Funktionalisierung und Fabrikation von rekombinanten Spinnenseidengerüsten für die Gewebezüchtung

DISSERTATION

zur Erlangung des akademischen Grades einer

DOKTORIN DER NATURWISSENSCHAFTEN

(Dr. rer. nat.)

im Promotionsprogramm „Polymerwissenschaft“ der Bayreuther Graduiertenschule für Mathematik und Naturwissenschaften der Universität Bayreuth (BayNAT)

vorgelegt von

Vanessa Tanja Troßmann

aus Helmbrechts

Bayreuth 2023

Die vorliegende Arbeit wurde in der Zeit von März 2016 bis März 2023 in Bayreuth am Lehrstuhl Biomaterialien unter Betreuung von Herrn Professor Dr. Thomas Scheibel angefertigt.

Vollständiger Abdruck der von der Bayreuther Graduiertenschule für Mathematik und Naturwissenschaften (BayNAT) der Universität Bayreuth genehmigten Dissertation zur Erlangung des akademischen Grades einer Doktorin der Naturwissenschaften (Dr. rer. nat.).

Form der Dissertation:	Kumulative Dissertation
Dissertation eingereicht am:	24.03.2023
Zulassung durch das Leitungsgremium:	03.04.2023
Wissenschaftliches Kolloquium:	23.10.2023

Amtierender Direktor: Prof. Dr. Jürgen Köhler

Prüfungsausschuss:

Prof. Dr. Thomas Scheibel	(Gutachter)
Prof. Dr. Hans-Werner Schmidt	(Gutachter)
Prof. Dr. Birte Höcker	(Vorsitz)
Prof. Dr. Ruth Freitag	

(Weitere Gutachterin: Prof. Dr. Christine Selhuber-Unkel)

þetta reddast.

Isländische Redewendung,

wenn man mit schwierigen Umständen konfrontiert wird.

„Wird schon! Am Ende werden die Dinge schon gut ausgehen, egal was passiert.“

Inhaltsverzeichnis

Zusammenfassung

Der menschliche Körper wird während des Lebens mit Krankheiten, Verletzungen und Verschleiß konfrontiert. Daher haben Biomaterialien zur Erhaltung und Förderung der Lebensqualität einen hohen Stellenwert in der Medizin erlangt. Ihr Ziel liegt darin, die Regeneration von eingeschränkten, verletzten oder verlorenen Körperfunktionen zu unterstützen, wiederherzustellen oder komplett zu übernehmen. Dabei sind die Anforderungen an Biomaterialien aufgrund der Diversität der Anwendungsbereiche jedoch sehr unterschiedlich. Während vorwiegend bioinerte Materialien minimal mit der Körperumgebung interagieren sollen, liegt das Ziel von bioaktiven Materialien in der Stimulation des umliegenden Gewebes. Deswegen haben sich gerade im Bereich der regenerativen Medizin und künstlichen Gewebezucht anwendungsspezifisch angepasste Biomaterialgerüste zu einem elementaren Bestandteil entwickelt. Solche stimulierenden, bioabbaubaren Gerüste bieten den Zellen zuerst eine geeignete, stabilisierende Kultivierungsmatrix, die über die Zeit abgebaut und durch die neu gebildete, zelluläre Mikroumgebung ersetzt wird. In diesem Zusammenhang sind die Adhäsion, das Wachstum, die Migration und die Differenzierung von Zellen entscheidende Faktoren, um die vollständige Funktion zu gewährleisten. Da die natürliche, zelluläre Mikroumgebung sehr komplex und gewebespezifisch ist, liegt ein Forschungsschwerpunkt in der Entwicklung und Herstellung von adaptierbaren und funktionalisierten Biomaterialgerüsten für die Gewebezucht und regenerative Medizin.

Aufgrund ihrer Eigenschaften, wie einer hohen Biokompatibilität, einer langsamen Bioabbaubarkeit und der vielfältigen Justierbarkeit, sind Materialien aus rekombinanten Spinnenseidenproteinen vielversprechende Kandidaten für die Anwendung als Biomaterialgerüst. Die rekombinante Produktion stellt die Herstellung ausreichender Proteinmengen mit gleichbleibender Qualität sicher und ermöglicht zusätzlich die Modifikation und Anpassbarkeit der Proteine auf genetischem Level. Die vorliegende Arbeit fokussierte sich auf die Herstellung und Charakterisierung von funktionalisierten Spinnseidengerüsten und deren potentielle Anwendungsgebiete in der Gewebezucht. Inspiriert vom natürlichen, repetitiven ADF4-Protein (*Araneus diadematus* Fibroin 4) des Abseilfadens der europäischen Gartenkreuzspinne, wurde in der Vergangenheit das rekombinante eADF4(C16)-Spinnenseidenprotein etabliert und weitere eADF4-Varianten generiert. In dieser Arbeit dienten das negativ geladene eADF4(C16)-, das positiv geladene eADF4(κ16)- und das zelladhäsive eADF4(C16)-RGD-Spinnenseidenprotein als Ausgangsmaterialien. Ein erster Teilbereich befasste sich mit der Entwicklung, Herstellung und Charakterisierung neuer eADF4-basierter Spinnenseidenvarianten durch Modifikation auf genetischer Ebene. Auf diese Weise wurde einerseits das ungeladene eADF4(Ω16)-Spinnenseidenprotein durch Aminosäureaustausch und andererseits mehrere, funktionalisierte, zelladhäsive Varianten durch die Fusion von kurzen bioaktiven Peptidsequenzen designt und rekombinant produziert.

Die Selbstassemblierung rekombinanter eADF4-basierter Proteine in Nanofibrillen und Gele wurde ebenfalls näher untersucht, da dieser Mechanismus bisher nur für eADF4(C16)-basierte Varianten beschrieben war. So zeigte sich, dass das ungeladene eADF4(Ω16) sehr schnell zu Fibrillen assemblierte, jedoch eine genaue Temperaturkontrolle brauchte, um ungewünschte Aggregation zu vermeiden. Im Gegensatz dazu, benötigte die positiv geladene eADF4(κ16)-

Variante zur Fibrillenbildung Ionen, die das Protein in Lösung stabilisierten und die Aggregation verlangsamten. Während die Anwesenheit eines organischen Co-Lösungsmittels (DMSO) die Selbstassemblierung von eADF4(C16) nahezu nicht beeinflusste, schien DMSO die Fibrillenbildung von eADF4(Ω16) zu stabilisieren und von eADF4(κ16) zu destabilisieren. Zusätzlich vorhandene Peptidmodifikationen ermöglichten eine bessere Kontrolle der Selbstassemblierung in wässriger Umgebung. Obwohl Säugetierzellen die Fibrillisierung von Spinnenseidenproteinen beeinflussten, bildeten sich immer noch physikalisch stabile 3D-Netzwerke aus. Dabei schienen sich negative Effekte der Zellen durch deren Interaktion mit RGD-Peptiden auszugleichen. All diese Erkenntnisse führten zur Entwicklung neuartiger Wirkstoffdepots auf Gel-Basis zur kontinuierlichen Freisetzung hydrophiler und hydrophober Substanzen und zur Optimierung von Biotinten durch die biochemische Stimulation von eingebrachten Zellen. Die entwickelten Gele eigneten sich für Biofabrikationsansätze und den Extrusionsdruck von formstabilen 3D-Konstrukten, wie dem Modell einer Aortenklappe.

Das ungeladene eADF4(Ω16) ermöglichte die Charakterisierung der Materialeigenschaften rekombinanter eADF4-Varianten basierend auf der Ladung, da nur eine Aminosäure im repetitiven Modul verändert war. Dadurch konnte der Mikrobenabstoßungsmechanismus von eADF4(C16)-basierten Spinnenseidengerüsten anhand eines molekularen Strukturmodells aufgeklärt werden. Das Fehlen von geladenen Aminosäuren führte bei eADF4(Ω16)-Gerüsten zu einer dichteren Anordnung der hydrophoben Proteinbereiche, mit denen Mikroben interagieren können. Durch die elektrostatische Abstoßung im negativ geladenen eADF4(C16) sind die resultierenden, hydrophoben Bereiche zu klein für eine Mikrobeninteraktion. Zudem zeigten eADF4(C16)-basierte Hydrogele auch *in vivo* eine exzellente Biokompatibilität ohne Immunantwort und eine langsame Bioabbaubarkeit. Im Gegensatz dazu zeigten positiv geladene eADF4(κ16)-Oberflächen im Vergleich zu eADF4(C16) und eADF4(Ω16) *in vitro* eine schnellere Degradation sowie eine erhöhte Adsorption und Umstrukturierung von Proteinen des Blutplasmas, was zu einer verstärkten Blutkoagulation führte.

Es wurde ebenfalls deutlich, dass positiv geladene Seidenoberflächen die Interaktion mit Zellen erhöhen. Zusätzlich förderte die Modifikation der eADF4-Varianten mit zelladhäsiven RGD-Peptiden generell die Interaktion mit Zellen und stimulierte diverse zelluläre Antworten unabhängig davon, welche Morphologie oder welcher Zelltyp verwendet wurden. So kontrahierten induzierte Kardiomyozyten synchron auf RGD-modifizierten Seidenfilmen, während eingekapselte HEK293 Produktionszellen in eADF4(C16)-RGD-Hydrogelen kontinuierlich einen Modellwirkstoff bildeten. Auch *in vivo* zeigten eADF4(C16)-RGD-Hydrogele eine gute Gewebeneubildung und Vaskularisierbarkeit.

In dieser Arbeit konnte außerdem die bioselektive Zellanheftung durch biochemische und topographische Modifikationen erreicht werden. So offenbarte die Analyse der funktionalisierten, zelladhäsiven Varianten mit elf Zelllinien und einer Co-Kultur, dass eADF4(C16)-KGD selektiv für Myoblasten ist. Zusätzlich ermöglichte die Modifikation von eigentlich zellabweisenden eADF4(C16)-Filmen mit diversen Oberflächentopographie-Gradienten eine gerichtete Interaktion und Ausrichtung von Zellen zur Entwicklung angepasster Implantatoberflächen. Dabei konnten auch zellspezifische Zusammenhänge zwischen Zell- und Strukturgröße nachgewiesen werden.

Summary

The human body is confronted with diseases, injuries and abrasion during life. Thus, biomaterials have gained high importance in medicine to maintain and promote life quality. Their aim is supporting, restoring or completely assuming the regeneration of restricted, injured or lost body functions. Due to diverse applications, the requirements for biomaterials differ. While mainly bioinert materials should minimally interact with the body surrounding, bioactive materials should actively stimulate the tissue. Thus, application-specifically adopted biomaterial scaffolds have evolved to an indispensable component in regenerative medicine and tissue engineering. Such stimulating, degradable scaffolds initially offer cells suitable, stabilizing culture matrices, which will be degraded and replaced by newly formed cellular microenvironment over time. In this context, adhesion, growth, migration, and differentiation of cells are essential factors to ensure complete function. Since the native, cellular microenvironment is complex and tissue-specific, the development and production of adjustable and functionalized biomaterial scaffolds for tissue engineering and regenerative medicine is currently focussed in science.

Due to their properties including high biocompatibility, slow biodegradation and versatile adjustability, materials made of recombinant spider silk proteins are promising candidates for application as biomaterial scaffolds. Recombinant production ensures fabrication of sufficient protein amounts with similar quality and allows the modification and adaption of proteins on the genetic level. The present work focussed on the production and characterization of functionalized spider silk scaffolds and their potential application fields in tissue engineering. Inspired by the natural, repetitive ADF4-protein (*Araneus diadematus* fibroin 4) of the dragline of the European garden spider, the recombinant eADF4(C16) spider silk protein has been established in the past and further eADF4-variants have been generated. Here, the negatively charged eADF4(C16), the positively charged eADF4(κ16) and the cell adhesive eADF4(C16)-RGD spider silk protein served as starting materials. A first part dealt with the development, production and characterization of new eADF4-based spider silk variants modified on genetic level. Thus, the uncharged eADF4(Ω16) and several, functionalized, cell adhesive variants were recombinantly produced after using amino acid exchange or fusing short bioactive peptide sequences, respectively.

The self-assembly of recombinant eADF4-based proteins into nanofibrils and gels has been investigated closer, since this mechanism has only been described for eADF4(C16)-based variants. It could be shown that uncharged eADF4(Ω16) self-assembled very fast into fibrils, however, a strict temperature control was necessary to avoid unintentional aggregation. In contrast, the positively charged eADF4(κ16) variant needed ions for fibril formation to stabilize proteins in solution and to avoid aggregation. While self-assembly of eADF4(C16) was almost unaffected in presence of an organic co-solvent (DMSO), it seemed to stabilize eADF4(Ω16) and to destabilize eADF4(κ16) fibril formation. Additional peptide modifications allowed better control of self-assembly in aqueous solution. Although mammalian cells influenced fibril formation of spider silk proteins, physically stable 3D-networks could be formed. Thereby, negative effects of the cells seemed to be compensated by their interaction with RGD-peptides. These findings led to the development of new, gel-based drug depots for continuous release of

hydrophilic and hydrophobic substances and to the optimization of bioinks by biochemical stimulation of encapsulated cells. The developed gels were suitable for biofabrication and extrusion printing of dimensionally stable 3D-constructs like the model of an aortic valve.

The uncharged eADF4(Ω16) allowed the characterization of properties of eADF4-based materials based on the charge, since only one amino acid was exchanged in the repetitive module. Thus, the microbe repellent mechanism of eADF4(C16)-based spider silk scaffolds could be clarified using a molecular structure model. The absence of charged amino acids led to denser arrangement of hydrophobic protein patches in eADF4(Ω16) scaffolds allowing microbe interaction. Due to electrostatic repulsion, the resulting, hydrophobic patches of negatively charged eADF4(C16) are too small for microbial interaction. In addition, eADF4(C16)-based hydrogels also showed excellent biocompatibility without immune response and slow biodegradation *in vivo*. In contrast, compared to eADF4(C16) and eADF4(Ω16), positively charged eADF4(κ16) surfaces displayed faster degradation and increased adsorption and restructuring of blood plasma proteins *in vitro* resulting in enhanced blood coagulation.

It also became clear that positively charged silk surfaces enhance cell interactions. Additionally, the modification of eADF4-variants with cell adhesive RGD peptides generally supported the interaction with cells and stimulated different cellular responses independent of the used morphology or cell type. For instance, induced cardiomyocytes synchronously contracted on RGD-modified silk films, while encapsulated HEK293 producer cells continuously released a model drug in eADF4(C16)-RGD hydrogels. The eADF4(C16)-RGD hydrogels also displayed good tissue formation and vascularization *in vivo*.

Furthermore, bioselective cell adhesion induced by biochemical and topographical modifications could be achieved in the present work. The analysis of functionalized, cell adhesive spider silk variants with eleven cell types and a co-culture showed that eADF4(C16)-KGD is selective for myoblasts. In addition, the modification of usually non-cell adhesive eADF4(C16) films with diverse surface topography gradients allowed guided interaction and orientation of cells for the development of adjusted implant surfaces. Thereby, cell-specific correlations between cell and topography size could be verified.

1. Einleitung

1.1. Anforderungen an Biomaterialien für biomedizinische Anwendungen

1.1.1. Entwicklungsgeschichte, Definition und Bedeutung von Biomaterialien

Da der Lebenszyklus eines Menschen mit Krankheiten, Verletzungen, Alterung und Verschleiß einhergeht, sind Biomaterialien ein wichtiges Werkzeug der modernen Medizin und fördern die menschliche Lebensqualität. [1] Ihr Ziel ist es, eingeschränkte oder verlorene Körperfunktionen wiederherzustellen, deren Regeneration anzuregen oder diese sogar komplett zu übernehmen. [1b, 1c, 2] Schon in der Antike wurden natürliche Materialien, wie Holz, Leder oder Elfenbein, als Prothesen genutzt, um verlorene Gliedmaßen strukturell zu ersetzen und dadurch ein gewisses Maß an Funktion zu erhalten. [3] Durch die Weiterentwicklung von Gewinnungs- und Verarbeitungstechnologien wurden auch Metalle und Legierungen genutzt, um Implantate als Zahn- oder Knochenersatz zu fertigen. [3] Bis ins Mittelalter wurden leicht verfügbare Materialien meistens als reines Mittel zum Zweck (z.B. Prothese oder Nahtmaterial) verwendet. [4] Mit der Zeit änderte sich jedoch der Fokus vom reinen Ersatzmaterial zum Material mit verbesserter Leistung und Funktionalität sowie breiterem Einsatzbereich für Zielgerichtete Anwendungen. [1a] Vor allem nach dem zweiten Weltkrieg rückten beispielsweise Silikone, Polyurethane, Titan oder rostfreier Edelstahl in den Fokus von Medizinern, um als Prothese, Implantat, Stent, Herzklappe oder Herzschrittmacher Anwendung zu finden. [4-5] Diese biologisch inerten, stabilen und nicht-responsiven Implantat-Materialien dominierten zunächst das Biomaterial-Feld, lösten jedoch oft eine negative Fremdkörperreaktion aus. [5-6] Durch das bessere Verständnis der Biomaterial-Körper-Reaktion, sollten Biomaterialien ab 1980 die körpereigene Regeneration unterstützen, anstatt verletztes oder kaputtes Gewebe einfach nur zu ersetzen. [5] Pionier-Studien über die Konstruktion einer künstlichen Haut (1980) [7] oder die Anwendung eines Gefäßersatzes im Hund (1989) [8], veranschaulichen die neue Denkweise vom reinem Ersatzmaterial zu einem unterstützenden Werkzeug der regenerativen Medizin als Beginn der heutigen Gewebezüchtung [9].

Aufgrund der Vielseitigkeit der eingesetzten Materialien und Anwendungsgebiete kursieren auch einige Definitionen des Begriffs „Biomaterial“. 1974 wurden pharmakologisch inerte Materialien, die in einen lebenden Organismus eingebracht werden, als Biomaterialien bezeichnet. [10] Später wurden alle Materialien unabhängig von der Materialart und des Ursprungs als Biomaterialien definiert, die mit Flüssigkeiten, Zellen oder Geweben des menschlichen Körpers in Kontakt kommen und für therapeutische, diagnostische und prothetische Zwecke verwendet werden ohne toxische Reaktionen im Körper auszulösen. [11] Die Bandbreite von Biomaterialien reicht dabei von biomedizinischen Geräten bis zu lebenden Strukturen. [6, 12] Die Gliederung von Biomaterialien ist aufgrund der vielen natürlichen oder synthetischen Materialien, Verarbeitungs- und Modifikationsmethoden sowie Anwendungsgebiete schwierig, aber auch nicht zwingend notwendig. [1c, 6, 13] Einordnungen erfolgen dabei aufgrund der Materialklasse (z.B. Metalle, Keramiken, Polymere und Komposite) oder des Anwendungsgebiets (z. B. Diagnostik, Therapie, medizinisches Gerät, Implantat oder Wirkstoffsystem). Zusätzlich können dauerhaft in den Körper eingesetzte Biomaterialien (z.B. Gelenkersatzmaterialien) von temporär eingebrachten Biomaterialien, wie Kathetern, oder

Zeit-abhängig abbaubaren Gerüsten zur Regeneration von Geweben abgegrenzt werden. [12, 14] Biomaterialien sollten daher eher als breit gefächertes Forschungsfeld betrachtet werden, in dem verschiedene Disziplinen und Materialien vereint werden. [10] Der Fokus liegt einerseits auf der Entwicklung und Charakterisierung von Materialien, um körpereigene Funktionen zu unterstützen, verbessern oder wiederherzustellen, aber andererseits auch in der Analyse von Geweben und Organen sowie den Wechselwirkungen zwischen dem eingebrachten Material und der Körperumgebung. [10] Die moderne Biomaterialforschung ist daher ein komplexes, inter- sowie multidisziplinäres Forschungsfeld und setzt sich aus den Fachgebieten Physik, Chemie, Medizin, Biologie und dem Ingenieurwesen zusammen. [5, 15]

1.1.2. Grundlegende Anforderungen an Biomaterialien

Aufgrund der breiten Varianz der Anwendungsgebiete unterscheiden sich die Anforderungen an Biomaterialien sehr stark. Als Gelenkersatz soll ein Implantat bestenfalls für den Rest des Lebens im Köper verbleiben und im Gewebe verwachsen, während Schrauben oder Platten nach der Heilung von Frakturen wieder entfernt werden. Große Gewebedefekte werden hingegen meistens sogar mithilfe eines bioabbaubaren Gerüsts behandelt, um die Regeneration zu unterstützen. Dabei spendet das Gerüst erst Stabilität für körpereigene Zellen, wird dann über die Zeit abgebaut und gleichzeitig durch neu gebildetes Gewebe ersetzt. [16] Dennoch sollen Biomaterialien, unabhängig von anwendungsspezifischen Anforderungen (siehe 1.1.3.), eine exzellente Biokompatibilität ohne Toxizität aufweisen und keine Entzündungs- oder Abstoßungsreaktionen zur Folge haben (**Abbildung 1**). [2, 6, 16] Zusätzlich sollen das Einbringen des Materials sowie seine Koexistenz mit minimalem Schaden von gesundem Gewebe durch eine Operation und ohne hypersensitive, allergische oder inflammatorische Reaktionen einhergehen. [1b, 2, 17]

Da die Biokompatibilität eines Materials gerade im Hinblick auf den Einsatz in der regenerativen Medizin der entscheidendste Faktor ist, muss die Immunantwort schon vom Design bis zur klinischen Translation mit bedacht werden. [18] Eine wichtige Studie von Homsy (1970) beschreibt die Inkompatibilität und den Funktionsverlust von potentiellen Implantat-Materialien. Es konnte gezeigt werden, dass viele dieser Materialien zytotoxische Substanzen absondern, welche zelluläre Funktionen einschränken und bis zum Zelltod führen. [19] Diese und viele weitere Studien veranlassten unter anderem die Internationale Organisation für Standardisierung (ISO) zur Entwicklung von normierten Tests zur Evaluierung der *in vitro* und *in vivo* Biokompatibilität durch direkten oder indirekten Kontakt mit potentiellen Implantationsmaterialien sowie deren Extrakten. [1b, 5] Nach erfolgreicher *in vitro* Biokompatibilitätsprüfung wird ein potentielles Implantationsmaterial auch *in vivo*, normalerweise subdermal oder intramuskulär, getestet. [1b, 5] Ein biokompatibles Material kann mit lebendem Gewebe oder Zellen des Empfängers koexistieren, ohne toxische Stoffe freizusetzen oder Entzündungen und Schäden zu bewirken. [2, 6] Dennoch muss jedes Material in seiner verarbeiteten Anwendungsform auf Biokompatibilität, Blutinteraktion und Fremdkörperreaktion getestet werden. [5] Die Blutverträglichkeit (Hämokompatibilität) ist wichtig, da Blutkoagulation und Thrombosebildung aufgrund von Blut-Material-Interaktionen unbedingt zu vermeiden sind. [6, 20]

Die Fremdkörperreaktion ist ein natürlicher Schutz-Mechanismus des Körpers, der immer zwischen Material und Körpergewebe auftritt und nach einer Implantation aufgrund der Verletzung und Entzündung des umliegenden Gewebes unvermeidbar ist. [21] Bei biokompatiblen Materialien wird die Wundheilungs- und Regenerationskaskade aktiviert und das Implantat im Körper integriert (**Abbildung 1A**). Sollte sich jedoch eine chronische, fibrotische Fremdkörperreaktion entwickeln, kommt es zur Kapselfibrose und Abstoßungsreaktion (**Abbildung 1B**). [21]

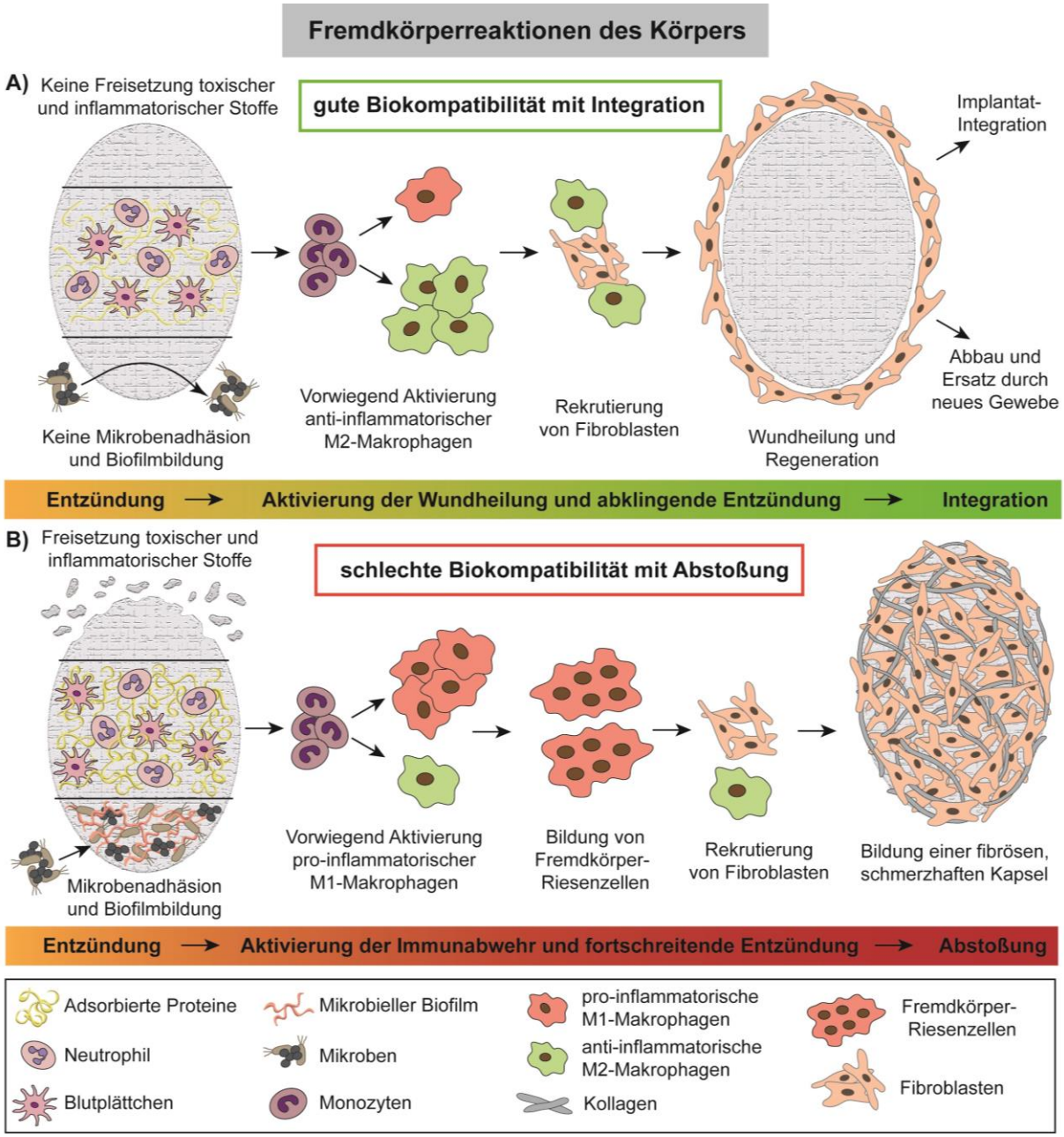

Abbildung 1: Mögliche Fremdkörperreaktionen zur Evaluation der Biokompatibilität eines Materials. **A)** Bei einer guten Biokompatibilität wird nach der Entzündung die Wundheilung aktiviert und das Implantat integriert. **B)** Bei einer schlechten Biokompatibilität wird durch die Entzündung die Immunabwehr aktiviert und es kommt zur Kapselfibrose und Abstoßung des Implantats. Die Freisetzung inflammatorischer Stoffe, die Adsorption und Umstrukturierung von Proteinen und Mikrobenadhäsion begünstigen die Aktivierung der Abstoßungskaskade.

Der Erfolg eines Implantats hängt stark von der Reaktion der Körperumgebung ab, welche primär durch die Interaktionen zwischen Materialoberfläche und dem umliegenden Gewebe gesteuert wird. [22] Bereits nach dem ersten Kontakt adsorbieren Proteine auf dem eingebrachten Implantat und bilden in kurzer Zeit eine komplette Proteinschicht aus. [22a, 23] Die Stärke dieser Protein-Oberflächen-Interaktionen ist dabei von den Eigenschaften und der Beschaffenheit der Materialien und der Körperflüssigkeit abhängig. Während beim Biomaterial die chemische Zusammensetzung, Struktur, Ladung, Benetzbarkeit, Hydrophobizität und Topographie wichtig sind, spielen bei der Flüssigkeit ihre generelle Zusammensetzung sowie die Struktur, Größe, Ladung und Faltungszustand der enthaltenen Proteine eine Rolle. [22a, 23-24] Aufgrund der Umstrukturierung und Zugänglichkeit von Proteinen entscheidet die Komposition der ausgebildeten Proteinschicht über die weiteren (Immun-) Reaktionen des Körpers, wie Blutkoagulation oder Zelladhäsion. [22a, 23a, 23c, 25] Sie ist daher entscheidend für den Ausgang der Fremdkörperreaktion, welche schlimmstenfalls zur Abstoßung und Explantation führt. [21-22, 26] Sollte die Abstoßungskaskade eingeleitet werden, stimulieren die Proteine Neutrophile, Blutplättchen und Mastzellen, die die Differenzierung von Monozyten zu Makrophagen aktivieren und den Verlauf der Fremdkörperreaktion entscheiden. [21, 26a, 27] Die sogenannten M1-Makrophagen bewirken Entzündungs- und Abstoßungsreaktionen, während die M2-Makrophagen für Heilung und Regeneration wichtig sind. [28] Die aktivierten M1-Makrophagen produzieren weitere Signalstoffe zur Bildung von sogenannten Fremdkörper-Riesenzellen, die Fibroblasten rekrutieren und zur Ausbildung einer Kollagen-haltigen, nicht-vaskularisierten Gewebekapsel (Fremdkörperkapsel) führen. [21, 26a] Diese Kapselfibrose kann zu Kontraktionen und Schmerzen führen oder medizinische Materialfunktionen, Wirkstofffreisetzung, Blutversorgung oder die Gewebeintegration beeinträchtigen. [28a] Eine gute Beschaffenheit ohne Korrosion und Verschleiß sowie die einwandfreie Funktion und Integration des Implantats sind entscheidend, da ansonsten weitere operative Eingriffe drohen. [2, 16, 29] So können auch Polymere, die für Katheter und andere Medizinprodukte verwendet werden, Biokompatibilitätsprobleme auslösen und das Risiko von Entzündungen erhöhen. [30] Da vor allem die Oberflächeneigenschaften eines Materials die Freisetzung toxischer Substanzen oder Abbauprodukte beeinflussen, ist deren Anpassung entscheidend für den anschließenden Erfolg eines potentiellen Implantats. [6, 30d, 31] Oberflächenmodifikationen und Beschichtungen sind eine elegante Lösung, um Immunreaktionen zu vermeiden. [30d, 31]

Im Rahmen der Biokompatibilität spielt auch die Mikrobenanheftung auf Implantations- und Kontaktmaterialien eine wichtige Rolle. Da von keiner Sterilität ausgegangen werden kann, bleibt ein Infektionsrisiko durch das Implantat bestehen. [16, 32] Der entscheidende Risikofaktor im Gesundheitswesen ist die Kontamination von Kontaktoberflächen mit potentiell pathogenen Mikroorganismen, die zu Irritationen, Entzündungen und teilweise schwerwiegenden Infektionen führen können, falls das menschliche Immunsystem diese nicht bekämpfen kann (**Abbildung 1B**). [32b, 33] Nach einer erfolgreichen Anheftung können Mikroben, wie Bakterien und Pilze, einen sogenannten Biofilm, also eine Schutzschicht vor dem endogenen Immunsystem, bilden, der auch die Zugänglichkeit von bekämpfenden Medikamenten, wie Antibiotika, einschränkt. [34] Ein solcher Biofilm kann auf Medizinprodukten, beispielsweise Implantaten und Kathetern, zu einer verringerten Einsatzdauer, Funktionsverlust, Explantation,

Entzündungen und schlimmstenfalls zum Tod führen. [34a, 34f, 35] In diesem Zusammenhang sind vor allem die durch den unbedachten Über-Einsatz von Antibiotika entstandenen, multi-resistenten, pathogenen Mikroben ein Problem, da konventionelle Behandlungsmethoden enorm eigeschränkt sind. [34f, 36] *Staphylococcus aureus* ist ein solcher multi-resistenter Krankenhauskeim, der für viele schwerwiegende Infektionen und Todesfälle verantwortlich ist. [37] Durch die eingeschränkten medikamentösen Behandlungsmethoden rücken Alternativmaterialien in den Fokus, die inhärente anti-adhäsive („non-fouling“) Eigenschaften besitzen und bereits die initiale Mikrobenanheftung unterbinden (**Abbildung 1A**). [38] Dafür wird die Oberfläche von kommerziellen Biomaterialien mit anti-adhäsiven oder anti-mikrobiellen Beschichtungen ausgestattet. [38c, 39] Bei der passiven Resistenz werden meist super-hydrophobe, hydrophile oder zwitterionische Polymer-basierte Materialien verwendet, damit Oberflächeninteraktionen mit Proteinen, aber auch Mikroben reduziert werden. [39c, 40] Bei der aktiven Resistenz, den sogenannten Kontakt-tötenden Materialien, werden kationische oder amphiphile Polymer- oder Kompositsysteme genutzt, die zusätzlich mit antimikrobiellen Peptiden oder Substanzen modifiziert sein können, um die Mikroben aktiv zu töten. [32d, 40c, 41] Da viele dieser Systeme jedoch gravierende Nachteile wie Instabilität und Zytotoxizität aufweisen [42], herrscht Optimierungs- und Forschungsbedarf bei der Entwicklung von funktionalen, biokompatiblen Biomaterialien. [5]

1.1.3. Biomaterialunterteilung für biomedizinische Anwendungen

Ideale Biomaterialien sollen vielseitig, einfach handhabbar, praktikabel, kostengünstig, biokompatibel, funktional, steril, ungiftig und anti-inflammatorisch sein. Diese Eigenschaften vereint bisher kein Biomaterial gleichzeitig, aber viele erfüllen zumindest einige dieser Kriterien. [43] Da Anforderungen zudem nicht pauschalisiert werden können, sollte ein Material im Hinblick auf die Anwendung und die dafür entscheidenden Parameter ausgewählt werden sowie die Eigenschaften des Zielgewebes bestmöglich imitieren. [6, 11] Dabei hängt die Performance von den Wechselwirkungen zwischen Materialoberfläche und Körperumgebung ab. [22a] Daher werden Biomaterialien oft spezifisch modifiziert und angepasst [44] und können in bioinert, bioaktiv und biomimetisch (Natur-imitierend) unterteilt werden (**Abbildung 2**).

Bioinert bedeutet, dass das Material biokompatibel, stabil und ungiftig ist, jedoch nicht-responsiv auf Umwelteinflüsse reagiert und minimal mit der Umgebung interagiert. [31] Bioinerte Materialien werden vorwiegend für biomedizinische Kontaktmaterialien verwendet, die mit Körperflüssigkeiten wie Blut, Urin, Speichel oder Tränen in Berührung kommen. Beispiele hierfür sind Gelenkersatzmaterialien, kardiovaskuläre Stents sowie intravaskuläre oder Harnwegs-Katheter, aber auch analytische und diagnostische Geräte für Biopsien. [30d] Neben der minimalen Gewebeinteraktion ist bei Implantaten mit Blutkontakt essentiell, dass keine Blutkoagulation, Thrombosen oder inflammatorischen Reaktionen hervorgerufen werden und sie der stetigen Belastung durch den Blutfluss standhalten. [20, 30d, 31a, 45] Auch Harnwegskatheter sollen stabil und flexibel sein, aber wenig Interaktionen zulassen, um Verkrustungen, Entzündungen und Infektionen zu vermeiden und ein schmerzfreies Entfernen zu gewährleisten. [24b, 30a-c, 46] Orthopädische und dentale Implantate benötigen ebenfalls eine hohe Beständigkeit und angemessene Festigkeit bei Belastung, um Folgeoperationen zu vermeiden und die Lebensqualität zu erhalten. [6, 47] Auch wenn der Kontakt mit Körper-

flüssigkeiten nicht gänzlich unterbunden werden kann, müssen Biomaterialien teilweise gut in das entsprechende Gewebe einwachsen, um die volle Funktionsfähigkeit erreichen zu können (z.B. Gefäß-, Gelenk-, oder Knochenersatz). [16, 45b, 47c] Diese Beispiele zeigen, dass ein gewisses Maß an biologischer Inertheit sinnvoll ist, um Mikroben- und Proteinadsorption zu verhindern und die Biokompatibilität zu gewährleisten, aber eine gerichtete Interaktion mit dem Biomaterial trotz allem gewünscht ist. [48] Materialien mit inhärenten, anti-adhäsiven („non-fouling“) Eigenschaften sind daher vielversprechend, da sie minimale Absorption von Proteinen, wie Fibrinogen und Lysozym, auf der Oberfläche zeigen. [49] Zudem können Komposit-Materialien und Oberflächenmodifikationen entwickelt werden, um Eigenschaften anzupassen und damit verbundene Körperreaktion zu steuern. [30d, 31a, 31b, 45a, 48, 50]

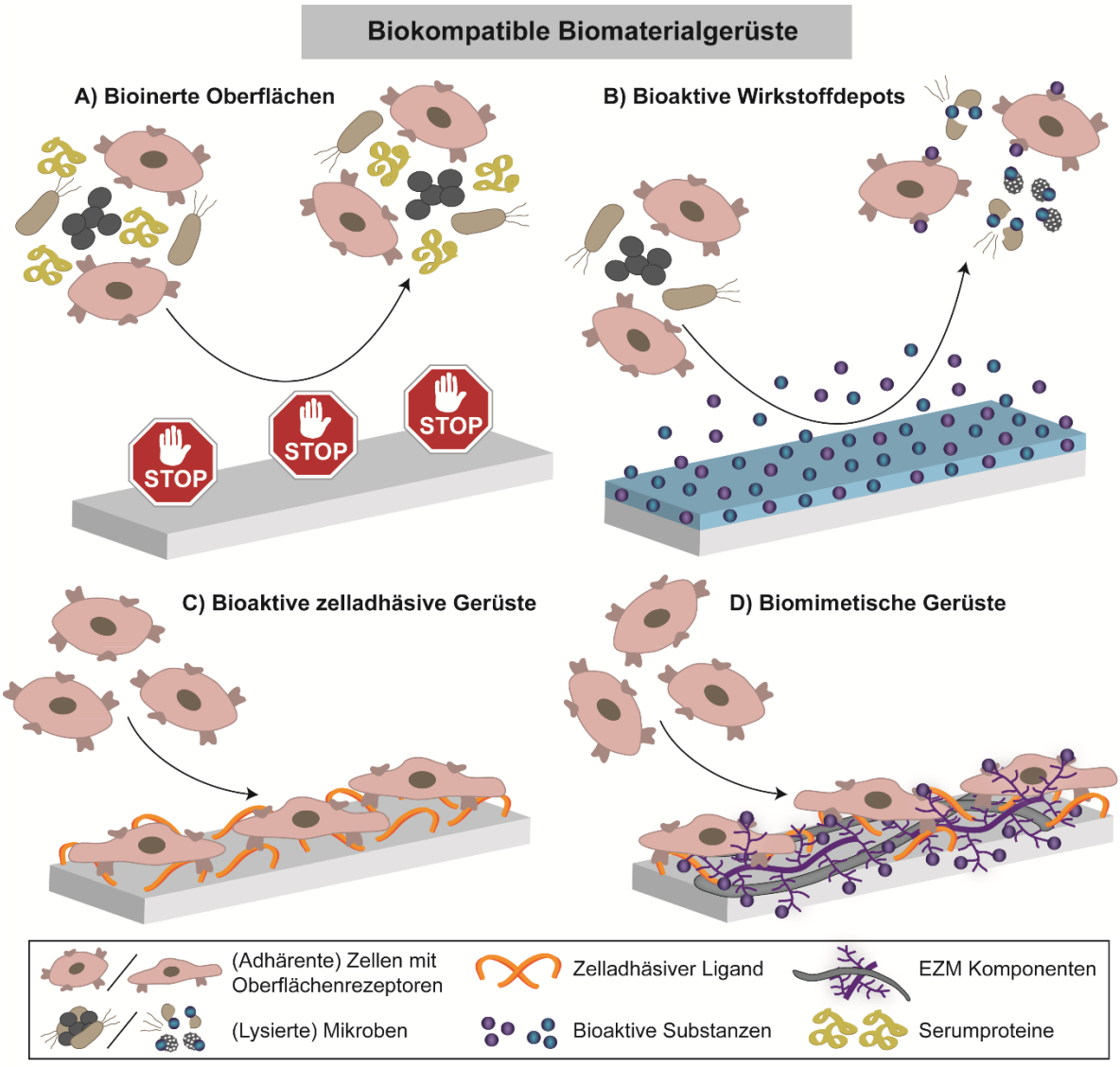

Abbildung 2: Biokompatible Biomaterialgerüste können in bioinert (**A**), bioaktiv (**B** und **C**) und biomimetisch (**D**) eingeteilt werden. Bei bioaktiven Materialien können Wirkstoffdepots (**B**) und zelladhäsive Gerüste (**C**) unterschieden werden.

Ein bioaktives Material soll mit der biologischen Umgebung interagieren, um zelluläre Funktionen zu stimulieren [31] und den Körper bei der Regeneration von verletztem oder eingeschränktem Gewebe zu unterstützen. [5-6] Dafür sind Bioabbaubarkeit, Reaktion auf

Umwelteinflüsse und eine kontrollierte Interaktion von Biomaterial-Oberflächen mit Proteinen und Zellen entscheidend. [5] Da viele Materialien per se nicht die passenden Eigenschaften für eine spezielle Anwendung zeigen, haben sich Funktionalisierungsmethoden für die Herstellung von stimulierenden Oberflächen entwickelt, um eine gerichtete Bioaktivität zu erzeugen (siehe 1.3.2). [31d, 51] Dabei wird oft nur die für die Interaktion nötige Grenzfläche modifiziert, während die restlichen Eigenschaften des Materials meist gleichbleiben.[31c, 31d, 51b, 52]

Viele Biomaterialien und daraus gefertigte Systeme können mit biologisch aktiven Substanzen modifiziert werden, um als Wirkstoff-freisetzende Depots (**Abbildung 2B**) oder Gewebegerüste (**Abbildung 2C**) eingesetzt zu werden. [53] So können mittlerweile implantierte Knochenschrauben, Nahtmaterialien, Wirkstoffsysteme und endovaskuläre Stents aus biologisch abbaubaren Biomaterialien zuerst eine beabsichtigte Funktion im Körper übernehmen und dabei vollständig vom Körper resorbiert und durch eigenes Gewebe ersetzt werden. [5, 54] Durch die Modifikation mit biologisch stimulierenden Faktoren, wie Proteinen, zelladhäsiven Peptiden oder Wachstumsfaktoren, werden bioaktive Materialien für eine verbesserte Interaktion mit Zellen kreiert. [55] Eine angepasste Oberflächentopographie kann helfen, die Biokompatibilität und die Zellantwort zu fördern. [51b, 56] Durch Kombination mehrerer Modifikationen ist es sogar möglich, multifunktionale Biomaterialien zu erschaffen, die eine höhere oder spezifischere biologische Aktivität oder Funktion zeigen. [57] So ermöglichen Materialien mit biochemischen Liganden und topographischer Stimulation zeitgleich eine verbesserte Verankerung und eine gerichtete Orientierung der Zellen auf dem Material. [58]

Neben bioaktiven Materialien haben sich auch biomimetische Gerüste entwickelt, um näher an die natürliche, extrazelluläre Matrix (EZM) heranzureichen (**Abbildung 2D**). [48, 51a, 59] Da in natürlichen Geweben physiologische Gradienten eine große Rolle spielen, wurden diverse Biomaterialsysteme mit chemischen und physikalischen Gradienten entwickelt. [60] Im Hinblick auf den natürlichen Gewebeaufbau mit seiner 3D-Struktur wurden daher auch bioaktive, poröse Gerüste und Hydrogelsyteme geschaffen, um den Zellen eine provisorische, stabilisierende Matrix vorzugeben, die darin wachsen und das Gewebe regenerieren. [53c, 61]

1.2. Natürlicher Aufbau von Geweben – die zelluläre Mikroumgebung

In ihrem natürlichen Gewebeumfeld sind Säugetierzellen in einer einzigartigen, komplexen und dynamischen Mikroumgebung mit diversen stimulierenden Faktoren eingebettet, die teilweise synergistisch, aber auch antagonistisch zelluläre Antworten und Funktionen bewirken. Dabei zeigen Mikroumgebungen in Säugetiergeweben stets einen ähnlichen Grundaufbau und gemeinsame Merkmale, die sich aus Komponenten der Teilbereiche „benachbarte Zellen“, „lösliche Faktoren“ und „umgebende EZM“ zusammensetzen. Die genaue Zusammensetzung ist dabei wiederum Gewebe-spezifisch und variabel, um spezifische Funktionen zu erfüllen (**Abbildung 3**). [62] Gerade bei differenzierbaren (Stamm-) Zellen ist diese Mikroumgebung enorm wichtig, da die vorhandenen (bio-) physikalischen und (bio-) chemischen Stimulatoren wichtige zelluläre Antworten der Entwicklung und Regeneration, wie Wachstum oder Differenzierung, regulieren. [63] *In vivo* nehmen die Zellen selbst einen entscheidenden Einfluss auf dieses dynamische System, weswegen ein grundlegendes Verständnis dieser komplexen Umgebung essentiell ist, um angepasste, biomimetische Gerüste

für gewünschte zelluläre Antworten zu kreieren. [64] Es besteht jedoch noch Forschungsbedarf, da viele intra- und interzelluläre Abläufe zwischen Zellen und Umgebung (z.B. zelluläre Signaltransduktionswege) nicht vollständig aufgeklärt sind und von chemischen, strukturellen oder mechanischen Signalen der Mikroumgebung abhängen. [62]

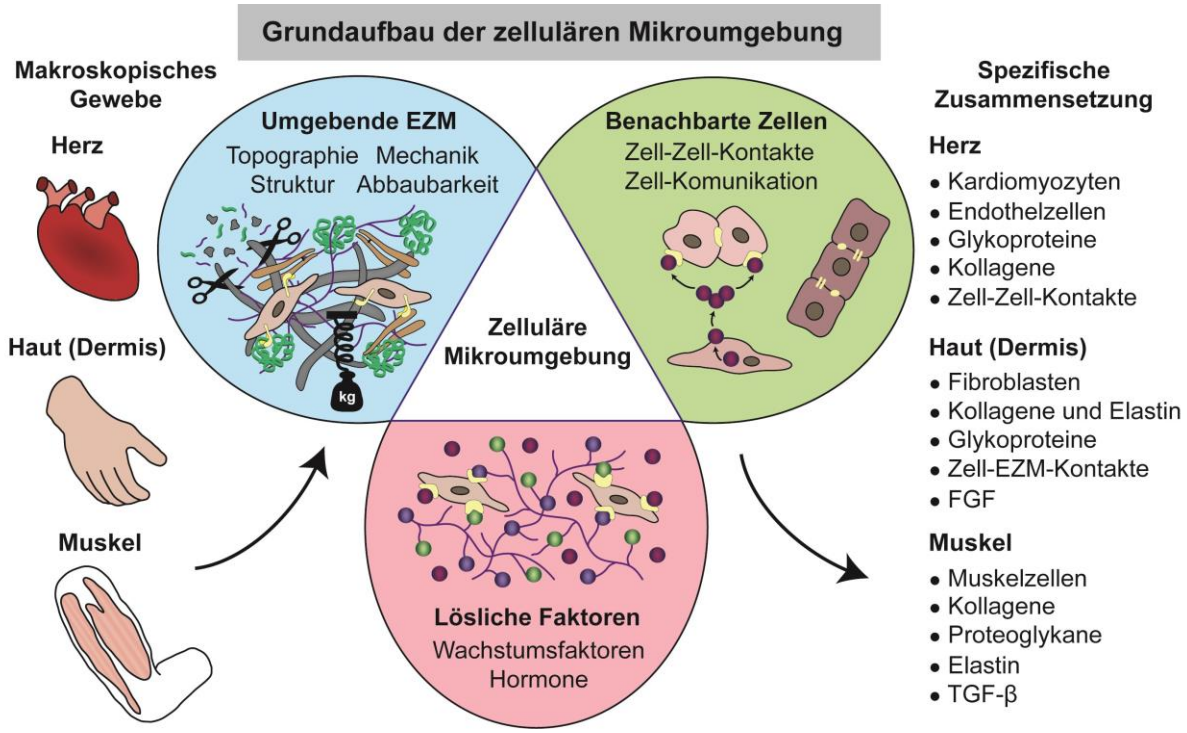

Abbildung 3: Alle Gewebe zeigen in ihrer Mikroumgebung einen ähnlichen Grundaufbau, der sich aus Komponenten der Teilbereiche „umgebende EZM“, „lösliche Faktoren“ und „benachbarte Zellen“ zusammensetzt. Dabei sind die einzelnen Komponenten jedoch Gewebe-spezifisch.

1.2.1. Lösliche Faktoren

Im natürlichen Gewebeverbund sind Zellen vielen, im wässrigen System gelösten Faktoren und Molekülen ausgesetzt. Dazu zählen beispielsweise Nährstoffe der zellulären Grundversorgung, wie Salze, Sauerstoff oder Glukose, aber auch andere gelöste Signalstoffe, zu denen Wachstumsfaktoren, Zytokine und Hormone gehören. [62, 65] Diese löslichen, biologisch hoch aktiven Stoffe werden freigesetzt, sobald keine direkte Zell-Zell-Kommunikation möglich ist, um nach Interaktion mit Oberflächenrezeptoren eine zelluläre Reaktion zu bewirken.[66] Durch extrazelluläre Ligandenbindung kommt es zu strukturellen Umlagerungen der Transmembran-proteine und zur Aktivierung intrazellulärer Signalweiterleitung (**Abbildung 4**). [55a, 66-67] Dabei können Signalstoffe durch Zirkulation oder Diffusion generell auf die gleiche Zelle (autokrin), auf benachbarte (parakrin) oder entfernte (endokrin) Zellen wirken. [62, 68] Zytokine haben entscheidende Funktionen bei der Immunabwehr und werden bei Verletzungen, Entzündungsreaktionen und Regenerationsprozessen von Immunzellen gebildet. [68-69] Wichtige Zytokine sind Interleukine (IL), Interferone, der Tumor-Nekrose-Faktor („TNF“) und der transformierende Wachstumsfaktor-β („TGF-β“). [68, 69b] Während der Gewebeentwicklung

und der Wundheilung sind Wachstumsfaktoren ebenfalls wichtig für die Zelldifferenzierung, da durch sie eine ganz spezifische, temporäre Mikroumgebung für die Zellen geschaffen wird. [62, 67f, 70] Zu den bekanntesten Wachstumsfaktoren in der EZM zählen neuronale („NGFs“), epidermale („EGFs“), transformierende („TGFs“), vaskuläre endotheliale („VEGFs“), Fibroblasten- („FGFs“) und Hepatozyten- („HGFs“) Wachstumsfaktoren sowie die Knochenmorphogenetischen-Proteine („BMPs“). [62, 71] Da die Zellstimulation stark von der räumlichen Anordnung, der lokalen Konzentration und der zeitlichen Verfügbarkeit des Signalstoffs abhängt, liegen Wachstumsfaktoren neben der löslichen Form auch in an EZM-Molekülen verankerter Form als Konzentrationsgradient vor. [62, 67e]

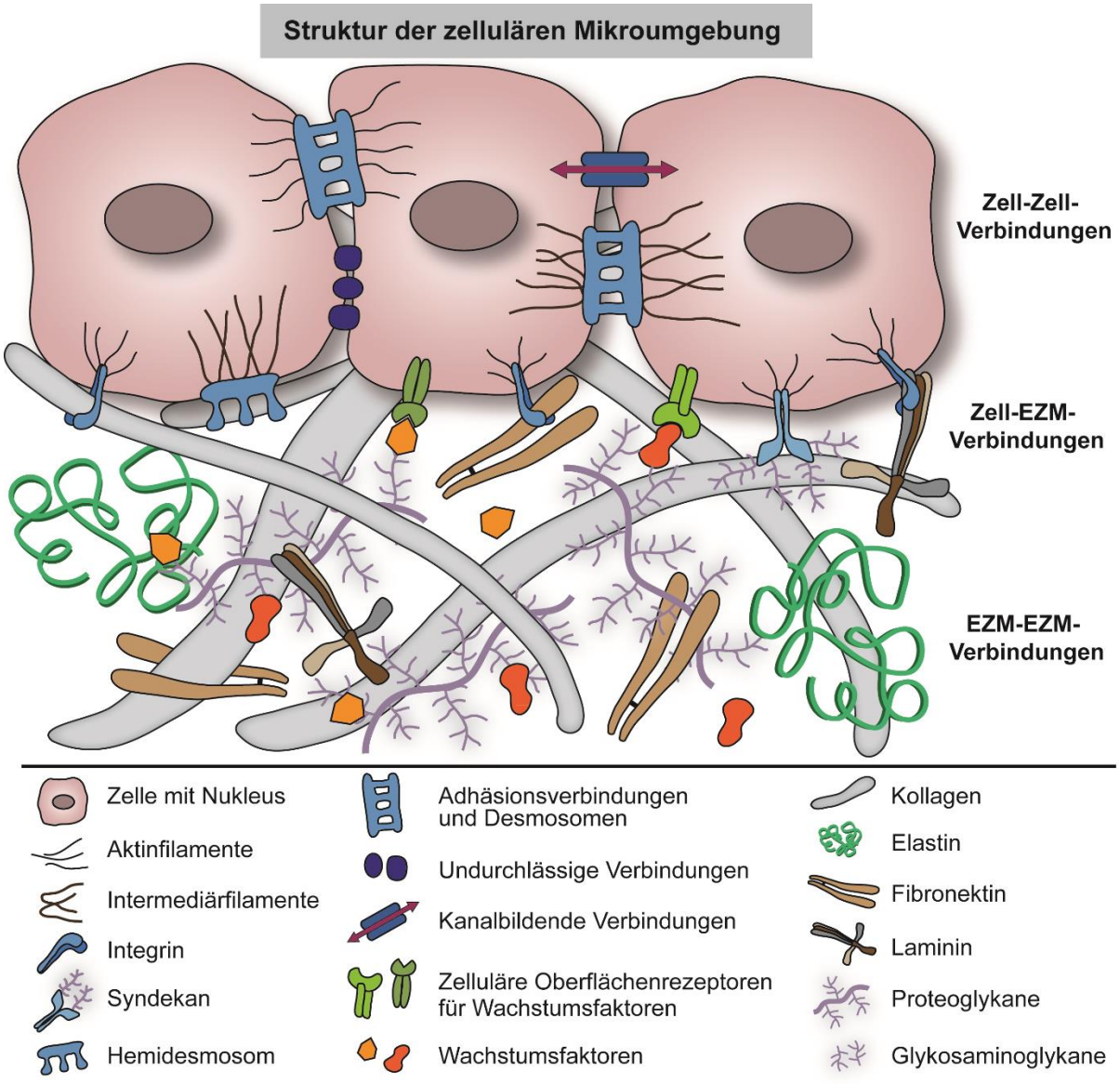

Abbildung 4: Natürlicher Aufbau von Geweben. Die zelluläre Mikroumgebung ist geprägt von Interaktionen zwischen Zellen, Signalstoffen und EZM-Komponenten. Dabei kann zwischen Zell-Zell-, Zell-EZM- und EZM-EZM-Kontakten unterschieden werden, die zur Vernetzung, Stimulation und Signalweiterleitung beitragen.

1.2.2. Nachbarzellen – Zell-Zell-Kontakte

Eine Grundvoraussetzung für den Erfolg multi-zellulärer Organismen ist die Fähigkeit von Zellen, sich mit der Umgebung zu verknüpfen, indem sie mit EZM-Komponenten und anderen Zellen interagieren. [72] Dabei kann die Kommunikation einer Zelle mit umliegenden Zellen Rezeptor-vermittelt (direkt) oder über Signalstoffe (indirekt) erfolgen. [62, 73] Da Zellen in Geweben im Verbund auftreten, bilden sie verschiedene direkte Zell-Zell-Kontakte und Signalwege für die Wechselwirkung miteinander aus, die essentiell für korrekte Zellfunktionen und Gewebemorphogenese sind. [62, 73b, 74] Unter direkten Zell-Zell-Kontakten werden physikalische Verbindungen („*Junctions*“) zwischen Zellen zusammengefasst. Dazu zählen undurchlässige Verbindungen („*Tight Junctions*“), Kanal-bildende Verbindungen („*Gap Junctions*“) und Ankerverbindungen („*Anchoring Junctions*“), wobei letztere auch als Zell-EZM-Verbindungen vorkommen (**Abbildung 4**). [62, 75] Undurchlässige Verbindungen sind dichte Zell-Zell-Kontakte und bestehen aus Multiprotein-Komplexen, die die Zellmembranen und das Zytoskelett von benachbarten Zellen verbinden. Ihre Aufgabe besteht einerseits darin, den Transport von Wasser, Nähr- und Signalstoffen sowie weiteren löslichen Bestandteilen zwischen den verbundenen Zellen zu unterbinden und andererseits, verschiedene Gewebearten voneinander zu trennen. [62, 75-76] Kanal-bildende Verbindungen bestehen aus Transmembran-Protein-Komplexen (z.B. Connexin), die Kanal- oder Porenstrukturen durch die Plasmamembran bilden, damit kleine Moleküle oder Ionen (Ca^{2+}) von Zelle zu Zelle weitergegeben werden können. Diese Kontakte zählen daher auch zu den Signal-vermittelnden Verbindungen, da sie im Metabolismus, der Zellphysiologie und für Zellfunktionen wichtig sind. [62, 75, 77] So ermöglicht Connexin bei der Signaltransduktion von elektrisch stimulierbaren Zellen, wie Kardiomyozyten, eine synchrone Kontraktion. [77-78] Zu den Ankerverbindungen zählen direkte Zell-Zell-Verbindungen, wie Adhäsionsverbindungen und Desmosomen, aber auch Hemidesmosomen, die bei Zell-EZM Interaktionen eine Rolle spielen. [75-76] Dabei werden bei Adhäsionsverbindungen jedoch Aktinfilamente angeregt, während bei Desmosomen und Hemidesmosomen die Intermediärfilamente angesprochen werden.[75] Wie undurchlässige, sind auch verankernde Verbindungen üblicherweise aus Multiprotein-Komplexen aufgebaut, und tragen dazu bei, dass Zellen und Gewebe ihre Form, Integrität und Zusammenhalt behalten, spielen aber auch bei der Signalübertragung und Mechanotransduktion eine Rolle. [62, 76]

1.2.3. Extrazelluläre Matrix

Zusammen mit den Nachbarzellen und den löslichen Faktoren hat die EZM in der natürlichen zellulären Mikroumgebung einen entscheidenden Einfluss auf die Entwicklung und Funktion von Zellen. [55a, 62, 63e, 79] So zeigen Binde- (Schutz) oder Muskelgewebe (Bewegung) eine ausgeprägte EZM-Komposition mit starken Zell-Matrix-Interaktionen [80], während im Herzen oder zentralen Nervensystem Zell-Zell-Kontakte entscheidender für die Funktion sind. [74b, 81] Dabei bietet die EZM nicht nur ein stabilisierendes Gerüst unter physischer oder mechanischer Belastung, sondern liefert eine dynamische 3D-Umgebung mit stimulierenden Faktoren, die zur Regulation der Zellfunktionen während der Morphogenese und Regeneration multizellulärer Organismen beitragen (**Abbildung 4**). [55a, 62, 63e, 79, 82] Diese komplexe, Gewebe-spezifische 3D-Matrix besteht aus vielen Molekülen und Proteinen, die vielfältige Morphologien, Strukturen und Faltungszuständen aufweisen und für die ihnen zugewiesenen

Funktionen wesentlich sind. [59c, 65, 83] Neben der strukturellen und mechanischen Unterstützung sind Proteine direkte Interaktionspartner für Zellrezeptoren (z. B. Integrine) oder enthalten Bindungsstellen für bioaktive Moleküle (z.B. Wachstumsfaktoren), um zelluläre Reaktionen, wie Wachstum oder Differenzierung, zu stimulieren. [83b, 84] Makroskopisch ist die EZM ein Hydrogel-artiges Netzwerk mit unlöslichen, ineinandergreifenden, strukturellen Makromolekülen, die als (bio-) chemische und (bio-) physikalische Interaktionsliganden dienen. [62, 67d, 79c, 85] Diese einzelnen Merkmale der zellulären Mikroumgebung, beispielsweise Adhäsionsliganden, Signalstoffe, topografische und strukturelle Merkmale, mechanische Eigenschaften und eine entsprechende biologische Abbaubarkeit, regulieren weitere zelluläre Antworten, wie Adhäsion, Spreiten, Wachstum, Migration, Differenzierung, aber auch Apoptose und Krebs. [55a, 62, 63e, 79a, 86] Obwohl die EZM-Zusammensetzung dynamisch ist und von Gewebe zu Gewebe variiert, sind die Hauptkomponenten faserbildende Proteine, wie Kollagen, Elastin, Fibronektin und Laminine, sowie stabilisierende und stimulierende Glykoproteine, Proteoglykane und die stark hydrierten Glykosaminoglykane (GAG). [55a, 79c, 83b, 85e, 85f] Dabei ist die Zusammensetzung der EZM meist nur eine Momentaufnahme, da die EZM ein hochdynamisches, strukturelles Netzwerk darstellt, das durch die Zellen kontinuierlich mittels löslicher Faktoren und Enzyme verändert und umstrukturiert wird. [79c, 85c, 85d]

1.2.3.1. EZM-Komponenten

Kollagene sind die häufigsten Proteine in Geweben von Säugetieren und stellen das wesentliche, wasserunlösliche, fibröse Strukturelement der EZM dar. [87] Da Kollagene hauptsächlich in Geweben mit hoher Belastung und Krafteinwirkung vorkommen, sind ihre mechanischen Eigenschaften, wie die hohe Steifheit sowie die enorme Druckaufnahme- und Zugfähigkeit, entscheidend. [88] Kollagene sind vorwiegend am Struktur-gebenden Aufbau von Geweben und bei der Regulation zellulärer Antworten, wie Adhäsion, Wanderung und Differenzierung, beteiligt [87], da Zellbindemotive (z.B. GFOGER, O repräsentiert Hydroxyprolin) zu finden sind. [89] Die Klasse der Struktur-gebenden Kollagene umfasst mindestens 28 Untertypen sowie weitere Proteine mit Kollagen-ähnlichen Domänen. [75, 87, 88b, 90] Die meisten Kollagene sind tripel-helikale Proteine und bestehen aus drei, teilweise unterschiedlichen α-Polypeptidketten, die vorwiegend aus dem repetitiven $(G\text{-}X\text{-}Y)_n$ - Motiv aufgebaut sind, bei dem Prolin- und 4-Hydroxyprolin-Reste sehr häufig die X und Y Positionen neben dem unpolaren Glyzin einnehmen. [87, 91] Kollagen Typ I repräsentiert dabei eine perfekte Tripel-Helix, was die regelmäßige Assemblierung zu Fibrillen bewirkt und die strukturellen Eigenschaften im Gewebe begründet. [87] Solche Kollagenfasern bestehen aus selbstassemblierten Kollagenfibrillen, die sich in einem charakteristischen, einzigartigen D-Bandenmuster (64 nm bis 67 nm) zusammenlagern. [88c, 92] Andere Kollagene zeigen Unterbrechungen in der Tripel-Helix-Struktur und können nicht bzw. nur mit Unterstützung in fibrilläre Strukturen assemblieren. [87] So bildet Kollagen Typ IV aufgrund von nicht-helikalen terminalen Domänen Netzwerke anstatt Fibrillen. [87, 88b, 90b] Da das Kollagen-Vorkommen Gewebe-spezifisch ist, findet sich Kollagen Typ I vorwiegend in Haut, Sehnen, Knochen und Bändern, während Typ IV in der Basalmembran auftritt. [88b]

Elastin ist für die Elastizität und Widerstandskraft von Geweben und Organen, wie Haut, Bändern, Arterien, Venen und Lunge, verantwortlich und somit und ein Gegenspieler zum steifen, festen Kollagen. [93] Während der Entwicklung und als Reaktion auf Verletzungen sind Fibroblasten, glatte Muskelzellen, Chondrozyten und Endothelzellen in der Lage, Tropoelastin als löslichen Vorläufer zu synthetisieren. [93a, 93b] Die Aminosäuresequenz beinhaltet abwechselnd hydrophile und hydrophobe Bereiche mit einem hohen Anteil (ca. 75 %) an Glyzin-, Valin-, Prolin- und Alanin-Resten, die in immer wiederkehrenden, repetitiven Motiven, wie VGVAPG, GVGVP, oder GGVP, auftreten. [93b, 94] Elastin kann an andere EZM-Komponenten binden, mit Fibrillin oder Fibulin interagieren und Enzym-katalysiert Mikrofibrillen bilden. Durch Zusammenlagerung werden elastische Fasern gebildet, die in Geweben Kräfte absorbieren. [93a, 94a, 95] Elastin hat noch weitere biologische Funktionen, wie direkte und indirekte Vermittlung von Zellsignalen und die Stimulation von zellulären Antworten und Chemotaxis. [96]

In der EZM befindet sich auch das Glykoprotein Fibronektin, welches aus zwei fast identischen Monomeren besteht, die am C-Terminus über zwei Disulfidbrücken kovalent verbunden und mit einer Vielzahl an funktionalen Domänen und Bereichen ausgestattet sind. [84c, 97] Fibronektin enthält Zellbindemotive für Integrine, wie RGD, PHSRN oder REDV, sowie Interaktionsstellen für Heparin, Kollagen oder Fibrin. [84c, 97] Die Matrix-Assemblierung von Fibronektin wird durch die Bindung eines Zellrezeptors, meistens dem $\alpha_1\beta_5$-Integrin and RGD, und anschließender Konformationsänderung aktiviert. Durch Umstrukturierung werden weitere Fibronektin-Bindestellen für intermolekulare Wechselwirkungen frei gelegt und es kommt zum Fibrillenwachstum. [84c, 97a, 98] Aufgrund der Anheftungsstellen für andere EZM-Proteine und Zellen spielt Fibronektin neben den Lamininen eine wichtige Rolle bei der Regulierung von intrazellulären Signaltransduktionswegen. [83b, 84c]

Laminine sind ebenfalls Glykoproteine und bestehen aus drei unterschiedlichen Polypeptid-Ketten (α, β, γ), die in unterschiedlichen Isoformen auftreten können und zu unterschiedlichen Strukturen und Funktionen führen. [97a, 99] Da Laminine eine Hauptkomponente der Basalmembran darstellen, sind sie entscheidend für eine gesunde Gewebeentwicklung und Morphogenese, spielen dadurch aber auch eine Rolle bei Fehlfunktionen und Krankheiten. [100] Auch bei Laminin scheint eine Zellrezeptor-gesteuerte Assemblierung zur Bildung der Basalmembran vorzuliegen. [98b, 101] Die räumliche, kreuzartige Struktur sowie das Vorhandensein weiterer globulärer Domänen ermöglichen eine gute Vermittlung und Mechanotransduktion zwischen Zell- und EZM-Komponenten. [99] Wie Fibronektin, enthält Laminin eine Vielzahl an Zellbindemotiven, wie RGD, IKVAV oder YIGSR, für Integrin-Interaktion sowie Bindedomänen für Heparin und Entactin. [97a] Aufgrund der vielen Bindestellen für Zellrezeptoren aber auch für Glukosamine, Proteoglykane oder Proteine fungiert Laminin als natürlicher Vernetzer und stimuliert zelluläre Funktionen, wie Adhäsion, Proliferation und Differenzierung. [97a, 99, 101] Weitere adhäsive Glykoproteine sind Vitronektin, Thrombospondin, Entactin und Tenascin. Sie tragen ebenfalls Zell-Interaktionsmotive (z.B. RGD oder KGD), vernetzen sich mit anderen EZM-Komponenten, wie Kollagen, Fibronektin oder Heparin, und wirken regulatorisch. [97a]

Proteoglykane und Glykosaminoglykane (GAG), wie Heparin und Hyaluron, sind weitere wichtige strukturelle, funktionelle und regulierende Biomakromoleküle in Geweben. Proteoglykane bestehen aus einem Protein, das mit einer oder mehreren, möglicherweise auch verschiedenen GAG-Ketten kovalent modifiziert ist. [79c, 102] Dabei stellen repetitive Disaccharide, bestehend aus verschiedenen Hexosaminen und Hexuronsäuren, die Grundeinheit von GAG dar, die zu langen, linearen, negativ geladenen Polysacchariden mit unterschiedlicher Größe zusammengesetzt werden. [79c, 102-103] Außer Hyaluron (Zellmembran, keine Sulfatgruppen), werden GAG im Golgi-Apparat innerhalb der Zelle hergestellt und Gewebe-spezifisch mit Sulfatgruppen modifiziert, wodurch heterogene und einzigartige Polymerketten entstehen. [79c, 102-103] Zur Regulation von Zellfunktionen können Proteoglykane und GAG direkt mit Zellrezeptoren interagieren oder bioaktive Signalstoffe binden. [79c, 102-104], Zudem können sie sich auch mit anderen EZM-Komponenten vernetzen und zur Organisation der EZM beitragen. [79c, 104] Zusätzlich können GAG und Proteoglykane Wasser binden, das osmotische Gleichgewicht kontrollieren und dem Gewebe mechanische Stabilität und Druckfestigkeit geben. [104b, 105] Somit zeigt die Diversität der EZM-Komponenten deutlich, wie multifunktional die extrazelluläre Mikroumgebung ist und wie daraus ein komplexes, miteinander verbundenes Netzwerk aus Zellen und Biomakromolekülen entstehen kann. [97a]

1.2.3.2. Zell-Matrix-Interaktionen

Um an Interaktionsliganden der EZM-Komponenten binden zu können, besitzen Zellen Oberflächenrezeptoren, die nach einer Wechselwirkung intrazelluläre Signaltransduktionswege aktivieren und zelluläre Antworten bewirken. [66, 106] Neben physischem Halt und Lokalisation können Zellen über eine entsprechende Adhäsion auch Signale in ihrer Mikroumgebung wahrnehmen. [72] Zudem übernehmen Oberflächenrezeptoren biologische Funktionen bei der Organisation und Strukturierung der EZM, da z.B. die Interaktion mit löslichem Fibronektin und die damit verbundenen Spannungskräfte eine Konformationsänderung bewirken, infolgedessen eine Fibrillenelongation und eine Netzwerk-Bildung eintritt. [84c]

Das Anheften und Spreiten von Zellen ist ein Zusammenspiel diverser Adhäsionskontakte, nämlich den fokalen Komplexen, fokalen Adhäsionen, fibrillären Adhäsionen und Podosomen. Diese Adhäsionssignalkomplexe interagieren mit EZM-Komponenten über Oberflächenrezeptoren und werden vom kontraktilen Aktin-Zytoskelett gesteuert. [84c] Während des Adhäsionsprozesses und der Zellmigration sind diese Adhäsionskontakte in verschiedenen Stadien ausgeprägt: Zunächst bilden sich kleine, punktartige fokale Komplexe am Rande der Filo- und Lamellipodien zur initialen Anheftung und Signaltransduktion aus. [72, 84c] Die fokalen Komplexe wandeln sich danach in flache, größere, längliche Zellausläufer in der Zellperipherie, die fokalen Adhäsionen, um. Diese vermitteln aufgrund der Interaktion assoziierter Proteine (z.B. Vinculin, Paxillin oder Talin) mit den Aktin-Mikrofilamenten und Stressfasern eine stabile Adhäsion. [72, 84c] Fibrilläre Adhäsionen sind längliche Bündel im zentralen Zellkörper und interagieren mit Fibrillen der EZM, um die Zelle auf dem Substrat anzuheften. [72, 84c] Podosomen sind kleine zylindrische Strukturen aus Vinculin und Paxillin und finden sich nur bei ausgewählten Zellen, wie Makrophagen oder Osteoklasten. [84c]

3D-Matrix-Adhäsionen unterscheiden sich von fokalen und fibrillären Adhäsionen auf 2D-Substraten durch die Expression wichtiger Matrix-Adhäsionsmoleküle, wie $\alpha_5\beta_1$- und $\alpha_v\beta_3$-Integrin-Oberflächenrezeptoren, Paxillin und anderen Komponenten des Zytoskeletts. Im Vergleich zu kommerzieller 2D-Kultur, zeigen diese *in vivo* wichtigen 3D-Matrix-Interaktionen keine klar trennbaren fokalen und fibrillären Adhäsionen, sondern sind zusammen entlang der fibrillären Umgebung lokalisiert und ausgeprägt, was ihre verstärkte biologische Funktion begründet. Gleichzeitig wird vermutet, dass die in 2D deutlich erkennbaren fokalen und fibrillären Adhäsionen Vorläufer für die 3D-Matrix-Adhäsionen darstellen, die durch die Kultur auf festen 2D-Substraten sehr stark exprimiert werden. [107]

Die wohl bekanntesten Oberflächenrezeptoren sind Integrine, eine Familie von transmembranen Glykoproteinen. [108] Integrine sind nicht-kovalent verbundene, heterodimere Multiproteinkomplexe und durch zwei verschiedene Untereinheiten, der α- und der β-Untereinheit, aufgebaut. [109] Die beiden extrazellulären Bereiche der α- und β-Untereinheit sind große Proteinkomplexe aus verschiedenen Domänen, während die Transmembran- und die intrazelluläre Domänen des Integrins im Vergleich relativ klein sind. [72, 109b, 110] Diese bidirektionalen Transmembran-Verbindungen leiten Signale über die Plasmamembran in beide Richtungen weiter und beeinflussen einerseits die Strukturierung und Integrität von Geweben (extrazellulär) und andererseits das Zellverhalten (intrazellulär). [72, 109a, 109c] Während die extrazellulären, Liganden-bindenden Adhäsionsdomänen mit kurzen Peptidsequenzen, anderen EZM-Makromolekülen oder zellulären Oberflächenproteinen interagieren [109c], ist der intrazelluläre, zytoplasmatische Bereich mit dem F-Aktin-Zytoskelett und Signalkomplexen verbunden. [72, 109a, 109c] Die spezifischen, Integrin-bindenden Peptidsequenzen der EZM-Komponenten beinhalten häufig saure Aminosäuren. [109a, 111] So können viele Integrine an das bekannte RGD-Tripeptid binden, das in EZM-Proteinen, wie Fibronektin, Laminin, Kollagen oder Vitronektin zu finden ist. [109c, 111-112] Dabei haben sowohl die RGD-flankierenden Aminosäurereste als auch die Konformation des RGD-tragenden Aminosäurebereichs einen Einfluss auf die Bindungsaffinität, wodurch sich spezifische Integrin-Selektivitäten zeigen. [112b, 113] Integrin-Rezeptoren können somit an verschiedene EZM-Komponenten binden, aber gleichzeitig kann ein EZM-Protein auch mit mehreren, unterschiedlichen Integrinen interagieren. [109c, 111-112] So konnten viele Integrine ihren Liganden zugeordnet werden, weswegen es beispielsweise eine Einteilung in Kollagen-, Laminin- und Leukozyten-spezifische Rezeptoren gibt. [109a, 109c, 112b] Da Integrine sowohl bei der Migration und Ausrichtung von Zellen als auch bei der Organisation des Zytoskeletts wichtig sind, liegt die Vermutung nahe, dass Zellen die Integrin-vermittelte Adhäsion zeitlich und räumlich regulieren können. [112a, 114] Einige Integrine sind nicht dauerhaft aktiv und müssen zur Ligandenbindung und Signalvermittlung erst durch Agonisten, wie Epinephrin oder Thrombin, aktiviert werden, was insbesondere bei eigentlich zirkulierenden Zellen (z.B. Blutzellen) wichtig ist. [109a, 112a] So würden dauerhaft aktive Integrine auf Blutplättchen zu Thrombosen durch Fibrinogen-Interaktion führen. [109a, 115] Bei ruhenden Leukozyten sind aktivierte Integrine wichtig bei der Immunabwehr, würden aber langfristig zu Entzündungen führen. [109a, 115] Neben der Verankerung haben Integrine aufgrund ihrer Membrangängigkeit aber auch sensorische und regulatorische Funktionen (z.B. Mechanotransduktion), da sie den extrazellulären Raum mit dem intrazellulären Zytoskelett verbrücken. [109a, 116] Diese dynamischen

EZM-Zytoskelett-Verbindungen aktivieren Signaltransduktions-Wege, die Zellantworten, wie Proliferation, Migration, Organisation des Zytoskeletts, Genexpression und Differenzierung sowie Überleben oder Apoptose steuern. [84c, 109a, 116a] Oft ist auch eine Integrin-basierte Adhäsion nötig, um eine Interaktion mit Wachstumsfaktoren zu ermöglichen. [109a, 117] Der Grund liegt darin, dass Wachstum und Überleben vieler Zellen neben Stimulation durch Signalstoffe genauso von einer Rezeptorvermittelten Substrat-Verankerung abhängig sind. [117-118] Ansonsten kommt es aufgrund unzureichender oder ungeeigneter Zell-EZM-Kontakte zum programmierten Zelltod. [119]

1.2.3.3. Biochemische Stimulatoren

Alle Komponenten der EZM enthalten per se schon biochemische Interaktionsliganden in ihrer Struktur. [65, 79c] Generell kann zwischen Zelladhäsionsliganden und immobilisierten Signalstoffen unterschieden werden, aber auch chemisch funktionale Gruppen (z.B. Carboxyl-, Amino- oder Methyl-Reste) können mit Zelloberflächen interagieren und Effekte bewirken. [62] Wie oben erwähnt, dienen EZM-Komponenten auch zur Immobilisierung von eigentlich löslichen Signalmolekülen, wie Wachstumsfaktoren, damit diese den Zellen zur Verfügung stehen.[83b, 120] Nicht-kovalente Interaktionen, wie elektrostatische oder Wasserstoff-Brücken-Bindungen, zwischen der EZM-Komponente und dem Signalstoff werden genutzt, um einerseits die Stabilität und Bioaktivität zu verbessern und andererseits eine räumliche Begrenzung der Moleküle zu erreichen. [62] Diese zeitliche und lokale Regulation ist wichtig für die Wachstumsfaktor-vermittelte Signaltransduktion, die anschließende Stimulation der zellulären Antworten und ein erfolgreiches Gewebewachstum. [120a]

Weitere wichtige biochemische Zelladhäsionsliganden sind kurze Peptidsequenzen in EZM-Proteinen, die mit spezifischen zellulären Oberflächenrezeptoren interagieren. [83a] Diese Interaktion aktiviert intrazelluläre Signaltransduktionswege und führt zum Anheften sowie zur Vernetzung der Zellen in der Mikroumgebung. [112c, 121] Mit Entdeckung des RGD-Peptids in Fibronektin [122] konnten Integrin-Interaktionen auf minimal nötige Aminosäuresequenzen herunter gebrochen [123] und weitere, zelladhäsive Peptidsequenzen in EZM-Proteinen beschrieben werden. [112c, 121b] Fibronektin enthält beispielsweise noch die Interaktionspeptide REDV, LDV und PHSRN [97b], während in Laminin neben RGD die Bindestellen IKVAV, YIGSR und IKLLI identifiziert wurden. [97a, 124] Dennoch bleibt RGD die bekannteste und häufigste zelladhäsive Sequenz. [97a, 112c, 121b] Interessanterweise, zeigen andere Peptide, wie KGD, KQAGDV, LDV, REDV und DGEA ein ähnliches Bindeverhalten wie RGD, was vermutlich auf den negativ geladenen Asparaginsäure-Rest zurückzuführen ist. [112c] Bei der KGD-Sequenz wird von einer zellstimulierenden Aktivität ausgegangen, da dieses Motiv vermehrt in zelladhäsiven Bereichen von Kollagen Typ XVII und Tensacin vorkommt. [97a, 125] Die kurzen Pentapeptide IKVAV und IKLLI in Laminin fördern Zelladhäsion und Neuritenwachstum. [124, 126] Dabei scheint der Isoleucin-Rest essentiell für die Zell-Bindefunktion von IKVAV sein, da eine Substitution durch Glycin zum Funktionsverlust führte. [124a] Das Zelladhäsionspeptid YIGSR, das ebenfalls in Laminin vorkommt, wird auch von einem Integrin Rezeptor erkannt. [127] Anhand dieser Beispiele zeigt sich, wie vielfältig die biochemische Zusammensetzung und die Stimulation zellulärer Mikroumgebungen sein kann.

1.2.4.4. Biophysikalische Faktoren

Durch die makromolekulare Komposition und die daraus entstandene Struktur der EZM werden viele biophysikalische Faktoren wie Topographie und mechanische Eigenschaften bereitgestellt. Sie bestimmt auch die biologische Abbaubarkeit für Zellen [62], welche Zell-Matrix-Interaktionen und zelluläres Wachstum regulieren. [128] Da einige EZM-Komponenten (z.B. Kollagen und Elastin) zu fibrillären Fasern assemblieren, sind diese für den Gewebe-spezifischen, hierarchischen Aufbau und anisotropen Charakter verantwortlich, deren Topographie Auswirkungen auf die Orientierung, Ausrichtung und Migration der Zellen hat. [85e, 129] Durch die strukturelle Anordnung der EZM als Hydrogel-Netzwerk bilden sich zudem verschieden große und dichte poröse Zwischenräume aus, die weitere lenkende Strukturen darstellen, an denen sich Zellen orientieren können. [62, 130] Zusätzlich sind auch Faserdichte und Faserdurchmesser wichtig, da biochemische Interaktionsstellen zugänglich werden, welche die topographisch regulierte Kontaktführung synergistisch unterstützen, und durch die Faserassemblierung die Mechanik beeinflusst wird. [131] Die mechanischen Eigenschaften der Mikroumgebung regulieren unter anderem die Entwicklung und Reifung von Geweben und Organen sowie die Regeneration von verletztem Gewebe, spielen aber auch bei der Krebsentwicklung eine Rolle. [132] Durch die diverse, spezifische Zusammensetzung reichen auch die mechanischen Eigenschaften (Elastizitätsmodul) von Geweben vom kPa- bis zum GPa-Bereich. [133] Dabei werden Steifheits-Bereiche und keine festen Werte angegeben, da viele Gewebe steife Komponenten für die Stabilität und elastische Bestandteile für die Kraftabsorption aufweisen. [133a] Während Knochen und Zähne zu den harten Geweben zählen, werden unter dem Oberbegriff weiche Gewebe eine Vielzahl unterschiedliche Gewebearten, wie Herz-, Leber-, Haut-, aber auch Neuro- bzw. Muskelgewebe, gelistet. [133] In diesem Zusammenhang, spielt die „Durotaxis“ eine Rolle, denn sie beschreibt die Mechanik-gesteuerte Migration von Zellen entlang eines Steifheits-Gradienten zu Bereichen mit höheren mechanischen Eigenschaften. [134] Die Matrixsteifheit beeinflusst auch die Differenzierung von Stammzellen [135], wobei Zellantworten durch ein komplexes Zusammenspiel weiterer Stimulatoren der Mikroumgebung reguliert sind. [62, 135e] Dennoch ist die passende Mechanik wichtig, da das beste Schlagverhalten embryonaler Kardiomyozyten auf Substraten mit der gleichen Elastizität wie im natürlichen Herzgewebe detektiert werden konnte, während Substrate mit einer Steifheit im Bereich von Narbengewebe das Schlagen unterbanden. [136]

Da sich Gewebe in einem ständigen Auf- und Abbau befinden und Zellen im Austausch mit der Mikroumgebung stehen, ändern sich auch mechanische und strukturelle Eigenschaften der EZM während der Entwicklung und Regeneration. [62, 137] Die zellgesteuerte Abbaubarkeit der EZM ist beim Aufbau und der Umstrukturierung von Geweben wichtig, um Migration, Proliferation und Differenzierung von Zellen zu steuern. [62, 138] Viele Säugetierzellen können spezifische Abbauenzyme (Proteasen), wie Plasmin, Elastase oder eine Vielzahl an Matrix-Metalloproteasen, sekretieren, um EZM-Komponenten während der Wundheilung und Geweberegeneration abzubauen. [62, 138] Dabei tragen die Protein-Komponenten der EZM verschiedene Protease-Schnittstellen in ihrer Aminosäuresequenz, um einen gezielten Abbau zu ermöglichen. [62] Bei der Betrachtung einzelner stimulierender Faktoren fällt auf, dass die natürliche Mikroumgebung sehr vernetzt ist und die Veränderung eines Parameters auch zur

Veränderung der anderen beiträgt. So ist der EZM-Abbau direkt mit der Veränderung der Mechanik und der strukturgebenden Komponenten verbunden. [62] Deswegen ist die Erstellung biomimetischer Systeme, die viele natürliche Parameter kombinieren, entscheidend für eine erfolgreiche Gewebezüchtung.

1.3. Zellkulturplattformen und Gewebezüchtung

1.3.1. Grundidee der Gewebezüchtung

Ein großes und andauerndes Problem des Gesundheitswesens ist seit jeher der Verlust und das Versagen von Organen und Geweben, welche oft durch Transplantationen, chirurgische Rekonstruktion oder medizinische Geräte ausgeglichen werden müssen. [9a] Es gibt jedoch weniger Spenderorgane als benötigt und das Risiko einer Abstoßung bleibt bestehen. Zudem kann jeder chirurgische Eingriff zu Folgeproblemen führen. [9a, 139] Medizinische Geräte und medikamentöse Therapien können zwar Teil-Funktionen übernehmen und erhalten, dennoch kann es zu Nebenwirkungen, einem Fortschreiten der Problematik oder einer Verschlechterung des Patientenzustands kommen. [9a, 139] Daher wurde bereits in den 1990er Jahren die klassische Idee der Gewebezüchtung („*Tissue Engineering*“) entwickelt. Sie kombiniert Prinzipien der Ingenieurwissenschaften und Biologie, um künstliches, biologisches Ersatzgewebe zu entwickeln. Dieses soll die Funktionen des geschädigten Organs oder Gewebes wiederherstellen, aufrechterhalten oder sogar verbessern. [9a, 140] In der Gewebezüchtung spielen (isolierte) Zellen, bioaktive Signalstoffe sowie künstliche Materialgerüste eine entscheidende Rolle, die frei kombinierbar sind und als reine Zelltherapie, azelluläre oder bereits besiedelte Gerüste verwendet werden (**Abbildung 5**). [9a, 139, 140b, 141] Dadurch werden (Stamm-) Zellbiologie, Materialforschung und Verarbeitungstechnologien vereint, um durch Alter, Trauma oder Krankheit geschädigte Gewebe und Organe zu unterstützen und zu ersetzen. [142] In der klassischen Zelltherapie (**Abbildung 5B (I)**) werden isolierte Zellen eines Spenders *in vitro* expandiert und eventuell umprogrammiert, um nach der Injektion in den Empfänger spezielle Funktionen zu übernehmen. Dabei braucht es keine aufwändige Operation und falls Spender und Empfänger die gleiche Person sind, können auch Immunreaktionen vermieden werden. [9a, 139, 141] Ein weiterer Ansatz basiert auf bioaktiven, angepassten Gerüsten, die azellulär in den Empfänger implantiert werden (**Abbildung 5B (II)**) und die körpereigene Regenerationsfähigkeit aktivieren sollen. Durch die Stimulation des umliegenden Gewebes werden Zellen animiert das Konstrukt zu besiedeln und die Neubildung von Gewebe zu fördern. [139, 143] Die Herstellung angepasster Gerüste mit biologisch aktiven Signalstoffen (z.B. Wachstumsfaktoren oder zelladhäsive Peptide) ist dabei entscheidend. [9a, 143] Durch die Kombination von Zellen und geeigneten Trägermatrizes können zelluläre Gerüste bereits außerhalb des Körpers geschaffen werden (**Abbildung 5B (III)**), um anschließend implantiert zu werden. [9a, 139, 140b] Gerüst-basierte Ansätze haben dabei den Vorteil, dass die Anhaftung und Verteilung von Zellen steuerbar sind, deren Funktionalität besser erhalten bleibt und auch größere Defekte behandelbar sind. [9a, 139, 141]

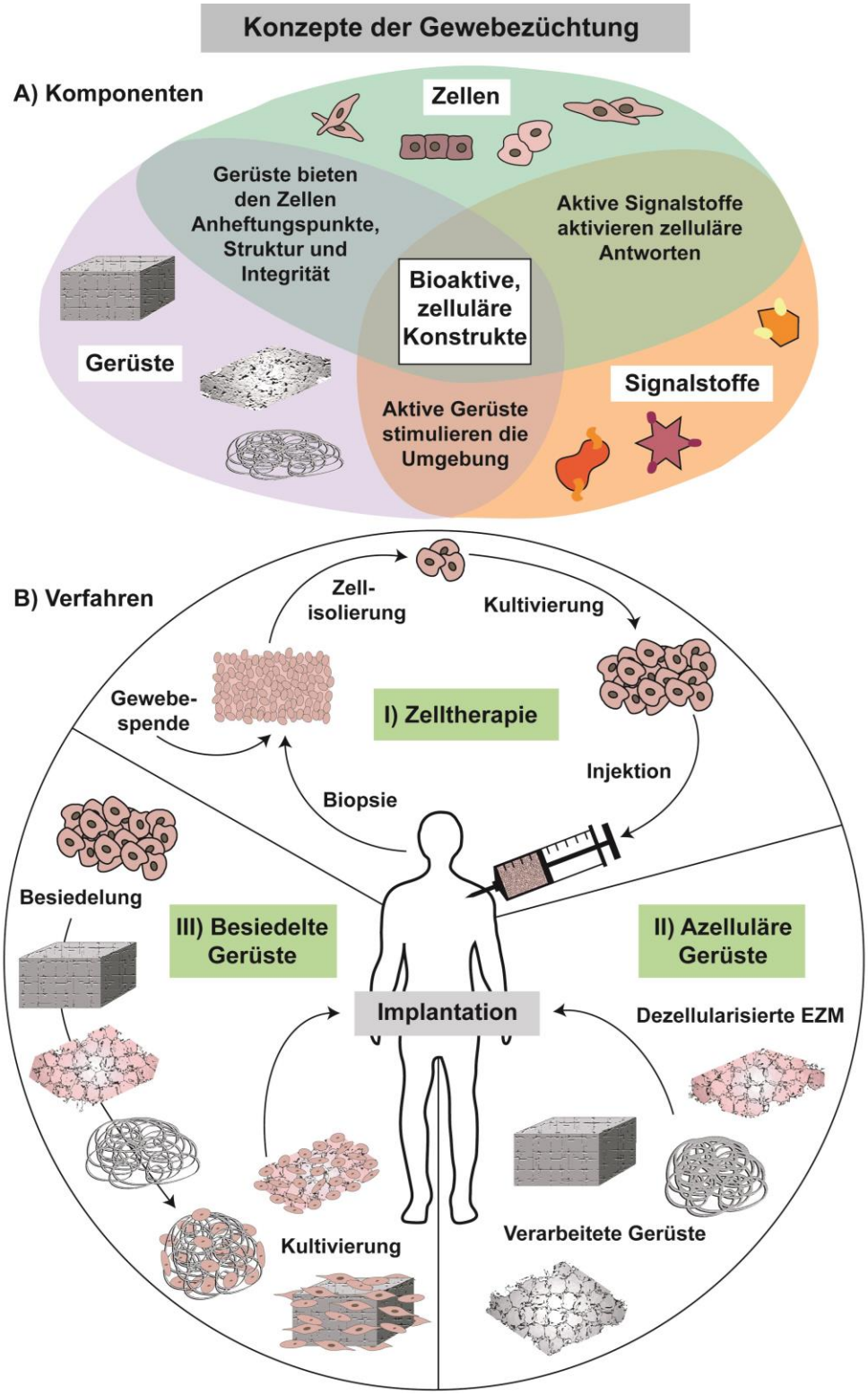

Abbildung 5: Klassische Konzepte der Gewebezüchtung. **A**) In der Gewebezüchtung werden Zellen, Signalmoleküle und Gerüste zu bioaktiven, zellulären Konstrukten verarbeitet. **B**) Es werden die reine Zelltherapie von azellulären oder bereits besiedelten Gerüsten unterschieden.

Diese klassischen Ansätze der Gewebezüchtung, auch als „*Top-Down*"-Strategien bezeichnet, befassen sich erst mit der Herstellung azellulärer, biokompatibler Gerüste, die anschließend von Zellen besiedelt werden (**Abbildung 6A**). Dafür werden unabhängig voneinander

biologisch abbaubare, natürliche oder synthetische Polymere zu aktiven Gerüsten verarbeitet und Zellen kultiviert, die anschließend auf das fertige Gerüst ausgesät werden. [144] Über die Zeit strukturieren die eingebrachten Zellen ihre Mikroumgebung um, indem sie das Gerüst allmählich abbauen und ihre eigene EZM sekretieren und anordnen. [144a, 144c, 144d] Neben der Zellbesiedelung muss auch die Kultivierung, eventuell durch ein Bioreaktor-System, optimiert werden, damit ein voll funktionsfähiges Konstrukt entstehen kann. [141, 145] Zusätzlich können bioaktive Signale in Form von Wachstumsfaktoren und Zytokinen, aber auch mechanische oder elektrische Stimulatoren verwendet werden, um die Anheftung, das Wachstum und die Differenzierung der Zellen zu regulieren. [144a, 144d] Für das Konstrukt-Design ist einerseits die Auswahl eines geeigneten, biokompatiblen Biomaterials mit ähnlichen physikalischen und strukturellen Eigenschaften des Zielgewebes und einer angepassten biologischen Abbaubarkeit entscheidend. [141] Andererseits sollen Adhäsion und Proliferation von Zellen ermöglicht und unterstützt werden, weswegen eine passende Porosität und chemische Interaktionsstellen nötig sind. [141] Dezellularisierte EZM-Gerüste aus natürlichen Geweben sind daher vielversprechend für die regenerative Medizin. [145-146] Weitere gängige Produktionstechniken für poröse 3D-Matrizes sind Gefriertrocknung, Auswaschung von Salzen oder Partikeln, chemisches oder gasförmiges Aufschäumen, thermisch induzierte Phasentrennung sowie Elektrospinn-Verfahren. [61a, 144c, 147] Es können aber auch additive Fertigungstechniken, wie Schmelzschicht-modellierung, diverse Lithographie-Methoden, selektives Laser-Sintern, 3D-Druck oder Elektronenstrahlschmelzen, verwendet werden. Die Computer-gestützte Modellierung ermöglicht dabei die Herstellung von Konstrukten mit geeigneter Porosität, kontrollierter Geometrie und angepasster Größe. [148]

Bei den klassischen „*Top-Down*“-Ansätzen kann jedoch oft nur der im Zielgewebe vorwiegend vorkommende Zelltyp isoliert, kultiviert und für die Geweberekonstruktion verwendet werden, ohne dass zusätzliche Nerven oder Blutbahnen eingebaut werden können. [144d] Zusätzlich ist die Zell-Verteilung eingeschränkt, wodurch die Besiedelung nach dem Aussäen nur auf der Oberseite und durch Zellmigration erfolgt. [141, 144a, 144c, 144d] Neben der geringen und ungleichmäßigen Zelldichte liegen weitere Nachteile in der langsamen Vaskularisierung und der limitierten, freien Diffusion von Nährstoffen und Sauerstoff. [141, 144b-d] Wegen der fehlenden Komplexität ist dieser Ansatz daher nur für einfach aufgebaute Gewebe geeignet. [141, 144a, 144c, 144d] Die geschaffenen Gerüste sollen Defekte im Gewebe räumlich ersetzen, damit die körpereigene Regeneration den komplexen Aufbau des Ziel-Gewebes noch anpasst. [144d]

Aufgrund dieser Nachteile haben sich sogenannte „*Bottom-Up*“-Strategien entwickelt, die Zellen von Anfang an in den Verarbeitungsprozess einschließen und mit Materialien kombinieren, um strukturierte Gewebekonstrukte zu schaffen (**Abbildung 6B**). Dieses modulare Baukastenprinzip soll es ermöglichen, mehrere kleine, naturähnliche, biomimetische Gewebestrukturen vom Nano- bis zum Mikro-Bereich zu erschaffen, die zu komplexeren Geweben zusammengesetzt werden können. [144, 149] Dabei können unabhängig voneinander kontrollierte Mikroumgebungen als Gewebebausteine aus diversen Zelltypen, Materialien, Gerüsten und Verarbeitungstechnologien hergestellt und zusammengelagert werden. [144d, 150] Eine räumliche Anordnung von Zellen kann dabei durch selbstorganisierte Zellaggregation in strukturgebende Mikroformen, eine Lagen-basierte Zell-Kultivierung, Mikrofabrikation zellbeladener Hydrogele oder 3D-Biodruck erfolgen. [144a, 144c, 149] Auch mikrofluidische

Verfahren und akustische, magnetische oder Oberflächenspannungs-induzierte Assemblierung können genutzt werden. [144c] Die nachfolgende Assemblierung der mikrostrukturierten Zell-Bausteine zu biomimetischen, makroskopischen Geweben kann durch gezielten Modulaufbau, Photovernetzung verschiedener Schichten, zufälliges Arrangieren der Module zur besseren Vaskularisierung, Stapeln von Zell-Schichten oder dem Gewebedruck erfolgen. [144a, 144c] Daher bieten diese Strategien im Vergleich zu „*Top-Down*"-Ansätzen eine räumliche und zeitliche Kontrolle von 3D-Strukturen, bessere Diffusion, höhere Zelldichten und die Herstellung komplexer Strukturen. [144c] Die Herausforderung dieser Methode liegt jedoch darin, die Eigenschaften der kleinen, modularen Mikroumgebungen zu erhalten und gleichzeitig ein komplexes, mechanisch stabiles und funktionsfähiges Gewebekonstrukt für potentielle Implantationen zu erschaffen. [144a] Ein auf dieser Methode aufgebautes Forschungsfeld zur Generation funktionaler Gewebegerüste ist die Biofabrikation (siehe 1.3.3.).

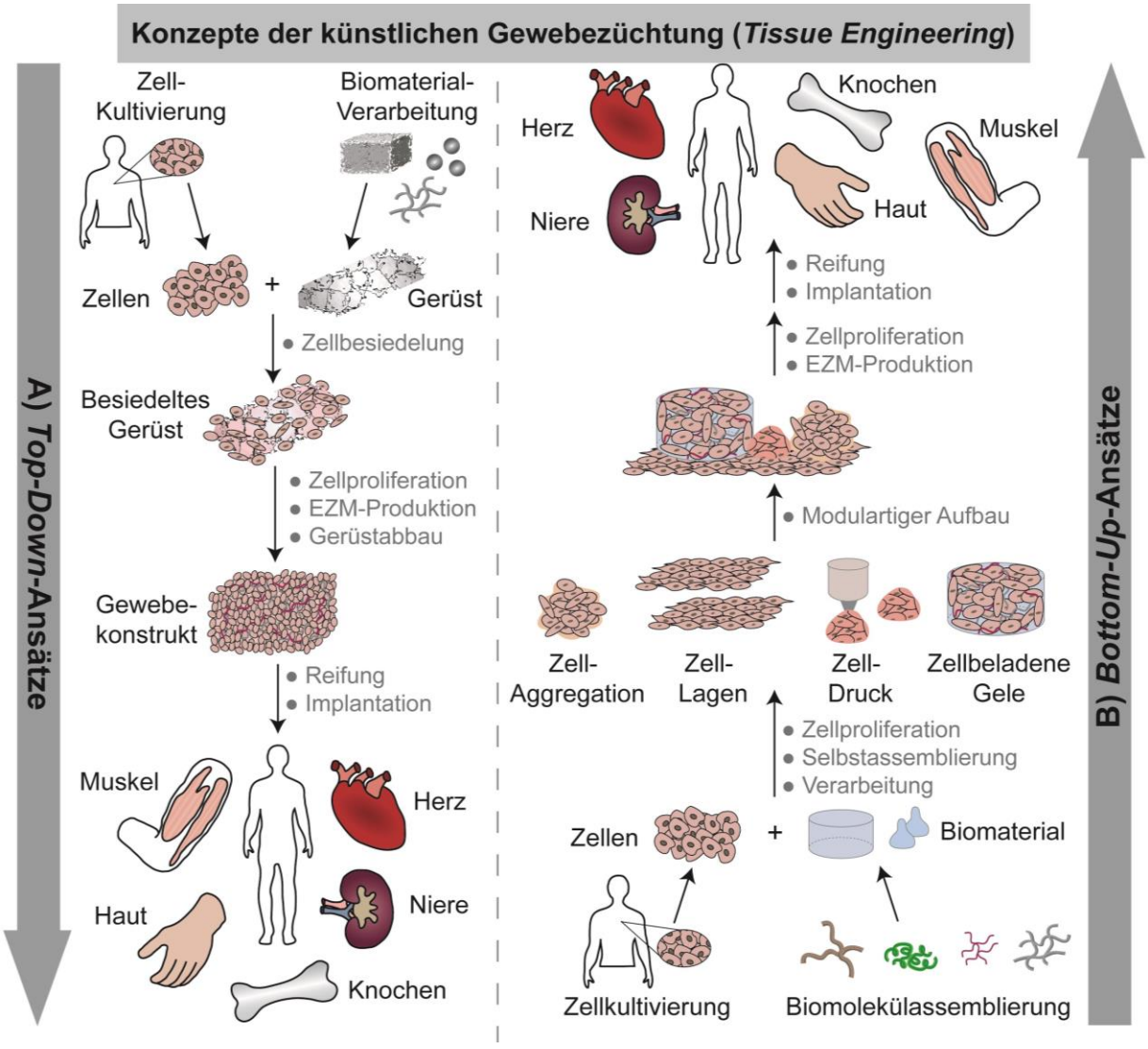

Abbildung 6: Konzepte der künstlichen Gewebezüchtung. **A**) Die klassischen „*Top-Down*"-Ansätze befassen sich getrennt mit der Kultivierung von Zellen und der Herstellung von Gerüsten und werden dann kombiniert, um Gewebekonstrukte zu generieren. **B**) „*Bottom-Up*"-Ansätze schließen Zellen bereits in den Materialverarbeitungsprozess ein, um modulare Mikroumgebungen zu schaffen, die zu komplexeren Strukturen zusammengesetzt werden können.

1.3.2. Entwicklung bioaktiver und biomimetischer Zellkultur-Plattformen

Um Zellen ein möglich naturnahes Umfeld zu bieten und bestimmte Antworten zu stimulieren, wurden Faktoren der spezifischen, zellulären Mikroumgebung in künstliche, biomimetische Biomaterial-Gerüste eingebaut (**Abbildung 7**). [59c, 151] Vielfältige Modifikationen und Funktionalisierungen ermöglichen die Entwicklung diverser 2D- und 3D-Gerüste für die Gewebezüchtung, um gerichtete Zellinteraktionen und gesteuertes Zellverhalten zu initiieren.

1.3.2.1. Funktionalisierte Gerüste für gerichtete Zellinteraktion

Eine Funktionalisierung vorhandener Gerüste mit stimulierenden Wachstumsfaktoren, EZM-Proteinen oder aktiven Peptiden dieser Komponenten stellt eine einfache und effektive Methode dar, um bioaktive, regulierende Matrizes für gerichtetes Zellverhalten zu generieren. [31b, 31d, 48, 51c, 51e-g, 55c, 152] Die Entdeckung des zelladhäsiven RGD-Peptids hat zu einem enormen Anstieg an Biomaterialmodifikationen geführt, um eine gerichtete Interaktion zwischen Zellen und Material herzustellen. [153] Die Identifikation weiterer, zelladhäsiver Peptidsequenzen [112c, 121b] führte zur Entwicklung angepasster Modifikationsstrategien, um spezifische Zell-Interaktions-Plattformen zu generieren. [31b, 48, 51e, 55c, 152c, 152d, 154] So scheint die Adhäsion, Proliferation und Differenzierung von neuronalen (Stamm-) Zellen beispielsweise auf und in IKVAV-modifizierten Gerüsten verbessert zu sein. [124a, 154b, 155] Da das YIGSR-Peptid Fibroblasten, Keratinozyten, glatte Muskelzellen, Epithelzellen und Endothelzellen stimuliert [127b, 154b, 156], findet es bei der Entwicklung von Haut-Äquivalenten und Blutgefäßen Anwendung. [157] Ein weiteres Zellinteraktions-Peptid ist die KGD-Sequenz, die $\alpha_5\beta_1$-, $\alpha_v\beta_1$- und $\alpha_{IIb}\beta_3$-Integrine bindet. [125, 158] Im Vergleich zu Volllängen-Proteinen zeigen Peptide entscheidende Vorteile, wie gute Biokompatibilität, einfache Modifikations-Strategien sowie hohe Zugänglichkeit, Selektivität und Bioaktivität, wenngleich auch ein Risiko von unzureichender Rezeptor-Interaktion bestehen bleibt. [152c, 153a, 159]

Neben biochemischen Funktionalisierungen gibt es auch (bio-) physikalische Material-modifikationen, wie topographische und strukturelle Merkmale, mechanische Eigenschaften, Abbaubarkeit eines Materials sowie elektrische Leitfähigkeit. [62, 160] Zellen können sich nach strukturellen Beschaffenheiten der Umgebung, wie Poren oder Fasern, ausrichten. [57b, 62, 161] Daher stellt die Anpassung der Oberflächentopographie eines Gerüsts eine einfache und effektive Modifikationsstrategie dar, um biologische Reaktionen nach einer Zell-Material-Interaktion zu steuern. [51b, 56b, 162] Die Substrat-Topographie beeinflusst nach dem ersten Zellkontakt zelluläre Antworten, wie Adhäsion, morphologische Umstrukturierung, Migration, Differenzierung und intrazelluläre Signalweiterleitung. [56b, 162b, 162c, 162e, 163] Dabei können sowohl Strukturen im Nanometer- als auch im Mikrometer-Bereich das Zellverhalten beeinflussen. [162b, 163a, 163b, 164] Zellen erkennen verschiedene Krümmungen und Strukturen in ihrer Umgebung und passen ihren Zellkörper und das F-Aktin-Zytoskelett entsprechend der modifizierten Oberflächen an. Sie richten sich also entlang von Rillen aus oder spreiten auf herausstehenden Säulen. [131b, 163c, 164b, 165] Topographische, formgebende Strukturen, wie Poren oder Rillen, können die fibrilläre Komposition der EZM nachahmen, was eine kontrollierte Interaktion und Kontaktführung auf Materialien unterstützt. [166]

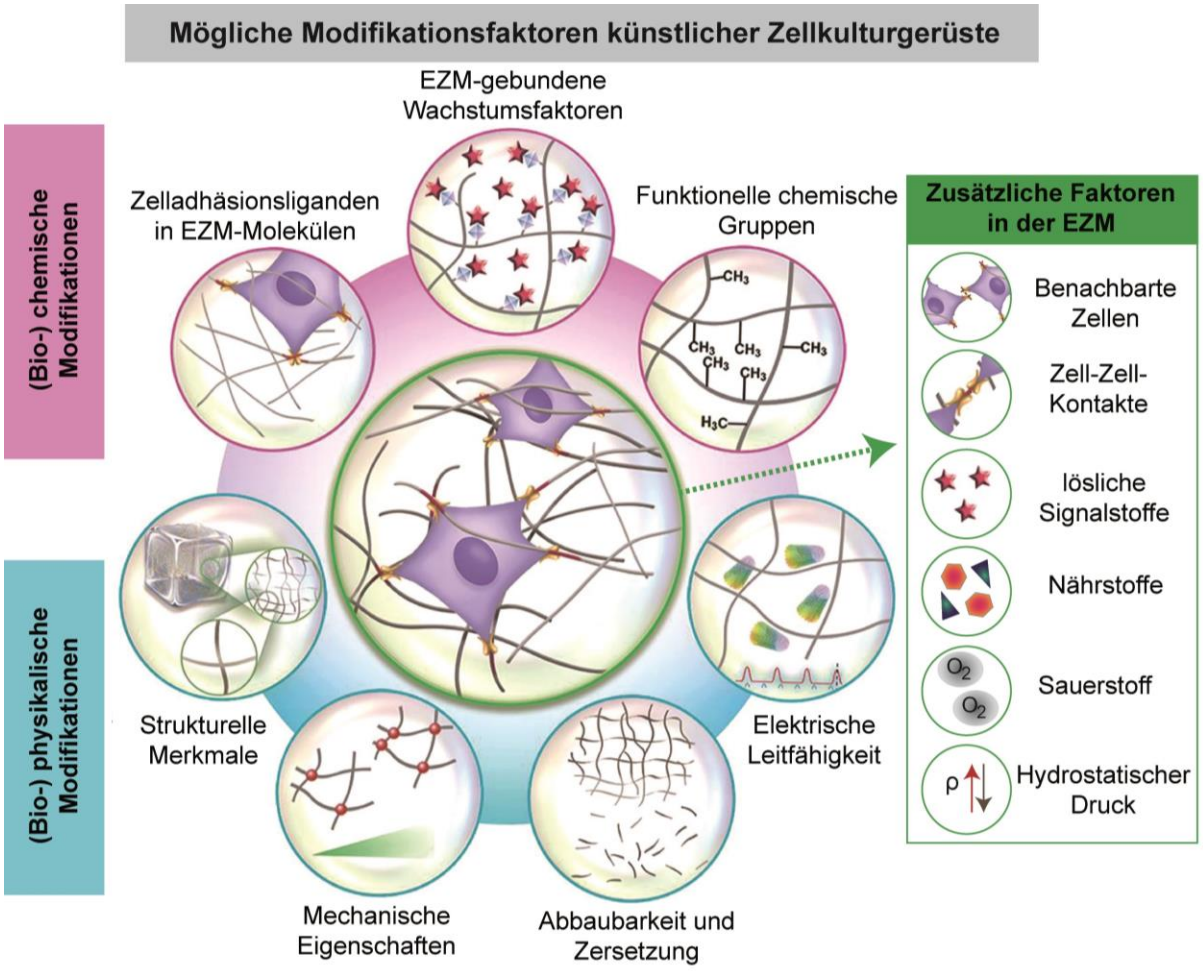

Abbildung 7: (Bio-) physikalische und (bio-) chemische Faktoren der zellulären Mikroumgebung dienen als Inspiration für die Entwicklung innovativer, biomimetischer Zellkultursysteme für die zielgerichtete und anwendungsorientierte Geweberegeneration. Modifiziert nach [62] und reproduziert mit freundlicher Genehmigung des Verlags American Chemical Society (Copyright © 2017, American Chemical Society).

1.3.2.2. Multifunktionale Zellkultur-Gerüste

Der Erfolg eines funktionalen Gewebes ist in der Regel nicht auf einen Regulator alleine sondern auf ein sehr komplexes Zusammenspiel vieler Komponenten zurückzuführen. Daher wurden multifunktionale Biomaterial-Gerüste entwickelt, die Kombinationen verschiedener Regulatoren aufweisen, um das natürliche System besser zu imitieren (**Abbildung 8**). [31b, 48, 57b] Hierfür wurden Materialdesign und Verarbeitungstechnologien stetig weiterentwickelt. [167] Synergistische Stimulation verschiedener Zelloberflächenrezeptoren kann unter anderem durch die Kombination von verschiedenen Peptiden erreicht werden. [31b, 48, 57b] So sorgt die Kombination von RGD- und YIGSR-Peptiden auf Fasern für ein besseres Neuritenwachstum [168], während Stimulation mit EGF und VEGF zu verbessertem Überleben von Endothelzellen führt [169]. Humane Stammzellen aus dem Knochenmark zeigen eine erhöhte Expression von osteogenen Markerproteinen, sobald sowohl RGD- als auch BMP-2-Peptide aus dem Knochenmorphogenetischen Protein-2 vorhanden sind. [170] Die Kombination aus Integrin- und Syndekan-Bindemotiven soll neben Zellen auch EZM-Komponenten, wie Proteoglykane und

Zytokine binden, um Biomaterialien eine komplexere Mikrostrukturierung zu geben. [48] Oberflächenstrukturen (z.B. Rillen) können mit RGD, YIGSR oder Kollagen funktionalisiert werden, damit der adhäsive Ligand die Anheftung und das Wachstum und die Topographie die Morphologie und die Ausrichtung der Zellen reguliert. [58, 165d, 171] Ferner kann eine verbesserte Endothelialisierung und Vaskularisierung durch die Adhäsion und Elongation von Zellen auf Fasern mit biochemischen Liganden (z.B. RGD oder VEGF) erreicht werden. [172] Auch die Änderung der mechanischen Eigenschaften eines Materials bei gleichzeitiger Modifikation mit Kollagen, Fibronektin, BMP-2 oder RGD führt zu unterschiedlicher Zelldifferenzierung. [173] Die Differenzierung von mesenchymalen Stammzellen wird beispielsweise synergistisch durch die Substrat-Steifheit, dessen Topographie und die Zell-Zell-Kontakte beeinflusst. [174] Da im natürlichen System Gradienten wichtig sind, ermöglichen lineare, orthogonale oder entgegengesetzte biochemische Signalgradienten eine räumliche Verteilung dieser stimulierenden Faktoren. [60e, 175] So können biochemische Gradienten zusätzlich mit mechanischen Gradienten kombiniert werden, da Gewebe auch verschiedene mechanische Eigenschaften aufweisen. [60c, 60d] Säugetierzellen zeigen entlang von Steifheitsgradienten eine verstärkte Migration von weicheren zu steiferen Substratbereichen. [176]

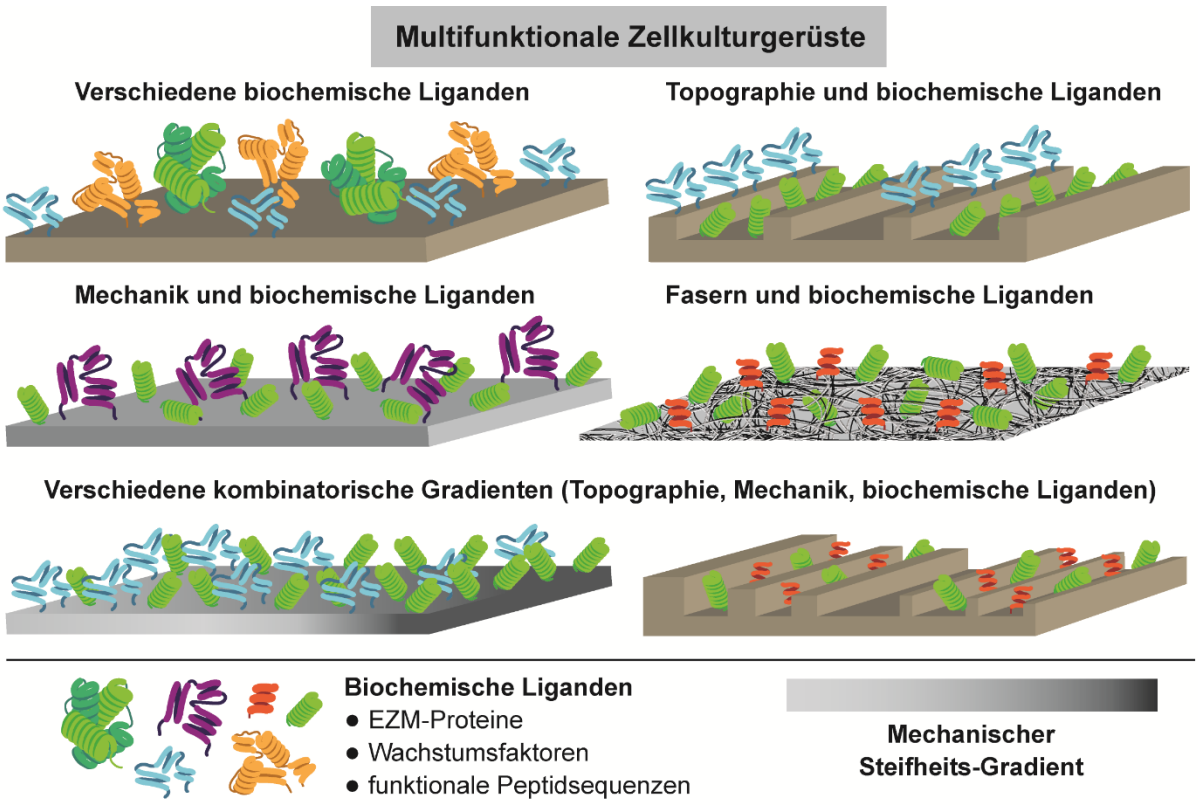

Abbildung 8: Multifunktionale Zellkulturgerüste kombinieren biochemische Liganden, wie EZM-Proteine, Wachstumsfaktoren und funktionale Peptidsequenzen, mit biophysikalischen Modifikationen, wie Oberflächenstrukturen oder veränderter Mechanik.

1.3.2.3. Signal- und Wirkstoff-modifizierte Gerüste

Viele EZM-Gerüste werden mit Signalstoffen funktionalisiert, um Zellen diese potenten Stimulatoren gezielt zur Verfügung zu stellen und biomimetische Mikroumgebungen zu generieren. [53b, 70b, 177] Beispielsweise können dentale Implantate bei Osteoporose zusätzlich

mit bioaktiven Modifikationen ausgestattet werden, um die Osteointegration in den Knochen zu verbessern und den Knochenabbau zu verhindern. [178] Auch Wirkstoffsysteme, welche Therapeutika stabilisieren und gezielt am Wirkort freisetzen, zählen zu wichtigen bioaktiven Gerüsten in der regenerativen Medizin und Gewebezüchtung. [177c, 179] In der medizinischen Therapie zeigen jedoch viele Wirkstoffe und Protein-basierte Therapeutika Limitierungen, wie Aggregation, geringe Pharmakokinetik, suboptimale biologische Verteilung, begrenzte Permeabilität sowie mangelnde Stabilität gegenüber Hydrolyse oder enzymatischem Abbau. Aufgrund der kurzen Halbwertszeit kommt es daher zu häufigen Injektionen oder Infusionen, was die Wirksamkeit reduziert und Nebenwirkungen, Kosten sowie Risiken einer Folgeinfektion erhöht. [180] Der Einbau von löslichen Faktoren kann über nicht-kovalente, physikalische Interaktionen oder chemische, kovalente Bindungen erfolgen. [181] Dabei muss jedoch die Bioaktivität der Stimulatoren geprüft werden, da diese von den Immobilisierungsstrategien, der Konzentration und der Zugänglichkeit abhängt. [62] Die Modifikation mit Signalstoffen kann durch direkte Beladung, elektrostatische Interaktionen, kovalente Bindungen oder zusätzliche Trägerstoffe erfolgen. [179a] Das direkte Einbringen eines Faktors ist zwar einfach, jedoch ist die Freisetzung durch Diffusion aufgrund des Schwellverhaltens des Materials meist schnell, kann aber durch Komposition und Vernetzungsgrad beeinflusst werden. [179a, 179b] Da Wachstumsfaktoren normal an EZM-Komponenten gebunden sind, ist eine elektrostatische Interaktion von Faktor und EZM-Molekülen (z.B. Heparin) eine elegante und naturnahe Immobilisierungsstrategie. [179a] Die kovalente Bindung von Aminosäuren des Wachstumsfaktors an reaktive Gruppen der Biopolymermatrix ermöglicht eine feste und lokale Verankerung am Gerüst. [179a, 179b] Eine kontrollierte Freisetzung eines Signalstoffs kann simultan mit dem Abbau des Gerüsts, z.B. eines Hydrogels, erreicht werden. [177c, 182] Für eine langsame und kontinuierliche Freisetzung können zudem abbaubare und nicht abbaubare Trägerstoffe, die mit dem Faktor beladen sind, kombiniert werden. [179a, 179b, 183] Dadurch werden zeitliche und räumliche Gradienten erzeugt, die durch die physikochemischen und biologischen Eigenschaften der verwendeten Materialien beeinflusst werden. [179a, 184] Das Risiko, dass Signal- und Wirkstoffe denaturieren, degradieren oder an biologischer Aktivität verlieren wird jedoch höher, je mehr verarbeitende Prozesse und chemische Reaktionen nötig sind. [177c, 179a] Daher liegt eine Weiterentwicklung in Zell-basierten Therapien, die Wirkstoff-produzierende Zellen in einer künstlichen 3D-Matrix kultivieren, um den Wirkstoff kontinuierlich am Wirkort freizusetzen. [185]

1.3.2.4. Bioaktive, biomimetische 3D-Gerüste

Die erfolgreiche Isolation und Kultivierung von Säugetierzellen, einschließlich diverser Stammzellen, war ein Meilenstein in der Forschung, um normale und krankhafte zelluläre Mechanismen aufzuklären, Zell- und Krankheitsmodelle zu entwickeln oder therapeutisch wichtige Substanzen (z.B. Antikörper) herzustellen. [186] Um die Zellkultur zu ermöglichen, wurde zunächst auf eine zweidimensionale (2D) Kultur zurückgegriffen, um dort wichtige Abläufe, wie die Herstellung von immortalisierten Zelllinien, zu etablieren. [186a] Da die Rezeptor-vermittelte Anhaftung in ihrer Umgebung für das Überleben und Wachstum von adhärenten Zellen essentiell ist [117-119], haben sich viele, auch großtechnische, Kultivierungs-methoden entwickelt. [186b] Dennoch zeigen Studien, dass sich zelluläres Verhalten und

Gewebeentwicklung in einer 2D-Kultur deutlich von einer 3D-Kultur unterscheiden. [187] 2D-Kulturplattformen spiegeln nicht die räumlichen Anforderungen der natürlichen, zellulären Mikroumgebung wieder, was zelluläre Interaktionen beeinflusst. [187a, 187c] So unterscheiden sich fokale und fibrilläre Adhäsionen auf 2D-Substraten im Vergleich zu einer 3D-Matrix in der Expression wichtiger Matrix-Adhäsionsmoleküle und Komponenten des Zytoskeletts. [107] Zusätzlich besteht der Verdacht, dass begrenzte oder unzureichende Zell-Zell-Kontakte zu einem veränderten zellulären Signaltransduktions-Verhalten führen können, was den Vergleich von 2D- und 3D-Daten enorm erschwert. [187a] Daher scheint eine 2D-Kultur nicht auszureichen und eine komplexere, multifunktionale 3D Umgebung nötig zu sein, um das *in vivo* beobachtete Zellverhalten auszulösen. [62, 188] Grundsätzlich ermöglichen biomimetische 2D-Gerüste ein generelles Grundverständnis und finden auch Anwendung bei Beschichtungen, die keine 3D-Struktur brauchen. Um für die Gewebezüchtung jedoch ein biomimetisches Abbild der natürlichen zellulären Mikroumgebung zu generieren, müssen diese Erkenntnisse auf 3D-basierte Systeme übertragen werden. [62, 189] Daher rückte die Entwicklung von bioaktiven, funktionalen und biomimetischen Gerüsten für die 3D-Zellkultur in den Fokus (**Abbildung 9**), um Zellen ein entsprechendes, möglichst natürliches 3D-Umfeld zu bieten. [62, 190] Im Hinblick auf die zelluläre EZM sind 3D-Hydrogel-Netzwerke aus natürlich vorkommenden oder künstlich hergestellten (Bio-) Polymeren vielversprechend, da sie Wasser aufnehmen können. [62, 191] Im Laufe der Zeit konnten Hydrogele mit angepasster Mechanik, Topographie, Abbaubarkeit sowie biochemischen Interaktionsliganden designt werden. [62, 191f, 192] Die Faser-beeinflusste Mechanik führt im Gewebe zu zellulärer Kommunikation und Mechanotrans-duktion, weswegen dieses komplexe und gleichzeitig dynamische Zusammenspiel zwischen Matrix- und Zell-Mechanik beim Design von künstlichen Gerüsten mit bedacht werden sollte. [62, 189, 193] Da die natürliche EZM einem ständigen Auf- und Abbau von Matrixkomponenten unterworfen ist, wurden künstliche Hydrogel-Systeme entwickelt, die auch einen enzymatischen, hydrolytischen oder photolytischen Abbau ermöglichen. [194] Zelladhäsive Liganden können durch natürliche Proteine mit intrinsischen Interaktionsstellen oder kurze Peptidsequenzen eingebracht werden. [192e] So werden IKVAV-modifizierte Hydrogele beispielsweise für Neurogenese und Stammzelldifferenzierung eingesetzt. [155a, 155c, 155e]

1.3.3. Biofabrikation

1.3.3.1. 3D-Biodruck-Entwicklung

In den letzten Jahrzehnten hat sich das Feld der Druckverfahren durch die Entwicklung von formgebenden 3D-Drucktechnologien zur Herstellung komplexer, mehrlagiger 3D-Konstrukte erweitert und sich als eine wichtige Verarbeitungsmethode in verschiedenen Forschungs- und Industriezweigen etabliert. [148a, 195] Generell kann zwischen dem nicht-biologischen, klassischen 3D-Druck und dem daraus entwickelten 3D-Biodruck unterschieden werden. Die klassische 3D-Druck-Technologie ist eine vielseitige, additive Fertigungsmethode zum schichtweisen Aufbau eines 3D-Konstrukts für die diverse Materialien, wie Metalle [196], Keramiken [197], Polymere [148b, 198] und Komposite [199], verwendet werden. [195b, 195c] Im Laufe der Zeit haben sich auch Hybrid-Systeme aus kommerziellen und additiven Fertigungs-methoden entwickelt, um komplexe, räumliche Konstrukte mit definierten Strukturen für die

Anwendung als Implantat oder Gewebematrix zu generieren. [148a, 200] Hybrid-Systeme ermöglichen die Herstellung von Gerüsten mit verschiedenen topographischen, mechanischen und teilweise (bio-) chemischen Modifikationen. Durch 3D-Druck und Elektrospinnen können beispielsweise gedruckte und Faser-Komponenten kombiniert werden. [148a, 200-201]

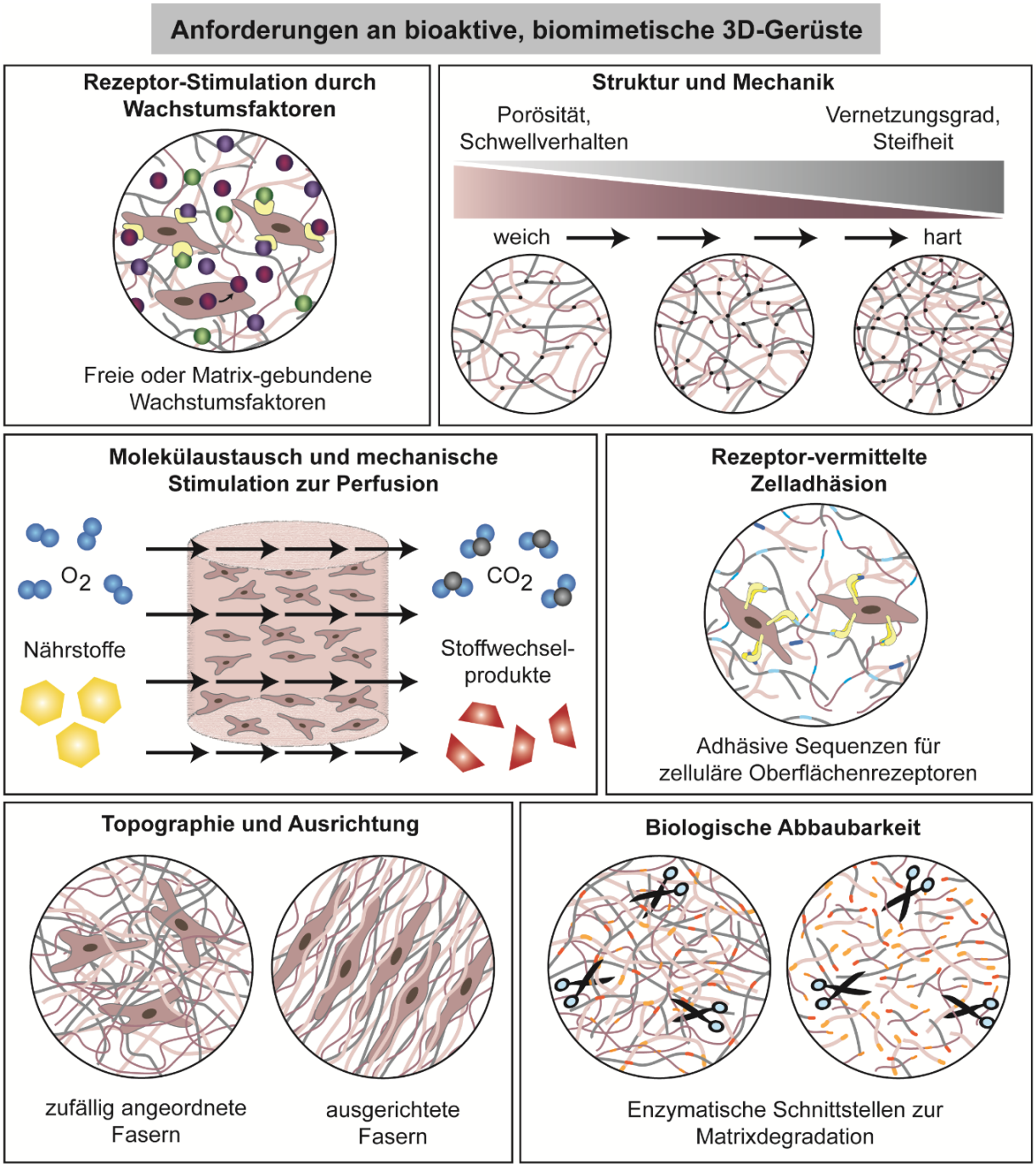

Abbildung 9: Künstliche, biomimetische 3D-Zellkulturgerüste sollen an die zelluläre Mikroumgebung angepasst sein. Entscheidende Faktoren sind biochemische Stimulation durch Adhäsionsliganden und Wachstumsfaktoren, mechanische und topographische Eigenschaften, die biologische Abbaubarkeit und der Molekülaustausch.

Da nicht-biologische Systeme auf Drucktechniken ohne Zellen basieren, werden oftmals Faser-produzierende Technologien und (Bio-) Tinten-basierte 3D-Biodruck-Ansätze miteinander

kombiniert. [200d, 202] Der generelle 3D-Druck-Prozess startet mit dem Erstellen eines Computer-basierten 3D-Modells. Dies erfolgt entweder durch Computer-gestützte Design- und Fertigungssoftware (CAD und CAM) und mathematischer Modellierung [203] oder anhand von Daten aus Bilderfassungstechnologien, wie der Computer- oder Magnetresonanztomographie. [148a, 195a] Die designten oder rekonstruierten 3D-Modelle werden in einem Computer-gesteuerten Schneideprozess in 2D-Querschnitte zerlegt und in einem auf den Drucker angepassten 3D-Schicht-für-Schicht-Modell übereinander gelagert, um den schichtweisen Druck zu ermöglichen. [148a, 195a] Aufgrund des Fortschritts und der Komplexität der 3D-Drucktechnologien sowie der Idee, personalisierte Implantate zu erzeugen, fand diese Verarbeitungsmethode auch Einzug im Bereich der regenerativen Medizin und Gewebezüchtung (**Abbildung 10**). [148a, 204] Im Vergleich zu kommerziellem, Zell-freiem 3D-Druck, basiert die 3D-Biodruck-Technologie als *Bottom-Up*-Prozess auf der Erschaffung naturnaher, hierarchisch geordneter Nachbildungen (Biomimikry), die durch die autonome, zelluläre Selbstorganisation und dem Erschaffen von funktionalen Mini-Gewebebausteinen erreicht wird. [195a] Dabei werden biologische oder bioinspirierte Grundbausteine, wie lebende Zellen, (Bio-) Makromoleküle und Biomaterialien, kombiniert und verarbeitet, um komplexe, therapeutische, lebende oder nicht-lebende 3D-Konstrukte und Modelle zu entwickeln. [205] Der 3D-Biodruck ist auch eine automatische, Computer-unterstütze Druckmethode, bei der es zu einem präzisen und schichtweisen Materialtransfer von biologisch relevanten Biomaterialien, Makromolekülen und Zellen kommt. Dadurch wird eine räumlich definierte, hierarchische Struktur generiert, um eine (oder mehrere) biologische Funktion(en) zu übernehmen. [206] Dabei müssen Parameter, wie Verarbeitungsmethode, Materialeigenschaften, Druck-Auflösung des Konstrukts sowie Effekte, die durch das Drucken auf die biologischen Materialien wirken, evaluiert werden, um ein funktionsfähiges 3D-Konstrukt zu erhalten. [206a]

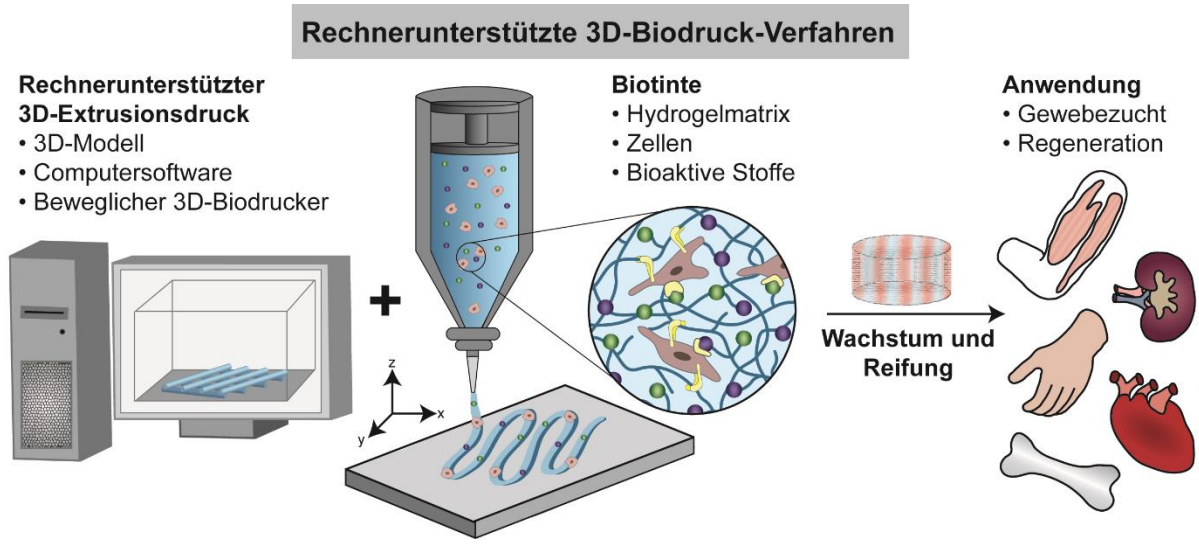

Abbildung 10: Rechnerunterstütze 3D-Biodruck-Verfahren verarbeiten Biotinten (bestehend aus einer Gelmatrix, Zellen und bioaktiven Substanzen) zu hierarchischen 3D-Konstrukten für den Gewebeersatz.

Beim 3D-Biodruck werden die drei Hauptmethoden Extrusions-, Tintenstrahl- (Inkjet) sowie laserunterstütztes Drucken unterschieden, die auch für nicht-biologische, azelluläre Zwecke verwendbar sind. [148a, 195a, 207] Neben den Druck-spezifischen Parametern, sind bei Biodrucktechnologien die Viskosität und die mechanischen Eigenschaften der Biotinte entscheidende Parameter für den anschließenden Druckerfolg. [148a, 207b] Beim laserunterstützten Biodruck liegt über einer Schicht aus Biotinte, eine Energie-absorbierende Opferschicht aus Polymer oder Metall. Durch die auftreffenden Laserpulse wird Energie übertragen und es bildet sich eine Hochdruckblase, die die Biotinte als Tröpfchen auf das Substrat befördert. [148a, 208] Da es sich beim laserunterstützten Biodruck um eine Nadel-freie, kontaktlose Drucktechnologie handelt, wirkt kaum mechanischer Stress auf die Zellen, was zu einer hohen Zellviabilität und Erhalt der Zellfunktionen führt und auch die Verwendung von hohen Zelldichten ermöglicht. [148a, 207b, 209] Beim Inkjet-Biodruck wird die Tinte, bestehend aus einem wenig viskosen Hydrogel-Vorläufer-Polymer und Zellen, durch eine Nadel tröpfchenweise, aber kontinuierlich als Schicht auf eine Oberfläche extrudiert und verfestigt sich. Die Tröpfchengröße wird dabei entweder thermisch oder Piezo-elektrisch gesteuert. [148a, 195a, 207, 210] Der Extrusions-basierte Biodruck ist auch unter dem Begriff automatisch-gesteuertes Dosieren („*Robotic Dispensing*“) bekannt und gilt aufgrund der Einfachheit und Kosteneffektivität gegenüber den anderen Techniken als am weitesten verbreitet. [211] Beim Extrusions-Biodruck werden hochviskose, scherverdünnende (Bio-) Tinten durch Druckkraft, die entweder pneumatisch oder mechanisch durch einen Kolben oder eine Schraube entsteht, als durchgängiges Filament durch eine Nadelöffnung extrudiert. Durch die Bewegung des Druckkopfes und/oder des Druckbetts dienen abgelegte Schichten auf der Substratoberfläche als Basis für die nächste extrudierte Schicht. [148a, 207b, 212] Ein wichtiger Vorteil dieser Methode ist die Verdruckbarkeit von (Bio-) Tinten aus unterschiedlichen Materialien und mit diversen rheologischen Eigenschaften. [148a, 195a, 207b, 212] Im Vergleich zum Inkjet-Druck mit niedrig-viskosen Materialien, führen hochviskose (Bio-) Tinten bei Extrusions-basierten Drucktechnologien zwar zu stabileren Konstrukten, die Überlebensrate der Zellen ist aber aufgrund der rheologischen Tinteneigenschaften meistens niedriger. Dies wird bei kleiner werdendem Düsendurchmesser und steigendem, angelegtem Druck noch verstärkt. [148a, 195a, 213] Neben dem Tintenmaterial entscheiden Prozess-Parameter, wie der angelegte Druck, der Durchmesser und die Beschaffenheit der Extrusions-Düse, die Druckgeschwindigkeit und die Druckdauer, letztlich über den Erfolg beim Biodrucken. [213b, 213c, 214]

1.3.3.2. Biotinten und Biofabrikation von 3D-Gerüsten

Bereits in den 1980er Jahren wurde die Grundlage für heutige Biofabrikationsansätze durch Verarbeitung von lebenden Zellen in einer künstlichen Matrix geschaffen. Isolierte Langerhans'sche Inselzellen wurden in Alginat verkapselt, konnten über 15 Wochen *in vitro* kultiviert werden und zeigten auch in Ratten für zwei bis drei Wochen Aktivität. [215] Ein deutlicher Vorteil liegt in der verlängerten Zellaktivität, da eingekapselte Zellen ein Jahr Funktion im Rattenmodell zeigten, während nicht eingekapselte Zellen nur zwei Wochen aktiv waren. [216] Zell-Verkapselung ist in der zielgerichteten Therapie, bei chronischen und neurologischen Erkrankungen wichtig, um eine kontinuierliche Produktion und Freisetzung von Wirkstoffen zu gewährleisten. [217] Die Freisetzung stimulierender Faktoren kann dabei

auch für gerichtete Regeneration und Gewebewachstum (z.B. im zentralen Nervensystem[218]) eingesetzt werden. Auch hier sind die physikochemischen Eigenschaften und die daraus resultierende Bio- und Zellkompatibilität der umgebenden Biomaterialmatrix-Komponenten entscheidende Faktoren für den Erfolg der zielgerichteten und regenerativen Therapie. [26d] Diese Verkapselungsstudien waren wichtig für die Entwicklung von Biotinten für Biofabrikationsprozesse zur Erstellung von stabilen, formgebenden Gerüsten für lebende Zellen. [219] Dabei ist ein druckbares Biomaterial natürlichen oder synthetischen Ursprungs die Basis der Biotinte, welche die zelluläre Mikroumgebung im Gewebe nachahmen soll. [211b, 220] Zusätzlich muss noch zwischen azellulären Biomaterial-Tinten und Biotinten unterschieden werden: Biotinten sind per Definition Zell-beinhaltende Biomaterial-Tinten, die durch Mischen von lebenden Zellen und Biomaterial formuliert werden. [219a] Es gelten die gleichen Anforderungen eines künstlichen Gewebegerüsts, wie Biokompatibilität, Sterilisierbarkeit bzw. Keimfreiheit, Funktionalisierbarkeit und anpassbare physikalische Eigenschaften, wie Mechanik oder Degradationsverhalten. [148a, 207b, 211b, 220a] Da Biotinten den Zellen mechanische Stabilität geben, aber auch biologische Funktionen und zelluläre Antworten stimulieren sollen, müssen die verwendeten Komponenten milde Gelierungsbedingungen und passende rheologische Eigenschaften aufweisen. Zudem müssen sie bei zellkompatiblen Temperaturen druckbar sein, um eine vorzeitige Degradation der Biomakromoleküle und Zellsterben zu verhindern. [148a, 207b, 211b, 213c, 220] Die Scherkräfte während des Druckprozesses müssen ebenfalls kontrolliert werden, um ein Gleichgewicht zwischen einer guten Druck-Auflösung und einer hohen Überlebensrate der Zellen zu gewährleisten. [213b, 213c, 221] Biofabrikationsprozesse sollen daher zum Lösen einiger bekannter Fabrikations-bedingter Probleme, wie einer schlechten Überlebensrate von Zellen, einer fehlenden hierarchischen Strukturierung während der zellulären Selbstorganisation, einer fehlenden Vaskularisierung zur Nährstoff- und Sauerstoffversorgung und einer eingeschränkten Reifung der entstandenen Gewebekonstrukte, beitragen. [205a] Denn obwohl der 3D-Biodruck sehr viele Vorteile aufweist, muss an den Drucktechniken, der Auflösung, Skalierbarkeit und Druckgeschwindigkeit nachgerüstet werden und die 3D-druckbaren Materialien und deren Biokompatibilität weiter charakterisiert werden. [148a]

Hydrogele aus natürlichen oder synthetischen Biopolymeren sind aufgrund ihrer Biokompatibilität, rheologischen Eigenschaften und Anpassbarkeit, perfekte Kandidaten für die Matrix-Komponente von Biotinten. [211b, 220, 222] Natürliche Matrix-Komponenten sind beispielsweise Kollagen-, Fibrin-, Agarose-, Alginat-, Hyaluronsäure-, Cellulose- und Seiden-basierte Gele.[219c, 220] Daneben stellen auch rekombinante Seiden-, Elastin- oder Kollagen-proteine geeignete Matrix-Komponenten dar, da sie auf die jeweiligen Anforderungen anpassbar sind. [222b] Etliche synthetische Polymere werden zwar als geeignetes Druck-Material für Biotinten gelistet, zeigen aber meistens keine gute Zellkompatibilität, weswegen sie in unmodifizierter Form eine untergeordnete Rolle für den 3D-Biodruck spielen. [220b] Viele der bisher entwickelten Biotinten müssen einen Kompromiss zwischen der Eignung für den Biofabrikationsprozess (Druckbarkeit, Auflösung) und der gewünschten biologischen Funktionen der eingekapselten Zellen finden. [223] Da sowohl die zelluläre Aktivität als auch die Formtreue des gedruckten Konstrukts erhalten bleiben soll, rücken vermehrt auch Stimuli-responsive Materialien und der 4D-Druckprozess in den Fokus. [223-224] Die Biofabrikation stellt

somit eine Schnittstelle zwischen der Zell- und Entwicklungsbiologie, den (Bio-) Materialwissenschaften und der Verarbeitungstechnik dar und ist damit ein interdisziplinäres Forschungsfeld, welches Biologie, Biochemie, Physik, Chemie sowie Lebens- und Ingenieurswissenschaften miteinander verbindet. [205]

1.4. Spinnenseide als Biomaterial

1.4.1. Natürliche Spinnenseide als Vorbild

Weibliche Radnetzspinnen sind in der Lage bis zu sechs verschiedene Seiden-Typen mit spezifischen Eigenschaften und Funktionen, sowie ein Seiden-ähnliches Protein mit Klebefunktion zu generieren. [225] Vor allem die Proteine des Abseilfadens der goldenen Seidenspinne (*Trichonephila clavipes*) und der europäischen Gartenkreuzspinne (*Araneus diadematus*) und deren Eigenschaften sind sehr gut charakterisiert. [225a-c, 226] Der Abseilfaden der Gartenkreuzspinne besteht aus mindestens zwei Proteinen, auch Spidroine genannt, dem *Araneus diadematus* Fibroin (ADF) 3 und 4. [226c, 227] Die mechanischen Eigenschaften der Spinnenseide gehen dabei auf die Komposition und Reihenfolge der Aminosäuren und damit auf die Gensequenz zurück. [228] Im natürlichen System ist eine repetitive Kern-Domäne von nicht-repetitiven N- und C-terminalen Domänen flankiert, die wichtig für die Lagerung der unstrukturierten Proteine in der Spinndrüse sind, aber auch die pH- und Salz-abhängige Faserassemblierung durch Zusammenlagerung initialisieren. [225d, 229] In der repetitiven Domäne finden sich Poly-Alanin-Bereiche, die in kristalline, β-Faltblatt-reiche Strukturen assemblieren. Diese sind wiederum in eine amorphe Matrix aus unstrukturierten, helikalen und Schleifen-reichen Sekundärstruktur-Bereichen eingebettet, die aus Glyzin-reichen Motiven, wie GPGXX, aufgebaut sind. [225b, 225d, 225f, 228b, 228c, 230] Die Anordnung dieser Sekundärstrukturen ist entscheidend für die mechanischen Eigenschaften der Spinnenseide, da die β-Faltblatt-reichen, kristallinen Bereiche für die Festigkeit und Stärke verantwortlich sind, während die amorphen Regionen die Elastizität, Dehnbarkeit und Kraftkompensation bewirken. [225b, 225d, 226b, 228b, 228c]

Die Kombination ihrer einzigartigen Eigenschaften, wie der hohen Biokompatibilität, dem geringen entzündungsfördernden Verhalten, der langsamen Bioabbaubarkeit sowie der gleichzeitig auftretenden mechanischen Festigkeit und Elastizität, macht Spinnenseide zu einem interessanten Biomaterial für biomedizinische und gewebetechnische Anwendungen. [231] So konnten beispielsweise natürliche Spinnenseidenfäden von *Trichonephila clavipes* erfolgreich zu Netzstrukturen prozessiert werden und eigneten sich anschließend für die Kultivierung von NIH/3T3 Maus-Fibroblasten. [232] Solche Netzstrukturen wurden zudem zur Herstellung eines zweischichtigen Hautmodells aus embryonalen Maus-Fibroblasten als Dermis und humanen HaCaT-Keratinozyten als Epidermis verwendet. [233] Die Zellinteraktion hängt dabei neben der chemischen Zusammensetzung auch von der präsentierten Topographie ab, da Säugetierzellen im Vergleich zu flachen Filmen eine verbesserte Ausrichtung auf Fasern aus prozessierter, natürlicher Spinnenseide aufweisen. [234]

1.4.2. Rekombinante Spinnenseidenproduktion

Auch wenn natürliche Spinnenseide ein hervorragendes Biomaterial darstellt, können nur geringe Mengen aus Spinnen gewonnen werden und eine Zucht ist aufgrund des territorialen, kannibalistischen Verhaltens der Spinnen sowie der Kosten nicht möglich. [225b] Daher wurden verschiedene, rekombinante Produktionssysteme entwickelt, um Spinnenseidenproteine in hoher Menge und mit gleichbleibender Qualität biotechnologisch zu produzieren. [226c, 227, 235] Als Produktionssysteme werden Bakterien, Hefen, Insekten, Säugetierzellen oder transgene Tiere oder Pflanzen verwendet. [225f, 231a] Dabei diente der Abseilfaden von *Trichonephila clavipes* als Vorlage zum Design von rekombinanten Spinnenseidenproteinen (6mer und 15mer), die durch sechs- oder fünfzehn-fache Wiederholung einer Konsensus-Sequenz entstanden sind. [236] Das rekombinante Spinnenseidenprotein 4RepCT konnte aus dem Abseilfaden von *Euprosthenops australis* entwickelt werden und besteht aus vier Wiederholungen eines Poly-Alanin- und eines Glycin-reichen Moduls sowie einer nicht-repetitiven C-terminalen Domäne. [237] Das für die vorliegende Dissertation verwendete rekombinante Spinnenseiden-System basiert auf Proteinen aus dem Abseilfaden der Europäischen Gartenkreuzspinne *Araneus diadematus*. Die Aminosäuresequenz der beiden in dieser Seide natürlich vorkommenden Spidroine ADF3 und ADF4 [238] diente als Vorbild für die rekombinanten Varianten. Während sich die zwei Konsensus-Module A und Q im rekombinanten eADF3$(AQ)_{12}$-Protein zwölf Mal alternierend wiederholen, wurde die eADF4(C16)-Variante aus 16 Wiederholungen einer Konsensus-Sequenz (C-Modul, Sequenz GSSAAAAAAAASGPGGYGPENQGPSGPGGYGPGGP) generiert. [226c, 227] Beide rekombinanten Proteine zählen zu den Prolin-reichen MaSp2-Proteinen (*Major ampullate spidroin-2*) und enthalten in ihren repetitiven Modulen einen Poly-Alanin-Bereich und Glyzin-reiche Abschnitte. [226c, 227, 238] Mithilfe gentechnischer und molekularbiologischer Verfahren wurden Gensequenzen der beschriebenen, künstlichen Spinnenseiden-Varianten generiert, um eine rekombinante Proteinproduktion in Bakterien, wie *Escherichia coli* (*E. coli*), zu ermöglichen (**Abbildung 11**). [226c, 227, 236-237] Wie ihre natürlichen Vorbilder zeichnen sich rekombinante Proteine ebenfalls durch mechanische Belastbarkeit, niedrige Inflammationslevel und hohe Biokompatibilität aus. [235c, 239]

1.4.3. Funktionalisierung rekombinanter Spinnenseidenproteine

Die Verwendung von gentechnischen und molekularbiologischen Verfahren ermöglicht die Modifikation und Funktionalisierung rekombinanter Spinnenseidenproteine schon auf Gen-Basis für Material-bezogene Anwendungen (**Abbildung 11**). [240] Auf diese Weise können spezifische Aminosäuren in den repetitiven Modulen ausgetauscht werden, um beispielsweise verschieden geladene Proteine zu erhalten. Im Fall von eADF4(C16) resultiert der Austausch der negativ geladenen Glutaminsäure gegen einen Lysin-Rest im positiven eADF4(κ16) [241], oder in der ungeladenen eADF4(Ω16)-Variante, wenn ein Glutamin verwendet wird [242]. Ferner können Modifikationen am N- oder C-terminalen Ende der Aminosäuresequenz platziert werden. So können weitere Module oder Peptide, beispielsweise mit einem Cystein-Rest, eingefügt werden, um freie spezifische Schwefelreste für Kopplungsreaktionen zur Verfügung zu haben. Auf diese Weise sind eADF4(C16-C*) (C-terminale Modifikation) und eADF4(C*-C16) (N-terminale Modifikation) als Varianten mit zusätzlichem, modifiziertem

Modul entstanden. [243] Eine N-terminale Addition einer kurzen Peptidsequenz führte zu ntag^{Cys}-eADF4(C16) [243] und ntag^{Cys}-eADF4(κ16) [244]. Die freie Thiolgruppe konnte anschließend mit Gold-Nanopartikeln, Biotin oder β-Galaktosidase funktionalisiert werden, was die vielseitige Anwendbarkeit zeigt. [243-245] Die ntag^{Cys}-eADF4(C16) Variante wurde auch mit einem zyklischen RGD-Peptid funktionalisiert, um eine verbesserte Zellinteraktion mit Spinnenseidenfilmen zu erreichen. [246]

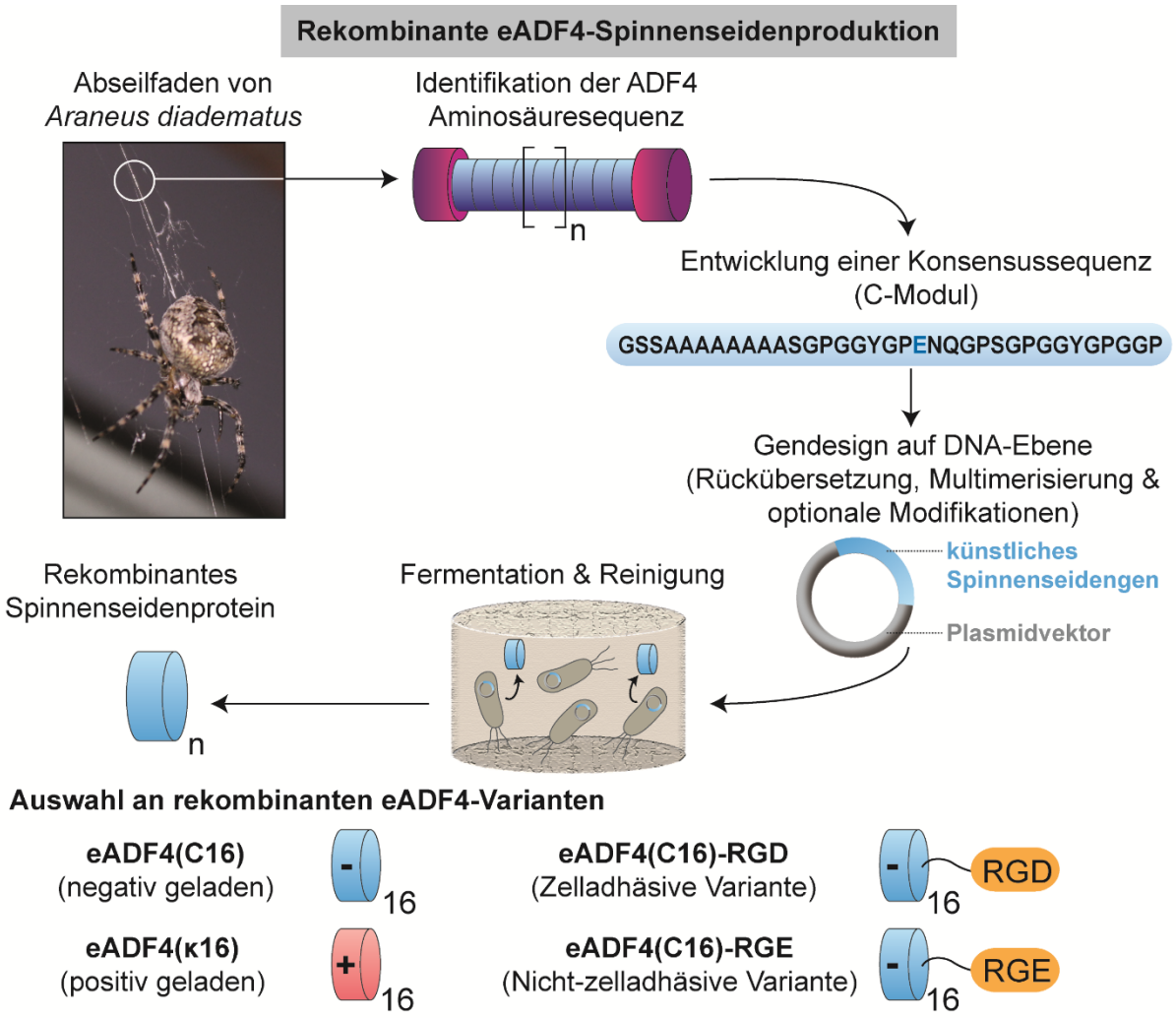

Abbildung 11: Rekombinante Spinnenseidenproduktion am Beispiel des negativ geladenen eADF4(C16). Nach der Identifikation der Aminosäuresequenz der repetitiven Proteine (Spidroine) des Abseilfadens von *Araneus diadematus*, wird eine Konsensus-Sequenz (C-Modul) entwickelt. Daraus wird ein Genkonstrukt generiert und in einen Plasmidvektor übertragen. Dieser ermöglicht die Fermentation zur Herstellung des Spinnenseidenproteins, das gereinigt werden muss. Dieses Klonierungssystem ermöglicht die Produktion modifizierter Spinnenseidenvarianten, beispielsweise der positiv geladenen eADF4(κ16)-Variante oder Peptid-funktionalisierter Varianten.

Im Vergleich wurde eADF4(C16) auch auf genetischer Ebene am C-Terminus mit einem adhäsiven RGD-Peptid und einem RGE-Kontroll-Peptid funktionalisiert, um eine stabile Modifikation zu generieren (**Abbildung 11**). [246] Auf diese Weise konnten weitere Peptid-modifizierte eADF4-Varianten generiert und prozessiert werden, um gerichtete

Zellinteraktion [247] oder kontrollierte Biomineralisation [248] zu ermöglichen. Enzymatische Proteaseschnittstellen für Cathepsine zwischen eADF4(C16) und einem Antigen-Peptid von Ovalbumin führten zu selektivem Schneiden. [249] Durch genetische Fusion wurden das grün fluoreszierende Protein (GFP) und das Enzym Esterase-2 N-terminal an eADF4(C16) gekoppelt. Beide Fusionsproteine konnten erfolgreich hergestellt und verarbeitet werden und behielten ihre fluoreszierenden beziehungsweise katalytischen Eigenschaften. [250] Zusätzlich wurden die beiden rekombinanten eADF3$(AQ)_{12}$ und eADF4(C16) Spinnenseidenproteine mit nicht-repetitiven N- und C-terminalen Domänen modifiziert, um das natürliche System möglichst genau zu imitieren. [229e, 251] Obwohl die meisten, modifizierten Varianten eine ähnliche Prozessierbarkeit wie die unmodifizierten Spinnenseidenproteine zeigten, können Veränderungen der grundlegenden Protein-Nettoladung und stark gegenteilig geladene Peptid-Sequenzen oder Domänen entscheidende Auswirkungen auf die Protein- oder Materialeigenschaften haben. [241, 247]

1.4.4. Spinnenseidengerüste für regenerative und medizinische Anwendungen

Die Modifikation von Spinnenseidengerüsten kann nicht nur auf genetischer Ebene erfolgen, sondern auch anhand von Verarbeitungsmethoden oder Kombination mit anderen Materialien. Rekombinante eADF4-Spinnenseidenproteine können in verschiedene Morphologien wie Filme, Beschichtungen, Partikel, Kapseln, Nanofibrillen, Hydrogele, Schäume, Einzelfasern und Vliese sowie Komposit-Materialien prozessiert werden. [225e] Da sich Spinnenseiden-materialien durch hohe Biokompatibilität, gering immunologisches Verhalten, langsame Degradation sowie mechanischer Belastbarkeit auszeichnen, sind sie für biomedizinische und gewebetechnische Anwendungen interessant (**Abbildung 12**). [231a, 231b, 235c, 239] So zeigen rekombinante eADF4-basierte Spinnenseidenproteine in verarbeiteter Form (z.B. Filme, Vliese oder Partikel) einen langsameren biologischen Abbau durch Modell-Enzyme als in löslicher Form. [252] Eine gute *in vivo* Biokompatibilität konnte für eADF4(C16)-basierte Materialien ebenfalls nachgewiesen werden. [249, 253] Da positiv geladene eADF4(κ16)-Partikel, im Vergleich zu negativ geladenen eADF4(C16)-basierten und neutral geladenen (Misch-) Partikeln, eine abweichende Protein-Corona bilden und eine erhöhte Blutkoagulation aufweisen, scheint die Biokompatibilität dieser Variante jedoch schlechter zu sein. [254]

1.4.4.1. Bioinerte und anti-adhäsive Spinnenseidenoberflächen

Aufgrund der Aminosäuren-Zusammensetzung zeigt eADF4(C16) im Hinblick auf die Zellinteraktion inhärente, anti-adhäsive Eigenschaften, die sich gut für biomedizinische Kontakt- und Implantat-Materialien einsetzen lassen. [246, 255] So konnten medizinisch relevante Polymermaterialien für Katheter mit eADF4(C16) beschichtet werden (**Abbildung 12**). Die Filme zeigten eine gute Stabilität, langsame Degradation durch Modell-Enzyme, sowie geringe Zellinteraktion. [256] Dünne eADF4(C16)-Beschichtungen auf Silikonimplantaten fungierten auch im *in vivo* Rattenmodell als biologischer Schutzschild und zeigten eine exzellente Biokompatibilität und Immunverträglichkeit, da sie die pro-inflammatorische Körperreaktion mit Kapselfibrose verhinderten. [253b, 253c] Viele natürlich vorkommende Spinnenseiden zeigen Mikroben-abstoßende Eigenschaften. [257] Beschichtungen aus rekombinanten eADF4(C16) zeigten auf rostfreien Stahl- und Silikonoberflächen eine deutlich verringerte Anhaftung von (potentiell) pathogenen Bakterien. [258] Auch eADF4(C16)-basierte strukturierte Filme und

Hydrogele konnten nicht von Mikroben besiedelt werden. [242] Zusätzlich erlaubt die biotechnologische Herstellung auch die Funktionalisierung rekombinanter Spinnenseiden-proteine mit antimikrobiellen Peptiden, um aktiv Mikroben-abtötende Materialien zu generieren. [257a, 259]

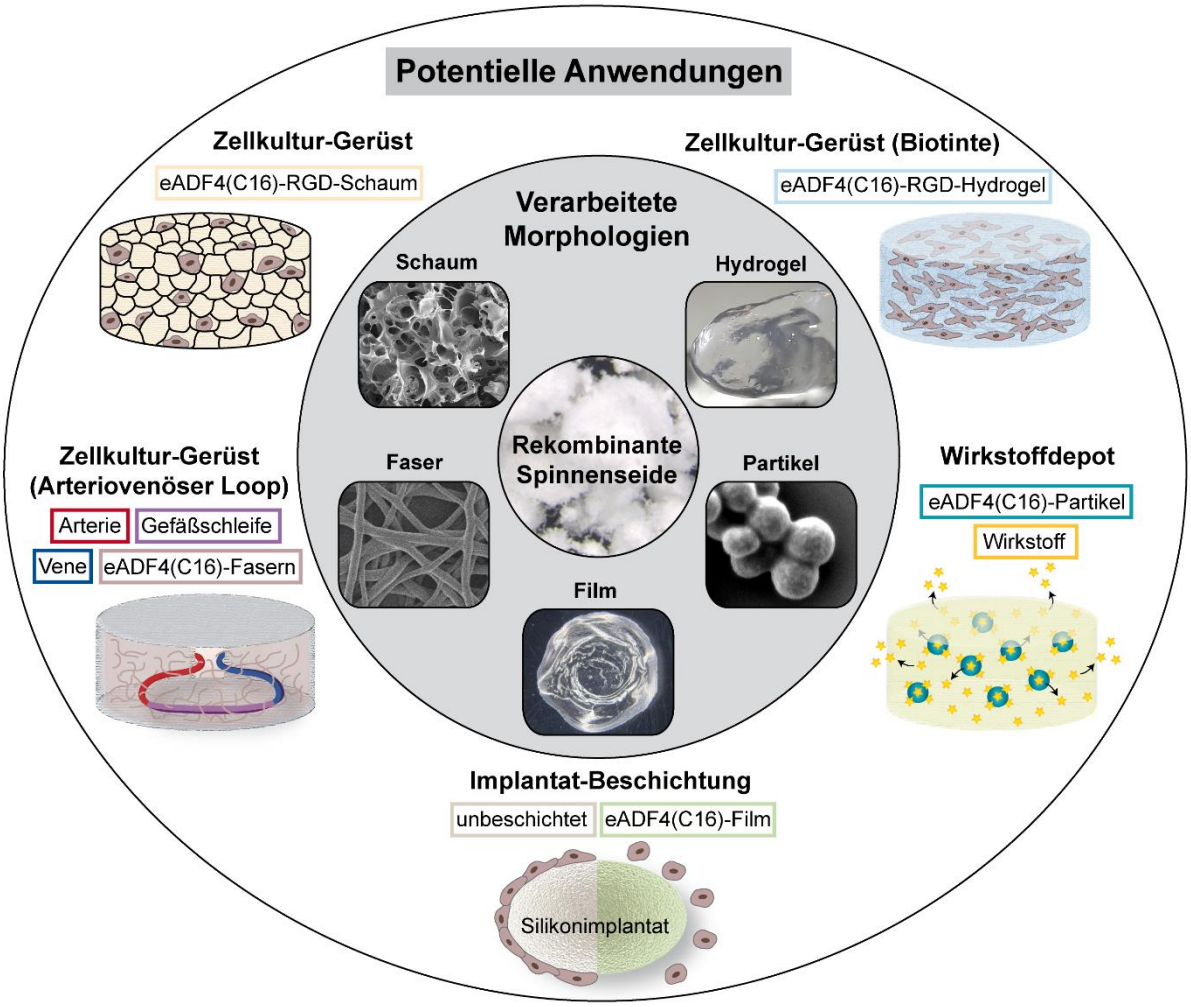

Abbildung 12: Rekombinante Spinnenseidenproteine können in Morphologien wie Filme, Partikel, Hydrogele, Schäume oder Fasern verarbeitet werden. Dadurch finden sie Anwendung als Implantat-Beschichtung, Wirkstoffdepot oder Zellkultur-Gerüst.

1.4.4.2. Spinnenseiden-basierte Gerüste für Gewebe- und Zellwachstum

Obwohl eADF4(C16)-basierte Materialien aufgrund ihrer Aminosäuren-Zusammensetzung keine zelladhäsiven Motive beinhalten und die Zelladhäsion reduziert ist [246, 255b], kann eine Zellinteraktion durch topographische Strukturen (z.B. Fasern oder Vliese) erreicht werden. [253a, 255a] So unterstützten rekombinante eADF4(C16)-Fasern die Bildung neuer Blutgefäße in einem Arteriovenösen Loop in Ratten (**Abbildung 12**). [253a] Strukturierte Filme aus verschiedenen, rekombinanten Seidenproteinen sind ebenfalls eine Möglichkeit, die Zellausrichtung und Kontaktführung zu beeinflussen. [260] Der positive Einfluss der Oberflächentopographie auf die Zellausrichtung konnte auch auf prozessierter, natürlicher Seide nachgewiesen werden. [234] Im Vergleich mit eADF4(C16) ermöglicht die Veränderung

der Nettoladung durch Aminosäureaustausch eine Zellinteraktion mit positiv geladenen eADF4(κ16)-Oberflächen. [255b, 256, 261] Aufgrund der elektrostatischen Wechselwirkungen zwischen negativ geladenen, zellulären Oberflächenmolekülen und positiv geladenen Oberflächen ist die ladungsgesteuerte Zelladhäsion ein bekannter Modifikationsmechanismus in der Zellkultur [262], der auf eADF4(κ16) und eADF4(C16) übertragbar ist.

Die genetische Modifikation mit zellstimulierenden Peptiden ermöglicht eine spezifische Interaktion mit Zellen. In diesem Kontext wurden eADF4-basierte rekombinante Spinnenseidenproteine mit dem zelladhäsiven RGD-Peptid funktionalisiert und zeigten deutlich verbesserte Zellinteraktion, unabhängig davon, ob Filme, Hydrogele oder Schäume verwendet wurden (**Abbildung 12**). [246, 261, 263] Die Modifikation eines anderen rekombinanten Spinnenseidenproteins (4RepCT, *Euprosthenops australis*) mit RGD-Sequenzen erhöhte ebenfalls die Zelladhäsion mit selbstassemblierten Filmen und Membranen. [264] Auf RGD-, IKVAV-, YIGSR- sowie RGE-funktionalisierten 4RepCT-Filmen zeigten Primär-Zellen nur bei der frühen Anhaftung entscheidende Unterschiede, während das generelle Zellwachstum auf allen Spinnenseidenvarianten verbessert war. [265] Pankreaszellen wiesen dagegen in RGD- und YIGSR-modifizierten 4RepCT-Schäumen eine gesteigerte Insulinproduktion auf, wobei die RGD-Variante *in vivo* in Mäusen die besten Ergebnisse erzielte. [266]

1.4.4.3. Spinnenseiden-basierte Systeme für Wirkstofffreisetzung

Wegen ihrer Eigenschaften eignen sich eADF4-basierte Spinnenseidenpartikel als System zur Freisetzung von Wirkstoffen, beispielsweise Peptid-Impfstoffen. [241, 249, 267] Aufgrund elektrostatischer Interaktionen zeigen negativ geladene eADF4(C16)- und positiv geladene eADF4(κ16)-Partikel eine bessere Ladungseffizienz und anschließende Freisetzung von Wirkstoffen, wenn die Substanzen entgegengesetzt geladen sind. [241, 267a] Zusätzlich ist die intrazelluläre Partikelaufnahme verbessert, wenn zellstimulierende Peptidmodifikationen angebracht sind. [247, 267d] Durch die Freisetzung der Modellsubstanzen Rinderserum-Albumin, Meerrettich-Peroxidase und Lysozym aus beladenen Hydrogelen beziehungsweise aus im Hydrogel-eingekapselten, beladenen Partikeln konnten eADF4(C16)-basierte Wirkstoff-freisetzende Depots entwickelt werden (**Abbildung 12**). [268] Für eine spätere Anwendung in der Krebstherapie wurden zusätzlich ein pH-Wert- und ein Redox-sensitives Kopplungssystem aus rekombinanten eADF4-Spinnenseidenvarianten entwickelt, welches eine gezielte Wirkstofffreisetzung bei einem bestimmten pH-Wert oder unter reduzierenden Bedingungen ermöglicht. [269] Auch Kompositmaterialien bestehend aus eADF4(C16)-Filmen oder Hydrogelen mit Antibiotika- und Antimykotika-beladenen, mesoporösen Silikapartikeln zeigten eine langsame und antimikrobiell wirksame Freisetzung der beladenen Substanzen, dabei aber keine Zytotoxizität. [270]

1.4.4.4. 3D-Spinnenseiden-Hydrogel-Gerüste und Biofabrikation

Durch ihre Aminosäuresequenz können eADF4(C16)-basierte Spinnenseidenproteine über einen Nukleationskeim-abhängigen Selbstassemblierungsmechanismus in β-Faltblatt-reiche Nanofibrillen assemblieren. In einem ersten Schritt bilden unstrukturierte Spinnenseidenproteine durch intramolekulare Interaktionen der Poly-Alanin-Bereiche metastabile Nukleationskeime. An diese lagern sich weitere ungefaltete Proteine durch

intermolekulare Wechselwirkungen an und strukturieren sich um, wodurch es zum Fibrillenwachstum kommt. [271] Liegen ausreichend hohe Proteinkonzentrationen vor, sind eADF4(C16)-basierte Spinnenseidenvarianten daher in der Lage nur durch physikalische Interaktionen nano-fibrilläre Hydrogel-Netzwerke auszubilden. [272] Zudem zeigen die Hydrogele viskoelastisches und scherverdünnendes Verhalten, weswegen sie als Matrix-material einer Biotinte für den 3D-Biodruck geeignet sind (**Abbildung 12**). [263b, 268, 270] Säugetierzellen sind ebenfalls in der Lage auf eADF4(C16)-RGD-Hydrogelen zu adhärieren und zu wachsen [263b, 270] Zusätzlich erlaubt der milde Gelierungsprozess bei 37 °C das Einkapseln von Säugetierzellen in einer 3D-Spinnenseidenmatrix ohne den Einsatz chemischer Quervernetzer, was die Druckbarkeit nicht nennenswert beeinflusst. [263b, 263c] Es ist außerdem möglich, Spinnenseidenhydrogele mit anderen Proteinen, wie Gelatine, zu mischen und als Biotinte in der Biofabrikation einzusetzen. [263c] Die Vielzahl der Studien, in denen funktionalisierte rekombinante Spinnenseide für die Gewebezüchtung verwendet wurde, bestätigt die große Bedeutung und Eignung von Materialien auf Basis von Spinnenseiden-proteinen in diesem Bereich.

2. Zielsetzung

Biomaterialgerüste sind essentielle Bestandteile der Gewebezucht und regenerativen Medizin, weil sie eine stabilisierende Kultivierungsmatrix für die eingebrachten Zellen darstellen, bis diese ihre eigene Mikroumgebung aufgebaut haben. Da das Ziel in der Unterstützung und der Regeneration von verletztem oder funktionslosem Ursprungsgewebe liegt, sollen diese Gewebegerüste eine erfolgreiche Zellantwort gewährleisten. In diesem Zusammenhang sind die Adhäsion, das Wachstum, die Migration und die Differenzierung von Zellen entscheidende Voraussetzungen, damit die vollständige Funktion wiederhergestellt werden kann. Zusätzlich ist die natürliche, zelluläre Mikroumgebung sehr komplex und Gewebe-spezifisch, weswegen ein besonderer Forschungsfokus auf dem Design und der Entwicklung von funktionalisierten und justierbaren Biomaterialgerüsten liegt. Es gibt daher eine ganze Reihe von Anforderungen (**Abbildung 13)**, die von einem anpassbaren Gewebegerüst erfüllt werden sollten.

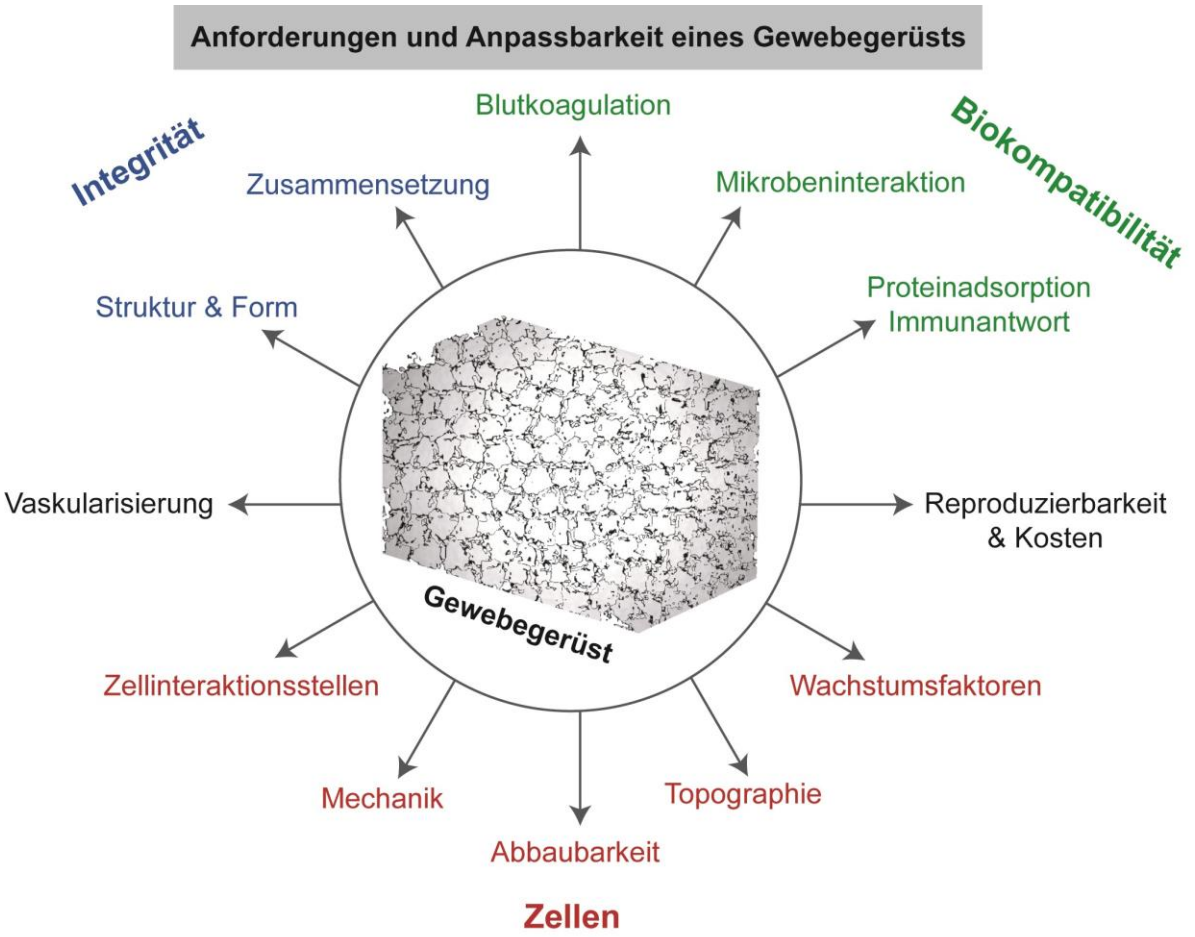

Abbildung 13: Anforderungen an künstliche Gewebegerüste, welche durch anpassbare, rekombinante Spinnenseidengerüste weitestgehend erfüllt werden sollen.

Aufgrund ihrer guten Biokompatibilität, langsamen Bioabbaubarkeit und den justierbaren, mechanischen Eigenschaften erfüllen Materialien auf Basis rekombinanter Spinnenseiden-proteine bereits einige Anforderungen von künstlichen Gewebegerüsten. Außerdem ermöglicht die rekombinante Herstellung die Funktionalisierung und Anpassbarkeit der Proteine auf

genetischem Level und stellt die Produktion des Ausgangsmaterials in ausreichender Menge mit gleichbleibender Qualität sicher, was für die Reproduzierbarkeit ein entscheidender Faktor ist. Das Ziel dieser Dissertation war daher die Herstellung und Charakterisierung von funktionalisierten Spinnenseidengerüsten für die Gewebezüchtung.

Basierend auf dem natürlichen ADF4-Protein des Abseilfadens der Gartenkreuzspinne (*Araneus diadematus*), dienten die negativ geladene eADF4(C16)-, die positiv geladene eADF4(κ16)- und die modifizierte eADF4(C16)-RGD-Spinnenseidenvariante als Ausgangsmaterial dieser Arbeit. Erste Modifikationen sollten auf genetischem Level erfolgen, indem zum einen das ungeladene eADF4(Ω16)-Spinnenseidenprotein durch Aminosäureaustausch und zum anderen funktionalisierte, zelladhäsive Varianten durch die Fusion mit kurzen bioaktiven Peptidsequenzen generiert und rekombinant hergestellt werden sollten. Der Einfluss dieser Peptide auf das Zellverhalten sollte mit verschiedenen Zelllinien untersucht werden, um selektive Varianten zu identifizieren. In diesem Kontext sollte zudem die Selbstassemblierung von rekombinanten Spinnenseidenproteinen in Nanofibrillen und Gele in Abhängigkeit von der Ladung, dem Lösungsmittel, den Peptidmodifikationen und anwesenden Zellen näher untersucht werden. Dies sollte die Entwicklung neuartiger Wirkstoffdepots zur kontinuierlichen Freisetzung hydrophiler und hydrophober Substanzen und der biochemischen Stimulation von Zellen ermöglichen. Eine gerichtete Zellinteraktion sollte aber auch durch variierende Prozessierungstechniken erreicht werden, um neben biochemischen Stimulatoren auch mechanische und topographische Effekte in die Gerüste einzubringen. Dabei sollten prozessierte Gradientenfilme natürliche Struktur- und Signalgradienten imitieren, um deren Einfluss auf Zellen zu analysieren. Die Oberflächentopographie sollte dabei die Adhäsion und die Ausrichtung der Zellen unterstützen und zur Identifikation von zellspezifischen Faktoren beitragen. Da rekombinante Spinnenseidenproteine auch in Anwesenheit von Säugetierzellen in mechanisch anpassbare und druckbare 3D-Netzwerke assemblieren können, sollten in dieser Arbeit auch Kompositionen und Eigenschaften von Biotinten näher charakterisiert werden. Dadurch sollte die Biofabrikation von komplexen Strukturen durch 3D-Extrusionsdruck optimiert werden. Gerade im Hinblick auf eine spätere Anwendung im menschlichen Körper, sollte zudem die Biokompatibilität von rekombinanten Spinnenseidengerüsten bezüglich Mikrobeninteraktion, Adsorption von Blutplasmaproteinen, Blutkoagulation und Immunantwort, sowie die biologische Abbaubarkeit *in vitro* evaluiert werden. Eine zusätzliche Untersuchung rekombinanter, eADF4(C16)-basierter Hydrogele im Rattenmodell sollte die Analyse der *in vivo* Immunantwort, Biodegradation und Vaskularisierbarkeit von Spinnenseidengerüsten komplettieren, um die Gewebeneubildung mit dem Aufbau neuer EZM bei simultanem Abbau der provisorischen Matrix zu verifizieren.

3. Synopsis

Die vorliegende Dissertation umfasst zwölf Teilarbeiten [57b, 242, 261, 273], die in Kapitel 7 vorgestellt werden. Es handelt sich dabei um zehn Daten-basierte Originalarbeiten und zwei Übersichts-Artikel, wovon acht als Erstautorin verfasst wurden. Die Schnittstelle dieser Teilarbeiten liegt in der Funktionalisierung, Fabrikation und Charakterisierung von bioaktiven, rekombinanten Spinnenseidengerüsten für die Anwendung in der Gewebezüchtung. Generell kann die vorliegende Arbeit in die drei großen Teilbereiche „Entwicklung, Herstellung und Charakterisierung funktionalisierter Spinnenseidenvarianten", „Analyse der Assemblierung von Spinnenseidenproteinen und deren Verarbeitung in hierarchische Strukturen" und „Biologische Evaluation von rekombinanten Spinnenseidengerüsten für die Gewebezüchtung" gegliedert werden. **Abbildung 14** veranschaulicht, welche Fragestellungen und Anforderungen an ein bioaktives Gerüst im Rahmen dieser Dissertation betrachtet und welche Methoden und Prozesse dafür verwendet wurden. Die dabei untersuchten Parameter wurden mit den Fragestellungen und Anforderungen in Relation gesetzt. Zudem werden sie durch die Farbabstufung den drei großen Teilbereichen (Pfeile in verschiedenen Grüntönen) zugeordnet und im Folgenden näher betrachtet.

Teilbereich I: Entwicklung, Herstellung und Charakterisierung funktionalisierter Spinnenseidenvarianten

Der erste Teilbereich dieser Dissertation fokussierte sich auf die Entwicklung, Herstellung und Charakterisierung neuer rekombinanter eADF4-Spinnenseidenvarianten im Hinblick auf deren potentiellen Einsatz in der Gewebezüchtung. Dabei entstand die ungeladene eADF4(Ω16)-Variante als Ergänzung zum negativ geladenen eADF4(C16) und positiv geladenen eADF4(κ16), die in sechs Teilarbeiten (**Teilarbeiten I, II, III, IV, V und VI**) zum Einsatz kam. Aufgrund der geringen Zelladhäsion auf eADF4(C16) wurde bereits vor Jahren das Integrin-bindende eADF4(C16)-RGD generiert, um eine gesteuerte Zellinteraktion zu ermöglichen [246]. In dieser Arbeit wurden eADF4(C16), eADF4(κ16) und eADF4(Ω16) mit weiteren kurzen, Zell-bindenden Peptiden aus natürlich vorkommenden EZM-Proteinen funktionalisiert, um eine zellspezifische Interaktion auszulösen. Eine selektive Anheftung bestimmter Zellen ist für die hierarchische Entwicklung von Geweben enorm wichtig und wird von der stark zellbindenden (zytophilen), jedoch zellunspezifischen RGD-Sequenz nicht gewährleistet (**Teilarbeiten I, II, XI und XII**).

Teilbereich II: Analyse der Assemblierung von Spinnenseidenproteinen und deren Verarbeitung in hierarchische Strukturen

Die Charakterisierung der Selbstassemblierung sowie die Verarbeitung rekombinanter Spinnenseidenproteine in Morphologien mit verschiedenen hierarchischen Strukturebenen sind weitere Bausteine zum Erstellen bioaktiver (Zellkultur-) Gerüste. In diesem Kontext ist hervorzuheben, dass sich Filme sehr gut als Substrat für diverse Basischarakterisierungen eignen, da sie einfach und schnell unter Verwendung einer geringen Proteinmenge herstellbar sind. Neben den charakteristischen Filmeigenschaften, wie Benetzbarkeit oder Protein-Sekundärstruktur, können auch potentielle Zellinteraktionen mit verschiedenen Seidenvarianten in Hochdurchsatz-Ansätzen analysiert werden (**Teilarbeiten I, II, III, IV und V**).

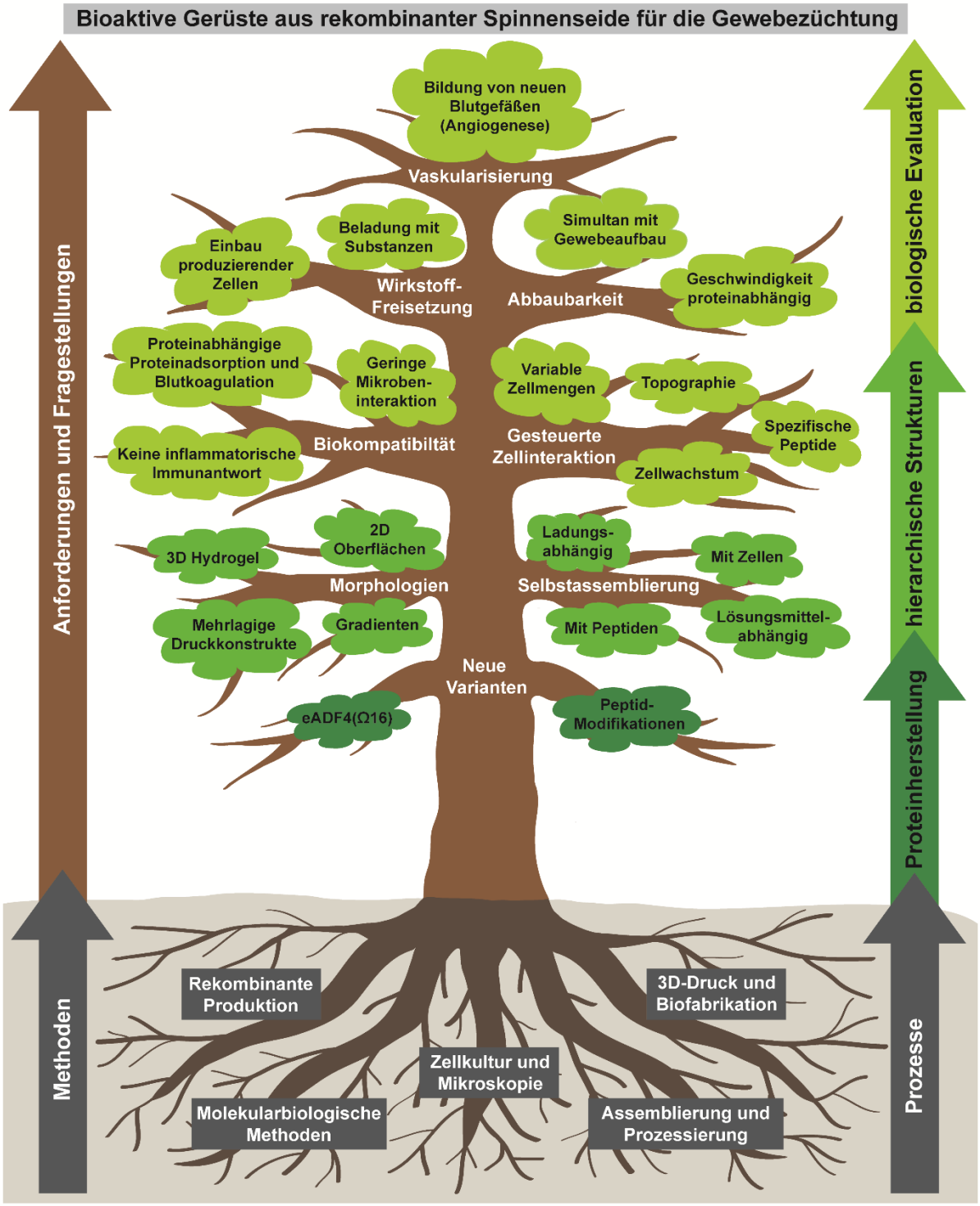

Abbildung 14: Übersicht über die in dieser Dissertation betrachteten Anforderungen und Fragestellungen (braun) zur Herstellung bioaktiver Spinnenseidengerüste sowie die dafür verwendeten Methoden und Prozesse (grau) und die untersuchten Parameter, die den drei großen Teilbereichen „Proteinherstellung“, „hierarchische Strukturen“ und „biologische Evaluation“ zugeordnet werden können (verschiedene Grüntöne).

Da Gradientenfilme eine gerichtete Zellanheftung ermöglichen können (**Teilarbeiten II, VII und XI**), wurden in dieser Arbeit Filmoberflächen mit biochemischen Signalgradienten aus zellbindenden (zytophilen) und zellabweisenden (zytophoben) Spinnenseidenvarianten

(**Teilarbeit II**) und Größengradienten mit diversen topographischen Oberflächenstrukturen generiert (**Teilarbeit VII**). Dennoch ist die Entwicklung einer 3D-Struktur für die Gewebezüchtung unerlässlich, um die natürliche Umgebung nachzuahmen. Durch intra- und intermolekulare Wechselwirkungen können eADF4(C16)-Varianten in Nano-Fibrillen [271a] und (zellbeladene) 3D Hydrogel-Netzwerke assemblieren [263b, 263c, 272a]. In dieser Dissertation wurde das Selbstassemblierungs- und Gelierungsverhalten rekombinanter eADF4-Varianten in Abhängigkeit von der Ladung, dem Lösungsmittel, zusätzlich angebrachten Peptidsequenzen und vorhandenen Zellen weiter analysiert (**Teilarbeiten IV, V, VI, VIII und IX**). Aufgrund ihrer rheologischen Eigenschaften eignen sich Seiden-Gele als azelluläre Tinten und Zell-beladene Biotinten für den 3D-Biodruck [263b, 263c, 274]. In dieser Arbeit konnten Spinnenseiden-basierte Hydrogele sowie Gele aus binären wässrig-organischen Mischungen in komplexe Strukturen verdruckt werden (**Teilarbeiten VI und VIII**). Zudem konnten druckbare Spinnenseiden-Biotinten mit verschiedenen Zellmengen generiert werden (**Teilarbeiten VIII und IX**).

Teilbereich III: Biologische Evaluation von rekombinanten Spinnenseidengerüsten für die Gewebezüchtung

Aufgrund der verschiedenen Kompositionen und Funktionen diverser Gewebe sind die biologischen und zellulären Anforderungen an ein bioaktives Gerüst für die Gewebezüchtung sehr vielfältig. Der wichtigste Parameter ist dabei sicherlich die Biokompatibilität eines Materials. Im Rahmen dieser Arbeit wurde die Biokompatibilität verschiedener Spinnenseiden-materialien einerseits *in vitro* anhand der Adsorption spezifischer Serumproteine (**Teilarbeiten II und III**), der Aktivierung der Blutkoagulation (**Teilarbeit III**) und der Interaktion verschiedener Mikroben (**Teilarbeiten IV und V**) untersucht. Anderseits konnte die exzellente Biokompatibilität von Spinnenseidenhydrogelen auch *in vivo* in einem Rattenmodell anhand der ausbleibenden Inflammations- und Immunantwort (**Teilarbeit X**) bestätigt werden.

Neben der Biokompatibilität spielt die gezielte Interaktion von Zellen mit dem eingebrachten Material eine entscheidende Rolle in der Gewebezüchtung. Durch die Fusion von Integrin-bindenden RGD-Peptiden konnte eine Interaktion von Zellen mit Spinnenseidengerüsten durch biochemische Stimulation gewährleistet werden (**Teilarbeiten I, II, IV, V, VIII, IX, X und XII**). Neben der erfolgreichen Zelladhäsion (**Teilarbeiten I und II**) waren auch Zellüberleben (**Teilarbeiten I, IV, V, VIII und IX**), Zellwachstum (**Teilarbeiten II, IV, V, IX und X**) und spezifische Zellfunktionen (**Teilarbeiten I, IX und X**) nachweisbar. Weiterhin konnten die im Rahmen dieser Doktorarbeit hergestellten Peptid-modifizierten Spinnenseidenvarianten für die selektive Anheftung ausgewählter Zelltypen genutzt werden, was eine Grundvoraussetzung für den Aufbau strukturierter Gewebe darstellt (**Teilarbeit II**). In diesem Kontext war auch die gerichtete Zellinteraktion durch einen biochemischen Signalgradienten (**Teilarbeit II**) und einen Größengradienten diverser Oberflächenstrukturen erfolgreich (**Teilarbeit VII**).

Im Hinblick auf die spätere Anwendung im Körper ist eine langsame, simultan zum Gewebe-aufbau angepasste Biodegradation der Gerüstmaterialien essentiell. Diese Gerüste bieten den Zellen zuerst Interaktionsstellen sowie die nötige Stabilität und werden nach der Gewebe-Rekonstruktion komplett durch körpereigene EZM ersetzt. Zusätzlich zu einer *in vitro* Abbau-Studie von fünf Spinnenseidenproteinen mit zwei Modell-Enzym-Mischungen (**Teilarbeit III**)

konnte eine langsame Biodegradation eADF4(C16)-basierter Hydrogele mit gleichzeitiger Gewebe-Neubildung in einem Rattenmodell nachgewiesen werden (**Teilarbeit X**).

Für einige medizinische Anwendungen ist eine gezielte Freisetzung bioaktiver, stimulierender Substanzen nötig. Diese Anforderung wurde in der vorliegenden Dissertation durch einen chemischen und einen Zell-basierten Weg gelöst (**Teilarbeiten VI und IX**). Einerseits wurde die Formulierung und Freisetzung von wasserunlöslichen, bioaktiven Stoffen mithilfe einer neu entwickelten Gel-Herstellungsmethode basierend auf wässrig-organischen Mischungen erreicht (**Teilarbeit VI**). Andererseits ermöglichte das Einkapseln modifizierter Produktionszellen in Spinnenseiden-Biotinten die kontinuierliche Produktion und Freisetzung eines bioaktiven, wasserlöslichen Faktors über einen längeren Zeitraum (**Teilarbeit IX**). Da die freie Diffusionsgrenze von Substanzen in Geweben bei etwa 200 µm liegt [275], ist die Ausbildung eines gut strukturierten Blutgefäßsystems innerhalb künstlicher Gewebe-Konstrukte essentiell für die Versorgung mit Nährstoffen und Sauerstoff und dem Abtransport von Stoffwechselprodukten und Kohlenstoffdioxid [276]. Im Rahmen dieser Arbeit wurde die erfolgreiche Vaskularisierung eADF4(C16)-basierter Hydrogele in einem *in vivo* Rattenmodell gezeigt, was entscheidend für die spätere Anwendung in der Gewebezucht ist (**Teilarbeit X**).

3.1. Entwicklung, Herstellung und Charakterisierung funktionalisierter Spinnenseidenvarianten

Um rekombinante Spinnenseidengerüste zu modifizieren, können Funktionalisierungen bereits in das entsprechende Genkonstrukt mittels molekularbiologischer Methoden eingebracht werden. [240] Nach der rekombinanten Herstellung liegt eine spezifische Proteinvariante vor, die eine nachträgliche, chemische Modifikation überflüssig macht. Auf diese Weise können bestimmte Aminosäuren gezielt ausgetauscht oder Peptidsequenzen innerhalb des Proteins eingebaut werden. Etablierte, molekularbiologische Techniken [227, 241, 246-247] wurden im Rahmen der vorliegenden Dissertation genutzt, um das Portfolio an neuartigen, modifizierten Spinnenseidenproteinen mittels rekombinanter Produktion zu erweitern (**Abbildung 15**).

3.1.1. eADF4(Ω16) als ungeladene Variante

Durch den gezielten Austausch der negativ geladenen Glutaminsäure (E) durch das ungeladene Glutamin (Q) in der repetitiven Einheit wurde das ungeladene eADF4(Ω16) generiert. Diese Variante erweiterte das Portfolio von negativ geladenen eADF4(C16)- und positiv geladenen eADF4(κ16)- Varianten und ermöglichte die Charakterisierung grundlegender Mechanismen und Eigenschaften von eADF4-basierten Spinnenseidenproteinen in Abhängigkeit von der Ladung. In den **Teilarbeiten IV und V** konnte eADF4(Ω16) dazu beitragen, den generellen Mechanismus der Mikrobenabstoßung von eADF4(C16)- und eADF3(AQ)-basierten Gerüsten auf molekularer Ebene aufzuklären und ein Modell zur Mikrobenadhäsion zu entwickeln (siehe 3.3.1.2.). Die Verwendung von eADF4(Ω16)-Beschichtungen ermöglichte in **Teilarbeit III** eine direkte und grundlegende Charakterisierung von ADF3- und ADF4-basierten Spinnenseidenproteinen basierend auf der Proteinladung und der zugrundeliegenden Proteinsequenz im Hinblick auf deren potentielle Anwendungen in der Biomedizin (siehe 3.3.1.1., 3.3.2.1. und 3.3.3.1). In den **Teilarbeiten IV, V und VI** wurde mittels eADF4(Ω16) das Assemblierungs-

verhalten eADF4-basierter Proteine in wässriger Umgebung oder in Anwesenheit von Kaliumphosphat oder organischem Co-Lösungsmittel in Abhängigkeit von der Proteinladung charakterisiert (siehe 3.2.1.1. und 3.2.1.2.). Außerdem zeigte sich in den **Teilarbeiten I, II und III** unabhängig voneinander, dass Materialien aus ungeladenem eADF4(Ω16) als zellabweisend (zytophob) eingestuft werden können (siehe 3.3.1.1. und 3.3.2.1.).

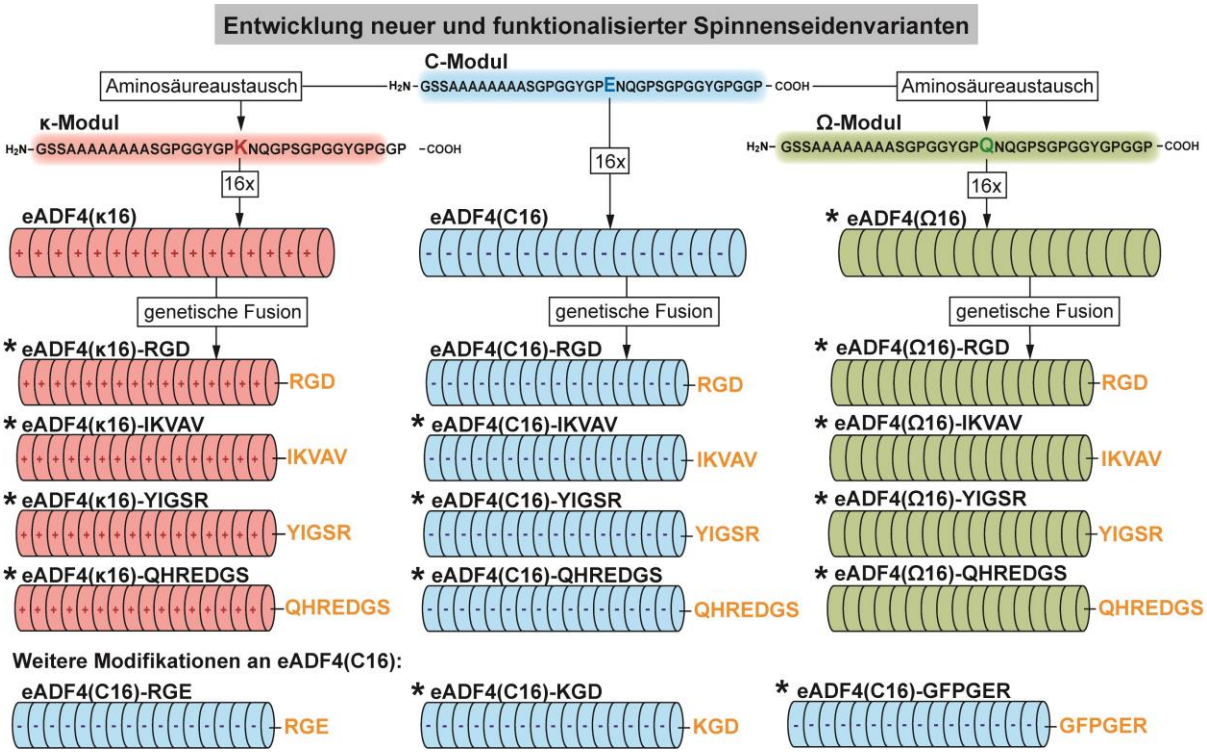

Abbildung 15: Übersicht eADF4-basierter rekombinanter Spinnenseidenproteine. Der negativ geladene Glutaminsäure-Rest (E) im ursprünglichen C-Modul wurde im κ-Modul durch einen positiv geladenen Lysin- (K) und im Ω-Modul durch einen ungeladenen Glutamin-Rest (Q) ersetzt. Durch 16-fache Wiederholung entstanden die rekombinanten Spinnenseidenproteine eADF4(C16), eADF4(κ16) und eADF4(Ω16). Durch genetische Fusion an das DNA-Konstrukt wurden diese Proteine mit kurzen Peptidsequenzen modifiziert, um eine gerichtete Zellinteraktion zu ermöglichen. Die mit einem * markierten Proteine wurden im Rahmen dieser Doktorarbeit designt und hergestellt. Modifiziert nach [273b] und reproduziert mit freundlicher Genehmigung des Verlags John Wiley & Sons (© 2023 The Authors. Advanced Healthcare Materials published by Wiley-VCH GmbH).

3.1.2. Peptid-modifizierte Spinnenseidenproteine

Die gerichtete Interaktion von Zellen mit Spinnenseidengerüsten stellte einen wichtigen Teil dieser Doktorarbeit dar. Infolgedessen wurden kurze, potentiell zelladhäsive Peptidsequenzen aus EZM-Proteinen an eADF4(C16), eADF4(κ16) und eADF4(Ω16) fusioniert, um eine Wechselwirkung mit zellulären Oberflächenrezeptoren zu erreichen. In **Teilarbeit I** wurden RGD-modifizierte eADF4(C16)-, eADF4(κ16)- und eADF4(Ω16)-Oberflächen als geeignete Interaktionsmatrizes für Stammzell-induzierte Kardiomyozyten identifiziert, welche zudem die Ausbildung zellspezifischer Funktionen unterstützten (siehe 3.3.2.3.). Die Funktionalisierung rekombinanter Spinnenseide mit weiteren Zellbindemotiven ermöglichte in **Teilarbeit II** außerdem eine selektive Adhäsion von speziellen Zelltypen (siehe 3.3.2.3.).

3.2. Analyse der Assemblierung von Spinnenseidenproteinen und deren Verarbeitung in hierarchische Strukturen

3.2.1. Charakterisierung der Selbstassemblierung von Spinnenseidenproteinen

Eine Grundanforderung eines erfolgreichen Gerüsts für die Gewebezucht liegt darin, Zellen eine 3D Umgebung für Interaktionen zu bieten. Von löslichen eADF4(C16)-basierten Spinnenseidenproteinen ist bereits bekannt, dass sie mittels eines Nukleationskeim-abhängigen Mechanismus aus einem intrinsisch unstrukturierten Zustand in β-Faltblatt-reiche Nanofibrillen assemblieren [271a]. Bei entsprechend hoher Proteinkonzentration, kann sich nur durch physikalische Wechselwirkungen und ohne zusätzliche Quervernetzer ein nanofibrilläres 3D Hydrogel-Netzwerk ausbilden [272a]. Diese Selbstassemblierung wird durch geladene Ionen, vor allem Phosphat-Ionen, unterstützt [263c, 271a, 274]. Außerdem beschleunigt das an eADF4(C16) fusionierte RGD-Peptid die Selbstassemblierung und Gelbildung [263c]. Daher wurde in dieser Dissertation das Selbstassemblierungsverhalten von eADF4-basierten rekombinanten Spinnenseidenproteinen weiter charakterisiert und ein Hauptaugenmerk auf den Einfluss von Proteinladung, Lösungsmittel, Fusionspeptiden und beigemengten Zellen gelegt. Die beobachteten Ergebnisse und daraus geschlussfolgerten Mechanismen wurden in **Tabelle 1** zusammengefasst. Es können auch mehrere Effekte gleichzeitig auftreten.

3.2.1.1. Einfluss der Proteinladung

Durch eADF4(Ω16) lag neben den bei physiologischem pH-Wert negativ geladenen eADF4(C16)- und positiv geladenen eADF4(κ16)-Proteinen eine ungeladene eADF4-Variante vor, weswegen die Selbstassemblierung in Abhängigkeit von der Proteinladung untersucht wurde. In den **Teilarbeiten IV, V und VI** stellte sich heraus, dass alle drei Spinnenseidenproteine in wässriger Umgebung grundsätzlich in der Lage waren, Nanofibrillen zu bilden. Das negativ geladene eADF4(C16) zeigte eine bekannte, langsame Assemblierung, bei der sich lösliche Proteine zu β-Faltblatt-reichen Nukleationskeimen zusammenlagern, mit denen lösliche Monomere interagieren, sich umstrukturieren und zum Fibrillenwachstum beitragen [271a]. Im Vergleich mit eADF4(C16) ist die positiv geladene eADF4(κ16)-Variante aufgrund von unkontrollierten Protein-Protein-Wechselwirkungen anfälliger für Proteinaggregation. Da eine Temperaturreduktion die Aggregation verstärkte, musste die Zeit-abhängige Aggregation durch verkürzte Dialyse bei RT verringert werden. Dabei konnte ein stabilisierender Effekt von noch vorhandenem Denaturierungsmittel (chaotropes Guanidiniumthiocyanat) festgestellt werden. Die ionischen Interaktionen mit eADF4(κ16) hielten das Protein in Lösung, verlangsamten die Aggregation und förderten die kontrollierte Selbstassemblierung durch intra- und inter-molekulare Wechselwirkungen (**Teilarbeit VI)**. Das ungeladene eADF4(Ω16) ist ebenfalls anfällig für Proteinaggregation. Im Gegensatz zu eADF4(C16) und eADF4(κ16) wurde eADF4(Ω16) zunächst bei 4 °C dialysiert, um eine vorwiegend Temperatur-gesteuerte Aggregation zu verlangsamen. Diese war bei eADF4(Ω16) aufgrund der vielen hydrophoben Bereiche in der Proteinsequenz verstärkt, da vermehrt unkontrollierte Protein-Protein-Interaktionen anstelle stabilisierender Protein-Lösungsmittel-Wechselwirkungen auftraten. Zeit-abhängige Aggregation spielte dagegen eine eher untergeordnete Rolle.

Tabelle 1: Einfluss und Effekt von Proteinladung, Lösungsmittel, Fusionspeptiden und beigemengten Zellen auf das Selbstassemblierungsverhalten von rekombinanten eADF4-basierten Spinnenseidenvarianten in Nanofibrillen. Abkürzungen: DMSO: Dimethylsulfoxid, SA: Selbstassemblierung, KPi: Kaliumphosphat, (0) direkte Zellzugabe, (+) Zellzugabe während des Fibrillen-Wachstums, (-) nicht vorhanden.

Parameter	Protein	Ladung	Peptid	Lösungs-mittel	Zellen	Effekt
Protein-ladung	eADF4(C16)	Negativ	-	Puffer	-	Langsame SA
	eADF4(κ16)	Positiv	-	Puffer	-	Schnelle, durch stabilisierende Ionen kontrollierte SA
	eADF4(Ω16)	Ungeladen	-	Puffer	-	Sehr schnelle, teilweise unkontrollierte SA
Lösungs-mittel (KPi)	eADF4(C16)	Negativ	-	Puffer & 150 mM KPi	-	Beschleunigte SA und stabile Gelbildung
	eADF4(κ16)	Positiv	-	Puffer & 150 mM KPi	-	Beeinträchtigung der SA und instabilere Gele
	eADF4(Ω16)	Ungeladen	-	Puffer & 150 mM KPi	-	Beschleunigte SA in Fibrillen und Ausfällen von Partikeln
Lösungs-mittel (DMSO)	eADF4(C16)	Negativ	-	Puffer & DMSO	-	Gleichbleibende SA und stabile Gele unabhängig von DMSO
	eADF4(κ16)	Positiv	-	Puffer & DMSO	-	Langsamere SA und instabilere Gele mit steigendem DMSO
	eADF4(Ω16)	Ungeladen	-	Puffer & DMSO	-	Langsamere SA und stabilere Gele mit steigendem DMSO
Fusions-peptid	eADF4(C16)	Negativ	Ja	Puffer	-	Beschleunigung der SA
	eADF4(κ16)	Positiv	Ja	Puffer	-	Stabilisierung der SA
	eADF4(Ω16)	Ungeladen	Ja	Puffer	-	Stabilisierung der SA
Zellen	eADF4(C16)	Negativ	-	Puffer & Medium	Ja	0) Beschleunigte SA +) Verlangsamte SA
	eADF4(C16)	Negativ	RGD	Puffer & Medium	Ja	0) Gleichbleibende SA +) Gleichbleibende SA
	eADF4(C16)	Negativ	RGE	Puffer & Medium	Ja	0) Verlangsamte SA +) Verlangsamte SA

Nach der Dialyse konnten sich dann die spezifischen hydrophoben Wechselwirkungen zwischen den Poly-Alanin-Bereichen ausbilden, welche zur Bildung von β-Faltblatt-reichen Nanofibrillen führten. Die Geschwindigkeit der bereits bekannten Nukleationskeim-abhängigen Assemblierung [271a] war bei eADF4(κ16) und eADF4(Ω16) jedoch stark beschleunigt (**Teilarbeit VI)**. Anhand von zeitabhängigen Trübungsmessungen (Gelierungskinetiken, **Abbildung 16**) zeigte sich, dass die Fibrillenbildung bei eADF4(κ16) nach etwa drei Stunden und bei eADF4(Ω16) nach einer Stunde abgeschlossen war, während bei eADF4(C16) einige Stunden (mindestens 16-20 h) benötigt wurden. Die erfolgreiche Bildung von Nanofibrillen konnte für eADF4(C16)-, eADF4(κ16)- und eADF4(Ω16)-Varianten außerdem mittels Transmissions-Elektronenmikroskopie (TEM) bestätigt werden (**Abbildung 17**). In **Teilarbeit VI** bildete eADF4(κ16) unter den beschriebenen stabilisierenden Bedingungen bei einer Proteinkonzentration von 20 mg/ml ein Hydrogel

(**Abbildung 16** (II)). Eine Konzentration von 10 mg/ml führte bei eADF4(Ω16) zu viskosen Lösungen, aber noch zu keinem stabilen Hydrogel (**Abbildung 16** (III)). Eine vollständige Hydrogel-Assemblierung konnte in den **Teilarbeiten IV und V** ab einer Konzentration von 20 mg/ml nachgewiesen werden.

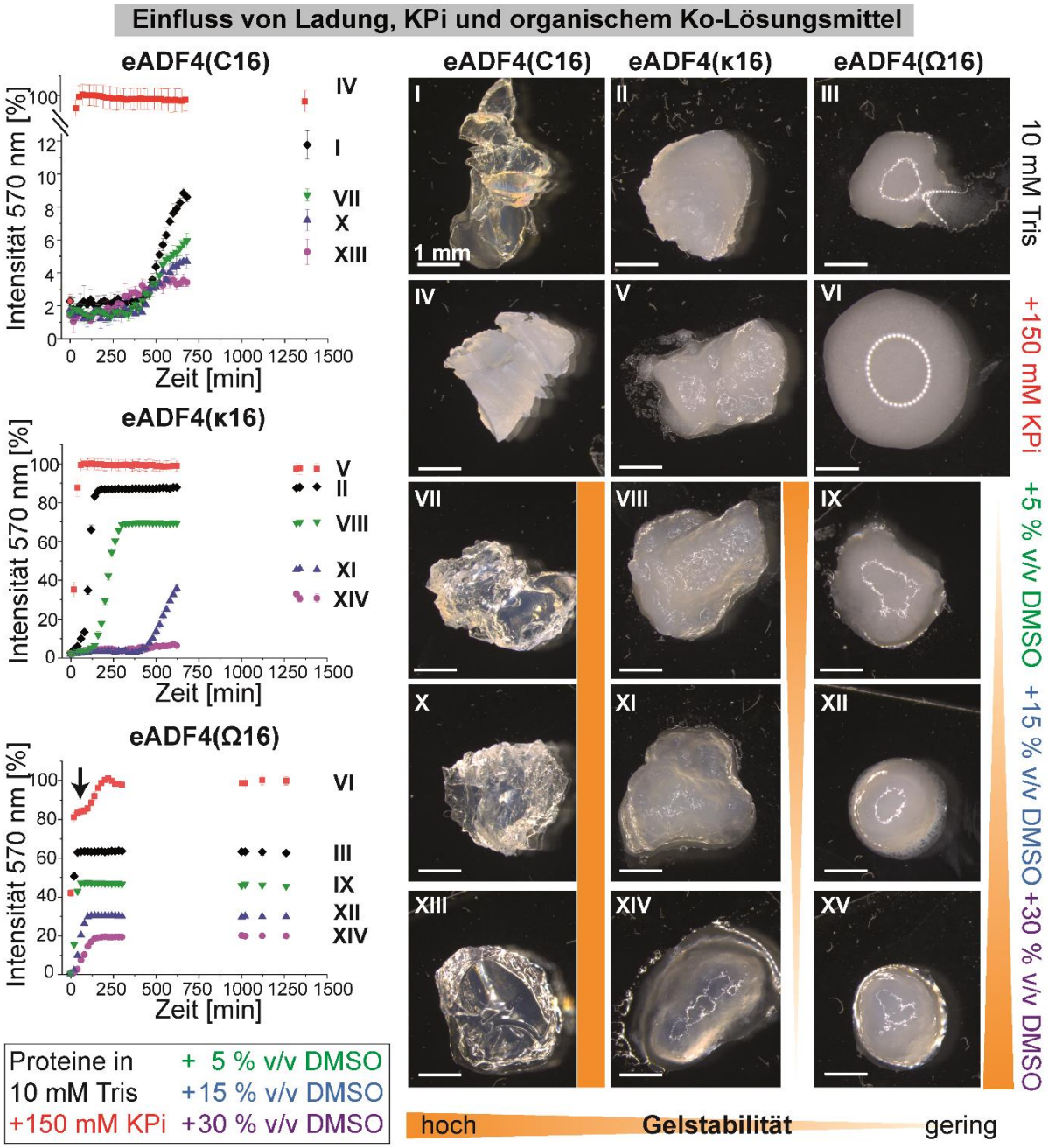

Abbildung 16: Zeit-abhängige Trübungsmessungen und Stereomikroskopieaufnahmen zeigen, wie Proteinladung, kosmotropes Kaliumphosphat (KPi) und organisches Lösungsmittel (DMSO) die Selbstassemblierung und Gelstabiliät von eADF4(C16), eADF4(κ16) und eADF4(Ω16) im wässrigen System beeinflussen. Modifiziert nach [273f] und reproduziert mit freundlicher Genehmigung des Verlags John Wiley and Sons (© 2021 The Authors. Angewandte Chemie International Edition published by Wiley-VCH GmbH).

3.2.1.2. Einfluss des Lösungsmittels

Bisher wurde die fibrilläre Selbstassemblierung von eADF4(C16)-basierten, rekombinanten Spinnenseidenproteinen in wässriger Pufferumgebung in An- oder Abwesenheit von verschiedenen Ionen und Komponenten aus Zellkulturmedien (Serumproteine (FCS), Zucker, Salze,…) analysiert [263c, 271a, 277]. Dabei konnte festgestellt werden, dass vor allem ionische Komponenten des Zellkulturmediums, wie Ca^{2+} [277a] oder kosmotropes Kaliumphosphat (KPi) [271a, 277b], die Fibrillisierung beschleunigten. In **Teilarbeit VI** wurde der KPi-induzierte Assemblierungsmechanismus von Seidenproteinen zu Nanofibrillen und Partikeln weiter charakterisiert. Für eADF4(C16) war bekannt, dass KPi bis zu einer Konzentration von 300 mM zu einer kontrollierten Nanofibrillen-Formation führt. Eine alleinige Präzipitation von Partikeln (ohne Fibrillenbildung) erfolgte erst bei KPi-Konzentrationen über 400 mM, was in der erhöhten Interaktion von eADF4(C16) mit Ionen des wässrigen Puffersystems begründet ist [271b]. Daher ermöglichte die Zugabe von 150 mM KPi zu eADF4(C16) eine schnellere Fibrillen-[271a] und Gelbildung (**Abbildung 16** (IV)). Im Gegensatz dazu führte die Anwesenheit von KPi beim positiv geladenen, Aggregations-anfälligen eADF4(κ16) zu einer Beeinträchtigung der Fibrillenbildung und zu instabileren Gelen (**Abbildung 16** (V)). Dies kann möglicherweise auf die Beschleunigung von unkontrollierten Proteininteraktionen zurückgeführt werden, bedarf jedoch weiterer Untersuchung. Beim ungeladenen eADF4(Ω16) bewirkte KPi eine verringerte Interaktion mit der wässrigen Pufferumgebung, weswegen Protein-Protein-Wechselwirkungen begünstigt waren. Folglich wurden Partikel schon bei niedrigerer KPi-Konzentration (ca. 150 mM) gebildet (**Abbildung 16** (VI)). Die Übergangsphase von Fibrillen zu Partikeln lag für eADF4(Ω16) zwischen 100 und 200 mM KPi, während sie bei eADF4(C16) zwischen 300 und 400 mM KPi zu finden war [271b]. Diese Verschiebung zu niedrigeren Partikel-Präzipitations-Konzentrationen wurde durch TEM-Aufnahmen und einem geringeren Ammoniumsulfat-Verbrauch bei der Reinigung bestätigt.

Weiterhin wurde in **Teilarbeit VI** der Einfluss von binären wässrig-organischen Mischungen auf das Selbstassemblierungsverhalten von eADF4-basierten Proteinen untersucht, um den Einbau und die stetige Freisetzung wasserunlöslicher Substanzen aus Spinnenseidengelen zu ermöglichen (siehe 3.3.4.). Dafür wurden wässrige Proteinlösungen anteilsmäßig mit dem amphiphilen, organischen Lösungsmittel Dimethylsulfoxid (5 %, 15 % und 30 % (v/v) DMSO) versetzt. Es wurden sowohl die Assemblierungskinetiken der Proteine anhand von Trübungsmessungen UV-Vis-spektroskopisch analysiert als auch die resultierenden, gelartigen Konstrukte auf ihre Stabilität geprüft und mittels Stereomikroskopie visualisiert (**Abbildung 16**). Dabei offenbarten sich sehr deutliche, von der Proteinladung abhängige Unterschiede. Während die negativ geladene eADF4(C16)-Variante unabhängig von beigemengten DMSO in einer ähnlichen Geschwindigkeit in gleichbleibend stabile, transparente Gele assemblierte (**Abbildung 16** (I, VII, X, XIII)), wurden die Gele der positiv geladenen eADF4(κ16)-Variante mit steigendem DMSO-Anteil instabiler und viskoser (**Abbildung 16** (II, VIII, XI, XIV)). Da die Beimengung von DMSO zusätzlich zu einer Verdünnung der Proteinkonzentration und einer deutlichen Verlangsamung der Assemblierung führte, könnten sich diese Änderungen ebenfalls negativ beeinflussen und zu der verringerten Gelstabilität geführt haben. Interessanterweise zeigte die ungeladene eADF4(Ω16)-Variante genau entgegengesetzte

Eigenschaften. Mit steigender Menge an DMSO und gleichzeitiger Reduktion der Proteinkonzentration wurden die resultierenden „Gele“ stabiler (**Abbildung 16** (III, IX, XII, XV)). Anhand der Trübungsmessungen wurde ersichtlich, dass mit zunehmender DMSO-Konzentration die Selbstassemblierung von eADF4(Ω16) langsamer ablief. Diese Ergebnisse zeigten deutlich, dass das amphiphile DMSO gut mit hydrophoben Bereichen in eADF4-basierten Proteinen interagieren kann. Vor allem bei eADF4(Ω16) unterstützt DMSO die Selbstassemblierung durch verbesserte Proteininteraktionen gegenüber Aggregation, sodass sogar bei geringerer Proteinkonzentration stabilere Gele entstehen.

3.2.1.3. Einfluss von Fusionspeptiden

Mit der Entwicklung der zelladhäsiven eADF4(C16)-RGD Variante [246] konnte der Selbstassemblierungsmechanismus Peptid-funktionalisierter Seidenvarianten analysiert werden. Die Anwesenheit des kurzen RGD-Fusionspeptids führte dabei zu einer schnelleren Assemblierung im Vergleich zu eADF4(C16) [277a]. Daher wurde die Selbstassemblierung Peptid-modifizierter Spinnenseidenvarianten im Rahmen dieser Arbeit weiter charakterisiert (**Teilarbeiten VIII und IX**). Die beschleunigte Fibrillen-Bildung eADF4(C16)-basierter Proteine durch ein Fusionspeptid konnte in **Teilarbeit VIII** anhand von Trübungsmessungen mit eADF4(C16)-RGD und der eADF4(C16)-RGE Kontrollvariante bestätigt werden (rote Kurven in **Abbildung 17B**). Sie konnte exemplarisch auch für eADF4(C16)-KGD, eADF4(C16)-IKVAV und eADF4(C16)-QHREDGS nachgewiesen werden. Zusätzlich ermöglichte das RGD-Fusionspeptid, dass eADF4(κ16) in fibrilläre Strukturen assemblierte (**Abbildung 17A**). Im Fall des ungeladenen, schnell assemblierenden eADF4(Ω16)-Proteins verlangsamte die RGD-Modifikation dagegen die Selbstassemblierungsgeschwindigkeit. Da das RGD-Peptid mit Arginin (R) und Asparaginsäure (D) zwei geladene Aminosäurereste beinhaltet, wird die Interaktion RGD-modifizierter Varianten mit der wässrigen Pufferumgebung erhöht. Der beobachtete Effekt kann auf andere, modifizierte Spinnenseidenvarianten übertragen werden, da die Fusionspeptide ebenfalls geladene Aminosäurereste beinhalten. Diese haben vor allem in Kombination mit den Aggregations-anfälligen eADF4(κ16)- und eADF4(Ω16)-Seidenproteinen eine stabilisierende Wirkung und ermöglichen eine kontrollierte Assemblierung basierend auf gerichteten inter- und intramolekularen Wechselwirkungen.

3.2.1.4. Einfluss von Zellen

Abschließend wurde die Selbstassemblierung von eADF4(C16)-basierten Seidenproteinen in Anwesenheit von Zellen untersucht. Es ist zwar bekannt, dass Säugetierzellen in eADF4(C16)- und eADF4(C16)-RGD-Hydrogele eingekapselt werden können [263b, 263c], jedoch wurde der zelluläre Einfluss auf deren Assemblierungsverhalten nicht näher charakterisiert. Daher wurde in **Teilarbeit VIII** der Effekt von Zellen direkt zu Beginn der Assemblierung, aber auch während des exponentiellen Fibrillen-Wachstums nach der Entstehung erster Nukleationskeime analysiert. Dafür wurden neben eADF4(C16) auch die zelladhäsive eADF4(C16)-RGD- und die nicht-zellbindende eADF4(C16)-RGE-Variante untersucht. Diese beiden Varianten eigneten sich gut zur Detektion möglicher zellulärer Unterschiede, da genau eine für die Zellinterkation essentielle Aminosäure ausgetauscht ist.

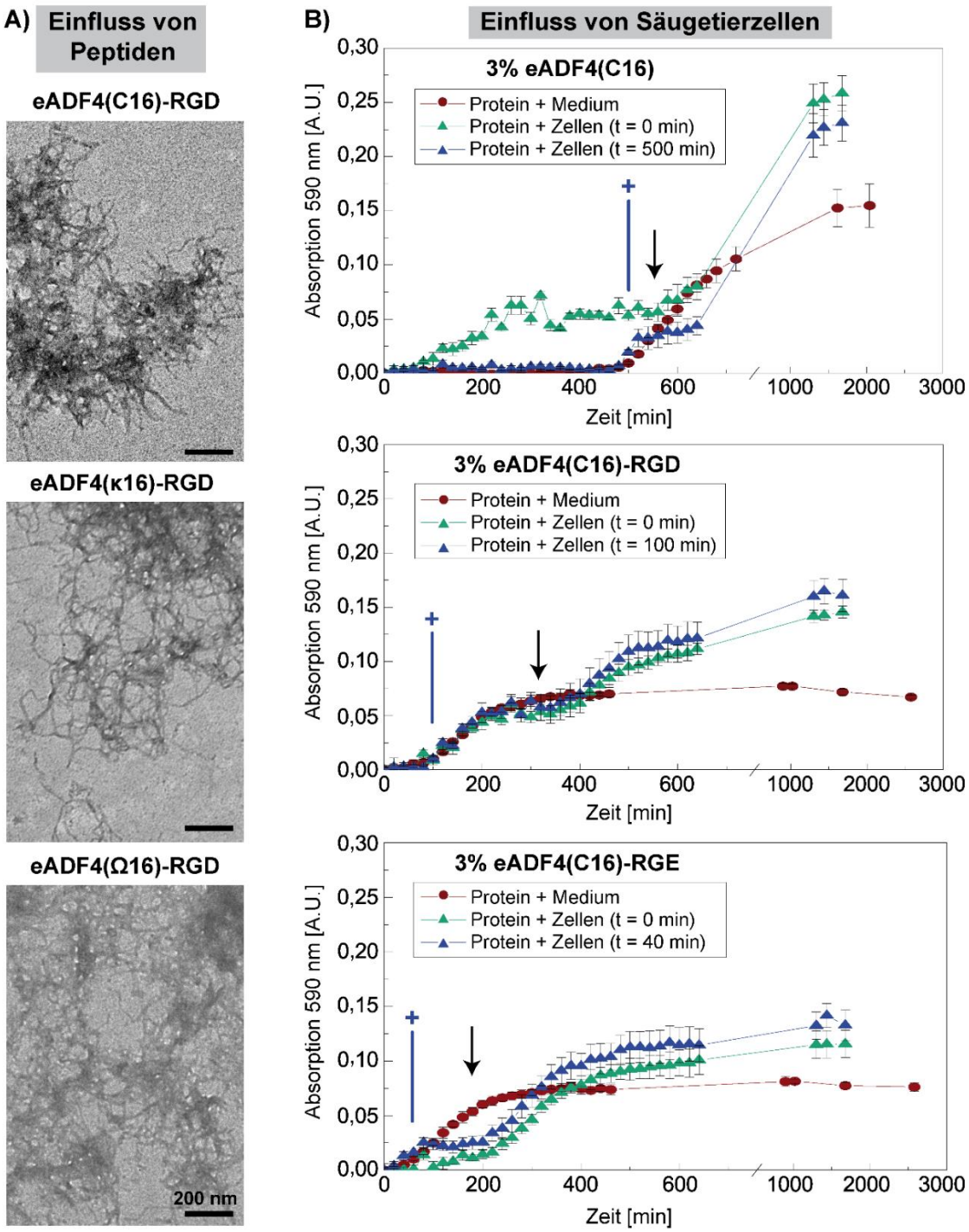

Abbildung 17: Einfluss von Peptidmodifikationen (**A, B**) und eingebrachten Zellen (**B**) auf die Fibrillen-und Gel-Bildung eADF4-basierter Spinnenseidenproteine. (**A**) TEM-Aufnahmen zeigen Nanofibrillen für RGD-modifizierte eADF4(C16)-, eADF4(κ16)- und eADF4(Ω16)-Seidenproteine. (**B**) Der Einfluss von BxPC3-Zellen auf das Selbstassemblierungsverhalten von eADF4(C16), eADF4(C16)-RGD und eADF4(C16)-RGE wurde anhand von Zeit-abhängigen Trübungsmessungen untersucht. Das + zeigt die Zugabe der Zellen während der Fibrillen-Elongationsphase an, während der Pfeil die Umstrukturierung des bereits gebildeten Nanofibrillen-Netzwerk kennzeichnet. Modifiziert nach [273d] und reproduziert mit freundlicher Genehmigung des Verlags John Wiley and Sons (© 2021 The Authors. Macromolecular Bioscience published by Wiley-VCH GmbH).

Es zeigte sich, dass die Zugabe von Zellen, sowohl von Beginn an als auch während der exponentiellen Fibrillen-Elongation, die Assemblierung von eADF4(C16)-RGD zunächst nicht beeinflusste, während bei eADF4(C16) und eADF4(C16)-RGE Unterschiede detektierbar waren (**Abbildung 17B**). Dabei schien die direkte Zellzugabe bei eADF4(C16) eine beschleunigende und bei eADF4(C16)-RGE eine verlangsamende Wirkung auf die Bildung von Nukleationskeimen zu haben (grüne Kurven in **Abbildung 17B**). Interessanterweise führte eine spätere Zellzugabe während der exponentiellen Fibrillen-Wachstumsphase (blaue Kurven und (+) in **Abbildung 17B**) bei diesen beiden Varianten zu einer Stagnation der Fibrillen-Elongation. Dies war auf die kurzfristige Zerstörung des bereits aufgebauten Fibrillen-Netzwerkes durch die Zellzugabe zurückzuführen. Die negativen Effekte, die zur verlangsamten Assemblierung führen, traten sicherlich auch bei der RGD-modifizierten Variante auf. Aufgrund der vorhandenen RGD-Interaktionsstellen für die Zellen, kam es aber zu einer zellgesteuerten Vernetzung von Proteinen und Fibrillen, welche die verlangsamenden Effekte ausgleichen konnte. Generell konnte in Anwesenheit von Zellen für alle Varianten ein intermediäres Plateau detektiert werden, welches ein Indikator für ein bereits gebildetes Hydrogel war (Pfeil in **Abbildung 17B**). Der nachfolgende, zweite Trübungsanstieg war ein Effekt der Neustrukturierung und Umlagerung des bereits geformten Fibrillen-Netzwerkes um die Zellen herum, was zu einem dichter gepackten, untereinander verbundenen Hydrogel führte. Diese erlangten Erkenntnisse konnten wiederum in **Teilarbeit IX** zur Vorgelierung von Spinnenseidenlösungen genutzt werden, um eine homogene Zellverteilung in den Hydrogelen zu erreichen.

3.2.2. Herstellung von Spinnenseidengerüsten

Rekombinante Spinnenseidenproteine können aufgrund ihres Selbstassemblierungsverhaltens und mithilfe diverser Prozessierungstechniken in anwendungsbezogene Morphologien verarbeitet werden. In dieser Arbeit lag der Fokus auf der Prozessierung und Charakterisierung von Filmen (**Abbildung 18**) und in der Analyse von nanofibrillären Gelen und deren Potential für die Biofabrikation zur Herstellung hierarchischer Strukturen (**Abbildung 19**).

3.2.2.1. (Gradienten-) Filme

Flache und strukturierte Filme können einfach durch Aufbringen („Gießen“) einer Proteinlösung auf einem geeigneten Substrat und dem anschließenden Verdampfen des Lösungsmittels hergestellt werden (**Abbildung 18**) [260, 278]. Die Filmdicke wird dabei durch die initiale Proteinkonzentration und die aufgebrachte Volumenmenge definiert [279]. In den **Teilarbeiten I, II, III, IV, V und VII** wurde dieses Gieß-Verfahren genutzt, um ohne hohen Materialverbrauch geeignete Oberflächen für anschließende physikalische und biologische Charakterisierungen (siehe 3.3.1.1., 3.3.1.2., 3.3.2. und 3.3.3.1.) zu generieren. Die beschriebene Film-Herstellungstechnik wurde in den **Teilarbeiten II und VII** noch erweitert, um verschiedene Arten von Gradientenfilmen für die Zellkultur zu prozessieren (siehe 3.3.2.2. und 3.3.2.3.). In **Teilarbeit II** erlaubte ein optimiertes Spritzenpumpen-Setup [248] das graduelle Mischen von eADF4(C16) und eADF4(C16)-RGD zur Herstellung eines entgegengesetzten, linearen Signalgradienten im resultierenden Film. Im Gegensatz dazu wurden in **Teilarbeit VII** topographische Struktur-Gradienten mittels Photolithographie erstellt, die als Negativ-

Abdruck für einen Stempel aus Polydimethylsiloxan (PDMS) dienten. Die hergestellten Stempel wurden auf Spinnenseidenlösungen aufgebracht, wodurch nach dem Verdampfen des Lösungsmittels ein Spinnenseidenfilm mit Oberflächen-Strukturgradienten geschaffen war.

Im Hinblick auf die anschließenden Analysen und Anwendungen war eine hohe Stabilität gegenüber Flüssigkeiten nötig, was durch die zusätzliche Nachbehandlung mit primären Alkoholen sichergestellt wurde [278]. Die Umstrukturierung ungeordneter und α-helikaler zu kristallinen, β-Faltblatt-reichen Proteinbereichen wurde anhand von Fourier-Transformations-Infrarot-Spektroskopie-Messungen (FTIR) und anschließender Fourier-Selbst-Dekonvolution (FSD) der Amid-I-Bande gezeigt (**Teilarbeiten I und III**). Rasterkraftmikroskopie-Aufnahmen zeigten, dass die Spinnenseidenfilme eine geringe Oberflächenrauheit aufwiesen, sich jedoch gemäß ihrer hydrophilen und hydrophoben Aminosäurebereiche ausrichteten (**Teilarbeiten I, III und VII**). Da die Kontaktwinkel von Wasser auf allen an der Luft getrockneten, eADF4-basierten Spinnenseidenfilmen unter 90° lagen, wurden sie als hydrophile Oberflächen eingestuft (**Teilarbeiten I, II, III und VII**). Einzig eADF4(C16)-Filme, die mit einem PDMS-Stempel hergestellt wurden, hatten aufgrund der Trocknung an der PDMS- anstelle der Luft-Grenzfläche einen deutlich hydrophoberen Charakter (**Teilarbeit VII**). Wie in den **Teilarbeiten IV, V und VII** gezeigt, konnten Oberflächenstrukturen sehr gut mittels Rasterkraft- und Rasterelektronenmikroskopie (REM) visualisiert werden. Die tatsächlichen Dimensionen des Strukturgradienten stimmten mit den ursprünglich designten überein (**Teilarbeit VII**).

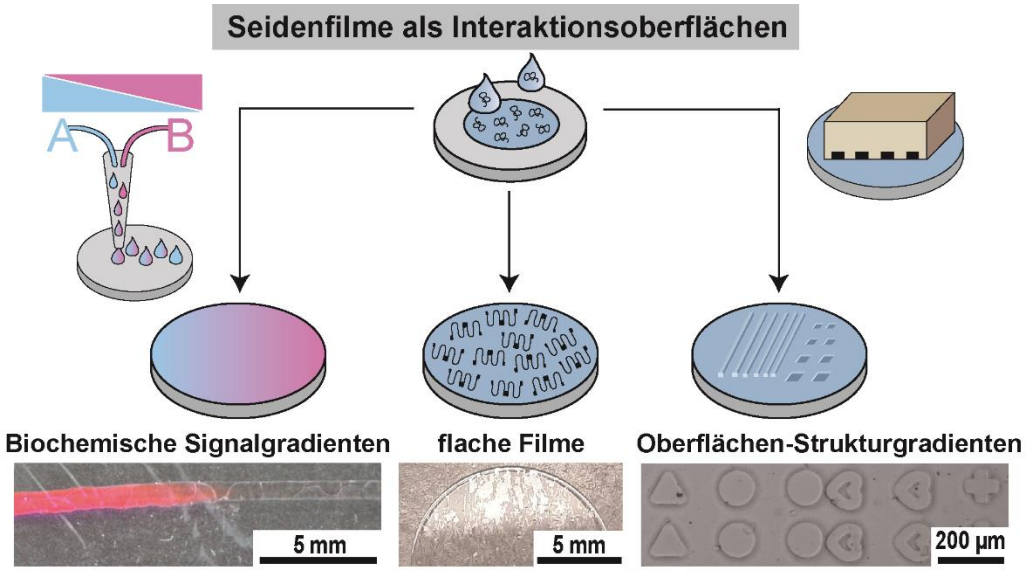

Abbildung 18: Übersicht der prozessierten, funktionalisierten Spinnenseidenfilme als potentielle Interaktionsoberflächen.

3.2.2.2. Hydrogele, Biotinten und Biofabrikation mittels 3D Extrusions-Biodruck

Aufgrund des bereits erwähnten Selbstassemblierungsprozesses rekombinanter Spinnenseidenproteine [271a] bilden sich bei geeigneter Proteinkonzentration, ohne den Einsatz chemischer Vernetzer, stabile, nanofibrilläre 3D Hydrogel-Netzwerke [272a] (siehe 3.2.1.). Das Vorhandensein eines binären organischen Lösungsmittelgemisches führte bei eADF4(C16)

zwar zu einer veränderten Fibrillenbildung, dennoch waren Selbstassemblierung und Gelformation in Gegenwart von DMSO uneingeschränkt möglich (**Teilarbeit VI**). Diese Tatsache und die Option, Säugetierzellen schon während der Gelbildung gleichmäßig in das Netzwerk einzukapseln [263b, 263c], eröffnen neue Möglichkeiten für die Anpassung und Optimierung von Gelen und (Bio-) Tinten. Die Gelbildung eADF4-basierter Spinnenseidenvarianten wurde anhand von Trübungsmessungen verfolgt und durch nachfolgende TEM-Aufnahmen bestätigt (**Teilarbeiten VI und VIII**). Außerdem wurde die zugrundeliegende Umstrukturierung von löslichen, unstrukturierten Proteinen zu β-Faltblatt-reichen Nano-Fibrillen anhand von FTIR-Messungen und anschließender FSD der relevanten Amid-I-Bande an vollständig gelierten Gelen nachgewiesen (**Teilarbeiten VI und IX**). Die entstandenen, porösen 3D-Gel-Matrices wurde zusätzlich mittels REM visualisiert. Dabei zeigten eADF4-basierte Hydrogele unabhängig von der verwendeten Variante (eADF4(C16), eADF4(C16)-RGD, eADF4(C16)-RGE, eADF4(Ω16)) eine Waben-ähnliche Struktur (**Teilarbeiten IV, V, VI und IX**). Zudem weisen Spinnenseiden-basierte Gele und Biotinten scherverdünnendes, viskoelastisches Verhalten, gute Formstabilität und Stresskompensation („Erholung“) auf, weswegen sie für den 3D-Biodruck verwendet werden können [263b, 263c, 268, 274]. In der vorliegenden Arbeit wurden die viskoelastischen, scherverdünnenden und stress-kompensierenden Eigenschaften weiterer Spinnenseiden-basierter Gele und Biotinten anhand von rheologischen Untersuchungen bestätigt (**Teilarbeiten VI, VIII und IX**). Zusätzlich konnte gezeigt werden, dass Spinnenseidenproteine, abhängig von der Formulierung und der genutzten Variante, zwischen 20 und 40 mg/ml zu stabilen, druckbaren (Bio-) Tinten assemblieren können und dadurch die mechanischen Eigenschaften angepasst werden können (**Teilarbeiten VI, VIII und IX**). Hervorzuheben ist dabei, dass diese für den Biodruck entscheidenden mechanischen Eigenschaften auch durch das Einbringen höherer Zelldichten bestehen blieben (**Teilarbeiten VIII und IX**).

Beim 3D-Biodruck mit Mikroventilen wird die Menge an extrudiertem Material neben dem angelegten Druck zusätzlich durch die Öffnungs- und Schließzeit des Mikroventils beeinflusst, wodurch punktuell extrudiert werden kann. Gedruckte Spinnenseidenfilamente und die daraus entstandenen Gitter-Konstrukte zeigen aufgrund der intermolekularen Wechselwirkungen und physikalischen Vernetzung eine hohe Formtreue. [263b, 263c] Spinnenseiden-basierte Gele können jedoch auch mittels pneumatischen Extrusionsdruck in formstabile Konstrukte verarbeitet werden [268]. Dabei wird die (Bio-)Tinte alleine durch den angelegten Druck extrudiert, was bei gut eingestellten Druckparametern zu einem durchgehenden Filament führt. In dieser Arbeit wurde der pneumatische 3D-Extrusionsdruck von rekombinanten Spinnenseidengelen und Biotinten für Biofabrikations-Anwendungen weiter analysiert (**Abbildung 19**, **Teilarbeiten VI, VIII und IX**). Sowohl eADF4(C16)-basierte Hydrogele als auch Gele aus wässrig-organischen Mischphasen bildeten wegen ihrer guten physikalischen Vernetzung im 3D-Extrusionsdruck durchgehende Filamente aus (**Teilarbeiten VI und VIII**). Außerdem konnten diese azellulären Tinten in formstabile, mehrlagige Konstrukte, wie das Miniatur-Modell einer menschlichen Aortenklappe (**Teilarbeit VIII**) oder Spinne (**Teilarbeit VI**), gedruckt werden (**Abbildung 19**). Aufgrund der viskoelastischen Eigenschaften und internen Vernetzung konnten Überhänge und kurze Verbindungen ohne Verwendung einer Stützstruktur oder Kollabieren des Konstrukts gedruckt werden. (**Abbildung 19** (Pfeil), **Teilarbeiten VI und VIII**).

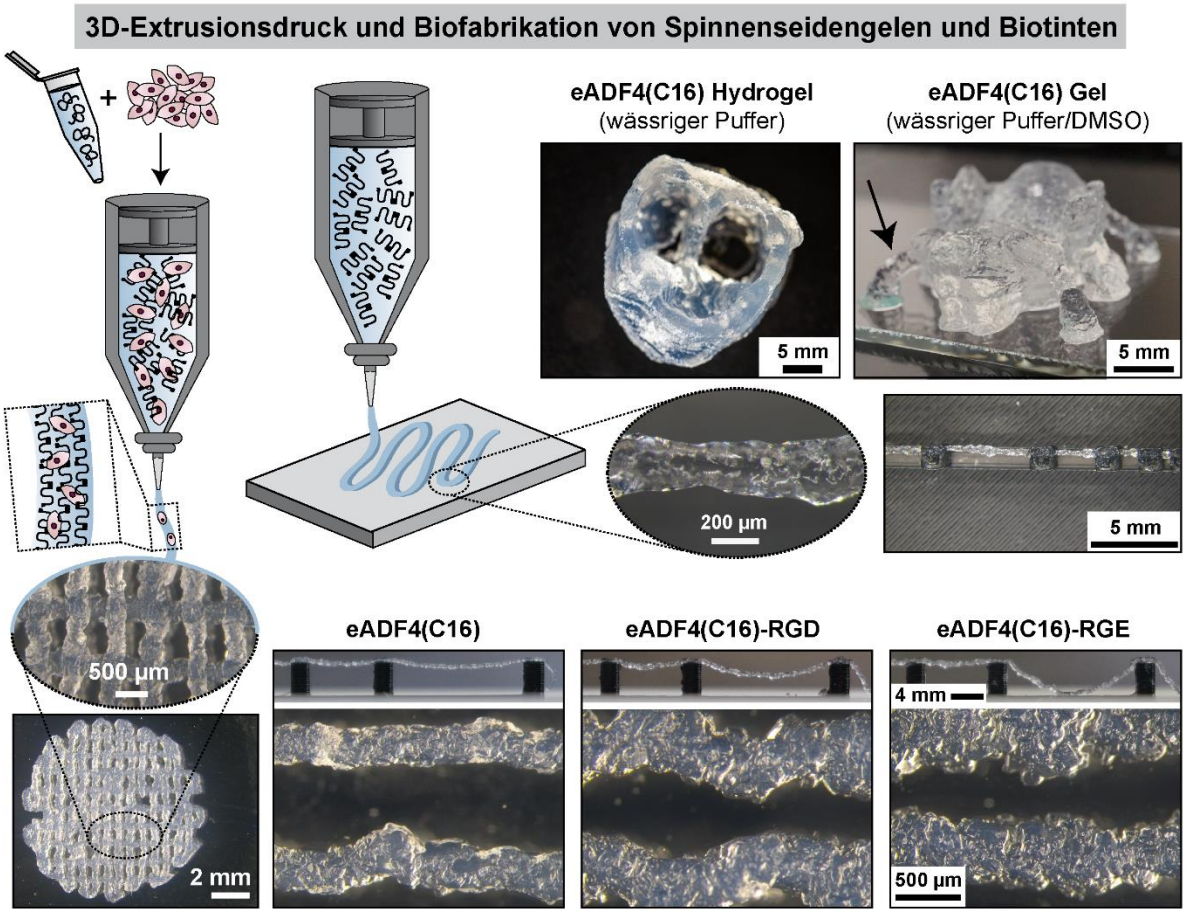

Abbildung 19: Übersicht der für die Biofabrikation hergestellten und mittels 3D-Extrusionsdruck prozessierten, Spinnenseiden-basierten Gele und Biotinten. Modifiziert nach [273d] und [273f] und reproduziert mit freundlicher Genehmigung des Verlags John Wiley and Sons (© 2021 The Authors. Macromolecular Bioscience published by Wiley-VCH GmbH, © 2021 The Authors. Angewandte Chemie International Edition published by Wiley-VCH GmbH).

Im Hinblick auf die Geweberegeneration ist die Verteilung und das Wachstum von Zellen in künstlichen Konstrukten ein entscheidender Faktor. In Vorarbeiten wurde eine Million Zellen pro Milliliter Seidenhydrogel eingebettet [263b, 263c]. In dieser Arbeit wurden drei eADF4(C16)-basierte Biotinten optimiert, verarbeitet und charakterisiert (**Teilarbeiten VIII und IX**). Neben eADF4(C16) wurden die Integrin-Bindesequenz-tragende eADF4(C16)-RGD- und die nicht-zelladhäsive eADF4(C16)-RGE-Variante analysiert. Dabei konnten höhere Zellmengen (fünf und zehn Millionen Zellen pro Milliliter finale Biotinte) homogen in den verschiedenen eADF4(C16)-Gelmatrizes verteilt werden (**Teilarbeiten VIII und IX**) ohne die Gelierung zu stören (**Abbildung 17**, **Teilarbeit VIII**). Während die eADF4(C16)- und die eADF4(C16)-RGD-basierten Biotinten auch mit hoher Zellzahl mit gleichbleibender Qualität verdruckt werden konnten, kam es bei der eADF4(C16)-RGE Biotinte durch die Zugabe von Medium und Zellen zu einer Verschlechterung der Tinten-Performance (**Abbildung 19**, **Teilarbeiten VIII und IX**). Selbst mit zehn Millionen Zellen pro Milliliter Tinte konnten die extrudierten Filamente von eADF4(C16) und eADF4(C16)-RGD einen Abstand von 16 mm überbrücken. Die intermolekularen Wechselwirkungen und die physikalische Vernetzung führten zu

ausreichend stabilen Druckfilamenten, um diese Distanz freihängend zu überwinden. Bei eADF4(C16)-RGE musste ein höherer Druck angelegt werden, um überhaupt ein zusammenhängendes Filament extrudieren zu können, was jedoch eine Überbrückung der 16 mm Distanz unmöglich machte (**Abbildung 19**, **Teilarbeit VIII**).

3.3. Biologische Evaluation von rekombinanten Spinnenseidengerüsten für die Gewebezüchtung

3.3.1. Biokompatibilität von Spinnenseidengerüsten

Biokompatibilität ist die Grundvoraussetzung eines Biomaterials für dessen späteren Einsatz in der Biomedizin, denn diese Materialien und deren Abbauprodukte dürfen keine Immun-, Entzündungs- und Abstoßungsreaktionen im Körper auslösen. Da eADF4(C16) als Beschichtung eines Silikonimplantats und als Impfstoffträger eine gute Biokompatibilität beschieden wurde [249, 253b, 253c], wurden in dieser Arbeit weitere Spinnenseiden-Varianten und Gerüste im Hinblick auf entscheidende Biokompatibilitäts-Parameter untersucht. Dazu zählen Adsorption von Blutplasmaproteinen und Aktivierung der Blutkoagulation (**Teilarbeit III**), Mikrobeninteraktion (**Teilarbeiten IV und V**) und die Rekrutierung von Immunzellen in einem *in vivo* Rattenmodell (**Teilarbeit X**).

3.3.1.1. Spezifische Adsorption von Blutplasmaproteinen und Blutkoagulation

Die Adsorption und Umstrukturierung von Proteinen auf Materialoberflächen nach Kontakt mit Köperflüssigkeiten, wie Blut oder Urin, ist entscheidend für die körpereigene Immunantwort mit potentiellen Entzündungs- oder Abstoßungsreaktionen und somit ein essentieller, zu untersuchender Parameter eines Biomaterials [22a]. Mit der ungeladenen eADF4(Ω16)-Variante konnte in **Teilarbeit III** eine ladungsabhängige Charakterisierung von eADF4-basierten Spinnenseidenfilmen hinsichtlich der Adsorption von Blutplasmaproteinen und der Aktivierung der Blutkoagulation erfolgen. Dazu wurde die Interaktion von Spinnenseidenoberflächen mit drei Proteinkomponenten aus dem Blutplasma (Albumin (HSA), Immunglobulin G (IgG), Fibrinogen) sowie menschlichem Blut untersucht. Die Adsorption der Blutplasma-Proteine HSA, IgG und Fibrinogen auf eADF4(C16)-, eADF4(κ16)- und eADF4(Ω16)-Oberflächen wurde anhand von Quarz-Mikrowaagen-Messungen (QCM-D) analysiert (**Abbildung 20**). Da weitere Körperreaktionen wie die Blutkoagulation stark von der Umstrukturierung von Fibrinogen abhängen, wurde ein Enzym-vermittelter Immuntest (ELISA) durchgeführt (**Abbildung 20**). Hierbei bindet ein spezifischer Antikörper an eine Peptidsequenz der γ-Kette des Fibrinogens, die nur im umstrukturierten Zustand, nicht aber im nativen Fibrinogen zugänglich ist. Abschließend wurde die Blutkoagulation und Ausbildung eines Fibrinnetzwerkes auf den Spinnenseidenfilmen mittels REM und konfokaler Lasermikroskopie (CLSM) nach Immunfärbung charakterisiert (**Abbildung 20**). Dabei zeigte sich sehr deutlich, dass auf der positiv geladenen eADF4(κ16)-Oberfläche eine erhöhte Proteinadsorption, Fibrinogen-Umstrukturierung und Blutkoagulation mit Ausbildung eines Fibrinnetzwerkes auftrat. Da sich diese Effekte auf den ungeladenen eADF4(Ω16)- und negativ geladenen eADF4(C16)-Filmen nicht zeigten, konnte von einer primär ladungs-gesteuerten, und gering Aminosäuresequenz-abhängigen Reaktion ausgegangen werden.

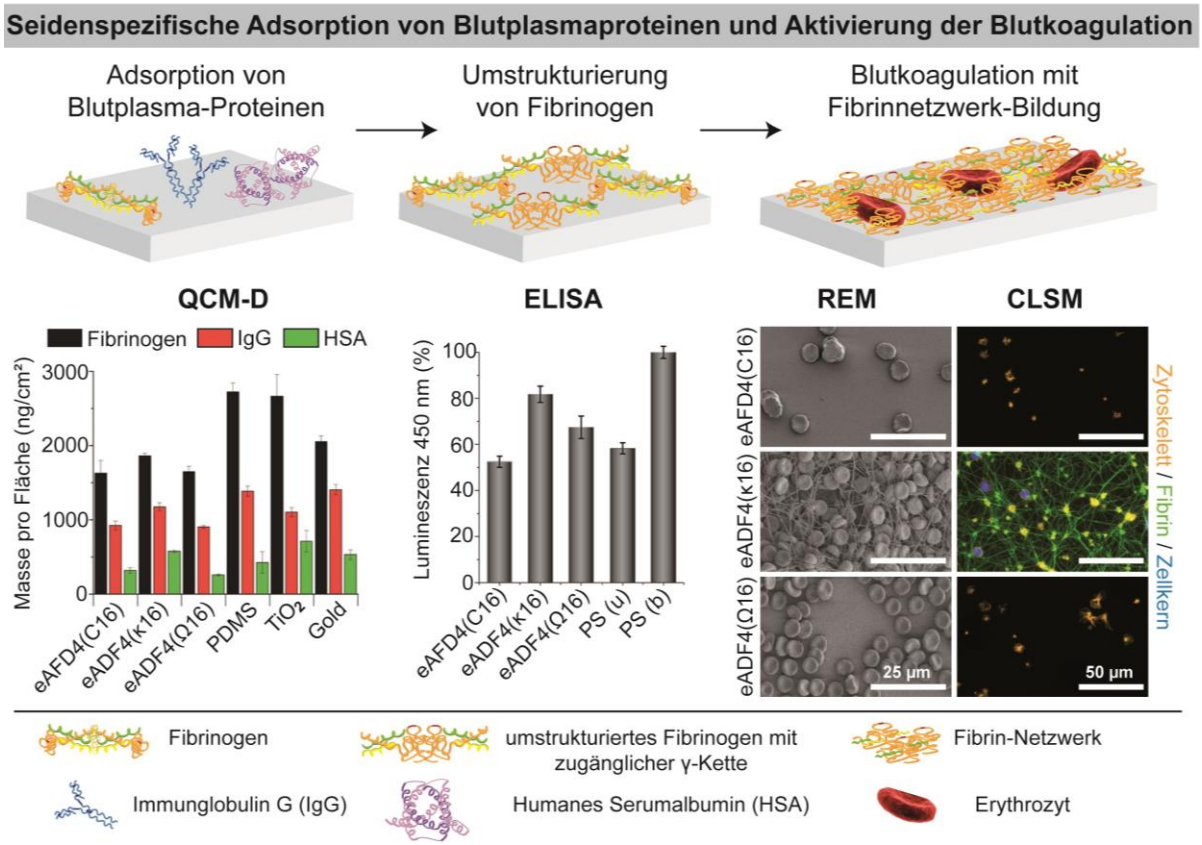

Abbildung 20: Ladungsabhängige Adsorption von Blutplasmaproteinen (Fibrinogen, IgG, HSA), Umstrukturierung von Fibrinogen und Blutkoagulation auf eADF4(C16)-, eADF4(κ16)- und eADF4(Ω16)-Filmen. Die Proteinadsorption von Fibrinogen, IgG und Albumin (HSA) wurde mittels QCM-D quantifiziert, während die Umstrukturierung von Fibrinogen mittels ELISA mit einem selektiven anti-γ-Antikörper detektiert wurde. Die Blutkoagulation und Ausbildung eines Fibrinnetzwerkes wurden mithilfe von REM- und CLSM-Aufnahmen visualisiert. Modifiziert nach [273h] und reproduziert mit freundlicher Genehmigung des Verlags American Chemical Society (Copyright © 2022, American Chemical Society).

3.3.1.2. Interaktion von Mikroben mit Spinnenseidengerüsten

Im Hinblick auf einen Einsatz in der Gewebezüchtung ist Mikrobenbefall von Implantaten ein Risikofaktor [280], da eine Biofilm-Bildung von pathogenen, multi-resistenten Stämmen schwerwiegende Entzündungen und Abstoßungsreaktionen zur Folge haben kann. [36a, 280a] Daher müssen bioselektive Gerüste entwickelt werden, die die Anheftung von Mikroben auf Materialoberflächen unterbinden, aber das Wachstum von Säugetierzellen ermöglichen. [281] Ein während dieser Dissertation verfasster Übersichtsartikel (**Teilarbeit XII**) betrachtet natürliche und rekombinante Spinnenseidenmaterialien, die eine Mikrobenanheftung unterbinden und selektive Zellinteraktionen ermöglichen. Zudem konnte in den **Teilarbeiten IV und V** mithilfe der ungeladenen eADF4(Ω16)-Spinnenseidenvariante der mikrobielle Abstoßungsmechanismus von rekombinanten eADF4(C16)- und eADF3(AQ)$_{12}$-basierten Gerüsten entschlüsselt werden. Die Interaktion mit Seidenmaterialien wurde mit Bakterien (*E. coli*, *Staphylococcus aureus* und *Streptococcus mutans*) und (Hefe-) Pilzen (*Pichia pastoris*

und *Candida albicans*) getestet. Anhand von Viabilitätsmessungen, Einzel-Zell-Adhäsions-Kraftmessungen und Adhäsionsstudien mit anschließenden REM-Aufnahmen wurde ein molekulares Struktur-Modell für die mikrobielle Interaktion mit (rekombinanten) Seidenmaterialien erstellt (**Abbildung 21**). Dieses basiert auf der Verteilung von hydrophoben, kristallinen und β-Faltblatt-reichen Proteinbereichen der Seidengerüste, die als potentielle Interaktionsstellen für Mikroben dienen.

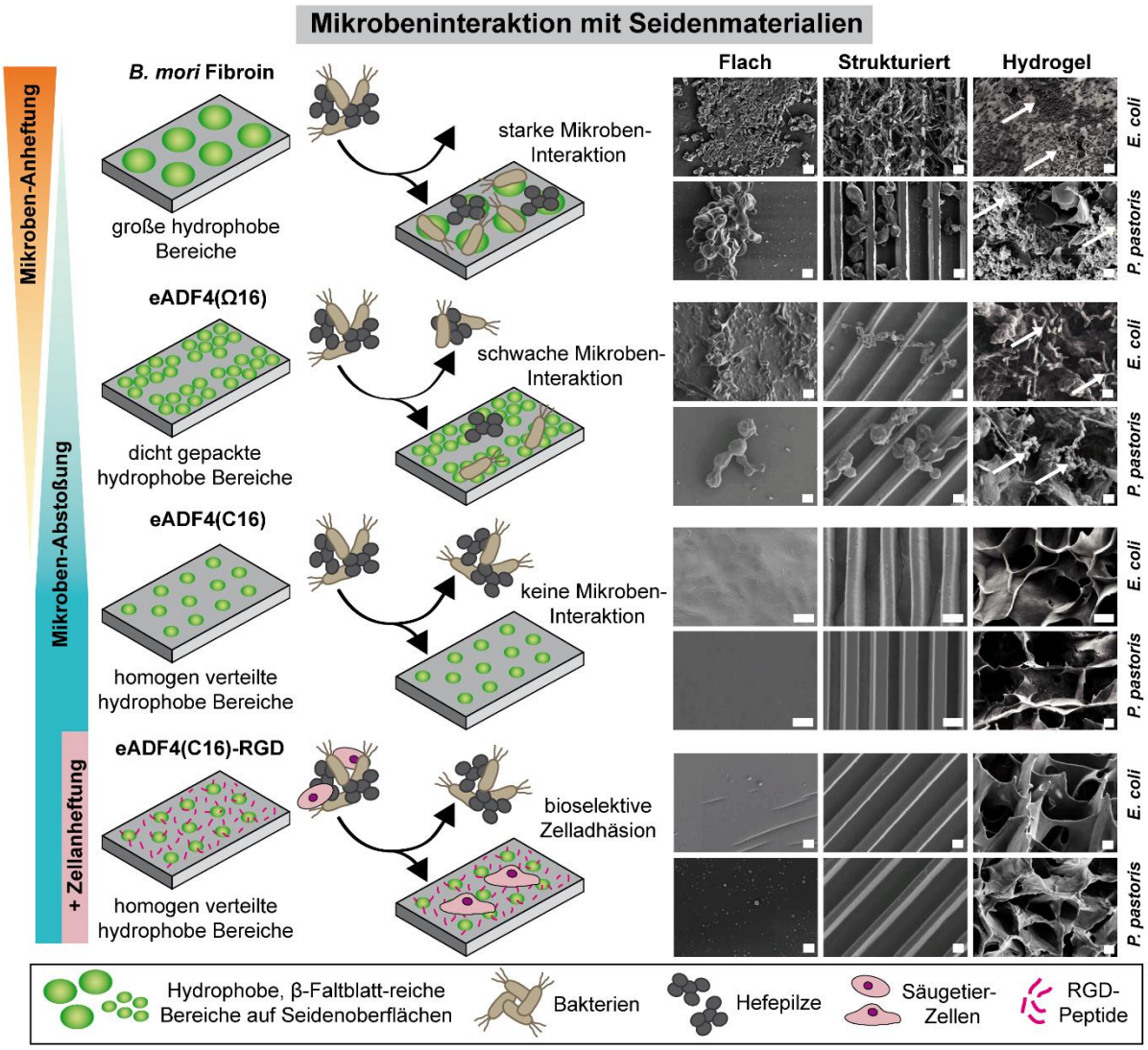

Abbildung 21: Die Proteinsequenz-abhängige Assemblierung von Seidenproteinen führt zur Ausbildung von hydrophoben, β-Faltblatt-reichen Bereichen mit unterschiedlicher Größe und Verteilung in Seidengerüsten (flacher und strukturierter Film, Hydrogel), was eine Interaktion von Mikroben (*E. coli* (Bakterien), *Pichia pastoris* (Hefepilze)) unterbinden oder fördern kann. Die großen hydrophoben Bereiche in *Bombyx mori* Seide und die dichte Anordnung kleiner Bereiche in eADF4(Ω16) stellen Anheftungspunkte dar, während die gleichmäßig verteilten, hydrophoben Bereiche in eADF4(C16)-basierten Proteinen keine Interaktion zulassen. Eine RGD-Modifikation ermöglicht gleichzeitig eine selektive Adhäsion von Säugetierzellen. Die Pfeile zeigen Mikroben in 3D-Hydrogelen. Maßstab entspricht 2 µm. Modifiziert nach [242a] und reproduziert mit freundlicher Genehmigung des Verlags Elsevier (© 2020 The Author(s). Published by Elsevier Ltd.).

Im Vergleich zu Spinnenseide sind die β-Faltblatt-reichen Bereiche bei *Bombyx mori* Seide größer und anders orientiert [282]. Diese großen, hydrophoben Bereiche sind der Grund für die enorme Mikrobenbesiedelung von Fibroin-Gerüsten (**Abbildung 21**). Die kleineren Bereiche der rekombinanten Spinnenseide erlauben keine Interaktion mit Mikroben, können aber aufgrund ihrer Verteilung während der Assemblierung, basierend auf der primären Aminosäuresequenz, zu Anheftungspunkten werden. Verglichen mit eADF3-Varianten haben eADF4-basierte Spinnenseidenproteine einen längeren, hydrophoben poly-Alanin-Bereich und einen kürzeren, amorphen Sequenzabschnitt im repetitiven Modul [227]. Daher tritt bei eADF3-basierten Proteinen ein Volumeneffekt der amorphen Bereiche auf, wodurch die kleinen, hydrophoben Bereiche gleichmäßig in die umgebende amorphe Matrix eingebettet sind. Da sich die repetitiven Module von eADF4(C16) und eADF4(Ω16) nur durch eine (geladene) Aminosäure unterscheiden, liegt der Grund für die unterschiedliche Assemblierung der hydrophoben Bereiche in der elektrostatischen Abstoßung. Bei eADF4(C16) tragen die negativ geladenen Glutaminsäure-Reste zur Abstoßung innerhalb des Proteins bei, wodurch kleine, gleichmäßig verteilte, hydrophobe Bereiche assemblieren (**Abbildung 21**). Die Fusion des RGD-Peptids beeinflusst diese Strukturierung nicht, weswegen eine bioselektive Adhäsion von Säugetierzellen möglich ist. Da bei eADF4(Ω16) aber keine Ladungseffekte auftreten, können sich die hydrophoben, β-kristallinen Bereiche viel dichter und ungleichmäßiger verteilt arrangieren und zu größeren hydrophoben Bereichen werden, wodurch Anheftungspunkte für Mikroben entstehen (**Abbildung 21**, **Teilarbeiten IV und V**).

3.3.1.3. *In vivo* Biokompatibilität von Seidenhydrogelen

Implantationsmaterialien für die Gewebezüchtung sowie deren Abbauprodukte dürfen keine Immun-, Entzündungs- und Abstoßungsreaktionen im Körper auslösen. In **Teilarbeit X** wurde die ausgezeichnete Biokompatibilität von eADF4(C16) und eADF4(C16)-RGD-Hydrogelen *in vivo* im Rattenmodell bestätigt. Vier Wochen nach der Implantation in einem Arteriovenösen Loop konnten im neu gebildeten Gewebe zwar Makrophagen, aber keine für die Immun- und Abstoßungsreaktion entscheidenden mehrkernigen Riesenzellen nachgewiesen werden. Eine spezifische Färbung von pro- und anti-inflammatorischen Makrophagen zeigte eine gleichmäßige Verteilung beider Zelltypen, was die hohe Biokompatibilität und das niedrige Stimulationsniveau der Entzündungs- und Immunantwort zeigte.

3.3.2. Gesteuerte Interaktion von Zellen mit Spinnenseidengerüsten

In dieser Dissertation stand die Funktionalisierung von Spinnenseidengerüsten im Fokus, um Interaktionen zwischen Material und Zellen zu unterstützen. Entscheidende Faktoren für eine erfolgreiche Gewebezüchtung sind eine gute Anheftung und ein kontinuierliches Wachstum der Zellen. Da Zellen in ihrer natürlichen EZM biochemischen, topographischen und mechanischen Reizen ausgesetzt sind, wurden zwei Übersichtsartikel (**Teilarbeiten XI und XII**) zu dieser Thematik verfasst. **Teilarbeit XI** befasste sich mit Modifikationsstrategien multifunktionaler Biomaterialien und deren (synergistischen) Effekte auf das Zellverhalten. In **Teilarbeit XII** wurden Spinnenseiden-basierte Materialien fokussiert, die die bioselektive Anheftung von Säugetierzellen bei gleichzeitiger Abstoßung von Mikroben zulassen.

3.3.2.1. Ladungsabhängige Zellinteraktion

Eine ladungsabhängige Analyse von eADF4(C16), eADF4(κ16) und eADF4(Ω16) im Hinblick auf deren Effekt auf das Zellverhalten erfolgte in den **Teilarbeiten I, II und III**. Eine Schlussfolgerung aus den drei Studien war, dass positiv geladene eADF4(κ16)-Oberflächen bei vielen Zelltypen zelluläre Antworten stimulieren konnten. Im Gegensatz dazu, zeigte die ungeladene eADF4(Ω16)-Variante keine zellstimulierende Wirkung, während das negative eADF4(C16) Zelltyp-abhängig geringe Zellinteraktionen ermöglichte. In **Teilarbeit I** konnten humane Stammzell-induzierte (hiPSC) Kardiomyozyten auf eADF4(κ16)-Filmen adhärieren und über 14 Tage kultiviert werden. Die Zellen zeigten im Vergleich zu RGD-modifizierten Varianten (siehe 3.3.2.3.) jedoch eine geringere Zellgröße und eine teilweise diffusere Expression der Kardiomyozyten-spezifischen Markerproteine (sarkomerisches α-Aktinin, kardiäres Troponin I und Connexin 43) sowie unregelmäßiges Schlagverhalten. Auf eADF4(C16) und eADF4(Ω16)-Oberflächen konnten die Zellen dagegen nicht anhaften. In **Teilarbeit III** unterstützte die positive Ladung von eADF4(κ16)-Beschichtungen zwar die Adhäsion von humanen BJ Haut-Fibroblasten, humanen HaCaT-Keratinozyten und neuronalen B50 Rattenzellen nach vier Stunden, ein Zellwachstum über sieben Tage war jedoch auf keiner der drei untersuchten Spinnenseidenvarianten besser als auf der Kontrolle (behandeltes Polystyrol). Durch die systematische Interaktionsanalyse von elf unterschiedlichen Zelltypen mit eADF4(C16), eADF4(κ16) und eADF4(Ω16) in **Teilarbeit II** wurde deutlich, dass das ungeladene eADF4(Ω16) als durchgehend zellabweisend (zytophob) eingestuft werden kann, da keiner der untersuchten Zelltypen gut auf dieser Variante anhaften konnte. Da auf positiv geladenen eADF4(κ16)-Filmen fast alle untersuchten Zelltypen, mit Ausnahme von humanen MG63 Knochen-Fibroblasten, eine moderate bis sehr gute Adhäsion und gutes Spreitverhalten zeigten, wurde diese Variante als zellbindend (zytophil) eingeordnet. Wie in Vorarbeiten bereits beschrieben [246, 255a, 256], wurden negativ geladene eADF4(C16)-Oberflächen per se als zytophob eingestuft, da die adhärenten Zellen eine runde Morphologie mit wenig F-Aktin-Expression aufwiesen.

3.3.2.2. Topographie-abhängige Zelladhäsion

Da Zellen in der natürlichen EZM durch Topographie stimuliert werden, können entsprechende Modifikationen zu einer verbesserten Zellinteraktion mit künstlichen Zellkulturgerüsten führen [283]. In **Teilarbeit VII** wurden zytophobe eADF4(C16)-Filme mit Oberflächenstruktur-gradienten, bestehend aus acht unterschiedlichen geometrischen Formen im Größenbereich von 40 µm bis 100 µm, modifiziert, um Zellinteraktionsstellen zu schaffen. Durch die Verwendung dieses Größengradienten und die systematische Analyse von acht Zelllinien aus verschiedenen Ursprungsgeweben zeigte sich, dass Zellen sehr unterschiedlich auf topographische Strukturen reagierten. In den CLSM-Aufnahmen (**Abbildung 22**) ist deutlich erkennbar, dass humane BJ Haut-Fibroblasten sehr stark durch Oberflächentopographie stimuliert werden, weil sie fast ausschließlich in den Vertiefungen anhafteten und ihre Zellform gemäß der vorgegebenen Form ausrichteten („Kontaktführung“). Da humane HaCaT-Keratinozyten auf flachen und strukturierten Filmen ähnlich anhafteten, wurden sie nicht durch die Topographie beeinflusst. Durch den Größengradienten konnte zudem ein Zusammenhang zwischen Zell- und Struktur-Größe im Adhäsionsverhalten ausgewählter Zellen gezeigt

werden. Humane BJ Haut-Fibroblasten und RN22 Ratten-Schwann-Zellen adhärierten unabhängig von der Größe in allen Vertiefungen, während kleinere Oberflächenstrukturen die Ausrichtung von humanen MG63 Knochen- und neuronalen B50 Ratten-Zellen mit geringerer Zellkörpergröße förderten (**Teilarbeit VII**).

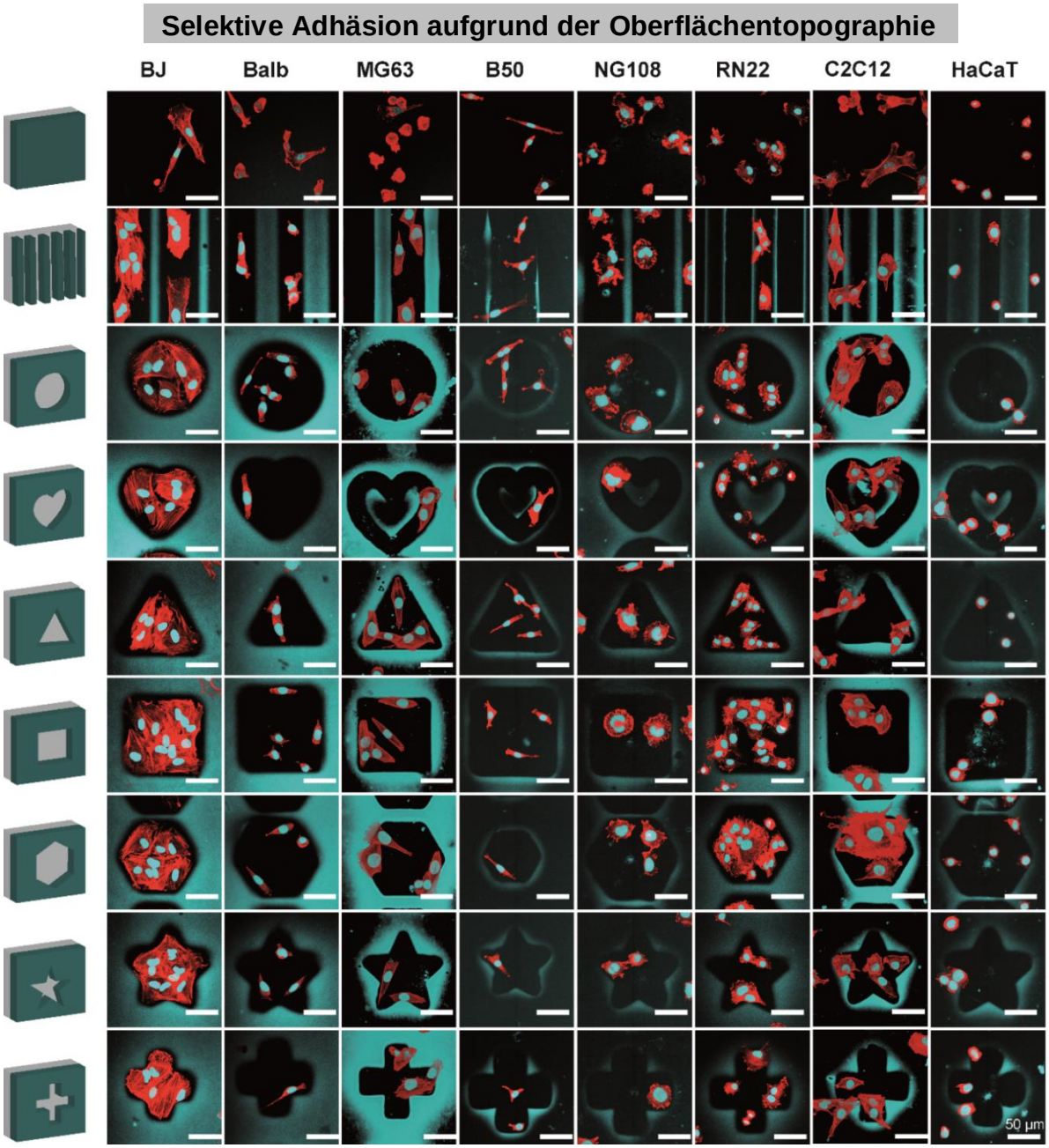

Abbildung 22: CLSM-Aufnahmen von acht Zelllinien (humane BJ-Haut-Fibroblasten, embryonale Balb 3T3 Maus-Fibroblasten, humane MG63 Knochen-Fibroblasten, B50 neuronale Ratten-Zellen, neuronale NG108 Hybrid-Zellen, RN22 Ratten-Schwann-Zellen, C2C12 Maus-Myoblasten und humane HaCaT-Keratinozyten) auf strukturierten eADF4(C16)-Filmen nach vier Stunden und Färben des F-Aktin-Zytoskeletts (Phalloidin-Rhodamin) und des Zellkerns (4‘6-Diamidin-2-Phenylindol (DAPI)). DAPI interagiert auch mit dem Spinnenseidenprotein, weswegen die Oberflächen-Vertiefungen auch angefärbt sind. Modifiziert nach [273g] und reproduziert mit freundlicher Genehmigung des Verlags John Wiley and Sons (© 2022 The Authors. Advanced Materials Interfaces published by Wiley-VCH GmbH).

3.3.2.3. Gerichtete Zellstimulation durch Fusionspeptide

Generell sind eine gute Adhäsion und kontinuierliches Wachstum von Zellen essentiell für die erfolgreiche Bildung und Regeneration von Geweben. Dabei sind die selektive Anhaftung und Proliferation von ausgewählten Zelltypen notwendig. In den letzten Jahrzehnten konnten viele zelluläre Bindemotive in EZM-Molekülen identifiziert werden [55c, 112c, 284]. In Vorarbeiten wurde die zelladhäsive eADF4(C16)-RGD-Variante entwickelt. [246] In dieser Dissertation wurden eADF4(C16), eADF4(κ16) und eADF4(Ω16) neben RGD mit fünf weiteren potentiell zelladhäsiven Fusionspeptiden aus natürlichen EZM-Proteinen modifiziert, um eine gerichtete Interaktion mit Zellrezeptoren zu induzieren. Dabei bestätigte sich, dass RGD-modifizierte Spinnenseidenfilme unabhängig von der Ladung der Seidenvariante Adhäsion und Wachstum von Zellen ermöglichten (**Teilarbeiten I und II**). In **Teilarbeit I** konnten hiPSC-Kardiomyozyten auf RGD-funktionalisierten Seidenfilmen anheften, kontrahieren sowie auf Medikamenten-Behandlung reagieren. Außerdem waren in **Teilarbeit II** alle elf untersuchten Säugetierzelllinien in der Lage in hoher Anzahl auf den RGD-modifizierten Seidenfilmen zu adhärieren (**Abbildung 23**). Zusätzlich zeigte ein Gradientenfilm aus eADF4(C16) und eADF4(C16)-RGD, dass die Zelladhäsion von embryonalen Balb 3T3 Maus-Fibroblasten mit steigender RGD-Konzentration zunahm. Zudem bestätigte die stetige Proliferation ausgewählter Zelllinien über sieben Tage die gerichtete Zellinteraktion mit den RGD-Peptiden (**Teilarbeit II**).

In **Teilarbeit II** offenbarte sich außerdem, dass die fusionierte KGD-Sequenz eine sehr selektive Adhäsion von C2C12 murinen Myoblasten auf Seidenoberflächen ermöglichte (**Abbildung 23**). Da die anderen zehn analysierten Zelltypen nicht bzw. wesentlich schwächer auf der eADF4(C16)-KGD Variante adhärieren konnten, wurde von einer spezifischen Wechselwirkung zwischen C2C12-Oberflächenrezeptoren und Oberflächen-exponierten KGD-Peptiden ausgegangen. Zusätzlich bestätigte ein Co-Kultur Experiment mit C2C12 Maus-Myoblasten und neuronalen B50 Ratten-Zellen die selektive Anheftung der Muskelzellen auf KGD-modifizierten Oberflächen. Zellbindende eADF4(C16)-RGD Oberflächen dienten dabei als Kontrolle, da beide Zelltypen bereits nach zwei Stunden Inkubationszeit auf dieser Seidenvariante adhärieren konnten (**Abbildung 23**).

3.3.3. Biologische Abbaubarkeit von Spinnenseidengerüsten

Die Biodegradation eines Biomaterials sollte an das jeweilige biomedizinische Anwendungsgebiet angepasst sein. Dementsprechend wird zwischen Langzeit-stabilen Materialien mit geringen Abbauraten und hoher Verschleißbeständigkeit, wie Implantat-Beschichtungen, und schnell abbaubaren Materialien, wie Medikamententrägern und Depots, unterschieden. Dazwischen finden sich noch Materialien für die Regeneration und den Aufbau von Geweben, bei denen die Biodegradation simultan mit dem Aufbau einer neuen EZM einhergeht.[285] In dieser Arbeit wurde zum einen ein enzymatischer *in vitro* Abbau von eADF3- und eADF4-basierten Beschichtungen (**Teilarbeit III**) und zum anderen der *in vivo* Abbau eADF4(C16)-basierter Hydrogele in einem Rattenmodell analysiert (**Teilarbeit X**).

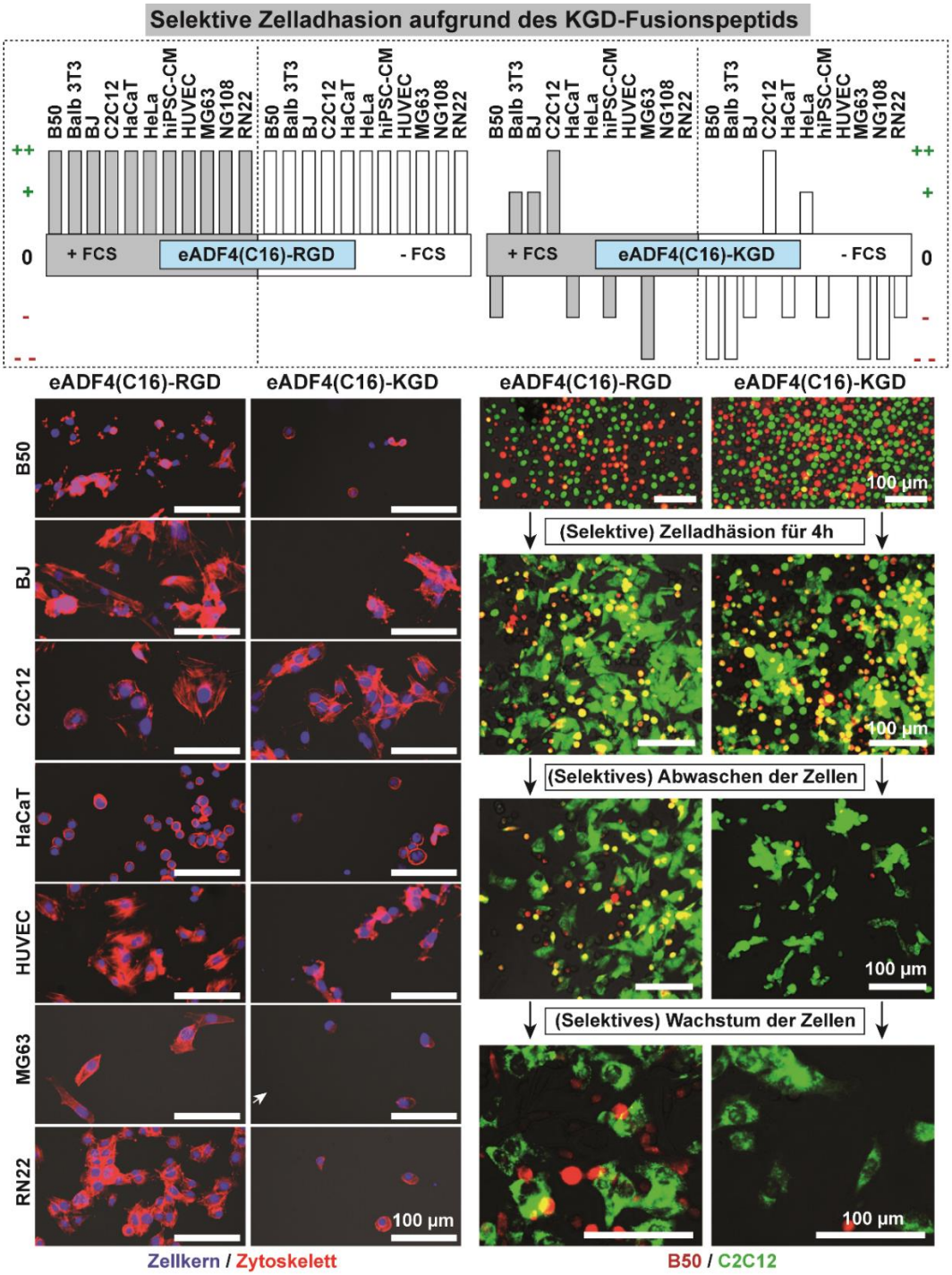

Abbildung 23: Im Vergleich der fluoreszenzmikroskopischen Aufnahmen von Filmen mit dem zellbindenden RGD-Peptid ermöglicht das KGD-Peptid eine selektive Interaktion von C2C12-Maus-Myoblasten, während andere Zelltypen gar nicht oder wesentlich schwächer interagieren (Aktin-Zytoskelett (Phalloidin-Rhodamin), Zellkern (DAPI)). Interaktionen aufgrund von unspezifischer Proteinadsorption von Serumkomponenten sind vernachlässigbar. In einer Co-Kultur von murinen C2C12-Myoblasten (grün, SYTO-Grün) und neuronalen B50 Rattenzellen (rot, Zell-Tracker-Rot) konnten C2C12-Moyblasten nach vier Stunden anhaften und spreiten, während nicht-adhärente B50-Zellen rund vorlagen und von den eADF4(C16)-KGD-Oberflächen abgewaschen werden konnten. Modifiziert nach [273b] und reproduziert mit freundlicher Genehmigung des Verlags John Wiley & Sons (© 2023 The Authors. Advanced Healthcare Materials published by Wiley-VCH GmbH).

3.3.3.1. Spinnenseidenprotein-abhängige *in vitro* Degradation

In **Teilarbeit III** wurde der Abbau von verschiedenen Spinnenseidenbeschichtungen mit dem Protease Mix PXIV aus *Streptomyces griseus* (Typ XIV, unspezifische Degradation) und dem Kollagenase Mix CHC aus *Clostridium histolyticum* (Typ IA, Schnittstelle -/P/X↓G/P/-, wobei X eine neutrale Aminosäure darstellt) über 15 Tage charakterisiert. Während eADF3-basierte Beschichtungen durch beide Enzym-Mischungen innerhalb von zwei Tagen vollständig abgebaut waren, zeigten sich bei den eADF4-Varianten ladungsspezifische Unterschiede. Die ungeladene eADF4(Ω16)- und die negativ geladene eADF4(C16)-Variante wiesen eine langsame Degradation auf, während positiv geladene eADF4(κ16)-Filme deutlich schneller durch den Protease Mix abgebaut wurden. Aufgrund des schnellen Degradationsverhaltens können eADF3-Varianten als Träger oder Depots für schnell freizusetzende Medikamente fungieren. Wenngleich Ladungs-abhängige Leistungsunterschiede auftraten, eignen sich die proteolytisch stabileren eADF4-Varianten für biomedizinische Anwendungen, zum Beispiel als Implantat-Beschichtung.

3.3.3.2. Langsame *in vivo* Biodegradation im Rattenmodell

Um die Stabilität und die biologische Abbaubarkeit von eADF4(C16)-basierten Morphologien näher zu untersuchen, wurde in **Teilarbeit X** die *in vivo* Biodegradation von eADF4(C16)- und eADF4(C16)-RGD-Hydrogelen nach Implantation in einem Arteriovenösen-Loop-Modell analysiert. Für den natürlichen Abbau sind Matrix-Metallo-Proteasen (MMP) verantwortlich [286]. Nach vier Wochen zeigte eine spezifische MMP-3-Färbung beider Seidengel-Varianten ein erhöhtes Vorkommen dieses Abbau-Enzyms. Da MMP-3 vorwiegend im neu gebildeten, vaskularisierten Gewebe der jeweiligen Konstrukte nachgewiesen wurde, ist davon auszugehen, dass der biologische Abbau der Seidenmatrix simultan mit der Entwicklung von neuer EZM und funktionalem Gewebe einhergeht. Der langsame Abbau eADF4(C16)-basierter Varianten konnte anhand von zwei und vier Wochen lang implantierten Hydrogelen bestätigt werden, weil sowohl die Größe als auch das Gewicht der Konstrukte über die Zeit abnahm.

3.3.4. Gezielte Freisetzung bioaktiver Substanzen aus Spinnenseidengerüsten

In der Krebstherapie werden Wirkstoffdepots zur Freisetzung bioaktiver Substanzen genutzt, um erkrankte Zellen gezielt zu bekämpfen und zu töten [287]. Diverse Einschränkungen, wie suboptimale biologische Verteilung sowie mangelnde und zeitlich begrenzte Stabilität, erschweren jedoch die Verwendung von Arzneistoffen [180d, 180f, 180g]. In dieser Dissertation konnte gezeigt werden, dass sich Spinnenseiden-basierte Gel-Systeme zur kontinuierlichen Freisetzung hydrophober und hydrophiler Wirkstoffe eignen (**Abbildung 24**). Um den Einbau und die stetige Freisetzung wasserunlöslicher, hydrophober Substanzen zu ermöglichen, wurden in **Teilarbeit VI** eADF4(C16)-Gele aus binären wässrig-organischen Mischungen als Wirkstoffdepots getestet. Durch die anteilige Verwendung (ein Drittel) des amphiphilen organischen Lösungsmittels DMSO konnte das schlecht wasserlösliche Krebsmedikament 6-Mercaptopurin [288] gleichmäßig in den Spinnenseidengelen verteilt werden, während der Wirkstoff in reinen Hydrogelen aggregierte. Der nicht-kovalente Einbau in der organischen Phase der Gele erlaubte anschließend eine kontinuierliche Freisetzung des hydrophoben Wirkstoffs aus dem Geldepot (Gel aus binären Mischungen, **Abbildung 24**). In **Teilarbeit IX**

wurden hingegen Spinnenseiden-basierte Biotinten zur stetigen Freisetzung eines Wirkstoffes (TNFR2-Fc-GpL, basierend auf Etanercept zur Behandlung von rheumatischen Erkrankungen und Psoriasis [289]) für die zielgerichtete Therapie entwickelt (Biotinte, **Abbildung 24**). Es zeigte sich, dass sowohl Biotinten aus eADF4(C16) als auch eADF4(C16)-RGD das Wachstum von HEK293 Produktionszellen förderten. Zudem konnte die kontinuierliche Produktion und Freisetzung des wasserlöslichen TNFR2-Fc-GpL Reporter-Fusionsproteins über einen Zeitraum von 14 Tagen anhand der angebrachten Luziferase aus *Gaussia princeps* (GpL) verfolgt werden. Die biologische Aktivität der extrazellulären TNFR2-Domäne wurde anhand der Interleukin-8 (IL-8) Produktion von HeLa-Zellen verifiziert. Normalerweise regt die Bindung des Tumor-Nekrose-Faktors (TNF) mit HeLa-Oberflächenrezeptoren (TNFR2) die pro-inflammatorische IL-8-Produktion an. In Anwesenheit des Fusionsproteins interagieren dessen TNFR2-Ligandenbindungsdomänen mit TNF, was eine Stimulation und IL-8-Produktion der HeLa-Zellen verhindert, und somit zu geringeren Entzündungsreaktionen führt (**Abbildung 24**).

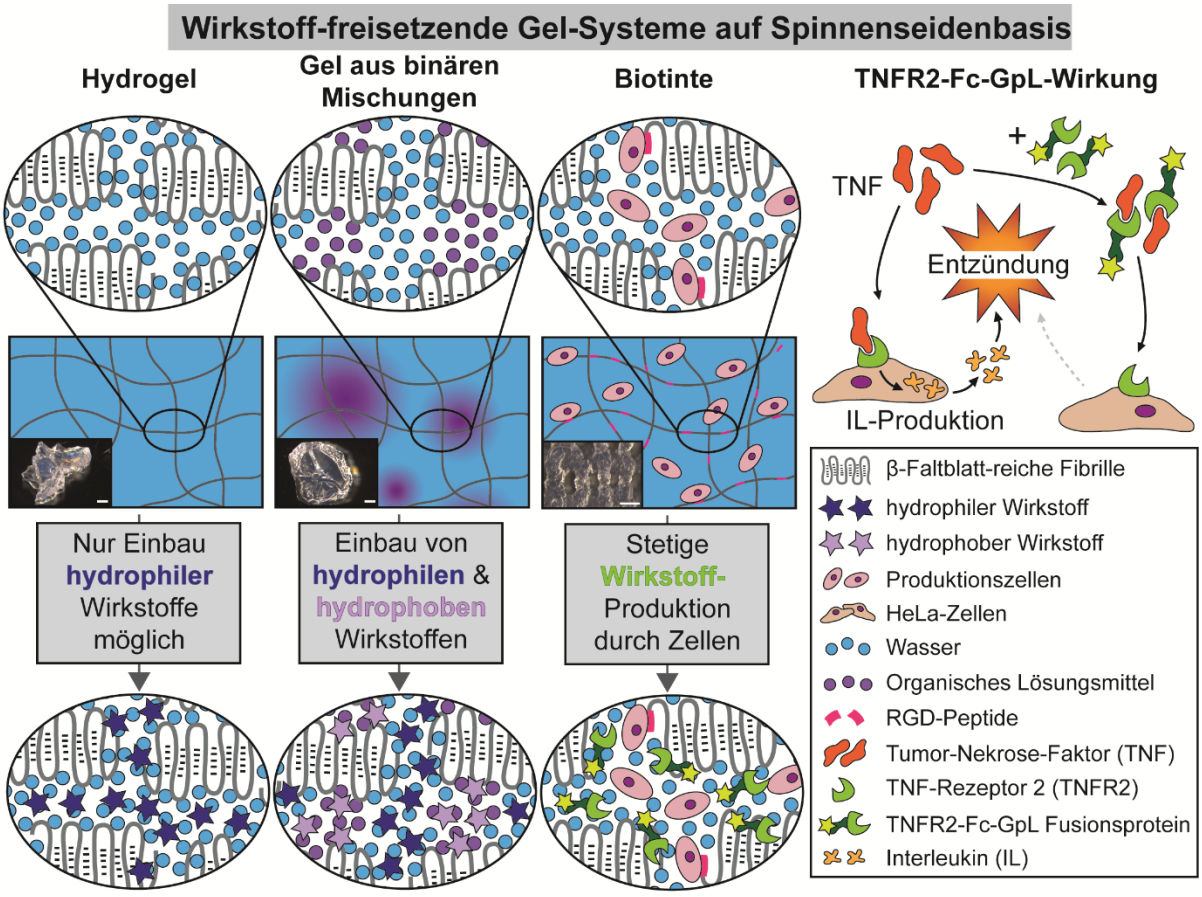

Abbildung 24: eADF4(C16)-basierte 3D-Spinnenseidenmatrizes als potentielle Wirkstoff-freisetzende Depots. Während in Hydrogele wasserlösliche, hydrophile Substanzen eingebaut werden, können hydrophobe Wirkstoffe in Gele aus binären Mischungen (Wasser/DMSO) formuliert und kontinuierlich freigesetzt werden. Zusätzlich können Produktionszellen in Spinnenseiden-Biotinten eingekapselt werden, um stetig ein wasserlösliches, therapeutisches Reporter-Fusionsprotein (TNFR2-Fc-GpL) zu produzieren und freizusetzen. TNFR2-Fc-GpL fängt den pro-inflammatorisch wirkenden TNF ab, wodurch eine Entzündungsreaktion (IL-Produktion) verhindert oder eingedämmt wird.

3.3.5. Vaskularisierbarkeit von Spinnenseidengerüsten

Da die freie Diffusionsgrenze von Substanzen in einem Konstrukt/Gewebe etwa 200 µm beträgt, ist die Vaskularisierung von künstlichen Gewebegerüsten durch Ausbildung neuer Blutgefäße eine Grundvoraussetzung für die Versorgung mit Sauerstoff und Nährstoffen sowie den Abtransport von Stoffwechselprodukten nach der Implantation [276]. In **Teilarbeit X** wurde analysiert, wie eADF4(C16)- und eADF4(C16)-RGD-Hydrogele in einem Arteriovenösen-Loop-Modell *in vivo* nach der (subkutanen) Implantation in Ratten vaskularisiert werden. Das Augenmerk lag dabei auf der Bildung von neuem Gewebe, besonders von Blutgefäßen im Rahmen der Angiogenese, auf möglichen Inflammations- und Immunreaktionen (siehe 3.3.1.3.) und der Bioabbaubarkeit (siehe 3.3.3.2.) nach zwei bzw. vier Wochen. Anhand einer µ-Computertomographischen (µCT) Analyse konnten der ursprüngliche Loop und die davon abzweigenden, neu gebildeten Blutgefäße innerhalb beider Hydrogel-Spezies visualisiert werden. Dabei unterstützten eADF4(C16)-RGD-Hydrogele die Absprossung und Bildung neuer Blutgefäße deutlich stärker als die eADF4(C16)-Variante (**Abbildung 25**).

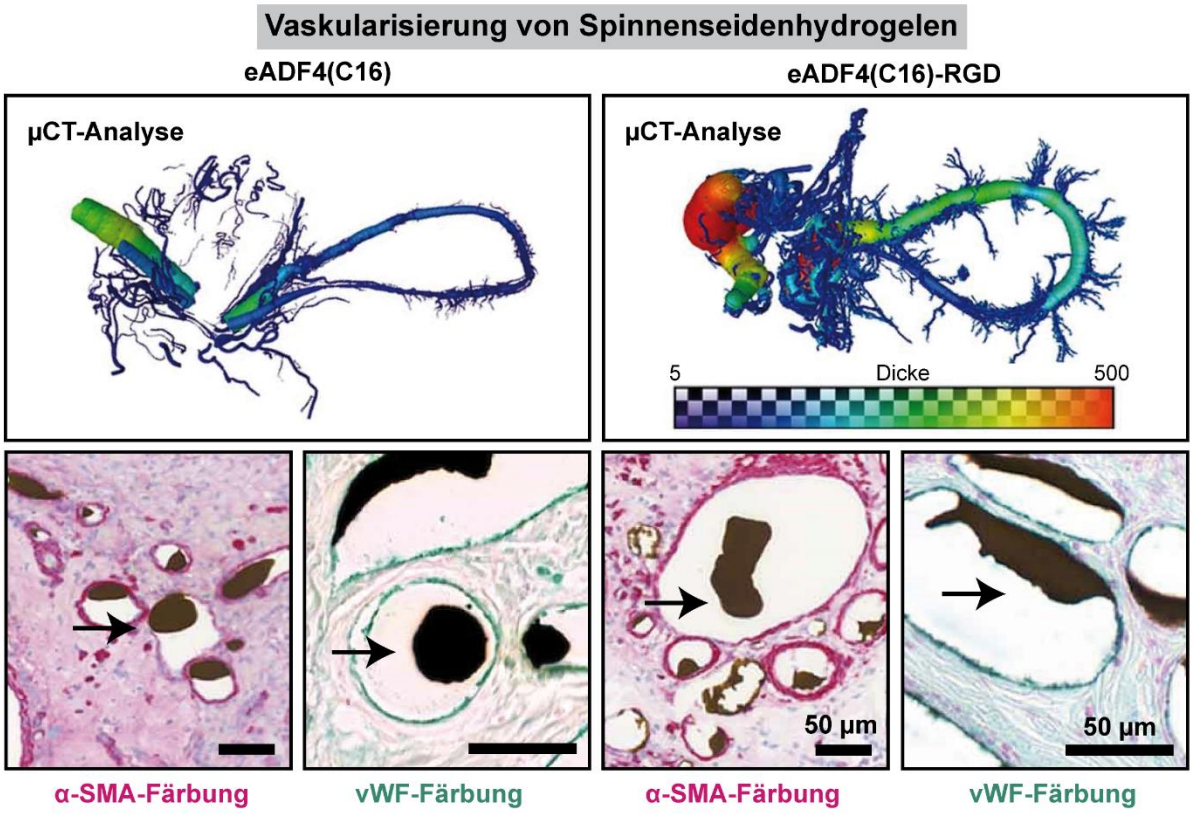

Abbildung 25:. Die Vaskularisierung von eADF4(C16)- und eADF4(C16)-RGD-Hydrogelen wurde i*n vivo* in einem Arteriovenösen-Loop-Modell in der Ratte untersucht. Die Bildung neuer Blutgefäße (Angiogenese) wurde nach vier Wochen anhand von µCT-Aufnahmen sowie spezifischer α-SMA- und vWF-Färbung histologischer Querschnitte gezeigt. Modifiziert nach [273c] und reproduziert mit freundlicher Genehmigung des Verlags IOP Publishing (© 2021 The Author(s). Published by IOP Publishing Ltd).

Histologische, Hämatoxylin/Eosin-gefärbte Querschnitte der Konstrukte bestätigten ebenfalls die Bildung von neuem Vaskulargewebe in der Umgebung des Loops. In beiden Hydrogel-Varianten zeigte die spezifische Färbung von Glattmuskel-Aktin (α-SMA) die neu gebildeten

Blutgefäße, während die Immun-Färbung des von-Willebrand-Faktors (vWF) das Vorhandensein von Endothelzellen an den Blutgefäßwänden verdeutlichte (**Abbildung 25**). Generell waren eADF4(C16)-RGD-Konstrukte im Vergleich mit eADF4(C16)-Gerüsten stabiler und wiesen eine deutlich höhere Anzahl an neuen Blutgefäßen auf. Die Ergebnisse aus **Teilarbeit X** bestätigten somit, dass sich eADF4(C16)-basierte Spinnenseiden-Hydrogele sehr gut für die Gewebezucht eignen und eine Modifikation mit dem Integrin-bindenden RGD-Peptid die Neubildung von Gewebe entscheidend fördert.

3.4. Fazit und Ausblick

Diese Dissertation konnte zeigen, dass rekombinante Spinnenseidengerüste aufgrund ihrer intrinsischen Eigenschaften (z.B. Biokompatibilität, Mikrobenabstoßung, Abbaubarkeit) vielfältig in der Gewebezüchtung eingesetzt werden können. Die vielseitige Prozessierbarkeit und diverse Funktionalisierungsmethoden ermöglichen die Herstellung angepasster Gerüste für spezifische Anwendungen. Die hier gewonnen Erkenntnisse können in Zukunft beispielsweise genutzt werden, um Implantatoberflächen gewebespezifisch zu modifizieren. Die Freisetzung bioaktiver Wirkstoffe kann genutzt werden, um gewünschte Zell-Interaktionen zu induzieren. Zusätzlich können anhand der identifizierten, selektiven Materialien hierarchisch strukturierte Gewebe entwickelt werden, die aus verschiedenen Zelltypen, Morphologien, Signalstoffen und Gradienten bestehen.

4. Literaturverzeichnis

[1] a) N. Huebsch, D. J. Mooney, *Nature* **2009**, 462, 426; b) G. M. Raghavendra, K. Varaprasad, T. Jayaramudu, in *Nanotechnology Applications for Tissue Engineering*, DOI: https://doi.org/10.1016/B978-0-323-32889-0.00002-9 (Eds: S. Thomas, Y. Grohens, N. Ninan), William Andrew Publishing, Oxford **2015**, p. 21; c) M. Ebrahimi, *Biomedical Journal* **2018**, 1, 3.

[2] S. Gobbi, *Biomedical Journal of Scientific & Technical Research* **2019**, 14.

[3] H. F. Hildebrand, *BioNanoMaterials* **2013**, 14, 119.

[4] B. D. Ratner, G. Zhang, in *Biomaterials Science (Fourth Edition)*, DOI: https://doi.org/10.1016/B978-0-12-816137-1.00002-7 (Eds: W. R. Wagner, S. E. Sakiyama-Elbert, G. Zhang, M. J. Yaszemski), Academic Press **2020**, p. 21.

[5] B. D. Ratner, *Annual Review of Biomedical Engineering* **2019**, 21, 171.

[6] S. Gobbi, G. Reinke, V. Gobbi, Y. Rocha, T. Sousa, M. Coutinho, **2020**, 9, 23.

[7] I. V. Yannas, J. F. Burke, *J Biomed Mater Res* **1980**, 14, 65.

[8] S. F. Badylak, G. C. Lantz, A. Coffey, L. A. Geddes, *J Surg Res* **1989**, 47, 74.

[9] a) R. Langer, J. P. Vacanti, *Science* **1993**, 260, 920; b) C. A. Vacanti, J. P. Vacanti, *Surg Technol Int* **1991**, I, 43.

[10] J. Black, *Journal of Biomedical Materials Research* **1982**, 16, 159.

[11] S. J. Kalita, in *Functional Nanostructures: Processing, Characterization, and Applications*, DOI: 10.1007/978-0-387-48805-9_4 (Ed: S. Seal), Springer New York, New York, NY **2008**, p. 168.

[12] A. C. Tathe, M. S. Ghodke, A. P. G. Nikalje, Y. B. Chavan, **2010**.

[13] S. Bose, D. Ke, H. Sahasrabudhe, A. Bandyopadhyay, *Prog Mater Sci* **2018**, 93, 45.

[14] a) E. T. J. Chong, J. W. Ng, P.-C. Lee, *BIO Integration* **2022**, DOI: 10.15212/bioi-2022-0009; b) P. Parida, A. Behera, S. Mishra, *International Journal of Advances in Applied Sciences* **2012**, 1.

[15] R. d. Moral, M. González, J. Navarro, P. C. Marijuán, *Information* **2011**, 2, 651.

[16] K. Borcherding, G. Schmidmaier, G. O. Hofmann, B. Wildemann, *Injury* **2021**, 52 Suppl 2, S106.

[17] D. F. Williams, *Biomaterials* **2008**, 29, 2941.

[18] K. Sadtler, A. Singh, M. T. Wolf, X. Wang, D. M. Pardoll, J. H. Elisseeff, *Nat. Rev. Mater.* **2016**, 1, 16040.

[19] C. A. Homsy, *Journal of Biomedical Materials Research* **1970**, 4, 341.

[20] M. Weber, H. Steinle, S. Golombek, L. Hann, C. Schlensak, H. P. Wendel, M. Avci-Adali, *Frontiers in Bioengineering and Biotechnology* **2018**, 6.

[21] A. Carnicer-Lombarte, S.-T. Chen, G. G. Malliaras, D. G. Barone, *Frontiers in Bioengineering and Biotechnology* **2021**, 9.

[22] a) T. R. Kyriakides, in *Host Response to Biomaterials*, DOI: https://doi.org/10.1016/B978-0-12-800196-7.00005-0 (Ed: S. F. Badylak), Academic Press, Oxford **2015**, p. 81; b) F. Wei, S. Liu, M. Chen, G. Tian, K. Zha, Z. Yang, S. Jiang, M. Li, X. Sui, Z. Chen, Q. Guo, *Frontiers in Bioengineering and Biotechnology* **2021**, 9.

[23] a) C. J. Wilson, R. E. Clegg, D. I. Leavesley, M. J. Pearcy, *Tissue Eng* **2005**, 11, 1; b) T. A. Horbett, R. A. Latour, in *Biomaterials Science (Fourth Edition)*, DOI: https://doi.org/10.1016/B978-0-12-816137-1.00042-8 (Eds: W. R. Wagner, S. E. Sakiyama-Elbert, G. Zhang, M. J. Yaszemski), Academic Press **2020**, p. 645; c) L. C. Xu, J. W. Bauer, C. A. Siedlecki, *Colloids Surf B Biointerfaces* **2014**, 124, 49.

[24] a) R. M. Visalakshan, M. N. MacGregor, S. Sasidharan, A. Ghazaryan, A. M. Mierczynska-Vasilev, S. Morsbach, V. Mailänder, K. Landfester, J. D. Hayball, K. Vasilev, *ACS Appl Mater Interfaces* **2019**, 11, 27615; b) M. Ramstedt, I. A. C. Ribeiro, H. Bujdakova, F. J. M. Mergulhão, L. Jordao, P. Thomsen, M. Alm, M. Burmølle, T. Vladkova, F. Can, M. Reches, M. Riool, A. Barros, R. L. Reis, E. Meaurio, J. Kikhney, A. Moter, S. A. J. Zaat, J. Sjollema, *Macromol Biosci* **2019**, 19, e1800384.

[25] B. G. Keselowsky, D. M. Collard, A. J. García, *J Biomed Mater Res A* **2003**, 66, 247.

[26] a) J. M. Anderson, A. Rodriguez, D. T. Chang, *Semin Immunol* **2008**, 20, 86; b) J. M. Anderson, *Annual Review of Materials Research* **2001**, 31, 81; c) S. Franz, S. Rammelt, D. Scharnweber, J. C. Simon, *Biomaterials* **2011**, 32, 6692; d) A. M. Rokstad, I. Lacík, P. de Vos, B. L. Strand, *Adv Drug Deliv Rev* **2014**, 67-68, 111; e) D. T. Luttikhuizen, M. C. Harmsen, M. J. Van Luyn, *Tissue Eng* **2006**, 12, 1955.

[27] a) Z. Xia, J. T. Triffitt, *Biomedical Materials* **2006**, 1, R1; b) J. M. Anderson, K. M. Miller, *Biomaterials* **1984**, 5, 5.

[28] a) E. M. Sussman, M. C. Halpin, J. Muster, R. T. Moon, B. D. Ratner, *Annals of Biomedical Engineering* **2014**, 42, 1508; b) A. Sica, A. Mantovani, *J Clin Invest* **2012**, 122, 787; c) B. N. Brown, B. D. Ratner, S. B. Goodman, S. Amar, S. F. Badylak, *Biomaterials* **2012**, 33, 3792; d) P. J. Murray, *Annu Rev Physiol* **2017**, 79, 541.

[29] a) M. Geetha, A. K. Singh, R. Asokamani, A. K. Gogia, *Progress in Materials Science* **2009**, 54, 397; b) R. I. M. Asri, W. S. W. Harun, M. Samykano, N. A. C. Lah, S. A. C. Ghani, F. Tarlochan, M. R. Raza, *Materials Science and Engineering: C* **2017**, 77, 1261; c) S. J. Gobbi, *Biomedical Journal of Scientific & Technical Research* **2018**, 12; d) M. Niinomi, *Journal of the Mechanical Behavior of Biomedical Materials* **2008**, 1, 30; e) A. Khemka, L. Frossard, S. J. Lord, B. Bosley, M. Al Muderis, *Acta Orthop* **2015**, 86, 740; f) D. Apostu, O. Lucaciu, C. Berce, D. Lucaciu, D. Cosma, *J Int Med Res* **2018**, 46, 2104.

[30] a) U. Braun, E. Lorenz, C. Weimann, H. Sturm, I. Karimov, J. Ettl, R. Meier, W. A. Wohlgemuth, H. Berger, M. Wildgruber, *Journal of the Mechanical Behavior of Biomedical Materials* **2016**, 64, 281; b) E. L. Lawrence, I. G. Turner, *Med Eng Phys* **2005**, 27, 443; c) R. C. L. Feneley, I. B. Hopley, P. N. T. Wells, *Journal of Medical Engineering & Technology* **2015**, 39, 459; d) P. Wyman, in *Coatings for Biomedical Applications*, DOI: https://doi.org/10.1533/9780857093677.1.3 (Ed: M. Driver), Woodhead Publishing **2012**, p. 3.

[31] a) Q. Wei, T. Becherer, S. Angioletti-Uberti, J. Dzubiella, C. Wischke, A. T. Neffe, A. Lendlein, M. Ballauff, R. Haag, *Angewandte Chemie International Edition* **2014**, 53, 8004; b) M. Pagel, A. G. Beck-Sickinger, *Biol Chem* **2017**, 398, 3; c) K. Kyzioł, Ł. Kaczmarek, A. Kyzioł, in *Handbook of Composites from Renewable Materials*, DOI: https://doi.org/10.1002/9781119441632.ch80 **2017**, p. 457; d) S. Pacelli, V. Manoharan, A. Desalvo, N. Lomis, K. S. Jodha, S. Prakash, A. Paul, *Journal of Materials Chemistry B* **2016**, 4, 1586.

[32] a) I.-S. Yeo, H.-Y. Kim, K. S. Lim, J.-S. Han, *The International Journal of Artificial Organs* **2012**, 35, 762; b) V. Russotto, A. Cortegiani, S. M. Raineri, A. Giarratano, *J Intensive Care* **2015**, 3, 54; c) E. Barth, Q. M. Myrvik, W. Wagner, A. G. Gristina, *Biomaterials* **1989**, 10, 325; d) E. M. Hetrick, M. H. Schoenfisch, *Chemical Society Reviews* **2006**, 35, 780.

[33] L. L. Leape, T. A. Brennan, N. Laird, A. G. Lawthers, A. R. Localio, B. A. Barnes, L. Hebert, J. P. Newhouse, P. C. Weiler, H. Hiatt, *New England Journal of Medicine* **1991**, 324, 377.

[34] a) J. W. Costerton, P. S. Stewart, E. P. Greenberg, *Science* **1999**, 284, 1318; b) P. S. Stewart, J. William Costerton, *The Lancet* **2001**, 358, 135; c) P. S. Stewart, *International Journal of Medical Microbiology* **2002**, 292, 107; d) M. M. Harriott, M. C. Noverr, *Antimicrob Agents Chemother* **2009**, 53, 3914; e) E. G. Di Domenico, S. G. Rimoldi, I. Cavallo, G. D'Agosto, E. Trento, G. Cagnoni, A. Palazzin, C. Pagani, F. Romeri, E. De Vecchi, M. Schiavini, D. Secchi, C. Antona, G. Rizzardini, R. B. Dichirico, L. Toma, D. Kovacs, G. Cardinali, M. T. Gallo, M. R. Gismondo, F. Ensoli, *BMC Microbiology* **2019**, 19, 228; f) F. Sun, F. Qu, Y. Ling, P. Mao, P. Xia, H. Chen, D. Zhou, *Future Microbiol* **2013**, 8, 877; g) G. G. Anderson, G. A. O'Toole, in *Bacterial Biofilms*, DOI: 10.1007/978-3-540-75418-3_5 (Ed: T. Romeo), Springer Berlin Heidelberg, Berlin, Heidelberg **2008**, p. 85; h) O. Ciofu, E. Rojo-Molinero, M. D. Macià, A. Oliver, *Apmis* **2017**, 125, 304.

[35] a) A. G. Gristina, *Science* **1987**, 237, 1588; b) R. Srinivasan, S. Santhakumari, P. Poonguzhali, M. Geetha, M. Dyavaiah, L. Xiangmin, *Frontiers in Microbiology* **2021**, 12.

[36] a) S. B. Levy, B. Marshall, *Nature Medicine* **2004**, 10, S122; b) D. Davies, *Nat Rev Drug Discov* **2003**, 2, 114; c) G. D. Wright, *Nat Rev Microbiol* **2007**, 5, 175; d) D. van Duin, D. L. Paterson, *Infect Dis Clin North Am* **2016**, 30, 377; e) H. Nikaido, *Annu Rev Biochem* **2009**, 78, 119.

[37] a) T. J. Foster, *J Clin Invest* **2004**, 114, 1693; b) J. A. Lindsay, M. T. Holden, *Trends Microbiol* **2004**, 12, 378; c) G. Ippolito, S. Leone, F. N. Lauria, E. Nicastri, R. P. Wenzel, *International Journal of Infectious Diseases* **2010**, 14, S7.

[38] a) D. Campoccia, L. Montanaro, C. R. Arciola, *Biomaterials* **2013**, 34, 8018; b) D. Campoccia, L. Montanaro, C. R. Arciola, *Biomaterials* **2013**, 34, 8533; c) V. B. Damodaran, N. S. Murthy, *Biomaterials Research* **2016**, 20, 18.

[39] a) C. L. Romanò, H. Tsuchiya, I. Morelli, A. G. Battaglia, L. Drago, *Bone & Joint Research* **2019**, 8, 199; b) R.-Y. Tsay, T. Imae, in *Encyclopedia of Biocolloid and Biointerface Science 2V Set*, DOI: https://doi.org/10.1002/9781119075691.ch11 **2016**, p. 145; c) U. Mahanta, M. Khandelwal, A. S. Deshpande, *J Mater Sci* **2021**, 56, 17915.

[40] a) S. Chen, L. Li, C. Zhao, J. Zheng, *Polymer* **2010**, 51, 5283; b) S. Krishnan, C. J. Weinman, C. K. Ober, *Journal of Materials Chemistry* **2008**, 18, 3405; c) R. Kenawy el, S. D. Worley, R. Broughton, *Biomacromolecules* **2007**, 8, 1359.

[41] a) B. Wang, Z. Ye, Y. Tang, Y. Han, Q. Lin, H. Liu, H. Chen, K. Nan, *Int J Nanomedicine* **2017**, 12, 111; b) M. R. E. Santos, A. C. Fonseca, P. V. Mendonça, R. Branco, A. C. Serra, P. V. Morais, J. F. J. Coelho, *Materials (Basel)* **2016**, 9; c) C. Wang, S. Feng, J. Qie, X. Wei, H. Yan, K. Liu, *Int J Pharm* **2019**, 554, 284; d) Y. Yang, Z. Cai, Z. Huang, X. Tang, X. Zhang, *Polymer Journal* **2018**, 50, 33; e) M. Zasloff, *Nature* **2002**, 415, 389; f) B. P. Lazzaro, M. Zasloff, J. Rolff, *Science* **2020**, 368; g) Y. Liu, L. Shi, L. Su, H. C. van der Mei, P. C. Jutte, Y. Ren, H. J. Busscher, *Chemical Society Reviews* **2019**, 48, 428.

[42] D. Campoccia, L. Montanaro, P. Speziale, C. R. Arciola, *Biomaterials* **2010**, 31, 6363.

[43] M. E. Karlovsky, L. Kushner, G. H. Badlani, *Curr Urol Rep* **2005**, 6, 376.

[44] a) M. W. Tibbitt, C. B. Rodell, J. A. Burdick, K. S. Anseth, *Proceedings of the National Academy of Sciences* **2015**, 112, 14444; b) Y. Wang, *Journal of Materials Science & Technology* **2016**, 32, 801; c) S. Bhat, A. Kumar, *Biomatter* **2013**, 3.

[45] a) P. Qi, M. F. Maitz, N. Huang, *Surface and Coatings Technology* **2013**, 233, 80; b) S. K. Jaganathan, E. Supriyanto, S. Murugesan, A. Balaji, M. K. Asokan, *BioMed Research International* **2014**, 2014, 459465; c) M. T. Lam, J. C. Wu, *Expert Rev Cardiovasc Ther* **2012**, 10, 1039.

[46] a) E. L. Lawrence, I. G. Turner, *J Mater Sci Mater Med* **2006**, 17, 147; b) J. H. Park, Y. W. Cho, I. C. Kwon, S. Y. Jeong, Y. H. Bae, *Biomaterials* **2002**, 23, 3991.

[47] a) R. Narayan, in *ASM Handbook*, Vol. 23 **2003**; b) F. F. Buechel, M. J. Pappas, in *Principles of Human Joint Replacement: Design and Clinical Application*, DOI: 10.1007/978-3-319-15311-7_1, Springer International Publishing, Cham **2015**, p. 1; c) S. S. Das, P. Chakraborti, *IOP Conference Series: Materials Science and Engineering* **2018**, 377, 012177; d) K. S. Katti, *Colloids and Surfaces B: Biointerfaces* **2004**, 39, 133; e) A. A. Khalifa, H. M. Bakr, *Arthroplasty* **2021**, 3, 32; f) M. F. Kunrath, C. Dahlin, *International Journal of Molecular Sciences* **2022**, 23, 2024; g) N. G. Fischer, C. Aparicio, *Colloids Surf B Biointerfaces* **2021**, 200, 111570.

[48] S. Spiller, F. Clauder, K. Bellmann-Sickert, A. G. Beck-Sickinger, *Biological Chemistry* **2021**, 402, 1271.

[49] a) L. Li, S. Chen, J. Zheng, B. D. Ratner, S. Jiang, *The Journal of Physical Chemistry B* **2005**, 109, 2934; b) Z. Zhang, M. Zhang, S. Chen, T. A. Horbett, B. D. Ratner, S. Jiang, *Biomaterials* **2008**, 29, 4285; c) K. L. Prime, G. M. Whitesides, *J. Am. Chem. Soc.* **1993**, 115, 10714; d) E. Ostuni, R. G. Chapman, R. E. Holmlin, S. Takayama, G. M. Whitesides, *Langmuir* **2001**, 17, 5605.

[50] S. Affatato, A. Ruggiero, M. Merola, *Composites Part B: Engineering* **2015**, 83, 276.

[51] a) D. Tsiapalis, A. De Pieri, M. Biggs, A. Pandit, D. I. Zeugolis, Vol. 3, ACS Publications, 2017, 1172; b) A. G. Harvey, E. W. Hill, A. Bayat, *Expert Rev Med Devices* **2013**, 10, 257; c) J. A. Hubbell, *Curr Opin Biotechnol* **1999**, 10, 123; d) P. Kingshott, G. Andersson, S. L. McArthur, H. J. Griesser, *Curr Opin Chem Biol* **2011**, 15, 667; e) H. Zhang, X. Zheng, W. Ahmed, Y. Yao, J. Bai, Y. Chen, C. Gao, *Biomacromolecules* **2018**, 19, 1746; f) H. Amani, H. Arzaghi, M. Bayandori, A. S. Dezfuli, H. Pazoki-Toroudi, A. Shafiee, L. Moradi, *Advanced Materials Interfaces* **2019**, 6, 1900572; g) N. R. Richbourg, N. A. Peppas, V. I. Sikavitsas, *Journal of Tissue Engineering and Regenerative Medicine* **2019**, 13, 1275.

[52] a) R. Williams, *Surface modification of biomaterials: Methods analysis and applications*, **2011**; b) N. Raval, D. Kalyane, R. Maheshwari, R. K. Tekade, in *Biomaterials and Bionanotechnology*, DOI: https://doi.org/10.1016/B978-0-12-814427-5.00017-2 (Ed: R. K. Tekade), Academic Press **2019**, p. 639; c) G. Wu, P. Li, H. Feng, X. Zhang, P. K. Chu, *Journal of Materials Chemistry B* **2015**, 3, 2024.

[53] a) A. Leonard, P. Koria, *J Bioact Compat Polym* **2017**, 32, 568; b) R. C. H. Gresham, C. S. Bahney, J. K. Leach, *Bioactive Materials* **2021**, 6, 1945; c) H. A. Santos, *Biomatter* **2012**, 2, 237; d) J. Li, D. J. Mooney, *Nat Rev Mater* **2016**, 1; e) T. R. Hoare, D. S. Kohane, *Polymer* **2008**, 49, 1993; f) O. S. Fenton, K. N. Olafson, P. S. Pillai, M. J. Mitchell, R. Langer, *Adv Mater* **2018**, DOI: 10.1002/adma.201705328e1705328.

[54] a) D. Das, Z. Zhang, T. Winkler, M. Mour, C. Gunter, M. Morlock, H. G. Machens, A. F. Schilling, *Adv Biochem Eng Biotechnol* **2012**, 126, 317; b) D. Hutmacher, M. B. Hürzeler, H. Schliephake, *International Journal of Oral & Maxillofacial Implants* **1996**, 11.

[55] a) D. E. Discher, D. J. Mooney, P. W. Zandstra, *Science* **2009**, 324, 1673; b) J. Li, Y. Liu, Y. Zhang, B. Yao, Z. Li, W. Song, Y. Wang, X. Duan, X. Yuan, X. Fu, *Frontiers in Cell and Developmental Biology* **2021**, 9, 640388; c) N. Huettner, T. R. Dargaville, A. Forget, *Trends in Biotechnology* **2018**, 36, 372.

[56] a) S. Zijl, A. S. Vasilevich, P. Viswanathan, A. L. Helling, N. R. M. Beijer, G. Walko, C. Chiappini, J. de Boer, F. M. Watt, *Acta Biomater* **2019**, 84, 133; b) M. Nikkhah, F. Edalat, S. Manoucheri, A. Khademhosseini, *Biomaterials* **2012**, 33, 5230; c) P.-Y.

Wang, W.-T. Li, J. Yu, W.-B. Tsai, *Journal of Materials Science: Materials in Medicine* **2012**, 23, 3015.

[57] a) D. Li, Q. Zheng, Y. Wang, H. Chen, *Polymer Chemistry* **2014**, 5, 14; b) A.-S. Mertgen, V. T. Trossmann, A. G. Guex, K. Maniura-Weber, T. Scheibel, M. Rottmar, *ACS Applied Materials & Interfaces* **2020**, 12, 21342.

[58] P. Y. Wang, H. Thissen, W. B. Tsai, *Biotechnology and bioengineering* **2012**, 109, 2104.

[59] a) A. R. Del Bakhshayesh, N. Asadi, A. Alihemmati, H. Tayefi Nasrabadi, A. Montaseri, S. Davaran, S. Saghati, A. Akbarzadeh, A. Abedelahi, *Journal of Biological Engineering* **2019**, 13, 85; b) D. Barik, K. Kundu, M. Dash, in *Biomimetic Biomaterials for Tissue Regeneration and Drug Delivery*, DOI: 10.1007/978-981-16-4566-2_1 (Ed: M. Dash), Springer Singapore, Singapore **2022**, p. 1; c) R. J. Wade, J. A. Burdick, *Mater. Today* **2012**, 15, 454.

[60] a) L. H. Nguyen, A. K. Kudva, N. S. Saxena, K. Roy, *Biomaterials* **2011**, 32, 6946; b) N. A. Hale, Y. Yang, P. Rajagopalan, *ACS Applied Materials & Interfaces* **2010**, 2, 2317; c) X. Tong, J. Jiang, D. Zhu, F. Yang, *ACS Biomater Sci Eng* **2016**, 2, 845; d) R. Sunyer, A. J. Jin, R. Nossal, D. L. Sackett, *PLoS One* **2012**, 7, e46107; e) Z. Y. Guan, C. Y. Wu, J. T. Wu, C. H. Tai, J. Yu, H. Y. Chen, *ACS Appl Mater Interfaces* **2016**, 8, 13812.

[61] a) T. M. Freyman, I. V. Yannas, L. J. Gibson, *Progress in Materials Science* **2001**, 46, 273; b) S. J. Hollister, *Nature Materials* **2005**, 4, 518; c) J. Zhu, *Biomaterials* **2010**, 31, 4639; d) T.-C. Ho, C.-C. Chang, H.-P. Chan, T.-W. Chung, C.-W. Shu, K.-P. Chuang, T.-H. Duh, M.-H. Yang, Y.-C. Tyan, *Molecules* **2022**, 27, 2902; e) E. Caló, V. V. Khutoryanskiy, *European Polymer Journal* **2015**, 65, 252; f) Q. Chai, Y. Jiao, X. Yu, *Gels* **2017**, 3.

[62] G. Huang, F. Li, X. Zhao, Y. Ma, Y. Li, M. Lin, G. Jin, T. J. Lu, G. M. Genin, F. Xu, *Chemical Reviews* **2017**, 117, 12764.

[63] a) S. J. Morrison, A. C. Spradling, *Cell* **2008**, 132, 598; b) A. Spradling, D. Drummond-Barbosa, T. Kai, *Nature* **2001**, 414, 98; c) A. Wilson, A. Trumpp, *Nat. Rev. Immunol.* **2006**, 6, 93; d) L. Li, T. Xie, *Annu. Rev. Cell Dev. Biol.* **2005**, 21, 605; e) D. T. Scadden, *Nature* **2006**, 441, 1075.

[64] a) S. W. Lane, D. A. Williams, F. M. Watt, *Nat. Biotechnol.* **2014**, 32, 795; b) S. M. Dellatore, A. S. Garcia, W. M. Miller, *Curr. Opin. Biotechnol.* **2008**, 19, 534; c) H. Wang, L. A. Leinwand, K. S. Anseth, *Nat. Rev. Cardiol.* **2014**, 11, 715.

[65] F. Rosso, A. Giordano, M. Barbarisi, A. Barbarisi, *J Cell Physiol* **2004**, 199, 174.

[66] M. C. Deller, E. Y. Jones, *Current Opinion in Structural Biology* **2000**, 10, 213.

[67] a) C.-H. Heldin, *Cell* **1995**, 80, 213; b) J. B. Spangler, I. Moraga, J. L. Mendoza, K. C. Garcia, *Annu Rev Immunol* **2015**, 33, 139; c) M. J. Wieduwilt, M. M. Moasser, *Cell Mol Life Sci* **2008**, 65, 1566; d) M. F. Brizzi, G. Tarone, P. Defilippi, *Curr. Opin. Cell Biol.* **2012**, 24, 645; e) S.-H. Kim, J. Turnbull, S. Guimond, *Journal of Endocrinology* **2011**, 209, 139; f) T. A. Wilgus, *Adv Wound Care (New Rochelle)* **2012**, 1, 249; g) M. A. Schwartz, V. Baron, *Current Opinion in Cell Biology* **1999**, 11, 197.

[68] J. M. Zhang, J. An, *Int Anesthesiol Clin* **2007**, 45, 27.

[69] a) P. Berraondo, M. F. Sanmamed, M. C. Ochoa, I. Etxeberria, M. A. Aznar, J. L. Pérez-Gracia, M. E. Rodríguez-Ruiz, M. Ponz-Sarvise, E. Castañón, I. Melero, *British Journal of Cancer* **2019**, 120, 6; b) S. F. Lowry, *Arch Surg* **1993**, 128, 1235.

[70] a) M. Schuldiner, O. Yanuka, J. Itskovitz-Eldor, D. A. Melton, N. Benvenisty, *Proceedings of the National Academy of Sciences* **2000**, 97, 11307; b) P. S. Briquez, J. A. Hubbell, M. M. Martino, *Adv Wound Care (New Rochelle)* **2015**, 4, 479.

[71] a) J. Taipale, J. Keski-Oja, *The FASEB Journal* **1997**, 11, 51; b) M. Lind, *Acta Orthopaedica Scandinavica* **1996**, 67, 407; c) S. A. Aaronson, *Science* **1991**, 254, 1146.
[72] M. R. Morgan, M. J. Humphries, M. D. Bass, *Nat Rev Mol Cell Biol* **2007**, 8, 957.
[73] a) S. Jin, C. F. Guerrero-Juarez, L. Zhang, I. Chang, R. Ramos, C.-H. Kuan, P. Myung, M. V. Plikus, Q. Nie, *Nature Communications* **2021**, 12, 1088; b) E. Armingol, A. Officer, O. Harismendy, N. E. Lewis, *Nature Reviews Genetics* **2021**, 22, 71.
[74] a) T. Xin, V. Greco, P. Myung, *Cell* **2016**, 164, 1212; b) I. Nitsan, S. Drori, Y. E. Lewis, S. Cohen, S. Tzlil, *Nat. Phys.* **2016**, 12, 472; c) E. Dejana, *Nat. Rev. Mol. Cell Biol.* **2004**, 5, 261.
[75] B. Alberts, A. Johnson, J. Lewis, M. Raff, K. Roberts, P. Walter, *Molekularbiologie der Zelle*, John Wiley & Sons, **2011**.
[76] K. Ebnet, *Histochem. Cell Biol.* **2008**, 130, 1.
[77] A. Rodríguez-Sinovas, J. A. Sánchez, L. Valls-Lacalle, M. Consegal, I. Ferreira-González, *Int J Mol Sci* **2021**, 22.
[78] S. Verheule, S. Kaese, *Front Pharmacol* **2013**, 4, 81.
[79] a) D. T. Scadden, *Cell* **2014**, 157, 41; b) W. P. Daley, S. B. Peters, M. Larsen, *J Cell Sci* **2008**, 121, 255; c) A. D. Theocharis, S. S. Skandalis, C. Gialeli, N. K. Karamanos, *Adv. Drug Delivery Rev.* **2016**, 97, 4.
[80] a) B. R. Freedman, D. J. Mooney, *Advanced Materials* **2019**, 31, 1806695; b) P. P. Purslow, *Frontiers in physiology* **2020**, 11, 495.
[81] W. H. Chooi, S. Y. Chew, *Biomaterials* **2019**, 197, 327.
[82] J. Engel, M. Chiquet, in *The Extracellular Matrix: an Overview*, DOI: 10.1007/978-3-642-16555-9_1 (Ed: R. P. Mecham), Springer Berlin Heidelberg, Berlin, Heidelberg **2011**, p. 1.
[83] a) W. Han, Y. Jang, A. García, DOI: 10.1016/B978-0-12-816137-1.00045-3 **2020**, p. 701; b) R. O. Hynes, *Science* **2009**, 326, 1216; c) D. E. Birk, P. Brückner, in *The Extracellular Matrix: an Overview*, DOI: 10.1007/978-3-642-16555-9_3 (Ed: R. P. Mecham), Springer Berlin Heidelberg, Berlin, Heidelberg **2011**, p. 77.
[84] a) A. L. Berrier, K. M. Yamada, *Journal of Cellular Physiology* **2007**, 213, 565; b) K. R. Legate, S. A. Wickström, R. Fässler, *Genes Dev* **2009**, 23, 397; c) B. Geiger, A. Bershadsky, R. Pankov, K. M. Yamada, *Nat Rev Mol Cell Biol* **2001**, 2, 793.
[85] a) A. S. Khalil, A. W. Xie, W. L. Murphy, *ACS Chem. Biol.* **2014**, 9, 45; b) F. M. Watt, W. T. S. Huck, *Nat. Rev. Mol. Cell Biol.* **2013**, 14, 467; c) J. K. Kular, S. Basu, R. I. Sharma, *Journal of Tissue Engineering* **2014**, 5, 2041731414557112; d) F. T. Bosman, I. Stamenkovic, *The Journal of Pathology* **2003**, 200, 423; e) J. K. Mouw, G. Ou, V. M. Weaver, *Nat. Rev. Mol. Cell Biol.* **2014**, 15, 771; f) C. Frantz, K. M. Stewart, V. M. Weaver, *J. Cell Sci.* **2010**, 123, 4195.
[86] a) J. D. Humphrey, E. R. Dufresne, M. A. Schwartz, *Nature Reviews Molecular Cell Biology* **2014**, 15, 802; b) P. Lu, V. M. Weaver, Z. Werb, *J. Cell Biol.* **2012**, 196, 395.
[87] K. E. Kadler, C. Baldock, J. Bella, R. P. Boot-Handford, *Journal of Cell Science* **2007**, 120, 1955.
[88] a) M. J. Buehler, *Proc Natl Acad Sci U S A* **2006**, 103, 12285; b) K. Gelse, E. Pöschl, T. Aigner, *Advanced Drug Delivery Reviews* **2003**, 55, 1531; c) P. Fratzl, K. Misof, I. Zizak, G. Rapp, H. Amenitsch, S. Bernstorff, *Journal of Structural Biology* **1998**, 122, 119.
[89] a) C. G. Knight, L. F. Morton, A. R. Peachey, D. S. Tuckwell, R. W. Farndale, M. J. Barnes, *J Biol Chem* **2000**, 275, 35; b) W. M. Zhang, J. Kapyla, J. S. Puranen, C. G. Knight, C. F. Tiger, O. T. Pentikainen, M. S. Johnson, R. W. Farndale, J. Heino, D. Gullberg, *J Biol Chem* **2003**, 278, 7270.

[90] a) J. Myllyharju, K. I. Kivirikko, *Annals of Medicine* **2001**, 33, 7; b) S. Ricard-Blum, *Cold Spring Harb Perspect Biol* **2011**, 3, a004978.
[91] B. Brodsky, A. V. Persikov, *Adv Protein Chem* **2005**, 70, 301.
[92] T. Ushiki, *Arch Histol Cytol* **2002**, 65, 109.
[93] a) J. H. Kristensen, M. A. Karsdal, in *Biochemistry of Collagens, Laminins and Elastin*, DOI: https://doi.org/10.1016/B978-0-12-809847-9.00030-1 (Ed: M. A. Karsdal), Academic Press **2016**, p. 197; b) S. G. Wise, G. C. Yeo, M. A. Hiob, J. Rnjak-Kovacina, D. L. Kaplan, M. K. Ng, A. S. Weiss, *Acta Biomater* **2014**, 10, 1532; c) S. M. Mithieux, A. S. Weiss, in *Advances in Protein Chemistry*, Vol. 70, Academic Press **2005**, p. 437.
[94] a) K. Wang, X. Meng, Z. Guo, *Frontiers in Cell and Developmental Biology* **2021**, 9; b) S. M. Mithieux, J. E. Rasko, A. S. Weiss, *Biomaterials* **2004**, 25, 4921.
[95] a) B. C. Starcher, *Thorax* **1986**, 41, 577; b) M. J. Rock, S. A. Cain, L. J. Freeman, A. Morgan, K. Mellody, A. Marson, C. A. Shuttleworth, A. S. Weiss, C. M. Kielty, *J Biol Chem* **2004**, 279, 23748.
[96] J. Halper, M. Kjaer, in *Progress in Heritable Soft Connective Tissue Diseases*, DOI: 10.1007/978-94-007-7893-1_3 (Ed: J. Halper), Springer Netherlands, Dordrecht **2014**, p. 31.
[97] a) J. Xu, D. Mosher, in *The Extracellular Matrix: an Overview*, DOI: 10.1007/978-3-642-16555-9_2 (Ed: R. P. Mecham), Springer Berlin Heidelberg, Berlin, Heidelberg **2011**, p. 41; b) R. Pankov, K. M. Yamada, *J Cell Sci* **2002**, 115, 3861.
[98] a) Y. Mao, J. E. Schwarzbauer, *Matrix Biology* **2005**, 24, 389; b) J. E. Schwarzbauer, J. L. Sechler, *Current Opinion in Cell Biology* **1999**, 11, 622.
[99] a) K. Beck, I. Hunter, J. Engel, *The FASEB Journal* **1990**, 4, 148; b) E. Hohenester, *Essays Biochem* **2019**, 63, 285.
[100] a) J. H. Miner, P. D. Yurchenco, *Annual Review of Cell and Developmental Biology* **2004**, 20, 255; b) A. Domogatskaya, S. Rodin, K. Tryggvason, *Annual Review of Cell and Developmental Biology* **2012**, 28, 523.
[101] E. Hohenester, P. D. Yurchenco, *Cell Adh Migr* **2013**, 7, 56.
[102] A. D. Theocharis, S. S. Skandalis, G. N. Tzanakakis, N. K. Karamanos, *The FEBS Journal* **2010**, 277, 3904.
[103] N. Afratis, C. Gialeli, D. Nikitovic, T. Tsegenidis, E. Karousou, A. D. Theocharis, M. S. Pavão, G. N. Tzanakakis, N. K. Karamanos, *The FEBS Journal* **2012**, 279, 1177.
[104] a) A. D. Theocharis, C. Gialeli, P. Bouris, E. Giannopoulou, S. S. Skandalis, A. J. Aletras, R. V. Iozzo, N. K. Karamanos, *The FEBS Journal* **2014**, 281, 5023; b) R. V. Iozzo, L. Schaefer, *Matrix Biology* **2015**, 42, 11.
[105] U. Freudenberg, Y. Liang, K. L. Kiick, C. Werner, *Adv. Mater.* **2016**, 28, 8861.
[106] a) C. A. Buck, A. F. Horwitz, *Annual review of cell biology* **1987**, 3, 179; b) S. K. Akiyama, K. Nagata, K. M. Yamada, *Biochimica et Biophysica Acta (BBA) - Reviews on Biomembranes* **1990**, 1031, 91.
[107] E. Cukierman, R. Pankov, D. R. Stevens, K. M. Yamada, *Science* **2001**, 294, 1708.
[108] a) R. O. Hynes, *Cell* **1987**, 48, 549; b) M. J. Humphries, *Biochem Soc Trans* **2000**, 28, 311.
[109] a) R. O. Hynes, *Cell* **2002**, 110, 673; b) T. A. Springer, J. H. Wang, *Adv Protein Chem* **2004**, 68, 29; c) J. D. Humphries, A. Byron, M. J. Humphries, *Journal of Cell Science* **2006**, 119, 3901.
[110] M. A. Arnaout, B. Mahalingam, J. P. Xiong, *Annu Rev Cell Dev Biol* **2005**, 21, 381.
[111] M. Humphries, *Journal of Cell Science* **1990**, 97, 585.

[112] a) A. van der Flier, A. Sonnenberg, *Cell and Tissue Research* **2001**, 305, 285; b) E. F. Plow, T. A. Haas, L. Zhang, J. Loftus, J. W. Smith, *Journal of Biological Chemistry* **2000**, 275, 21785; c) E. Ruoslahti, *Annu. Rev. Cell Dev. Biol.* **1996**, 12, 697.

[113] a) T. G. Kapp, F. Rechenmacher, S. Neubauer, O. V. Maltsev, E. A. Cavalcanti-Adam, R. Zarka, U. Reuning, J. Notni, H.-J. Wester, C. Mas-Moruno, J. Spatz, B. Geiger, H. Kessler, *Scientific Reports* **2017**, 7, 39805; b) B. S. Ludwig, H. Kessler, S. Kossatz, U. Reuning, *Cancers (Basel)* **2021**, 13.

[114] a) C. E. Schmidt, A. F. Horwitz, D. A. Lauffenburger, M. P. Sheetz, *J Cell Biol* **1993**, 123, 977; b) S. P. Palecek, C. E. Schmidt, D. A. Lauffenburger, A. F. Horwitz, *J Cell Sci* **1996**, 109 (Pt 5), 941; c) D. A. Lauffenburger, A. F. Horwitz, *Cell* **1996**, 84, 359; d) S. P. Palecek, J. C. Loftus, M. H. Ginsberg, D. A. Lauffenburger, A. F. Horwitz, *Nature* **1997**, 385, 537.

[115] O. J. Mezu-Ndubuisi, A. Maheshwari, *Pediatric Research* **2021**, 89, 1619.

[116] a) A. Katsumi, A. W. Orr, E. Tzima, M. A. Schwartz, *J Biol Chem* **2004**, 279, 12001; b) T. D. Ross, B. G. Coon, S. Yun, N. Baeyens, K. Tanaka, M. Ouyang, M. A. Schwartz, *Curr Opin Cell Biol* **2013**, 25, 613.

[117] a) M. A. Schwartz, R. K. Assoian, *Journal of cell science* **2001**, 114 Pt 14, 2553; b) R. K. Assoian, *J Cell Biol* **1997**, 136, 1.

[118] P. Chiarugi, *IUBMB Life* **2008**, 60, 301.

[119] a) S. M. Frisch, H. Francis, *J Cell Biol* **1994**, 124, 619; b) S. M. Frisch, R. A. Screaton, *Current Opinion in Cell Biology* **2001**, 13, 555.

[120] a) J. Zhu, R. A. F. Clark, *J. Invest. Dermatol.* **2014**, 134, 895; b) M. M. Martino, P. S. Briquez, A. Ranga, M. P. Lutolf, J. A. Hubbell, *Proc. Natl. Acad. Sci. U. S. A.* **2013**, 110, 4563.

[121] a) B. M. Gumbiner, *Cell* **1996**, 84, 345; b) K. M. Yamada, *J Biol Chem* **1991**, 266, 12809; c) T. H. Barker, *Biomaterials* **2011**, 32, 4211.

[122] a) M. D. Pierschbacher, E. G. Hayman, E. Ruoslahti, *Journal of Cellular Biochemistry* **1985**, 28, 115; b) M. D. Pierschbacher, E. Ruoslahti, *Nature* **1984**, 309, 30.

[123] a) E. Ruoslahti, M. D. Pierschbacher, *Cell* **1986**, 44, 517; b) E. Ruoslahti, M. D. Pierschbacher, *Science* **1987**, 238, 491.

[124] a) K. Tashiro, G. C. Sephel, B. Weeks, M. Sasaki, G. R. Martin, H. K. Kleinman, Y. Yamada, *J Biol Chem* **1989**, 264, 16174; b) K. Tashiro, A. Monji, I. Yoshida, Y. Hayashi, K. Matsuda, N. Tashiro, Y. Mitsuyama, *Biochem J* **1999**, 340 (Pt 1), 119.

[125] P. Nykvist, K. Tasanen, T. Viitasalo, J. Käpylä, J. Jokinen, L. Bruckner-Tuderman, J. Heino, *The Journal of biological chemistry* **2001**, 276, 38673.

[126] M. Manthorpe, E. Engvall, E. Ruoslahti, F. M. Longo, G. E. Davis, S. Varon, *Journal of Cell Biology* **1983**, 97, 1882.

[127] a) J. Graf, R. C. Ogle, F. A. Robey, M. Sasaki, G. R. Martin, Y. Yamada, H. K. Kleinman, *Biochemistry* **1987**, 26, 6896; b) J. Graf, Y. Iwamoto, M. Sasaki, G. R. Martin, H. K. Kleinman, F. A. Robey, Y. Yamada, *Cell* **1987**, 48, 989.

[128] a) S. Huang, D. E. Ingber, *Nature Cell Biology* **1999**, 1, E131; b) B.-Z. Katz, E. Zamir, A. Bershadsky, Z. Kam, K. M. Yamada, B. Geiger, *Molecular Biology of the Cell* **2000**, 11, 1047.

[129] a) C. Chaubaroux, F. Perrin-Schmitt, B. Senger, L. Vidal, J. C. Voegel, P. Schaaf, Y. Haikel, F. Boulmedais, P. Lavalle, J. Hemmerlé, *Tissue Eng., Part C* **2015**, 21, 881; b) K. Sheets, S. Wunsch, C. Ng, A. S. Nain, *Acta Biomater.* **2013**, 9, 7169.

[130] a) M. Osmond, S. M. Bernier, M. B. Pantcheva, M. D. Krebs, *Biotechnol. Bioeng.* **2017**, 114, 915; b) S. Jana, A. Cooper, M. Zhang, *Adv. Healthcare Mater.* **2013**, 2, 557.

[131] a) S. Meehan, A. S. Nain, *Biophys. J.* **2014**, 107, 2604; b) A. I. Teixeira, G. A. Abrams, P. J. Bertics, C. J. Murphy, P. F. Nealey, *J. Cell Sci.* **2003**, 116, 1881; c) P. P. Provenzano, D. R. Inman, K. W. Eliceiri, S. M. Trier, P. J. Keely, *Biophys. J.* **2008**, 95, 5374.

[132] a) N. M. Ayad, S. Kaushik, V. M. Weaver, *Philosophical Transactions of the Royal Society B* **2019**, 374, 20180215; b) T. Mammoto, D. E. Ingber, *Development* **2010**, 137, 1407; c) S. Huang, D. E. Ingber, *Cancer Cell* **2005**, 8, 175; d) F. Kai, H. Laklai, V. M. Weaver, *Trends Cell Biol.* **2016**, 26, 486; e) C. C. DuFort, M. J. Paszek, V. M. Weaver, *Nat. Rev. Mol. Cell Biol.* **2011**, 12, 308.

[133] a) S. Nemir, J. L. West, *Ann. Biomed. Eng.* **2010**, 38, 2; b) H. Abé, K. Hayashi, M. Sato, in *Data Book on Mechanical Properties of Living Cells, Tissues, and Organs*, DOI: 10.1007/978-4-431-65862-7_3 (Eds: H. Abé, K. Hayashi, M. Sato), Springer Japan, Tokyo **1996**, p. 291; c) H. Abé, K. Hayashi, M. Sato, in *Data Book on Mechanical Properties of Living Cells, Tissues, and Organs*, DOI: 10.1007/978-4-431-65862-7_2 (Eds: H. Abé, K. Hayashi, M. Sato), Springer Japan, Tokyo **1996**, p. 3.

[134] a) A. Shellard, R. Mayor, *Nature* **2021**, 600, 690; b) A. Shellard, R. Mayor, *Developmental Cell* **2021**, 56, 227; c) J. A. Espina, C. L. Marchant, E. H. Barriga, *The FEBS Journal* **2022**, 289, 2736.

[135] a) A. J. Steward, D. J. Kelly, *J Anat* **2015**, 227, 717; b) L. He, G. Si, J. Huang, A. D. T. Samuel, N. Perrimon, *Nature* **2018**, 555, 103; c) K. H. Vining, D. J. Mooney, *Nat Rev Mol Cell Biol* **2017**, 18, 728; d) D. Dado, M. Sagi, S. Levenberg, A. Zemel, *Regenerative Medicine* **2012**, 7, 101; e) S.-B. Han, J.-K. Kim, G. Lee, D.-H. Kim, *Advanced Biosystems* **2020**, 4, 2000247; f) A. J. Engler, S. Sen, H. L. Sweeney, D. E. Discher, *Cell* **2006**, 126, 677.

[136] A. J. Engler, C. Carag-Krieger, C. P. Johnson, M. Raab, H. Y. Tang, D. W. Speicher, J. W. Sanger, J. M. Sanger, D. E. Discher, *J. Cell Sci.* **2008**, 121, 3794.

[137] J. D. Humphrey, E. R. Dufresne, M. A. Schwartz, *Nat. Rev. Mol. Cell Biol.* **2014**, 15, 802.

[138] a) G. Murphy, J. Gavrilovic, *Curr. Opin. Cell Biol.* **1999**, 11, 614; b) V. Ellis, G. Murphy, *FEBS Lett.* **2001**, 506, 1.

[139] J. Mayer, J. Blum, E. Wintermantel, in *Medizintechnik: Life Science Engineering*, DOI: 10.1007/978-3-540-93936-8_17 (Eds: E. Wintermantel, S.-W. Ha), Springer Berlin Heidelberg, Berlin, Heidelberg **2009**, p. 373.

[140] a) R. M. Nerem, *Medical and Biological Engineering and Computing* **1992**, 30, CE8; b) R. M. Nerem, *Annals of Biomedical Engineering* **1991**, 19, 529.

[141] J. Carvalho, P. Herthel, D. Gomes, A. Góes, DOI: 10.5772/53337 **2013**, p. 295.

[142] a) A. S. Mao, D. J. Mooney, *Proc Natl Acad Sci U S A* **2015**, 112, 14452; b) T. Ramos, L. Moroni, *Tissue Eng Part C Methods* **2020**, 26, 91.

[143] J. A. Hubbell, *Bio/technology* **1995**, 13, 565.

[144] a) J. W. Nichol, A. Khademhosseini, *Soft Matter* **2009**, 5, 1312; b) R. Annamalai, D. Armant, H. Matthew, *PloS one* **2014**, 9, e84287; c) T. Lu, Y. Li, T. Chen, *International journal of nanomedicine* **2013**, 8, 337; d) T. Schmidt, Y. Xiang, X. Bao, T. Sun, *Processes* **2021**, 9, 935.

[145] H. C. Ott, T. S. Matthiesen, S. K. Goh, L. D. Black, S. M. Kren, T. I. Netoff, D. A. Taylor, *Nat. Med.* **2008**, 14, 213.

[146] a) S. F. Badylak, *Ann Biomed Eng* **2014**, 42, 1517; b) S. F. Badylak, D. Taylor, K. Uygun, *Annu Rev Biomed Eng* **2011**, 13, 27; c) C. Quint, Y. Kondo, R. J. Manson, J. H. Lawson, A. Dardik, L. E. Niklason, *Proc. Natl. Acad. Sci. U. S. A.* **2011**, 108, 9214.

[147] a) Q. L. Loh, C. Choong, *Tissue Eng., Part B* **2013**, 19, 485; b) R. S. Ambekar, B. Kandasubramanian, *Industrial & Engineering Chemistry Research* **2019**, 58, 6163; c) A. Cheng, Z. Schwartz, A. Kahn, X. Li, Z. Shao, M. Sun, Y. Ao, B. D. Boyan, H. Chen, *Tissue Engineering Part B: Reviews* **2019**, 25, 14.

[148] a) Z. Xie, M. Gao, A. O. Lobo, T. J. Webster, *Polymers (Basel)* **2020**, 12; b) J. R. H. Sta. Agueda, Q. Chen, R. D. Maalihan, J. Ren, Í. G. M. da Silva, N. P. Dugos, E. B. Caldona, R. C. Advincula, *MRS Communications* **2021**, 11, 197; c) A. P. Moreno Madrid, S. M. Vrech, M. A. Sanchez, A. P. Rodriguez, *Materials Science and Engineering: C* **2019**, 100, 631.

[149] D. L. Elbert, *Current Opinion in Biotechnology* **2011**, 22, 674.

[150] V. J. Neubauer, A. Döbl, T. Scheibel, *Materials (Basel)* **2021**, 14.

[151] a) N. Huang, S. Li, *Ann. Biomed. Eng.* **2011**, 39, 1201; b) W. F. Liu, C. S. Chen, *Mater. Today* **2005**, 8, 28.

[152] a) M. Salmerón-Sánchez, M. J. Dalby, *Chemical Communications* **2016**, 52, 13327; b) A. Cipitria, M. Salmeron-Sanchez, *Advanced Healthcare Materials* **2017**, 6, 1700052; c) K. Hosoyama, C. Lazurko, M. Muñoz, C. D. McTiernan, E. I. Alarcon, *Frontiers in Bioengineering and Biotechnology* **2019**, 205; d) P. Jurczak, J. Witkowska, S. Rodziewicz-Motowidło, S. Lach, *Advances in colloid and interface science* **2020**, 276, 102083.

[153] a) U. Hersel, C. Dahmen, H. Kessler, *Biomaterials* **2003**, 24, 4385; b) S. L. Bellis, *Biomaterials* **2011**, 32, 4205.

[154] a) B. K. Mann, A. T. Tsai, T. Scott-Burden, J. L. West, *Biomaterials* **1999**, 20, 2281; b) K. G. Sreejalekshmi, P. D. Nair, *Journal of Biomedical Materials Research Part A* **2011**, 96A, 477.

[155] a) W. Sun, T. Incitti, C. Migliaresi, A. Quattrone, S. Casarosa, A. Motta, *J Tissue Eng Regen Med* **2017**, 11, 1532; b) R. Patel, M. Santhosh, J. K. Dash, R. Karpoormath, A. Jha, J. Kwak, M. Patel, J. H. Kim, *Polymers for Advanced Technologies* **2019**, 30, 4; c) Y. Yin, W. Wang, Q. Shao, B. Li, D. Yu, X. Zhou, J. Parajuli, H. Xu, T. Qiu, A. K. Yetisen, N. Jiang, *Biomaterials Science* **2021**, 9, 2887; d) T. H. Perera, X. Lu, L. A. Smith Callahan, *J Funct Biomater* **2020**, 11; e) A. Farrukh, F. Ortega, W. Fan, N. Marichal, J. I. Paez, B. Berninger, A. D. Campo, M. J. Salierno, *Stem Cell Reports* **2017**, 9, 1432.

[156] S. P. Massia, S. S. Rao, J. A. Hubbell, *J Biol Chem* **1993**, 268, 8053.

[157] a) H.-W. Jun, J. West, *Journal of Biomaterials Science, Polymer Edition* **2004**, 15, 73; b) Y.-Y. Kim, H. Li, Y. S. Song, H.-S. Jeong, H.-Y. Yun, K. J. Baek, N. S. Kwon, Y. K. Shin, K.-C. Park, D.-S. Kim, *Journal of Tissue Viability* **2018**, 27, 117; c) J. H. Yoon, J. Kim, H. Lee, S. Y. Kim, H.-H. Jang, S. H. Ryu, B. J. Kim, T. G. Lee, *Biochemical and Biophysical Research Communications* **2012**, 428, 416.

[158] a) H. Minoux, C. Chipot, D. Brown, B. Maigret, *Journal of Computer-Aided Molecular Design* **2000**, 14, 317; b) X. Lu, J. Davies, D. Lu, M. Xia, B. Wattam, D. Shang, Y. Sun, M. Scully, V. Kakkar, *Cell Commun Adhes* **2006**, 13, 171.

[159] V. Apostolopoulos, J. Bojarska, T.-T. Chai, S. Elnagdy, K. Kaczmarek, J. Matsoukas, R. New, K. Parang, O. P. Lopez, H. Parhiz, *Molecules* **2021**, 26, 430.

[160] A. Higuchi, Q. D. Ling, Y. Chang, S. T. Hsu, A. Umezawa, *Chem. Rev.* **2013**, 113, 3297.

[161] P. Zorlutuna, N. Annabi, G. Camci-Unal, M. Nikkhah, J. M. Cha, J. W. Nichol, A. Manbachi, H. Bae, S. Chen, A. Khademhosseini, *Adv. Mater.* **2012**, 24, 1782.

[162] a) M. Ermis, E. Antmen, V. Hasirci, *Bioactive Materials* **2018**, 3, 355; b) A. T. Nguyen, S. R. Sathe, E. K. Yim, *J Phys Condens Matter* **2016**, 28, 183001; c) D. M. Kalaskar,

F. Alshomer, **2016**; d) E. Luong-Van, I. Rodriguez, H. Y. Low, N. Elmouelhi, B. Lowenhaupt, S. Natarajan, C. T. Lim, R. Prajapati, M. Vyakarnam, K. Cooper, *Journal of Materials Research* **2013**, 28, 165; e) D. Hamilton, S. Ghrebi, H. Kim, B. Chehroudi, D. Brunette, **2008**, DOI: 10.1201/b18990-2461.

[163] a) R. G. Flemming, C. J. Murphy, G. A. Abrams, S. L. Goodman, P. F. Nealey, *Biomaterials* **1999**, 20, 573; b) X. Le, G. E. Poinern, N. Ali, C. M. Berry, D. Fawcett, *Int J Biomater* **2013**, 2013, 782549; c) J. Rychly, B. J. Nebe, *BioNanoMaterials* **2013**, 14, 153; d) C.-Y. Yang, W.-Y. Huang, L.-H. Chen, N.-W. Liang, H.-C. Wang, J. Lu, X. Wang, T.-W. Wang, *Journal of Materials Chemistry B* **2021**, 9, 567.

[164] a) J. Ballester-Beltran, M. J. Biggs, M. J. Dalby, M. Salmeron-Sanchez, A. Leal-Egana, *Frontiers in Materials* **2015**, 2, 39; b) T. Naganuma, *Nanoscale* **2017**, 9, 13171.

[165] a) X. Walboomers, W. Monaghan, A. Curtis, J. Jansen, *Journal of Biomedical Materials Research: An Official Journal of The Society for Biomaterials, The Japanese Society for Biomaterials, and The Australian Society for Biomaterials* **1999**, 46, 212; b) C. Matschegewski, S. Staehlke, R. Loeffler, R. Lange, F. Chai, D. P. Kern, U. Beck, B. J. Nebe, *Biomaterials* **2010**, 31, 5729; c) C. Matschegewski, S. Staehlke, H. Birkholz, R. Lange, U. Beck, K. Engel, J. B. Nebe, *Materials* **2012**, 5, 1176; d) C. Mörke, H. Rebl, B. Finke, M. Dubs, P. Nestler, A. Airoudj, V. Roucoules, M. Schnabelrauch, A. Körtge, K. Anselme, *ACS Applied Materials & Interfaces* **2017**, 9, 10461; e) A. Mathur, S. W. Moore, M. P. Sheetz, J. Hone, *Acta Biomater* **2012**, 8, 2595.

[166] a) P. Clark, P. Connolly, A. S. Curtis, J. A. Dow, C. D. Wilkinson, *J Cell Sci* **1991**, 99 (Pt 1), 73; b) G. Abagnale, A. Sechi, M. Steger, Q. Zhou, C.-C. Kuo, G. Aydin, C. Schalla, G. Müller-Newen, M. Zenke, I. G. Costa, P. van Rijn, A. Gillner, W. Wagner, *Stem Cell Reports* **2017**, 9, 654.

[167] a) M. W. Tibbitt, C. B. Rodell, J. A. Burdick, K. S. Anseth, *Proc Natl Acad Sci U S A* **2015**, 112, 14444; b) Y. Shao, J. Fu, *Advanced Materials* **2014**, 26, 1494.

[168] L. Zhu, K. Wang, T. Ma, L. Huang, B. Xia, S. Zhu, Y. Yang, Z. Liu, X. Quan, K. Luo, D. Kong, J. Huang, Z. Luo, *Advanced Healthcare Materials* **2017**, 6, 1600860.

[169] P. Lequoy, F. Murschel, B. Liberelle, S. Lerouge, G. De Crescenzo, *Acta Biomaterialia* **2016**, 29, 239.

[170] I. Bilem, P. Chevallier, L. Plawinski, E. D. Sone, M. C. Durrieu, G. Laroche, *Acta Biomaterialia* **2016**, 36, 132.

[171] P.-Y. Wang, T.-H. Wu, W.-B. Tsai, W.-H. Kuo, M.-J. Wang, *Colloids and Surfaces B: Biointerfaces* **2013**, 110, 88.

[172] a) K. Wang, X. Chen, Y. Pan, Y. Cui, X. Zhou, D. Kong, Q. Zhao, *BioMed Research International* **2015**, 2015, 865076; b) M. Dettin, A. Zamuner, M. Roso, G. Iucci, V. Samouillan, R. Danesin, M. Modesti, M. T. Conconi, *Journal of Peptide Science* **2015**, 21, 786; c) W. Zheng, Z. Wang, L. Song, Q. Zhao, J. Zhang, D. Li, S. Wang, J. Han, X.-L. Zheng, Z. Yang, D. Kong, *Biomaterials* **2012**, 33, 2880; d) A. G. Guex, D. Hegemann, M. N. Giraud, H. T. Tevaearai, A. M. Popa, R. M. Rossi, G. Fortunato, *Colloids and Surfaces B: Biointerfaces* **2014**, 123, 724.

[173] a) O. F. Zouani, J. Kalisky, E. Ibarboure, M.-C. Durrieu, *Biomaterials* **2013**, 34, 2157; b) A. P. Kourouklis, K. B. Kaylan, G. H. Underhill, *Biomaterials* **2016**, 99, 82.

[174] a) A. S. Mao, J. W. Shin, D. J. Mooney, *Biomaterials* **2016**, 98, 184; b) A. Parandakh, A. Anbarlou, M. Tafazzoli-Shadpour, A. Ardeshirylajimi, M.-M. Khani, *Colloids and Surfaces B: Biointerfaces* **2019**, 173, 194.

[175] a) Y. Ma, G. M. Policastro, Q. Li, J. Zheng, R. Jacquet, W. J. Landis, M. L. Becker, *Biomacromolecules* **2016**, 17, 1486; b) L. Liu, B. D. Ratner, E. H. Sage, S. Jiang, *Langmuir* **2007**, 23, 11168.

[176] a) C. M. Lo, H. B. Wang, M. Dembo, Y. Wang, *Biophys. J.* **2000**, 79, 144; b) B. C. Isenberg, P. A. DiMilla, M. Walker, S. Kim, J. Y. Wong, *Biophys. J.* **2009**, 97, 1313; c) B. Harland, S. Walcott, S. X. Sun, *Phys. Biol.* **2011**, 8, 015011.

[177] a) Z. Yan, H. Yin, M. Nerlich, C. G. Pfeifer, D. Docheva, *Journal of Experimental Orthopaedics* **2018**, 5, 1; b) A. H. Zisch, M. P. Lutolf, J. A. Hubbell, *Cardiovascular Pathology* **2003**, 12, 295; c) Y. Tabata, *Pharmaceutical science & technology today* **2000**, 3, 80.

[178] C. Zhang, T. Zhang, T. Geng, X. Wang, K. Lin, P. Wang, *Frontiers in Bioengineering and Biotechnology* **2021**, 9, 591796.

[179] a) A. K. A. Silva, C. Richard, M. Bessodes, D. Scherman, O. W. Merten, *Biomacromolecules* **2009**, 10, 9; b) J. K. Tessmar, A. M. Göpferich, *Advanced Drug Delivery Reviews* **2007**, 59, 274; c) S. J. Buwalda, T. Vermonden, W. E. Hennink, *Biomacromolecules* **2017**, 18, 316; d) N. Oliva, J. Conde, K. Wang, N. Artzi, *Accounts of Chemical Research* **2017**, 50, 669; e) F. Camponeschi, A. Atrei, G. Rocchigiani, L. Mencuccini, M. Uva, R. Barbucci, *Gels* **2015**, 1, 3.

[180] a) R. Jaini, D. Hannaman, J. M. Johnson, R. M. Bernard, C. Z. Altuntas, M. M. delasAlas, P. Kesaraju, A. Luxembourg, C. F. Evans, V. K. Tuohy, *Molecular Therapy* **2006**, 14, 416; b) S. Day, K. Acquah, P. Mruthyunjaya, D. S. Grossman, P. P. Lee, F. A. Sloan, *Am J Ophthalmol* **2011**, 152, 266; c) J. J. Arnold, A. Campain, D. Barthelmes, J. M. Simpson, R. H. Guymer, A. P. Hunyor, I. L. McAllister, R. W. Essex, N. Morlet, M. C. Gillies, *Ophthalmology* **2015**, 122, 1212; d) W. R. Strohl, *BioDrugs* **2015**, 29, 215; e) J. G. Ghosh, A. A. Nguyen, C. E. Bigelow, S. Poor, Y. Qiu, N. Rangaswamy, R. Ornberg, B. Jackson, H. Mak, T. Ezell, V. Kenanova, E. de la Cruz, A. Carrion, B. Etemad-Gilbertson, R. G. Caro, K. Zhu, V. George, J. Bai, R. Sharma-Nahar, S. Shen, Y. Wang, K. K. Subramanian, E. Fassbender, M. Maker, S. Hanks, J. Vrouvlianis, B. Leehy, D. Long, M. Prentiss, V. Kansara, B. Jaffee, T. P. Dryja, M. Roguska, *Nature Communications* **2017**, 8, 14837; f) A. D. AlQahtani, D. O'Connor, A. Domling, S. K. Goda, *Biomedicine & Pharmacotherapy* **2019**, 113, 108750; g) N. Ibeanu, R. Egbu, L. Onyekuru, H. Javaheri, P. T. Khaw, G. R. Williams, S. Brocchini, S. Awwad, *Pharmaceutics* **2020**, 12.

[181] E. S. Place, N. D. Evans, M. M. Stevens, *Nat. Mater.* **2009**, 8, 457.

[182] M. Yamamoto, Y. Ikada, Y. Tabata, *Journal of Biomaterials Science, Polymer Edition* **2001**, 12, 77.

[183] A. B. Ennett, D. Kaigler, D. J. Mooney, *Journal of Biomedical Materials Research Part A* **2006**, 79A, 176.

[184] C. Fischbach, D. J. Mooney, *Biomaterials* **2007**, 28, 2069.

[185] a) G. Orive, E. Santos-Vizcaino, J. L. Pedraz, R. M. Hernandez, J. E. Vela Ramirez, A. Dolatshahi-Pirouz, A. Khademhosseini, N. A. Peppas, D. F. Emerich, *Progress in Retinal and Eye Research* **2019**, 68, 67; b) D. F. Emerich, S. R. Winn, P. M. Hantraye, M. Peschanski, E. Y. Chen, Y. Chu, P. McDermott, E. E. Baetge, J. H. Kordower, *Nature* **1997**, 386, 395; c) D. F. Emerich, G. Orive, C. Thanos, J. Tornoe, L. U. Wahlberg, *Adv Drug Deliv Rev* **2014**, 67-68, 131; d) F. Thorsen, T. A. Read, M. Lund-Johansen, B. B. Tysnes, R. Bjerkvig, *Cell Transplant* **2000**, 9, 773; e) T. A. Read, D. R. Sorensen, R. Mahesparan, P. O. Enger, R. Timpl, B. R. Olsen, M. H. Hjelstuen, O. Haraldseth, R. Bjerkvig, *Nat Biotechnol* **2001**, 19, 29; f) T. Visted, R. Bjerkvig, P. Ø. Enger, *Neuro-oncology* **2001**, 3, 201; g) G. Orive, R. M. a. Hernández, A. R. Gascón, M. Igartua, J. L. Pedraz, *TRENDS in Biotechnology* **2002**, 20, 382; h) O. Hauser, E. Prieschl-Grassauer, B. Salmons, *Current opinion in molecular therapeutics* **2004**, 6, 412; i) J. K. Gandhi, E. C. Opara, E. M. Brey, *Therapeutic delivery* **2013**, 4, 327.

[186] a) M. Jedrzejczak-Silicka, *New insights into cell culture technology* **2017**, 1; b) O. W. Merten, *Philos Trans R Soc Lond B Biol Sci* **2015**, 370, 20140040.

[187] a) S. Alhaque, M. Themis, H. Rashidi, *Philos Trans R Soc Lond B Biol Sci* **2018**, 373; b) M. Simian, M. J. Bissell, *J Cell Biol* **2017**, 216, 31; c) A. Abbott, *Nature* **2003**, 424, 870.

[188] a) O. Guillame-Gentil, O. Semenov, A. S. Roca, T. Groth, R. Zahn, J. Vörös, M. Zenobi-Wong, *Advanced Materials* **2010**, 22, 5443; b) B. M. Baker, C. S. Chen, *Journal of Cell Science* **2012**, 125, 3015; c) L. G. Griffith, M. A. Swartz, *Nature Reviews Molecular Cell Biology* **2006**, 7, 211.

[189] J. A. Burdick, W. L. Murphy, *Nat. Commun.* **2012**, 3, 1269.

[190] a) W. L. Murphy, T. C. McDevitt, A. J. Engler, *Nature Materials* **2014**, 13, 547; b) M. P. Lutolf, P. M. Gilbert, H. M. Blau, *Nature* **2009**, 462, 433.

[191] a) M. W. Tibbitt, K. S. Anseth, *Biotechnol. Bioeng.* **2009**, 103, 655; b) K. Y. Lee, D. J. Mooney, *Chemical Reviews* **2001**, 101, 1869; c) A. Higuchi, Q. D. Ling, S. T. Hsu, A. Umezawa, *Chem. Rev.* **2012**, 112, 4507; d) N. Annabi, A. Tamayol, J. A. Uquillas, M. Akbari, L. E. Bertassoni, C. Cha, G. Camci-Unal, M. R. Dokmeci, N. A. Peppas, A. Khademhosseini, *Adv. Mater.* **2014**, 26, 85; e) J. J. Green, J. H. Elisseeff, *Nature* **2016**, 540, 386; f) K. A. Kyburz, K. S. Anseth, *Ann Biomed Eng* **2015**, 43, 489.

[192] a) J. L. Drury, D. J. Mooney, *Biomaterials* **2003**, 24, 4337; b) M. Guvendiren, J. A. Burdick, *Curr Opin Biotechnol* **2013**, 24, 841; c) D. Seliktar, *Science* **2012**, 336, 1124; d) S. Mantha, S. Pillai, P. Khayambashi, A. Upadhyay, Y. Zhang, O. Tao, H. M. Pham, S. D. Tran, *Materials (Basel)* **2019**, 12; e) S. Ahadian, R. B. Sadeghian, S. Salehi, S. Ostrovidov, H. Bae, M. Ramalingam, A. Khademhosseini, *Bioconjugate Chem.* **2015**, 26, 1984.

[193] a) R. K. Das, V. Gocheva, R. Hammink, O. F. Zouani, A. E. Rowan, *Nat. Mater.* **2016**, 15, 318; b) O. Chaudhuri, L. Gu, D. Klumpers, M. Darnell, S. A. Bencherif, J. C. Weaver, N. Huebsch, H. p. Lee, E. Lippens, G. N. Duda, D. J. Mooney, *Nat. Mater.* **2016**, 15, 326; c) H. Wang, A. S. Abhilash, n. Chen, S. Christopher, R. G. Wells, V. B. Shenoy, *Biophys. J.* **2014**, 107, 2592; d) A. S. Abhilash, n. Baker, M. Brendon, B. Trappmann, n. Chen, S. Christopher, n. Shenoy, B. Vivek, *Biophys. J.* **2014**, 107, 1829; e) X. Ma, M. E. Schickel, M. D. Stevenson, A. L. Sarang-Sieminski, K. J. Gooch, S. N. Ghadiali, R. T. Hart, *Biophys. J.* **2013**, 104, 1410; f) P. A. Janmey, R. T. Miller, *J. Cell Sci.* **2011**, 124, 9.

[194] a) P. M. Kharkar, K. L. Kiick, A. M. Kloxin, *Chem. Soc. Rev.* **2013**, 42, 7335; b) N. Iqbal, A. S. Khan, A. Asif, M. Yar, J. W. Haycock, I. U. Rehman, *International Materials Reviews* **2019**, 64, 91; c) D. W. Hutmacher, J. C. Goh, S. H. Teoh, *Ann Acad Med Singap* **2001**, 30, 183; d) Z. Sheikh, S. Najeeb, Z. Khurshid, V. Verma, H. Rashid, M. Glogauer, *Materials (Basel)* **2015**, 8, 5744; e) G. BaoLin, P. X. Ma, *Sci China Chem* **2014**, 57, 490.

[195] a) S. V. Murphy, A. Atala, *Nature Biotechnology* **2014**, 32, 773; b) Y. Bozkurt, E. Karayel, *Journal of Materials Research and Technology* **2021**, 14, 1430; c) N. Shahrubudin, T. C. Lee, R. Ramlan, *Procedia Manufacturing* **2019**, 35, 1286.

[196] a) J. Ni, H. Ling, S. Zhang, Z. Wang, Z. Peng, C. Benyshek, R. Zan, A. K. Miri, Z. Li, X. Zhang, J. Lee, K. J. Lee, H. J. Kim, P. Tebon, T. Hoffman, M. R. Dokmeci, N. Ashammakhi, X. Li, A. Khademhosseini, *Materials Today Bio* **2019**, 3, 100024; b) K. Chua, I. Khan, R. Malhotra, D. Zhu, *Engineered Regeneration* **2021**, 2, 288; c) L. F. Velásquez-García, Y. Kornbluth, *Annual Review of Biomedical Engineering* **2021**, 23, 307.

[197] a) Z. Chen, Z. Li, J. Li, C. Liu, C. Lao, Y. Fu, C. Liu, Y. Li, P. Wang, Y. He, *Journal of the European Ceramic Society* **2019**, 39, 661; b) L. C. Hwa, S. Rajoo, A. M. Noor, N. Ahmad, M. B. Uday, *Current Opinion in Solid State and Materials Science* **2017**, 21, 323.

[198] a) P. Szymczyk-Ziółkowska, M. B. Łabowska, J. Detyna, I. Michalak, P. Gruber, *Biocybernetics and Biomedical Engineering* **2020**, 40, 624; b) R. Pugliese, B. Beltrami, S. Regondi, C. Lunetta, *Annals of 3D Printed Medicine* **2021**, 2, 100011.

[199] a) S. Singh, S. Ramakrishna, F. Berto, *Material Design & Processing Communications* **2020**, 2, e97; b) F. Alam, V. R. Shukla, K. M. Varadarajan, S. Kumar, *Journal of the Mechanical Behavior of Biomedical Materials* **2020**, 103, 103576; c) E. H. Tümer, H. Y. Erbil, *Coatings* **2021**, 11, 390.

[200] a) S. M. Giannitelli, P. Mozetic, M. Trombetta, A. Rainer, *Acta Biomaterialia* **2015**, 24, 1; b) C. Vaquette, W. Fan, Y. Xiao, S. Hamlet, D. W. Hutmacher, S. Ivanovski, *Biomaterials* **2012**, 33, 5560; c) H. Saniei, S. Mousavi, *Polymer* **2020**, 196, 122467; d) D.-L. Yang, F. Faraz, J.-X. Wang, N. Radacsi, *Advanced Materials Technologies* **2022**, 7, 2101309.

[201] a) L. Moroni, R. Schotel, D. Hamann, J. R. de Wijn, C. A. van Blitterswijk, *Advanced Functional Materials* **2008**, 18, 53; b) D. Sooriyaarachchi, H. J. Minière, S. Maharubin, G. Z. Tan, *Tissue Engineering and Regenerative Medicine* **2019**, 16, 29.

[202] a) A. De Pieri, A. M. Byerley, C. R. Musumeci, F. Salemizadehparizi, M. A. Vanderhorst, K. Wuertz-Kozak, *JOR Spine* **2020**, 3, e1117; b) Y.-Z. Yu, L.-L. Zheng, H.-P. Chen, W.-H. Chen, Q.-X. Hu, *Advances in Manufacturing* **2014**, 2, 231.

[203] T. J. Horn, O. L. A. Harrysson, *Science Progress* **2012**, 95, 255.

[204] a) G. Gao, X. Cui, *Biotechnology Letters* **2016**, 38, 203; b) G. Saini, N. Segaran, J. L. Mayer, A. Saini, H. Albadawi, R. Oklu, *J Clin Med* **2021**, 10.

[205] a) V. Mironov, T. Trusk, V. Kasyanov, S. Little, R. Swaja, R. Markwald, *Biofabrication* **2009**, 1, 022001; b) W. Sun, *Biofabrication* **2009**, 1, 010201.

[206] a) V. Mironov, N. Reis, B. Derby, *Tissue Eng* **2006**, 12, 631; b) V. Mironov, *Expert Opinion on Biological Therapy* **2005**, 5, 1111.

[207] a) C. Mandrycky, Z. Wang, K. Kim, D.-H. Kim, *Biotechnology Advances* **2016**, 34, 422; b) S. Kyle, Z. M. Jessop, A. Al-Sabah, I. S. Whitaker, *Advanced Healthcare Materials* **2017**, 6, 1700264.

[208] F. Guillemot, A. Souquet, S. Catros, B. Guillotin, *Nanomedicine* **2010**, 5, 507.

[209] a) L. Koch, S. Kuhn, H. Sorg, M. Gruene, S. Schlie, R. Gaebel, B. Polchow, K. Reimers, S. Stoelting, N. Ma, P. M. Vogt, G. Steinhoff, B. Chichkov, *Tissue Eng Part C Methods* **2010**, 16, 847; b) B. Hopp, T. Smausz, N. Kresz, N. Barna, Z. Bor, L. Kolozsvári, D. B. Chrisey, A. Szabó, A. Nógrádi, *Tissue Eng* **2005**, 11, 1817; c) M. Gruene, A. Deiwick, L. Koch, S. Schlie, C. Unger, N. Hofmann, I. Bernemann, B. Glasmacher, B. Chichkov, *Tissue Eng Part C Methods* **2011**, 17, 79.

[210] a) T. Xu, J. Jin, C. Gregory, J. J. Hickman, T. Boland, *Biomaterials* **2005**, 26, 93; b) T. Xu, C. A. Gregory, P. Molnar, X. Cui, S. Jalota, S. B. Bhaduri, T. Boland, *Biomaterials* **2006**, 27, 3580.

[211] a) J. Malda, J. Visser, F. P. Melchels, T. Jüngst, W. E. Hennink, W. J. A. Dhert, J. Groll, D. W. Hutmacher, *Advanced Materials* **2013**, 25, 5011; b) S. P. Tarassoli, Z. M. Jessop, T. Jovic, K. Hawkins, I. S. Whitaker, *Frontiers in Bioengineering and Biotechnology* **2021**, 9.

[212] C. C. Chang, E. D. Boland, S. K. Williams, J. B. Hoying, *J Biomed Mater Res B Appl Biomater* **2011**, 98, 160.

[213] a) J. Emmermacher, D. Spura, J. Cziommer, D. Kilian, T. Wollborn, U. Fritsching, J. Steingroewer, T. Walther, M. Gelinsky, A. Lode, *Biofabrication* **2020**, 12, 025022; b) K. Nair, M. Gandhi, S. Khalil, K. C. Yan, M. Marcolongo, K. Barbee, W. Sun, *Biotechnology Journal* **2009**, 4, 1168; c) A. Panwar, L. P. Tan, *Molecules* **2016**, 21, 685.

[214] B. Webb, B. J. Doyle, *Bioprinting* **2017**, 8, 8.

[215] F. Lim, A. M. Sun, *Science* **1980**, 210, 908.

[216] G. M. O'Shea, M. F. Goosen, A. M. Sun, *Biochim Biophys Acta* **1984**, 804, 133.

[217] a) G. Orive, E. Santos, D. Poncelet, R. M. Hernández, J. L. Pedraz, L. U. Wahlberg, P. De Vos, D. Emerich, *Trends in Pharmacological Sciences* **2015**, 36, 537; b) H. Gurruchaga, L. Saenz del Burgo, J. Ciriza, G. Orive, R. M. Hernández, J. L. Pedraz, *Expert Opinion on Drug Delivery* **2015**, 12, 1251.

[218] I. Elliott Donaghue, R. Tam, M. V. Sefton, M. S. Shoichet, *J Control Release* **2014**, 190, 219.

[219] a) J. Groll, J. A. Burdick, D. W. Cho, B. Derby, M. Gelinsky, S. C. Heilshorn, T. Jüngst, J. Malda, V. A. Mironov, K. Nakayama, A. Ovsianikov, W. Sun, S. Takeuchi, J. J. Yoo, T. B. F. Woodfield, *Biofabrication* **2018**, 11, 013001; b) J. Groll, T. Boland, T. Blunk, J. A. Burdick, D.-W. Cho, P. D. Dalton, B. Derby, G. Forgacs, Q. Li, V. A. Mironov, L. Moroni, M. Nakamura, W. Shu, S. Takeuchi, G. Vozzi, T. B. F. Woodfield, T. Xu, J. J. Yoo, J. Malda, *Biofabrication* **2016**, 8, 013001; c) M. Hospodiuk, M. Dey, D. Sosnoski, I. T. Ozbolat, *Biotechnology advances* **2017**, 35, 217.

[220] a) J. Gopinathan, I. Noh, *Biomaterials Research* **2018**, 22, 11; b) J. Nulty, R. Schipani, R. Burdis, D. J. Kelly, in *Polymer-Based Additive Manufacturing: Biomedical Applications*, DOI: 10.1007/978-3-030-24532-0_9 (Ed: D. M. Devine), Springer International Publishing, Cham **2019**, p. 187.

[221] A. Blaeser, D. F. Duarte Campos, U. Puster, W. Richtering, M. M. Stevens, H. Fischer, *Advanced Healthcare Materials* **2016**, 5, 326.

[222] a) S. V. Murphy, A. Skardal, A. Atala, *J Biomed Mater Res A* **2013**, 101, 272; b) T. Jungst, W. Smolan, K. Schacht, T. Scheibel, J. Groll, *Chemical Reviews* **2016**, 116, 1496.

[223] D. Chimene, K. K. Lennox, R. R. Kaunas, A. K. Gaharwar, *Annals of Biomedical Engineering* **2016**, 44, 2090.

[224] a) L. Moroni, T. Boland, J. A. Burdick, C. De Maria, B. Derby, G. Forgacs, J. Groll, Q. Li, J. Malda, V. A. Mironov, C. Mota, M. Nakamura, W. Shu, S. Takeuchi, T. B. F. Woodfield, T. Xu, J. J. Yoo, G. Vozzi, *Trends in Biotechnology* **2018**, 36, 384; b) A. Sydney Gladman, E. A. Matsumoto, R. G. Nuzzo, L. Mahadevan, J. A. Lewis, *Nat. Mater.* **2016**, 15, 413; c) N. J. Kanu, E. Gupta, U. K. Vates, G. K. Singh, *RSC Advances* **2019**, 9, 38209; d) Ayushi, U. Kumar Vates, S. Mishra, N. Jee Kanu, *Materials Today: Proceedings* **2021**, 47, 3313; e) S. Tibbits, *Architectural Design* **2014**, 84, 116; f) Z. Fu, L. Ouyang, R. Xu, Y. Yang, W. Sun, *Materials Today* **2022**, 52, 112; g) J. A. Serna, L. Rueda-Gensini, D. N. Céspedes-Valenzuela, J. Cifuentes, J. C. Cruz, C. Muñoz-Camargo, *Polymers (Basel)* **2021**, 13.

[225] a) J. G. Hardy, L. M. Römer, T. R. Scheibel, *Polymer* **2008**, 49, 4309; b) L. Römer, T. Scheibel, *Prion* **2008**, 2, 154; c) F. Vollrath, *Reviews in Molecular Biotechnology* **2000**, 74, 67; d) L. Eisoldt, A. Smith, T. Scheibel, *Materials Today* **2011**, 14, 80; e) E. Doblhofer, A. Heidebrecht, T. Scheibel, *Applied Microbiology and Biotechnology* **2015**, 99, 9361; f) M. Ramezaniaghdam, N. D. Nahdi, R. Reski, *Frontiers in Bioengineering and Biotechnology* **2022**, 10.

[226] a) M. Heim, D. Keerl, T. Scheibel, *Angewandte Chemie International Edition* **2009**, 48, 3584; b) M. Heim, L. Römer, T. Scheibel, *Chemical Society Reviews* **2010**, 39, 156; c) T. Scheibel, *Microb Cell Fact* **2004**, 3, 14.
[227] D. Huemmerich, C. W. Helsen, S. Quedzuweit, J. Oschmann, R. Rudolph, T. Scheibel, *Biochemistry* **2004**, 43, 13604.
[228] a) A. Rising, H. Nimmervoll, S. Grip, A. Fernandez-Arias, E. Storckenfeldt, D. P. Knight, F. Vollrath, W. Engström, *Zoolog Sci* **2005**, 22, 273; b) J. M. Gosline, P. A. Guerette, C. S. Ortlepp, K. N. Savage, *Journal of Experimental Biology* **1999**, 202, 3295; c) C. Y. Hayashi, N. H. Shipley, R. V. Lewis, *Int J Biol Macromol* **1999**, 24, 271.
[229] a) F. Hagn, L. Eisoldt, J. G. Hardy, C. Vendrely, M. Coles, T. Scheibel, H. Kessler, *Nature* **2010**, 465, 239; b) G. Askarieh, M. Hedhammar, K. Nordling, A. Saenz, C. Casals, A. Rising, J. Johansson, S. D. Knight, *Nature* **2010**, 465, 236; c) L. Eisoldt, C. Thamm, T. Scheibel, *Biopolymers* **2012**, 97, 355; d) L. Eisoldt, J. G. Hardy, M. Heim, T. R. Scheibel, *Journal of Structural Biology* **2010**, 170, 413; e) M. Saric, L. Eisoldt, V. Döring, T. Scheibel, *Advanced Materials* **2021**, 33, 2006499.
[230] S. Winkler, D. L. Kaplan, *Reviews in Molecular Biotechnology* **2000**, 74, 85.
[231] a) T. B. Aigner, E. DeSimone, T. Scheibel, *Advanced Materials* **2018**, 30, 1704636; b) S. Salehi, K. Koeck, T. Scheibel, *Molecules* **2020**, 25, 737; c) A. P. Kiseleva, P. V. Krivoshapkin, E. F. Krivoshapkina, *Front Chem* **2020**, 8, 554; d) Y. Gu, L. Yu, J. Mou, D. Wu, P. Zhou, M. Xu, *e-Polymers* **2020**, 20, 443.
[232] J. W. Kuhbier, C. Allmeling, K. Reimers, A. Hillmer, C. Kasper, B. Menger, G. Brandes, M. Guggenheim, P. M. Vogt, *PLOS ONE* **2010**, 5, e12032.
[233] H. Wendt, A. Hillmer, K. Reimers, J. W. Kuhbier, F. Schäfer-Nolte, C. Allmeling, C. Kasper, P. M. Vogt, *PLoS One* **2011**, 6, e21833.
[234] K. Yazawa, K. Hidaka, J. Negishi, *Langmuir* **2022**, 38, 7766.
[235] a) A. Heidebrecht, T. Scheibel, *Adv Appl Microbiol* **2013**, 82, 115; b) D. R. Whittall, K. V. Baker, R. Breitling, E. Takano, *Trends Biotechnol* **2021**, 39, 560; c) A. Rising, M. Widhe, J. Johansson, M. Hedhammar, *Cellular and Molecular Life Sciences* **2011**, 68, 169; d) J. A. Kluge, O. Rabotyagova, G. G. Leisk, D. L. Kaplan, *Trends in Biotechnology* **2008**, 26, 244.
[236] O. S. Rabotyagova, P. Cebe, D. L. Kaplan, *Biomacromolecules* **2009**, 10, 229.
[237] a) M. Hedhammar, A. Rising, S. Grip, A. S. Martinez, K. Nordling, C. Casals, M. Stark, J. Johansson, *Biochemistry* **2008**, 47, 3407; b) M. Stark, S. Grip, A. Rising, M. Hedhammar, W. Engström, G. Hjälm, J. Johansson, *Biomacromolecules* **2007**, 8, 1695.
[238] P. A. Guerette, D. G. Ginzinger, B. H. F. Weber, J. M. Gosline, *Science* **1996**, 272, 112.
[239] M. Widhe, H. Bysell, S. Nystedt, I. Schenning, M. Malmsten, J. Johansson, A. Rising, M. Hedhammar, *Biomaterials* **2010**, 31, 9575.
[240] M. Saric, T. Scheibel, *Current Opinion in Biotechnology* **2019**, 60, 213.
[241] E. Doblhofer, T. Scheibel, *J Pharm Sci* **2015**, 104, 988.
[242] a) S. Kumari, G. Lang, E. DeSimone, C. Spengler, V. T. Trossmann, S. Lücker, M. Hudel, K. Jacobs, N. Krämer, T. Scheibel, *Materials Today* **2020**, 41, 21; b) S. Kumari, G. Lang, E. DeSimone, C. Spengler, V. T. Trossmann, S. Lücker, M. Hudel, K. Jacobs, N. Krämer, T. Scheibel, *Data in Brief* **2020**, 32, 106305.
[243] K. Spieß, S. Wohlrab, T. Scheibel, *Soft Matter* **2010**, 6, 4168.
[244] H. M. Herold, T. B. Aigner, C. E. Grill, S. Krüger, A. Taubert, T. Scheibel, *Bioinspired, Biomimetic and Nanobiomaterials* **2019**, 8, 99.
[245] G. Lang, C. Grill, T. Scheibel, *Angewandte Chemie International Edition* **2022**, 61, e202115232.

[246] S. Wohlrab, S. Müller, A. Schmidt, S. Neubauer, H. Kessler, A. Leal-Egaña, T. Scheibel, *Biomaterials* **2012**, 33, 6650.
[247] M. B. Elsner, H. M. Herold, S. Müller-Herrmann, H. Bargel, T. Scheibel, *Biomaterials Science* **2015**, 3, 543.
[248] V. J. Neubauer, T. Scheibel, *ACS Biomater Sci Eng* **2020**, 6, 5599.
[249] M. Lucke, I. Mottas, T. Herbst, C. Hotz, L. Römer, M. Schierling, H. M. Herold, U. Slotta, T. Spinetti, T. Scheibel, G. Winter, C. Bourquin, J. Engert, *Biomaterials* **2018**, 172, 105.
[250] M. Humenik, M. Mohrand, T. Scheibel, *Bioconjugate Chemistry* **2018**, 29, 898.
[251] A. Heidebrecht, L. Eisoldt, J. Diehl, A. Schmidt, M. Geffers, G. Lang, T. Scheibel, *Adv Mater* **2015**, 27, 2189.
[252] S. Müller-Herrmann, T. Scheibel, *ACS Biomaterials Science & Engineering* **2015**, 1, 247.
[253] a) D. Steiner, G. Lang, L. Fischer, S. Winkler, P. Greil, T. Fey, T. Scheibel, R. Horch, A. Arkudas, *Tissue Engineering Part A* **2019**, 25; b) P. H. Zeplin, N. C. Maksimovikj, M. C. Jordan, J. Nickel, G. Lang, A. H. Leimer, L. Römer, T. Scheibel, *Advanced Functional Materials* **2014**, 24, 2658; c) P. H. Zeplin, A. K. Berninger, N. C. Maksimovikj, P. van Gelder, T. Scheibel, H. Walles, *Handchir Mikr* **2014**, 46, 336.
[254] A. C. G. Weiss, H. M. Herold, S. Lentz, M. Faria, Q. A. Besford, C.-S. Ang, F. Caruso, T. Scheibel, *ACS Applied Materials & Interfaces* **2020**, 12, 24635.
[255] a) A. Leal-Egaña, G. Lang, C. Mauerer, J. Wickinghoff, M. Weber, S. Geimer, T. Scheibel, *Advanced Engineering Materials* **2012**, 14, B67; b) J. Petzold, T. B. Aigner, F. Touska, K. Zimmermann, T. Scheibel, F. B. Engel, *Advanced Functional Materials* **2017**, 27, 1701427.
[256] C. B. Borkner, S. Wohlrab, E. Möller, G. Lang, T. Scheibel, *ACS Biomaterials Science & Engineering* **2017**, 3, 767.
[257] a) D. Sonnleitner, C. Sommer, T. Scheibel, G. Lang, *Materials Science and Engineering: C* **2021**, 131, 112458; b) S. Wright, S. L. Goodacre, *BMC Research Notes* **2012**, 5, 326; c) S. Zhang, D. Piorkowski, W. R. Lin, Y. R. Lee, C. P. Liao, P. H. Wang, I. M. Tso, *J Exp Biol* **2019**, 222.
[258] a) C. Sommer, H. Bargel, N. Raßmann, T. Scheibel, *MRS Communications* **2021**, 11, 356; b) R. H. Zha, P. Delparastan, T. D. Fink, J. Bauer, T. Scheibel, P. B. Messersmith, *Biomaterials Science* **2019**, 7, 683.
[259] a) D. Chouhan, N. Thatikonda, L. Nilebäck, M. Widhe, M. Hedhammar, B. B. Mandal, *ACS Applied Materials & Interfaces* **2018**, 10, 23560; b) S. C. Gomes, I. B. Leonor, J. F. Mano, R. L. Reis, D. L. Kaplan, *Biomaterials* **2011**, 32, 4255.
[260] F. Bauer, S. Wohlrab, T. Scheibel, *Biomaterials Science* **2013**, 1, 1244.
[261] T. U. Esser, V. T. Trossmann, S. Lentz, F. B. Engel, T. Scheibel, *Materials Today Bio* **2021**, 11, 100114.
[262] a) A. Blau, *Current Opinion in Colloid & Interface Science* **2013**, 18, 481; b) A. Leal-Egaña, A. Díaz-Cuenca, A. R. Boccaccini, *Advanced Materials* **2013**, 25, 4049; c) M. De Rosa, M. Carteni', O. Petillo, A. Calarco, S. Margarucci, F. Rosso, A. De Rosa, E. Farina, P. Grippo, G. Peluso, *Journal of Cellular Physiology* **2004**, 198, 133.
[263] a) J. P. M. Kramer, T. B. Aigner, J. Petzold, K. Roshanbinfar, T. Scheibel, F. B. Engel, *Sci Rep* **2020**, 10, 8789; b) K. Schacht, T. Jüngst, M. Schweinlin, A. Ewald, J. Groll, T. Scheibel, *Angewandte Chemie International Edition* **2015**, 54, 2816; c) E. DeSimone, K. Schacht, A. Pellert, T. Scheibel, *Biofabrication* **2017**, 9, 044104; d) K. Schacht, J. Vogt, T. Scheibel, *ACS Biomater Sci Eng* **2016**, 2, 517.

[264] a) M. Widhe, N. D. Shalaly, M. Hedhammar, *Biomaterials* **2016**, 74, 256; b) N. D. Shalaly, M. Ria, U. Johansson, K. Åvall, P.-O. Berggren, M. Hedhammar, *Biomaterials* **2016**, 90, 50; c) C. P. Tasiopoulos, L. Gustafsson, W. van der Wijngaart, M. Hedhammar, *ACS Biomater Sci Eng* **2021**, 7, 3332.

[265] M. Widhe, U. Johansson, C.-O. Hillerdahl, M. Hedhammar, *Biomaterials* **2013**, 34, 8223.

[266] U. Johansson, M. Ria, K. Åvall, N. Dekki Shalaly, S. V. Zaitsev, P. O. Berggren, M. Hedhammar, *PLoS One* **2015**, 10, e0130169.

[267] a) A. Lammel, M. Schwab, M. Hofer, G. Winter, T. Scheibel, *Biomaterials* **2011**, 32, 2233; b) M. Hofer, G. Winter, J. Myschik, *Biomaterials* **2012**, 33, 1554; c) C. Blüm, A. Nichtl, T. Scheibel, *Advanced Functional Materials* **2014**, 24, 763; d) M. B. Schierling, E. Doblhofer, T. Scheibel, *Biomaterials Science* **2016**, 4, 1515.

[268] S. Kumari, H. Bargel, M. U. Anby, D. Lafargue, T. Scheibel, *ACS Biomaterials Science & Engineering* **2018**, 4, 1750.

[269] H. M. Herold, A. Döbl, S. Wohlrab, M. Humenik, T. Scheibel, *Biomacromolecules* **2020**, 21, 4904.

[270] S. Kumari, H. Bargel, T. Scheibel, *Macromolecular Rapid Communications* **2020**, 41, 1900426.

[271] a) M. Humenik, M. Magdeburg, T. Scheibel, *Journal of Structural Biology* **2014**, 186, 431; b) U. K. Slotta, S. Rammensee, S. Gorb, T. Scheibel, *Angewandte Chemie International Edition* **2008**, 47, 4592.

[272] a) K. Schacht, T. Scheibel, *Biomacromolecules* **2011**, 12, 2488; b) S. Rammensee, D. Huemmerich, K. D. Hermanson, T. Scheibel, A. R. Bausch, *Applied Physics A* **2006**, 82, 261.

[273] a) H. Bargel, V. T. Trossmann, C. Sommer, T. Scheibel, *Beilstein Journal of Nanotechnology* **2022**, 13, 902; b) V. T. Trossmann, T. Scheibel, *Advanced Healthcare Materials* **2023**, 12, 2202660; c) D. Steiner, S. Winkler, S. Heltmann-Meyer, V. T. Trossmann, T. Fey, T. Scheibel, R. E. Horch, A. Arkudas, *Biofabrication* **2021**, 13, 045003; d) A. Lechner, V. T. Trossmann, T. Scheibel, *Macromolecular Bioscience* **2022**, 22, 2100390; e) V. T. Trossmann, S. Heltmann-Meyer, H. Amouei, H. Wajant, R. E. Horch, D. Steiner, T. Scheibel, *Biomacromolecules* **2022**, 23, 4427; f) V. J. Neubauer, V. T. Trossmann, S. Jacobi, A. Döbl, T. Scheibel, *Angewandte Chemie International Edition* **2021**, 60, 11847; g) S. Lentz, V. T. Trossmann, T. Scheibel, *Advanced Materials Interfaces* **2023**, 10, 2201936; h) S. Lentz, V. T. Trossmann, C. B. Borkner, V. Beyersdorfer, M. Rottmar, T. Scheibel, *ACS Applied Materials & Interfaces* **2022**, 14, 31751.

[274] E. DeSimone, K. Schacht, T. Jungst, J. Groll, T. Scheibel, *Pure and Applied Chemistry* **2015**, 87, 737.

[275] K. Groebe, P. Vaupel, *Int J Radiat Oncol Biol Phys* **1988**, 15, 691.

[276] E. C. Novosel, C. Kleinhans, P. J. Kluger, *Adv Drug Deliv Rev* **2011**, 63, 300.

[277] a) E. DeSimone, K. Schacht, T. Scheibel, *Materials Letters* **2016**, 183, 101; b) M. Humenik, A. M. Smith, S. Arndt, T. Scheibel, *Journal of Structural Biology* **2015**, 191, 130.

[278] a) S. Wohlrab, K. Spieß, T. Scheibel, *Journal of Materials Chemistry* **2012**, 22, 22050; b) K. Spiess, R. Ene, C. D. Keenan, J. Senker, F. Kremer, T. Scheibel, *Journal of Materials Chemistry* **2011**, 21, 13594.

[279] C. B. Borkner, S. Lentz, M. Müller, A. Fery, T. Scheibel, *ACS Applied Polymer Materials* **2019**, 1, 3366.

[280] a) J. M. Schierholz, J. Beuth, *J Hosp Infect* **2001**, 49, 87; b) K. Johansson, R. Jimbo, P. Östlund, S. Tranæus, J. P. Becktor, *Implant Dent* **2017**, 26, 778.

[281] J. Fu, W. Zhu, X. Liu, C. Liang, Y. Zheng, Z. Li, Y. Liang, D. Zheng, S. Zhu, Z. Cui, S. Wu, *Nature Communications* **2021**, 12, 6907.

[282] a) E. Metwalli, U. Slotta, C. Darko, S. V. Roth, T. Scheibel, C. M. Papadakis, *Applied Physics A* **2007**, 89, 655; b) A. M. Anton, A. Heidebrecht, N. Mahmood, M. Beiner, T. Scheibel, F. Kremer, *Biomacromolecules* **2017**, 18, 3954; c) C. Guo, J. Zhang, J. S. Jordan, X. Wang, R. W. Henning, J. L. Yarger, *Biomacromolecules* **2018**, 19, 906.

[283] a) M. Ventre, C. F. Natale, C. Rianna, P. A. Netti, *Journal of The Royal Society Interface* **2014**, 11, 20140687; b) J. Huang, Y. Chen, C. Tang, Y. Fei, H. Wu, D. Ruan, M. E. Paul, X. Chen, Z. Yin, B. C. Heng, W. Chen, W. Shen, *Cellular and Molecular Life Sciences* **2019**, 76, 505.

[284] L. M. Weber, K. N. Hayda, K. Haskins, K. S. Anseth, *Biomaterials* **2007**, 28, 3004.

[285] V. Castagnola, E. Castagnola, C. Bergaud, D. Ricci, *Frontiers in Bioengineering and Biotechnology* **2021**, 9.

[286] a) H. Laronha, J. Caldeira, *Cells* **2020**, 9; b) H.-D. Haubeck, in *Lexikon der Medizinischen Laboratoriumsdiagnostik*, DOI: 10.1007/978-3-662-48986-4_2044 (Eds: A. M. Gressner, T. Arndt), Springer Berlin Heidelberg, Berlin, Heidelberg **2019**, p. 1589.

[287] a) J. B. Wolinsky, Y. L. Colson, M. W. Grinstaff, *J Control Release* **2012**, 159, 14; b) P. Zahedi, R. Yoganathan, M. Piquette-Miller, C. Allen, *Expert Opinion on Drug Delivery* **2012**, 9, 567; c) T. Zhang, Y. Tang, W. Zhang, S. Liu, Y. Zhao, W. Wang, J. Wang, L. Xu, K. Liu, *Journal of Materials Chemistry B* **2018**, 6, 1216.

[288] X. Gao, M. Ma, C. M. Pedersen, R. Liu, Z. Zhang, H. Chang, Y. Qiao, Y. Wang, *Chemistry – An Asian Journal* **2021**, 16, 3658.

[289] a) R. L. Yung, *Curr Opin Investig Drugs* **2001**, 2, 216; b) E. Ducharme, J. M. Weinberg, *Expert Opinion on Biological Therapy* **2008**, 8, 491; c) D. Kivelevitch, B. Mansouri, A. Menter, *Biologics* **2014**, 8, 169.

5. Publikationsliste

I. Esser, T. U.*; **Trossmann, V. T.***; Lentz, S.; Engel, F. B.§ & Scheibel, T.§ (2021) Designing of spider silk proteins for human induced pluripotent stem cell-based cardiac tissue engineering. *Materials Today Bio* **11**: 100114.

II. **Trossmann, V. T.** & Scheibel, T (2023) Design of Recombinant Spider Silk Proteins for Cell Type Specific Binding. *Advanced Healthcare Materials* **12**: 2202660.

III. Lentz, S.*; **Trossmann, V. T.***; Borkner, C. B.; Beyersdorfer, V.; Rottmar, M. & Scheibel, T. (2022) Structure-Property Relationship Based on the Amino Acid Composition of Recombinant Spider Silk Proteins for Potential Biomedical Applications. *ACS Applied Materials & Interfaces* **14**: 31751.

IV. Kumari, S.*; Lang, G.*; DeSimone, E.; Spengler, C.; **Trossmann, V. T.**; Lücker, S.; Hudel, M.; Jacobs, K.; Krämer, N. & Scheibel, T. (2020) Engineered spider silk-based 2D and 3D materials prevent microbial infestation. *Materials Today* **41**: 21.

V. Kumari, S.*; Lang, G.*; DeSimone, E.; Spengler, C.; **Trossmann, V. T.**; Lücker, S.; Hudel, M.; Jacobs, K.; Krämer, N. & Scheibel, T. (2020) Data for microbe resistant engineered recombinant spider silk protein based 2D and 3D materials. *Data in Brief* **32**: 106305.

VI. Neubauer, V. J.; **Trossmann, V. T.**; Jacobi S.; Döbl, A. & Scheibel, T. (2021) Recombinant Spider Silk Gels Derived from Aqueous-Organic Solvents as Depots for Drugs. *Angewandte Chemie International Edition* **60**: 11847.

Deutsche Version: Neubauer, V. J.; **Trossmann, V. T.**; Jacobi S.; Döbl, A. & Scheibel, T. (2021) Rekombinante Spinnenseidengele aus wässrig-organischen Mischphasen als Wirkstoffdepots. *Angewandte Chemie* **133**: 11953.

VII. Lentz, S.*; **Trossmann, V. T.*** & Scheibel, T. (2022) Selective Topography Directed Cell Adhesion on Spider Silk Surfaces. *Advanced Materials Interfaces* **10**: 2201936.

VIII. Lechner, A.*; **Trossmann, V. T.*** & Scheibel, T. (2021) Impact of Cell Loading of Recombinant Spider Silk Based Bioinks on Gelation and Printability. *Macromolecular Bioscience* **22**: 2100390.

IX. **Trossmann, V. T.***; Heltmann-Meyer, S.*; Amouei, H; Wajant, H.; Horch, R. E.; Steiner, D.§ & Scheibel, T.§ (2022) Recombinant Spider Silk Bioinks for Continuous Protein Release by Encapsulated Producer Cells. *Biomacromolecules* **23**: 4427.

X. Steiner, D.; Winkler, S.; Heltmann-Meyer, S.; **Trossmann, V. T.**; Fey, T.; Scheibel, T.; Horch, R. E. & Arkudas, A. (2021) Enhanced vascularization and de novo tissue formation in hydrogels made of engineered RGD-tagged spider silk proteins in the arteriovenous loop model. *Biofabrication* **13**: 045003.

XI. Mertgen, A.-S.*; **Trossmann, V. T**.*.; Guex, A. G.§; Maniura-Weber, K.; Scheibel, T. & Rottmar, M.§ (2020) Multifunctional Biomaterials: Combining Material Modification Strategies for Engineering of Cell-Contacting Surfaces. *ACS Applied Materials & Interfaces* **12**: 21342.

XII. Bargel, H.*; **Trossmann, V. T.***; Sommer, C. & Scheibel, T. (2022) Bioselectivity of silk protein-based materials and their bio-inspired applications. *Beilstein Journal of Nanotechnology* **13**: 902.

Nicht Teil dieser Dissertation:

XIII. Scheibel, T.; **Trossmann, V. T.**; Lechner, A.; Bargel, H.; Humenik, M. & Zurovec, M. (2022) Bioinspirierte Klebstoffe zur Anwendung in wässrigen Flüssigkeiten. *Adhaesion Kleben & Dichten* **66**: 34.

XIV. Neubauer, V. J.; Hüter, F.; Wittmann, J.; **Trossmann, V. T.**; Kleinschrodt, C.; Alber-Laukant, B.; Rieg, F. & Scheibel, T. (2022) Flow Simulation and Gradient Printing of Fluorapatite- and Cell-Loaded Recombinant Spider Silk Hydrogels. *Biomolecules* **12**: 1413.

XV. **Trossmann, V. T.** & Scheibel T. (2023) Spider silk and blend biomaterials: Recent advances and future opportunities. In *Silk-Based Biomaterials for Tissue Engineering, Regenerative and Precision Medicine*, 2nd Edition (Editors: S. C. Kundu, R. L. Reis), Elsevier Ltd: p. 133.

XVI. **Trossmann, V. T.**; Lentz, S. & Scheibel, T. (2023) Factors Influencing Properties of Spider Silk Coatings and Their Interactions within a Biological Environment. *Journal of Functional Biomaterials* **14**: 434.

XVII. Schaefer N.; Andrade Mier, M. S.; Sonnleitner, D.; Murenu, N.; Ng, X. J.; Lamberger, Z.; Buechner, M.; **Trossmann, V. T.**; Schubert, D. W.; Scheibel T. & Lang G. (2023) Rheological and Biological Impact of Printable PCL-Fibers as Reinforcing Fillers in Cell-Laden Spider-Silk Bio-Inks. *Small Methods* **7**: 2201717.

* gleichberechtigte Co-Autorenschaft

§ gleichberechtige korrespondierende Co-Autorenschaft

6. Darstellung des Eigenanteils

Die Ergebnisse der vorliegenden Dissertation sind teilweise in Zusammenarbeit mit Kooperationspartnern entstanden und führten zur Entstehung von zwölf Teilarbeiten. Im Folgenden werden die einzelnen Beiträge der entsprechenden Autoren zu den jeweiligen Veröffentlichungen gesondert aufgeführt.

Teilarbeit I

Die Ergebnisse dieser Studie wurden bereits im Journal *Materials Today Bio* veröffentlicht und werden hier mit freundlicher Genehmigung des Verlags Elsevier reproduziert (© 2021 The Author(s). Published by Elsevier Ltd.).

Esser, T. U.*; **Trossmann, V. T.***; Lentz, S.; Engel, F. B.[§] & Scheibel, T.[§] (2021) Designing of spider silk proteins for human induced pluripotent stem cell-based cardiac tissue engineering. *Materials Today Bio* **11**: 100114.

https://doi.org/10.1016/j.mtbio.2021.100114

* gleichberechtigte Co-Autorenschaft

[§] gleichberechtige korrespondierende Co-Autorenschaft

Die Studie wurde von Tilman U. Esser, Felix B. Engel, Thomas Scheibel und mir konzeptioniert. Das Gen-Design, die rekombinante Herstellung und die biochemische Analyse der Spinnenseidenproteine wurden von mir durchgeführt. Die Prozessierung in Filme und deren Analyse mittels Kontaktwinkelmessungen erfolgte durch mich. Sarah Lentz führte die FTIR- und AFM-Messungen und die entsprechende Datenanalyse durch. Tilman U. Esser etablierte die humane pluripotente Stammzellkultur und die Differenzierung zu Kardiomyozyten. Die Interaktions- und Viabilitäts-Studien von induzierten Kardiomyozyten auf Spinnenseidenfilmen mit dazugehörigen Färbungen und Mikroskopie-Aufnahmen wurden von Tilman U. Esser durchgeführt. Die Analyse des Schlagverhaltens von Kardiomyozyten und deren Reaktion auf Medikamenten-Stimulation erfolgte durch Tilman U. Esser. Nach Diskussion der Ergebnisse mit allen Autoren wurde das Manuskript von Tilman U. Esser und mir verfasst und zusammen mit Sarah Lentz, Felix B. Engel und Thomas Scheibel editiert und fertig gestellt.

Teilarbeit II

Die Ergebnisse dieses Projekts wurden bereits im Journal *Advanced Healthcare Materials* veröffentlicht und werden hier mit freundlicher Genehmigung des Verlags John Wiley & Sons reproduziert (© 2023 The Authors. Advanced Healthcare Materials published by Wiley-VCH GmbH).

Trossmann, V. T. & Scheibel, T (2023) Design of Recombinant Spider Silk Proteins for Cell Type Specific Binding. *Advanced Healthcare Materials* **12**: 2202660.

https://doi.org/10.1002/adhm.202202660

Die Studie wurde von Thomas Scheibel und mir konzipiert. Die funktionalisierten Spinnenseidenproteine wurde von mir designt und kloniert. Bei der rekombinanten Herstellung und Reinigung der Proteine wurde ich von den technischen Assistenten Andreas Schmidt und Johannes Diehl sowie den wissenschaftlichen Hilfskräften Vivien Beyersdorfer und Kathrin Döhla unterstützt. Die Reinheit der Proteine wurde von mir durch biochemische Analyse anhand von SDS-Page, Western Blot sowie Fluoreszenz- und CD-Spektroskopie überprüft. MALDI-TOF-Analysen wurden von Andreas Schmidt durchgeführt. Ich prozessierte die Spinnenseidenvarianten in Filme und charakterisierte die Benetzbarkeit mittels Wasser-Kontaktwinkelmessungen. Gradientenfilme mit biochemischen Signalgradienten wurden von meiner Forschungsstudentin Christina Heinritz unter meiner Betreuung prozessiert. Die Zellkulturexperimente wurden von mir mit Unterstützung von Eva Möller, Alexandra Pellert und Nicole Pittel durchgeführt. Tilman U. Esser und Felix. B. Engel lieferten freundlicherweise humane induzierte Kardiomyozyten. Zellfärbungen, mikroskopische Bildaufnahmen, Datenauswertung und das Erstellen von Abbildungen erfolgten durch mich. Das Manuskript wurde von mir verfasst und mit Thomas Scheibel editiert und fertig gestellt.

Teilarbeit III

Die Ergebnisse dieser Studie wurden bereits im Journal *ACS Applied Materials & Interfaces* veröffentlicht und werden hier mit freundlicher Genehmigung des Verlags American Chemical Society reproduziert (Copyright © 2022, American Chemical Society).

Lentz, S.*; **Trossmann, V. T.***; Borkner, C. B.; Beyersdorfer, V.; Rottmar, M. & Scheibel, T. (2022) Structure-Property Relationship Based on the Amino Acid Composition of Recombinant Spider Silk Proteins for Potential Biomedical Applications. *ACS Applied Materials & Interfaces* **14**: 31751.

https://doi.org/10.1021/acsami.2c09590

* gleichberechtigte Co-Autorenschaft

Die Studie wurde von Sarah Lentz, Thomas Scheibel und mir konzipiert. Die rekombinante Proteinherstellung erfolgte durch Johannes Diehl, Andreas Schmidt und mich. Sarah Lentz prozessierte Spinnenseidenfilme und erstellte zudem elektrokinetische Strömungspotentiale von löslichen Proteinen und, mit Unterstützung von Anja Caspari, von Filmen. Die Isoelektrische Fokussierung löslicher Proteine mit anschließendem Western Blot habe ich durchgeführt. Für die Analyse der Filme führte Sarah Lentz AFM-, KPFM-, GATR-FTIR- und Wasser-Kontaktwinkelmessungen und Datenanalysen durch. Die Studien zum enzymatischen Abbau wurden von Sarah Lentz, Christian B. Borkner, Vivien Beyersdorfer und mir durchgeführt. Die Proteinadsorptions-Messungen wurden von Christian B. Borkner und Sarah Lentz durchgeführt und ausgewertet. Der ELISA zur Umstrukturierung von Fibrinogen wurde von mir etabliert. Sarah Lentz führte die Blutkoagulations-Tests in Zusammenarbeit mit Eike Müller und Markus Rottmar durch. Die Zellkultur-Tests mit anschließender Auswertung wurden von mir mit der Unterstützung von Sarah Lentz durchgeführt. Nach wissenschaftlicher Diskussion wurde das Manuskript von Sarah Lentz und mir vorbereitet, von Markus Rottmar und Thomas Scheibel editiert und von Sarah Lentz, Thomas Scheibel und mir finalisiert.

Teilarbeit IV

Die Ergebnisse dieser Studie wurden bereits im Journal *Materials Today* veröffentlicht und werden hier mit freundlicher Genehmigung des Verlags Elsevier reproduziert (© 2020 The Author(s). Published by Elsevier Ltd.).

Kumari, S.*; Lang, G.*; DeSimone, E.; Spengler, C.; **Trossmann, V. T.**; Lücker, S.; Hudel, M.; Jacobs, K.; Krämer, N. & Scheibel, T. (2020) Engineered spider silk-based 2D and 3D materials prevent microbial infestation. *Materials Today* **41**: 21.

https://doi.org/10.1016/j.mattod.2020.06.009

* gleichberechtigte Co-Autorenschaft

Die Konzeption dieser Studie wurde von Sushma Kumari, Gregor Lang und Thomas Scheibel entwickelt. Sushma Kumari führte die *in vitro* Versuche zur Abstoßung von *E. coli* und *P. pastoris* sowie die Co-Kultur-Experimente mit Säugetierzellen auf Filmen und Hydrogelen durch. Gregor Lang bereitete flache und strukturierte Seidenoberflächen vor, führte die REM-Messungen durch und analysierte die Daten. Elise DeSimone unterstützte die 3D-Co-Kultur-Experimente. Das Gen-Design, die rekombinante Herstellung und die biochemische Analyse des ungeladenen eADF4(Ω16)-Spinnenseidenproteins erfolgte durch mich. Ferner assistierte ich Sushma Kumari bei der Vorbereitung und Handhabung der eADF4(Ω16)-Proben. Susanne Lücker, Martina Hudel und Norbert Krämer führten die *in vitro* Versuche mit *S. mutans* und *C. albicans* durch. Die Vorbereitung und anschließenden Kraft-Distanz-Messungen der Proben erfolgten durch Christian Spengler und Karin Jacobs. Nach wissenschaftlicher Diskussion der Ergebnisse mit allen Autoren wurde das Manuskript von Sushma Kumari und Gregor Lang verfasst. Elise DeSimone, Christian Spengler, Karin Jacobs, Thomas Scheibel und ich leisteten schriftliche Beiträge und editierten das Manuskript.

Teilarbeit V

Die Ergebnisse dieser Studie wurden bereits im Journal *Data in Brief* veröffentlicht und werden hier mit freundlicher Genehmigung des Verlags Elsevier reproduziert (© 2020 The Author(s). Published by Elsevier Inc.).

Kumari, S.*; Lang, G.*; DeSimone, E.; Spengler, C.; **Trossmann, V. T.**; Lücker, S.; Hudel, M.; Jacobs, K.; Krämer, N. & Scheibel, T. (2020) Data for microbe resistant engineered recombinant spider silk protein based 2D and 3D materials. *Data in Brief* **32**: 106305.

https://doi.org/10.1016/j.dib.2020.106305

* gleichberechtigte Co-Autorenschaft

Da Teilarbeit V ist als eigenständig publizierte *Supporting Information* mit weiteren Daten und Informationen zu Teilarbeit IV zu verstehen ist, decken sich die Autoren und die Beschreibung der Anteile (inkl. Eigenanteile) mit Teilarbeit IV. Daher wird auf die Beschreibung von Teilarbeit IV verwiesen.

Teilarbeit VI

Die Ergebnisse dieser Studie wurden bereits im Journal *Angewandte Chemie International Edition* veröffentlicht und werden hier mit freundlicher Genehmigung des Verlags John Wiley and Sons reproduziert (© 2021 The Authors. Angewandte Chemie International Edition published by Wiley-VCH GmbH).

Neubauer, V. J.; **Trossmann, V. T.**; Jacobi S.; Döbl, A. & Scheibel, T. (2021) Recombinant Spider Silk Gels Derived from Aqueous-Organic Solvents as Depots for Drugs. *Angewandte Chemie International Edition* **60**: 11847.

https://doi.org/10.1002/anie.202103147

Deutsche Version

Neben der englischen Version wurde auch eine deutschsprachige Variante im Journal *Angewandte Chemie* veröffentlicht und wird hier mit freundlicher Genehmigung des Verlags John Wiley and Sons reproduziert (© 2021 Die Autoren. Angewandte Chemie veröffentlicht von Wiley-VCH GmbH).

Neubauer, V. J.; **Trossmann, V. T.**; Jacobi S.; Döbl, A. & Scheibel, T. (2021) Rekombinante Spinnenseidengele aus wässrig-organischen Mischphasen als Wirkstoffdepots. *Angewandte Chemie* **133**: 11953.

https://doi.org/10.1002/ange.202103147

Das Konzept dieser Studie wurde von Vanessa J. Neubauer und Thomas Scheibel entworfen. Die Methode der Dialyse gegen ein organisches Lösungsmittel zur Herstellung von Gelen wurde von Vanessa J. Neubauer mit ihrer Forschungsstudentin Sofia Jacobi etabliert. Die Assemblierungskinetiken der Spinnenseidenproteine mit anschließender mikroskopischer Analyse wurden von mir durchgeführt. Sofia Jacobi erstellte das Freisetzungsprofil für Fluorescein und bereitete Proben für REM-Messungen mit Hendrik Bargel und TEM-Aufnahmen mit Anika Winkler vor. Weiterhin unterstützte sie Vanessa J. Neubauer bei den rheologischen Messungen. Die Rheologie-Auswertung und die Sekundärstruktur-Bestimmung anhand von ATR-FTIR-Spektroskopie erfolgte durch Vanessa J. Neubauer. Die 3D-Druckversuche und die Bildaufnahmen erfolgten in Zusammenarbeit von Vanessa J. Neubauer, Annika Lechner und mir. Annika Lechner erstellte zudem das Wirkstofffreisetzungs-Profil von β-Mercaptopurin. Die wissenschaftliche Diskussion der Ergebnisse durch Vanessa J. Neubauer, Thomas Scheibel und mich führte zur Entwicklung eines Assemblierungsmodells in Anwesenheit von organischem Co-Lösungsmittel. Das Manuskript wurde von Vanessa J. Neubauer verfasst und von allen Autoren editiert und vollendet.

Teilarbeit VII

Die Ergebnisse dieses Projekts wurden bereits im Journal *Advanced Materials Interfaces* veröffentlich und werden hier mit freundlicher Genehmigung des Verlags John Wiley and Sons reproduziert (© 2022 The Authors. Advanced Materials Interfaces published by Wiley-VCH GmbH).

Lentz, S.*; **Trossmann, V. T.*** & Scheibel, T. (2022) Selective Topography Directed Cell Adhesion on Spider Silk Surfaces. *Advanced Materials Interfaces* **10**: 2201936.

https://doi.org/10.1002/admi.202201936

* gleichberechtigte Co-Autorenschaft

Das Projekt wurde von Sarah Lentz, Thomas Scheibel und mir konzeptioniert. Die Methodik zur Herstellung strukturierter Oberflächen-(Gradienten) mittels Photolithographie wurde von Sarah Lentz mit Unterstützung ihres Forschungsstudenten Marcel Höferth etabliert. Die strukturierten Spinnenseidenfilme wurden von Sarah Lentz und mir hergestellt. Sarah Lentz übernahm die Charakterisierung dieser Filme anhand von REM-Aufnahmen sowie AFM-, GATR-FTIR- und Wasser-Kontaktwinkelmessungen mit der entsprechenden Datenanalyse. Die Zellkulturexperimente mit anschließender Färbung sowie Licht- und Fluoreszenzmikroskopie wurden von mir in Zusammenarbeit mit Sarah Lentz durchgeführt. Während Sarah Lentz die Bildaufnahmen mittels REM übernahm, führte ich die konfokale Lasermikroskopie der Proben durch. Das Manuskript wurde von mir mit Unterstützung von Sarah Lentz verfasst und von Thomas Scheibel editiert.

Teilarbeit VIII

Die Ergebnisse dieser Studie wurden bereits im Journal *Macromolecular Bioscience* veröffentlicht und werden hier mit freundlicher Genehmigung des Verlags John Wiley and Sons reproduziert (© 2021 The Authors. Macromolecular Bioscience published by Wiley-VCH GmbH).

Lechner, A.*; **Trossmann, V. T.*** & Scheibel, T. (2021) Impact of Cell Loading of Recombinant Spider Silk Based Bioinks on Gelation and Printability. *Macromolecular Bioscience* **22**: 2100390.

https://doi.org/10.1002/mabi.202100390

* gleichberechtigte Co-Autorenschaft

Annika Lechner, Thomas Scheibel und ich entwarfen das Konzept dieser Studie. Annika Lechner stellte eADF4(C16)-Hydrogele her und führte den Druck-Vergleich anhand von 3D-gedruckten Hydrogelen in Form von menschlichen Aortenklappen durch und etablierte den Filament-Kollaps-Test. Die rheologischen Messungen von Hydrogelen (Temperatur-abhängig) und von Biotinten mit anschließender Datenauswertung erfolgte durch Annika Lechner. Die Biotinten wurden von mir hergestellt. Die Aufnahme der Gelierungskinetiken erfolgte durch mich. Der Filament-Kollaps-Test verschiedener Spinnenseiden-Biotinten wurde von Annika

Lechner und mir durchgeführt und mikroskopisch von mir analysiert. Die Zellkultur und die Analyse der Viabilität erfolgten durch mich. Annika Lechner und ich werteten die Ergebnisse aus und diskutierten diese mit Thomas Scheibel. Annika Lechner und ich verfassten das Manuskript und stellten dieses nach dem Editieren durch Thomas Scheibel fertig.

Teilarbeit IX

Die Ergebnisse dieser Studie wurden bereits im Journal *Biomacromolecules* veröffentlicht und werden hier mit freundlicher Genehmigung des Verlags American Chemical Society reproduziert (Copyright © 2022, American Chemical Society).

Trossmann, V. T.*; Heltmann-Meyer, S.*; Amouei, H; Wajant, H.; Horch, R. E.; Steiner, D.[§] & Scheibel, T.[§] (2022) Recombinant Spider Silk Bioinks for Continuous Protein Release by Encapsulated Producer Cells. *Biomacromolecules* **23**: 4427.

https://doi.org/10.1021/acs.biomac.2c00971

* gleichberechtigte Co-Autorenschaft

[§] gleichberechtige korrespondierende Co-Autorenschaft

Stefanie Heltmann-Meyer, Dominik Steiner, Thomas Scheibel und ich entwarfen das Konzept dieser Studie. Ich habe die Hydrogele und Biotinten prozessiert und die Sekundärstruktur anhand von GATR-FTIR-Spektroskopie sowie die mechanischen Eigenschaften mittels rheologischer Charakterisierung mit anschließender Datenauswertung ermittelt. Claudia Stemmann führte REM- und Anika Winkler TEM-Messungen durch. Weiterhin übernahm ich Zellfärbungen mit anschließender konfokaler Lasermikroskopie. Ich verarbeitete die Biotinten mittels 3D Biodruck und dokumentierte die gedruckten Konstrukte mittels Stereomikroskopie-Aufnahmen. Stefanie Heltmann-Meyer führte den WST-8- und den Luziferase-Test durch und ermittelte die Freisetzung des Fusionsproteins mit entsprechender Datenanalyse. Die HEK293 Produktionszellen wurden von Hanna Amouei hergestellt. Hanna Amouei führte zudem den Western Blot und das TNF-Neutralisierungs-Experiment zum Aktivitätsnachweis durch. Nach wissenschaftlicher Diskussion der Ergebnisse wurde das Manuskript von mir verfasst. Die anderen Autoren editierten das Manuskript, welches von Thomas Scheibel und mir fertig gestellt wurde.

Teilarbeit X

Die Ergebnisse dieser Studie wurden bereits im Journal *Biofabrication* veröffentlicht und werden hier mit freundlicher Genehmigung des Verlags IOP Publishing reproduziert (© 2021 The Author(s). Published by IOP Publishing Ltd).

Steiner, D.; Winkler, S.; Heltmann-Meyer, S.; **Trossmann, V. T.**; Fey, T.; Scheibel, T.; Horch, R. E. & Arkudas, A. (2021) Enhanced vascularization and de novo tissue formation in hydrogels made of engineered RGD-tagged spider silk proteins in the arteriovenous loop model. *Biofabrication* **13**: 045003.

https://doi.org/10.1088/1758-5090/ac0d9b

Das Konzept dieser Studie wurde von Stefanie Heltmann-Meyer, Dominik Steiner, Thomas Scheibel und mir erstellt. Die Spinnenseiden-Hydrogele wurden von mir unter sterilen Bedingungen hergestellt. Stefanie Heltmann-Meyer und Sophie Winkler führten die Implantations- und Explantations-Experimente durch und stellten die Versorgung der Versuchstiere sicher. Die µCT-Analysen wurden von Tobias Fey durchgeführt. Die Anfertigung histologischer Schnitte und Antikörper-Färbungen erfolgte durch Ilse Arnold-Herberth, während Stefanie Heltmann-Meyer und Sophie Winkler die anschließenden Bildaufnahmen mit Auswertung durchführten. Nach wissenschaftlicher Diskussion der Ergebnisse mit allen Autoren wurde das Manuskript von Dominik Steiner verfasst, von allen Autoren editiert und fertig gestellt.

Teilarbeit XI

Dieser Übersichtsartikel wurde bereits im Journal *ACS Applied Materials & Interfaces* veröffentlicht und wird hier mit freundlicher Genehmigung des Verlags American Chemical Society reproduziert (Copyright © 2020, American Chemical Society).

Mertgen, A.-S.*; **Trossmann, V. T**.*.; Guex, A. G.[§]; Maniura-Weber, K.; Scheibel, T. & Rottmar, M.[§] (2020) Multifunctional Biomaterials: Combining Material Modification Strategies for Engineering of Cell-Contacting Surfaces. *ACS Applied Materials & Interfaces* **12**: 21342.

https://doi.org/10.1021/acsami.0c01893

* gleichberechtigte Co-Autorenschaft

[§] gleichberechtige korrespondierende Co-Autorenschaft

Die Konzeptionierung dieses Übersichtsartikels begannen Anne-Sophie Mertgen und Markus Rottmar. Anne-Sophie Mertgen und ich führten Literaturrecherchen durch, formulierten Textabschnitte und gestalteten Abbildungen. An der Einleitung und am Fazit mit Zukunftsperspektive arbeiteten Anne-Sophie Mertgen und ich zu gleichen Teilen. Der Hauptteil, der sich auf den biologischen Effekt und die Herstellung und Charakterisierung von multifunktionalen Biomaterialien fokussierte, wurde aufgeteilt: Während sich Anne-Sophie Mertgen auf Kombinationen chemischer Oberflächenmodifikationen fokussierte, bestand mein Teil aus biochemischen Funktionalisierungen, die mit topographischen oder mechanischen Modifikationen kombiniert wurden. Das Manuskript wurde von Anne-Sophie und mir verfasst und von allen Autoren editiert und finalisiert.

Teilarbeit XII

Dieser Übersichtsartikel wurde bereits im Journal *Beilstein Journal of Nanotechnology* veröffentlicht und wird mit freundlicher Genehmigung des Beilstein Instituts gemäß dem *Full Beilstein-Institut Open Access Licence Agreement 1.2* reproduziert (© 2022 Bargel *et al.*; licensee Beilstein-Institut)

Bargel, H.*; **Trossmann, V. T.***; Sommer, C. & Scheibel, T. (2022) Bioselectivity of silk protein-based materials and their bio-inspired applications. *Beilstein Journal of Nanotechnology* **13**: 902.

https://doi.org/10.3762/bjnano.13.81

* gleichberechtigte Co-Autorenschaft

Das Konzept dieses Übersichtsartikels wurde von Hendrik Bargel, Christoph Sommer und Thomas Scheibel entworfen und editiert. Hendrik Bargel, Christoph Sommer und ich führten Literaturrecherchen durch und formulierten entsprechende Textabschnitte. Die Abbildungen für den Artikel wurden von mir erstellt und von Hendrik Bargel editiert. Die Aufteilung des Artikels wurde folgendermaßen gegliedert: Die Einleitung wurde von Hendrik Bargel und mir verfasst. Hendrik Bargel schrieb zusätzlich den Paragraphen über natürliche Seidenproteine. Während ich mich im Hauptteil auf den Abschnitt über rekombinante Spinnenseiden-Technologien und zelladhäsive Spinnenseidenoberflächen fokussierte, bereiteten Christoph Sommer und Hendrik Bargel die Paragraphen über antimikrobielle und antiadhäsive Seiden-basierte Oberflächen vor. Das Manuskript wurde von Thomas Scheibel editiert und von Hendrik Bargel und mir finalisiert.

7. Teilarbeiten

7.1. Teilarbeit I

Teilarbeit I wurde 2021 unter dem Titel „*Designing of spider silk proteins for human induced pluripotent stem cell-based cardiac tissue engineering*“ im Journal *Materials Today Bio* veröffentlicht.

Esser, T. U.*; **Trossmann, V. T.***; Lentz, S.; Engel, F. B.§ & Scheibel, T.§ (2021) Designing of spider silk proteins for human induced pluripotent stem cell-based cardiac tissue engineering. *Materials Today Bio* **11**: 100114.

https://doi.org/10.1016/j.mtbio.2021.100114

* gleichberechtigte Co-Autorenschaft

§ gleichberechtigte korrespondierende Co-Autorenschaft

Materials Today Bio 11 (2021) 100114

Contents lists available at ScienceDirect

Materials Today Bio

journal homepage: www.journals.elsevier.com/materials-today-bio

Designing of spider silk proteins for human induced pluripotent stem cell-based cardiac tissue engineering

T.U. Esser [a,1], V.T. Trossmann [b,1], S. Lentz [b], F.B. Engel [a,c,**], T. Scheibel [b,d,*]

[a] Experimental Renal and Cardiovascular Research, Department of Nephropathology, Institute of Pathology, Friedrich-Alexander-Universität Erlangen-Nürnberg (FAU), Erlangen, 91054, Germany
[b] Lehrstuhl Biomaterialien, Prof.-Rüdiger-Bormann Straße 1, Bayreuth, 95447, Germany
[c] MURCE, Muscle Research Center Erlangen, Erlangen, Germany
[d] Bayreuther Zentrum für Kolloide und Grenzflächen (BZKG), Bayerisches Polymerinstitut (BPI), Bayreuther Zentrum für Molekulare Biowissenschaften (BZMB), Bayreuther Materialzentrum (BayMAT), Universitätsstraße 30, Universität Bayreuth, Bayreuth, D-95447, Germany

A B S T R A C T

Materials made of recombinant spider silk proteins are promising candidates for cardiac tissue engineering, and their suitability has so far been investigated utilizing primary rat cardiomyocytes. Herein, we expanded the tool box of available spider silk variants and demonstrated for the first time that human induced pluripotent stem cell (hiPSC)-derived cardiomyocytes attach, contract, and respond to pharmacological treatment using phenylephrine and verapamil on explicit spider silk films. The hiPSC-cardiomyocytes contracted for at least 14 days on films made of positively charged engineered *Araneus diadematus fibroin 4* (eADF4(κ16)) and three different arginyl-glycyl-aspartic acid (RGD)-tagged spider silk variants (positively or negatively charged and uncharged). Notably, hiPSC-cardiomyocytes exhibited different morphologies depending on the spider silk variant used, with less spreading and being smaller on films made of eADF4(κ16) than on RGD-tagged spider silk films. These results indicate that spider silk engineering is a powerful tool to provide new materials suitable for hiPSC-based cardiac tissue engineering.

1. Introduction

Cardiovascular disease is one of the most common causes of death worldwide [1]. Despite great advances in reducing the acute mortality of cardiovascular disease through identification of risk factors (e.g. physical inactivity, high fat diet, high blood pressure, and smoking), education and diagnosis, as well as minimizing cardiomyocyte loss (e.g. antiplatelet therapy, optimized hospitalization, acute percutaneous coronary intervention), the prevalence of heart failure is rising [1]. Thus, there is a great need for novel therapies to improve heart function. Moreover, it is becoming more apparent that data derived from animal models are often not translatable into clinical practice [2–4]. Therefore, researchers in the field are working toward developing predictive human engineered cardiac tissues to model cardiac diseases [5–7], screen for therapeutic drugs [7,8], as well as repair modalities for the injured heart [9–11]. A cornerstone of this development is the advent of human induced pluripotent stem cells (hiPSCs) and protocols for their efficient differentiation into cardiac lineages [12–15]. The hiPSCs can be derived from patients' own cells and easily modified by the genome editing technology, Clustered Regularly Interspaced Short Palindromic Repeats (CRISPR)/ CRISPR-associated protein 9 (Cas9) to introduce or correct specific mutations or to introduce reporters for monitoring specific processes [16,17].

The most advanced engineered cardiac tissues are based on cast collagen matrices [5,7], in which tissue organization can be enhanced by electrical and mechanical stimulation [18]. However, contractile forces generated by engineered heart tissues (0.05–2 mN/mm^2 [19]) are still significantly smaller than forces generated by native tissue (approx. 50 mN/mm^2 [20]). This might, for example, be due to suboptimal mechanical properties of the utilized matrix and the fabrication approach (casting). Only few other materials have been utilized for cardiac tissue

Abbreviations: AFM, atomic force microscopy; APTES, (3-aminopropyl) triethoxysilane; ATR, attenuated total reflection; DPBS, Dulbecco's phosphate-buffered saline; eADF4, Engineered *Araneus diadematus* fibroin 4; EthHD1, ethidium homodimer 1; FT-IR, Fourier-transform infrared (spectroscopy); hiPSC, human-induced pluripotent stem cell; IPTG, isopropyl-β-D-thiogalactoside; SDS-PAGE, sodium dodecyl sulfate-polyacrylamide gel electrophoresis; MALDI-TOF, matrix-assisted laser desorption/ionization time-of-flight.

* Corresponding author. Lehrstuhl Biomaterialien, Prof.-Rüdiger-Bormann Straße 1, Bayreuth, 95447, Germany.
** Corresponding author. Experimental Renal and Cardiovascular Research, Department of Nephropathology, Institute of Pathology, Friedrich-Alexander-Universität Erlangen-Nürnberg (FAU), Erlangen, 91054, Germany.
E-mail addresses: felix.engel@uk-erlangen.de (F.B. Engel), thomas.scheibel@bm.uni-bayreuth.de (T. Scheibel).
[1] Authors contributed equally to the work.

https://doi.org/10.1016/j.mtbio.2021.100114
Received 15 March 2021; Received in revised form 1 May 2021; Accepted 8 May 2021
Available online 15 May 2021

engineering, such as fibrin [9,18,21] and gelatin methacrylate [22,23]. Expansion of the number of materials suitable for cardiac tissue engineering will be necessary to identify one with optimized mechanical properties and to enable fabrication approaches beyond casting to generate hierarchically structured tissues including, for example, a vasculature, which is required for the creation of thick heart tissues. Limited by the rate of diffusion, the maximum thickness of non-vascularized myocardial tissue *in vitro* generally ranges from 50 to 100 μm, but this can be increased to around 200 μm through perfusion and high oxygen content and even to 0.5 mm when using an advanced perfusion bioreactor [24,25].

In order to identify 3D printable new materials, suitable for tissue engineering, the ones made of silk proteins are promising candidates [26–29]. We have previously demonstrated that materials made of natural silkworm silk and recombinant silk proteins are suitable for cardiac tissue engineering [30–32]. Recombinant spider silk proteins are non-cytotoxic, show no immunogenicity [27,33,34] and can be produced at a large scale with high purity and consistent quality [35–37]. Furthermore, their biological and mechanical properties can be engineered by genetic modifications, and they can be functionalized with growth factors or peptides specific for cardiomyocyte or cardiovascular needs [38–42], which confers a definite advantage over naturally derived (silk) proteins. A further advantage is the processability of recombinant spider silk proteins into 3D scaffolds without the need of additives or crosslinkers, such as hydrogels or foams, which can mimic the environment of natural tissue [43,44]. Our spider silk hydrogels show viscoelastic and shear-thinning behavior and could be 3D bioprinted in the presence or absence of encapsulated cells [38,45].

Our studies are based on the recombinant spider silk protein eADF4(C16), which is composed of 16 repeats of the C-module (Sequence: GSSAAAAAAAASGPGGYGPENQGPSGPGGYGPGGP) based on the *Araneus diadematus* fibroin (ADF4) of the European garden spider [37]. One glutamic acid residue (E) in each C-module yields a negative net charge in eADF4(C16) at neutral pH [37]. Although the material is highly biocompatible, previous studies showed that several cell types could not adhere to films made thereof [39,46], as most cells also have a negatively charged surface and prefer positively charged surfaces for attachment [47,48]. Further, the protein amino acid sequence of eADF4(C16) lacks any cell-binding motifs [39,46]. When eADF4(C16) is modified with the tripeptide arginyl-glycyl-aspartic acid (RGD) cell adhesion motif or the glutamic acid residues are replaced by lysine ones, yielding the positively charged variant eADF4(κ16), rat neonatal cardiomyocytes can attach to films made of both proteins [31,32]. These results suggested that materials made of specifically engineered spider silk proteins can be used for cardiac tissue engineering.

In this work, we expanded the number of spider silk variants tested. Further, we showed for the first time that hiPSC-cardiomyocytes can efficiently attach, spread, contract, and respond to pharmacological treatment on films made of explicit eADF4 variants.

2. Materials and methods

If not stated otherwise, all chemicals were purchased from Carl Roth, Germany.

2.1. Production of recombinant spider silk variants

The cell-binding RGD-peptide was genetically fused to the C-terminus of eADF4(κ16) and the eADF4(Ω16) variant (Fig. 1A) using our established cloning strategy [37,39]. Therein, all recombinant eADF4-based spider silk variants contain an N-terminally fused T7 tag enabling detection by western blot analysis. While eADF4(C16) was purchased from AMSilk GmbH in a high quality, all other recombinant eADF4-based spider silk proteins were produced via time-dependent fed-batch fermentation in *Escherichia coli BL21 gold* (*DE3*) as described previously [37]. In brief, the protein synthesis was initialized by adding 0.5 mM isopropyl-β-D-thiogalactoside at 30 °C. While eADF4(C16)-RGD [39] was produced for 4 h, eADF4(κ16) [41] and eADF4(Ω16) [40] variants were expressed for 2 h at 37 °C due to faster protein degradation and inclusion body formation. After production, all recombinant spider silk proteins were purified as described previously [37,39–41]. After cell disruption, a heat step was used to denature residual *E. coli* proteins and an ammonium sulfate precipitation to yield spider silk particles. After several washing steps to remove residual *E.coli* DNA or salt, the spider silk particles were lyophilized and stored at −20 °C. The purity of the recombinant spider silk proteins was confirmed by ultraviolet visual (UV–Vis) spectroscopy,

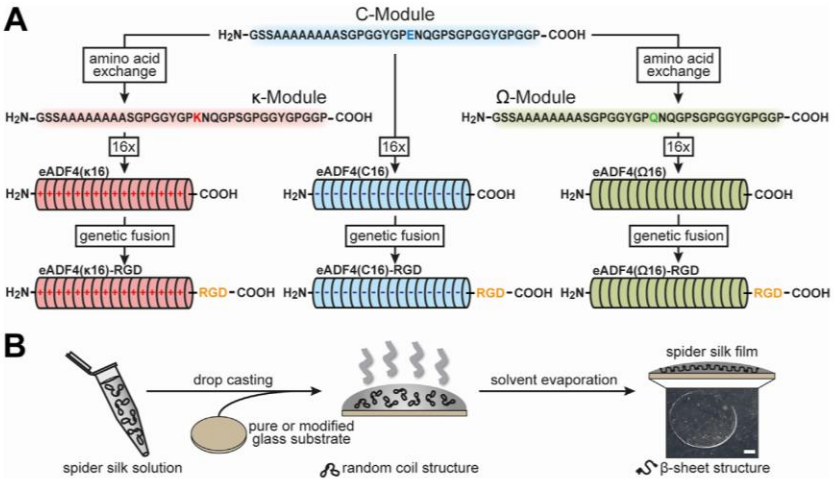

Fig. 1. Design and processing of recombinant spider silk proteins based on ADF4. A The negatively charged glutamic acid (E) residue of the C-module, reflecting the consensus sequence of the core domain of the natural *Araneus diadematus* fibroin 4, was replaced by a positively charged lysine (K) or an uncharged glutamine (Q) residue to generate the κ- or the Ω-module, respectively. These modules were repeated 16 times to obtain the charged recombinant spider silk variants eADF4(C16), eADF4(κ16), or the uncharged eADF4(Ω16). Additionally, by genetically fusing an integrin-binding sequence RGD at the C-terminus, eADF4(C16)-RGD, eADF4(κ16)-RGD and eADF4(Ω16)-RGD were generated. **B** For film casting, the recombinant spider silk proteins were dissolved in a formic acid-water mixture (5:1 v/v). The spider silk solutions were drop-cast on glass substrates to obtain films with 0.5 mg protein per cm^2. For negatively charged eADF4(C16) variants, the glass substrates were modified using (3-aminopropyl) triethoxysilane (APTES) before film casting to generate a positive surface. During solvent evaporation, β-sheets formed making the spider silk films water-insoluble. Scale bar: 2 mm.

sodium dodecyl sulfate-polyacrylamide gel electrophoresis (SDS-PAGE), Western Blot, fluorescence spectroscopy, and matrix-assisted laser desorption/ionization time-of-flight (MALDI-TOF) mass spectrometry to be >98% as described previously [37,39].

2.2. Spider silk film casting

Recombinant spider silk protein films were cast on glass slides (Thermo Fisher Scientific, Germany) with an area of 1 cm^2 by a drop-casting process (Fig. 1B). For negatively charged eADF4(C16) variants, glass slides were functionalized using (3-aminopropyl) triethoxysilane (APTES) (Sigma-Aldrich, Germany) before film casting to prevent film detachment due to electrostatic repulsion as described previously [31,32]. In brief, after washing using acetone (VWR, Germany) and water, the glass slides were incubated in ethanol (VWR, Germany)/APTES mixture (250:1 (v/v)) for 5 h at room temperature. Afterwards, the glass slides were incubated for 1 h at 70 °C to stabilize the APTES functionalization. Before film casting, the APTES-functionalized and the pure glass slides were washed using water and ethanol. All eADF4 variants were solved at a concentration of 5 mg/ml in a formic acid/water mixture (5:1 (v/v)) in a step-wise manner in which the protein powder was first solved in formic acid (VWR, Germany) for 30 min before water was added. 100 μL spider silk solution was dropped on glass slides. After evaporation of the solvent, spider silk films containing 0.5 mg spider silk protein per cm^2 were obtained and stored at dry and dark conditions until further use. Formic acid was used for film casting, as the obtained films were already water-insoluble making a subsequent treatment afterwards unnecessary [49–51]. The resulting films were used as-cast for subsequent experiments without any further washing steps or treatment afterwards.

2.3. Fourier transform infrared spectroscopy

Fourier transform infrared (FT-IR) spectroscopy was performed using a Bruker Tensor 27 FT-IR-spectrometer with Mercury Cadmium Telluride (MCT)-detector (Bruker, Rheinstetten, Germany) coupled with a Hyperion 1000 FT-IR microscope (Bruker Rheinstetten, Germany) with an attenuated total reflection (ATR) lens (20x). The germanium crystal was brought into contact with the sample. The FT-IR spectra were recorded in reflectance mode in a wavenumber range of 4000 cm^{-1}–800 cm^{-1} with a spectral resolution of 4 cm^{-1}. One hundred scans were recorded for each spectrum. Atmospheric compensation and background spectra in air were applied to each spectrum. The spectra were smoothened with five points, and the baseline was corrected using the rubber band method with 64 baseline points and one iteration. Fourier self-deconvolution (FSD) and curve fitting were performed as described previously [52,53].

2.4. Atomic force microscopy

For surface topography characterization, the recombinant spider silk films on glass were analyzed in tapping mode using a Dimension Icon atomic force microscope (Bruker, Karlsruhe, Germany) with a resolution of 512 to 512 data points at 1 Hz. OTESPA-R3 silicon cantilevers with a spring constant of 26 Nm^{-1} were used. The scan size was 50 μm–50 μm. Images were processed with Nanoscope analysis 1.5 afterwards, plane fitted and flattened with first-order fits.

2.5. Water contact angle measurements

Water contact angle measurements were conducted on spider silk coatings as well as untreated and silanized glass slides at a Surftens-universal tensiometer (OEG GmbH, Germany) using the SCA-20 software and the sessile drop method. Therefore, water droplets were applied on the surface of recombinant spider silk films or appropriate glass substrates. After 10 s equilibration time at room temperature an image was taken, and the contact angle was analyzed. (Nine measurements per condition n = 9).

2.6. Human induced pluripotent stem cells culture and cardiac differentiation

Human induced pluripotent stem cells (hiPSCs) were cultured in StemMACS iPS-Brew XF (Miltenyi Biotec, Germany) on Matrigel™-coated multiwell culture plates. Medium change was performed daily. For maintenance culture, hiPSCs were passaged at 75%–80% confluency using ethylene diamine tetra acetic acid (EDTA, 0.5 mM, Thermo Fisher Scientific) and re-plated in StemMACS iPS-Brew XF supplemented with 10 μM rho-associated protein kinase (ROCK)-inhibitor (Y-27632, Selleck Chemicals). For subsequent differentiation, hiPSCs were dissociated into single cells using Accutase (Sigma-Aldrich) and re-plated in StemMACS iPS-Brew XF supplemented with ROCK-inhibitor at a density of ~21,000 cells/cm^2. A cardiac differentiation protocol based on that described by Lian and coworkers was used [15]. At 80%–90% confluency, cardiac differentiation was initiated by exchanging the culture medium to differentiation medium (M_{Diff}) comprising Roswell Park Memorial Institute (RPMI) 1640 medium (Thermo Fisher Scientific) supplemented with 2% B-27 Minus Insulin (Thermo Fisher Scientific) and 100 μM L-ascorbic acid (Sigma-Aldrich). For the first 24 h (day 0–1), culture medium was further supplemented with 8–10 μM CHIR-99021 (Sigma Aldrich). Subsequently, medium was exchanged to M_{Diff} without additional supplementation. On day 3 of differentiation, medium was exchanged to conditioned M_{Diff} comprising equal parts of fresh M_{Diff} and M_{Diff} from days 1–3 of differentiation, and supplemented with 5 μM IWR-1 (Selleck Chemicals). Fresh M_{Diff} without additional supplementation was added on day 5 of differentiation. Subsequently, on day 7 of differentiation culture medium was exchanged to maintenance medium (M_{Main}) comprising RPMI 1640 supplemented with 2% B-27 Supplement (Thermo Fisher Scientific). Cardiomyocytes were purified by switching to lactate selection medium comprising Glucose-free RPMI 1640 (Thermo Fisher Scientific) supplemented with 5 mM sodium-lactate (Sigma-Aldrich) and 100 mM L-ascorbic acid. Metabolic selection was performed for 4–5 days starting on day 9–11 of differentiation, after which culture medium was changed back to M_{Main} for continued maintenance.

2.7. Cardiomyocyte culture on recombinant spider silk films

Cardiomyocytes were dissociated on day 15–22 of differentiation by incubation with Accutase for 30 min at 37 °C. 200,000 cells in M_{Main} supplemented with 1% RevitaCell (Thermo Fisher Scientific) were seeded per coverslip and left to attach for 24 h. Coverslips were then washed with Dulbecco's phosphate-buffered saline (DPBS, Thermo Fisher Scientific) and subsequently cultured in M_{Main}, with medium changes every 2 days.

2.8. Live-dead-staining

Cardiomyocytes cultured on spider silk films for 72 h were incubated with 1 mM Calcein, 2 mM Ethidium Homodimer-1 (EthHD1) and 5 μg/mL Hoechst 33421 (all Thermo Fisher Scientific) in DPBS for 30 min at 37 °C. Cells were subsequently washed with fresh DPBS and directly mounted onto glass slides using Fluoromount-G (Thermo Fisher Scientific). Samples were imaged immediately on a Keyence BZ-9000 epifluorescence microscope equipped with a 20x Plan Apo objective (Nikon). $Calcein^+$ and $Ethidium\ Homodimer\text{-}1^+$ cells were counted manually using Hoechst to distinguish autofluorescent debris.

2.9. Immunofluorescence staining

Cardiomyocytes were washed with DPBS and fixed with 4% paraformaldehyde for 15 min at room temperature. Samples were washed

and permeabilized (0.5% Triton X-100 in phosphate buffered saline [PBS]), followed by incubation with blocking buffer (5% bovine serum albumin [BSA], 0.2% Tween-20 in PBS). Samples were incubated with primary antibody overnight at 4 °C. The following antibodies were used at the indicated dilution: anti-sarcomeric α-actinin (abcam, ab9465, 1:500); anti-cardiac troponin-I (abcam, ab56357, 1:500); anti-connexin 43 (abcam, ab11370, 1:250). Secondary antibody incubation was performed for 1 h at room temperature: donkey anti-mouse Alexa Fluor 647 (1:500); donkey anti-rabbit Alexa Fluor 488 (1:500); donkey anti-goat Alexa Fluor 594 (1:500). All antibodies were diluted in blocking buffer. Samples were counterstained with 4′,6-diamidino-2-phenylindole (DAPI) and mounted onto glass slides using Fluoromount G. Images were acquired using a laser scanning confocal microscope (LSM 800, Zeiss) equipped with a 20x Plan-APOCHROMAT and a 63x Plan-APOCHROMAT oil immersion objective (both Zeiss).

2.10. Quantification of immunofluorescence staining

For quantification of cardiomyocyte size, images (~320 × 320 μm) of hiPSC-cardiomyocytes, immunofluorescently stained for sarcomeric α-actinin and counterstained with DAPI, were used. Intensity thresholds were set for each image individually, and the area of α-actinin signal was measured. Nuclei were counted and outlined manually, and their size was recorded. All analyses were performed using the Fiji image processing package of ImageJ [54].

2.11. Contraction analysis

Videos of beating cardiomyocytes were recorded at 15 frames per second using a Keyence BZ-9000 microscope equipped with a 20x Plan Fluor objective (Nikon). The number of contractions in each video (10 s) was extrapolated to obtain beats per minute (bpm). The beating frequency calculated from three to four videos were averaged for each sample. Contraction profiles were generated using the MUSCLEMOTION plugin [55] for the image processing software ImageJ/FIJI [54]. For analysis of drug response, baseline contraction behavior was recorded first. Then, 50 μM phenylephrine was added to the culture medium. Videos were recorded after incubating the samples for 10 min at 37 °C. Subsequently, 1 μM verapamil was added, followed by an additional incubation for 10 min at 37 °C and a final recording.

2.12. Statistics

Statistical analyses were conducted in PRISM 5 (*GraphPad*). Statistical significance was determined by one-way analysis of variance (ANOVA), followed by a *post hoc* test according to Tukey, assuming normal distribution, or two-way ANOVA when indicated. P-values of <0.05 were considered to indicate significant differences between the groups tested.

3. Results and discussion

3.1. Analysis of spider silk variant films as scaffolds for hiPSC cardiomyocytes

Negatively charged eADF4(C16) is based on 16 repeats of the consensus sequence of ADF4 and has been established almost two decades ago [37]. In recent years, modifications of this recombinant protein comprised the introduction of an RGD-tag in eADF4(C16)-RGD [39]. Furthermore, the exchange of all glutamic acid residues with lysine or glutamine ones, yielded positively charged eADF4(κ16) [41], and uncharged eADF4(Ω16) [40], respectively. Herein, to further extend the range of modified spider silk proteins, RGD-fusions with eADF4(κ16) and eADF4(Ω16) were generated (Fig. 1A).

Spider silk films were processed on untreated and 3-aminopropyltriethoxysilane (APTES)-functionalized (i.e. silanized) glass substrates at a density of 0.5 mg protein per cm^2. The differently charged and RGD-modified spider silk proteins were successfully processed into flat films. The positively charged eADF4(κ16) and uncharged eADF4(Ω16) variants were stably fixed on the negatively charged glass substrates without treatment beforehand. In contrast, silanization was used to immobilize films made of the negatively charged eADF4(C16) and eADF4(C16)-RGD variants. All films were stable during all experiments, including long-term cell cultivation. No apparent degradation or detachment was detected, confirming results from previous experiments using spider silk films [31,32,34,56].

The secondary structure of recombinant spider silk films was analyzed using FT-IR spectroscopy. In the herein used approach, a subsequent treatment of the spider silk proteins afterwards was not necessary [49–51], since the initial β-sheet content was sufficiently high, after processing from the very beginning, turning the recombinant spider silk films water-insoluble [51,52]. All recombinant spider silk variants showed nearly the same broad curve shape of amide I (1,600 cm^{-1} – 1,700 cm^{-1}) and amide II (1,570 cm^{-1} – 1,540 cm^{-1}) bands (Supplementary Fig. 1A).

Fourier self-deconvolution (FSD) and curve fitting were used to evaluate the secondary structure content of the amide I region (Supplementary Fig. 1B, Table 1) [53].

Primary cell attachment to biomaterial surfaces is influenced by surface topography and, in most cases, by the surface roughness of a material. The surface topography of flat 2D spider silk films was determined without further washing using AFM (Fig. 2A). The height images (Fig. 2A, AFM pictures, upper row) showed a smooth surface topography for eADF4(C16) and eADF4(Ω16) variants. However, the height AFM pictures indicated circular patches in the cases of eADF4(C16)-RGD, eADF4(Ω16) and eADF4(Ω16)-RGD films, which were also visible in the related phase images (Fig. 2A, lower row). These phase images represent the delay of the oscillation of the cantilever in tapping mode. The phase signal is sensitive to different material-related properties like composition, stiffness/softness and viscoelastic properties [57]. These patches on eADF4(C16)-RGD, eADF4(Ω16) and eADF4(Ω16)-RGD films (Fig. 2A, lower row) indicated different viscoelastic properties of the patches in comparison to the rest of the film. The patches could result from microphase separation of hydrophobic and hydrophilic parts of the protein as published previously [51,52]. Thereby, during film assembly the hydrophilic parts (GGX and GPGX motifs) of the eADF4-variants separate from the hydrophobic parts (polyalanine stretches), leading to structural patches with crystalline areas embedded in an amorphous matrix. The coupled RGD sequence affected the size of these patches in case of the negatively and uncharged variants, as they were smaller for eADF4(C16)-RGD and eADF4(Ω16)-RGD compared to eADF4(Ω16). In contrast, both positively charged films, eADF4(κ16) and eADF4(κ16)-RGD, showed a smooth film surface without any patches despite salt crystals distributed over the entire surface. These salt crystals were increasing the apparent total surface roughness.

Table 1
Secondary structure content [%] of recombinant spider silk films determined using FSD analysis according to Hu et al. [53].

Secondary structure	eADF4(C16)	eADF4(C16)-RGD	eADF4(κ16)	eADF4(κ16)-RGD	eADF4(Ω16)	eADF4(Ω16)-RGD
β-sheets	31.0 ± 0.4	34.4 ± 0.9	24.7 ± 7.9	28.1 ± 1.0	27.4 ± 2.0	26.9 ± 1.4
random coils	35.4 ± 0.5	34.4 ± 0.3	36.9 ± 3.7	34.1 ± 0.7	34.5 ± 0.3	34.9 ± 1.3
α-helices	11.5 ± 0.3	10.9 ± 0.1	12.2 ± 0.7	11.1 ± 0.4	11.2 ± 0.3	11.5 ± 0.5
β-turns	19.7 ± 0.3	18.8 ± 0.3	23.4 ± 1.5	20.1 ± 0.9	20.1 ± 1.5	20.4 ± 0.5
others	2.5 ± 1.5	1.5 ± 0.8	2.7 ± 2.2	6.6 ± 0.6	6.7 ± 0.4	6.4 ± 0.8

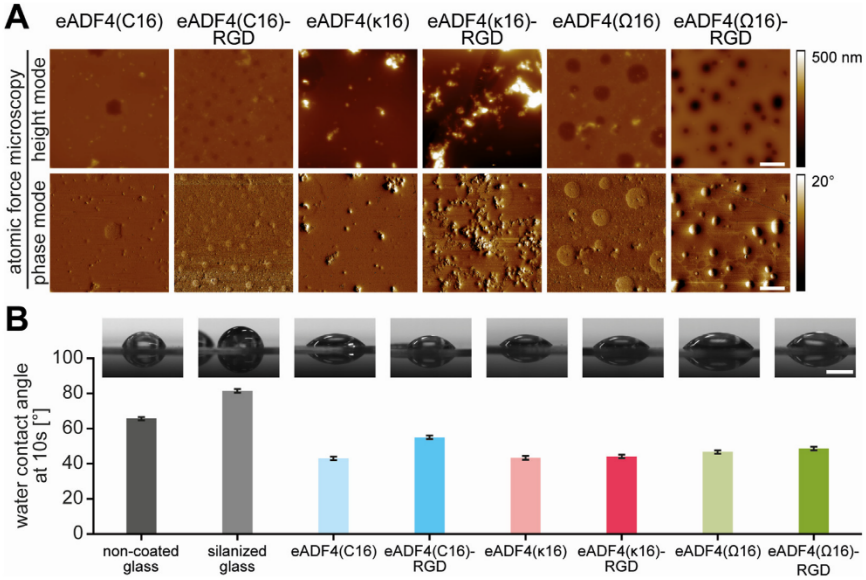

Fig. 2. Spider silk film surface characterization. A Film surface topography was determined using atomic force microscopy (AFM) in tapping mode in air. Scale bar: 10 μm **B** Water contact angles on spider silk films and non-coated and silanized glass materials were determined after 10 s using the sessile drop method. Scale bar: 1 mm.

Finally, water contact angle measurements were performed to evaluate the surface hydrophobicity of the films (Fig. 2B). Surfaces with a water contact angle below 90° are characterized as hydrophilic, while water contact angles above this threshold are indicative of hydrophobic surfaces. Untreated and APTES-functionalized (silanized) glass slides showed contact angles around 66° and 81°, respectively, and are *per se* defined as hydrophilic surfaces. Nevertheless, spider silk surfaces were more hydrophilic, indicated by a better spread water droplet (Fig. 2B). All spider silk variants, except eADF4(C16)-RGD, showed contact angles between 43° and 49°. The slightly higher contact angle of 55° for eADF4(C16)-RGD in comparison to eADF4(C16) confirmed results of a former study [31]. The presence of salt crystals on eADF4(κ16)-based spider silk films showed no influence on the water contact angle and surface hydrophobicity [32].

3.2. Human induced pluripotent stem cell-cardiomyocytes attach to films of distinct spider silk variants

In order to evaluate the spider silk variants' suitability for human cardiac tissue engineering applications, human induced pluripotent stem cell (hiPSC)-cardiomyocytes were seeded on silk films, and the viability of attached cells was determined after 3 days using Calcein and Ethidium Homodimer-1 (EthHD1) staining. As a control adhesion matrix, Matrigel™ was used, representing a laminin-rich mixture of extracellular matrix (ECM) proteins. While Matrigel™ is typically used to culture hiPSC-cardiomyocytes *in vitro*, it is not suitable for clinical translation, due to its tumor-related origin and associated safety concerns. In addition, the composition of Matrigel™ is not fully defined and is also subject to lot-to-lot variability [58].

High viability was found on films made of RGD-modified spider silk variants, irrespective of their charge, comparable to the viability of hiPSC-cardiomyocytes on Matrigel™ (Fig. 3A). Similarly, cells on eADF4(κ16) films exhibited high viability. In contrast, the degree of viability was significantly reduced on eADF4(C16) and eADF4(Ω16) films (similar to glass controls). Considering the non-cytotoxic nature of spider silk proteins [27,33,34], the reduced viability is probably due to a lack of proper cell attachment. Note, our experience shows also that non-proliferative cardiomyocytes undergo cell death when seeded at very low densities. Importantly, part of the seeded cells is dead as a result of metabolic selection during differentiation and cell dissociation. These dead cells stick to surfaces (in our case also

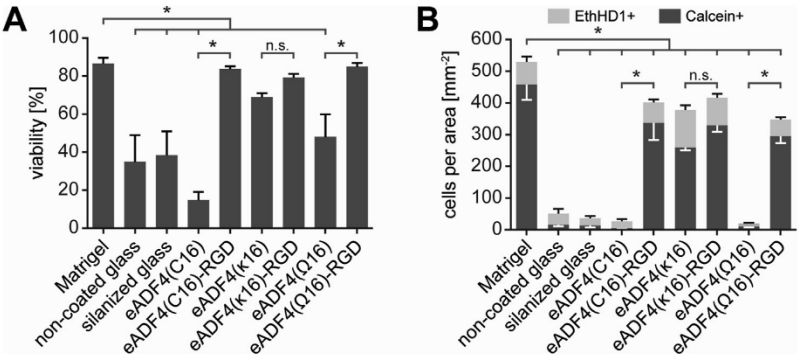

Fig. 3. hiPSC-cardiomyocytes adhere to films made of several spider silk variants. A Percentage of viable cells on spider silk films made of different variants 3 days after seeding as determined by Calcein and Ethidium Homodimer-1 (EthHD1) staining. Data are mean ± standard error (SE) of the mean. *: $p < 0.05$, one-way ANOVA followed by a *post hoc* test according to Tukey. **B** Count of viable (Calcein+) and dead (EthHD1+) cells per area on spider silk films 3 days after seeding. N = 4 independent experiments. Data are mean ± standard error of the mean. *: $p < 0.05$, one-way ANOVA followed by a *post hoc* test according to Tukey.

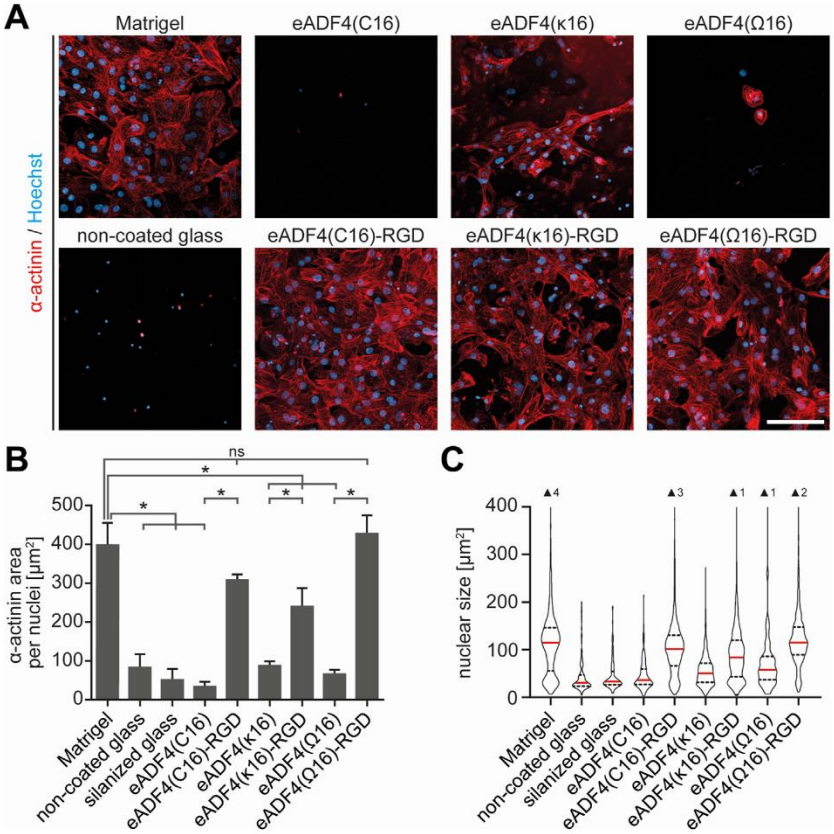

Fig. 4. hiPSC-cardiomyocytes display different morphologies depending on the spider silk variant used as scaffold. A Immunofluorescence staining for hiPSC-cardiomyocyte marker protein sarcomeric α-actinin (red) 3 days after seeding. Scale bar: 100 μm. **B** Quantification of sarcomeric α-actinin immunofluorescence signal area, normalized to nuclei count 3 days after seeding. Data from four independent experiments are presented as mean ± standard error of the mean. *: $p < 0.05$, one-way ANOVA followed by a *post hoc* test according to Tukey. **C** Violin plots of nuclear size 3 days after seeding. Data from four independent experiments are presented (n = 101 to 1944). Red lines: median; dashed lines: 1st and 3rd quartile. ▲: number of data points outside of the depicted range.

non-coated glass) independently of adhesion motifs and thus are overrepresented on films to which hiPSC-derived cardiomyocytes adhere only inefficiently.

To further examine the interaction of hiPSC-cardiomyocytes with the different surfaces, the absolute numbers of live (Calcein^{+}) and dead (EthidiumHD1^{+}) cells were assessed (Fig. 3B). The number of cells on unmodified eADF4(C16) and eADF4(Ω16) films were very low and comparable to glass controls, where only a few viable cells were found. In contrast, the amounts were markedly higher on RGD-modified spider silk variants, as well as eADF4(κ16). Importantly, the number of viable cells on eADF4(κ16) films was comparable to that observed for eADF4(κ16)-RGD ones. No significant differences were observed between the different RGD-modified variants. The observed higher number of attached cells on Matrigel™, compared to RGD-variant and eADF4(κ16) films, might be explained by the greater variety of cell adhesion motifs and integrin recognition sites, as Matrigel™ comprises a multitude of extracellular matrix (ECM) proteins [59]. In addition, growth factors present in Matrigel™ might promote attachment.

Attachment on eADF4(κ16) films appeared to be mediated by its charge, since the primary amino acid sequence of this spider silk sequence contains no cell-binding motif [46], and the cell membrane of mammalian cells is mainly negatively charged and interacts preferentially with polycationic surfaces [32,47,48]. The attachment efficiency to eADF4(κ16) films was comparable with the efficiencies of eADF4(C16)-RGD or eADF4(Ω16)-RGD ones. Interestingly, the RGD-modification of eADF4(κ16) did not further improve cell attachment. This suggested that the peptide motif of eADF4(κ16)-RGD has no additional, synergistic effect on initial adhesion to the positively charged surface.

3.3. hiPSC-cardiomyocytes exhibit different morphologies depending on the spider silk variant

Immunofluorescent staining of sarcomeric α-actinin revealed hiPSC-cardiomyocyte spreading on RGD-modified variants, similar to Matrigel™-controls, 3 days after seeding (Fig. 4A). In contrast, on eADF4(C16) and eADF4(Ω16) films, hiPSC-cardiomyocytes remained rounded and did not spread. Notably, while being comparable in number (Fig. 3B), the hiPSC-cardiomyocytes on eADF4(κ16) films appeared less spread and smaller than those on eADF4(κ16)-RGD films (Fig. 4A). To obtain an estimation of cardiomyocyte size, the area of α-actinin staining was determined as well as the number of nuclei of a given field of view (Fig. 4B). Our analyses showed that the few cardiomyocytes attached to unmodified variants, irrespective of charge, exhibited the smallest α-actinin areas/nuclei with values comparable to those of cells on glass controls. The analyses further revealed that cardiomyocytes spread most on films made of RGD-variants, with α-actinin/nuclei levels highest for cells grown on Matrigel™, eADF4(Ω16)-RGD and eADF4(C16)-RGD and slightly smaller for cells on eADF4(κ16)-RGD. Notably, the analyses confirmed that cells on eADF4(κ16) films exhibited a significantly lower α-actinin area per nuclei compared with cells on eADF4(κ16)-RGD.

To validate these results, nuclear size was quantified as an indirect indicator of cardiomyocyte cell size. Notably, cells usually maintain a roughly constant nuclear-to-cytoplasmic volume ratio [60]. It has been previously shown that during maturation, the increase in cardiomyocyte size is accompanied by an increase in size of the nuclei [61].

As shown in Fig. 4C, nuclear size data were in agreement with α-actinin area/nuclei data, whereby the average nuclear size was largest

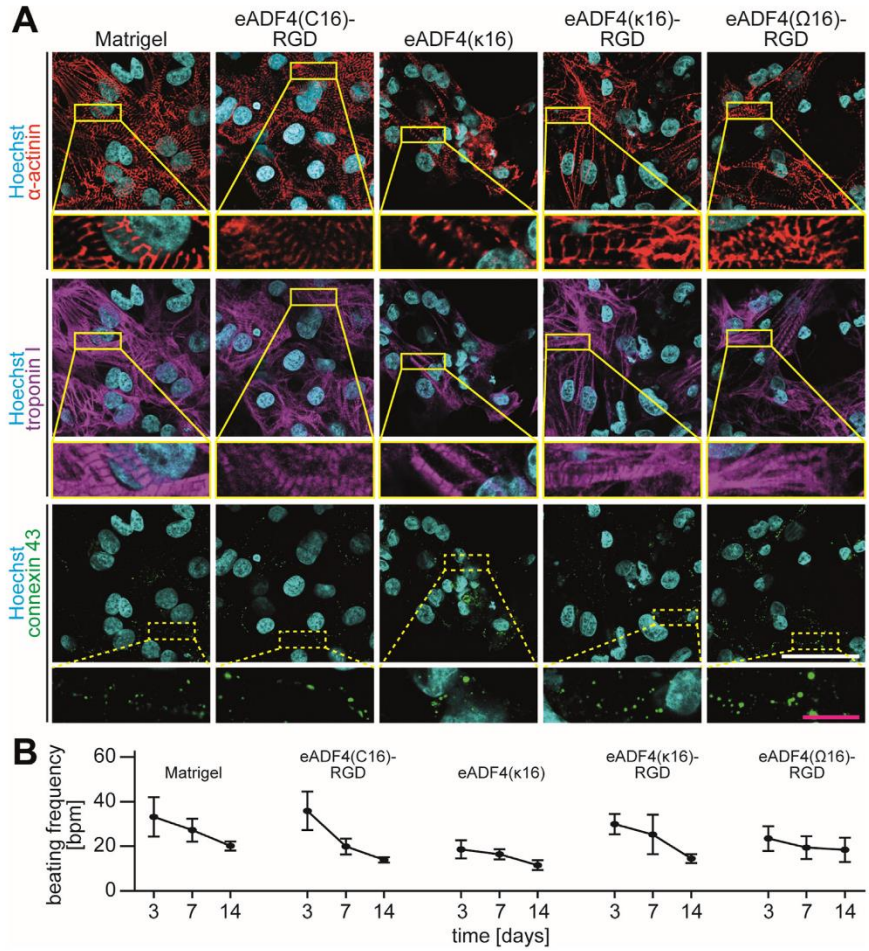

Fig. 5. Long-term cultivation of hiPSC-cardiomyocytes on spider silk films. **A** Immunofluorescence staining of the hiPSC-cardiomyocyte marker proteins sarcomeric α-actinin (red), cardiac troponin I (magenta) and connexin 43 (green) 14 days after seeding. White scale bar: 50 μm; magenta scale bar: 10 μm. **B** Beating frequency of hiPSC-cardiomyocytes at 3, 7 and 14 days after seeding. Data from 3 independent experiments are presented as mean ± standard error of the mean.

on eADF4(Ω16)-RGD, surpassing sizes on both eADF4(C16)-RGD and eADF4(κ16)-RGD as well as Matrigel™.

In summary, hiPSC-cardiomyocytes attachment did not correlate with cell size, as hiPSC-cardiomyocytes attached on eADF4(κ16) films were markedly smaller than those attached on films made of RGD-modified variants. These findings are in agreement with reports that RGD-mediated integrin signaling is required for hypertrophic responses in cardiomyocytes [62,63].

3.4. Long-term cultivation of hiPSC-cardiomyocytes on spider silk films

To evaluate the possibility of long-term cultivation of hiPSC-cardiomyocytes on spider silk films, cultures were analyzed for up to 14 days. Immunofluorescent staining for α-actinin revealed a striated pattern, typical for hiPSC-cardiomyocytes, on all RGD-modified spider silk variants, similar to that on Matrigel™ (Fig. 5A). hiPSC-cardiomyocytes cultured on eADF4(κ16) remained smaller, even after this prolonged culture period. Additionally, cardiac troponin I (cTnI), an isoform of troponin I associated with hiPSC-cardiomyocytes maturation, was found in a striated pattern on RGD-modified variants, whereas it appeared more disorganized on eADF4(κ16) (Fig. 5A). Further, the gap junction protein connexin 43 could be identified at cell-to-cell contacts, suggesting electrical coupling (Fig. 5A). In accordance, spontaneous contractions of hiPSC-cardiomyocytes were observed on films made of RGD-modified variants and eADF4(κ16) as early as 24 h after seeding, and consistently by day 3 of culture. Connexin 43 was not specifically localized to longitudinal termini of cardiomyocytes (i.e. intercalated discs) on either of the matrices investigated, but distributed around the entire cells, suggesting that hiPSC-derived cardiomyocytes did not undergo advanced maturation on spider silk films compared to Matrigel™.

Of note, hiPSC-cardiomyocytes on RGD-modified variants and Matrigel™ contracted synchronously across each field of view, while contractions on eADF4(κ16) were asynchronous (Supplementary Fig. 2), which appears to result from the smaller cell size and, therefore, lower coverage and cell-to-cell contact impairing electrical coupling.

To investigate hiPSC-cardiomyocyte contractility on spider silk variant films over time, cultures were analyzed for up to 14 days, and the beating behavior was recorded (Fig. 5B). An overall reduction in beating frequency was observed with increasing culture time (influence of culture time: $p < 0.05$ determined by two-way ANOVA). However, no significant differences between RGD-modified variants, eADF4(κ16) or Matrigel™ were observed at either time point (day 3, 7 or 14). These findings indicated that films made of these spider silk variants supported long-term culture and did not impair hiPSC-cardiomyocyte contractility.

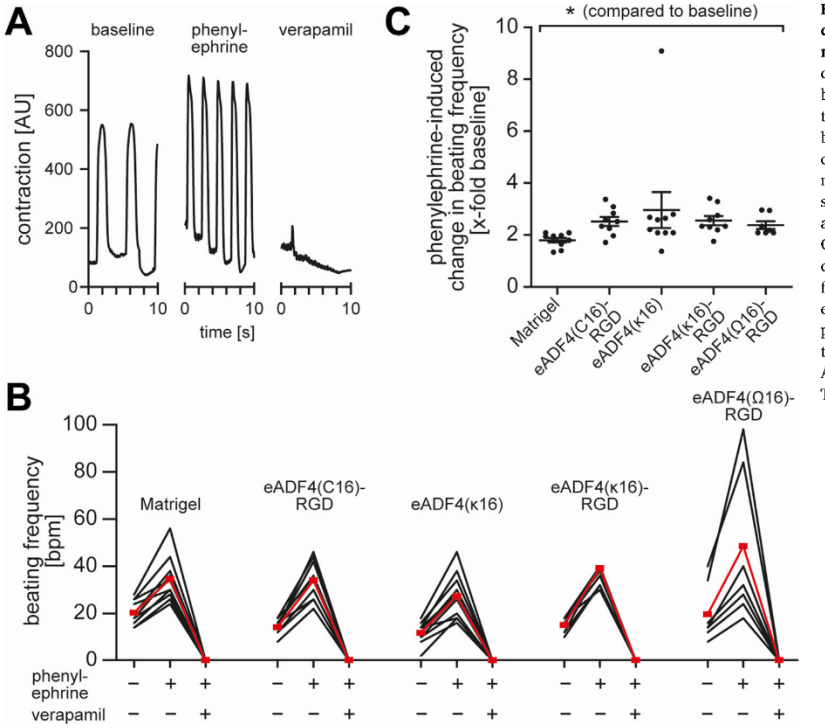

Fig. 6. hiPSC-cardiomyocytes on selected spider silk films are responsive to drug treatment. **A** Scheme of workflow and exemplary contraction profiles of hiPSC-cardiomyocytes at baseline and in response to adrenergic stimulation (50 μM phenylephrine) and calcium channel blockade (1 μM verapamil). **B** Beating frequencies of hiPSC-cardiomyocytes upon treatment with phenylephrine and verapamil on spider silk films. Individual samples (n = 7 to 10) are shown in black; means are shown in red. **C** Quantification of the increase in beating frequencies upon phenylephrine treatment. Data from 4 (3 for eADF4(Ω16)-RGD) independent experiments are presented as individual data points (black dots) and mean ± standard error of the mean (gray bars). *: $p < 0.05$, one-way ANOVA followed by a post hoc test according to Tukey.

3.5. hiPSC-cardiomyocytes on spider silk films respond to pharmacological stimulation

Next, cells were treated with phenylephrine, an adrenergic agonist, and subsequently verapamil, an inhibitor of L-type calcium channels, and the contractions were recorded (Fig. 6A). Phenylephrine induced a significant increase in beating frequency of hiPSC-cardiomyocytes on all spider silk variants tested, while verapamil abolished beating (Fig. 6B and C). A 1.7–2.9-fold increase in beating frequency was detected upon phenylephrine treatment.

4. Conclusion

Two Previous studies have established that spider silk materials made of eADF4 variants are very suitable and promising materials for tissue engineering and biomedical applications, as spider silk materials are highly biocompatible and cause no unspecific immune response [27,33,34]. From the findings presented here, we deduce that these materials are also promising scaffolds for cardiac tissue engineering. Interestingly, while hiPSC-cardiomyocytes could not adhere to eADF4(C16) without additional modification, they could be cultivated on specifically engineered spider silk variants. We conclude that specific modified spider silk variants, tailored to tissue-specific requirements, can be utilized to engineer human cardiac tissues aiming at modeling human diseases, screening for therapeutic drugs, and improving heart function in patients. This is an important observation, as it might allow to design strategies for selective growth of cardiomyocytes in the future, and thus might help in designing hierarchically structured cardiac tissues. Further, hiPSC-cardiomyocytes exhibited selective cell behavior on films made of the different spider silk variants, which might be of advantage for certain applications. The smaller cell size in contact with eADF4(κ16) surfaces might allow the generation of cardiac tissues with a higher cardiomyocyte density, which might, therefore, exhibit a higher contractile force. Such a construct could then also be enlarged by subsequent stimulation with pro-hypertrophic agents. In the context of 3D printing, a smaller cell size might also be of advantage, for example, regarding shear stress.

Credit author statement

TUE, VTT, and SL carried out experimental work and analyzed data; TUE, VTT, FBE, and TS wrote the original draft of the manuscript; FBE and TS conceptualized and supervised the study; all authors revised and approved the final version of the manuscript.

Declaration of competing interest

The authors declare the following financial interests/personal relationships which may be considered as potential competing interests:

Prof. Scheibel is co-founder and shareholder of AMSilk GmbH.

Acknowledgments

The authors would like to thank Isabel Schoenauer for assistance in confirming stem cell pluripotency, Jana Petzold for technical advice, as well as Annika Döbl, Kaveh Roshanbinfar and Ingo Thievessen for critical discussions. Support from the Elite Network of Bavaria is also acknowledged. This work was supported by the Deutsche Forschungsgemeinschaft [DFG, German Research Foundation, grant numbers: Projektnummer 326998133 – TRR 225 (subproject C01 to F.B.E. and T.S.) and INST 410/91-1 FUGG (to F.B.E.)].

Appendix A. Supplementary data

Supplementary data to this article can be found online at https://doi.org/10.1016/j.mtbio.2021.100114.

References

[1] S.S. Virani, A. Alonso, E.J. Benjamin, M.S. Bittencourt, C.W. Callaway, A.P. Carson, A.M. Chamberlain, A.R. Chang, S. Cheng, F.N. Delling, L. Djousse, M.S.V. Elkind, J.F. Ferguson, M. Fornage, S.S. Khan, B.M. Kissela, K.L. Knutson, T.W. Kwan, D.T. Lackland, T.T. Lewis, J.H. Lichtman, C.T. Longenecker, M.S. Loop, P.L. Lutsey, S.S. Martin, K. Matsushita, A.E. Moran, M.E. Mussolino, A.M. Perak, W.D. Rosamond, G.A. Roth, U.K.A. Sampson, G.M. Satou, E.B. Schroeder, S.H. Shah, C.M. Shay, N.L. Spartano, A. Stokes, D.L. Tirschwell, L.B. VanWagner, C.W. Tsao, E. American Heart Association Council on, C. Prevention Statistics, S. Stroke Statistics, Heart disease and stroke statistics-2020 update: a report from the American heart association, Circulation 141 (2020) e139 e596, https://doi.org/10.1161/CIR.0000000000000757.

[2] S. Lecour, H.E. Botker, G. Condorelli, S.M. Davidson, D. Garcia-Dorado, F.B. Engel, P. Ferdinandy, G. Heusch, R. Madonna, M. Ovize, M. Ruiz-Meana, R. Schulz, J.P. Sluijter, L.W. Van Laake, D.M. Yellon, D.J. Hausenloy, ESC working group cellular biology of the heart: position paper: improving the preclinical assessment of novel cardioprotective therapies, Cardiovasc. Res. 104 (2014) 399 411, https://doi.org/10.1093/cvr/cvu225.

[3] S. Clauss, C. Bleyer, D. Schuttler, P. Tomsits, S. Renner, N. Klymiuk, R. Wakili, S. Massberg, E. Wolf, S. Kaab, Animal models of arrhythmia: classic electrophysiology to genetically modified large animals, Nat. Rev. Cardiol. 16 (2019) 457 475, https://doi.org/10.1038/s41569-019-0179-0.

[4] C.J. Perry, A.J. Lawrence, Hurdles in basic science translation, Front. Pharmacol. 8 (2017) 478, https://doi.org/10.3389/fphar.2017.00478.

[5] M. Tiburcy, J.E. Hudson, P. Balfanz, S. Schlick, T. Meyer, M.L. Chang Liao, E. Levent, F. Raad, S. Zeidler, E. Wingender, J. Riegler, M. Wang, J.D. Gold, I. Kehat, E. Wettwer, U. Ravens, P. Dierickx, L.W. van Laake, M.J. Goumans, S. Khadjeh, K. Toischer, G. Hasenfuss, L.A. Couture, A. Unger, W.A. Linke, T. Araki, B. Neel, G. Keller, L. Gepstein, J.C. Wu, W.H. Zimmermann, Defined engineered human myocardium with advanced maturation for applications in heart failure modeling and repair, Circulation 135 (2017) 1832 1847, https://doi.org/10.1161/CIRCULATIONAHA.116.024145.

[6] J.T. Hinson, A. Chopra, N. Nafissi, W.J. Polacheck, C.C. Benson, S. Swist, J. Gorham, L. Yang, S. Schafer, C.C. Sheng, A. Haghighi, J. Homsy, N. Hubner, G. Church, S.A. Cook, W.A. Linke, C.S. Chen, J.G. Seidman, C.E. Seidman, Titin mutations in iPS cells define sarcomere insufficiency as a cause of dilated cardiomyopathy, Science 349 (2015) 982 986, https://doi.org/10.1126/science.aaa5458.

[7] Y. Zhao, N. Rafatian, N.T. Feric, B.J. Cox, R. Aschar-Sobbi, E.Y. Wang, P. Aggarwal, B. Zhang, G. Conant, K. Ronaldson-Bouchard, A. Pahnke, S. Protze, J.H. Lee, L. Davenport Huyer, D. Jekic, A. Wickeler, H.E. Naguib, G.M. Keller, G. Vunjak-Novakovic, U. Broeckel, P.H. Backx, M. Radisic, A platform for generation of chamber-specific cardiac tissues and disease modeling, Cell 176 (2019) 913 927, https://doi.org/10.1016/j.cell.2018.11.042, e18.

[8] M. Lemme, B.M. Ulmer, M.D. Lemoine, A.T.L. Zech, F. Flenner, U. Ravens, H. Reichenspurner, M. Rol-Garcia, G. Smith, A. Hansen, T. Christ, T. Eschenhagen, Atrial-like engineered heart tissue: an in vitro model of the human atrium, Stem Cell Rep. 11 (2018) 1378 1390, https://doi.org/10.1016/j.stemcr.2018.10.008.

[9] P. Menasche, V. Vanneaux, A. Hagege, A. Bel, B. Cholley, A. Parouchev, I. Cacciapuoti, R. Al-Daccak, N. Benhamouda, H. Blons, O. Agbulut, L. Tosca, J.H. Trouvin, J.R. Fabreguettes, V. Bellamy, D. Charron, E. Tartour, G. Tachdjian, M. Desnos, J. Larghero, Transplantation of human embryonic stem cell-derived cardiovascular progenitors for severe ischemic left ventricular dysfunction, J. Am. Coll. Cardiol. 71 (2018) 429 438, https://doi.org/10.1016/j.jacc.2017.11.047.

[10] R. Madonna, L.W. Van Laake, H.E. Botker, S.M. Davidson, R. De Caterina, F.B. Engel, T. Eschenhagen, F. Fernandez-Aviles, D.J. Hausenloy, J.S. Hulot, S. Lecour, J. Leor, P. Menasche, M. Pesce, C. Perrino, F. Prunier, S. Van Linthout, K. Ytrehus, W.H. Zimmermann, P. Ferdinandy, J.P.G. Sluijter, ESC Working Group on Cellular Biology of the Heart: position paper for Cardiovascular Research: tissue engineering strategies combined with cell therapies for cardiac repair in ischaemic heart disease and heart failure, Cardiovasc. Res. 115 (2019) 488 500, https://doi.org/10.1093/cvr/cvz010.

[11] L. Gao, Z.R. Gregorich, W. Zhu, S. Mattapally, Y. Oduk, X. Lou, R. Kannappan, A.V. Borovjagin, G.P. Walcott, A.E. Pollard, V.G. Fast, X. Hu, S.G. Lloyd, Y. Ge, J. Zhang, Large cardiac muscle patches engineered from human induced-pluripotent stem cell derived cardiac cells improve recovery from myocardial infarction in swine, Circulation 137 (2018) 1712 1730, https://doi.org/10.1161/circulationaha.117.030785.

[12] L. Cyganek, M. Tiburcy, K. Sekeres, K. Gerstenberg, H. Bohnenberger, C. Lenz, S. Henze, M. Stauske, G. Salinas, W.-H. Zimmermann, G. Hasenfuss, K. Guan, Deep phenotyping of human induced pluripotent stem cell derived atrial and ventricular cardiomyocytes, JCI Insight 3 (2018), https://doi.org/10.1172/jci.insight.99941.

[13] J.H. Lee, S.I. Protze, Z. Laksman, P.H. Backx, G.M. Keller, Human pluripotent stem cell-derived atrial and ventricular cardiomyocytes develop from distinct mesoderm populations, Cell Stem Cell 21 (2017) 179 194, https://doi.org/10.1016/j.stem.2017.07.003, e4.

[14] S.I. Protze, J. Liu, U. Nussinovitch, L. Ohana, P.H. Backx, L. Gepstein, G.M. Keller, Sinoatrial node cardiomyocytes derived from human pluripotent cells function as a biological pacemaker, Nat. Biotechnol. 35 (2016) 56 68, https://doi.org/10.1038/nbt.3745.

[15] X. Lian, J. Zhang, S.M. Azarin, K. Zhu, L.B. Hazeltine, X. Bao, C. Hsiao, T.J. Kamp, S.P. Palecek, Directed cardiomyocyte differentiation from human pluripotent stem cells by modulating Wnt/beta-catenin signaling under fully defined conditions, Nat. Protoc. 8 (2013) 162 175, https://doi.org/10.1038/nprot.2012.150.

[16] C. Long, H. Li, M. Tiburcy, C. Rodriguez-Caycedo, V. Kyrychenko, H. Zhou, Y. Zhang, Y.L. Min, J.M. Shelton, P.P.A. Mammen, N.Y. Liaw, W.H. Zimmermann, R. Bassel-Duby, J.W. Schneider, E.N. Olson, Correction of diverse muscular dystrophy mutations in human engineered heart muscle by single-site genome editing, Sci. Adv. 4 (2018), eaap9004, https://doi.org/10.1126/sciadv.aap9004.

[17] Y.H. Sun, H.K.J. Kao, C.W. Chang, A. Merleev, J.L. Overton, D. Pretto, S. Yechikov, E. Maverakis, N. Chiamvimonvat, J.W. Chan, D.K. Lieu, Human induced pluripotent stem cell line with genetically encoded fluorescent voltage indicator generated via CRISPR for action potential assessment post-cardiogenesis, Stem Cells 38 (2020) 90 101, https://doi.org/10.1002/stem.3085.

[18] K. Ronaldson-Bouchard, S.P. Ma, K. Yeager, T. Chen, L. Song, D. Sirabella, K. Morikawa, D. Teles, M. Yazawa, G. Vunjak-Novakovic, Advanced maturation of human cardiac tissue grown from pluripotent stem cells, Nature 556 (2018) 239 243, https://doi.org/10.1038/s41586-018-0016-3.

[19] M.N. Hirt, A. Hansen, T. Eschenhagen, Cardiac tissue engineering: state of the art, Circ. Res. 114 (2014) 354 367, https://doi.org/10.1161/CIRCRESAHA.114.300522.

[20] G. Hasenfuss, L.A. Mulieri, E.M. Blanchard, C. Holubarsch, B.J. Leavitt, F. Ittleman, N.R. Alpert, Energetics of isometric force development in control and volume-overload human myocardium. Comparison with animal species, Circ. Res. 68 (1991) 836 846, https://doi.org/10.1161/01.res.68.3.836.

[21] K. Breckwoldt, D. Letuffe-Breniere, I. Mannhardt, T. Schulze, B. Ulmer, T. Werner, A. Benzin, B. Klampe, M.C. Reinsch, S. Laufer, A. Shibamiya, M. Prondzynski, G. Mearini, D. Schade, S. Fuchs, C. Neuber, E. Kramer, U. Saleem, M.L. Schulze, M.L. Rodriguez, T. Eschenhagen, A. Hansen, Differentiation of cardiomyocytes and generation of human engineered heart tissue, Nat. Protoc. 12 (2017) 1177 1197, https://doi.org/10.1038/nprot.2017.033.

[22] J. Lee, V. Manoharan, L. Cheung, S. Lee, B.H. Cha, P. Newman, R. Farzad, S. Mehrotra, K. Zhang, F. Khan, M. Ghaderi, Y.D. Lin, S. Aftab, P. Mostafalu, M. Miscuglio, J. Li, B.B. Mandal, M.A. Hussain, K.T. Wan, X.S. Tang, A. Khademhosseini, S.R. Shin, Nanoparticle-based hybrid Scaffolds for deciphering the role of multimodal cues in cardiac tissue engineering, ACS Nano 13 (2019) 12525 12539, https://doi.org/10.1021/acsnano.9b03050.

[23] S.R. Shin, C. Zihlmann, M. Akbari, P. Assawes, L. Cheung, K. Zhang, V. Manoharan, Y.S. Zhang, M. Yuksekkaya, K.T. Wan, M. Nikkhah, M.R. Dokmeci, X.S. Tang, A. Khademhosseini, Reduced graphene oxide-GelMA hybrid hydrogels as Scaffolds for cardiac tissue engineering, Small 12 (2016) 3677 3689, https://doi.org/10.1002/smll.201600178.

[24] C. Patra, A.R. Boccaccini, F.B. Engel, Vascularisation for cardiac tissue engineering: the extracellular matrix, Thromb. Haemost. 113 (2015) 532 547, https://doi.org/10.1160/TH14-05-0480.

[25] T.U. Esser, K. Roshanbinfar, F.B. Engel, Promoting vascularization for tissue engineering constructs: current strategies focusing on HIF-regulating scaffolds, Expet Opin. Biol. Ther. 19 (2019) 105 118, https://doi.org/10.1080/14712598.2019.1561855.

[26] Y. Song, H. Wang, F. Yue, Q. Lv, B. Cai, N. Dong, Z. Wang, L. Wang, Silk-based biomaterials for cardiac tissue engineering, Adv. Healthc. Mater. (2020), e2000735, https://doi.org/10.1002/adhm.202000735.

[27] S. Salehi, K. Koeck, T. Scheibel, Spider silk for tissue engineering applications, Molecules 25 (2020), https://doi.org/10.3390/molecules25030737.

[28] C. Holland, K. Numata, J. Rnjak-Kovacina, F.P. Seib, The biomedical use of silk: past, present, future, Adv. Healthc. Mater. 8 (2019), e1800465, https://doi.org/10.1002/adhm.201800465.

[29] B. Kundu, N.E. Kurland, S. Bano, C. Patra, F.B. Engel, V.K. Yadavalli, S.C. Kundu, Silk proteins for biomedical applications: bioengineering perspectives, Prog. Polym. Sci. 39 (2014) 251 267, https://doi.org/10.1016/j.progpolymsci.2013.09.002.

[30] C. Patra, S. Talukdar, T. Novoyatleva, S.R. Velagala, C. Muhlfeld, B. Kundu, S.C. Kundu, F.B. Engel, Silk protein fibroin from Antheraea mylitta for cardiac tissue engineering, Biomaterials 33 (2012) 2673 2680, https://doi.org/10.1016/j.biomaterials.2011.12.036.

[31] J.P.M. Kramer, T.B. Aigner, J. Petzold, K. Roshanbinfar, T. Scheibel, F.B. Engel, Recombinant spider silk protein eADF4(C16)-RGD coatings are suitable for cardiac tissue engineering, Sci. Rep. 10 (2020) 8789, https://doi.org/10.1038/s41598-020-65786-4.

[32] J. Petzold, T.B. Aigner, F. Touska, K. Zimmermann, T. Scheibel, F.B. Engel, Surface features of recombinant spider silk protein eADF4(kappa 16)-made materials are well-suited for cardiac tissue engineering, Adv. Funct. Mater. 27 (2017), https://doi.org/10.1002/adfm.201701427.

[33] D. Steiner, G. Lang, L. Fischer, S. Winkler, T. Fey, P. Greil, T. Scheibel, R.E. Horch, A. Arkudas, Intrinsic vascularization of recombinant eADF4(C16) spider silk matrices in the arteriovenous loop model, Tissue Eng. 25 (2019) 1504 1513, https://doi.org/10.1089/ten.tea.2018.0360.

[34] P.H. Zeplin, N.C. Maksimovikj, M.C. Jordan, J. Nickel, G. Lang, A.H. Leimer, L. Römer, T. Scheibel, Spider silk coatings as a bioshield to reduce periprosthetic fibrous capsule formation, Adv. Funct. Mater. 24 (2014) 2658 2666, https://doi.org/10.1002/adfm.201302813.

[35] L. DeFrancesco, Hanging on a thread, Nat. Biotechnol. 35 (2017) 496 499, https://doi.org/10.1038/nbt.3894.

[36] A. Heidebrecht, T. Scheibel, Recombinant production of spider silk proteins, Adv. Appl. Microbiol. 82 (2013) 115 153, https://doi.org/10.1016/b978-0-12-407679-2.00004-1.

[37] D. Huemmerich, C.W. Helsen, S. Quedzuweit, J. Oschmann, R. Rudolph, T. Scheibel, Primary structure elements of spider dragline silks and their contribution to protein solubility†, Biochemistry 43 (2004) 13604 13612, https://doi.org/10.1021/bi048983q.

[38] K. Schacht, T. Jungst, M. Schweinlin, A. Ewald, J. Groll, T. Scheibel, Biofabrication of cell-loaded 3D spider silk constructs, Angew Chem. Int. Ed. Engl. 54 (2015) 2816 2820, https://doi.org/10.1002/anie.201409846.

[39] S. Wohlrab, S. Muller, A. Schmidt, S. Neubauer, H. Kessler, A. Leal-Egana, T. Scheibel, Cell adhesion and proliferation on RGD-modified recombinant spider silk proteins, Biomaterials 33 (2012) 6650 6659, https://doi.org/10.1016/j.biomaterials.2012.05.069.

[40] S. Kumari, G. Lang, E. DeSimone, C. Spengler, V.T. Trossmann, S. Lücker, M. Hudel, K. Jacobs, N. Krämer, T. Scheibel, Engineered spider silk-based 2D and 3D materials prevent microbial infestation, Mater. Today (2020), https://doi.org/10.1016/j.mattod.2020.06.009.

[41] E. Doblhofer, T. Scheibel, Engineering of recombinant spider silk proteins allows defined uptake and release of substances, J. Pharm. Sci. 104 (2015) 988 994, https://doi.org/10.1002/jps.24300.

[42] M. Saric, T. Scheibel, Engineering of silk proteins for materials applications, Curr. Opin. Biotechnol. 60 (2019) 213 220, https://doi.org/10.1016/j.copbio.2019.05.005.

[43] K. Schacht, T. Scheibel, Controlled hydrogel formation of a recombinant spider silk protein, Biomacromolecules 12 (2011) 2488 2495, https://doi.org/10.1021/bm200154k.

[44] K. Schacht, J. Vogt, T. Scheibel, Foams made of engineered recombinant spider silk proteins as 3D Scaffolds for cell growth, ACS Biomater. Sci. Eng. 2 (2016) 517 525, https://doi.org/10.1021/acsbiomaterials.5b00483.

[45] E. DeSimone, K. Schacht, A. Pellert, T. Scheibel, Recombinant spider silk-based bioinks, Biofabrication 9 (2017), 044104, https://doi.org/10.1088/1758-5090/aa90db.

[46] A. Leal-Egaña, G. Lang, C. Mauerer, J. Wickinghoff, M. Weber, S. Geimer, T. Scheibel, Interactions of fibroblasts with different morphologies made of an engineered spider silk protein, Adv. Eng. Mater. 14 (2012) B67 B75, https://doi.org/10.1002/adem.201180072.

[47] A. Blau, Cell adhesion promotion strategies for signal transduction enhancement in microelectrode array in vitro electrophysiology: an introductory overview and critical discussion, Curr. Opin. Colloid Interface Sci. 18 (2013) 481 492, https://doi.org/10.1016/j.cocis.2013.07.005.

[48] M. De Rosa, M. Carteni, O. Petillo, A. Calarco, S. Margarucci, F. Rosso, A. De Rosa, E. Farina, P. Grippo, G. Peluso, Cationic polyelectrolyte hydrogel fosters fibroblast spreading, proliferation, and extracellular matrix production: implications for tissue engineering, J. Cell. Physiol. 198 (2004) 133 143, https://doi.org/10.1002/jcp.10397.

[49] K. Spiess, R. Ene, C.D. Keenan, J. Senker, F. Kremer, T. Scheibel, Impact of initial solvent on thermal stability and mechanical properties of recombinant spider silk films, J. Mater. Chem. 21 (2011) 13594 13604, https://doi.org/10.1039/c1jm11700a.

[50] I.C. Um, H.Y. Kweon, K.G. Lee, Y.H. Park, The role of formic acid in solution stability and crystallization of silk protein polymer, Int. J. Biol. Macromol. 33 (2003) 203 213, https://doi.org/10.1016/j.ijbiomac.2003.08.004.

[51] S. Wohlrab, K. Spiess, T. Scheibel, Varying surface hydrophobicities of coatings made of recombinant spider silk proteins, J. Mater. Chem. 22 (2012) 22050 22054, https://doi.org/10.1039/c2jm35075k.

[52] C.B. Borkner, S. Lentz, M. Müller, A. Fery, T. Scheibel, Ultrathin spider silk films: insights into spider silk assembly on surfaces, ACS Appl. Polym. Mater. 1 (2019) 3366 3374, https://doi.org/10.1021/acsapm.9b00792.

[53] X. Hu, D. Kaplan, P. Cebe, Determining beta-sheet crystallinity in fibrous proteins by thermal analysis and infrared spectroscopy, Macromolecules 39 (2006) 6161 6170, https://doi.org/10.1021/ma0610109.

[54] J. Schindelin, I. Arganda-Carreras, E. Frise, V. Kaynig, M. Longair, T. Pietzsch, S. Preibisch, C. Rueden, S. Saalfeld, B. Schmid, J.Y. Tinevez, D.J. White, V. Hartenstein, K. Eliceiri, P. Tomancak, A. Cardona, Fiji: an open-source platform for biological-image analysis, Nat. Methods 9 (2012) 676 682, https://doi.org/10.1038/nmeth.2019.

[55] L. Sala, B.J. van Meer, L.G.J. Tertoolen, J. Bakkers, M. Bellin, R.P. Davis, C. Denning, M.A.E. Dieben, T. Eschenhagen, E. Giacomelli, C. Grandela, A. Hansen, E.R. Holman, M.R.M. Jongbloed, S.M. Kamel, C.D. Koopman, Q. Lachaud, I. Mannhardt, M.P.H. Mol, D. Mosqueira, V.V. Orlova, R. Passier, M.C. Ribeiro, U. Saleem, G.L. Smith, F.L. Burton, C.L. Mummery, MUSCLEMOTION: a versatile open software tool to quantify cardiomyocyte and cardiac muscle contraction in vitro and in vivo, Circ. Res. 122 (2018) e5 e16, https://doi.org/10.1161/CIRCRESAHA.117.312067.

[56] C.B. Borkner, S. Wohlrab, E. Möller, G. Lang, T. Scheibel, Surface modification of polymeric biomaterials using recombinant spider silk proteins, ACS Biomater. Sci. Eng. 3 (2016) 767 775, https://doi.org/10.1021/acsbiomaterials.6b00306.

[57] W. Giurlani, E. Berretti, M. Innocenti, A. Lavacchi, Measuring the thickness of metal coatings: a review of the methods, Coatings 10 (2020), https://doi.org/10.3390/coatings10121211.

[58] C.S. Hughes, L.M. Postovit, G.A. Lajoie, Matrigel: a complex protein mixture required for optimal growth of cell culture, Proteomics 10 (2010) 1886 1890, https://doi.org/10.1002/pmic.200900758.

[59] G. Benton, I. Arnaoutova, J. George, H.K. Kleinman, J. Koblinski, Matrigel: from discovery and ECM mimicry to assays and models for cancer research, Adv. Drug Deliv. Rev. 79 80 (2014) 3 18, https://doi.org/10.1016/j.addr.2014.06.005.

[60] L.D. Vukovic, P. Jevtic, L.J. Edens, D.L. Levy, New insights into mechanisms and functions of nuclear size regulation, Int Rev Cell Mol Biol 322 (2016) 1 59, https://doi.org/10.1016/bs.ircmb.2015.11.001.

[61] A.M. Gerdes, M.C. Morales, V. Handa, J.A. Moore, M.R. Alvarez, Nuclear size and DNA content in rat cardiac myocytes during growth, maturation and aging, J. Mol. Cell. Cardiol. 23 (1991) 833 839, https://doi.org/10.1016/0022-2828(91)90216-9.

[62] R.S. Ross, C. Pham, S.Y. Shai, J.I. Goldhaber, C. Fenczik, C.C. Glembotski, M.H. Ginsberg, J.C. Loftus, Beta1 integrins participate in the hypertrophic response of rat ventricular myocytes, Circ. Res. 82 (1998) 1160 1172, https://doi.org/10.1161/01.res.82.11.1160.

[63] M. Brancaccio, E. Hirsch, A. Notte, G. Selvetella, G. Lembo, G. Tarone, Integrin signalling: the tug-of-war in heart hypertrophy, Cardiovasc. Res. 70 (2006) 422 433, https://doi.org/10.1016/j.cardiores.2005.12.015.

SUPPLEMENTAL MATERIAL

Designing of spider silk proteins for hiPSC-based cardiac tissue engineering

Tilman U. Esser[a,e], Vanessa T. Trossmann[b,e], Sarah Lentz[b], Felix B. Engel[a,c,*], Thomas Scheibel[b,d,*]

[a]Experimental Renal and Cardiovascular Research, Department of Nephropathology, Institute of Pathology, Friedrich-Alexander-Universität Erlangen-Nürnberg (FAU), 91054 Erlangen, Germany;

[b]Lehrstuhl Biomaterialien, Prof.-Rüdiger-Bormann Straße 1, 95447 Bayreuth, Germany;

[c]MURCE, Muscle Research Center Erlangen, Erlangen, Germany.

[d]Bayreuther Zentrum für Kolloide und Grenzflächen (BZKG), Bayerisches Polymerinstitut (BPI), Bayreuther Zentrum für Molekulare Biowissenschaften (BZMB), Bayreuther Materialzentrum (BayMAT), Universitätsstraße 30, Universität Bayreuth, Bayreuth D-95447, Germany,

***Corresponding authors:**

felix.engel@uk-erlangen.de

thomas.scheibel@bm.uni-bayreuth.de

[e]authors contributed equally to the work

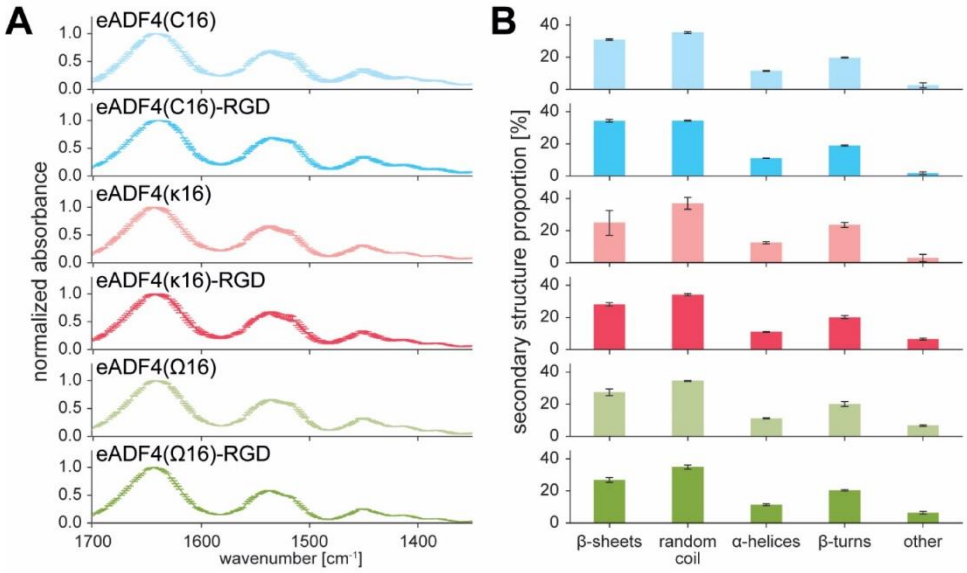

Supplementary Figure 1: Absorbance spectra and Fourier self-deconvoluted secondary structure components of spider silk films

A Absorbance spectra of spider silk films showing amide I, II and III bands determined using attenuated total reflection-Fourier transform infrared (ATR-FTIR) spectroscopy. **B** Secondary structure components were calculated using Fourier self-deconvolution of the amide I band.

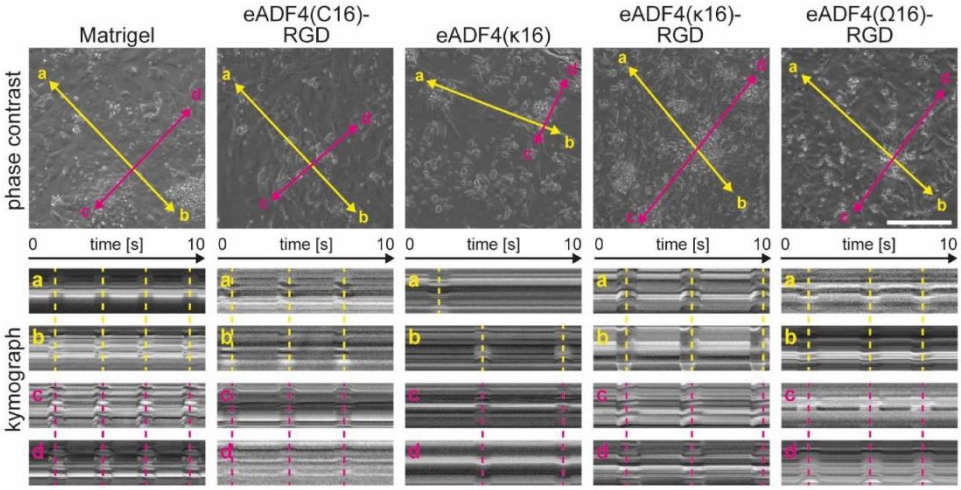

Supplementary Figure 2: Synchronous and asynchronous contractions of hiPSC cardiomyocytes on spider silk films

Kymograph analyses of representative videos of hiPSC-cardiomyocytes 3 days after seeding. *Top row*: still images of videos with arrows indicating kymograph axes. Scale bar: 200 µm. *Bottom rows*: Kymograph plots at positions indicated above (a, b, c, d). Dashed lines indicate contractions.

7.2. Teilarbeit II

Teilarbeit II wurde 2023 unter dem Titel „*Design of Recombinant Spider Silk Proteins for Cell Type Specific Binding*“ im Journal *Advanced Healthcare Materials* veröffentlicht.

Trossmann, V. T. & Scheibel, T (2023) Design of Recombinant Spider Silk Proteins for Cell Type Specific Binding. *Advanced Healthcare Materials* **12**: 2202660.

https://doi.org/10.1002/adhm.202202660

RESEARCH ARTICLE

ADVANCED HEALTHCARE MATERIALS
www.advhealthmat.de

Design of Recombinant Spider Silk Proteins for Cell Type Specific Binding

*Vanessa Tanja Trossmann and Thomas Scheibel**

Cytophilic (cell-adhesive) materials are very important for tissue engineering and regenerative medicine. However, for engineering hierarchically organized tissue structures comprising different cell types, cell-specific attachment and guidance are decisive. In this context, materials made of recombinant spider silk proteins are promising scaffolds, since they exhibit high biocompatibility, biodegradability, and the underlying proteins can be genetically functionalized. Here, previously established spider silk variants based on the engineered *Araneus diadematus* fibroin 4 (eADF4(C16)) are genetically modified with cell adhesive peptide sequences from extracellular matrix proteins, including IKVAV, YIGSR, QHREDGS, and KGD. Interestingly, eADF4(C16)-KGD as one of 18 tested variants is cell-selective for C2C12 mouse myoblasts, one out of 11 tested cell lines. Co-culturing with B50 rat neuronal cells confirms the cell-specificity of eADF4(C16)-KGD material surfaces for C2C12 mouse myoblast adhesion.

1. Introduction

Cells are enveloped in a complex and dynamic microenvironment including an extracellular matrix (ECM), soluble factors, and neighboring cells decisive for cellular responses and functions.[1] The ECM is an essential regulator of cell behavior, since it provides interaction sites for cells important for physical and mechanical support.[2] Due to the regulatory effects of the ECM,[3] tissue engineering aims to generate artificial, biomimetic matrix substitutes, which maintain, support, or restore the regeneration of tissues.[4] Therefore, either biofunctionalized, acellular scaffolds, or pre-cultured tissue constructs combining cells and artificial ECM materials are used to promote tissue regeneration and formation.[5] Tissue-specific elements should be implemented to construct a biomimetic extracellular microenvironment imitating the natural one.[6] Ideally, an artificial scaffold supports a guided and selective interaction of tissue-specific cells to enable the formation of hierarchically organized tissue structures.[5e,f,j,7] Functionalization using stimulating growth factors, ECM proteins or active fragments and peptides thereof is widely used to design bioactive surfaces to control cellular responses.[5e,f,j,7d,8]

The cell adhesive activity of the tripeptide Arg–Gly–Asp (in one letter code: RGD) has been identified in the 1980s, and this sequence can be found in different ECM proteins, such as fibronectin, representing a prime example for a minimal necessary peptide sequence recognized by cellular receptors (integrins).[9] This decisive discovery has enabled the development of functionalized materials to promote cell interactions.[5j,8h,10] Since RGD is a peptide sequence recognized by various integrin receptors, it interacts with many cell types.[11] However, selective attachment and growth of desired cells and simultaneous non-adhesion of other cells are crucial factors to generate hierarchically structured tissue constructs. Besides RGD, other cell-binding peptides sequences have been identified over time stimulating cellular responses and enabling the generation of cell-contacting surfaces.[5f,j,7a,d,8g,h,12] Some examples of other cell adhesive peptides are Ile–Lys–Val–Ala–Val (IKVAV) derived from laminin,[13] Tyr–Ile–Gly–Ser–Arg (YIGSR) derived from laminin,[14] Lys–Gly–Asp (KGD) derived from collagen and barbourin,[15] Gly–Phe–Hyp–Gly–Glu–Arg (GFOGER) derived from collagen,[16] Gln–His–Arg–Glu–Asp–Gly–Ser (QHREDGS) derived from angiopoietin,[17] Arg–Glu–Asp–Val (REDV) derived from fibronectin,[18] or Asp–Gly–Glu–Ala (DGEA) again derived from collagen.[19]

Materials made of the engineered recombinant spider silk protein Araneus diadematus fibroin 4 (eADF4) and its variants have been shown to be promising candidates for tissue engineering due to their low inflammatory properties, good biocompatibility, and possible biodegradability.[20] Specific genetic engineering

V. T. Trossmann, T. Scheibel
Chair of Biomaterials
Engineering Faculty
University of Bayreuth
Prof.-Rüdiger-Bormann-Straße 1, 95447 Bayreuth, Germany
E-mail: thomas.scheibel@bm.uni-bayreuth.de
T. Scheibel
Bayreuth Center for Colloids and Interfaces (BZKG)
Bavarian Polymer Institute (BPI)
Bayreuth Center for Molecular Biosciences (BZMB)
Bayreuth Center for Material Science (BayMAT)
University of Bayreuth
Universitätsstraße 30, 95447 Bayreuth, Germany

The ORCID identification number(s) for the author(s) of this article can be found under https://doi.org/10.1002/adhm.202202660

DOI: 10.1002/adhm.202202660

ADVANCED SCIENCE NEWS
www.advancedsciencenews.com

ADVANCED HEALTHCARE MATERIALS
www.advhealthmat.de

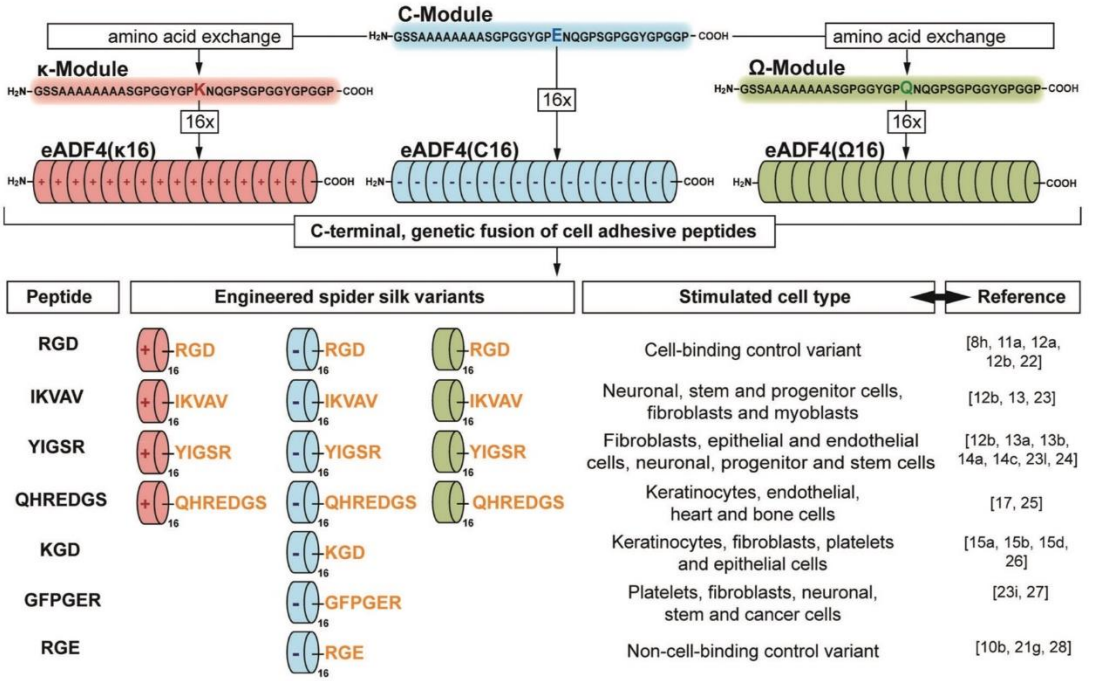

Figure 1. Design of recombinant spider silk proteins based on Araneus diadematus fibroin 4 (ADF4) carrying cell binding peptides for cell type specific interaction. The consensus sequence of ADF4 inspired the engineering of the C-module for recombinant production. In κ- or Ω-modules, the negatively charged glutamic acid (E) residues have been replaced by either positively charged lysine (K) or uncharged glutamine (Q) residue, respectively. The appropriate recombinant engineered spider silk proteins eADF4(C16) (negative net charge), eADF4(κ16) (positive net charge), and eADF4(Ω16) (neutral net charge) comprise 16 repeats of the respective modules. Cell binding peptides identified in the depicted references were genetically fused to the C-terminal end of the respective protein. IKVAV, YIGSR, QHREDGS, KGD, and GFPGER were selected due to their reported cell-specific stimulating effects (Table 1). RGD- and RGE-tagged variants served as well-established cell-binding and non-cell-binding controls, respectively.

of the recombinant protein enables a task-specific functionalization of materials made thereof.[21] In the present study, new recombinant spider silk proteins were modified with peptide tags for guided cell attachment. The cell adhesive peptides IKVAV, YIGSR, QHREDGS, KGD, and GFPGER were each genetically fused to previously established eADF4(C16), eADF4(κ16), and eADF4(Ω16) (**Figure 1**). After recombinant production and characterization, the obtained 18 spider silk proteins were processed into films, analyzed concerning cell adhesion using 11 different mammalian cell types and categorized into cell-adhesive (cytophilic), non-cell-adhesive (cytophobic), and cell-selective variants.

2. Results and Discussion

2.1. Production and Characterization of New Spider Silk Variants

The consensus sequence of the repetitive core motif of *Araneus diadematus* fibroin 4 (ADF4) has been used as template for the engineered recombinant spider silk variants eADF4(C16) (negatively charged),[21a] eADF4(κ16) (positively charged),[21b] and eADF4(Ω16) (uncharged).[21c,d] These variants have been previously modified with RGD-tags to enhance cell attachment.[21e,g] Here, the eADF4-based spider silk proteins were functionalized with further cell-interaction peptides due to a previously reported cell-type specificity allowing guided and selective cell attachment (**Table 1** and Figure 1).

In case of the collagen-derived GFOGER tag, a proline (P) residue was part of the sequence instead of the naturally occurring hydroxy-proline (O) due to the recombinant production of this spider silk variant using *Escherichia coli* (*E. coli*) bacteria, which lack the enzymes for respective post-translational modifications.[29] Recombinant production was successful for all 18 spider silk variants used in our experiments (Figure 1).[21a–e,g] Table S1, Supporting Information, summarizes important protein parameters including the number of charged amino acid residues, the isoelectric point, or the molecular weight (MW). For uncharged eADF4(Ω16) variants, the influence of charged amino acid tags on the isoelectric point is more pronounced than for negatively charged eADF4(C16) or positively charged eADF4(κ16) spider silk proteins. Since the addition of peptides increases the MW by around 1000 Da (i.e., only around 2 % of the MW), the physico-chemical properties, except the desired cell interaction and stimulation, should be driven by the underlying spider silk protein. The correct gene expression and high purity of produced eADF4-based variants could be confirmed using

Table 1. Reported biological effects of peptides used herein. Besides the cytophilic RGD sequence, other cell-interaction peptides showing cell-type specificity were used in this study to allow guided and selective cell attachment.

Peptide	Origin	Biological Effect	References
RGD	Fibronectin	Activation of different integrin receptors enabling increased adhesion, spreading, proliferation, migration, and differentiation of various cell types including stem cells	[8h, 11a, 12a,b, 22]
IKVAV	Laminin	Increased attachment, proliferation, viability, and differentiation of neuronal cells, neuronal progenitor cells as well as stem cells; enhanced neurite growth and extension; attachment of fibroblasts; adhesion, growth and differentiation of myoblasts; adhesion and growth of cancer cells	[12b, 13, 23]
YIGSR	Laminin	Improved adhesion, spreading, migration, and growth of endothelial cells; attachment, spreading, and stress fiber formation of fibroblasts; increased adhesion and extension of epithelial cells; enhanced adhesion, growth, viability, and differentiation of neuronal cells, neuronal progenitor cells and stem cells; enhanced neurite growth and extension; interaction of cancer cells	[12b, 13a,b, 14a,c, 23l, 24]
QHREDGS	Angiopoietin	Enhanced endothelial cell survival, metabolism, and tube formation; promoted survival of heart cells; polarization of macrophages; attachment and survival of keratinocytes; inhibited apoptosis of stem cells; enhanced osteoblast differentiation, bone matrix deposition, and mineralization	[17, 25]
KGD	Collagen	Enhanced keratinocyte adhesion and spreading; reduced platelet aggregation; enhanced epithelial cell and fibroblast adhesion	[15a,b,d, 26]
GFOGER	Collagen	Increased adhesion of platelets and human neuronal stem/progenitor and fibrosarcoma cells; chondrogenic differentiation of human bone mesenchymal stem cells; adhesion and spreading of fibroblasts	[23i, 27]
RGE	Control	No cell attachment including fibroblasts and endothelial cells	[10b, 21g, 28]

matrix-assisted laser desorption/ionization mass spectrometry with time-of-flight (MALDI-TOF) analysis (Table S1 and Figure S1, Supporting Information) as well as silver-stained sodium dodecyl sulfate polyacrylamide gel electrophoresis (SDS-PAGE), fluorescence, and circular dichroism (CD) spectroscopy (Figure S2, Supporting Information). MALDI-TOF spectra showed one sharp peak around the expected MW for all variants (Figure S1, Supporting Information). Minor variations could result from natural measurement fluctuations and possible ionic interactions (e.g., Na^+) with the matrix.[30] Silver-stained SDS-PAGs (Figure S2A, Supporting Information) displayed single bands at a MW of around 65 kDa for eADF4(C16)-, at around 48 kDa for eADF4(κ16)- and at around 55 kDa for eADF4(Ω16)-based variants. Incomplete and irregular binding capacities of negatively charged SDS to differently charged recombinant spider silk proteins led to a different charge distribution and explained the different migration behavior of these variants.[21a] Since tyrosine-rich recombinant spider silk proteins contain no tryptophan, but *E. coli* proteins comprise on average 1.5 % Trp residues,[21a,31] protein purity could be confirmed using fluorescence spectroscopy indicating the absence of an intrinsic Trp (347 nm) and the presence of a high Tyr (303 nm) fluorescence signal (Figure S2B, Supporting Information). Furthermore, regardless of fused peptides, far-UV CD spectra verified the random coil secondary structure in solution for all 18 variants, indicated by a broad minimum around 205 nm and a plateau around 219 nm (Figure S2C, Supporting Information).[21a,g,32]

2.2. Analysis of Spider Silk Films regarding Cell Type Specific Adhesion

Spider silk films (0.5 mg protein per 1 cm^2) were produced using drop-casting on polystyrene surfaces followed by post-treatment using ethanol vapor to induce β-sheet formation making the films water insoluble, but preserving surface exposition of the peptide tags as reported previously.[21e,g,32,33] Since surface hydrophobicity influences protein and cell interaction, water contact angles (WCA) were determined and revealed that all 18 spider silk films provided hydrophilic surfaces (WCA below 90°) (Figure S3, Supporting Information).[21f,34]

To analyze specific cell interactions as described in literature (Table 1), all spider silk films were investigated regarding the adhesion behavior (t = 4 h) of 11 different mammalian cell lines originating from several tissues (**Table 2**). Cell attachment was analyzed in absence and presence of fetal calf serum (FCS) or comparable supplements to screen influences of adsorbed serum proteins on cell adhesion.[23l,28,35]

Table 2. Cell type, tissue origin, and reasons for the selection of the cells. Abbreviations: HUVECs: human umbilical vein endothelial cells, hiPSC-CMs: human induced pluripotent stem cell derived cardiomyocytes.

Cell type	Tissue Origin	Reason
BJ fibroblasts	Human skin	GFPGER, KGD, YIGSR, IKVAV
Balb 3T3 fibroblasts	Mouse embryo	GFPGER, KGD, YIGSR, IKVAV
C2C12 myoblasts	Mouse muscle	IKVAV
HaCaT keratinocytes	Human skin	KGD, QHREDGS
B50 neuronal cells	Mouse nerve	IKVAV, YIGSR
RN22 Schwann cells	Rat nerve	IKVAV, YIGSR
NG108 cell hybrids	Rat-mouse nerve	IKVAV, YIGSR
HeLa epithelial cells	Human cervix carcinoma	IKVAV, YIGSR
HUVECs	Human vascular system	QHREDGS, YIGSR
hiPSC-CMs	Human heart	QHREDGS, IKVAV
MG63 fibroblasts	Human osteosarcoma	QHREDGS, GFPGER

ADVANCED SCIENCE NEWS
www.advancedsciencenews.com

ADVANCED HEALTHCARE MATERIALS
www.advhealthmat.de

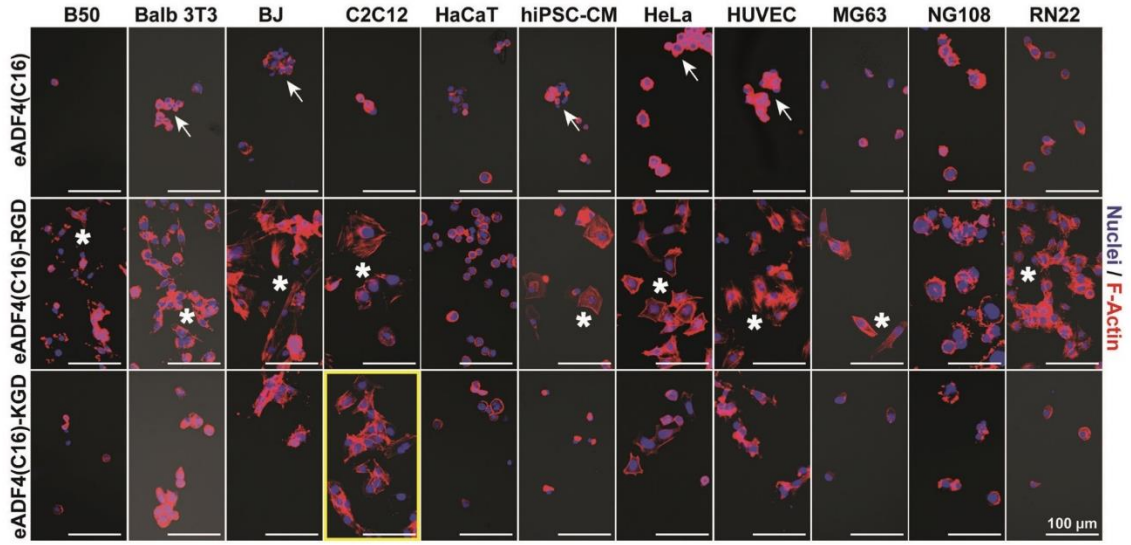

Figure 2. Cell adhesion on films made of eADF4(C16) (cytophobic), eADF4(C16)-RGD (cytophilic), and eADF4(C16)-KGD (cell selective). Cell adhesion and spreading of rat B50 neuronal cells, mouse Balb 3T3 embryonal fibroblasts, human BJ fibroblasts, mouse C2C12 myoblasts, human HaCaT keratinocytes, human induced pluripotent stem cell derived cardiomyocytes (hiPSC-CM), human HeLa cervix carcinoma cells, human umbilical vein endothelial cells (HUVEC), human MG63 bone fibroblasts, mouse-rat NG108 neuronal hybrid cells, and rat RN22 Schwann cells on different spider silk films were recorded after 4 h of incubation using fluorescence microscopy. Therefore, cell nuclei and F-actin cytoskeleton of fixed cells were stained using DAPI (blue) and Phalloidin (red), respectively. White arrows point towards round cellular aggregates showing small cell body sizes and preferring cell–cell-contacts, but no/little cell–matrix interactions. White asterisks highlight clearly spread cells exhibiting enhanced cell body sizes. The yellow box marks the selectivity of C2C12 myoblasts on the eADF4(C16)-KGD variant. Scale bars: 100 µm.

After 4 h of incubation, cell nuclei (4′,6-diamidino-2-phenylindole, DAPI, blue) and the F-actin cytoskeleton (phalloidin–rhodamine B, phalloidin, red) of adhered cells were visualized using fluorescence staining to determine, if a spider silk variant shows a cytophobic or a cytophilic character. Cytophobicity does not equate with cytotoxicity, since recombinant eADF4-based spider silk materials are highly biocompatible, non-cytotoxic, and cause no inflammatory or allergic reaction.[20b,36] The cytophilicity of spider silk variants was classified as very good (++), good (+), moderate (0), bad (−), and very bad (−) regarding the total number of attached cells, their spreading behavior and the cell body size. Cytophobic spider silk surfaces were characterized by a low number of sporadically distributed cells exhibiting a round morphology with a low F-actin expression resulting in a small cell body size. Moreover, cells could not form proper, adequate cell-material adhesions leading to a reduced surface attachment and formation of cellular aggregates or clusters comprising several individual cells, which prefer cell-to-cell contacts compared to cell–matrix-interactions. In contrast, on cytophilic surfaces, many cells adhered uniformly distributed and showed a clear F-actin expression with identifiable filaments of the cytoskeleton and distinct focal adhesions leading to clearly enhanced cell spreading. On moderately cytophilic surfaces some small cell aggregates as well as some partially spread cells were visible exhibiting a round morphology with reduced cell body size and some F-actin expression indicated as stress fibers.

Figure 2 shows representative fluorescence images of all cell types on spider silk surfaces made of the cytophobic eADF4(C16), the cytophilic eADF4(C16)-RGD, and eADF4(C16)-KGD in presence of FCS. Furthermore, cell numbers of four selected, representative fluorescence images per eADF4(C16), eADF4(C16)-RGD, and eADF4(C16)-KGD were counted for every cell line and summed up to quantify cell adhesion behavior on these spider silk variants (Figure S5, Supporting Information). It was expected that eADF4(C16) films would be cytophobic, since the amino acid sequence of eADF4(C16) lacks any cell binding motifs.[21e,g,33,36b,37] This assumption could be verified, because the few detected cells displayed a round, less spread morphology showing F-actin expression mainly around the cell nuclei. Either sporadically distributed cells, for example, for B50 neuronal or MG63 osteosarcoma cells, or cellular aggregates, as seen for Balb 3T3 and BJ fibroblasts, human induced pluripotent stem cell (hiPSC)-CM, HeLa cells, or human umbilical vein endothelial cells (HUVEC), were visible (Figure 2, white arrows). RN22 Schwann cells seemed to be an exception, since more cells attached (Figure S5, Supporting Information). These cells formed F-actin containing stress fibers for mechanotransduction and migration instead of focal adhesions. Importantly, due to the low cell amount, non-specific cell attachment based on serum protein adsorption could be excluded.

Since RGD is a widespread and abundant cell (integrin) interaction peptide used for enhancing cytophilicity of biomaterials,[8g,h,10b,11c,38] strong cell interaction with

ADVANCED SCIENCE NEWS
www.advancedsciencenews.com

ADVANCED HEALTHCARE MATERIALS
www.advhealthmat.de

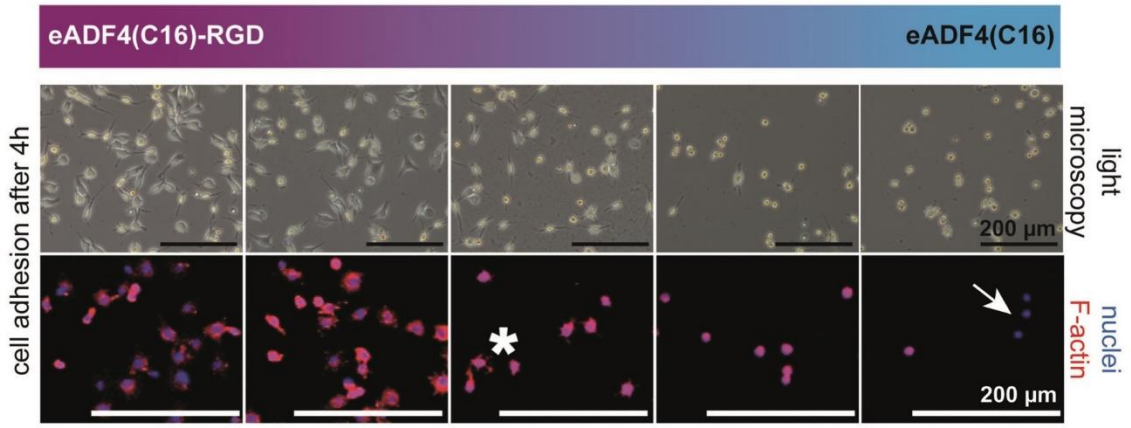

Figure 3. Adhesion of Balb 3T3 fibroblasts on a gradient film from eADF4(C16)-RGD towards eADF4(C16) after 4 h of incubation. Cell adhesion with increasing availability of cell interaction peptide was analyzed after 4 h using light microscopy (before washing) and confocal microscopy after washing, fixing, and staining the attached cells. Cell nuclei and F-actin cytoskeleton were stained using DAPI (blue) and Phalloidin (red), respectively. The white arrow points towards round, only DAPI-stained cells without any F-actin expression. The white asterisk highlights cells starting to form focal adhesions and F-actin stress fibers. Scale bars: 200 µm.

eADF4(C16)-RGD surfaces was expected.[21e,g,39] For all investigated cell types, high cell numbers and a spread morphology with F-actin-containing focal adhesions could be detected on eADF4(C16)-RGD (Figure 2, white asterisks). HaCaT keratinocytes always exhibited a round morphology with a uniform F-actin expression around the cell nuclei, since they need proper cell–cell-contacts. Due to the short incubation time, NG108 hybrid cells did not outgrow any neurites or axons. Other studies using RGD-modified spider silk surfaces confirmed high cytophilicity of this peptide.[23l,35e,40]

The silk-specific adhesion of murine Balb 3T3 fibroblasts was further evaluated on gradient films made of eADF4(C16) and eADF4(C16)-RGD after 2 h (Figure S4A, Supporting Information) and 4 h (**Figure 3**) in comparison to eADF4(C16), eADF4(C16)-RGD, and glass controls (Figure S4B, Supporting Information). Confocal images revealed only little cell numbers, some did not even show any F-actin expression (Figure 3 and Figure S4, white arrows, Supporting Information), attached at areas consisting of mainly eADF4(C16), and most of these round cells could be washed off. With increasing eADF4(C16)-RGD content, presumably at a 50:50 ratio, the first focal adhesions and F-actin stress fibers appeared and cell spreading enhanced (Figure 3 and Figure S4, white asterisks, Supporting Information). It was concluded that around 75% w/w of eADF4(C16)-RGD content is sufficient to enable complete cell attachment. Other studies using RGD gradients also showed improved cell attachment and spreading with increasing RGD ligand density.[41]

The collagen-derived KGD peptide tag was chosen to enhance interactions with keratinocytes, fibroblasts, and epithelial cells.[15a,b,d,26] Interestingly, here, eADF4(C16)-KGD films were highly selective for C2C12 myoblasts, which attached in a spread morphology with F-actin containing focal adhesions comparable to eADF4(C16)-RGD (Figure 2, yellow box), while other cell types showed less interactions (Figure S5, Supporting Information). In presence of FCS, the eADF4(C16)-KGD variant provided a moderate primary interaction surface for some cells (e.g., Balb 3T3, BJ, HeLa, and HUVEC), whereas the other investigated cell lines (B50, HaCaT, hiPSC-CM, MG63, NG108 and RN22) showed similar responses as seen on eADF4(C16) surfaces.

All film- and cell-interactions were visualized using bar charts (**Figure 4**). Based on our results, eADF4(C16), eADF4(C16)-RGE, eADF4(C16)-GFPGER, and eADF4(Ω16) were categorized as cytophobic spider silk variants. These results verified the expectations, since eADF4(C16)-RGE was used as a non-cell-binding control variant[21g,42] and the uncharged eADF4(Ω16), like negatively charged eADF4(C16), does not contain cell interaction sites.[21e,37a,43] The exchange of post-translationally modified hydroxy-proline (GFOGER) to proline (GFPGER) residues obviously also reduced cell binding properties.

Polycationic material surfaces are known to enhance unspecific cell-material interactions due to serum protein adsorption as well as higher affinity of mostly negatively charged cell membrane components.[33,44] Here, our positively charged spider silk variants also enhanced cell interactions and cytophilicity. Previous studies have already shown that positively charged eADF4(κ16) displayed enhanced cell-stimulation behavior compared to negatively charged eADF4(C16) and uncharged eADF4(Ω16) materials.[21e,h,33,37b] Many cell types already showed improved adhesion and spreading on eADF4(κ16) surfaces in presence as well as absence of FCS. Thus, although some FCS-related, cell-type specific effects (e.g., Balb 3T3 or hiPSC-CM adhesion on eADF4(κ16) or Balb 3T3 and RN22 attachment on eADF4(C16)) were visible, unspecific cell adhesion to surface-adsorbed serum proteins played a subordinate role on these spider silk surfaces.

The laminin-derived IKVAV peptide was expected to interact mainly with neuronal cells, but also fibroblasts, myoblasts, or cancer cells.[12b,13,23] eADF4(κ16)-IKVAV films were cytophilic for many cell types. Although eADF4(κ16)-IKVAV showed no FCS effect, the absence or presence of serum proteins or sup-

ADVANCED SCIENCE NEWS
www.advancedsciencenews.com

ADVANCED HEALTHCARE MATERIALS
www.advhealthmat.de

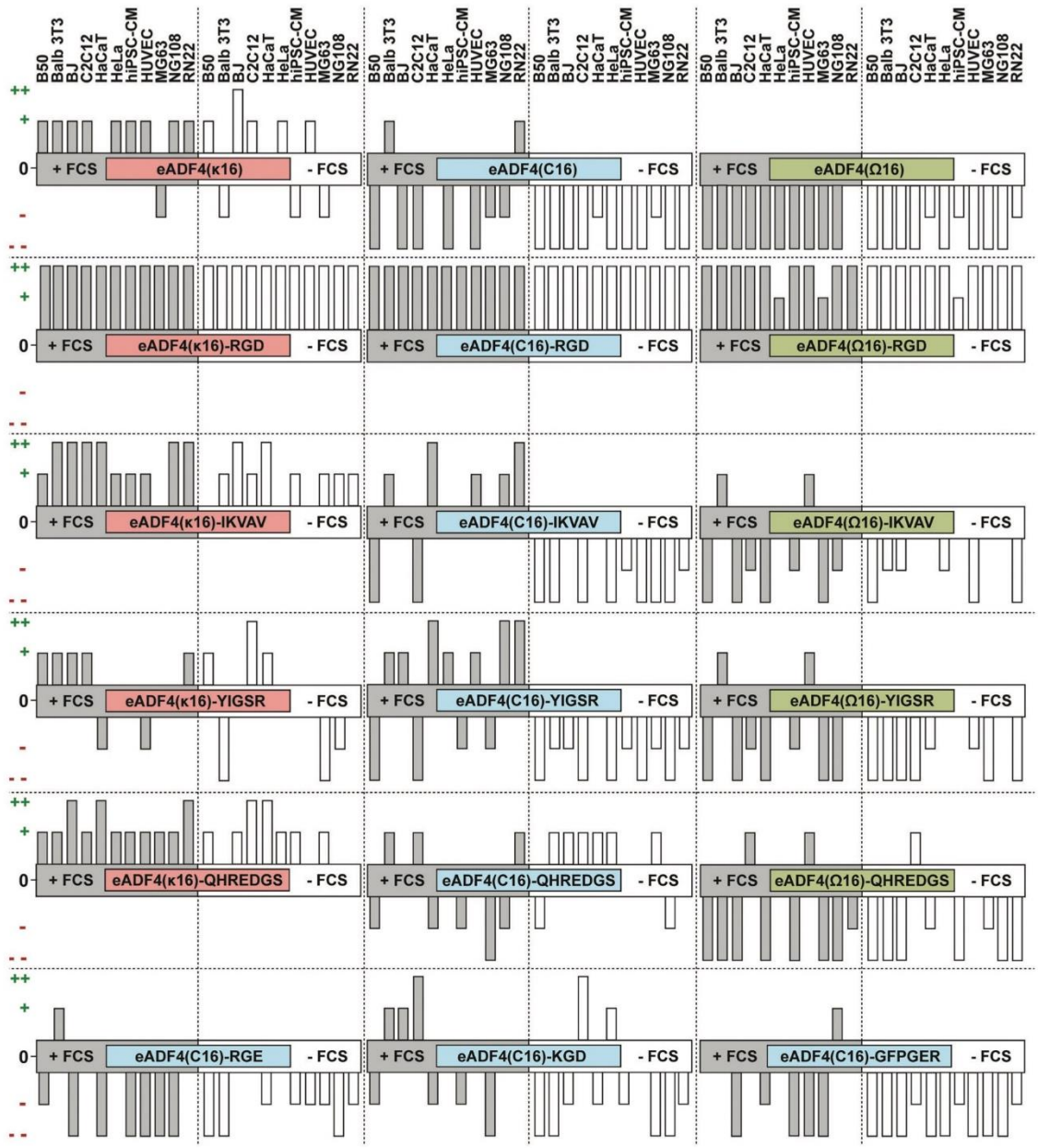

Figure 4. Adhesion of mammalian cell lines on films made of different recombinant spider silk proteins after 4 h of incubation. 11 cell lines were incubated on 18 different spider silk films in the absence or presence of FCS. Adhesion after 4 h of incubation was analyzed using fluorescence microscopy after fixing and staining attached cells. The adhesion was ranked as follows by the number of attached cells and their spreading behavior: very good (++), good (+), neutral (0), bad (−), and very bad (−).

plements could be used to selectively guide cellular attachment on eADF4(C16)-IKVAV and eADF4(Ω16)-IKVAV surfaces. There, the IKVAV peptide seemed to promote primary attachment of Balb 3T3 fibroblasts, HUVECs as well as selected neuronal cells (e.g., NG108 hybrid and RN22 Schwann cells).

The laminin-derived YIGSR peptide has been shown to stimulate neuronal cells, endothelial cells, fibroblasts, keratinocytes, and cancer cells.[12b,13a,b,14a,c,23l,24] Interestingly, the charge effect of eADF4(κ16)-YIGSR was not as strong as on the other positively charged eADF4(κ16) variants, but a clear FCS effect could be identified in case of this variant. While Balb 3T3 fibroblasts and C2C12 myoblasts adhered to eADF4(κ16)-YIGSR in presence of FCS, only C2C12 myoblasts remained their strong cell attachment in absence of serum. FCS addition also enabled a cell-type specific adhesion on eADF4(C16)-YIGSR and eADF4(Ω16)-YIGSR surfaces. Since HaCaT keratinocytes, RN22 Schwann, NG108 hybrid cells, HUVECs, Balb 3T3, and BJ fibroblasts showed good attachment on eADF4(C16)-YIGSR films, this variant could also be used for neuronal or skin tissue engineering.

The angiopoietin-derived QHREDGS peptide tag should enhance interaction of surfaces with endothelial cells, cardiomyocytes, myoblasts, stem cells, or bone cells.[17,25] The cytophilicity of positively charged eADF4(κ16)-QHREDGS mainly resulted from the already known charge effect. However, the QHREDGS modification seemed to stimulate C2C12 myoblast attachment charge-independently. Furthermore, eADF4(C16)-QHREDGS showed FCS-influenced cell type selectivity, since attachment of MG63 bone fibroblasts and HaCaT keratinocytes was reduced in presence and enhanced in absence of supplements. HUVECs exhibited a moderate or good attachment behavior on the QHREDGS-modified spider silk variants indicating to some extent an interaction of cell surface receptors with the surface.

The shown systematic evaluation classified eADF4(C16)-RGD as cytophilic, eADF4(C16)-KGD as cell-selective, and eADF4(C16)-RGE as cytophobic, clearly demonstrating how sensitive cellular receptors recognize peptide sequences and interact with specific amino acid sequences, although only one amino acid residue differs. The modification of eADF4(C16) with RGD, RGE, and KGD sequences allowed the analysis regardless of charge effects, since the proteins exhibited identical physico-chemical properties due to similar charge distribution (one positively charged arginine [R] or lysine [K] and one negatively charged glutamic acid [E] or aspartic acid [D]). For RGE, the exchange of aspartic acid (D) with glutamic acid (E) increased the length of the side group by one CH_2-unit leading to a reduced cell interaction[21g,23l,28b,42b,45] explained by a reduced binding affinity due to steric hindrance inside the integrin binding pocket.[10b] Several integrin receptors recognize and bind RGD[11a,12a,46] and some are also able to bind KGD.[47] The binding affinity of RGD-specific integrins could be lower for KGD due to the shorter lysine (K) versus arginine (R) residue leading to a cell-type dependent interaction explaining the divergent cell attachment behavior.[47] However, it is also assumed that C2C12 myoblasts express cellular receptors, which are able to specifically interact with KGD. The $\alpha_5\beta_1$ and the $\alpha_v\beta_1$ integrins, both binding RGD,[46a] also interact with the ectodomain of collagen XVII, which contains several KGD peptide sequences.[15b,46b,47] Furthermore, several studies have shown that snake venom poisons containing KGD peptide sequences could interact with cellular surface receptors, for instance $\alpha_{IIb}\beta_3$ and $\alpha_5\beta_1$.[15a,c,26a,48] However, receptor affinity and specificity as well as successful integrin–peptide interactions are strongly influenced by the amino acid following the important recognition sequence. While a KGDW sequence promoted $\alpha_{IIb}\beta_3$-binding, a KGDD sequence showed enhanced interaction with the $\alpha_5\beta_1$ integrin.[15a,c] Furthermore, KGDK and KGDR showed strong interaction with $\alpha_5\beta_1$ and the $\alpha_v\beta_1$ integrins, while KGDM and KGDQ were less efficient.[15b] In our case, the serine-residue that follows the KGD sequence seems to beneficially support the interaction with surface receptors of C2C12 myoblasts.

The subsequent amino acid residues are also decisive for integrin affinity and specific cell attachment to RGD[5j,8h,11b,35e,49] and YIGSR- or IKVAV-containing peptides.[13a,c,14c] Since these studies confirmed the importance of specific amino acid residues upfront and after the appropriate cell recognition site, the cell interaction and specificity of the here presented spider silk variants could also be an effect of the flanking amino acid residues.

2.3. Selective Myoblast Attachment on eADF4(C16)-KGD Films in Co-Culture

Since in natural tissue (e.g., muscle tissue) a heterotypic communication between cells occur, different co-culture systems combining, for instance, myoblasts with endothelial cells[50] or fibroblasts[51] have been evolved to improve cellular responses. Moreover, previously published studies have shown that the co-culture of neural cells and muscle cells has stimulating effect on both cell types and promotes the formation of functional muscle or neuronal tissue.[52] However, since adhesion and growth of tissue-specific cells are decisive for generating hierarchically organized tissue structures, the selective cell attachment of C2C12 myoblasts on eADF4(C16)-KGD was demonstrated in a co-culture model with B50 neuronal cells and eADF4(C16)-RGD as a control (**Figure 5**). The described cell-specific serum/supplement effect was used to enhance selective C2C12 attachment, while simultaneously prohibiting B50 adhesion. After washing off unattached cells, the adhered cells were incubated in full media. The specific, time-dependent life cell tracking yielded green fluorescing C2C12 myoblasts (Syto 9) and red fluorescing B50 neuronal cells (Red CMTPX) in single and co-culture experiments on spider silk films directly after seeding (Figure 5). However, some B50 neuronal cells displayed no fluorescence indicating no uptake of the dye (Figure 5, white triangles). Both fluorescence dyes are membrane permeable, but not permanently integrated inside the cells. The red CMTPX dye is supposed to be metabolized into non-cell membrane permeable products inside the cell, and the DNA intercalating Syto 9 dye should only show high fluorescence signals after contact with nucleic acids. Thus, only cells with ingested dyes showed fluorescence as confirmed by the low background signal. Yellow cross-signals can occur if differently stained cells are arranged on top of each other and their fluorescence signals overlap.[52g] However, despite several washing steps, some dye molecules might also have interacted with the cell surface and could be released into the cell culture media triggered by osmosis and diffusion. Thus, the subsequent uptake

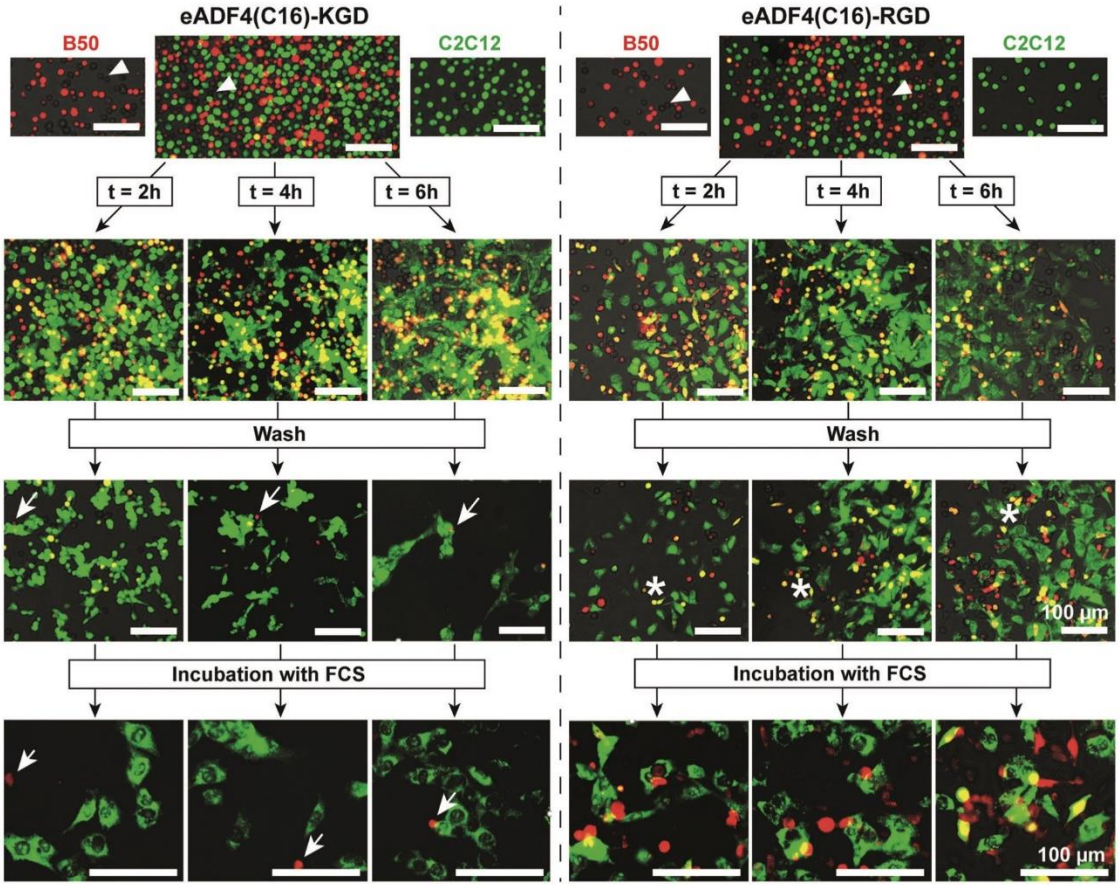

Figure 5. Selective attachment and spreading of C2C12 mouse myoblasts and detachment of B50 rat neuronal cells upon incubation on films made of eADF4(C16)-KGD. Labeled C2C12 mouse myoblasts (green) and B50 rat neuronal cells (red) were incubated for 2, 4, or 6 h on films made of eADF4(C16)-KGD and eADF4(C16)-RGD in the absence of FCS. After washing with 1× PBS, only C2C12 myoblasts were attached on eADF4(C16)-KGD films, while B50 neuronal cells could not attach to this silk variant and were washed off. In contrast, on eADF4(C16)-RGD films both cell lines could attach and spread. After further 20–24 h of incubation in presence of FCS, cells were still attached. On eADF4(C16)-KGD surfaces a selective growth of C2C12 myoblasts was possible. White triangles highlight unlabeled B50 cells. White arrows point towards sporadically attached, remaining red stained B50 neuronal cells on eADF4(C16)-KGD. White asterisks highlight cells showing a yellow fluorescence cross signal after uptake of both dyes. Scale bars: 100 µm.

of an opposite dye by a cell is possible, also resulting in a yellow fluorescence cross-signal (Figure 5, white asterisks).

After 2, 4, and 6 h incubation time, individual wells containing the co-culture were washed with phosphate buffered saline (PBS) to remove unattached cells, and incubated in fresh FCS-containing media (Dulbecco's modified Eagle's medium [DMEM]) overnight to ensure survival of the remaining cells. Subsequent fluorescence microscopy revealed that on eADF4(C16)-KGD films primarily myoblasts (Figure 5, green cells) adhered and spread, while only a few round, non-spread B50 neuronal cells (Figure 5, red cells, white arrows) could be identified. In contrast, both cell types adhered and spread on cytophilic eADF4(C16)-RGD, which consequently led to a higher yellow fluorescence cross-signal. The apparently larger area of green fluorescence could be explained by the larger cell body size of spread C2C12 myoblasts compared to B50 neuronal cells, which was also noticeable in single culture after nuclei and F-actin staining (Figure 3).

After initial cell attachment, cell proliferation is an important pre-requisite for successful tissue engineering requiring nutrients, growth factors, and soluble plasma proteins present in FCS or comparable supplements. Thus, cell proliferation of seven cell lines from different mammalian tissues was investigated conducting a cell titer blue assay over 8 days on eADF4(C16), eADF4(C16)-RGD, and eADF4(C16)-KGD films to confirm selective proliferation of C2C12 myoblasts on KGD-functionalized surfaces (Figure S6, Supporting Information). The cytophobic character of eADF4(C16) could be verified, because none of the investigated cell lines grew. In contrast, the high cytophilicity of eADF4(C16)-RGD was confirmed, since the cell number of all

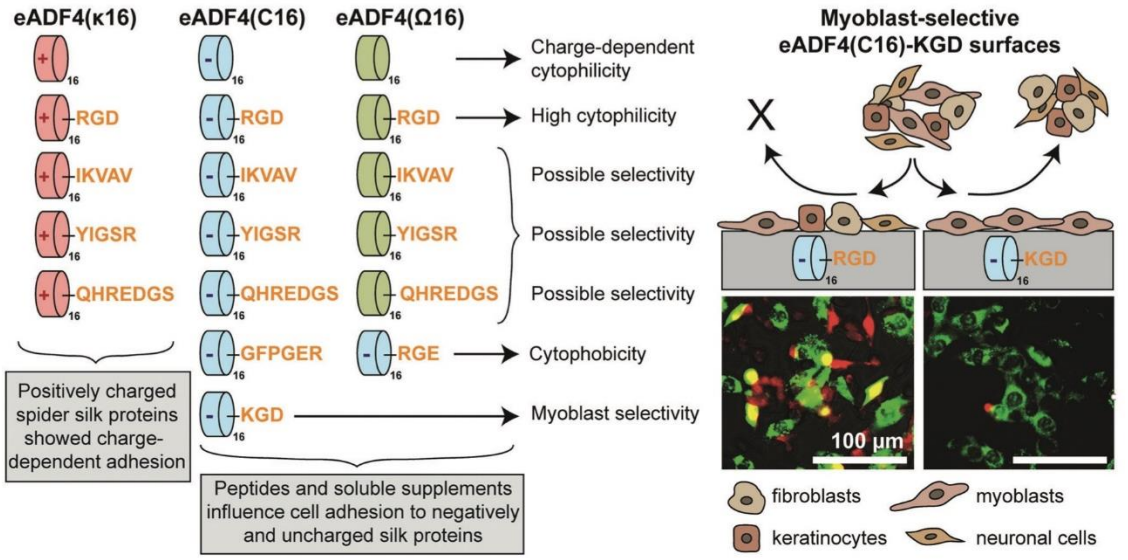

Figure 6. Summary of identified cellular responses to different spider silk variants. Non-tagged eADF4-based spider silk variants showed a charge-dependent cytophilicity, which could be enhanced by introducing the RGD-sequence. Generally, positively charged eADF4(κ16)-surfaces improved cell adhesion, while specific peptide tags mainly influenced cell adhesion on negatively and uncharged eADF4(C16)- and eADF4(Ω16)-variants. Although IKVAV-, YIGSR-, and QHREDGS-surfaces showed possible cell type selectivity, eADF4(C16)-KGD was identified as a myoblast-specific spider silk variant allowing selective cell attachment.

cell lines increased over the investigated incubation time. Since only C2C12 myoblasts displayed proliferation on eADF4(C16)-KGD films and the other cell lines behaved as on eADF4(C16), cell selective behavior of this variant was verified. These results also confirmed that cell attachment and cell proliferation are different cellular responses, since BJ fibroblasts showed good cell attachment (Figures 2 and 4), but no proliferation on the eADF4(C16)-KGD surface.

3. Conclusion

The present study showed that genetic modification of recombinant spider silk proteins enables the processing of cell type specific silk materials (**Figure 6**). In general, a charge-dependent cytophilicity of non-tagged eADF4-based spider silk variants was visible, since only positively charged eADF4(κ16) allowed cell adhesion, while negatively charged eADF4(C16)- and uncharged eADF4(Ω16)-films showed a cytophobic character. However, the cytophilicity of these spider silk variants could be increased by introducing the integrin-binding RGD-sequence regardless of protein charge.

Functionalization of recombinant spider silk proteins with other short peptide tags from ECM proteins allowed specific cell attachment. In this context, the peptide tags mainly influenced specific cell interactions with surfaces made of negatively charged eADF4(C16)- and uncharged eADF4(Ω16)-variants, as positively charged eADF4(κ16)-surfaces generally improved cell adhesion. The present study revealed that modifying spider silk proteins with IKVAV-, YIGSR-, and QHREDGS-peptides partly led to cell specific interactions with possible selectivity. However, functionalization with the KGD-peptide allowed selective attachment and growth of myoblasts, which could also be confirmed using a co-culture experiment with neuronal cells (Figure 6). These findings enable a tissue-specific application of engineered spider silk materials. Since spider silk proteins are very versatile and could be processed into different morphologies, the range of possible applications is quite broad. Spider silk films can be used as implant coatings to enhance the performance and integration of supportive implants by improved, selected cellular attachment and ingrowth with simultaneously reduced microbial infection and fibrosis.[21c,d,36b,37c] Furthermore, 3D-printable hydrogel networks with adjustable mechanical properties enable the encapsulation of specific cells in appropriate hydrogels with subsequent processing in adopted 3D structures.[39b,42b,53] Further morphologies with different topographical features are fibers, fiber bundles, or nonwoven meshes, as well as porous foams for the cultivation of cells.[20a,b]

4. Experimental Section

If not stated otherwise, all chemicals were purchased from Carl Roth.

Molecular Cloning: The repetitive core domain of natural ADF4 dragline silk served as model for designing the negatively charged eADF4(C16). For recombinant production using *E. coli*, the consensus sequence, also called C-module (sequence: GSSAAAAAAAAS GPGGYG-PENQGPSGPGGYGPGGP) was repeated 16 times and N-terminally functionalized with a T7 tag for specific detection.[21a] Using this strategy, the positively charged eADF4(κ16),[21b] the uncharged eADF4(Ω16),[21c,d] as well as the C-terminally modified eADF4(C16)-RGD,[21g] eADF4(C16)-RGE,[21g] eADF4(κ16)-RGD,[21e] and eADF4(Ω16)-RGD[21e] variants had been generated previously. For functionalizing recombinant spider

silk proteins with further peptide sequences, codon optimized DNA oligonucleotides (Table S1, Supporting Information) were designed for seamless cloning. Single-stranded oligo-nucleotides (Eurofins Genomics, Germany) were annealed using a temperature gradient (95 to 4 °C, 1 °C min^{-1}) in a thermocycler (Bio-Rad Laboratories, Germany). The digestion with *Bam HI* and *Hind III* restriction enzymes (New England Biolabs GmbH, Germany) enabled insertion into a cloning vector and subsequent ligation with respective spider silk proteins.[21a,g] Successful generation of the appropriate DNA gene constructs was confirmed by sequencing (Eurofins Genomics, Germany).

Recombinant Protein Production: eADF4(C16) was purchased from AMSilk GmbH, Germany. For all other variants, time-dependent fed-batch fermentations using *E. coli BL21 gold (DE3)* were conducted.[21a] While eADF4(C16)-variants[21a] were synthesized for 4 h, eADF4(κ16)-[21b] and eADF4(Ω16)-[21c,d] genes were expressed for 2 h at 30 °C to avoid protein degradation and inclusion body formation. For protein purification,[21a–e,g] cells were disrupted, and residual *E. coli* proteins were separated from heat-stable spider silk proteins using a heat step. After precipitation, washing, and freeze-drying, spider silk proteins were stored at −20 °C.

Protein Analysis: To confirm protein purity, MALDI-TOF analysis, SDS-PAGE with subsequent silver staining, as well as fluorescence and Far-UV CD spectroscopy were conducted.[21a,g] Proteins were dissolved in 6 M guanidinium thiocyanate at room temperature (RT). For MALDI-TOF analysis, the protein solutions were treated with ZipTip C4 pipette tips (Millipore, Germany) to desalt and concentrate the proteins. For elution, a SA-matrix containing 60% acetonitrile and 0.1 % trifluoroacetic acid was used. MALDI-TOF spectra were recorded using a Bruker Daltonics Autoflex (Bruker, Germany) equipped with a 337 nm laser in linear mode and an acceleration voltage between 20 and 40 kV (n = 1). To analyze soluble proteins, silk solutions were dialyzed against 10 mM Tris/HCl buffer overnight using dialysis membranes with a MW cutoff of 6–8 kDa (Spectra/Por, Thermo Fisher Scientific GmbH, Germany). While eADF4(C16) and eADF4(κ16) variants were dialyzed at RT,[21b] dialysis of eADF4(Ω16) silk variants was conducted at 4 °C[21c] to reduce protein aggregation. For SDS-PAGE, proteins were incubated with Laemmli buffer (95 °C, 15 min) and analyzed using 5 µg protein, 12.5 % gels, and silver staining (n = 2). Since recombinant spider silk proteins contain Tyr but no Trp residues, potential *E. coli* contaminants could be identified by Trp fluorescence at 347 nm, because *E. coli* proteins comprised on average 1.5 % Trp residues.[21a,31] Fluorescence spectra were recorded using a FP 6500 spectrofluorimeter (Jasco, Japan) and protein concentrations of 0.5 mg mL^{-1}, black cuvettes, a step size of 0.5 nm and a scan speed of 100 nm min^{-1}. The excitation wavelength was either 275 nm (Tyr) or 295 nm (Trp), while the emission was recorded between 300 and 400 nm with bandwidths of 5 nm. Three spectra were recorded and averaged. As soluble spider silk proteins were unstructured, far-UV CD spectroscopy between 190 and 300 nm was conducted to determine secondary structure.[21a] CD spectra were recorded in triplicates on a J-815 CD spectrometer (Jasco, Japan) using concentrations of 0.2 mg mL^{-1}, cuvettes with a path length of 0.1 cm, an integration time of 1 s, and a scan speed of 50 nm min^{-1}. Three spectra were recorded and averaged.

Spider Silk Film Preparation: For film casting, spider silk variants were dissolved in 1,1,1,3,3,3-hexafluoro-2-ispropanol (HFIP) at a concentration of 10 mg mL^{-1} at RT overnight. The needed volume of silk solution was adjusted to the corresponding area of the used nontreated polystyrene surface (Sarstedt or Nunc, Thermo Fisher Scientific, Germany) to obtain films containing 0.5 mg spider silk protein per cm^2 after solvent evaporation. Since cast spider silk films exhibit a mainly α-helical or random coil structure making them water soluble, post-treatment using ethanol vapor in a desiccator was conducted to induce a structural transition into water insoluble β-sheets.[54]

Gradient Film Production: Gradient films mimicking a biochemical signaling gradient were produced in a modified and adopted manner as described previously.[21f] Therefore, eADF4(C16) (cytophobic) and eADF4(C16)-RGD (cytophilic) were dissolved in HFIP (10 mg mL^{-1}). Two 1 mL gastight glass syringes with Luer-lock connection (Hamilton, series 1000, Germany) were connected to in-house built tubing systems (Braun GmbH, Germany and Scientific Commodities Inc., USA) and mixing units consisting of tube adapters (Braun GmbH, Germany) and conical polyethylene tips (Sarstedt, Germany) to enable protein blending according to the applied inverse flow profiles of a Nemesys S syringe pump system (Cetoni GmbH, Germany). Besides linear gradients with steps lasting from 0.1 s, blocks with 100% of the corresponding spider silk variant flanked the gradient ends. Gradient and control films were produced at a total flow rate of 400 µL h^{-1} on glass substrates (Thermo Fisher Scientific, Germany) fixed on a mobile unit of a Harvard syringe pump system (Model 33, Harvard Apparatus, USA) moving with a continuous speed of 0.16 mm s^{-1}. Generated films were post-treated using ethanol vapor.

Water Contact Angle Measurements: To analyze the surface wettability of spider silk films and polystyrene, static WCA measurements were conducted using a Surftens-universal tensiometer (OEG GmbH, Germany) and the sessile drop method at RT. After an equilibration time of 10 s, an image was recorded and the contact angle was analyzed. Five measurements per condition were conducted (n = 5) and averaged (e.g., mean ± standard deviation [SD]). Each individual droplet was also measured five times in the software and averaged.

Cell Culture: The following chemicals were used for different cell culture studies: DMEM (BioSell, Germany), RPMI 1640 (Roswell Park Memorial Institute, Sigma-Aldrich, Germany), Eagle's minimum essential medium (EMEM, ATCC, Germany), FCS (BioSell, Germany), GlutaMax (Gibco, Thermo Fisher Scientific, Germany), Gentamycin-Sulfate (Sigma-Aldrich, Germany), trypsin (BioSell, Germany), 1× PBS (Sigma-Aldrich, Germany), non-essential amino acids (NEAA, Sigma-Aldrich, Germany), and trypan blue (Sigma-Aldrich, Germany). Human skin BJ fibroblasts (CRL-2522, ATCC, USA) were cultured in EMEM supplemented with 10% v/v FCS, 1% v/v GlutaMax, and 0.1% v/v gentamycin sulfate. Human bone MG-63 osteosarcoma fibroblasts (CRL-1427, ATCC, USA) were cultured in EMEM supplemented with 10% v/v FCS, 1% v/v GlutaMax, 1 % v/v NEAA, and 0.1% v/v gentamycin sulfate. Mouse M-MSV Balb/3T3 fibroblasts (ECACC, Sigma-Aldrich, Germany), rat nerve B50 neuronal cells (ECACC, Sigma-Aldrich, Germany), mouse C2C12 myoblasts (CLR-1772, ATCC, USA), mouse-rat NG108-15 somatic cell hybrids from glio- and neuroblastoma (HB-12317, ATCC, USA), human skin HaCaT keratinocytes (DKFZ, CLS, Germany), and immature, bipolar rat RN 22 Schwann cells (ECACC, Sigma-Aldrich, Germany) were cultured in DMEM supplemented with 10% v/v FCS, 1% v/v GlutaMax, and 0.1% v/v gentamycin sulfate. Human HeLa epithelial cells from a cervix carcinoma (ACC 57, DSMZ, Germany) were cultured in RPMI 1640 supplemented with 10% v/v FCS, 1% v/v GlutaMax, and 0.1% v/v gentamycin sulfate. HUVEC from the human umbilical cord (INS-Cl-1002, InSCREENeX GmbH, Germany) were cultured in huVEC basal medium (INS-ME-1011) supplemented with 5.7 % v/v supplements (INS-ME-1011BS, both InSCREENeX GmbH, Germany) and 0.1 % v/v gentamycin sulfate in gelatine-coated cell culture flasks. hiPSC derived cardiomyocytes were provided by Tilman Esser and Prof. Felix B. Engel (Nephropathology, University Hospital Erlangen, Germany) and cultured as published previously.[21e]

All cell types were cultivated using a cell culture incubator (HeraCell, Thermo Fisher Scientific, Germany) at humidified conditions containing 5 % CO_2 at 37 °C. Sub-culturing of cells was conducted using trypsin, except for hiPSC-cardiomyocytes. The hiPSC-cardiomyocytes were differentiated from hiPSC as described previously and sub-cultured using accutase.[21e] Cell numbers and viability was determined using trypan blue and an automated cell counter (TC20, Bio-Rad Laboratories, Germany). Prior to use in cell culture, (gradient) films were UV-sterilized for 30 min and washed using 1× PBS.

Cell Adhesion Analysis on Gradient Films: Balb 3T3 fibroblasts were seeded at a density of 10 000 cells per cm^2 in FCS-containing DMEM and incubated for 2 or 4 h in a cell incubator at 37 °C to analyze the influence of increasing RGD-density on cell attachment. Three spider silk gradient films were analyzed per condition (n = 3), while glass, eADF4(C16), and eADF4(C16)-RGD surfaces served as controls. Light microscopical images were recorded using a Leica DM IL LED microscope and the appropriate LAS 4.8 software (Leica, Germany) before washing to visualize also non-attached cells. After washing, cells were fixed using 3.7 % v/v paraformaldehyde (PFA) in 1× PBS (30 min, ambient conditions) and permeabilized using 0.1% v/v Triton X-100 in 1× PBS

(20 min, ambient conditions). Afterwards, the cell nuclei and the F-actin cytoskeleton were fluorescently stained (60 min, dark, RT) using 300 nM 4′,6-diamidino-2-phenylindole dihydrochloride (DAPI, Sigma-Aldrich, Germany) and 200 nM phalloidin tetramethyl rhodamine B isothiocyanate (Phalloidin-red, Sigma-Aldrich, Germany) in 1× PBS, respectively. Prior to imaging, the staining solution was exchanged with fresh 1× PBS. The gradient films were imaged using the DMI 8 confocal laser scanning microscope equipped with lasers using excitation wavelength of 405 nm (DAPI) and 552 nm (Phalloidin-red) and the appropriate LAS X software (Leica, Germany). Three individual gradient films were analyzed per incubation time ($n = 3$).

Cell Adhesion Assay for 4 h and Evaluation of Cell Adhesion Behavior: For each spider silk variant, three individual wells were analyzed with cells ($n = 3$), while untreated wells served as controls. To investigate the effect of added serum proteins, the cell adhesion behavior was analyzed in presence and absence of FCS. For each cell type, 10 000 cells per well (96 well plate) were seeded in 150 µL of the respective media and allowed to attach for 4 h at 37 °C. After 4 h, the cells were fixed, permeabilized, and fluorescently stained (300 nM DAPI and 200 nM Phalloidin-red) as mentioned above. To evaluate cell adhesion behavior, cell numbers as well as the morphology and spreading behavior of attached cells were analyzed using a Leica DMI 3000B fluorescence microscope with a 20× objective and the LAS X software (Leica, Germany). A high cell number combined with clear cell spreading and a visible, organized F-actin expression indicated a very good cell attachment (++) and classified the spider silk as cell-adhesive. As soon as the number of attached cells was reduced, but cell spreading was visible, or many cells were visible starting to form a F-actin cytoskeleton, the variant was classified as "good" (+). If a surface showed moderate number of attached cells, which formed some focal adhesions or stress fibers, indicated by some F-actin filaments, the respective spider silk variant showed moderate cell adhesion behavior (0). In contrast, spider silk variants showing few attached cells exhibiting a mainly round morphology without a clear F-actin cytoskeleton formation were classified as poor adhesive surfaces (−). As soon as only a few sporadic round cells were detectable showing no or less F-actin expression, the cell attachment was very poor (−), and the silk surfaces were classified as a cell-repellent. Furthermore, cell numbers of four selected, representative fluorescence images ($n = 4$) per condition (eADF4(C16), eADF4(C16)-RGD, eADF4(C16)-KGD) were counted for every cell line and summed up to quantify cell adhesion behavior on these spider silk variants.

Co-Culture for Selective Attachment: To demonstrate spider silk selective cell attachment, co-culture experiments using mouse C2C12 myoblasts and rat B50 neuronal cells were conducted on eADF4(C16)-KGD (cell-specific for C2C12 myoblasts) and eADF4(C16)-RGD (cytophilic) spider silk films. C2C12 myoblasts and B50 neuronal cells were stained with Syto 9 DNA stain (green, Invitrogen, Thermo Fisher Scientific, Germany) and CellTracker Red CMTPX (red, Invitrogen, Thermo Fisher Scientific, Germany), respectively, to enable specific recognition of the respective cell type using fluorescence microscopy afterwards ($n = 3$). Confluent cells were incubated with 1 µM DNA stain or cell mask in DMEM for 1 h. Afterwards, both cell layers were washed several times using 1× PBS to remove excess surface bound dye. After sub-culturing using trypsin, cells were resuspended in DMEM without FCS, and 10 000 cells per cm^2 were seeded on eADF4(C16)-KGD and eADF4(C16)-RGD films. Wells without spider silk films and individually cultured cells on silk films served as control. The staining success was verified using a Leica DMI 3000B fluorescence microscope equipped with a 10× and a 20× objective and the LAS X software (Leica, Germany). Fluorescence microscopy was conducted at different timepoints ($t = 0$, 2, 4, and 6 h) before and after washing (1× PBS) to check cell adhesion behavior. After washing, FCS-containing DMEM FCS was added. To confirm cell selectivity of eADF4(C16)-KGD compared to eADF4(C16)-RGD, the same samples were imaged again using fluorescence microscopy on the next day.

Cell Proliferation Assay: A proliferation assay over 8 days was conducted on spider silk films made of eADF4(C16) (cytophobic), eADF4(C16)-RGD (cytophilic), and eADF4(C16)-KGD (cell-specific for C2C12 myoblasts) using seven different cell types (mouse C2C12 myoblasts, human BJ fibroblasts, human HaCaT keratinocytes, human MG63 osteosarcoma fibroblasts, rat RN22 Schwann cells, rat B50 neuronal cells, and mouse-rat NG108-15 somatic hybrid cells). For each spider silk variant, four different wells were analyzed ($n = 4$) and averaged (e.g., mean ± SD), while wells without films served as controls. For each cell type, 5000 cells per 1 cm^2 were seeded in 150 µL media containing 10% FCS and incubated at 37 °C. To evaluate cell proliferation, a CellTiter-Blue cell viability assay (Promega, USA) was conducted on day 1, 3 or 4, 6, and 8. After washing using 1× PBS, 150 µL of 10% v/v CellTiter-Blue reagent in the respective cell culture media were added and incubated for 2.5 h. Samples without cells served as blanks to determine self-degradation of resazurin over time. The averaged blank samples were subtracted from the measured values. The viability of cells could be determined by their metabolic turnover of resazurin (blue) to resofurin (pink, $\lambda_{ex} = 530$ nm, $\lambda_{em} = 590$ nm) by viable cells. Therefore, 100 µL of respective supernatants were transferred to a black 96 well plate (Nunc, Thermo Fisher Scientific, Germany) and measured at 590 nm using a plate reader system (Mithras LB940, Berthold Technologies, Germany).

Statistical Analysis: A pre-processing of the data was not performed. The respective information about sample sizes and data presentation was added at the appropriate experimental procedures. Further statistical analyses were not conducted.

Supporting Information

Supporting Information is available from the Wiley Online Library or from the author.

Acknowledgements

The authors acknowledge the funding from the Deutsche Forschungsgemeinschaft (DFG, German Research Foundation)—project number 326998133-TRR225 (funded sub-project: C01). Support from the Elite Network of Bavaria is also acknowledged. The authors thank Andreas Schmidt, Johannes Diehl, Andreas Kumschier, Comfort Ajala, Vivien Beyersdorfer, Kathrin Döhla, and Thomas Göbbel for supporting protein production and purification. Andreas Schmidt is also acknowledged for MALDI-TOF measurements. Alexandra Pellert, Eva Möller, and Nicole Pittel are acknowledged for supporting cell culture. The authors also want to thank Christina Heinritz for assistance in gradient film generation and Dr. Vanessa Neubauer for critical discussions. Final thanks to Prof. Felix B. Engel and Tilman Esser for providing hiPSC-derived cardiomyocytes.

Open access funding enabled and organized by Projekt DEAL.

Conflict of Interest

T.S. is co-founder and shareholder of AMSilk GmbH.

Data Availability Statement

The data that support the findings of this study are available from the corresponding author upon reasonable request.

Keywords

bioactive peptides, bioselectivity, cell co-culture, cytophilic surfaces, gradient materials

Received: October 14, 2022
Revised: December 19, 2022
Published online:

[1] a) G. Huang, F. Li, X. Zhao, Y. Ma, Y. Li, M. Lin, G. Jin, T. J. Lu, G. M. Genin, F. Xu, *Chem. Rev.* **2017**, *117*, 12764; b) D. T. Scadden, *Nature* **2006**, *441*, 1075.

[2] a) J. Engel, M. Chiquet, in *The Extracellular Matrix: An Overview* (Ed: R. P. Mecham), Springer, Berlin **2011**, p. 1; b) A. D. Theocharis, S. S. Skandalis, C. Gialeli, N. K. Karamanos, *Adv. Drug Delivery Rev.* **2016**, *97*, 4; c) W. P. Daley, S. B. Peters, M. Larsen, *J. Cell Sci.* **2008**, *121*, 255.

[3] D. E. Discher, D. J. Mooney, P. W. Zandstra, *Science* **2009**, *324*, 1673.

[4] a) R. Langer, J. P. Vacanti, *Science* **1993**, *260*, 920; b) J. L. Carvalho, P. H. de Carvalho, D. A. Gomes, A. M. de Goes, *Adv. Biomater. Sci. Biomed. Appl.* **2013**, *11*, 295; c) C. A. Vacanti, J. P. Vacanti, *Surg. Technol. Int.* **1991**, *I*, 43; d) U. A. Stock, J. P. Vacanti, *Annu. Rev. Med.* **2001**, *52*, 443.

[5] a) B. P. Chan, K. W. Leong, *Eur. Spine J.* **2008**, *17*, 467; b) S. Hinderer, S. L. Layland, K. Schenke-Layland, *Adv. Drug Delivery Rev.* **2016**, *97*, 260; c) F. J. O'Brien, *Mater. Today* **2011**, *14*, 88; d) S. M. Choi, P. Chaudhry, S. M. Zo, S. S. Han, in *Cutting-Edge Enabling Technologies for Regenerative Medicine* (Eds: H. J. Chun, C. H. Park, I. K. Kwon, G. Khang), Springer, Singapore **2018**, p. 161; e) S. Pacelli, V. Manoharan, A. Desalvo, N. Lomis, K. S. Jodha, S. Prakash, A. Paul, *J. Mater. Chem. B* **2016**, *4*, 1586; f) M. Pagel, A. G. Beck-Sickinger, *Biol. Chem.* **2017**, *398*, 3; g) K. Borcherding, G. Schmidmaier, G. O. Hofmann, B. Wildemann, *Injury* **2021**, *52*, S106; h) X. Zhao, in *Bioactive Materials in Medicine* (Eds: X. Zhao, J. M. Courtney, H. Qian), Woodhead Publishing, Cambridge, UK **2011**, p. 1; i) J. Najdanović, J. Rajković, S. Najman, in *Biomaterials in Clinical Practice: Advances in Clinical Research and Medical Devices* (Eds: F. Zivic, S. Affatato, M. Trajanovic, M. Schnabelrauch, N. Grujovic, K. L. Choy), Springer International Publishing, Cham **2018**, p. 333; j) S. Spiller, F. Clauder, K. Bellmann-Sickert, A. G. Beck-Sickinger, *Biol. Chem.* **2021**, *402*, 1271.

[6] a) J. A. DeQuach, V. Mezzano, A. Miglani, S. Lange, G. M. Keller, F. Sheikh, K. L. Christman, *PLoS One* **2010**, *5*, e13039; b) Y. Zhang, Y. He, S. Bharadwaj, N. Hammam, K. Carnagey, R. Myers, A. Atala, M. Van Dyke, *Biomaterials* **2009**, *30*, 4021; c) D. Lam, H. A. Enright, J. Cadena, S. K. G. Peters, A. P. Sales, J. J. Osburn, D. A. Soscia, K. S. Kulp, E. K. Wheeler, N. O. Fischer, *Sci. Rep.* **2019**, *9*, 4159; d) D. Olvera, B. N. Sathy, D. J. Kelly, *ACS Biomater. Sci. Eng.* **2020**, *6*, 5145; e) A. Shridhar, B. G. Amsden, E. R. Gillies, L. E. Flynn, *Front. Bioeng. Biotechnol.* **2019**, *7*, 402.

[7] a) A.-S. Mertgen, V. T. Trossmann, A. G. Guex, K. Maniura-Weber, T. Scheibel, M. Rottmar, *ACS Appl. Mater. Interfaces* **2020**, *12*, 21342; b) K. Kyzioł, Ł. Kaczmarek, A. Kyzioł, in *Handbook of Composites from Renewable Materials* (Eds: V. K. Thakur, M. K. Thakur, M. R. Kessler), Scrivener Publishing, Beverly, MA **2017**, p. 457; c) R. Fraioli, S. Neubauer, F. Rechenmacher, B. M. Bosch, K. Dashnyam, J. H. Kim, R. A. Perez, H. W. Kim, F. J. Gil, M. P. Ginebra, J. M. Manero, H. Kessler, C. Mas-Moruno, *Biomater. Sci.* **2019**, *7*, 1281; d) H. Zhang, X. Zheng, W. Ahmed, Y. Yao, J. Bai, Y. Chen, C. Gao, *Biomacromolecules* **2018**, *19*, 1746.

[8] a) P. Jurczak, J. Witkowska, S. Rodziewicz-Motowidło, S. Lach, *Adv. Colloid Interface Sci.* **2020**, *276*, 102083; b) H. Amani, H. Arzaghi, M. Bayandori, A. S. Dezfuli, H. Pazoki-Toroudi, A. Shafiee, L. Moradi, *Adv. Mater. Interfaces* **2019**, *6*, 1900572; c) A. Cipitria, M. Salmeron-Sanchez, *Adv. Healthcare Mater.* **2017**, *6*, 1700052; d) J. A. Hubbell, *Curr. Opin. Biotechnol.* **1999**, *10*, 123; e) N. R. Richbourg, N. A. Peppas, V. I. Sikavitsas, *J. Tissue Eng. Regener. Med.* **2019**, *13*, 1275; f) M. Salmerón-Sánchez, M. J. Dalby, *Chem. Commun.* **2016**, *52*, 13327; g) K. Hosoyama, C. Lazurko, M. Muñoz, C. D. McTiernan, E. I. Alarcon, *Front. Bioeng. Biotechnol.* **2019**, *7*, 205; h) N. Huettner, T. R. Dargaville, A. Forget, *Trends Biotechnol.* **2018**, *36*, 372.

[9] a) E. Ruoslahti, M. D. Pierschbacher, *Cell* **1986**, *44*, 517; b) M. D. Pierschbacher, E. Ruoslahti, *Nature* **1984**, *309*, 30; c) M. D. Pierschbacher, E. G. Hayman, E. Ruoslahti, *J. Cell. Biochem.* **1985**, *28*, 115; d) M. D. Pierschbacher, E. Ruoslahti, *Proc. Natl. Acad. Sci. USA* **1984**, *81*, 5985.

[10] a) S. L. Bellis, *Biomaterials* **2011**, *32*, 4205; b) U. Hersel, C. Dahmen, H. Kessler, *Biomaterials* **2003**, *24*, 4385.

[11] a) M. Pfaff, in *Integrin-Ligand Interaction*, Springer, Boston, MA **1997**, p. 101; b) T. G. Kapp, F. Rechenmacher, S. Neubauer, O. V. Maltsev, E. A. Cavalcanti-Adam, R. Zarka, U. Reuning, J. Notni, H.-J. Wester, C. Mas-Moruno, J. Spatz, B. Geiger, H. Kessler, *Sci. Rep.* **2017**, *7*, 39805; c) W. M. Han, Y. C. Jang, A. J. García, in *Biomaterials Science*, 4th ed. (Eds: W. R. Wagner, S. E. Sakiyama-Elbert, G. Zhang, M. J. Yaszemski), Academic Press, Cambridge, MA, USA **2020**, p. 701.

[12] a) E. Ruoslahti, *Annu. Rev. Cell Dev. Biol.* **1996**, *12*, 697; b) K. G. Sreejalekshmi, P. D. Nair, *J. Biomed. Mater. Res., Part A* **2011**, *96A*, 477; c) F. R. Maia, S. J. Bidarra, P. L. Granja, C. C. Barrias, *Acta Biomater.* **2013**, *9*, 8773; d) J. Xu, D. Mosher, in *The Extracellular Matrix: An Overview* (Ed: R. P. Mecham), Springer, Berlin **2011**, p. 41; e) B. K. Mann, A. T. Tsai, T. Scott-Burden, J. L. West, *Biomaterials* **1999**, *20*, 2281; f) K. M. Yamada, *J. Biol. Chem.* **1991**, *266*, 12809.

[13] a) K. Tashiro, G. C. Sephel, B. Weeks, M. Sasaki, G. R. Martin, H. K. Kleinman, Y. Yamada, *J. Biol. Chem.* **1989**, *264*, 16174; b) Y. Yin, W. Wang, Q. Shao, B. Li, D. Yu, X. Zhou, J. Parajuli, H. Xu, T. Qiu, A. K. Yetisen, N. Jiang, *Biomater. Sci.* **2021**, *9*, 2887; c) R. Patel, M. Santhosh, J. K. Dash, R. Karpoormath, A. Jha, J. Kwak, M. Patel, J. H. Kim, *Polym. Adv. Technol.* **2019**, *30*, 4; d) T. H. Perera, S. M. Howell, L. A. S. Callahan, *Biomacromolecules* **2019**, *20*, 3009; e) W. Sun, T. Incitti, C. Migliaresi, A. Quattrone, S. Casarosa, A. Motta, *J. Tissue Eng. Regener. Med.* **2017**, *11*, 1532.

[14] a) S. P. Massia, S. S. Rao, J. A. Hubbell, *J. Biol. Chem.* **1993**, *268*, 8053; b) J. Graf, Y. Iwamoto, M. Sasaki, G. R. Martin, H. K. Kleinman, F. A. Robey, Y. Yamada, *Cell* **1987**, *48*, 989; c) J. Graf, R. C. Ogle, F. A. Robey, M. Sasaki, G. R. Martin, Y. Yamada, H. K. Kleinman, *Biochemistry* **1987**, *26*, 6896; d) H.-W. Jun, J. West, *J. Biomater. Sci., Polym. Ed.* **2004**, *15*, 73.

[15] a) R. M. Scarborough, J. W. Rose, M. A. Hsu, D. R. Phillips, V. A. Fried, A. M. Campbell, L. Nannizzi, I. F. Charo, *J. Biol. Chem.* **1991**, *266*, 9359; b) P. Nykvist, K. Tasanen, T. Viitasalo, J. Käpylä, J. Jokinen, L. Bruckner-Tuderman, J. Heino, *J. Biol. Chem.* **2001**, *276*, 38673; c) H. Minoux, C. Chipot, D. Brown, B. Maigret, *J. Comput.-Aided Mol. Des.* **2000**, *14*, 317; d) J. Salber, S. Gräter, M. Harwardt, M. Hofmann, D. Klee, J. Dujic, H. Jinghuan, J. Ding, S. Kippenberger, A. Bernd, J. Groll, J. P. Spatz, M. Möller, *Small* **2007**, *3*, 1023.

[16] a) C. G. Knight, L. F. Morton, A. R. Peachey, D. S. Tuckwell, R. W. Farndale, M. J. Barnes, *J. Biol. Chem.* **2000**, *275*, 35; b) W.-M. Zhang, J. Käpylä, J. S. Puranen, C. G. Knight, C.-F. Tiger, O. T. Pentikäinen, M. S. Johnson, R. W. Farndale, J. Heino, D. Gullberg, *J. Biol. Chem.* **2003**, *278*, 7270.

[17] a) N. T. Feric, C. C. H. Cheng, M. C. Goh, V. Dudnyk, V. Di Tizio, M. Radisic, *Biomater. Sci.* **2014**, *2*, 1384; b) L. A. Reis, L. L. Y. Chiu, J. Wu, N. Feric, C. Laschinger, A. Momen, R.-K. Li, M. Radisic, *Circ.: Heart Failure* **2015**, *8*, 333; c) J. W. Miklas, S. M. Dallabrida, L. A. Reis, N. Ismail, M. Rupnick, M. Radisic, *PLoS One* **2013**, *8*, e72956.

[18] a) J. A. Hubbell, S. P. Massia, N. P. Desai, P. D. Drumheller, *Bio/Technology* **1991**, *9*, 568; b) S. P. Massia, J. A. Hubbell, *J. Biol. Chem.* **1992**, *267*, 14019; c) Y. Liu, A. Mahara, Y. Kambe, Y.-I. Hsu, T. Yamaoka, *Biomater. Sci.* **2021**, *9*, 1034.

[19] a) M. Mehta, C. M. Madl, S. Lee, G. N. Duda, D. J. Mooney, *J. Biomed. Mater. Res., Part A* **2015**, *103*, 3516; b) A. Jha, E. Moore, *J. Mater. Res.* **2021**, *37*, 77.

[20] a) T. B. Aigner, E. DeSimone, T. Scheibel, *Adv. Mater.* **2018**, *30*, 1704636; b) S. Salehi, K. Koeck, T. Scheibel, *Molecules* **2020**, *25*, 737; c) A. Leal-Egaña, T. Scheibel, *Biotechnol. Appl. Biochem.* **2010**, *55*, 155.

[21] a) D. Huemmerich, C. W. Helsen, S. Quedzuweit, J. Oschmann, R. Rudolph, T. Scheibel, *Biochemistry* **2004**, *43*, 13604; b) E. Doblhofer, T. Scheibel, *J. Pharm. Sci.* **2015**, *104*, 988; c) S. Kumari, G. Lang, E.

DeSimone, C. Spengler, V. T. Trossmann, S. Lücker, M. Hudel, K. Jacobs, N. Krämer, T. Scheibel, *Mater. Today* **2020**, *41*, 21; d) S. Kumari, G. Lang, E. DeSimone, C. Spengler, V. T. Trossmann, S. Lücker, M. Hudel, K. Jacobs, N. Krämer, T. Scheibel, *Data Brief* **2020**, *32*, 106305; e) T. U. Esser, V. T. Trossmann, S. Lentz, F. B. Engel, T. Scheibel, *Mater Today Bio* **2021**, *11*, 100114; f) V. J. Neubauer, T. Scheibel, *ACS Biomater. Sci. Eng.* **2020**, *6*, 5599; g) S. Wohlrab, S. Müller, A. Schmidt, S. Neubauer, H. Kessler, A. Leal-Egaña, T. Scheibel, *Biomaterials* **2012**, *33*, 6650; h) M. B. Elsner, H. M. Herold, S. Müller-Herrmann, H. Bargel, T. Scheibel, *Biomater. Sci.* **2015**, *3*, 543.

[22] J. D. Humphries, A. Byron, M. J. Humphries, *J. Cell Sci.* **2006**, *119*, 3901.

[23] a) T.-Y. Cheng, M.-H. Chen, W.-H. Chang, M.-Y. Huang, T.-W. Wang, *Biomaterials* **2013**, *34*, 2005; b) T. H. Perera, X. Lu, L. A. S. Callahan, *J. Funct. Biomater.* **2020**, *11*, 15; c) A. Farrukh, S. Zhao, A. del Campo, *Front. Mater.* **2018**, *5*, 62; d) A. Farrukh, J. I. Paez, M. Salierno, W. Fan, B. Berninger, A. del Campo, *Biomacromolecules* **2017**, *18*, 906; e) A. Farrukh, F. Ortega, W. Fan, N. Marichal, J. I. Paez, B. Berninger, A. d. Campo, M. J. Salierno, *Stem Cell Rep.* **2017**, *9*, 1432; f) S. K. Powell, J. Rao, E. Roque, M. Nomizu, Y. Kuratomi, Y. Yamada, H. K. Kleinman, *J. Neurosci. Res.* **2000**, *61*, 302; g) M. Nomizu, B. S. Weeks, C. A. Weston, W. H. Kim, H. K. Kleinman, Y. Yamada, *FEBS Lett.* **1995**, *365*, 227; h) M. Yamada, Y. Kadoya, S. Kasai, K. Kato, M. Mochizuki, N. Nishi, N. Watanabe, H. K. Kleinman, Y. Yamada, M. Nomizu, *FEBS Lett.* **2002**, *530*, 48; i) R. A. Que, J. Arulmoli, N. A. Da Silva, L. A. Flanagan, S.-W. Wang, *J. Biomed. Mater. Res., Part A* **2018**, *106*, 1363; j) Y. Wu, Q. Zheng, J. Du, Y. Song, B. Wu, X. Guo, *J. Huazhong Univ. Sci. Technol., Med. Sci.* **2006**, *26*, 594; k) I. C. Yasa, N. Gunduz, M. Kilinc, M. O. Guler, A. B. Tekinay, *Sci. Rep.* **2015**, *5*, 16460; l) M. Widhe, U. Johansson, C.-O. Hillerdahl, M. Hedhammar, *Biomaterials* **2013**, *34*, 8223; m) G. A. Silva, C. Czeisler, K. L. Niece, E. Beniash, D. A. Harrington, J. A. Kessler, S. I. Stupp, *Science* **2004**, *303*, 1352; n) B. Li, T. Qiu, P. Zhang, X. Wang, Y. Yin, S. Li, *Cell Proliferation* **2014**, *47*, 133; o) E. Sieni, B. Bazzolo, F. Pieretti, A. Zamuner, A. Tasso, M. Dettin, M. T. Conconi, *Bioelectrochemistry* **2020**, *136*, 107626.

[24] a) M. Matsuzawa, F. F. Weight, R. S. Potember, P. Liesi, *Int. J. Dev. Neurosci.* **1996**, *14*, 283; b) M. J. Cooke, T. Zahir, S. R. Phillips, D. S. Shah, D. Athey, J. H. Lakey, M. S. Shoichet, S. A. Przyborski, *J. Biomed. Mater. Res., Part A* **2010**, *93*, 824; c) W. Wang, L. Guo, Y. Yu, Z. Chen, R. Zhou, Z. Yuan, *J. Biomed. Mater. Res., Part A* **2015**, *103*, 1703; d) Y. Iwamoto, F. A. Robey, J. Graf, M. Sasaki, H. K. Kleinman, Y. Yamada, G. R. Martin, *Science* **1987**, *238*, 1132; e) G. Sarfati, T. Dvir, M. Elkabets, R. N. Apte, S. Cohen, *Biomaterials* **2011**, *32*, 152.

[25] a) F. Rask, S. M. Dallabrida, N. S. Ismail, Z. Amoozgar, Y. Yeo, M. A. Rupnick, M. Radisic, *J. Biomed. Mater. Res., Part A* **2010**, *95A*, 105; b) F. Rask, A. Mihic, L. Reis, S. M. Dallabrida, N. S. Ismail, K. Sider, C. A. Simmons, M. A. Rupnick, R. D. Weisel, R.-K. Li, M. Radisic, *Soft Matter* **2010**, *6*, 5089; c) L. A. Reis, L. L. Y. Chiu, Y. Liang, K. Hyunh, A. Momen, M. Radisic, *Acta Biomater.* **2012**, *8*, 1022; d) H. Cai, F.-Y. Wu, Q.-L. Wang, P. Xu, F.-F. Mou, S.-J. Shao, Z.-R. Luo, J. Zhu, S.-S. Xuan, R. Lu, H.-D. Guo, *FASEB J.* **2019**, *33*, 8306; e) S. Mandla, L. D. Huyer, Y. Wang, M. Radisic, *ACS Biomater. Sci. Eng.* **2019**, *5*, 4542; f) Y. Xiao, L. A. Reis, N. Feric, E. J. Knee, J. Gu, S. Cao, C. Laschinger, C. Londono, J. Antolovich, A. P. McGuigan, M. Radisic, *Proc. Natl. Acad. Sci. USA* **2016**, *113*, E5792; g) L. T. Dang, N. T. Feric, C. Laschinger, W. Y. Chang, B. Zhang, G. A. Wood, W. L. Stanford, M. Radisic, *Biomaterials* **2014**, *35*, 7786.

[26] a) K. Oshikawa, S. Terada, *J. Biochem.* **1999**, *125*, 31; b) K. Tasanen, J. A. Eble, M. Aumailley, H. Schumann, J. Baetge, H. Tu, P. Bruckner, L. Bruckner-Tuderman, *J. Biol. Chem.* **2000**, *275*, 3093.

[27] a) R. Mhanna, E. Öztürk, Q. Vallmajo-Martin, C. Millan, M. Müller, M. Zenobi-Wong, *Tissue Eng., Part A* **2014**, *20*, 1165; b) P. Castillo-Briceño, D. Bihan, M. Nilges, S. Hamaia, J. Meseguer, A. García-Ayala, R. W. Farndale, V. Mulero, *Mol. Immunol.* **2011**, *48*, 826.

[28] a) H.-B. Lin, W. Sun, D. F. Mosher, C. García-Echeverría, K. Schaufelberger, P. I. Lelkes, S. L. Cooper, *J. Biomed. Mater. Res.* **1994**, *28*, 329; b) H.-B. Lin, C. García-Echeverría, S. Asakura, W. Sun, D. F. Mosher, S. L. Cooper, *Biomaterials* **1992**, *13*, 905.

[29] a) G. L. Rosano, E. A. Ceccarelli, *Front. Microbiol.* **2014**, *5*, 172; b) S. Sahdev, S. K. Khattar, K. S. Saini, *Mol. Cell. Biochem.* **2008**, *307*, 249.

[30] S. Hosseini, S. O. Martinez-Chapa, in *Fundamentals of MALDI-ToF-MS Analysis: Applications in Bio-diagnosis Tissue Engineering and Drug Delivery*, Springer, Singapore **2017**, p. 1.

[31] F. R. Blattner, G. Plunkett 3rd, C. A. Bloch, N. T. Perna, V. Burland, M. Riley, J. Collado-Vides, J. D. Glasner, C. K. Rode, G. F. Mayhew, J. Gregor, N. W. Davis, H. A. Kirkpatrick, M. A. Goeden, D. J. Rose, B. Mau, Y. Shao, *Science* **1997**, *277*, 1453.

[32] K. Spieß, S. Wohlrab, T. Scheibel, *Soft Matter* **2010**, *6*, 4168.

[33] J. Petzold, T. B. Aigner, F. Touska, K. Zimmermann, T. Scheibel, F. B. Engel, *Adv. Funct. Mater.* **2017**, *27*, 1701427.

[34] S. Wohlrab, K. Spieß, T. Scheibel, *J. Mater. Chem.* **2012**, *22*, 22050.

[35] a) J. G. Steele, G. Johnson, W. D. Norris, P. A. Underwood, *Biomaterials* **1991**, *12*, 531; b) P. A. Underwood, F. A. Bennett, *J. Cell Sci.* **1989**, *93*, 641; c) P. A. Underwood, P. A. Bean, *Cells Mater.* **1996**, *6*, 20; d) P. A. Underwood, P. A. Bean, S. M. Mitchell, J. M. Whitelock, *J. Immunol. Methods* **2001**, *247*, 217; e) M. Widhe, N. D. Shalaly, M. Hedhammar, *Biomaterials* **2016**, *74*, 256; f) M. Widhe, H. Bysell, S. Nystedt, I. Schenning, M. Malmsten, J. Johansson, A. Rising, M. Hedhammar, *Biomaterials* **2010**, *31*, 9575.

[36] a) D. Steiner, S. Winkler, S. Heltmann-Meyer, V. T. Trossmann, T. Fey, T. Scheibel, R. E. Horch, A. Arkudas, *Biofabrication* **2021**, *13*, 045003; b) P. H. Zeplin, N. C. Maksimovikj, M. C. Jordan, J. Nickel, G. Lang, A. H. Leimer, L. Römer, T. Scheibel, *Adv. Funct. Mater.* **2014**, *24*, 2658; c) M. Lucke, I. Mottas, T. Herbst, C. Hotz, L. Römer, M. Schierling, H. M. Herold, U. Slotta, T. Spinetti, T. Scheibel, G. Winter, C. Bourquin, J. Engert, *Biomaterials* **2018**, *172*, 105.

[37] a) A. Leal-Egaña, G. Lang, C. Mauerer, J. Wickinghoff, M. Weber, S. Geimer, T. Scheibel, *Adv. Eng. Mater.* **2012**, *14*, B67; b) C. B. Borkner, S. Wohlrab, E. Möller, G. Lang, T. Scheibel, *ACS Biomater. Sci. Eng.* **2017**, *3*, 767; c) P. H. Zeplin, A.-K. Berninger, N. C. Maksimovikj, P. Van Gelder, T. Scheibel, H. Walles, *Handchirurgie Mikrochirurgie Plastische Chirurgie* **2014**, *46*, 336.

[38] I. Pountos, M. Panteli, A. Lampropoulos, E. Jones, G. M. Calori, P. V. Giannoudis, *BMC Med.* **2016**, *14*, 103.

[39] a) J. P. M. Kramer, T. B. Aigner, J. Petzold, K. Roshanbinfar, T. Scheibel, F. B. Engel, *Sci. Rep.* **2020**, *10*, 8789; b) K. Schacht, T. Jüngst, M. Schweinlin, A. Ewald, J. Groll, T. Scheibel, *Angew. Chem., Int. Ed.* **2015**, *54*, 2816.

[40] a) E. Bini, C. W. P. Foo, J. Huang, V. Karageorgiou, B. Kitchel, D. L. Kaplan, *Biomacromolecules* **2006**, *7*, 3139; b) J. Zhao, H. Qiu, D.-l. Chen, W.-x. Zhang, D.-c. Zhang, M. Li, *Int. J. Biol. Macromol.* **2013**, *56*, 106; c) M. Widhe, J. Johansson, M. Hedhammar, A. Rising, *Biopolymers* **2012**, *97*, 468; d) C. P. Tasiopoulos, L. Gustafsson, W. van der Wijngaart, M. Hedhammar, *ACS Biomater. Sci. Eng.* **2021**, *7*, 3332; e) C. P. Tasiopoulos, M. Widhe, M. Hedhammar, *ACS Appl. Mater. Interfaces* **2018**, *10*, 14531; f) C. P. Tasiopoulos, S. Petronis, H. Sahlin, M. Hedhammar, *ACS Appl. Bio Mater.* **2020**, *3*, 577.

[41] a) A. Lagunas, J. Comelles, E. Martínez, E. Prats-Alfonso, G. A. Acosta, F. Albericio, J. Samitier, *Nanomedicine* **2012**, *8*, 432; b) B. P. Harris, J. K. Kutty, E. W. Fritz, C. K. Webb, K. J. L. Burg, A. T. Metters, *Langmuir* **2006**, *22*, 4467; c) X. Tong, J. Jiang, D. Zhu, F. Yang, *ACS Biomater. Sci. Eng.* **2016**, *2*, 845.

[42] a) V. T. Trossmann, S. Heltmann-Meyer, H. Amouei, H. Wajant, R. E. Horch, D. Steiner, T. Scheibel, *Biomacromolecules* **2022**, *23*, 4427; b) A. Lechner, V. T. Trossmann, T. Scheibel, *Macromol. Biosci.* **2021**, *22*, 2100390.

[43] S. Lentz, V. T. Trossmann, C. B. Borkner, V. Beyersdorfer, M. Rottmar, T. Scheibel, *ACS Appl. Mater. Interfaces* **2022**, *14*, 31751.

[44] a) A. Leal-Egana, A. Díaz-Cuenca, A. Boccaccini, *Adv. Mater.* **2013**, *25*, 4049; b) A. Blau, *Curr. Opin. Colloid Interface Sci.* **2013**, *18*, 481; c) M. De Rosa, M. Carteni', O. Petillo, A. Calarco, S. Margarucci, F. Rosso, A. De Rosa, E. Farina, P. Grippo, G. Peluso, *J. Cell. Physiol.* **2004**, *198*, 133.
[45] U. Johansson, M. Ria, K. Åvall, N. D. Shalaly, S. V. Zaitsev, P.-O. Berggren, M. Hedhammar, *PLoS One* **2015**, *10*, e0130169.
[46] a) M. Barczyk, S. Carracedo, D. Gullberg, *Cell Tissue Res.* **2009**, *339*, 269; b) O. Schussler, J. C. Chachques, M. Alifano, Y. Lecarpentier, *J. Cardiovasc. Transl. Res.* **2021**, *15*, 179.
[47] J. Heino, *BioEssays* **2007**, *29*, 1001.
[48] R. A. Lazarus, R. S. McDowell, *Curr. Opin. Biotechnol.* **1993**, *4*, 438.
[49] M. D. Pierschbacher, E. Ruoslahti, *J. Biol. Chem.* **1987**, *262*, 17294.
[50] a) T. Sasagawa, T. Shimizu, S. Sekiya, Y. Haraguchi, M. Yamato, Y. Sawa, T. Okano, *Biomaterials* **2010**, *31*, 1646; b) D. W. van der Schaft, A. C. van Spreeuwel, H. C. van Assen, F. P. Baaijens, *Tissue Eng., Part A* **2011**, *17*, 2857.
[51] S. T. Cooper, A. L. Maxwell, E. Kizana, M. Ghoddusi, E. C. Hardeman, I. E. Alexander, D. G. Allen, K. N. North, *Cell Motil. Cytoskeleton* **2004**, *58*, 200.
[52] a) S. Ostrovidov, S. Ahadian, J. Ramon-Azcon, V. Hosseini, T. Fujie, S. P. Parthiban, H. Shiku, T. Matsue, H. Kaji, M. Ramalingam, H. Bae, A. Khademhosseini, *J. Tissue Eng. Regener. Med.* **2017**, *11*, 582; b) M. Das, J. W. Rumsey, N. Bhargava, M. Stancescu, J. J. Hickman, *Biomaterials* **2010**, *31*, 4880; c) J. X. Jiang, R. C. Choi, N. L. Siow, H. H. Lee, D. C. Wan, K. W. Tsim, *J. Biol. Chem.* **2003**, *278*, 45435; d) M. Das, J. W. Rumsey, C. A. Gregory, N. Bhargava, J. F. Kang, P. Molnar, L. Riedel, X. Guo, J. J. Hickman, *Neuroscience* **2007**, *146*, 481; e) M. Das, J. W. Rumsey, N. Bhargava, M. Stancescu, J. J. Hickman, *Biomaterials* **2009**, *30*, 5392; f) X. Guo, M. Gonzalez, M. Stancescu, H. H. Vandenburgh, J. J. Hickman, *Biomaterials* **2011**, *32*, 9602; g) A. S. Smith, S. L. Passey, N. R. Martin, D. J. Player, V. Mudera, L. Greensmith, M. P. Lewis, *Cells Tissues Organs* **2016**, *202*, 143; h) J. W. Santoso, X. Li, D. Gupta, G. C. Suh, E. Hendricks, S. Lin, S. Perry, J. K. Ichida, D. Dickman, M. L. McCain, *APL Bioeng.* **2021**, *5*, 036101.
[53] a) E. DeSimone, K. Schacht, A. Pellert, T. Scheibel, *Biofabrication* **2017**, *9*, 044104; b) K. Schacht, T. Scheibel, *Biomacromolecules* **2011**, *12*, 2488.
[54] K. Spiess, R. Ene, C. D. Keenan, J. Senker, F. Kremer, T. Scheibel, *J. Mater. Chem.* **2011**, *21*, 13594.

ADVANCED HEALTHCARE MATERIALS

Supporting Information

for *Adv. Healthcare Mater.*, DOI 10.1002/adhm.202202660

Design of Recombinant Spider Silk Proteins for Cell Type Specific Binding

*Vanessa Tanja Trossmann and Thomas Scheibel**

WILEY-VCH

Supplementary Information

Design of Recombinant Spider Silk Proteins for Cell Type Specific Binding

*Vanessa Tanja Trossmann and Thomas Scheibel**

Vanessa Tanja Trossmann, Prof. Dr. Thomas Scheibel

Lehrstuhl Biomaterialien, Fakultät für Ingenieurswissenschaften, Universität Bayreuth, Prof.-Rüdiger-Bormann-Straße 1, 95447 Bayreuth, Germany

Prof. Dr. Thomas Scheibel

Bayreuther Zentrum für Kolloide und Grenzflächen (BZKG), Bayerisches Polymerinstitut (BPI), Bayreuther Zentrum für Molekulare Biowissenschaften (BZMB), Bayreuther Materialzentrum (BayMAT), Universität Bayreuth, Universitätsstraße 30, 95447 Bayreuth, Germany

* Corresponding author: Prof. Dr. Thomas Scheibel

E-Mail: thomas.scheibel@bm.uni-bayreuth.de

Table S1: Properties of recombinant spider silk proteins. Note: One positively charged amino acid (arginine) is located in the N-Terminally fused T7 tag and not within the silk sequence. Abbreviations: total number of amino acids (AA), molecular weight (MW), isoelectric point (pI), number of negatively charged amino acids (- AA), number of positively charged amino acids (+ AA).

	pI	- AA	+ AA	AA	MW_{theo} (Da)	MW_{det} (Da)
eADF4(C16)	3.5	16	1	576	47,698	47,747
eADF4(C16)-RGD	3.6	17	2	587	48,583	48,649
eADF4(C16)-KGD	3.6	17	2	587	48,555	48,614
eADF4(C16)-RGE	3.7	17	2	587	48,597	48,669
eADF4(C16)-GFPGER	3.7	17	2	590	48,899	48,894
eADF4(C16)-IKVAV	3.7	16	2	589	48,766	48,762
eADF4(C16)-YIGSR	3.7	16	2	589	48,832	48,916
eADF4(C16)-QHREDGS	3.8	18	2	589	48,880	48,864
eADF4(Ω16)-QHREDGS	6.5	2	2	585	48,606	48,596
eADF4(Ω16)	7.7	0	1	576	47,683	47,694
eADF4(Ω16)-RGD	7.7	1	2	587	48,567	48,640
eADF4(Ω16)-IKVAV	8.5	0	2	589	48,750	48,813
eADF4(Ω16)-YIGSR	8.5	0	2	589	48,816	48,833
eADF4(κ16)-QHREDGS	9.7	2	18	585	48,607	48,803
eADF4(κ16)	9.7	0	17	576	47,683	47,740
eADF4(κ16)-RGD	9.7	1	18	587	48,568	48,648
eADF4(κ16)-YIGSR	9.7	0	18	589	48,816	48,898
eADF4(κ16)-IKVAV	9.7	0	18	589	48,750	48,801

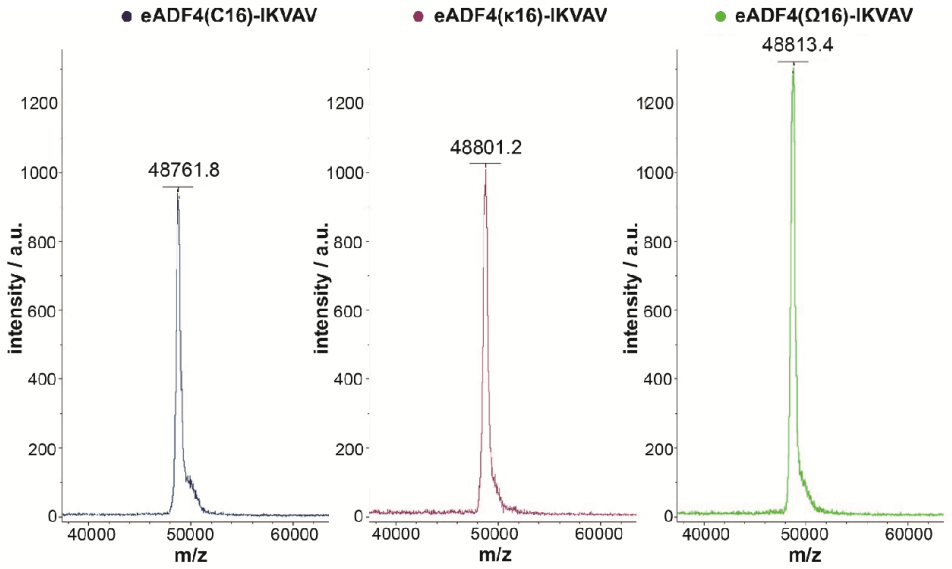

Figure S1: MALDI-TOF spectra of recombinant spider silk proteins. Purified recombinant eADF4-based spider silk proteins (1 mg ml^{-1}) were analyzed using MALDI-TOF to determine their molecular weight (MW). MALDI-TOF spectra are exemplarily shown for eADF4(C16)-IKVAV, eADF4(κ16)-IKVAV and eADF4(Ω16)-IKVAV.

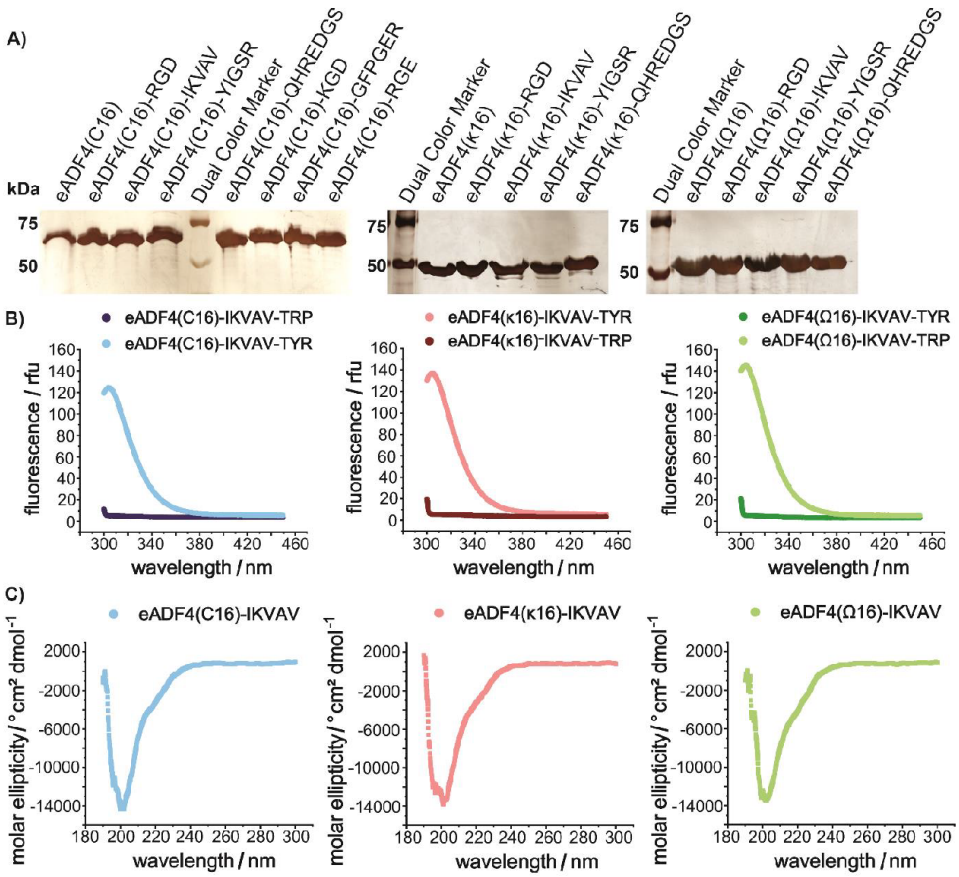

Figure S2: Biochemical characterization of recombinant spider silk proteins. A) 5 µg of purified recombinant spider silk proteins eADF4(C16), eADF4(κ16), eADF4(Ω16) and their respective modified variants were analyzed using silver staining after SDS-PAGE. **B)** Purity of recombinant spider silk proteins was analyzed by detecting specific tyrosine (303 nm, light curve) and tryptophan (347 nm, dark curve) fluorescence emission. While recombinant spider silk proteins contain abundant tyrosine residues, tryptophan fluorescence is a highly sensitive indicator of *E. coli* contaminations. **C)** Secondary structure of soluble spider silk proteins was determined using far-UV circular dichroism spectroscopy. Fluorescence (B) and circular dichroism (C) spectra are exemplarily shown for eADF4(C16)-IKVAV, eADF4(κ16)-IKVAV and eADF4(Ω16)-IKVAV.

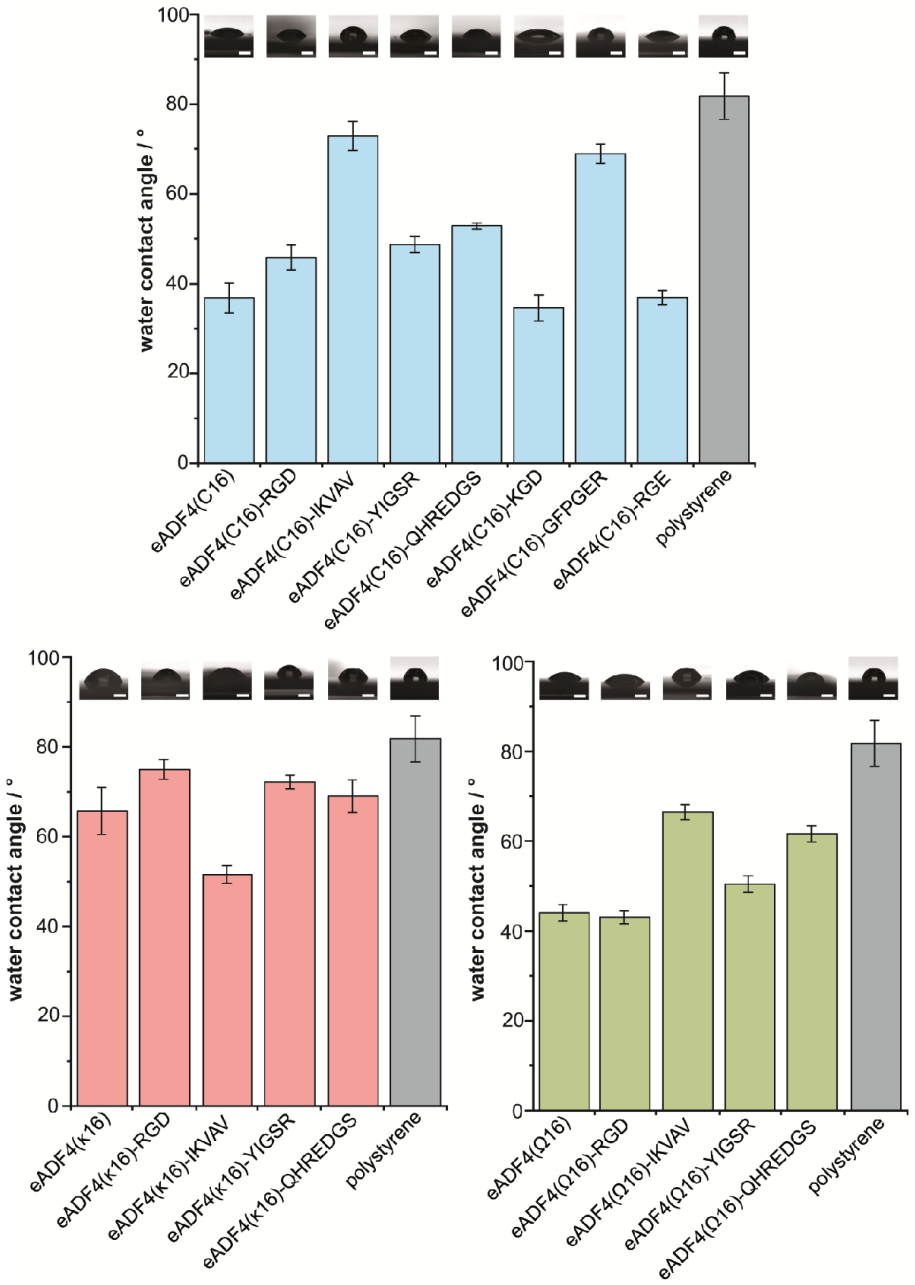

Figure S3: Surface hydrophobicity of recombinant spider silk films. Water contact angle measurements using the sessile drop method were conducted on recombinant spider silk film surfaces and polystyrene surfaces as a control. Scale bar: 1 mm.

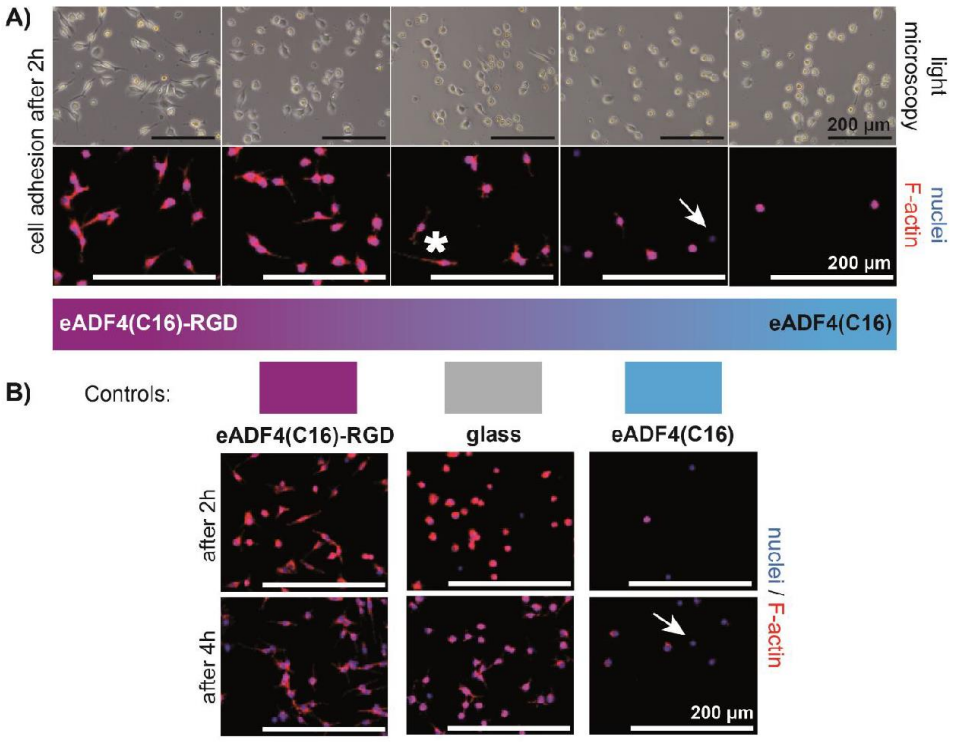

Figure S4: Adhesion of Balb 3T3 fibroblasts on a gradient film made of eADF4(C16) and eADF4(C16)-RGD after 2h and on eADF4(C16), eADF4(C16)-RGD and glass control surfaces after 2 h and 4 h. Cell adhesion on an eADF4(C16)/eADF4(C16)-RGD gradient film showing increasing availability of RGD (A) as well as on control surfaces (B) were analyzed using light microscopy (before washing) and confocal microscopy after washing, fixing and staining the attached cells. Cell nuclei and F-actin cytoskeleton were stained using DAPI (blue) and Phalloidin (red), respectively. White arrows point towards round, only DAPI-stained cells without any F-actin expression. The white asterisk highlights cells starting to form focal adhesions and F-actin stress fibers. Scale bars: 200 µm.

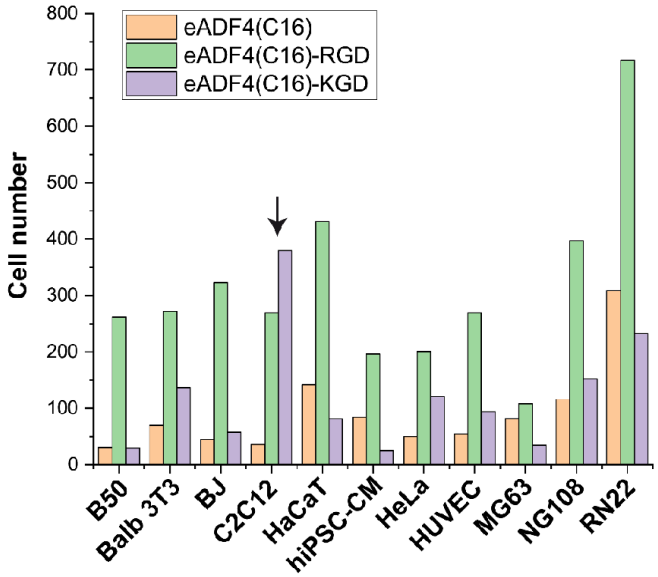

Figure S5: Quantification of attached cells on eADF4(C16) (cytophobic), eADF4(C16)-RGD (cytophilic) and eADF4(C16)-KGD (cell selective). Adhered cells (B50 neuronal cells, mouse Balb 3T3 embryonal fibroblasts, human BJ fibroblasts, mouse C2C12 myoblasts, human HaCaT keratinocytes, human induced pluripotent stem cell derived cardiomyocytes (hiPSC-CM), human HeLa cervix carcinoma cells, human umbilical vein endothelial cells (HUVEC), human MG63 bone fibroblasts, mouse-rat NG108 neuronal hybrid cells, and rat RN22 Schwann cells) on eADF4(C16), eADF4(C16)-RGD and eADF4(C16)-KGD of four selected images were counted and summed up. The black arrow point towards C2C12 cells visualizing the cell selectivity of eADF4(C16)-KGD.

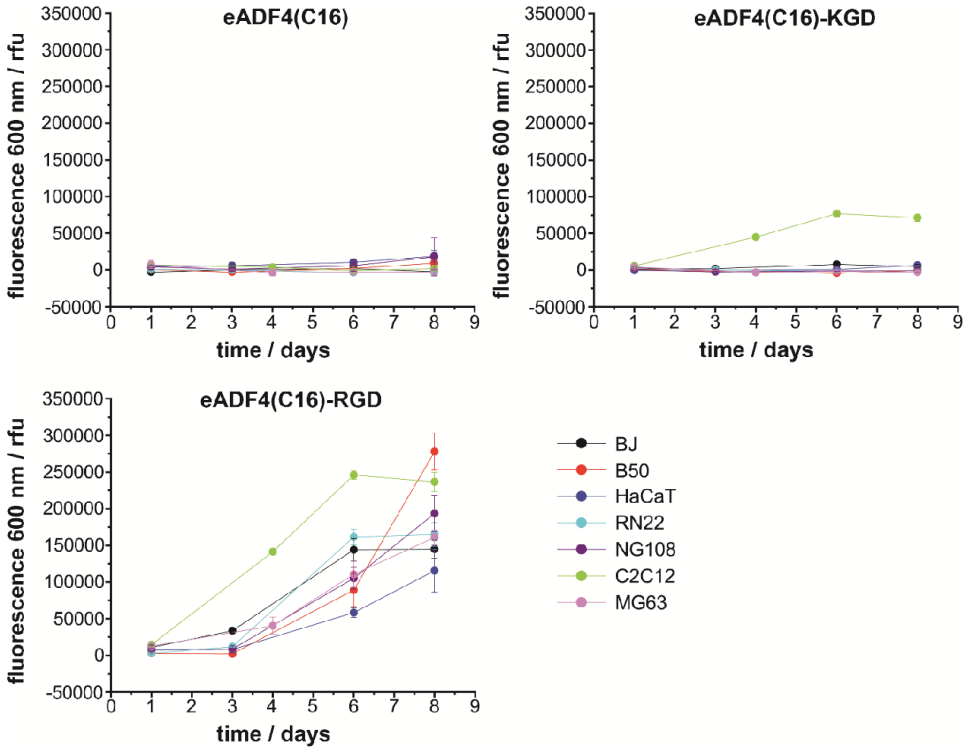

Figure S6: Proliferation of different cell lines on films made of eADF4(C16) (cytophobic), eADF4(C16)-RGD (cytophilic) and eADF4(C16)-KGD (cell selective) over 8 days using the cell titer blue assay. Cell proliferation on different silk surfaces was quantified for human BJ fibroblasts, rat B50 neuronal cells, human HaCaT keratinocytes, rat RN22 Schwann cells, mouse NG108 neuronal cells, mouse C2C12 myoblasts and human MG63 osteoblasts using the cell titer blue assay over 8 days.

Table S2: DNA-oligonucleotides used for genetic fusion of peptide sequences. For each peptide, two matching single stranded DNA-oligonucleotides were designed considering the codon usage of the *E. coli* host system and the established seamless cloning strategy using *Bam HI* and *Hind III* restriction enzymes. Both DNA sequences are displayed in 5' to 3' direction.

Peptide	Sequence (5' → 3')
IKVAV	GATCCATGGGCGGTGGCTCTGGTGGTATTAAAGTGGCGGTGTCTCCGGGTTAATGAA
	AGCTTTCATTAACCCGGAGACACCGCCACTTTAATACCACCAGAGCCACCGCCCATG
YIGSR	GATCCATGGGCGGTGGCTCTGGTGGTTATATTGGTTCGAGATCTCCGGGTTAATGAA
	AGCTTTCATTAACCCGGAGATCTCGAACCAATATAACCACCAGAGCCACCGCCCATG
QHREDGS	AGGAGGATCCATGGGCGGTCAGCATCGTGAAGATGGCAGCGGTTAATGAAAGCTTACTG
	CAGTAAGCTTTCATTAACCGCTGCCATCTTCACGATGCTGACCGCCCATGGATCCTCCT
KGD	GATCCATGGGCGGTGGCTCTGGTGGTAAAGGTGACTCTCCGGGTTAATGAA
	AGCTTTCATTAACCCGGAGAGTCACCTTTACCACCAGAGCCACCGCCCATG
GFPGER	GATCCATGGGCGGTGGCTCTGGTGGTGGTTTTCCGGGTGAAAGATCTCCGGGTTAATGAA
	AGCTTTCATTAACCCGGAGATCTTTCACCCGGAAAACCACCACCAGAGCCACCGCCCATG

7.3. Teilarbeit III

Teilarbeit III wurde 2022 unter dem Titel „*Structure-Property Relationship Based on the Amino Acid Composition of Recombinant Spider Silk Proteins for Potential Biomedical Applications*“ im Journal *ACS Applied Materials & Interfaces* veröffentlicht.

Lentz, S.*; **Trossmann, V. T.***; Borkner, C. B.; Beyersdorfer, V.; Rottmar, M. & Scheibel, T. (2022) Structure-Property Relationship Based on the Amino Acid Composition of Recombinant Spider Silk Proteins for Potential Biomedical Applications. *ACS Applied Materials & Interfaces* **14**: 31751.

https://doi.org/10.1021/acsami.2c09590

* gleichberechtigte Co-Autorenschaft

ACS APPLIED MATERIALS & INTERFACES

www.acsami.org Research Article

Structure–Property Relationship Based on the Amino Acid Composition of Recombinant Spider Silk Proteins for Potential Biomedical Applications

Sarah Lentz, Vanessa T. Trossmann, Christian B. Borkner, Vivien Beyersdorfer, Markus Rottmar, and Thomas Scheibel*

Cite This: *ACS Appl. Mater. Interfaces* 2022, 14, 31751–31766 Read Online

ACCESS | Metrics & More | Article Recommendations | Supporting Information

ABSTRACT: Improving biomaterials by engineering application-specific and adjustable properties is of increasing interest. Most of the commonly available materials fulfill the mechanical and physical requirements of relevant biomedical applications, but they lack biological functionality, including biocompatibility and prevention of microbial infestation. Thus, research has focused on customizable, application-specific, and modifiable surface coatings to cope with the limitations of existing biomaterials. In the case of adjustable degradation and configurable interaction with body fluids and cells, these coatings enlarge the applicability of the underlying biomaterials. Silks are interesting coating materials, e.g., for implants, since they exhibit excellent biocompatibility and mechanical properties. Herein, we present putative implant coatings made of five engineered recombinant spider silk proteins derived from the European garden spider *Araneus diadematus* fibroins (ADF), differing in amino acid sequence and charge. We analyzed the influence of the underlying amino acid composition on wetting behavior, blood compatibility, biodegradability, serum protein adsorption, and cell adhesion. The outcome of the comparison indicates that spider silk coatings can be engineered for explicit biomedical applications.

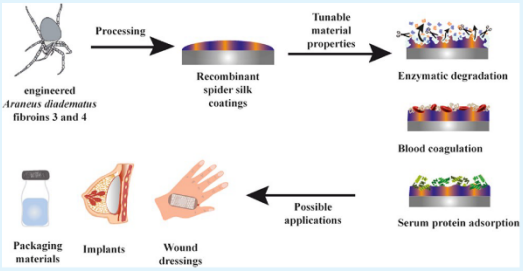

KEYWORDS: *recombinant spider silk proteins, blood coagulation, enzymatic degradation, cell adhesion, protein adsorption, surface properties*

1. INTRODUCTION

One main goal of biomaterials' development is the improvement of their application specificity.[1] However, the performance of a biomaterial strongly depends on its interaction with the surrounding biological environment, which is mainly driven by interactions on the material's surface.[2,3] The crucial step in this process is the formation of a protein layer on the surface of the material within a short time after contact.[2−6] Protein−material interactions are influenced and directed by the properties of the material as well as the body fluid, such as general composition, size, charge, stability, folding, and structure of included proteins. In the case of the biomaterial, its chemical composition, charge, hydrophobicity, wettability, topography, and structure are highly important.[2,4−8] A protein layer formed on the material surface, also named a biocorona, affects subsequent cellular mechanisms, such as cell adhesion, since protein segments accessible for cell surface receptors might influence their adhesion and further cell fate.[2,8,9] However, the foreign body response, inflammation, fibrous capsule formation, and thus a potential rejection reaction of the body are also determined by the adsorbed protein layer.[2,10,11] Since several material surface properties, including roughness, wettability, and charge, trigger responses upon contact with body fluids, such as protein adsorption and cell-related behavior,[2,4,7−9,12] the control of surface properties of biomaterials is one key factor for their successful application in biomedical applications, tissue engineering, and regenerative medicine.[3,7,13] However, depending on the desired field of application, the demands on biomaterials' surface properties are quite different. The class of bioinert materials should interact minimally with the host environment, while bioactive and biospecific materials should actively interact with the biological surrounding and adjacent tissue to stimulate, promote, and guide cellular responses.[1,3,13−16]

Received: May 29, 2022
Accepted: June 20, 2022
Published: July 5, 2022

https://doi.org/10.1021/acsami.2c09590
ACS Appl. Mater. Interfaces 2022, 14, 31751−31766

ACS Applied Materials & Interfaces www.acsami.org Research Article

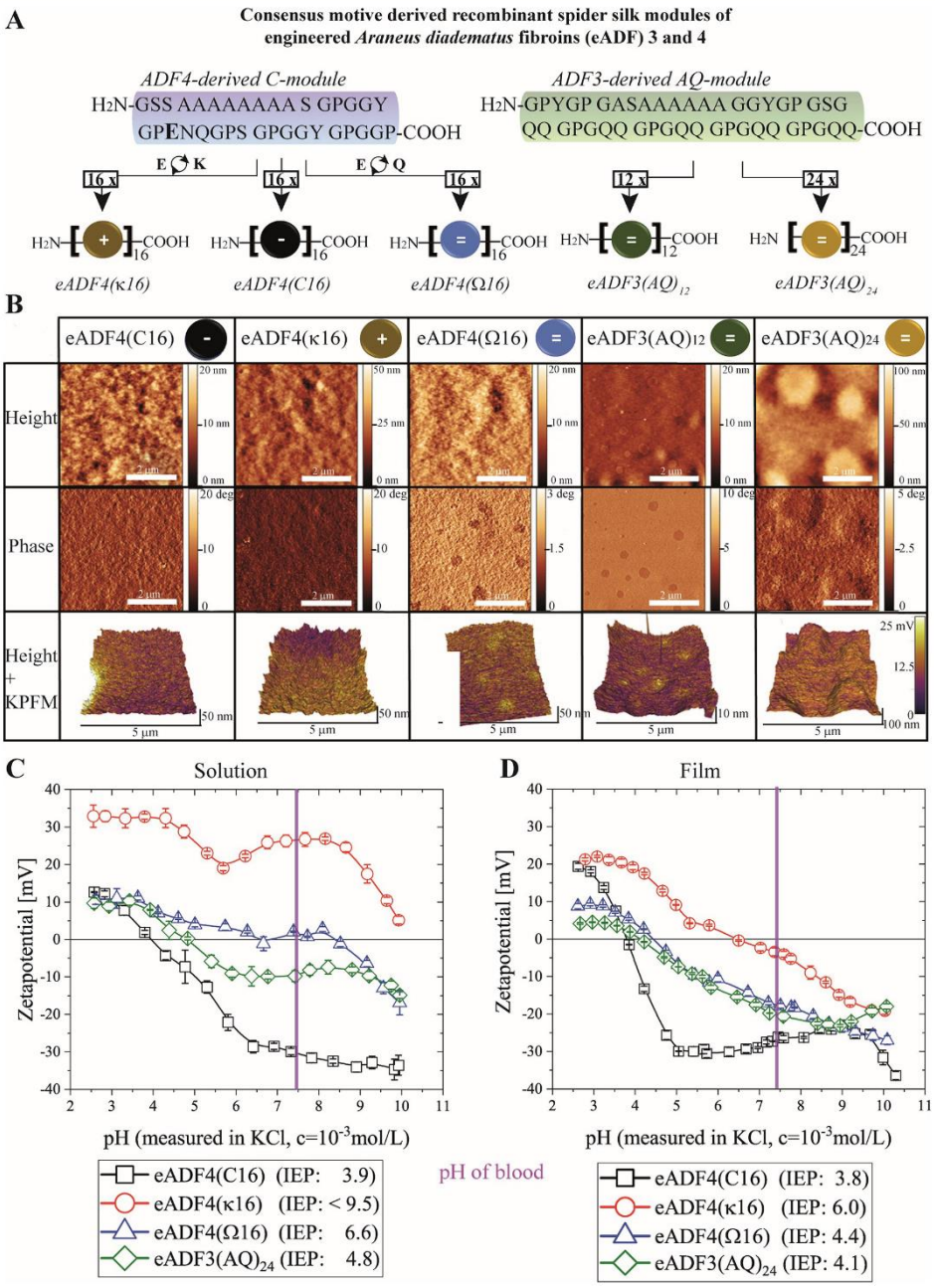

Figure 1. (A) Schematic representation of the amino acid consensus sequences of ADF3 and ADF4 named AQ- and C-modules and the resulting engineered *A. diadematus* fibroins eADF3(AQ)$_{12}$ (48 kDa), eADF3(AQ)$_{24}$ (96 kDa), eADF4(C16) (48 kDa), eADF4(κ16) (48 kDa), and eADF4(Ω16) (48 kDa). ⊖ depicts the zero net charge, ⊕ depicts the positive net charge, and ⊖ depicts the negative net charge. (B) Atomic force microscopy (AFM) images of dry protein films. The last lane depicts Kelvin probe force microscopy (KPFM) images, showing the surface potential (mV) of the spider silk films related to the cantilever overlaid by topography images of these films. (C) Representative ζ potential curves of recombinant spider silk proteins in solution versus pH. (D) Representative streaming potential curves of recombinant spider silk films versus pH. The films made of the recombinant spider silk proteins are the negatively charged variant eADF4(C16) (black curves), the positively charged variant eADF4(κ16) (red curves), and the uncharged variants eADF4(Ω16) (blue curve) and eADF3(AQ)$_{24}$ (green curves). (n = 3 at each pH value.) The purple line indicates the pH of human blood of ~7.4.[37]

https://doi.org/10.1021/acsami.2c09590
ACS Appl. Mater. Interfaces 2022, 14, 31751−31766

On the one hand, bioinert surfaces are used for many different biomedical contact materials interacting with blood, tear fluid, urine, or saliva.[12,17] Thereby, it must be distinguished between in vivo applications, including cardiovascular stents, urine or intravascular catheters, guidewires and ocular devices, or medical devices, which come in direct contact with the patient, and ex vivo applications related to diagnostics and analytical methods of body fluids or biopsies.[12,17] In this context, it is important to mention that blood-contacting devices, such as catheters, artificial heart bladders, or stents, should not only prevent adhesion with the surrounding tissues but also inhibit thrombosis and immunological responses.[3,17−19] Today, the most commonly used materials for such applications are polymeric materials, such as polyurethanes (PUs), poly(tetrafluoroethylene) (PTFE), latex, and silicone-based materials, due to their easy processing and suitable physical properties. However, several of these materials comprise low biocompatibility, increased susceptibility to infection, risk of incrustation, or trigger inflammatory responses as serious disadvantages.[18,20,21] On the other hand, bioactive surfaces are specifically designed, modified, and functionalized to actively engage with the surrounding tissue for their application in drug delivery as a local depot of bioactive substances as well as in tissue engineering and regeneration to support cellular responses, including adhesion, proliferation, or differentiation.[13−16,22]

From the problems associated with bone tissues, including implant loosening, poor healing, and permanent defect or infections, it is clear that such bioactive implants should support tissue integration, prevent microbial infections, and stimulate cells.[23] As mentioned before, many implants are made of polymeric materials but also metals, ceramics, and composites are used, and in addition to difficulties in processing, they also have serious disadvantages in terms of biocompatibility, degradability, and foreign body reaction.[24] In recent years, customizable, application-specific, and modifiable surface coatings have become more and more important to overcome the known limitations and drawbacks of different biomaterials.[13,15,17,23,25] These coatings could be generated using materials like phosphorylcholine or polymers, such as poly(ethylene glycol) (PEG), and naturally occurring biopolymers and proteins, such as extracellular matrix components (e.g., hyaluronic acid and collagen I) or chitosan, as well as hydroxyapatite or silver.[15,17,23,25]

In this context, coatings made of recombinant silk proteins are promising candidates for modifying a wide range of biomaterials, because they are biocompatible, do not trigger an inflammatory response, and can be adapted to a specific application. Since recombinant spider silk-based materials consist of amino acids, they are nontoxic and biodegradable and, therefore, well suited for various biomedical applications.[18,26−30] The dragline spider silk of the European garden spider *Araneus diadematus* comprises at least two major ampullate spidroins (MaSp), the so-called *A. diadematus* fibroins (ADF) 3 and 4.[31−33] A sequence alignment of ADF3 and ADF4 revealed a pairwise identity of 58.1%, mainly deriving from polyalanine and amorphous sequence motifs containing glycine and proline residues (Figure SI1). Although showing similar amounts of proline, alanine, and glycine residues, they differ significantly in the content of glutamine and serine residues, with ADF4 containing more serine and fewer glutamine residues than ADF3.[31] ADF3 represents a more hydrophilic spider silk protein based on the amino acid composition, while ADF4 has a more hydrophobic character.[33] In an established recombinant approach, consensus sequences of the core domains of both proteins, namely, eADF4(C), eADF3(Q), and eADF3(A), have been multimerized, resulting in eADF4(C16) and eADF3(AQ)$_{12}$ or eADF3(AQ)$_{24}$ (Figure 1A).[32,34] To investigate the impact of protein net charge more closely, the uncharged eADF4(Ω16) variant and the positively charged eADF4(κ16) variant were developed.[29,35,36]

Here, recombinant spider silk film surfaces were analyzed concerning their suitability for biomedical applications based on their amino acid composition. We gained insights into the surface properties of spider silk coatings concerning the impact of the underlying amino acid composition including the charge. With these findings, we identified possible biomedical application fields of coatings made of each variant.

2. RESULTS AND DISCUSSION

2.1. Surface Topography and Surface Potential.

Atomic force microscopy (AFM) was used to image the surface topography of spider silk films made of five different spider silk variants, as depicted in Figure 1. Both the eADF3- and the eADF4-derived variants showed smooth and relatively featureless surfaces (Figure 1B). The root-mean-square (rms) roughness of all spider silk films was below 5 nm (Figure SI2).

Films made of eADF3(AQ)$_{12}$ and eADF3(AQ)$_{24}$ showed large patches on the surface, with eADF3(AQ)$_{24}$ being bigger than that of eADF3(AQ)$_{12}$, likely due to the larger molecular weight of this protein. Interestingly, the phase image of the uncharged eADF4(Ω16) showed similar patches as observed for eADF3(AQ)$_{12}$, while the charged variants eADF4(C16) and eADF4(κ16) showed no patchy areas. The surface potential of the detected nanostructures and phase-separated domains were visualized using Kelvin probe force microscopy (KPFM). KPFM measurements qualitatively showed that the patchy character of the phase images of eADF4(Ω16), eADF3(AQ)$_{12}$, and eADF3(AQ)$_{24}$ arose from phase separation of the hydrophilic and hydrophobic motifs of the proteins, indicative of phase-separated (slightly more hydrophobic) β-sheets, which increase the surface potential compared to non-β-sheet areas of the surface.[38−40] Coatings made of recombinant spider silk protein films will mostly be in contact with body fluids. The most important body fluid is human blood with a pH of 7.4.[37] Therefore, electrokinetic measurements, namely, streaming potential measurements of recombinant spider silk coatings and ζ-potential measurements of recombinant spider silk proteins in solution versus pH, were performed to show the surface charge behavior over the pH range from 2.5 to 10 (Figure 1C,D). Furthermore, an isoelectric focusing (IEF) gel electrophoresis of soluble, dialyzed proteins (Figure SI3) was conducted to determine the isoelectric point (IEP) of the spider silk variants. Since a homogeneous gel staining was not possible for the used spider silk proteins, a subsequent western blot analysis was conducted detecting the N-terminally fused T7-tag with a horseradish peroxidase (HRP)-conjugated T7-antibody. The theoretical expected and the experimentally determined IEPs are shown in Table 1. Recombinant spider silk films on silicon were used for streaming potential measurements, and, therefore, the water contact angles on silicon were important for discussing the streaming potential results. Recombinant spider silk protein films showed water contact angles (WCAs) from 50° (eADF4(Ω16)) to 55° (eADF4(κ16)) to more hydrophobic

https://doi.org/10.1021/acsami.2c09590
ACS Appl. Mater. Interfaces 2022, 14, 31751−31766

Table 1. Comparison of Isoelectric Points (IEPs) of Recombinant Spider Silk Proteins[a]

protein	calculated IEP (mV)	IEP estimated from IEF gel	ζ-potential (solution) (mV)	streaming potential (film) (mV)
eADF4(C16)	3.5	4.5	3.9	3.8
eADF4(κ16)	9.7	>8.3	>9.5	6.0
eADF4(Ω16)	7.7	7.8–8.3	6.6	4.4
eADF3$(AQ)_{24}$	7.8	8.3	4.8	4.1

[a]Calculated theoretical IEPs, IEPs estimated from an IEF gel electrophoresis (pH gradient gel), and IEPs of ζ-potential measurements of recombinant spider silk proteins in solution versus IEPs of streaming potential measurements (n = 3 at each pH).

WCA of 70° (eADF4(C16)) up to ~80° (eADF3$(AQ)_{24}$) (see Figure 2).

For the negatively charged variant eADF4(C16), the theoretical IEP of 3.5 was close to the measured IEP in solution ($IEP_{C16,solution}$ = 3.9) and on films ($IEP_{C16,film}$ = 3.8). With a large band at around 4.5, the IEP derived from the IEF gel analysis was also in a similar range (Figure SI3). eADF4(C16) is the most acidic recombinant spider silk protein investigated in this study because of its amino acid sequence, which comprises 16 additional COOH-groups from glutamic acid residues in the repetitive units. The eADF4(κ16) variant is positively charged because the glutamic acid in its consensus motif is substituted by 16 basic lysines. In solution, eADF4(κ16) showed a positive ζ-potential over the entire pH range, which is a typical curve course for protonated samples. The theoretical IEP is at 9.7. The IEP was not observable in the electrokinetic measurements in solution, probably because of too much dissolved CO_2. Additionally, with the IEF gel analysis, it was also not possible to make a precise statement for soluble eADF4(κ16) because the used IEF setup was only designed for the separation of proteins with an IEP range between 3.0 and 8.5 according to the manufacturer. Due to the fact that eADF4(κ16) stays inside the gel pocket and only a very light band was visible, we assume an IEP of above 8.5 (Figure SI3). The streaming potential of eADF4(κ16) films showed a different course of the curve (Figure 1). This is due to the more hydrophobic surface of the film (WCA ~ 55°) compared to that of eADF4(κ16) in solution. In the eADF4(Ω16) variant, the 16 glutamic acid in the repetitive unit are substituted with 16 glutamine residues. Consequently, the eADF4(Ω16) protein comprises more amide functional groups than eADF4(C16). The IEP in solution is a bit lower than the theoretical IEP (7.7), but the curve between pH 6 and 8.5 is always close to zero (Table 1 and Figure 2C). In the IEF gel analysis, three bands were detected for eADF4(Ω16) in an IEP range between 7.8 and 8.3 (Figure SI3), which are close to the theoretical IEP. It is a known mechanism that *Escherichia coli* bacteria start protein degradation N-terminally,[41,42] and, for instance, the missing of methionine as the first amino acid is already known for recombinant spider silk proteins.[30] As a consequence, the free N-terminal amino group is located at different amino acid residues, which could influence the IEP of uncharged proteins more than the IEP of highly charged proteins explaining the three bands for eADF4(Ω16). Furthermore, the IEF gel also showed three bands in the same IEP range between 7.8 and 8.3 for the uncharged eADF3$(AQ)_{12}$ (Figure SI3). For eADF3$(AQ)_{24}$, only one band was detectable at an IEP of around 8.3, which corresponded with the theoretical IEP. Streaming potentials of only one of the eADF3-derived variants were measured, because eADF4-$(AQ)_{12}$ and eADF3$(AQ)_{24}$ just differ in molecular weight. The ζ-potential in solution is more acidic (IEP: 4.8) than the

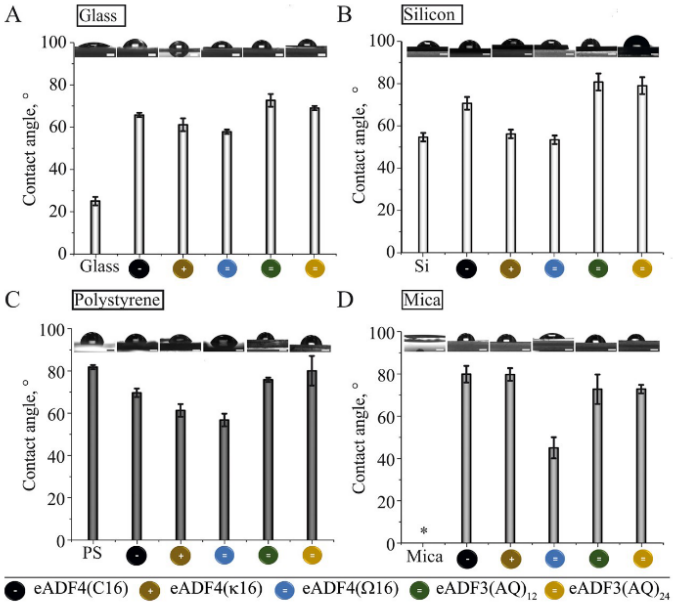

Figure 2. Water contact angles (static drop) of spider silk films in comparison to blank substrates; (A) glass, (B) silicon, (C) polystyrene (PS), and (D) mica. The recombinant spider silk films were post-treated with methanol overnight prior to water contact angle measurements. *Contact angle measurements were not possible due to the complete spreading of the water droplet. Scale bars are 1 mm (n = 9).

https://doi.org/10.1021/acsami.2c09590
ACS Appl. Mater. Interfaces 2022, 14, 31751−31766

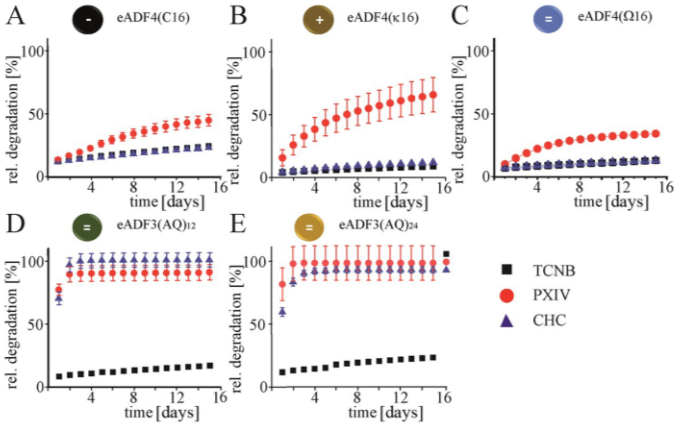

Figure 3. Enzymatic degradation of eADF4(C16) (A), eADF4(κ16) (B), eADF4(Ω16), eADF3$(AQ)_{12}$, and (D) eADF3$(AQ)_{24}$ (E) films in the presence of protease mixture PXIV of *S. griseus* and collagenase CHC from *C. histolyticum* (type IA), as indicated over 15 days at room temperature (RT). The TCNB samples contained no enzyme and served as controls. The enzyme and buffer solutions were exchanged every 24 h (n = 2).

theoretical IEP (IEP: 7.8) as well as the streaming potential (IEP: 4.1).

2.2. Wetting Behavior and Secondary Structure of Recombinant Spider Silk Protein Films. The substrate on which spider silk films are cast on has an impact on spider silk phase separation and on the spider silk film surface properties.[18,38,39] Therefore, in addition to silicium, as stated above, additional surfaces with different hydrophobicities, such as mica, glass, and polystyrene (PS), were used as substrates to analyze the water contact angle (WCA). The structural differences (secondary structure) of the silk films were analyzed using grazing angle attenuated total reflection Fourier transform infrared spectroscopy (GATR-FTIR) before and after post-treatment with MeOH. As cast, the normalized GATR-FTIR spectra of all recombinant spider silk films showed a unimodal peak around 1658−1661 cm^{-1}, assigned to random coil structures (Figure SI4). After post-treatment with MeOH vapor, the GATR-FTIR spectra showed a bimodal curve shape. The β-sheet content increased for all variants, as seen by a shift of the maximum of the GATR-FTIR spectra to the β-sheet-assigned area (1628−1630 cm^{-1}) (Figure SI4).[43] For eADF4(C16) and eADF4(Ω16) films, there was no apparent difference in the secondary structure content on the different substrates. eADF4(κ16) films cast on mica showed a higher random coil content than on the other substrates (higher peak at 1658 cm^{-1}) (Figure SI4). For eADF3-derived proteins, a bimodal curve shape could be observed, and for all four substrates, the random coil content was higher than for the eADF4-derived variants (Figure SI4). In principle, the increase in the β-sheet content turned the recombinant spider silk films water-insoluble.[39] Therefore, all WCA measurements were performed after post-treatment. The WCA of uncoated mica was close to zero, and the drop spread entirely over the surface immediately after its contact with the surface.[44]

The contact angle increased with increasing surface hydrophobicity from mica to glass to silicon to polystyrene (Figure 2). eADF3-derived variants showed WCAs between 69° and 81° regardless of the underlying substrate on all four different substrates. Furthermore, there was no significant difference between the WCA of eADF3$(AQ)_{12}$ and eADF3-$(AQ)_{24}$ on the same substrate, indicating that the molecular weight in this case did not affect WCA. eADF4-derived variants showed different behavior (Figure 2), and the WCA decreased in the order of eADF4(C16) > eADF4(κ16) > eADF4(Ω16) independent of the underlying substrate.

In general, as reported previously,[39] upon coating with recombinant spider silk proteins, all surfaces showed an inverted WCA compared to the uncoated substrates. Here, inverted WCA means that surfaces that were hydrophobic before coating turned more hydrophilic upon coating with spider silk proteins. Vice versa, uncoated, hydrophilic substrates turned more hydrophobic upon spider silk coating. Strikingly, the underlying substrate had less influence on the film formation of the uncharged recombinant spider silk variants, and the uncharged eADF4(Ω16) surfaces always showed the lowest WCAs. These results led to the assumption that the charge of the protein plays an important role in the resulting water contact angles and, thus, surface hydrophilicity and wetting behavior. The ratios between the WCA of the uncoated and the coated substrates showed a clear trend regardless of the absolute values. This led to the assumption that the increase/decrease of WCA is independent of the protein but specific to the substrates; e.g., coating glass with recombinant spider silk proteins led to a 40% increase of WCA compared to that of the uncoated substrate (see Table SI1).

2.3. Biodegradation of Spider Silk Films. To analyze the biodegradability of spider silk films, they were incubated in the presence of protease mixture PXIV from *Streptomyces griseus* (type XIV) and a collagenase (CHC) from *Clostridium histolyticum* (type IA), which reflects model enzymes for digestive and wound proteases, respectively, and represents prominent candidates for evaluating the proteolytic stability of silk proteins.[45−49] As expected, enzymatic degradation was highly dependent on the underlying amino acid sequence (Figure 3). Films of both recombinant eADF3 spider silk variants were almost completely degraded within the first 48 h in the presence of both enzymatic mixtures, because the ADF3-derived variants are more hydrophilic than ADF4-derived variants. It is known that a hydrophilic network allows a fast inflow of the enzymes in the bulk material, leading to increased cleavage of the peptide bonds.[50] In contrast, eADF4-based films could not be digested by collagenase CHC. The

https://doi.org/10.1021/acsami.2c09590
ACS Appl. Mater. Interfaces 2022, 14, 31751−31766

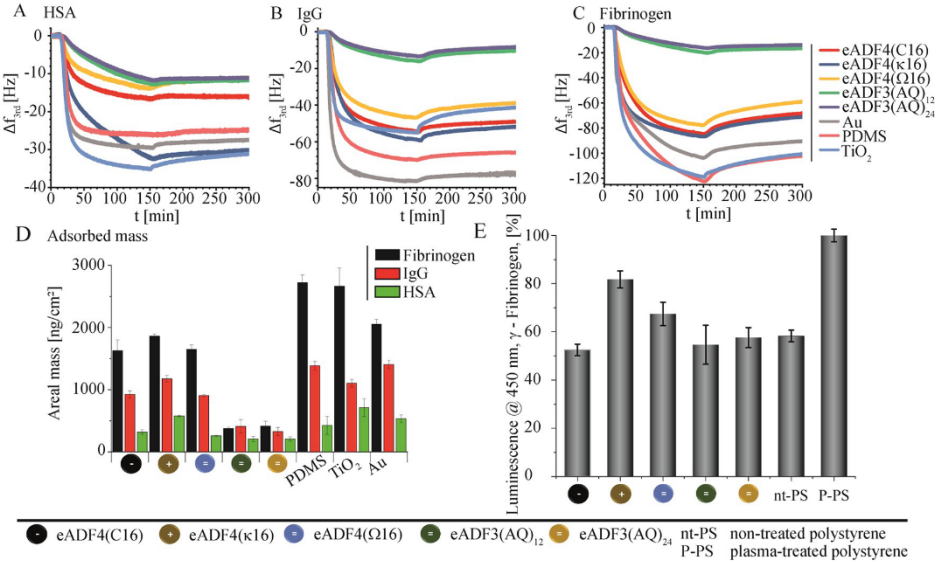

Figure 4. Third overtone (Δf_{3rd}) of quartz crystal frequency of protein adsorption is shown for the spider silk films. (A) HSA, (B) IgG, and (C) fibrinogen were added to various surfaces, as depicted in the legend. All samples were washed with PBS buffer from 150 min until 300 min to remove the loosely adsorbed protein. The adsorbed areal mass of serum proteins was calculated using the Sauerbrey equation or the viscoelastic Kelvin–Voigt model, depending on the protein behavior. The blank Au–QCM-D surface, TiO_2, and PDMS were used as reference substrates. (D) The adsorbed areal mass is shown at maximum during serum protein adsorption before the PBS buffer flow and desorption started. The amount of the adsorbed mass to spider silk films is in the order of eADF4(κ16) > eADF4(C16) ≈ eADF4(Ω16) > eADF3$(AQ)_{12}$ ≈ eADF3$(AQ)_{24}$ (n = 3). (E) Indirect enzyme-linked immunosorbent assay (ELISA) determining the restructuring of human fibrinogen by detecting the usually hidden carboxyl-terminal peptide of the γ-chain using a monoclonal mouse anti-γ-chain antibody (2 μg mL^{-1}) and a secondary antibody with a HRP function (1:10 000). Luminescence was measured at 450 nm. Nontreated and oxygen plasma polystyrene served as control.

measured signal was as low as for the buffer control and, thus, a result of washing. Protease XIV digested eADF4-based films but to a much lower extent than ADF3-based ones. Among the eADF4 variants, films of the positively charged eADF4(κ16) showed the fastest proteolytic degradation (Figure 3A–C). After 15 days, approximately 45% of the eADF4(C16) films, 35% of the eADF4(Ω16) films, and 70% of the eADF4(κ16) spider silk films were degraded by protease XIV. Proteases of the mix PXIV exhibit an unspecific cleavage pattern, while the collagenases of mix CHC cleave at −/P/X↓G/P/− (with X representing a neutral amino acid).[45] In eADF4-based proteins, only one such pattern, namely, −/P/S/G/P/− could be found. In contrast, eADF3(AQ)-based proteins showed the −/P/Y/G/P/− and three further −/P/G/Q/Q/G/P/− amino acid motifs. We assume that all motifs in eADF3(AQ)-based proteins could be cleaved by the CHC collagenase mix and that the serine in eADF4-based variants reduced the enzyme interaction.

The previously published results showed that soluble, unstructured eADF4(C16) proteins are degraded orders of magnitude faster than β-sheet-rich spider silk films.[45] In a soluble state, the intrinsically unstructured spider silk proteins are freely accessible to enzymes leading to enhanced enzymatic interaction and degradation rate.[45] In contrast, in the bulk state in the films, the protein sequence is densely packed,[38] leading to a decelerated enzymatic degradation rate.[45]

2.4. Formation of a Protein Layer on Spider Silk Film Surfaces. *2.4.1. Adsorption of Essential Blood Serum Proteins.* The first response to the implantation of biomaterials is the formation of a protein layer on its surface. Therefore, controlling protein adsorption is crucial for enhancing the biocompatibility of a material.[2−6] Protein adsorption on biomaterial surfaces is influenced by a multitude of parameters, including chemical composition, charge, wettability, and topography.[2−6] Thus, protein adsorption on spider silk films was determined using three essential blood proteins, human serum albumin (HSA), immunoglobulin G (IgG), and fibrinogen (Fib).[6] Quartz crystal microbalance (QCM) measurements allowed calculating the adsorbed mass of the respective proteins on the spider silk films in situ based on the third overtone of the frequency of the respective protein (Figure 4A–C). Therefore, the three essential blood proteins were floated 150 min over coatings of recombinant spider silk proteins and three reference materials poly(dimethylsiloxane) (PDMS), TiO_2, and gold (Au), which are often used in biomedical applications. After 150 min, the coatings were flushed for another 150 min with phosphate-buffered saline (PBS) buffer to remove the loosely bound protein from the surface. The adsorbed mass (Figure 4D) represents the adsorbed mass after washing with 1× PBS. A slight change in frequency was observed for all three blood proteins by washing the films with 1× PBS. As a consequence, just small amounts of proteins were loosely bound to the surface. Strikingly, fibrinogen was less prone to adsorb on silk surfaces than on the control materials (Figure 4C,D). Comparing films made of the spider silk variants, the adsorption of fibrinogen and IgG was higher on films made of eADF4 variants than on that of eADF3 variants (Figure 4), indicating a clear sequence but not really charge-dependent protein adsorption, as eADF4(Ω16) is also uncharged. The direct comparison of

https://doi.org/10.1021/acsami.2c09590
ACS Appl. Mater. Interfaces 2022, 14, 31751−31766

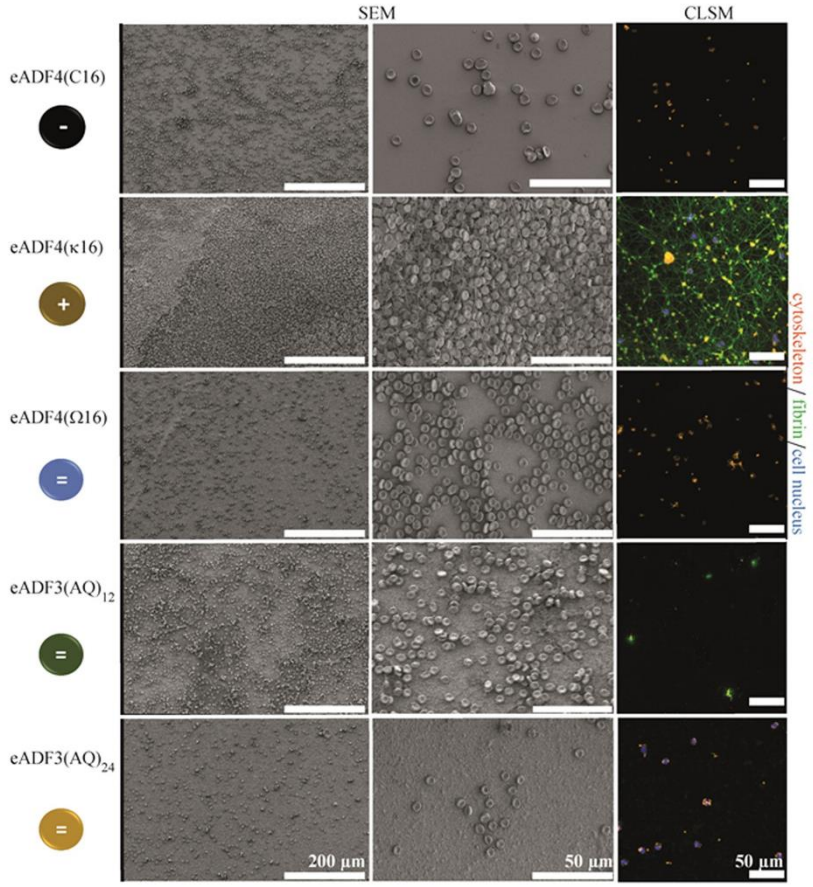

Figure 5. SEM and CLSM images of spider silk films incubated in whole human blood at dynamic conditions (10 rpm) for 35 min. The blood incubated samples were immuno-stained to visualize the cytoskeleton, fibrin (green), and the cell nuclei (blue) (CLSM) or they were dehydrated and sputter-coated with 10 nm gold (SEM). Scale bars are as indicated for the first row of 200 μm and for the last two rows of 50 μm (n = 3).

uncharged spider silk variants showed that the protein adsorption on eADF3$(AQ)_{12}$ and eADF4$(AQ)_{24}$ was significantly decreased compared to that on eADF4(Ω16). This finding is likely based on a higher hydrophobicity of ADF4-based materials. Several studies support this finding, as fibrinogen adsorption is enhanced on hydrophobic surfaces.[6,51,52] However, in addition to the sequence-dependent differences of protein adsorption between eADF3 and eADF4 variants, a clear surface charge effect could be observed when only considering differently charged eADF4 spider silk proteins. While the negatively charged eADF4(C16) and uncharged eADF4(Ω16) surfaces adsorbed nearly the same amount of proteins, the positively charged eADF4(κ16) variant exhibited higher protein adsorption for all investigated serum proteins (Figure 4D). Thus, the combination of a positively charged and hydrophobic surface led to higher protein adsorption, as all other spider silk variant films showed lower protein adsorption. This supports the assumption that a combination of amino acid composition and charge of a coating is the reason for specific protein adsorption. Generally, the spider silk film surfaces showed a protein adsorption behavior for the model proteins in the order of eADF4(κ16) > eADF4(C16) ≈ eADF4(Ω16) > eADF3$(AQ)_{12}$ ≈ eADF3-$(AQ)_{24}$. A study by Kidoaki and Matsuda analyzing the same serum proteins showed that surfaces with carboxyl functional groups generally showed the lowest protein adsorption. In that case, fibrinogen adsorption was stronger compared to that of albumin and IgG adsorption.[53] Our results indicated that the adsorption of the selected model proteins is dependent on the amino acid sequence as well as the surface charge of spider silk films or a combination of both. Since albumin and fibrinogen are negatively charged at physiological pH,[54] a mostly electrostatically driven interaction of negatively charged proteins and positively charged spider silk films could be an explanation for the results of eADF4 variants, with almost identical primary structures differing only in individual residues.[55,56] Since hydrophilic material surfaces with a neutral charge seemed to be more resistant to protein adsorption,[57] and eADF3 variants are more hydrophilic than eADF4 variants, the reduced protein adsorption noted there is more likely dependent on the underlying (hydrophilic) primary structure.

2.4.2. Conformational Changes of Fibrinogen during Adsorption on Spider Silk Surfaces. Serum proteins adsorbed

https://doi.org/10.1021/acsami.2c09590
ACS Appl. Mater. Interfaces 2022, 14, 31751−31766

ACS Applied Materials & Interfaces www.acsami.org Research Article

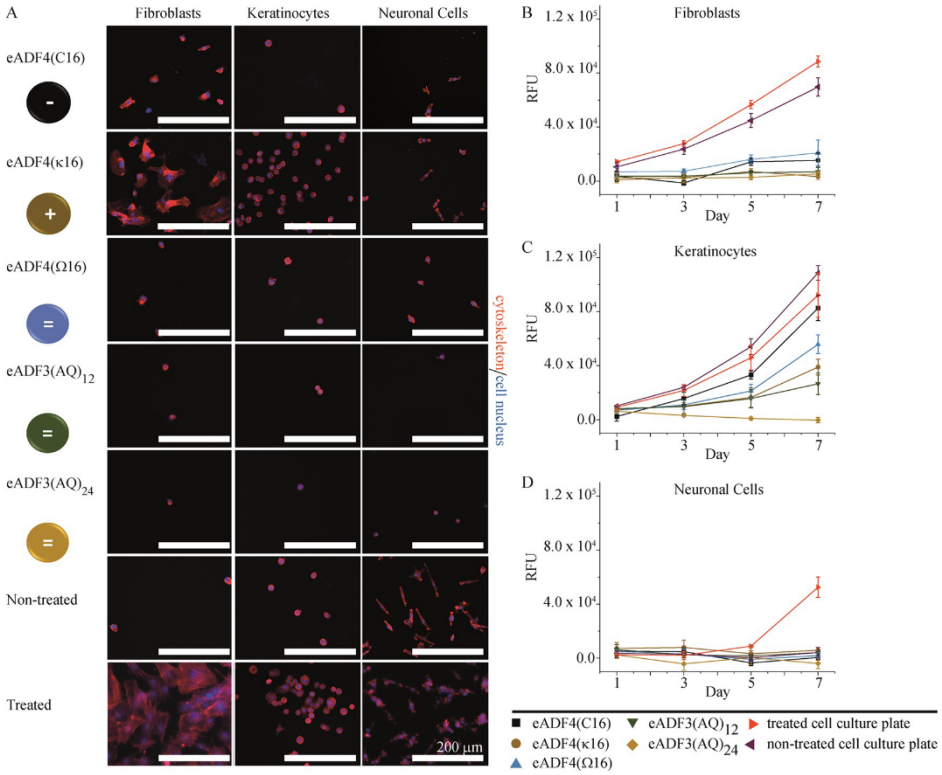

Figure 6. Adhesion and proliferation of human BJ fibroblasts, human HaCaT keratinocytes, and rat B50 neuronal cells on spider silk films made of eADF4(C16), eADF4(κ16), eADF4(Ω16), eADF3(AQ)$_{12}$, and eADF4(AQ)$_{24}$ and polystyrene surfaces as controls. (A) Primary cell adhesion in the presence of FCS was analyzed using fluorescence microscopy after 4 h of cultivation. Cell nuclei and F-actin cytoskeleton were stained using DAPI (blue) and phalloidin−rhodamine (red), respectively. (B−D) Proliferation of mammalian cells over 7 days was investigated by measuring the resofurin fluorescence of metabolized resazurin of the cell titer blue assay on days 1, 3, 5, and 7 (n = 3).

on biomaterial surfaces can influence a biomaterial's behavior; for instance, fibrinogen can trigger platelet adhesion and blood coagulation on such a surface.[6] Interestingly, it is not the total amount of surface-bound fibrinogen but its conformation and the accessibility of cryptic binding sites, exposed by the restructuring of fibrinogen during adsorption, that are decisive for subsequent platelet interaction and blood coagulation, enhancing the risk of cardiovascular diseases.[6,58,59] Thus, in addition to the quantification of total fibrinogen mass using QCM-D, the conformational changes of fibrinogen due to adsorption on spider silk surfaces were analyzed. Therefore, an indirect enzyme-linked immunosorbent assay (ELISA) with the mouse monoclonal antibody 2.G2.H9 explicitly binding to the carboxyl-terminal peptide of the human fibrinogen γ-chain was conducted to detect conformation-specific accessibility (Figure 4E).[59,59] For eADF4-based films, the highest amount of restructured fibrinogen was obtained in the case of the positively charged eADF4(κ16) variant, followed by the uncharged eADF4(Ω16) and the negatively charged eADF4-(C16) variant (Figure 4E). Interestingly, the conformational change of fibrinogen on uncharged eADF3(AQ)$_{12}$ and eADF3(AQ)$_{24}$ films was at a similar level as for the negatively charged eADF4(C16) variant.

Comparing adsorption (QCM-D) and conformational changes (ELISA) of fibrinogen on spider silk film surfaces showed that generally less fibrinogen is adsorbed on hydrophilic eADF3 variants, but restructuring takes place in all cases. Although eADF4(C16) films showed a higher total adsorption, the conformational changes of fibrinogen were at similar levels compared to that of eADF3 variants. Furthermore, the level of fibrinogen restructuring was only slightly enhanced on uncharged eADF4(Ω16) films compared to those of eADF4-(C16) and eADF3(AQ)-based ones. These results rebut a fibrinogen restructuring based on the spider silk sequences. Since the highest fibrinogen restructuring takes place on the positively charged eADF4(κ16) variant, which at the same time also adsorbs the highest fibrinogen amount, the combination of a hydrophobic amino acid sequence with a positive charge seems to trigger the unfavorable conformational change of fibrinogen. As mentioned before, hydrophilic material surfaces with a neutral charge are more resistant to protein adsorption,[57] which could explain the better performance of eADF3-based variants. Furthermore, the negative charge of fibrinogen at physiological pH[52] could explain its enhanced interaction with aminated and, thus, positively charged surfaces compared to negatively charged, carboxylated surfaces.[55,56]

2.5. Interaction of Human Blood with Spider Silk Film Surfaces. In addition to the protein adsorption and fibrinogen conformation analysis, spider silk films were also analyzed for

https://doi.org/10.1021/acsami.2c09590
ACS Appl. Mater. Interfaces 2022, 14, 31751−31766

inducing blood coagulation to complete the blood compatibility analysis of spider silk surfaces. As mentioned before, the control of blood coagulation, to either prevent or promote it, is of utmost importance for biomedical applications. Blood coagulation is a complex cascade influenced by different factors, including protein adsorption and restructuring, platelet adhesion and their activation, coagulation, and thrombosis.[6,11] Here, the spider silk films were analyzed regarding blood clotting and fibrin formation, which were mainly enhanced on the positively charged, hydrophobic eADF4(κ16) films (Figure 5). Scanning electron microscopy (SEM) and confocal laser scanning microscopy (CLSM) of stained fibrin networks revealed that surfaces made of uncharged eADF3$(AQ)_{12}$, eADF3$(AQ)_{24}$, eADF4(Ω16), or the negatively charged eADF4(C16) did not induce blood clotting or fibrin formation since only erythrocytes were detectable. However, the positively charged eADF4(κ16) induced severe blood clotting and fibrin formation, as depicted previously,[60] with erythrocytes being entrapped in a fibrillar fibrin network (Figure 5). The results of the blood coagulation assay are in line with the serum protein adsorption and the fibrinogen restructuring (Figure 4). Especially the adsorption and restructuring of fibrinogen are central processes triggering subsequent platelet activation and the blood coagulation cascade.[6,58,59] Furthermore, fibrinogen represents the precursor molecule of fibrin, which is the predominant structural component in blood coagulation/clotting and thrombus formation.[6] Since positively charged eADF4(κ16) surfaces exhibited the highest amount and restructuring of adsorbed fibrinogen, enhanced blood coagulation and fibrin expression have been expectable. These results are in accordance with a previous study on the formation of a biomolecular corona on spider silk films and particles made of eADF4(C16) and eADF4(κ16), showing enhanced protein adsorption, fibrin network formation, and blood clotting on the positively charged silk, independent of the morphology.[60]

In this study, erythrocytes were also visible on all investigated samples, but the whole human blood was in a coagulated state after contact with eADF4(κ16) materials, while it was still liquid in the case of eADF4(C16) ones.[60] This finding confirmed that the adsorption of erythrocytes on surfaces has a negligible effect on subsequent blood coagulation and thrombus formation.

Sperling et al. have already shown that the coagulation and the fibrin network formation are enhanced on positively charged surfaces but not on negatively or uncharged surfaces, supporting our findings.[52] The blood coagulation response on the positively charged eADF4(κ16) could be based on negatively charged proteins or molecules, e.g., heparin interacting via ionic interactions or activating further blood coagulation cascades.[52]

2.6. Mammalian Cell Interaction with Spider Silk Films. For biomedical applications, tissue encapsulation is another important issue and should either be prevented, e.g., for catheters[18] or implants,[27] or specific cell adhesion should be supported, e.g., in tissue regeneration.[30] Surface charge, in accordance with surface roughness or wettability, can regulate cell adhesion on a material.[8,18,22] It is relevant to determine the relationship between the underlying spider silk protein sequence and cellular adhesion and growth. Therefore, primary cell adhesion after 4 h and cell growth over 7 days on spider silk films were investigated using three mammalian cell lines (human dermal fibroblasts (BJ), rat neuronal cells (B50), human keratinocytes (HaCaT); Figure 6). The primary cell adhesion after 4 h was analyzed using fluorescence microscopy of stained cell nuclei (4′,6-diamidino-2-phenylindole (DAPI)) and the F-actin cytoskeleton (phalloidin) (Figure 6A). Fluorescence microscopy revealed indeed that the positively charged spider silk film surface supported early cell attachment and expression of F-actin stress fibers; however, cells also attached to eADF4(C16) and eADF4(Ω16) surfaces. In contrast, only a few cells adhered to uncharged eADF$(AQ)_{12}$ and eADF3$(AQ)_{24}$ spider silk films, showing a round morphology without spreading or enhanced F-actin production. These results showed a sequence-dependent cell adhesion, indicating that the more hydrophobic eADF4 spider silk variants promote primary cell adhesion. The cell proliferation assay of these mammalian cell lines showed that none of the investigated spider silk surfaces promoted cell growth as strong as polystyrene surfaces (Figure 6B−D). Since eADF4 and eADF3 amino acid sequences do not contain any specific cell interaction motifs,[61] mainly the structural arrangement of hydrophobic and hydrophilic parts and to a lower extent the different charges are responsible for the primary cell interaction. Usually, cells prefer positively charged surfaces for cell adhesion due to their negatively charged cell surface.[38−40] One previously published study analyzed cardiomyocyte attachment on non-post-treated eADF4(C16), eADF4(κ16), and eADF4(Ω16) films cast from formic acid on glass substrates and showed that only the positively charged variant promoted cardiomyocyte attachment.[40] Another study showed that mammalian cells could grow on post-treated eADF4(κ16) but not on eADF4(C16) coatings cast from aqueous solutions on catheter surfaces.[18] However, in comparison to our results, these studies used different substrates, pretreatments, solvents, and post-treatment methods, making a direct correlation difficult. Thus, we conclude that cell adhesion could be influenced by these parameters to be cytophilic or cytophobic. We assume that the pretreatment with ozone used here to enable a homogeneous film formation led to a different structural assembly of the amino acid sequence of eADF4-based variants compared to the other studies using the same spider silk variants. Thus, the surface properties could be changed leading to a reduced mammalian cell interaction. However, if an application requires cell adhesion and growth, spider silk proteins have to be further modified and functionalized (e.g., with an RGD-motif) to enable cell attachment and growth on silk scaffolds, as shown previously.[30,40] Thus, in correlation with protein adsorption (Figure 4) and blood coagulation (Figure 5), the negatively charged eADF4(C16) and the uncharged eADF4(Ω16), eADF3$(AQ)_{12}$, and eADF3$(AQ)_{24}$ variants reflect promising coating materials for, e.g., catheters (as shown previously)[18] or stents, where interactions with cells should be decreased.

3. CONCLUSIONS

The interaction of a biomaterial with the surrounding biological environment is crucial for its performance, and it is eligible if this is controllable depending on the application.[2,3] Since the implant surfaces come in direct contact with different physiological body fluids, the surfaces of medical devices that should not interact with these fluids, like catheters, implants, or contact lenses,[12,17] as well as packaging materials, have to be modified, e.g., with coatings, to protect or stabilize such implants.[62,63] Further, surfaces could enhance wound healing by activating blood coagulation[64,65] or act as a stationary drug

https://doi.org/10.1021/acsami.2c09590
ACS Appl. Mater. Interfaces 2022, 14, 31751−31766

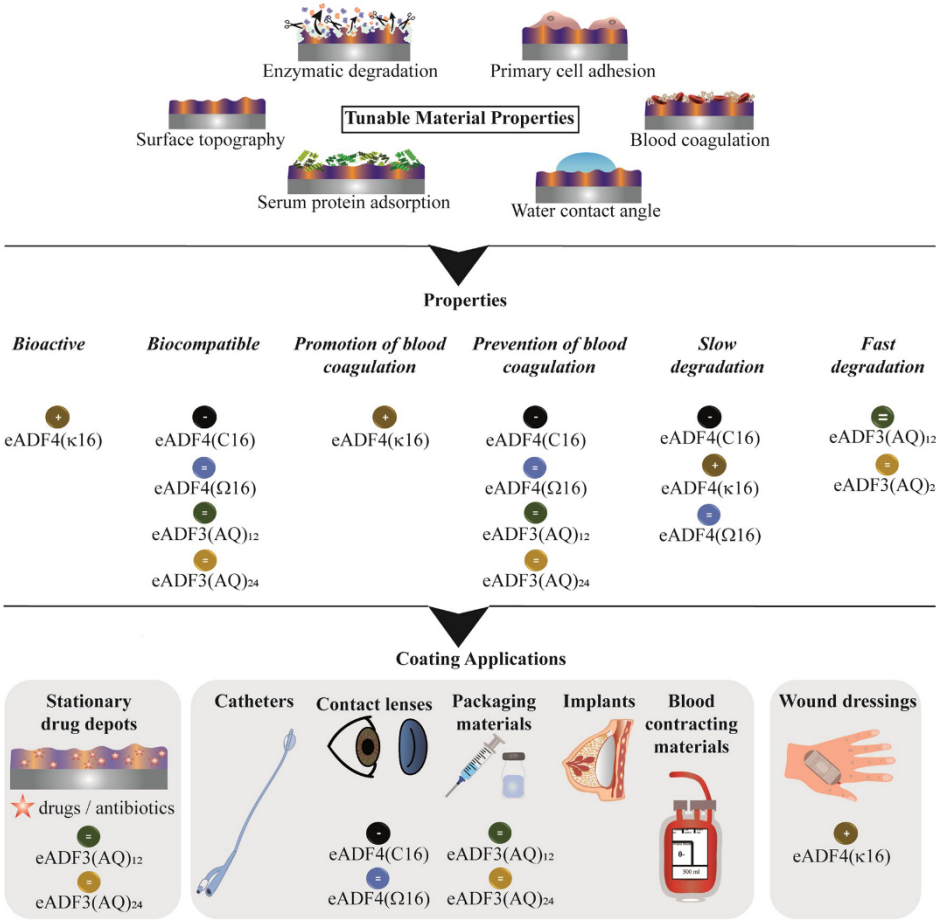

Figure 7. Summary of properties and tentative biomedical applications for films made of five different spider silk variants.

depot releasing bioactive molecules.[63] Particularly, with regard to the mentioned applications, recombinant spider silk materials interact differently with serum proteins, whole human blood, and mammalian cells depending on the underlying protein sequence (Figure 7).

Among the tested spider silk derivatives, eADF4(C16) and eADF4(Ω16) are promising candidates for applications as a coating material for implants or medical devices coming in direct contact with different physiological body fluids, as well as storage materials for, e.g., drugs or growth factors with long lifetime. Films made of both proteins are biocompatible and combine necessary requirements, including a smooth surface, slow biodegradation and resistance against proteolytic enzymes, low adsorption and conformational change of blood serum proteins, (partial) microbial repellence, no blood coagulation, and cell repellence of different mammalian cell lines.

Since films made of eADF3(AQ)$_{12}$ and eADF3(AQ)$_{24}$ also combine these important features except long-time stability, they are promising candidates for similar applications but where fast biodegradation is desired. Furthermore, due to their fast biodegradation, coatings made thereof are appropriate candidates for stationary depots releasing bioactive substances, such as drugs or antibiotics.

In contrast, coatings made of the positively charged eADF4(κ16) seem to be biologically active, as they promote the adsorption of blood serum proteins, blood coagulation, and cell adhesion of selected mammalian cell lines. Nevertheless, coatings made thereof are also degradable by digestive proteases. Due to the enhanced stimulation of blood coagulation, eADF4(κ16) films are promising candidates for, e.g., wound dressings.

4. EXPERIMENTAL SECTION

4.1. Materials. All chemicals were purchased from Roth (Karlsruhe, Germany) with analytical grade if not stated otherwise. eADF4(C16) was purchased from AMSilk GmbH (Planegg/München, Germany). The IEF SERVAGel IEF 3−10 Starter kit was purchased from Serva. Protease mixture (PXIV) from *S. griseus* (type XIV), collagenase (CHC) from *C. histolyticum* (type IA), formic acid, human fibrinogen, recombinant human albumin (HSA), and immunoglobulin (IgG) from rabbit serum were purchased from Sigma-Aldrich (Munich, Germany). Bovine fibrinogen was purchased from TCI (TCI Europe N.V., Zwijndrecht, Belgium). 5/6-Carboxyfluorescein succinimidyl ester (NHS-fluorescein) was pur-

https://doi.org/10.1021/acsami.2c09590
ACS Appl. Mater. Interfaces 2022, 14, 31751−31766

chased from Thermo Fisher Scientific (Darmstadt, Germany). Dimethylformamide (DMF) and ethanol were purchased from VWR (Darmstadt, Germany). Poly(dimethylsiloxane) (PDMS) (Sylgard 184 Silicone Elastomer) was purchased from Dow Corning (Wiesbaden, Germany). Q-Sense Ti sensor chips (QSX 310 Ti) were purchased from LOT-QuantumDesign GmbH (Darmstadt, Germany). The used water was ultrapure (Milli-Q) and obtained using a Merck Millipore system (Billerica, MA). Antibodies for fibrinogen ELISA were purchased from Santa Cruz Animal Health. ECL Western Plus and LimuLight detection solutions were purchased from Merck. The cell titer blue assay was purchased from Promega.

4.2. Production of eADF4(Ω16), eADF4(κ16), eADF3(AQ)$_{12}$, and eADF3(AQ)$_{24}$. Silk proteins were recombinantly produced using *E. coli* (BL21 gold (DE3)) in a fermenter using the fed-batch technique.[32] The recombinant spider silk proteins eADF3(AQ)$_{12}$ and eADF3(AQ)$_{24}$ were purified using a heating step and ammonium sulfate precipitation, as described previously.[32] eADF4(κ16) was produced as reported earlier.[29] eADF4(Ω16) was also purified, as described previously.[36]

4.3. Processing of eADF3 and eADF4 Spider Silk Proteins into Films. For film casting, all eADF3- and eADF4-based recombinant spider silk proteins were dissolved in formic acid at a concentration of 5 mg mL^{-1} for 1−2 h at room temperature. Since different substrates and sample sizes were necessary for the performed characterization methods, the appropriate film casting procedures are explained at the beginning of each respective analysis paragraph.

4.4. Characterization of Surface Topography and Surface Potential of Spider Silk Films. *4.4.1. Preparation of Protein Films.* The recombinant spider silk films were cast (c = 5 mg mL^{-1}) onto freshly RCA-cleaned, ozone-treated Si-wafers. The post-treatment was performed in MeOH$_{abs.}$ vapor overnight.

4.4.2. Atomic Force Microscopy (AFM). For surface morphology characterization, film surfaces were analyzed in tapping mode using a Dimension 3100 Nanoscope V (Bruker, Karlsruhe, Germany) with a resolution of 512 to 512 data points at 0)12 to 1 Hz. Silicon cantilevers (OTESPA-R3, Bruker, Karlsruhe, Germany) were used with a force constant of 26 N m^{-1}. The average roughness R_a was calculated in an area of 25 μm^2. Silicon cantilevers (OTESPA-R3, Bruker, Karlsruhe, Germany) were used with a force constant of 26 N m^{-1}. The average arithmetic roughness R_a was calculated in an area of 25 μm^2.

4.4.3. Kelvin Probe Force Microscopy (KPFM). For analyzing the surface potential of spider silk films, KPFM measurements were performed on a Cypher ES (Oxford Instruments, Asylum Research, Santa Barbara) in air at an ambient temperature and pressure. The instrument was operated in a dual-frequency mode (DFM). Topographic images were recorded simultaneously with KPFM images (512 × 512 lines, 1 Hz, 5 μm × 5 μm). An asylum electrolever tip with a conductive coating (TI/Ir) (Asyelec.01-R2, f = 75 kHz, k = 2.8 N m^{-1}) was used for KPFM measurements.

4.5. Electrokinetic Measurements of Spider Silk Proteins. *4.5.1. Streaming Potential Measurements of Recombinant Spider Silk Films.* Si-wafers (2 cm × 1 cm) were cleaned with alkaline RCA cleaning. Therefore, the Si-wafers were placed into a Teflon sample holder and a mixture consisting of ammonia hydroxide, hydrogen peroxide, and Milli-Q-water (1:1:5). The Si-wafers were stirred for 1 h, at 70 °C, and afterward thoroughly rinsed with MQ-water and dried with a N_2 flow. The recombinant spider silk films were cast by drop-casting. Therefore, all recombinant spider silk proteins were dissolved in formic acid (c = 5 mg mL^{-1}). The Si-wafer surfaces were activated using O_2-plasma (Plasma Technology, Mini-Flecto, 1 min, 100% power, 0.1 mbar, 100% O_2). Afterward, 200 μL of the recombinant spider silk solution was cast onto the Si-wafer and the formic acid was evaporated overnight. Then, the dried films were placed in a methanol atmosphere for 24 to post-treat the films. Finally, the films were dried at room temperature. The ζ-potential was determined with streaming potential measurements using a SurPASS 3 (Anton Paar, Austria). The post-treated recombinant spider silk films were inserted into the cylindrical cell equipped with Ag/AgCl electrodes. As electrolyte solution, KCl (c = 0.001 M) was used. The pressure changed during the measurement in the range of 600−200 mbar. The acidic or alkaline pH region measurements were started at neutral pH. 0.1 M HCl or 0.1 M KOH solutions were used for pH adjustment. The measurement was repeated at least twice for each recombinant spider silk protein with three measurements at each pH. The ζ-potential was calculated according to Smoluchowski.

4.5.2. Electrokinetic Measurements of Soluble Spider Silk Proteins. For characterizing the isoelectric point of proteins in solution, the hydrophilic eADF3(AQ)$_{24}$ was directly dissolved in 1 mM potassium chloride (KCl) at a concentration of 1 mg mL^{-1}. The hydrophobic eADF4-based proteins were dissolved in 6 M guanidinium thiocyanate (GuaSCN) at a concentration of 1−2 mg mL^{-1} for 30 min at room temperature and dialyzed against 0.001 M KCl overnight. The dialysis was conducted using membranes with a molecular weight cutoff of 6−8 kDa at room temperature (eADF4(C16), eADF4(κ16)) and at 4 °C for eADF4(Ω16). The pH-dependent electrokinetic measurements in solution were performed via electrophoresis with a Zetasizer Ultra Red from Malvern Instruments Ltd. and an MPT-3 autotitrator. For the pH-depending ζ-potential measurements, the recombinant spider silk proteins, dissolved in 0.001 M KCl, were titrated by adding either 0.1 M KOH or HCl aqueous solutions until pH 10 or 2.5. Three measurements were recorded for each sample at each pH value.

4.5.3. Isoelectric Focusing by Gel Electrophoresis. For isoelectric focusing (IEF) of the recombinant spider silk proteins, the IEF gel electrophoresis starter kit (pH 3−10, SERVA) was conducted according to the manufacturer's protocol. Therefore, all proteins were dissolved in 6 M GuaSCN and dialyzed against 10 mM Tris/HCl (pH 7.5) overnight using again membranes with a molecular weight cutoff of 6−8 kDa at room temperature (eADF4(C16), eADF4(κ16), eADF3(AQ)$_{12}$, and eADF3(AQ)$_{24}$) and at 4 °C for eADF4(Ω16). Protein samples were mixed with an IEF sample loading buffer. Five micrograms of the appropriate protein was loaded on IEF gels (pH 3−10). For IEF gel electrophoresis, the related anode and cathode buffers were used. Gel electrophoresis was conducted for 60 min at 100 V, 60 min at 200 V, and 30 min at 500 V. After gel electrophoresis, one IEF standard marker band was separated and silver-stained. A western blot was conducted with the remaining gel to transfer the proteins to a PVDF membrane and to allow detection of the fused T7-tag by interaction with an HRP-conjugated T7-antibody. After blocking the membrane with 5% w/v milk powder in 1× PBS and incubation with a conjugated T7-antibody (1:5000 dilution in 1× PBS), protein bands were visualized by incubating the membrane with the LumiLight detection solution for 15 min in the dark at room temperature. Chemiluminescence was detected on a Hoefer device (Hoefer, Germany).

4.6. Wetting Behavior of Recombinant Spider Silk Films on Different Substrates. *4.6.1. Preparation of Protein Films.* For analyzing the influence of different substrates on the wetting behavior of spider silk films, polished (111) silicon wafers (CrysTec GmbH, Berlin, Germany), RCA-cleaned glass slides, and mica sheets were cut into pieces of 1 cm^2 and cleaned by rinsing with toluene, acetone, water, and acetone before coating. Polystyrene (PS) surfaces were rinsed with ethanol. Silk solutions (V = 200 μL) were placed in the substrate center and dried overnight at ambient conditions to obtain films with 0.5 mg protein per 1 cm^2. For post-treatment, samples were placed in a desiccator with 20 mL methanol at the bottom. The desiccator was evacuated (p = 10^{-1} mbar) to generate a saturated methanol atmosphere, and samples were incubated overnight.

4.6.2. Fourier Transform Infrared (FTIR) Spectroscopy. For determining the secondary structure of spider silk films, grazing angle attenuated total reflection (GATR) FTIR spectroscopy was performed using the VariGATR accessory (Harrick Scientific Products Inc., Pleasantville) on a Bruker Tensor 27 FTIR-spectrometer with an MCT detector (Bruker, Rheinstetten, Germany). For absorbance measurements, a grazing angle of 62° was used. One hundred and forty scans from 4000 to 800 nm^{-1} were averaged at a resolution of 2 cm^{-1}.

4.6.3. Water Contact Angle Measurements. To analyze wettability, static contact angles of water were determined on

https://doi.org/10.1021/acsami.2c09590
ACS Appl. Mater. Interfaces 2022, 14, 31751−31766

different spider silk films on various substrates using the OEG contact angle system (Surftens Universal, OEG, Frankfurt(Oder), Germany). Contact angles were analyzed using the SURFTENS software (OEG, Frankfurt(Oder), Germany) and a Laplace Young fit.

4.7. Biodegradation of Recombinant Spider Silk Films.

4.7.1. Protein Labeling. Recombinant spider silk proteins were dissolved in 6 M GuaSCN and dialyzed against 20 mM *N*-(2-hydroxyethyl)piperazine-*N*′-ethanesulfonic acid (HEPES) (pH 7.1) using membranes with a molecular weight cutoff of 6−8 kDa at room temperature (eADF4(C16), eADF4(κ16), eADF3(AQ)$_{12}$, and eADF3(AQ)$_{24}$) and at 4 °C for eADF4(Ω16). A 10-fold molar excess of the NHS-fluorescein was dissolved in dimethylformamide (DMF) and added to the protein solution (1 h, RT), with the exception of eADF4(Ω16) (1 h, 4 °C). The labeled proteins were precipitated using 1 M potassium phosphate (K-Pi, pH 7.0) overnight (4 °C). The resulting particles were thoroughly washed three times using a water−DMF mixture (1:1, v/v), followed by pure water to remove salt and a nonspecifically bound fluorescence dye. Afterward, the labeled protein particles were dissolved in 6 M GdmSCN and dialyzed against ammonium bicarbonate buffer (20 mM, pH 9.0) to remove the remaining free fluorescein. Ammonium bicarbonate was chosen, as it decomposes into the volatile components NH_3, CO_2, and H_2O during the lyophilization process without any remaining salts. The success of labeling was confirmed by UV/vis analysis (Nanodrop ND 1000, Thermo Scientific), and the determined degree of labeling (n(fluoresceine)/n(protein)) was 0.90 for eADF4(C16), 1.93 for eADF4(κ16), 1.33 for eADF4(Ω16), 0.86 for eADF3(AQ)$_{12}$, and 1.26 for eADF4(AQ)$_{24}$. Afterward, the proteins were freeze-dried (Alpha 1-2 LD plus freeze dryer, Martin Christ Gefriertrockungsanlagen GmbH, Germany).

4.7.2. Preparation of Protein Films. For degradation experiments, fluorescein-labeled protein solutions were cast in nontreated 48-well plates (Nunc, Thermo Scientific, Germany) and dried at ambient conditions overnight to obtain films with 0.5 mg protein per 1 cm^2. For post-treatment, 250 μL of 75% ethanol was added onto the films and air-dried overnight at ambient conditions.

4.7.3. Enzymatic Degradation Assay. Degradation experiments were performed according to Müller-Herrmann and Scheibel.[45] Experiments were performed in the TCNB buffer (50 mM Tris/HCl, 10 mM $CaCl_2$, 150 mM NaCl, 0.05% Brij 35, pH 7.5) at room temperature. The fluorescein-labeled eADF3 and eADF4 spider silk films were incubated with 250 μL of PXIV or CHC solution (175 μg mL^{-1} in TCNB buffer) for 15 days. Control experiments without enzymes were conducted in 250 μL of TCNB buffer. Buffers and enzyme solutions were changed every 24 h. The experiments were performed in sextuplicates, and the fluorescence intensity of the supernatant was measured every day using a Mithras LB940 plate reader system (Berthold Technologies, Germany) (λ_{ex} = 485 nm, λ_{em} = 535 nm) in a black plate (Nunc, Thermo Scientific, Germany). To calculate the protein concentration in the supernatant and determine the relative degradation ($m_{degraded}/m_{initial}$) of the protein, a calibration curve was made for the labeled proteins.

4.8. Protein Adsorption on Recombinant Spider Silk Films.

4.8.1. Sensor Chip Coatings. For quantifying protein adsorption on spider silk films, QCM-D resonators (5 MHz, AT-cut, Cr/Au; Quartz Pro Sweden AB, Järfälla, Sweden) were cleaned using a 10 min UV/ozone treatment (PSD-Pro Series, Novascann, Ames). For spider silk coating, chips were spin-coated (67 rps, 3 s acceleration ramp, 30 s; K.L.M. SCE-150 jr, Schaefer Technologie GmbH, Germany) with a 30 μL protein solution (4 mg mL^{-1}) in formic acid, yielding spider silk films with a thickness of 15−20 nm.[52] The coated sensor chips were post-treated in a methanol atmosphere overnight and mounted in the standard Q-Sense flow module (QFM 401, Biolin Scientific, Västra, Frölunda, Sweden). For PDMS coating of QCM-D resonators, thin PDMS films were applied to resonators, as reported by Bračič et al.[66] A stock solution of 10% (w/w) PDMS with a base-to-curing agent ration of 10:1 (w/w) was prepared by dissolving the reaction mixture in toluene and shaking overnight. For resonator coatings, the PDMS solution was diluted with toluene to 0.5% (w/w) followed by shaking overnight. Sensor chips were spin-coated (83 rps, 3 s acceleration ramp, 60 s) with 40 μL of PDMS solution (0.5% (w/w)). The PDMS-coated sensor chips were cured overnight at 80 °C in a drying cabinet. Such a spin-coating process leads to films with a thickness of 23.1 ± 1.1 nm if applied on silicon wafers. Film thickness was determined by scratching the film with a scalpel, measuring the scratched area using AFM, and applying step analysis using NanoScope Analysis 1.5 (Bruker, Karlsruhe, Germany).

4.8.2. Blood Serum Protein Solutions. Fibrinogen was layered on top of 1× PBS and gently agitated in an Eppendorf thermomixer (300 rpm, 37 °C; Eppendorf AG, Hamburg, Germany) overnight. IgG and HAS were reconstituted in 1× PBS overnight at 4 °C. Protein concentrations were determined in the UV/vis region using a Nanodrop ND 1000 ($E_{280\ nm}^{1\%}$(Fibrinogen) = 15.1, $E_{279\ nm}^{1\%}$(HSA) = 5.3, $E_{280\ nm}^{1\%}$(IgG) = 14.0) and set to 1 mg mL^{-1}. Working aliquots of HSA and IgG were stored at −20 °C. Fibrinogen solutions were freshly prepared before usage.

4.8.3. QCM-D Measurements. All equilibration and adsorption steps were performed in a 1× PBS buffer at a volume flow of 10 mL min^{-1} at 21 °C with a Q-Sense E4 (Biolin Scientific, Västra Frölunda, Sweden). The coated sensor chips were equilibrated in PBS buffer and then flushed with 1 mg mL^{-1} of the particular blood serum proteins for 135 min, followed by a 210 min buffer flow. Frequency and dissipation data were monitored for the 3rd, 5th, 9th, and 11th overtones. The change in the areal mass density $\Delta\rho_A$ for a specific overtone n is proportional to the change in frequency Δf and is described by the Sauerbrey equation (eq 1)[67]

$$\Delta\rho_A = -\frac{\rho_q h_q}{f_0}\frac{\Delta f}{n} = -C\frac{\Delta f}{n} \quad (1)$$

The mass sensitivity constant C depends on the density (ρ_q), the thickness (h_q), and the fundamental frequency (f_0) of the quartz crystal.[68] The Sauerbrey equation can be used to estimate the mass change of a rigidly adsorbed layer on the chip surface in air or vacuum and also in the liquid medium, as long as the damping of oscillation is not sufficiently large.[69] If the damping is too large, a viscoelastic model has to be applied, which will consider the change in the dissipation factor D by measuring the oscillation decay.[68] The hydrodynamic thickness can be calculated by fitting Δf and ΔD at different overtones using the Voigt model with Q-tools software (Biolin Scientific, Västra Frölunda, Sweden). Areal mass was estimated by the conversion of thickness into mass using the bulk density (1370 kg m^{-3}) of the protein−material. The areal mass of HSA on all surfaces, as well as fibrinogen and IgG adsorption on eADF3(AQ)$_{12}$ and eADF3(AQ)$_{24}$, was determined using the Sauerbrey equation due to the more rigid character of these thin adsorbed serum protein layers. The Voigt model was used for the areal mass calculation of all other samples due to their more viscoelastic character.

4.9. Quantification of Conformational Changes during Fibrinogen Adsorption on Recombinant Spider Silk Films.

4.9.1. Preparation of Films. For investigating conformational changes of human fibrinogen during protein adsorption on spider silk surfaces, nontreated 96-well polystyrene tissue culture plates (Nunc, Thermo Scientific, Germany) were pretreated using UV/ozone (PSD-Pro Series, Novascan, Ames) for 10 min to enable a homogeneous film formation after solvent evaporation. 42 μL of the respective spider silk solution was drop-cast in each well and dried overnight at ambient conditions to obtain films containing 0.5 mg protein per 1 cm^2. For post-treatment, 100 μL of ethanol (75% v/v) was added to each film, removed after 1 h incubation, and evaporated overnight to induce β-sheets to make the films water-insoluble.

4.9.2. Indirect Enzyme-Linked Immunosorbent Assay (ELISA). Human plasma fibrinogen (Sigma-Aldrich, Germany) was resolubilized in a 0.9% (w/v) saline solution at a concentration of 1 mg mL^{-1} at RT. 50 μL of fibrinogen solution was pipetted on films and control wells to obtain a protein amount of 50 μg per well (five wells per condition). Uncoated wells on the spider silk film-containing plate, as well as an oxygen plasma pretreated (60 s, 100% O_2) 96-well polystyrene plate, served as controls (five wells per condition). The

https://doi.org/10.1021/acsami.2c09590
ACS Appl. Mater. Interfaces 2022, 14, 31751−31766

samples were incubated overnight at 4 °C to allow fibrinogen adsorption and restructuring on the different surfaces. After removal of the fibrinogen solution, the samples were washed twice using 150 μL 1× PBS. The samples were incubated with 150 μL blocking solution (1% w/v bovine serum albumin in 1× PBS) for 5 h to block nonspecific protein interactions. Afterward, the samples were again washed twice using 1× PBS and incubated with 100 μL monoclonal mouse antifibrinogen γ primary antibody (IgG1, sc-81620, clone 2.G2.H9, 2 μg mL^{-1} in blocking solution, Santa Cruz Biotechnology, Germany) for 90 min at RT. After another round of washing with 1× PBS, 100 μL of the secondary antibody carrying a horseradish peroxidase (HRP) function (m-IgG1 BP-HRP, sc-525415, 1:10 000 v/v in 1× PBS, Santa Cruz Biotechnology, Germany) was added to the samples and incubated for 90 min. The samples were washed again with 1× PBS and developed with 50 μL of ECL Plus substrate solution (1:50 v/v solution A and solution B) for 15 min. Several controls (three wells per condition) were added to the assay, namely, 100 μL of pure fibrinogen, substrate, primary, and secondary antibody solutions, as well as adsorbed fibrinogen incubated with either one or both antibodies with or without substrate solution to detect nonspecific protein binding or substrate degradation. The luminescence of the resulting product correlating with fibrinogen adsorption was quantified at a wavelength of 450 nm using an endpoint measurement on a SpectraMax iD5 plate reader system (Molecular Devices, Germany).

4.10. Interaction of Human Blood with Recombinant Spider Silk Films. *4.10.1. Preparation of Films.* After solving in formic acid, recombinant spider silk proteins (c = 10 mg mL^{-1}) were cast onto piranha cleaned (3:1 ratio H_2SO_4 and H_2O_2 (30%), 15 min, RT) cover borosilicate glass and dried overnight. For post-treatment, the samples were placed in a methanol-saturated atmosphere overnight. Afterward, the recombinant spider silk proteins were dried at room temperature.

4.10.2. Blood Coagulation Assays. According to the described procedure, the blood coagulation assays were performed with whole human blood.[60,70] Human blood was collected from healthy human volunteers by standard venipuncture into S-Monovette tubes (Sarstedt), partially heparinized to a final concentration of 0.43 IU mL^{-1}, and used within 1 h upon withdrawal. Informed consent was obtained in compliance with the ethics approval BASEC No. PB_2016-00816 from the local ethics committee, St. Gallen, Switzerland. Spider silk films were placed in custom Teflon molds, incubated with whole human blood on an orbital shaker (Polymax, Heidolph) for 35 and 40 min, washed with PBS, and then prepared for SEM or CLSM imaging, as described previously.[70] Two independent experiments were performed with duplicate samples each and analyzed by CLSM (n = 2) and SEM (n = 2). Representative images are depicted.

4.11. Mammalian Cell Culture on Recombinant Spider Silk Films. *4.11.1. Preparation of Films.* Nontreated 48-well and 96-well polystyrene tissue culture plates (Nunc, Thermo Scientific, Germany) were pretreated using UV/ozone (PSD-Pro Series, Novascan, Ames) for 10 min to ensure a homogeneous film formation after solvent evaporation.

One hundred microliters (48-well plates) and 32 μL (96-well plates) of silk solutions were drop-cast in appropriate wells and dried overnight at ambient conditions to obtain films showing 0.5 mg protein per 1 cm^2 after solvent evaporation. For post-treatment, 250 μL (48-well plate) or 100 μL (96-well plate) of 75% (v/v) ethanol were added to each film and evaporated overnight to induce β-sheets and make the films water-insoluble. Before cell culture analysis, spider silk films were sterilized using UV treatment for 30 min and washed once with 1× PBS.

4.11.2. Mammalian Cell Cultivation. Human BJ fibroblasts (ATCC, CRL-2522) were cultivated in Eagle's minimum essential medium (EMEM) (LGC Standards GmbH, Germany), and human HaCaT keratinocytes (CLS, cell lines service, Germany) and rat B50 neuronal cells (ECACC, Public Health, England) were cultivated in Dulbecco's modified Eagle's medium (DMEM) (Biosell GmbH, Germany) supplemented with 10% (v/v) fetal calf serum (FCS) (Biosell GmbH, Germany) 1% (v/v) GlutaMAX (Gibco, Thermo Scientific) and 0.1% (v/v) gentamycin sulfate (Sigma-Aldrich, Germany) in a cell culture incubator (HERAcell 150i, Thermo Scientific, Germany) in a controlled atmosphere (5% CO_2, 95% relative humidity) at 37 °C. BJ fibroblasts, HaCaT keratinocytes, and B50 neuronal cells were subcultured using trypsinization. Cell viability and cell number were determined using trypan blue (Sigma-Aldrich, U.K.) and an automated cell counter (TC20, BioRad Laboratories Ltd., U.K.). All cell culture experiments were conducted with media containing 10% (v/v) FCS, 1% (v/v) GlutaMAX, and 0.1% (v/v) gentamycin sulfate.

4.11.3. Initial Cell Adhesion on Silk Films. To evaluate early cell attachment, all three cell lines were seeded at a density of 10 000 cells per cm^2 on spider silk films and control plates (treated (Nunclon, Thermo Scientific, Germany) and nontreated (Nunc, Thermo Scientific, Germany) 48-well polystyrene tissue culture plates) (n = 3). After 4 h of incubation in a cell culture incubator (HERAcell 150i, Thermo Scientific, Germany) in a humidified atmosphere (5% CO_2) at 37 °C, the cells were washed with 1× PBS and fixed using 3.7% (v/v) paraformaldehyde (Carl Roth, Germany) in 1× PBS at ambient conditions. Cell samples were incubated in 0.1% (v/v) Triton X-100 (Carl Roth, Germany) in 1× PBS to permeabilize the cell membrane prior to fluorescence staining. The cell nuclei were stained using 300 nM 4′,6-diamidino-2-phenylindole and dihydrochloride (DAPI, Thermo Scientific), while F-actin cytoskeleton was visualized using 200 nM phalloidin−rhodamine (Sigma-Aldrich, Germany). Primary cell adhesion was analyzed using a fluorescence microscope (DMI3000B, Leica, Germany) and the associated LAS X software (Leica, Germany).

4.11.4. Cell Proliferation on Silk Films. To evaluate cell growth on spider silk films, all three cell lines were seeded at a density of 5000 cells per cm^2 on spider silk films and control plates (treated (Nunclon, Thermo Scientific, Germany) and nontreated (Nunc, Thermo Scientific, Germany) 48-well polystyrene tissue culture plates) (n = 4) and incubated at 37 °C in a humidified atmosphere (5% CO_2) in a cell culture incubator (HERAcell 150i, Thermo Scientific, Germany). After 1, 3, 5, and 7 days of incubation, cell viability and growth were analyzed using the cell titer blue assay (alamarBlue, Promega, Germany). Therefore, cell samples were washed with 1× PBS and incubated with 150 μL of 10% (v/v) cell titer blue reagent in appropriate cell culture media in a humidified atmosphere (5% CO_2) in a cell culture incubator (HERAcell 150i, Thermo Scientific, Germany) at 37 °C. As mammalian cells can metabolize resazurin (blue) to resofurin (pink), cell viability and thus cell growth could be determined by measuring the resofurin fluorescence at 590 nm. A sample without cells was used as a blank control to determine the self-degradation of resazurin during the incubation time. After incubation, 100 μL of the supernatant was pipetted to a black 96-well plate (Nunc, Thermo Scientific, Germany) and measured at 590 nm using a Mithras LB940 plate reader system (Berthold Technologies, Germany).

■ ASSOCIATED CONTENT

Supporting Information

The Supporting Information is available free of charge at https://pubs.acs.org/doi/10.1021/acsami.2c09590.

Sequence comparison, amino acid sequence blast, root-mean-square roughness of spider silk films, IEF gel and western blot of soluble spider silk proteins, normalized FTIR spectra on different substrates in the amide I region, and the ratio of water contact angles (PDF)

■ AUTHOR INFORMATION

Corresponding Author

Thomas Scheibel − *Lehrstuhl Biomaterialien, Fakultät für Ingenieurwissenschaften, Universität Bayreuth, 95447 Bayreuth, Germany; Bayerisches Polymerinstitut (BPI),*

https://doi.org/10.1021/acsami.2c09590
ACS Appl. Mater. Interfaces 2022, 14, 31751−31766

Bayreuther Zentrum für Kolloide und Grenzflächen (BZKG), Bayreuther Zentrum für Molekulare Biowissenschaften (BZMB), Bayreuther Materialzentrum (BayMAT), Universität Bayreuth, 95440 Bayreuth, Germany;
orcid.org/0000-0002-0457-2423;
Email: thomas.scheibel@bm.uni-bayreuth.de

Authors

Sarah Lentz – *Lehrstuhl Biomaterialien, Fakultät für Ingenieurwissenschaften, Universität Bayreuth, 95447 Bayreuth, Germany*

Vanessa T. Trossmann – *Lehrstuhl Biomaterialien, Fakultät für Ingenieurwissenschaften, Universität Bayreuth, 95447 Bayreuth, Germany*

Christian B. Borkner – *Lehrstuhl Biomaterialien, Fakultät für Ingenieurwissenschaften, Universität Bayreuth, 95447 Bayreuth, Germany*

Vivien Beyersdorfer – *Lehrstuhl Biomaterialien, Fakultät für Ingenieurwissenschaften, Universität Bayreuth, 95447 Bayreuth, Germany*

Markus Rottmar – *Laboratory for Materials-Biology Interactions, Empa Swiss Federal Laboratories for Materials Science and Technology, CH-9014 St. Gallen, Switzerland;*
orcid.org/0000-0001-7636-428X

Complete contact information is available at:
https://pubs.acs.org/10.1021/acsami.2c09590

Author Contributions

S.L. and V.T.T. contributed equally to this work. The design of the experiments was performed by S.L., V.T.T., and T.S. S.L. produced the films and performed the AFM, KPFM, GATR-FTIR, and the water contact angle measurements. V.T.T. designed and produced the eADF4(Ω16) variant. C.B.B., V.B., S.L., and V.T.T performed the enzymatic degradation. C.B.B. and S.L. performed the QCM-D measurements. S.L. and M.R. performed the blood coagulation tests. V.T.T. and S.L. performed the cell culture tests. S.L. performed the electrokinetic measurements. V.T.T. performed the IEF gel electrophoresis, western blot, and the ELISA test. Preparation of the paper was performed by V.T.T. and S.L. T.S. supervised the studies and edited the paper.

Funding

This project has been funded by the Deutsche Forschungsgemeinschaft (DFG, German Research Foundation) project numbers 326998133–TRR225 subproject C01 (T.S.) and DFG SCHE603/23-1 (T.S).

Notes

The authors declare the following competing financial interest(s): T.S. is a cofounder and shareholder of AmSilk GmbH.

■ ACKNOWLEDGMENTS

The authors thank Prof. Laforsch for access to the Harrick VariGATR, Anja Caspari for the streaming potential measurements, and PD Dr. Alla Synytska for the possibility to measure the electrokinetic measurements.

■ REFERENCES

(1) Bhat, S.; Kumar, A. Biomaterials and bioengineering tomorrow's healthcare. *Biomatter* **2013**, *3*, No. e24717.
(2) Kyriakides, T. R. Molecular Events at Tissue–Biomaterial Interface. In *Host Response to Biomaterials* Badylak, S. F., Ed.; Academic Press: Oxford, 2015; Chapter 5, pp 81–116.
(3) Wei, Q.; Becherer, T.; Angioletti-Uberti, S.; Dzubiella, J.; Wischke, C.; Neffe, A. T.; Lendlein, A.; Ballauff, M.; Haag, R. Protein Interactions with Polymer Coatings and Biomaterials. *Angew. Chem., Int. Ed.* **2014**, *53*, 8004–8031.
(4) Wilson, C. J.; Clegg, R. E.; Leavesley, D. I.; Pearcy, M. J. Mediation of biomaterial–cell interactions by adsorbed proteins: a review. *Tissue Eng.* **2005**, *11*, 1–18.
(5) Horbett, T. A.; Latour, R. A. Adsorbed Proteins on Biomaterials. In *Biomaterials Science*, 4th ed.; Wagner, W. R.; Sakiyama-Elbert, S. E.; Zhang, G.; Yaszemski, M. J., Eds.; Academic Press, 2020; Chapter 2.1.2, pp 645–660.
(6) Xu, L.-C.; Bauer, J. W.; Siedlecki, C. A. Proteins, platelets, and blood coagulation at biomaterial interfaces. *Colloids Surf., B* **2014**, *124*, 49–68.
(7) Visalakshan, R. M.; MacGregor, M. N.; Sasidharan, S.; Ghazaryan, A.; Mierczynska-Vasilev, A. M.; Morsbach, S.; Mailänder, V.; Landfester, K.; Hayball, J. D.; Vasilev, K. Biomaterial Surface Hydrophobicity-Mediated Serum Protein Adsorption and Immune Responses. *ACS Appl. Mater. Interfaces* **2019**, *11*, 27615–27623.
(8) Hoshiba, T.; Yoshikawa, C.; Sakakibara, K. Characterization of Initial Cell Adhesion on Charged Polymer Substrates in Serum-Containing and Serum-Free Media. *Langmuir* **2018**, *34*, 4043–4051.
(9) Keselowsky, B. G.; Collard, D. M.; García, A. J. Surface chemistry modulates fibronectin conformation and directs integrin binding and specificity to control cell adhesion. *J. Biomed. Mater. Res., Part A* **2003**, *66A*, 247–259.
(10) Anderson, J. M.; Rodriguez, A.; Chang, D. T. Foreign body reaction to biomaterials. *Semin. Immunol.* **2008**, *20*, 86–100.
(11) Anderson, J. M. Biological Responses to Materials. *Annu. Rev. Mater. Res.* **2001**, *31*, 81–110.
(12) Luensmann, D.; Jones, L. Protein deposition on contact lenses: The past, the present, and the future. *Contact Lens Anterior Eye* **2012**, *35*, 53–64.
(13) Pagel, M.; Beck-Sickinger, A. G. Multifunctional biomaterial coatings: synthetic challenges and biological activity. *Biol. Chem.* **2017**, *398*, 3–22.
(14) Mertgen, A.-S.; Trossmann, V. T.; Guex, A. G.; Maniura-Weber, K.; Scheibel, T.; Rottmar, M. Multifunctional Biomaterials: Combining Material Modification Strategies for Engineering of Cell-Contacting Surfaces. *ACS Appl. Mater. Interfaces* **2020**, *12*, 21342–21367.
(15) Pacelli, S.; Manoharan, V.; Desalvo, A.; Lomis, N.; Jodha, K. S.; Prakash, S.; Paul, A. Tailoring biomaterial surface properties to modulate host-implant interactions: implication in cardiovascular and bone therapy. *J. Mater. Chem. B* **2016**, *4*, 1586–1599.
(16) Kyzioł, K.; Kaczmarek, Ł.; Kyzioł, A.Surface Functionalization of Biomaterials. *Handbook of Composites from Renewable Materials*; John Wiley & Sons, Inc., 2017; Vol. *4*, pp 457–490.
(17) Wyman, P. Hydrophilic Coatings for Biomedical Applications in and Ex Vivo. *Coatings for Biomedical Applications*; Elsevier, 2012; pp 3–42.
(18) Borkner, C. B.; Wohlrab, S.; Möller, E.; Lang, G.; Scheibel, T. Surface Modification of Polymeric Biomaterials Using Recombinant Spider Silk Proteins. *ACS Biomater. Sci. Eng.* **2017**, *3*, 767–775.
(19) Qi, P.; Maitz, M. F.; Huang, N. Surface modification of cardiovascular materials and implants. *Surf. Coat. Technol.* **2013**, *233*, 80–90.
(20) Lawrence, E. L.; Turner, I. G. Materials for urinary catheters: a review of their history and development in the UK. *Med. Eng. Phys.* **2005**, *27*, 443–453.
(21) Braun, U.; Lorenz, E.; Weimann, C.; Sturm, H.; Karimov, I.; Ettl, J.; Meier, R.; Wohlgemuth, W. A.; Berger, H.; Wildgruber, M. Mechanic and surface properties of central-venous port catheters after removal: A comparison of polyurethane and silicon rubber materials. *J. Mech. Behav. Biomed. Mater.* **2016**, *64*, 281–291.
(22) Zhang, H.; Zheng, X.; Ahmed, W.; Yao, Y.; Bai, J.; Chen, Y.; Gao, C. Design and Applications of Cell-Selective Surfaces and Interfaces. *Biomacromolecules* **2018**, *19*, 1746–1763.

(23) Borcherding, K.; Schmidmaier, G.; Hofmann, G. O.; Wildemann, B. The rationale behind implant coatings to promote osteointegration, bone healing or regeneration. *Injury* **2021**, *52*, S106−S111.
(24) Kiradzhiyska, D. D.; Mantcheva, R. Overview of Biocompatible Materials and Their Use in Medicine. *Folia Med.* **2019**, *61*, 34−40.
(25) Zhang, B. G. X.; Myers, D. E.; Wallace, G. G.; Brandt, M.; Choong, P. F. M. Bioactive coatings for orthopaedic implants-recent trends in development of implant coatings. *Int. J. Mol. Sci.* **2014**, *15*, 11878−11921.
(26) Borkner, C. B.; Elsner, M. B.; Scheibel, T. Coatings and films made of silk proteins. *ACS Appl. Mater. Interfaces* **2014**, *6*, 15611−15625.
(27) Zeplin, P. H.; Maksimovikj, N. C.; Jordan, M. C.; Nickel, J.; Lang, G.; Leimer, A. H.; Römer, L.; Scheibel, T. Spider silk coatings as a bioshield to reduce periprosthetic fibrous capsule formation. *Adv. Funct. Mater.* **2014**, *24*, 2658−2666.
(28) Aigner, T. B.; DeSimone, E.; Scheibel, T. Biomedical Applications of Recombinant Silk-Based Materials. *Adv. Mater.* **2018**, *30*, No. 1704636.
(29) Doblhofer, E.; Schmid, J.; Rieß, M.; Daab, M.; Suntinger, M.; Habel, C.; Bargel, H.; Hugenschmidt, C.; Rosenfeldt, S.; Breu, J.; Scheibel, T. Structural Insights into Water-Based Spider Silk Protein−Nanoclay Composites with Excellent Gas and Water Vapor Barrier Properties. *ACS Appl. Mater. Interfaces* **2016**, *8*, 25535−25543.
(30) Wohlrab, S.; Müller, S.; Schmidt, A.; Neubauer, S.; Kessler, H.; Leal-Egaña, A.; Scheibel, T. Cell adhesion and proliferation on RGD-modified recombinant spider silk proteins. *Biomaterials* **2012**, *33*, 6650−6659.
(31) Guerette, P. A.; Ginzinger, D. G.; Weber, B. H. F.; Gosline, J. M. Silk Properties Determined by Gland-Specific Expression of a Spider Fibroin Gene Family. *Science* **1996**, *272*, 112−115.
(32) Huemmerich, D.; Helsen, C. W.; Quedzuweit, S.; Oschmann, J.; Rudolph, R.; Scheibel, T. Primary Structure Elements of Spider Dragline Silks and Their Contribution to Protein Solubility. *Biochemistry* **2004**, *43*, 13604−13612.
(33) Eisoldt, L.; Smith, A.; Scheibel, T. Decoding the secrets of spider silk. *Mater. Today* **2011**, *14*, 80−86.
(34) Heidebrecht, A.; Eisoldt, L.; Diehl, J.; Schmidt, A.; Geffers, M.; Lang, G.; Scheibel, T. Biomimetic Fibers Made of Recombinant Spidroins with the Same Toughness as Natural Spider Silk. *Adv. Mater.* **2015**, *27*, 2189−2194.
(35) Kumari, S.; Lang, G.; DeSimone, E.; Spengler, C.; Trossmann, V. T.; Lücker, S.; Hudel, M.; Jacobs, K.; Krämer, N.; Scheibel, T. Data for microbe resistant engineered recombinant spider silk protein based 2D and 3D materials. *Data Brief* **2020**, *32*, No. 106305.
(36) Kumari, S.; Lang, G.; DeSimone, E.; Spengler, C.; Trossmann, V. T.; Lücker, S.; Hudel, M.; Jacobs, K.; Krämer, N.; Scheibel, T. Engineered spider silk-based 2D and 3D materials prevent microbial infestation. *Mater. Today* **2020**, *41*, 21.
(37) Kellum, J. A. Determinants of blood pH in health and disease. *Crit. Care* **2000**, *4*, No. 6.
(38) Borkner, C. B.; Lentz, S.; Müller, M.; Fery, A.; Scheibel, T. Ultrathin Spider Silk Films: Insights into Spider Silk Assembly on Surfaces. *ACS Appl. Polym. Mater.* **2019**, *1*, 3366−3374.
(39) Wohlrab, S.; Spieß, K.; Scheibel, T. Varying surface hydrophobicities of coatings made of recombinant spider silk proteins. *J. Mater. Chem.* **2012**, *22*, 22050−22054.
(40) Esser, T. U.; Trossmann, V. T.; Lentz, S.; Engel, F. B.; Scheibel, T. Designing of spider silk proteins for human induced pluripotent stem cell-based cardiac tissue engineering. *Mater. Today Bio* **2021**, *11*, No. 100114.
(41) Varshavsky, A. The N-end rule pathway and regulation by proteolysis. *Protein Sci.* **2011**, *20*, 1298−1345.
(42) Humbard, M. A.; Surkov, S.; De Donatis, G. M.; Jenkins, L. M.; Maurizi, M. R. The N-degradome of *Escherichia coli*: limited proteolysis in vivo generates a large pool of proteins bearing N-degrons. *J. Biol. Chem.* **2013**, *288*, 28913−28924.
(43) Hu, X.; Kaplan, D.; Cebe, P. Determining beta-sheet crystallinity in fibrous proteins by thermal analysis and infrared spectroscopy. *Macromolecules* **2006**, *39*, 6161−6170.
(44) Metya, A.; Ghose, D.; Ray, N. R. Development of hydrophobicity of mica surfaces by ion beam sputtering. *Appl. Surf. Sci.* **2014**, *293*, 18−23.
(45) Müller-Herrmann, S.; Scheibel, T. Enzymatic Degradation of Films, Particles, and Nonwoven Meshes Made of a Recombinant Spider Silk Protein. *ACS Biomater. Sci. Eng.* **2015**, *1*, 247−259.
(46) Li, M.; Ogiso, M.; Minoura, N. Enzymatic degradation behavior of porous silk fibroin sheets. *Biomaterials* **2003**, *24*, 357−365.
(47) Zhao, C.; Wu, X.; Zhang, Q.; Yan, S.; Li, M. Enzymatic degradation of *Antheraea pernyi* silk fibroin 3D scaffolds and fibers. *Int. J. Biol. Macromol.* **2011**, *48*, 249−255.
(48) Bauer, C. A.; Löfqvist, B.; Pettersson, G. Studies on the catalytic mechanism of a serine protease from *Streptomyces griseus*. *Eur. J. Biochem.* **1974**, *41*, 45−49.
(49) Wolters, G. H. J.; Vos-Scheperkeuter, G. H.; Lin, H.-C.; van Schilfgaarde, R. Different roles of class I and class II *Clostridium histolyticum* collagenase in rat pancreatic islet isolation. *Diabetes* **1995**, *44*, 227−233.
(50) Maziz, A.; Leprette, O.; Boyer, L.; Blatché, C.; Bergaud, C. Tuning the properties of silk fibroin biomaterial via chemical cross-linking. *Biomed. Phys. Eng. Express* **2018**, *4*, No. 065012.
(51) Rodrigues, S. N.; Gonçalves, I. C.; Martins, M. C. L.; Barbosa, M. A.; Ratner, B. D. Fibrinogen adsorption, platelet adhesion and activation on mixed hydroxyl-/methyl-terminated self-assembled monolayers. *Biomaterials* **2006**, *27*, 5357−5367.
(52) Sperling, C.; Maitz, M. F.; Grasso, S.; Werner, C.; Kanse, S. M.; Positively, A. Charged Surface Triggers Coagulation Activation Through Factor VII Activating Protease (FSAP). *ACS Appl. Mater. Interfaces* **2017**, *9*, 40107−40116.
(53) Kidoaki, S.; Matsuda, T. Adhesion Forces of the Blood Plasma Proteins on Self-Assembled Monolayer Surfaces of Alkanethiolates with Different Functional Groups Measured by an Atomic Force Microscope. *Langmuir* **1999**, *15*, 7639−7646.
(54) Bernabeu, P.; Caprani, A. Influence of surface charge on adsorption of fibrinogen and/or albumin on a rotating disc electrode of platinum and carbon. *Biomaterials* **1990**, *11*, 258−264.
(55) Agashe, M.; Raut, V.; Stuart, S. J.; Latour, R. A. Molecular Simulation To Characterize the Adsorption Behavior of a Fibrinogen γ-Chain Fragment. *Langmuir* **2005**, *21*, 1103−1117.
(56) Evans-Nguyen, K. M.; Tolles, L. R.; Gorkun, O. V.; Lord, S. T.; Schoenfisch, M. H. Interactions of Thrombin with Fibrinogen Adsorbed on Methyl-, Hydroxyl-, Amine-, and Carboxyl-Terminated Self-Assembled Monolayers. *Biochemistry* **2005**, *44*, 15561−15568.
(57) Ostuni, E.; Chapman, R. G.; Holmlin, R. E.; Takayama, S.; Whitesides, G. M. A Survey of Structure−Property Relationships of Surfaces that Resist the Adsorption of Protein. *Langmuir* **2001**, *17*, 5605−5620.
(58) Sivaraman, B.; Latour, R. A. The relationship between platelet adhesion on surfaces and the structure versus the amount of adsorbed fibrinogen. *Biomaterials* **2010**, *31*, 832−839.
(59) Lovely, R. S.; Kazmierczak, S. C.; Massaro, J. M.; D'Agostino, R. B., Sr.; O'Donnell, C. J.; Farrell, D. H. Gamma' fibrinogen: evaluation of a new assay for study of associations with cardiovascular disease. *Clin. Chem.* **2010**, *56*, 781−788.
(60) Weiss, A. C. G.; Herold, H. M.; Lentz, S.; Faria, M.; Besford, Q. A.; Ang, C.-S.; Caruso, F.; Scheibel, T. Surface Modification of Spider Silk Particles to Direct Biomolecular Corona Formation. *ACS Appl. Mater. Interfaces* **2020**, *12*, 24635−24643.
(61) Leal-Egaña, A.; Lang, G.; Mauerer, C.; Wickinghoff, J.; Weber, M.; Geimer, S.; Scheibel, T. Interactions of Fibroblasts with Different Morphologies Made of an Engineered Spider Silk Protein. *Adv. Eng. Mater.* **2012**, *14*, B67−B75.
(62) Kazmierska, K.; Ciach, T. Bioactive Coatings for Minimally Invasive Medical Devices: Surface Modification in the Service of Medicine. *Recent Pat. Biomed. Eng.* **2010**, *2*, 1−14.

https://doi.org/10.1021/acsami.2c09590
ACS Appl. Mater. Interfaces 2022, 14, 31751−31766

(63) Böttcher, H. Bioactive Sol-Gel Coatings. *J. Prakt. Chem.* **2000**, *342*, 427−436.
(64) Li, Z.; Milionis, A.; Zheng, Y.; Yee, M.; Codispoti, L.; Tan, F.; Poulikakos, D.; Yap, C. H. Superhydrophobic hemostatic nanofiber composites for fast clotting and minimal adhesion. *Nat. Commun.* **2019**, *10*, No. 5562.
(65) Shiu, H. T.; Goss, B.; Lutton, C.; Crawford, R.; Xiao, Y. Controlling whole blood activation and resultant clot properties by carboxyl and alkyl functional groups on material surfaces: a possible therapeutic approach for enhancing bone healing. *J. Mater. Chem. B* **2014**, *2*, 3009−3021.
(66) Bračič, M.; Mohan, T.; Kargl, R.; Griesser, T.; Hribernik, S.; Köstler, S.; Stana-Kleinschek, K.; Fras-Zemljič, L. Preparation of PDMS ultrathin films and patterned surface modification with cellulose. *RSC Adv.* **2014**, *4* (23), 11955−11961.
(67) Sauerbrey, G. Verwendung von Schwingquarzen zur Wägung dünner Schichten und zur Mikrowägung. *Z. Physik* **1959**, *155* (2), 206−222.
(68) Liu, G.; Zhang, G. Basic principles of QCM-D. In *QCM-D Studies on Polymer Behavior at Interfaces*; Springer, 2013; pp 1−8.
(69) Liu, G.; Zhang, G. *QCM-D Studies on Polymer Behavior at Interfaces*; Springer, 2013.
(70) Weidenbacher, L.; Muller, E.; Guex, A. G.; Zündel, M.; Schweizer, P.; Marina, V.; Adlhart, C.; Vejsadová, L.; Pauer, R.; Spiecker, E.; Maniura-Weber, K.; Ferguson, S. J.; Rossi, R. M.; Rottmar, M.; Fortunato, G. In Vitro Endothelialization of Surface-Integrated Nanofiber Networks for Stretchable Blood Interfaces. *ACS Appl. Mater. Interfaces* **2019**, *11* (6), 5740−5751.

https://doi.org/10.1021/acsami.2c09590
ACS Appl. Mater. Interfaces 2022, 14, 31751−31766

Supporting Information

Structure-property relationship based on the amino acid composition of recombinant spider silk proteins for potential biomedical applications

Sarah Lentz[‡,†], *Vanessa T. Trossmann*[‡,†], *Christian B. Borkner*[‡], *Vivien Beyersdorfer*[‡], *Markus Rottmar*[§] *and Thomas Scheibel*[*,‡,x]

[‡] *Lehrstuhl Biomaterialien, Fakultät für Ingenieurwissenschaften, Universität Bayreuth, Rüdiger-Bormann-Str. 1, 95447 Bayreuth, Germany*

§ Laboratory for Materials-Biology Interactions, Empa Swiss Federal Laboratories for Materials Science and Technology, CH-9014 St. Gallen, Switzerland

** Bayerisches Polymerinstitut (BPI), Bayreuther Zentrum für Kolloide und Grenzflächen (BZKG), Bayreuther Zentrum für Molekulare Biowissenschaften (BZMB), Bayreuther Materialzentrum (BayMAT), Universität Bayreuth, Universitätsstr. 30, 95440 Bayreuth, Germany*

E-Mail: thomas.scheibel@bm.uni-bayreuth.de

[†] contributed equally

[x] corresponding author

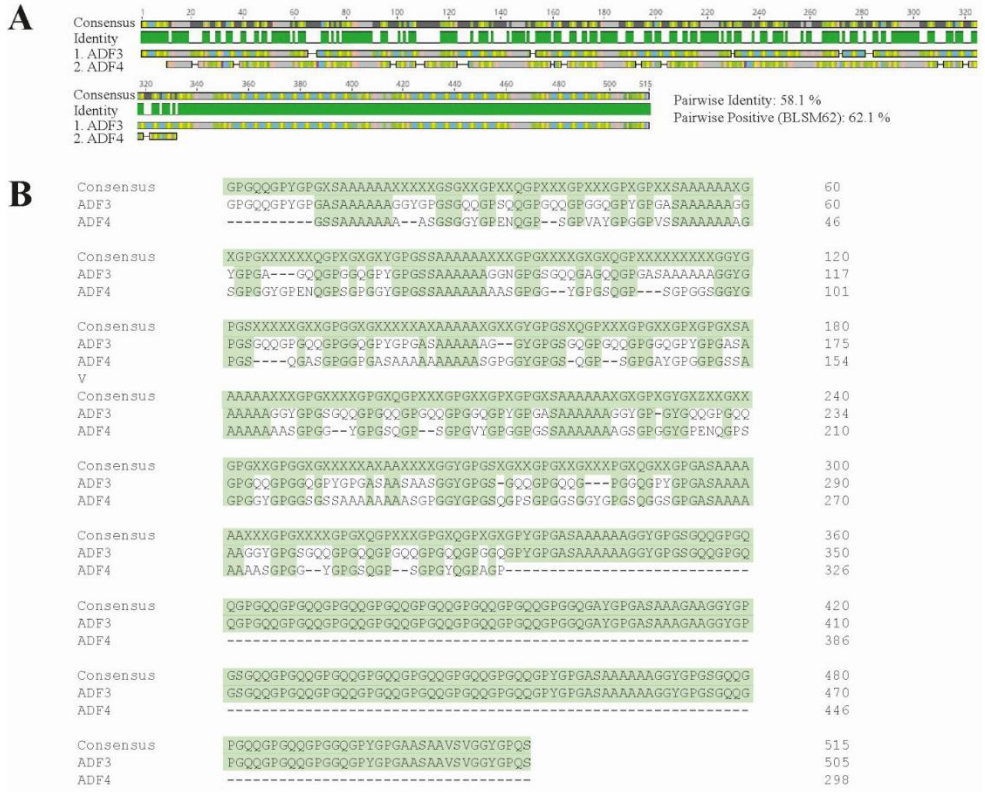

Figure SI 1: A) Sequence comparison of natural amino acid sequences of *Araneus diadematus* fibroin 3 and 4. Homology and identity of both amino acid sequences are shown. B) Amino acid sequence blast of the so far identified parts of the natural amino acid sequences ADF3 and ADF4. The algorithm BLSM62 was used for the comparison. The known sequence of ADF3 comprises 505 aa and that of ADF4 298aa.

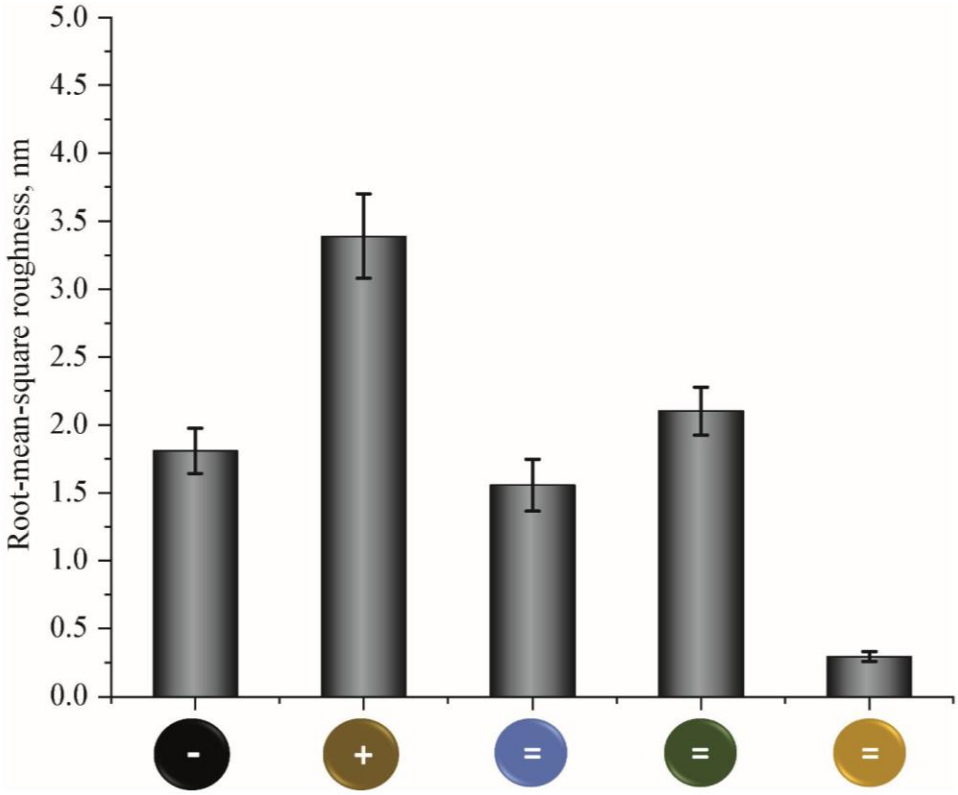

Figure SI 2: Root-mean-suare roughness (nm) of recombinant spider silk films as shown in figure 1. The black button reflects the negatively charged eADF4(C16), the brown one the positively charged eADF4(κ16), the blue one the uncharged variant eADF4(Ω16), and the green one depicts for eADF3$(AQ)_{12}$ and the yellow one for eADF3$(AQ)_{24}$.

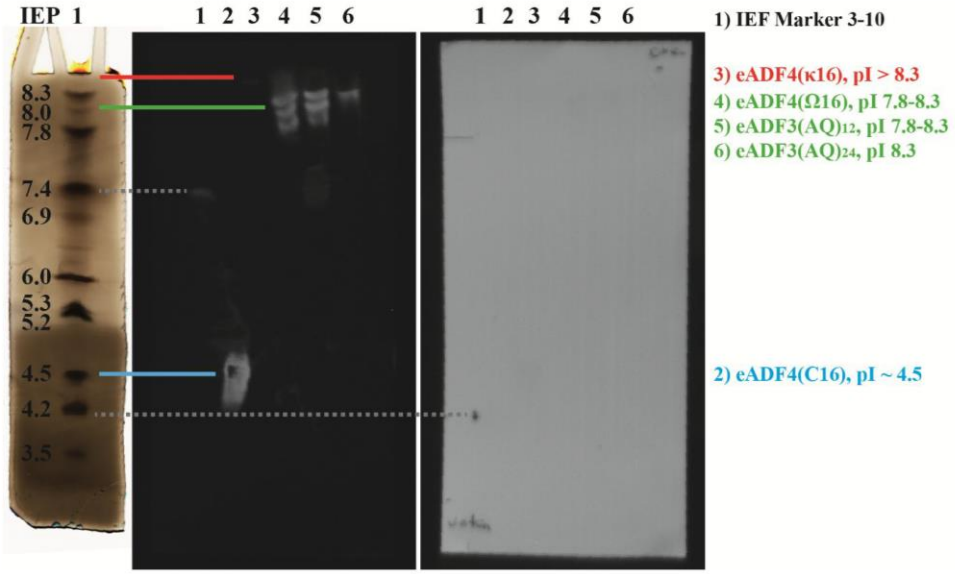

Figure SI 3: Isoelectric focussing (IEF) of soluble recombinant spider silk proteins eADF4(C16), eADF4(κ16), eADF4(Ω16), eADF3(AQ)$_{12}$ and eADF3(AQ)$_{24}$ for determination ot the isoelectric point (IEP). An IEF gel electrophoresis using the SERVA*Gel*™ IEF 3-10 Starter Kit was performed with dialyzed, soluble spider silk proteins in native state according to manufacturers prototcol. The subsequent western blot enabled protein visualization by detecting the N-terminally fused T7-tag using an HRP-conjugated T7 antibody (1:5000), since a homogeneous protein staining, e.g. silver staining, was not possible due to individual protein characteristics. However, the IEF marker was additionally silver stained for a better allocation of the individual IEP-indicating bands. The grey dashed lines show the bands visible on the blot that were used for classification.

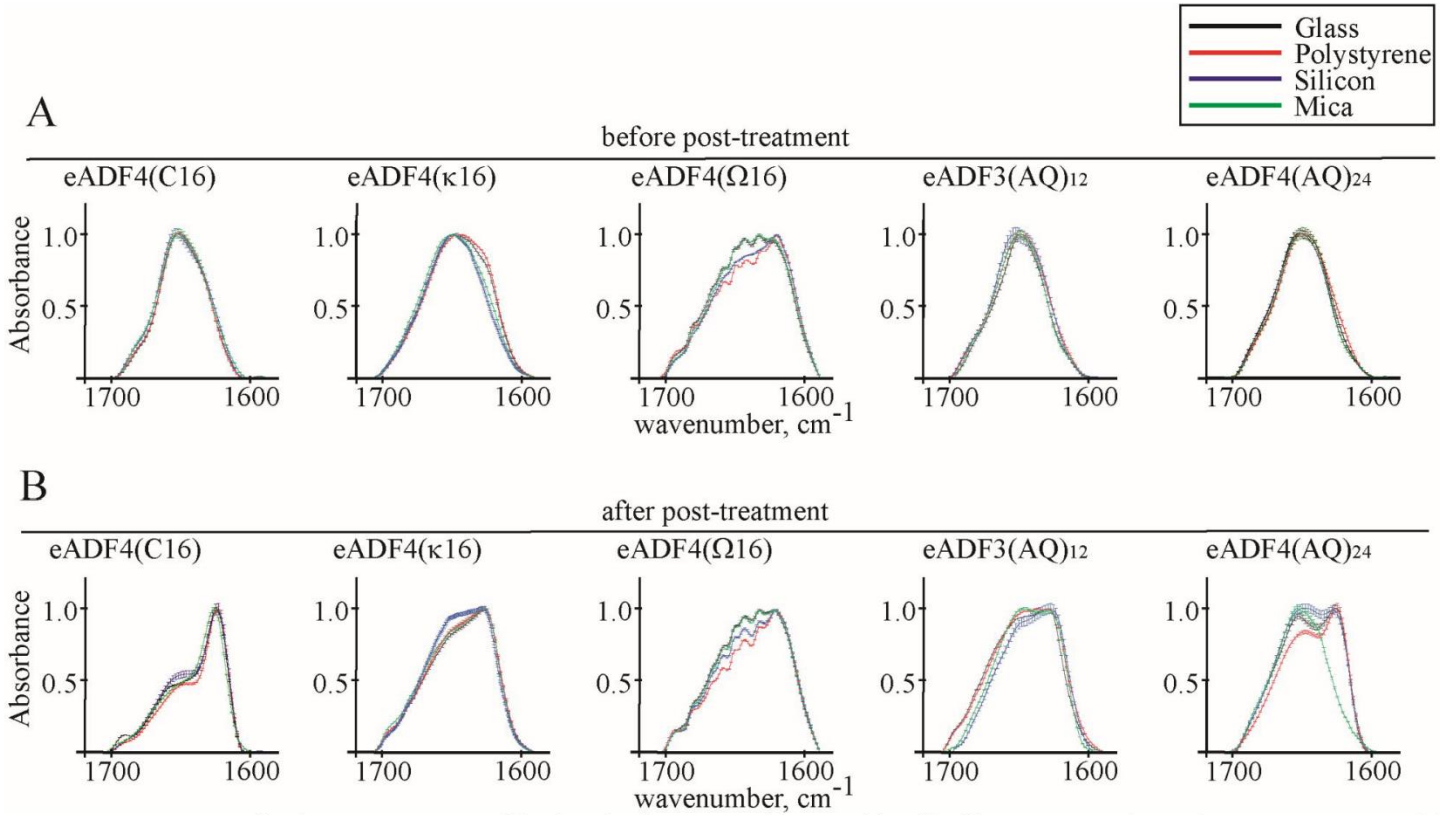

Figure SI 4: Normalized FTIR-spectra (amide I band) of (A) recombinant spider silk films as-cast and (B) after post-treatment with methanol. Films were cast on glass (black), polystyrene (red), silicon (blue) and mica (green). Samples were analyzed in quintuplets. Post-treatment leads to a peak shift from ~1660 cm-1 (mainly random coil) to ~1626 cm-1 (mainly ß-sheet).

Table SI 1: Ratio of water contact angles of uncoated substrates to recombinant spider silk coated substrates.

Protein	Glass/Protein	PS/Protein	Si/Protein	Mica/Protein
eADF4(C16)	0.4	1.2	0.8	0.01
eADF4(κ16)	0.4	1.3	1.0	0.01
eADF4(Ω16)	0.4	1.4	1.0	0.02
$eADF3(AQ)_{12}$	0.4	1.1	0.7	0.01
$eADF3(AQ)_{24}$	0.4	1.0	0.7	0.01
Average ± SD	0.4 ± 0.0	1.2 ± 0.2	0.8 ± 0.2	0.01 ± 0.0

7.4. Teilarbeit IV

Teilarbeit IV wurde 2020 unter dem Titel „Engineered spider silk-based 2D and 3D materials prevent microbial infestation“ im Journal *Materials Today* veröffentlicht.

Kumari, S.*; Lang, G.*; DeSimone, E.; Spengler, C.; **Trossmann, V. T.**; Lücker, S.; Hudel, M.; Jacobs, K.; Krämer, N. & Scheibel, T. (2020) Engineered spider silk-based 2D and 3D materials prevent microbial infestation. *Materials Today* **41**: 21.

https://doi.org/10.1016/j.mattod.2020.06.009

* gleichberechtigte Co-Autorenschaft

Materials Today • Volume 41 • December 2020 RESEARCH

ELSEVIER

RESEARCH: Original Research

Engineered spider silk-based 2D and 3D materials prevent microbial infestation

Sushma Kumari [1,†], Gregor Lang [1,2,†], Elise DeSimone [1], Christian Spengler [3], Vanessa T. Trossmann [1], Susanne Lücker [4], Martina Hudel [5], Karin Jacobs [3], Norbert Krämer [4], Thomas Scheibel [1,6,7,8,9,*]

[1] Department of Biomaterials, Faculty of Engineering Science, University of Bayreuth, Prof.-Rüdiger-Bormann-Str. 1, 95447 Bayreuth, Germany
[2] Biopolymer Processing Group, Faculty of Engineering Science, University of Bayreuth, Ludwig-Thoma-Str. 36A, 95447 Bayreuth, Germany
[3] Department of Experimental Physics and Center for Biophysics, Saarland University, 66123 Saarbrücken, Germany
[4] Medical Center for Dentistry, Department of Paediatric Dentistry, Medical Center Gießen and Marburg, Justus-Liebig University Gießen, Schlagenzahl 14, 35392 Gießen, Germany
[5] Institute of Medical Microbiology, Justus-Liebig University Gießen, Schubertstraße 81, 35392 Gießen, Germany
[6] Bayreuth Center for Material Science and Engineering (BayMAT), Germany
[7] Bavarian Polymer Institute (BPI), Germany
[8] Bayreuth Center for Colloids and Interfaces (BZKG), Germany
[9] Bayreuth Center for Molecular Biosciences (BZMB), University of Bayreuth, Universitätsstraße 30, 95447 Bayreuth, Germany

Biofilm formation, especially of antimicrobiotic-resistant microbial strains, are a major problem in health care. Therefore, there is great interest in developing advanced materials that are selectively inhibiting microbial adhesion to surfaces, but at the same time promoting mammalian cell growth. In nature, some spider silks have evolved to repel microbes, a feature that could be used in biomaterials. To unravel how microbe repellence can be achieved in engineered spider silk, different recombinant spider silk proteins based on the consensus sequences of *Araneus diadematus* dragline silk proteins (fibroin 3 and 4) were processed into 2D-patterned films and 3D-hydrogels. Strikingly, protein structure characteristics on the nanoscale are the basis for the detected microbe-repellence. Designed spider silk materials promoted mammalian cell attachment and proliferation while inhibiting microbial infestation, demonstrating the great potential of these engineered spider silk-based materials as bio-selective microbial-resistant coatings in biomedical as well as technical applications.

Introduction

Pathogenic microbial contaminations of surfaces, when exposed to patients, significantly increase the risk of infection, and represent a severe problem in the public health care sector [1,2]. Biofilm formation on biomedical devices, such as prosthetics, medical implants, contact lenses, and catheters, not only limits their functionality and lifetime but can also cause life-threatening infections [3,4]. Consequently, microbial biofilm generation and nosocomial infection during conventional medical therapy have significantly increased mortality as well as healthcare costs worldwide in the last decade. Outside of the clinical setting, diseases associated with food contamination as well as biofouling of material surfaces in contact with water supply systems are considered major health issues [5]. There are several interacting parameters that have ultimately led to this problem, however, the most critical is the evolution of antimicrobial-resistant (or even multi-drug resistant) [6] microbes due to the overuse of antibiotics [7,8]. Furthermore, microbial colonization can subsequently lead to formation of

* Corresponding author.
E-mail address: Scheibel, T. (thomas.scheibel@bm.uni-bayreuth.de)
† These authors contributed equally to this work.

https://doi.org/10.1016/j.mattod.2020.06.009

almost irremovable biofilms, hardly accessible for antibiotics as, after becoming a dense colony, the microbes secrete a protective coating, making it much more difficult to eradicate biofilms in contrast to isolated microbes [9,10].

One example of a "superbug" is methicillin-resistant *Staphylococcus aureus*, a major cause of community-acquired infections resulting in high morbidity and mortality rates in hospital-acquired infections [11]. Concerning treatment of these infections, glycopeptide antibiotics (GPAs) targeting the acyl-D-alanyl-D-alanine (D-Ala-D-Ala) terminus of the growing peptidoglycans on the outer surface of the Gram-positive bacteria's cytoplasmatic membrane are considered the last, non-antibiotic resort for medical treatment [12]. Nevertheless, glycopeptide-resistant organisms cause new problems, as they significantly reduce antibiotic affinity by replacing the D-Ala-D-Ala terminus with D-alanyl-D-lactate (D-Ala-D-Lac) or D-alanyl-D-serine (D-Ala-D-Ser), prompting the search for second generation drugs and new strategies to inhibit spreading of such pathogens by new hygiene standards and for materials with explicit microbial repelling surfaces [13]. In this context, biomaterials with inherent non-fouling properties would provide new opportunities of long-term protection, especially when they can be used as surface coating materials for already existing products. However, one draw-back of such surfaces is that they often repel any kind of cells, even human ones, making it difficult to employ them in applications such as tissue engineering [14].

As one critical step in biofilm formation is the initial adherence of pathogenic microbes onto a material's surface [9], inhibiting microbial attachment is a favorable approach to develop material surfaces resistant to biofilm formation [15,16]. There are two main approaches for inhibiting surface attachment, referred to as either active or passive resistance. While passively resistant surfaces are typically made of super hydrophilic or hydrophobic as well as zwitterionic or other synthetic polymers [17–19], actively resistant ones are often "contact killing" materials, such as cationic polymers, amphiphilic polymers, antimicrobial peptides and polymeric/composite materials loaded with antimicrobial agents [20–25]. Although these approaches can combat microbial infection by inhibiting mechanisms of persistence and adaptation, several drawbacks exist, such as instability under physiological conditions, cytotoxicity to mammalian cells, inflammatory responses, a narrow antimicrobial spectrum, and implications for transmitting multidrug resistance [26]. Further, antimicrobial activity has been mostly investigated in terms of its effectiveness against bacteria, although fungal infections also contribute significantly to patient morbidity and mortality. Moreover, fungal infections can readily form polymicrobial biofilms with enhanced resistance to antifungal drugs, further limiting therapeutic options [27]. Therefore, efficient mitigation of microbial infection associated with both bacteria and fungi is required for the future development of broad-range multifunctional material coatings.

Spider silk exhibits extraordinary mechanical properties, surpassing the toughness of other polymer fibers, and further displays excellent biocompatibility useful for biomedical applications [28,29]. Remarkably, most spider silk webs withstand microbial omnipresence and remain resistant to microbial decomposition for years, irrespective of environmental impacts such as humidity, temperature, and location, though being composed of proteins and therefore of amino acids, which would be a valuable source of nutrition for microbes. Only few studies have been published examining microbe-repelling effects of natural spider silk [30], and so far, the underlying mechanism remains ambiguous. This is because the surface of silk fibers consists of varying mixtures of spidroins, glycoproteins and lipids, and the composition of the surface further depends on the spider species as well as environmental conditions [31]. In some cases, even antimicrobial peptides might be implemented in the spider silk coatings [32,33]. So far, the resistance of spider silk fibers against microbial infestation has only been macroscopically described, but not assigned to single material components such as lipids, glycoproteins, silk proteins or material features of these composite materials. Recently published results indicate that bacterial infestation and decomposition of spider silk is inhibited by bacteriostatic or microbe repellent properties rather than by antibacterial means [34,35]. The authors of this study further hypothesized, that the complex network of interconnected crystalline and non-crystalline structures might prevent accessibility of nitrogen, which is necessary for bacterial growth.

Here, 2D and 3D scaffolds based on explicit individual recombinant spider silk proteins, based on sequences of the dragline silk of the European garden spider *Araneus diadematus*, were found to withstand microbial infestation depending on the structural features of the material's surfaces. Two engineered *Araneus diadematus* fibroins eADF3 and eADF4 and variants thereof were utilized, based on consensus sequences of the core domains of the naturally occurring fibroins 3 and 4 [36,37]. Materials made of polyanionic eADF4(C16), the best investigated of these variants, display absence of toxicity, lack of immune reactivity and slow biodegradation [38,39]. As eADF4(C16) lacks cell binding motifs, like most so far identified spider silk proteins, eADF4 (C16)-coated implants and catheters display significantly reduced adhesion and proliferation of mammalian cells as compared to non-treated ones [40,41]. When transplanted *in vivo* in rats, eADF4(C16)-coated silicone implants exhibited a substantial reduction in capsular fibrosis [40]. However, cell attachment to eADF4-based materials could be promoted by generating defined surface topographies, such as films with micrometer wide stripes or non-woven mats, on both of which good cell adhesion and proliferation could be detected due to the precisely controlled topography, dimensions and an increased surface area [42,43]. As a second approach, genetically modifying eADF4(C16) with the cell-binding motif RGD (Arginine-Glycine-Aspartate) promoted mammalian cell adhesion and proliferation with good cell viability in 2D and 3D materials [44,45]. Interestingly, even without sterilization, surfaces of materials based on the used recombinant spider silk protein eADF4(C16) were commonly free of microbes [46,34].

To systematically analyze microbe repellence, an extensive study was performed applying a diverse selection of different biofilm forming microbes, representing pathogenic bacteria (*S. mutans*, *S. aureus*, *E. coli*) and fungi/yeasts (*C. albicans*, *P. pastoris*) (Fig. 1a and Ref. [62]). Unlike the complex mixture/composite of natural spider silk fibers, recombinant technologies provide pure and perfectly defined proteins and materials made thereof, which are intrinsically non-toxic. Consequently, it was hypoth-

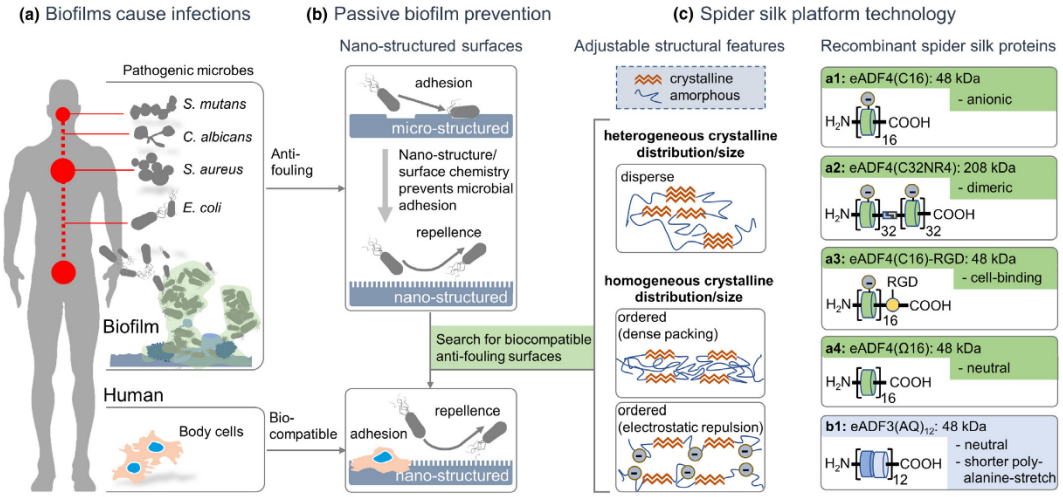

FIGURE 1

Schematic overview of the strategy to prevent biofilm formation using a spider silk platform technology. Various biofilm-forming microbes representing pathogenic bacteria and fungi as well as *P. pastoris* (model system) (a) were chosen to verify previously established concepts of passive biofilm prevention by nano-structured surfaces (b) using the established recombinant spider silk platform technology (c). It is predicted, as previously published, that particularly charge and amino acid sequence contribute to the homogeneity of crystallite size and distribution. Biotechnological engineering allows for systematic adaption of e.g. molecular weight (a1 vs. a2) and bio-functionality (a1 vs. a3) not affecting the crystallite properties of the underlying silk proteins. On the other hand, changes such as charge (a1 vs. a4) or amino acid sequence (a1 vs. b1) are expected to impact crystallite size and distribution. Combining microbe-repellant structural features with the ability to modify the intrinsically bio-compatible spider silk proteins with cell-adhesion motifs (a3) resulted in distinct bio-selective 2D and 3D spider silk materials.

esized, that anti-fouling effects of spider silk surfaces might not be attributed to toxic effects or explicit amino acid sequences, but to nano-structural features. Numerous technical [47,48] as well as natural [49,50] examples have shown the achievement of anti-fouling properties by nano-scaled topographies (Fig. 1b) [51]. Here, biotechnological design and recombinant production of different spider silk proteins was applied as a platform technology to systematically study the impact of the β-sheet structure-based nano-crystallites concerning anti-fouling performance (Fig. 1c). To test the hypothesis of nano-topographical effects leading to microbe-repellence, we investigated the impact of the bio-functionalization with a cell-binding motif (RGD), which doesn't change the basic crystallite-structural features of eADF4 (C16) and has the potential of supporting bio-selective mammalian cell growth with simultaneous microbe repellence (Fig. 1c: a1, a3). To evaluate the impact of molecular weight as well as terminal domains, eADF4(C32NR4) was included within this study as its non-repetitive terminal domain causes dimerization resulting in an apparent MW of 208 kDa (Fig. 1c: a2). As no structural differences between the core-domains of these proteins and that of eADF4(C16) could be detected [36], anti-fouling properties were expected to be the same.

On the other hand, structural changes and thus changed microbe-repellent properties were predicted to be induced by varying charges or different amino acid sequence motifs. To analyze the impact of charge, all negatively charged glutamic acid residues (E) in the consensus sequence of eADF4(C16) were replaced by uncharged glutamine residues (Q), resulting in the so far not examined neutral recombinant spider silk variant eADF4(Ω16) (Fig. 1c: a4). We predicted that loss of electrostatic repulsion would impact the homogeneous crystalline distribution as found in the eADF4(C16) structure leading to rather heterogenous packing, clustering, and distribution of β-sheet structures in eADF4(Ω16)-based materials. This feature could be already seen in self-assembly studies with much faster kinetics than that of the charged variant (data not shown). Although, the fibroin 3-based protein variant $eADF3(AQ)_{12}$ is also uncharged, the amino acid sequence significantly differs in length of the polyalanine as well as glycine-rich sequence motif with direct implications on β-sheet size/crystallite size as well as amorphous regions (Fig. 1c: b1). It is expected that the larger amorphous regions in $eADF3(AQ)_{12}$ sterically separate the crystal parts, leading to a more homogeneous distribution of crystals similar to those found in eADF4(C16), which are based on electrostatic repulsion (Fig. 1c: b1). This structural feature inhibits self-assembly into crystalline nanofibrils [36,52].

Importantly, recombinant spider silk proteins can be processed into solid morphologies such as films (representing the potential use as coatings of medical devices or bio-plastic foils as packaging materials) [41,53–56] or soft hydrogels (which are highly relevant in the fields of tissue engineering and biofabrication) [57–59]. Thus, the experimental design included the use of smooth and structured films as well as hydrogels. For comparison, regenerated *B. mori* fibroin was included representing a

non-spider silk type with a significantly different amino acid sequence and, respectively, slightly different structural features as well as crystal size, poly(caprolactone) (PCL) as a broadly applied biopolymer, and gelatin, a protein-based material which is often used in the context of tissue engineering and biofabrication (i.e. 3D-bioprinting together with cells) [60,61]. To explicitly analyze their suitability in the field of tissue engineering and biofabrication, the bio-selectivity of 2D and 3D materials made of recombinant spider silk proteins was tested in a post-operative contamination model including microbes and fibroblasts.

Results

Bacterial and fungal repellent properties of recombinant spider silk films

To systematically investigate the absence of microbes and the putative bacterial and fungal repellent properties of distinct spider silk surfaces, films of the negatively charged recombinant spider silk proteins eADF4(C16) and eADF4(C32NR4) and the uncharged eADF4(Ω16) and eADF3$((AQ)_{12})$ were fabricated to test the influence of the primary structure, molecular weight, net charge and the presence of a terminal assembly domain (see Table 1 in Ref. [62]) on microbial adhesion.

At first, we investigated biofilm formation on 2D-surfaces using *E. coli* and *P. pastoris*. Microbial viability was quantified using the CellTiter-Blue assay. The negligible adhesion of *E. coli* and *P. pastoris* on eADF4(C16), eADF4(C32NR4), and eADF3$((AQ)_{12})$ as well as eADF4(C16)-RGD films resulted in low fluorescence intensity in comparison to that of consolidated biofilm formation on eADF4(Ω16), *B. mori* fibroin and PCL films with much higher microbial viability (Fig. 2a). To the best of our knowledge, this bacterial and fungal repellent properties of materials made of recombinant spider silk are unique, and, as shown, even materials prepared from regenerated *B. mori* fibroin, which resemble to some extend the composition and properties of spider silk proteins but not at the amino acid sequence and nanostructural level, do not show such behavior.

Methicillin-resistant *Staphylococcus aureus* (MRSA) is a widespread problem in hospitals and is a highly infectious pathogen responsible for numerous fatalities worldwide. To investigate single bacterial adhesion forces of pathogens in contact with 2D spider silk surfaces, we used *S. aureus* which represents an established model organism for single cell adhesion tests. The forces involved in *S. aureus* adhesion on various film surfaces were previously quantified using atomic force microscopy (AFM) in force spectroscopy mode on single bacterial probes [63,64]. A single *S. aureus* cell was immobilized on a tipless AFM cantilever and pressed with a maximum force of 300 pN onto silanized glass slides coated with eADF4(C16), eADF4(C32NR4), eADF4(Ω16), eADF3$((AQ)_{12})$, *B. mori* fibroin, and PCL, the latter two acting as controls. Direct contact was allowed for some microseconds (termed 0 s in the following) or additional 5 s of surface delay time before the single bacterium was lifted and the adhesion force F_{ad} was measured. This contact time of several seconds is a simple method which has been previously established to investigate bacterial adhesion to various materials [65,66], and, therefore, the results obtained here could be directly compared to previous ones. The forces were normalized ($F_{ad\ (biopolymer\ coating)}$/ $F_{ad\ (silanized\ glass)}$), and the statistically

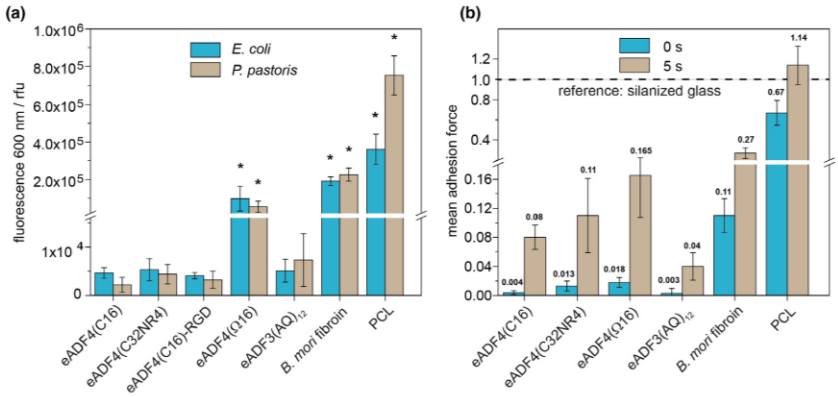

FIGURE 2

Bacterial and fungal repellent properties of 2D scaffolds made of recombinant spider silk proteins. (a) Viability of *E. coli* (blue) and *P. pastoris (brown) cells* on films of eADF4(C16), eADF4(C32NR4), eADF4(C16)-RGD, eADF3$((AQ)_{12})$, *B. mori* fibroin, and PCL, after incubation for 24 h at 37 °C. Microbial viability was quantified using the CellTiter-Blue assay by measuring the transformation of the blue fluorescent dye resazurin into red fluorescent resorufin using 530 nm excitation and 600 nm emission filters in a microplate reader. Each result is an average of five experiments, and the error bars designate the standard deviations. Student's t-test was performed for statistical analysis, * indicates significant difference to eADF4(C16) ($p < 0.05$). (b) Adhesion force measurements upon short contact using single *S. aureus* probes on silanized glass coated with eADF4(C16), eADF4(C32NR4), eADF4(Ω16), eADF3$((AQ)_{12})$, *B. mori* fibroin, and PCL, the latter two serving as controls. Representative normalized mean adhesion forces were obtained from 25 force-distance curves performed on each surface for 0 s (blue) as well as 5 s (brown) surface delay time using one and the same cell immobilized on a cantilever with a nominal spring constant of 0.03 N m^{-1}. Forces were referred to the values measured on uncoated silanized glass (4.8 ± 2.4 nN). It was detected that all distributions of adhesion forces were significantly different with p values below 0.001.

weighted mean adhesion force was determined. Thereby, the recombinant spider silk films made of eADF4(C16), eADF4(C32NR4), and eADF3($(AQ)_{12}$), yielded an extremely low bacterial adhesion force (Fig. 2b). The initial adhesive force at 0 s was slightly, but significantly higher on eADF4(Ω16) film surfaces (factor ~4.5) and even higher on surfaces of *B. mori* fibroin (factor ~28) and of PCL films (factor ~168) in comparison to that of eADF4(C16) films. At a surface delay time of 5 s, the adhesive forces increased in all cases, but still adhesion forces on the three recombinant spider silk protein-based films (eADF4(C16), eADF4(C32NR4), and eADF3$(AQ)_{12}$) were significantly lower than on the control materials (*B. mori* fibroin and PCL). These quantitative adhesion force measurements results of one model pathogen clearly indicated that explicit spider silk surfaces do not allow strong adhesion of *S. aureus* upon first contact while other surfaces do, an observation that is complementary to the biofilm formation assays made with the other bacteria and yeast strains.

This finding is intriguing, since the amino acid building blocks between the different silk proteins are similar with only slight differences. However, these differences are the basis of distinct structural features with significant impact on protein folding and e.g. fibril self-assembly [36,52]. The microbe-repellent properties of these different silks seem to be directly based on these structural features. To confirm that microbe-repellence is based on structural but not topographical features, flat spider silk films were compared to micro-patterned ones (2 μm wide grooves, 1 μm wide and 4 μm high ridges) concerning microbial adhesion. The surface topography of spider silk films has previously been shown to influence mammalian cell attachment and proliferation making this experiment important [42]. Suspended bacteria (*E. coli* and *S. mutans*) as well as fungi (*P. pastoris* and *C. albicans*) were seeded on top of all smooth and patterned films for 12 h at 37 °C (see also Ref. [62]). After washing to remove non-adherent microbes, films were air dried for microscopic analysis of microbial growth. Scanning electron microscope (SEM) images clearly showed that both smooth and patterned films of eADF3 and eADF4 variants (with the exception of eADF4(Ω16), Fig. 3d) substantially restricted the attachment, growth and microbial colonization of bacteria as well as fungi (Fig. 3a–c, e) and (Fig. 1 in Ref. [62]), and confirmed the superior repellence of spider silk 2D films as compared to *B. mori* fibroin and PCL (Fig. 3f and g). This finding confirmed the strict dependence of microbe adhesion to protein-structural surface pattern but not on surface topography, which was surprising since the grooves were expected to provide optimal niches for bacterial and fungal physical attachment, being thought to provide at least some impact on microbe adhesion. The microbe-repellence structural features were overruling any effect that the topography would normally have, which was also exhibited in the control groups. This property could have far-reaching impact on future applications, as for instance, *C. albicans* is an opportunistic, common fungal pathogen found in hospitals and is known to be highly infectious and life threatening.

Next, we investigated whether this protein structure-based bacterial and fungal repellent properties are restricted to the surface of explicit spider silk films or if they are generic, that is, the feature is retained when other spider silk morphologies (with identical protein structures) are prepared, such as hydrogels. Spider silk proteins can be processed into shear thinning hydrogels which can be 3D printed [45], and one possible application is their use as scaffolds in tissue regeneration. Therefore, bacterial and fungal repellent properties would complement other interesting features such as non-toxicity and biodegradability of recombinant spider silk hydrogels [38,39,55]. These properties, in combination with a controllable adhesion of mammalian cells, would boost their applicability in various biomedical applications, especially in biofabrication, i.e. the simultaneous printing of cells and materials (i.e. bioinks) for tissue regeneration [67].

Bacterial and fungal repellent properties of spider silk hydrogels

To monitor their bacterial and fungal repellent properties, spider silk hydrogels were incubated with *E. coli* and *P. pastoris* for 24 h at 37 °C. As a control, hydrogels of regenerated *B. mori* fibroin [68] and GelMA [69,70] as a further commonly used biomaterial were incubated in an identical manner. Subsequently, all hydrogels were washed carefully to remove non-adherent bacteria, and an alamar blue viability assay was used to determine *E. coli* and *P. pastoris* (see Ref. [62]). Spider silk hydrogels with microbes showed little alamar blue fluorescence, exemplarily shown for eADF4(C16) and eADF4(C16)-RGD (Fig. 4a) and (Fig. 2, Table 2, 3 in Ref. [62]). SEM images of lyophilized hydrogels clearly indicated that bacteria and fungi were not adhering and growing on and within recombinant spider silk hydrogels (Fig. 4b (i-ii) and c (i-ii)) even upon incubation for 10 days (Fig. 2, Table 2, 3 in Ref. [62]). Importantly, in this study, adhesion of microbial cells to eADF4(Ω16) hydrogels endorsed the microbe-repellence structural features of spider silk in 3D surfaces as well to some extent (Fig. 4d (i-ii)). It can be clearly seen that *B. mori* fibroin and GelMA hydrogels enabled *E. coli* and *P. pastoris* cells to adhere and colonize, and within both *B. mori* fibroin and GelMA hydrogels, microbial biofilms could be easily detected (Fig. 4e (i-ii) and f (i-ii)).

Bio-selective properties of spider silk films and hydrogels

Since the identified bacterial and fungal repellent properties of distinct spider silk materials can be distinguished from the previously determined topography-dependent adhesion of mammalian cells, we wanted to elucidate whether it is possible to trigger a bio-selective behavior, which represses the growth of microbes but enhances mammalian cell attachment and proliferation on spider silk materials. To improve mammalian cell adhesion, we used eADF4(C16)-RGD known to interact with integrin receptors to promote mammalian cell attachment [44,45,58]. Importantly, all other physicochemical characteristics of this variant are indistinguishable to that of eADF4(C16) including pronounced bacterial and fungal repellent properties to resist biofilm formation as shown above.

Hydrogels made of eADF4(C16) and eADF4(C16)-RGD were used to encapsulate BALB/3T3 fibroblasts yielding bioinks for biofabrication and were then inoculated with *E. coli* and *P. pastoris* for 6 h to mimic a situation similar to that of a tissue regeneration scenario as found for post-operative infection (Fig. 3 in Ref. [62]). After 6 h of incubation, hydrogels were washed carefully to remove non-adherent cells (mammalian as well as microbial), and the hydrogels were further incubated with fresh cell

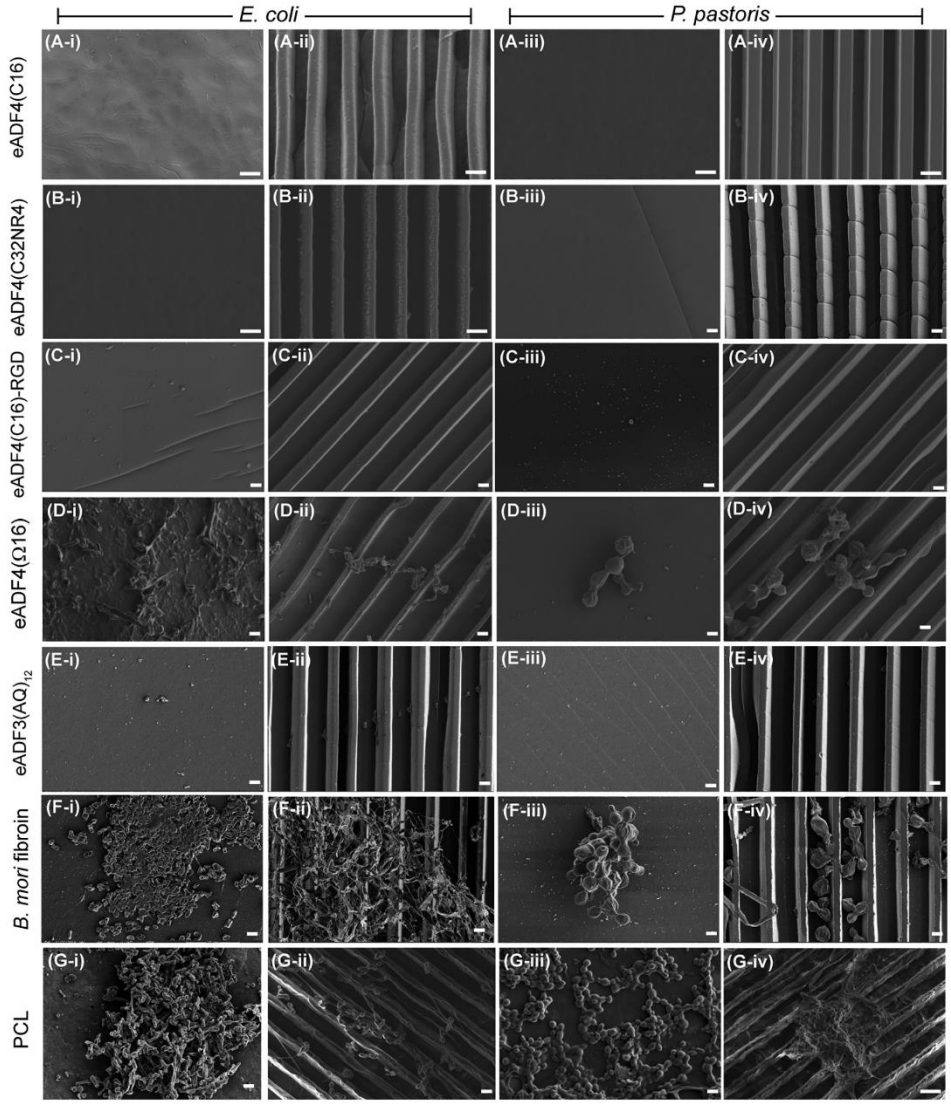

FIGURE 3

Bacterial and fungal repellent properties of films made of recombinant spider silk proteins. SEM images showing (i & iii) plane and (ii & iv) micro-patterned surfaces of films made of (a) eADF4(C16), (b) eADF4(C32NR4), (c) eADF4(C16)-RGD, (d) eADF4(Ω16), (e) eADF3$(AQ)_{12}$, (f) *B. mori* fibroin and (g) PCL after 12 h of incubation with (i & ii) *E. coli* and (iii & iv) *P. pastoris* at 37 °C. Scale bars = 2 μm.

culture media. Viability of microbes and fibroblasts was evaluated by microscopy and live/dead staining after 3, 6, and 10 days of incubation (Fig. 5a–d). Encapsulated fibroblasts showed good viability within the hydrogels made of eADF4(C16) and eADF4(C16)-RGD over a culture period of 10 days (Fig. 5e), while no bacterial and fungi growth/contamination could be detected during the entire cultivation period (Fig. 5f and g), since the microbes could not adhere to the hydrogels to start colony formation and did not manifest a biofilm. As expected, introduction of the RGD-sequence stimulated the proliferation of BALB/3T3 fibroblasts in contrast to eADF4(C16) hydrogels in which very little proliferation was observed.

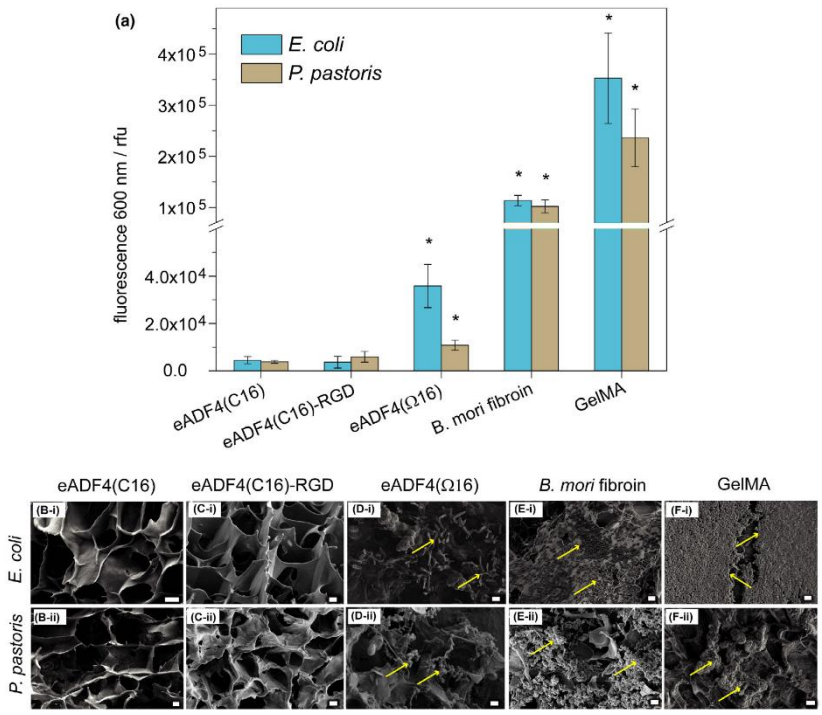

FIGURE 4

Bacterial and fungal repellent properties of spider silk and other hydrogels. (a) Viability of microbial cells on hydrogels made of eADF4(C16), eADF4(C16)-RGD, eADF4(Ω16), *B. mori* fibroin and GelMA after 24 h incubation with *E. coli* and *P. pastoris* at 37 °C. Microbial viability was quantified using the alamar blue assay by measuring the transformation of the blue fluorescent dye resazurin into red fluorescent resorufin with 530 nm excitation and 600 nm emission filters in a microplate reader. Minimal adhesion of *E. coli* and *P. pastoris* on eADF4(C16) and eADF4(C16)-RGD hydrogels resulted in low fluorescence intensity in comparison to adhesion on eADF4(Ω16), *B. mori* fibroin and GelMA hydrogels with higher microbial viability. Each result is an average of three experiments, and the error bars designate the standard deviations. Student's *t*-test was performed for statistical analysis, *indicates significant difference to eADF4(C16) ($p < 0.05$). SEM images of hydrogels prepared from (b) eADF4(C16), (c) eADF4(C16)-RGD, (d) eADF4(Ω16), (e) *B. mori* fibroin and (f) GelMA after 24 h of incubation with (i) *E. coli* and (ii) *P. pastoris*. Arrows show biofilm or microbial cells on hydrogels. Scale bars = 2 μm.

Discussion

Microbial adhesion tests with different pathogenic microorganisms using both bacteria (*S. mutans*, *S. aureus*, and *E. coli*) and fungi (*C. albicans*, and *P. pastoris*) demonstrated microbe repellence of distinct recombinant spider silk materials. None of the tested microbes could manifest biofilms on selected recombinant spider silk films, hydrogel surfaces or within hydrogels. The inherent property of bacterial and fungal repellent performance of distinct spider silk materials is related to the structural features of the underlying proteins responsible for the formation of hydrophobic patches [52,71]. The used protein platform technology (Fig. 6a), confirmed the correlation of adhesion of microorganisms with the presence of hydrophobic patches (Fig. 6b, and c). As shown schematically, based on the primary sequence, hydrophobic patches can be engineered due to either intermolecular charge-charge repulsion as in eADF4(C16) and eADF4(C32NR4) or a volume effect of the amorphous region in eADF3 $(AQ)_{12}$. In contrast, the absence of charge in eADF4(Ω16) induces a denser and less homogeneous packing of nano ß-crystallites, creating new anchoring sites for microbes. On the mesoscale, microbial cell attachment most readily occurs on surfaces which are rougher, more hydrophobic, and positively charged. Distinct silk proteins, such as spider silk and silkworm silk, feature structural differences e.g. concerning the β-sheet crystallite size (spider silk: ~7 nm, *B. mori* fibroin ~14–200 nm) and crystallite orientation [54,72,73], both influencing the dimensions of the respective hydrophobic patches. Our study demonstrated that 2D and 3D surfaces of *B. mori* fibroin with larger hydrophobic patches than that of spider silk are easily accessible for microbial manifestation. Finally, RGD-modified spider silk with homogeneous hydrophobic patches showed repellence of microbes but allowed selective mammalian cell adhesion and proliferation.

In comparison to natural spider silk with its composite surface layer, it is highly interesting that no additional components such as glycoproteins, lipids or antimicrobial agents but only the structural features of individual recombinant spider silk proteins

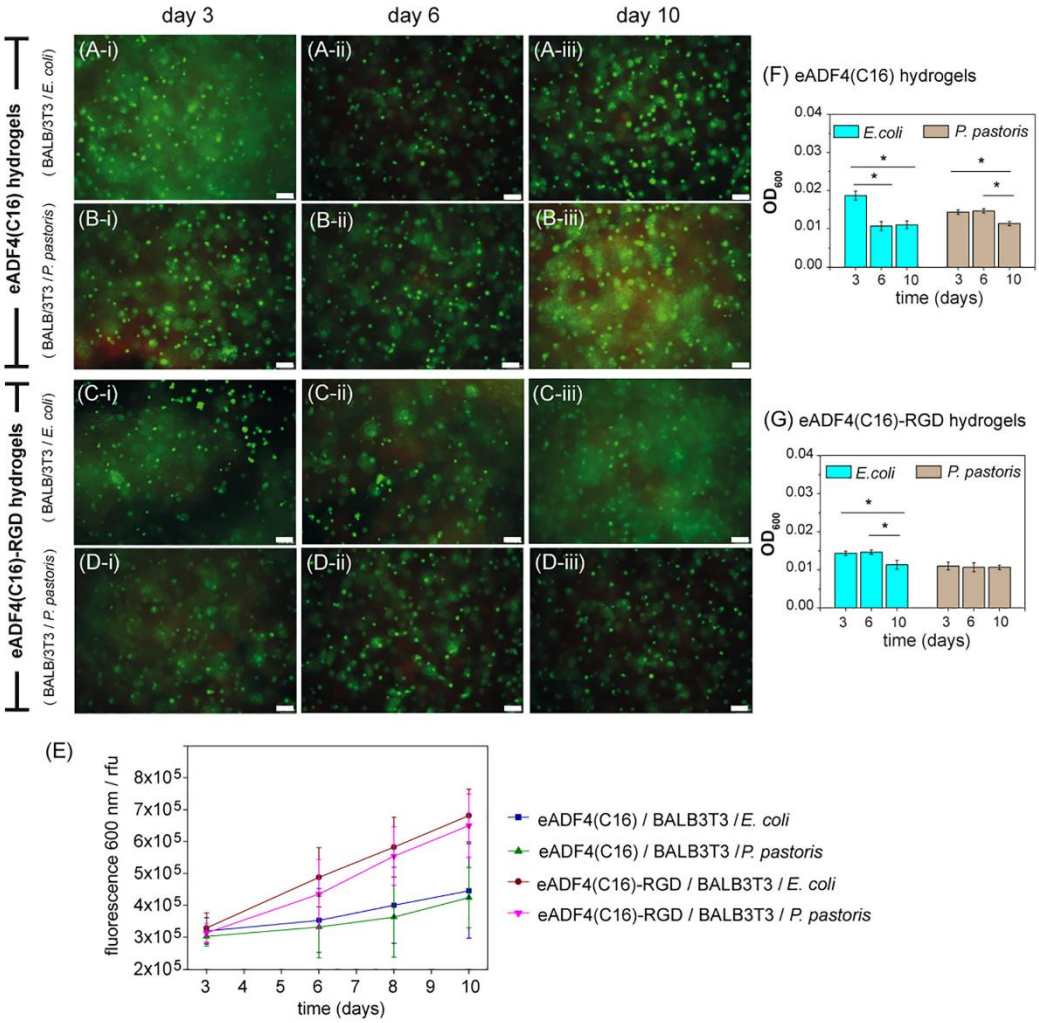

FIGURE 5

Bacterial and fungal repellent properties of 3D scaffolds made of eADF4(C16) and eADF4(C16)-RGD in a post-operative contamination model containing microbes and mammalian cells. Fluorescence images of (a and b) eADF4(C16) and (c and d) eADF4(C16)-RGD hydrogels with encapsulated BALB/3T3 fibroblasts (i.e. bioinks for biofabrication) and cultured with (a and c) *E. coli* and (b and d) *P. pastoris* for (i) 3 days, (ii) 6 days, and (iii) 10 days. Scale bars = 100 μm. The cells were stained with calcein A/M (live cells: green) and ethidium homo dimer I (dead cells: red). Ethidium homodimer I also stained the hydrogels yielding an unspecific red background fluorescence (a–d). Proliferation of mouse fibroblasts (BALB/3T3) in presence of microbes was measured over 10 days using (e) the absorbance of cell titer blue. Microbial growth of *E. coli* and *P. pastoris* in fresh media was measured using (f and g) optical density at 600 nm (OD_{600}) with microbial inoculated hydrogels (after washing) and after incubation for 12 h at 37 °C. Each result is an average of three experiments and the error bars designate the standard deviation. Student's *t*-test was performed for statistical analysis, $*p < 0.05$.

are necessary to generate a microbe-repellent spider silk surface. To the best of our knowledge, this is a completely new finding which opens the door for novel applications of spider silk materials, e.g., as bioselective coatings in various biomedical applications as for the preparation of bioinks for biofabrication and regeneration medicine.

Methods

Protein design and production of recombinant spider silk proteins: eADF4(C16) was purchased from AMSilk GmbH (Planegg, Germany). The recombinant spider silk proteins eADF4(C16)-RGD, eADF4(C32NR4) and $eADF3(AQ)_{12}$ were produced and purified as described previously [36,44]. To generate the uncharged

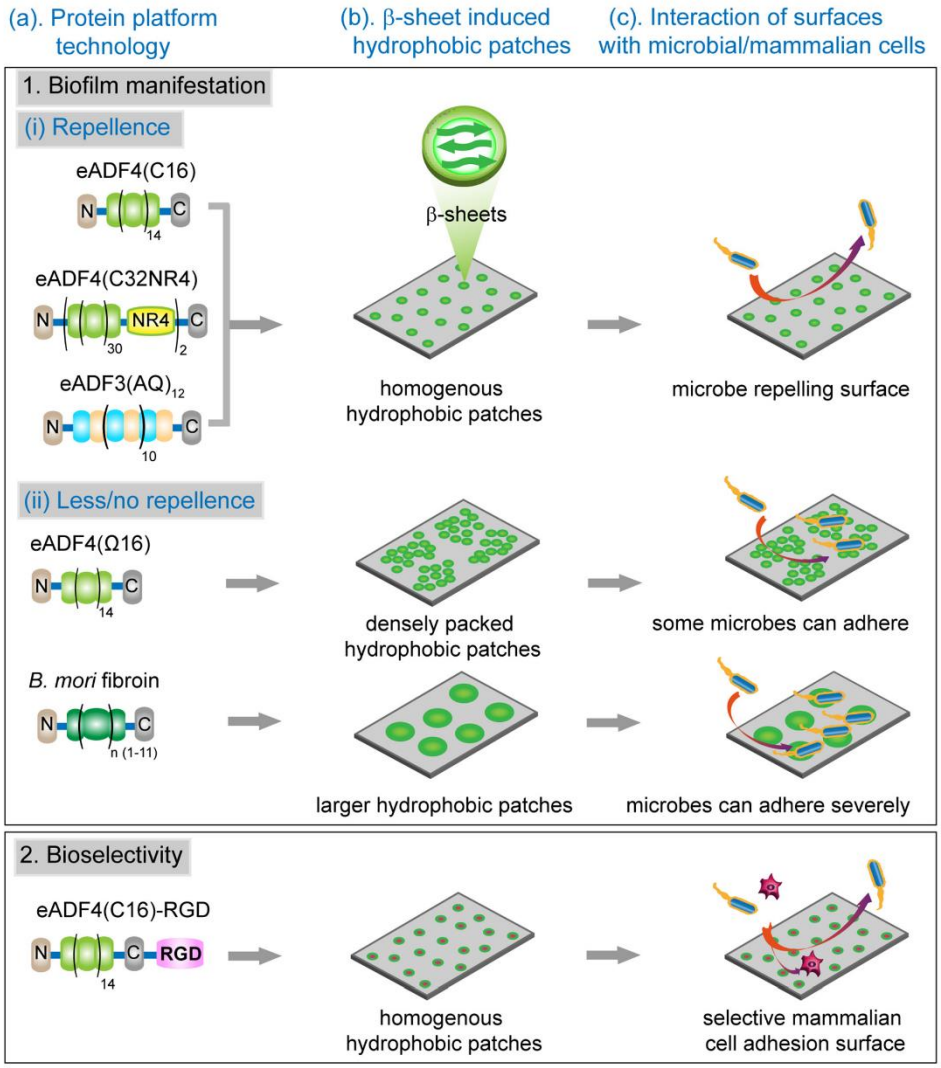

FIGURE 6

Schematic illustration of the microbial behavior on silk materials with (1) repellent/non-repellent and (2) bioselective surfaces. (a) Recombinant spider silk variant/silkworm silk, (b) β-sheet formation yields hydrophobic surface patches with unique distribution and dimensions. (c) Homogeneous hydrophobic patch distribution of eADF4(C16), dimeric eADF4(C32NR4), and eADF3$((AQ)_{12})$ shows microbe repellence characteristics. The absence of charge-charge repulsion or steric effects in eADF4(Ω16) leads to dense packing of hydrophobic patches and structured larger hydrophobic patches in *B. mori* fibroin favoring the attachment of microbial cells. eADF4(C16)-RGD allows selective mammalian cell attachment with simultaneous microbe repellence.

eADF4(Ω16) variant, the glutamic acid residues (E) of the consensus sequence of eADF4(C16) were exchanged with glutamine (Q) ones. The recombinant spider silk protein eADF4(Ω16) was produced in *E. coli* BL21 gold (DE3) and purified following a protocol as described previously [36]. Briefly, after cell disruption eADF4 (Ω16) was purified using a heat step and an ammonium sulphate precipitation.

Bombyx mori (B. mori) fibroin protein: Regenerated fibroin solutions were prepared as described previously [68] by dissolving degummed (boiled for 30 min in 0.02 M sodium carbonate) silk fibres in 9.3 M LiBr solution, dialysis against ultrapure water (Milli-Q) for 2 d at 4 °C, centrifugation at 8500 rpm for 45 min at 4 °C, and collection of the supernatant. The *B. mori* fibroin solutions had a final concentration of ~6% w/v and were stored

at 4 °C until use. To produce flat and patterned films, solutions were freeze-dried and processed in the same way as spider silk and PCL.

Production of flat and patterned films: All flat and patterned films of proteins and polycaprolactone (PCL; Perstorp AB) were produced by film casting onto patterned polydimethylsiloxane (PDMS; Sylgard 184 Silicone Elastomer, Dow Corning) substrates. PDMS stamps were produced by casting of a 10:1 mixture of PDMS pre-polymer and curing agent (degassed for 20 min) on a photo-lithographically patterned waver to generate the desired geometry (12 × 12 mm area with 2 μm wide grooves, ridges with a width of 1 μm and a height of 4 μm). After curing at 80 °C for 90 min, the stamps were solidified and could be easily peeled off. To produce patterned films, proteins and PCL were dissolved in 1,1,1,3,3,3,-hexafluoro-2-propanol (HFIP; Alpha Aesar) at a concentration of 100 mg/mL (room temperature, overnight). To generate films with a thickness of 10–15 μm, 250 μL of solution (corresponding to 25 mg of protein/polymer) were poured into the stamp, and the solvent was subsequently evaporated at room temperature. The dried patterned films were removed and post-treated with 100% ethanol for 1 h to render the silk protein water insoluble upon induction of β-sheet structures. To ensure that only material properties determined the results of microbial growth experiments, all samples (including PCL films) were treated the same way. After post-treatment, the samples were stored sterile in 70% ethanol at 4 °C.

Bacteria and yeast culture on films: *Streptococcus mutans* (DSMZ 20523, Braunschweig) and *Candida albicans* (patient isolate), stored at −80 °C, were thawed at RT, fractionally spread on Columbia blood agar (PB 5039A, oxoid, Wesel) and incubated for 48 h at 37 °C and 5% CO_2. Afterwards, an overnight culture was prepared in BBLTM Schaedler Broth medium (Becton Dickinson, Sparks MD, USA), and then the culture was diluted (1:10) with Schaedler Broth medium (see also Ref [62]).

Escherichia coli BL21(DE3)-gold (Novagen, Merck, Darmstadt, Germany), stored at −80 °C, was thawed at RT and inoculated in Luria–Bertani medium (LB), at 37 °C with constant shaking at 150 rpm until an optical density (OD_{600}) between 0.8 and 1 was reached (corresponding to a viable count of approx. 10^7–10^8 CFU mL ^{1}). The *E. coli* culture was diluted (1:10) with LB medium.

Pichia pastoris X33 (wild type, Invitrogen, Germany) was inoculated in YPD-media and allowed to grow for 24 h at 30 °C with constant shaking at 150 rpm. The *P. pastoris* culture was diluted (1:10) with YPD medium.

Staphylococcus aureus (strain SA113), stored at −20 °C, was thawed and cultured on blood agar plates for three days at 37 °C. Then, one colony from a plate was transferred into 5 mL of sterile tryptic soy broth (TSB) and cultured overnight at 150 rpm, 37 °C. For each experiment, 40 μL of the culture were transferred into 4 mL fresh TSB and cultured for another 2.5 h at 37 °C. The bacterial culture was washed three times with sterile phosphate buffered saline (PBS). The final suspension of bacteria in PBS was stored at 4 °C and used no longer than 6 h.

Silk and polymer films were taken out of 70% ethanol, subsequently washed with PBS (8.18 g NaCl, 0.2 g KCl, 0.24 g anhydrous KH_2PO_4, 1.78 g $Na_2HPO_4 \times 2H_2O$, 1 L distilled water, pH 7.4, Sigma Aldrich, St. Louis, Missouri, USA), and incubated in 5 mL of diluted microbial solution (as described above) in petri dishes (Φ 5 cm) for 60 h (5% CO_2, 37 °C). Then, the films were removed and carefully washed with PBS to remove non-adherent bacteria and yeast cells and dried at room temperature for subsequent SEM imaging.

Adhesion force measurements: A single *S. aureus* cell was attached to a tipless AFM cantilever (MLCT-0 with a nominal spring constant of 0.03 N/m from Bruker Nano, Santa Barbara, Ca, USA) coated with polydopamine that was calibrated before each set of experiments [63,64]. Force-distance measurements were performed using a Bioscope Catalyst from Bruker-Nano in PBS at room temperature. The maximum force with which the cell was pressed onto the surfaces was set to 300 pN. On each surface, 25 force-distance curves were performed for 0 s and 5 s of additional surface delay time with one and the same cell, the total number of individual cells being twelve. The results obtained from three of these cells were not used for the analysis as their adhesion forces were less than 5% of the mean adhesion force of the remaining cells indicating that the adhesive strengths of these cells were not representative for the totality of *S. aureus* cells used. Nine more cells were tested on eADF4 (C16), *B. mori* fibroin, and PCL with identical parameters under the same conditions. Approaching speed towards the surfaces was set to 800 nm/s for 0 s of surface delay time and 100 nm/s for 5 s of surface delay time. Retraction speed was 800 nm/s. To test the results of adhesion measurements for statistical significance, all adhesion force distributions were analyzed in pairs by a Man–Whitney-*U*-test with the software Matlab.

Bacterial and yeast cell viability: Adhesion of *E. coli* and *P. pastoris* to silk and polymer films or hydrogels was measured by analysis of cell vitality using the CellTiter-Blue assay after culturing for 24 h at 37 °C. Samples incubated with bacterial and yeast cells were washed with phosphate buffered saline (PBS; Sigma-Aldrich) three times, and then incubated with 10% CellTiter-Blue (Promega) in PBS for 3 h at 37 °C. Transformation of the blue fluorescent dye resazurin into red fluorescent resorufin (λ_{ex} = 530 nm; λ_{em} = 590 - nm) was measured using a plate reader (Mithras LB 940, Berthold, Bad Wildbad) with a counting time of 0.5 s.

Preparation of eADF4(C16), eADF4(C16)-RGD and eADF4(Ω16) hydrogels: Lyophilized eADF4(C16) and eADF4(C16)-RGD were dissolved in 6 M guanidinium thiocyanate (GdmSCN) at 5 mg/mL and dialyzed using dialysis membranes with a molecular weight cutoff of 6–8 kDa against 10 mM Tris/HCl, pH 7.5 overnight at room temperature. Subsequent dialysis against 20% w/v poly (ethylene glycol) (PEG, 20,000 g/mol) at a volume ratio of PEG/eADF4(C16) solution of 100:1 was used to remove water by osmotic pressure and to adjust 30 mg/mL (3% w/v) spider silk solutions. Hydrogels were self-assembled after an overnight incubation at 37 °C. For the preparation of eADF4(Ω16) hydrogels, due to the faster self-assembly of fibrils, all steps were carried out at 4 °C, and hydrogels were prepared at a concentration of 20 mg/mL (2% w/v).

For post-operative contamination experiments, 1×10^6 BALB/3T3 fibroblasts were added to 3% w/v eADF4(C16) and eADF4(C16)-RGD spider silk solutions before gelation in an incubator at 37 °C.

Preparation of B. mori fibroin hydrogels: *B. mori* fibroin hydrogels were prepared using sonication-induced gelation, as previously reported [68]. In brief, 4% (w/v) aqueous silk fibroin solution in a 15 mL conical tube was ultra-sonicated (Ultrasonic Homogenizers HD 3100, BANDELIN) at 50% amplitude (21 W) for 30 s, and overnight incubation at 37 °C induced gelation.

Preparation of methacrylated gelatin hydrogels: Gelatin Methacrylate (GelMA) was produced upon reacting gelatin solutions (gelatin from bovine skin, Type B, ~225 g Bloom, Sigma-Aldrich) with methacrylic anhydride (Sigma-Aldrich) following previously described protocols [69,70]. After the dissolution of 10% (w/v) gelatin in 0.1 M CB buffer (3.18 g sodium carbonate and 5.86 g sodium bicarbonate in 1L distilled water) at 60 °C, one sixth of 1% (v/v) methacrylic anhydride was added dropwise every 30 min for 3 h. The solution was vigorously stirred for another 1 h, diluted with 0.1M CB, and dialyzed for 2 days against ultrapure (Milli-Q) water at 37 °C. The solution was then freeze-dried in a lyophilizer to obtain methacrylamide-modified gelatin as a dry white powder.

Methacrylamide-modified gelatin hydrogel was obtained by UV exposure of 5% (w/v) GelMA solution in 24 well cell culture vessels at 365 nm using an ultraviolet lamp (Benda, type NU -4 KL) for 15 min in the presence of 0.5 mg/mL of the photoinitiator 2-hydroxy-4′-(2-hydroxyethoxy)-2-methylpropiophenone (Irgacure- 2959, Sigma-Aldrich).

Bacteria and yeast culture with hydrogels: Hydrogels were incubated with 1 mL of diluted liquid cultures of *E. coli* and *P. pastoris* for 12 h at 37 °C. Hydrogels were washed with phosphate buffered saline (PBS; Sigma-Aldrich) three times to remove non-adherent bacteria and yeast cells and then lyophilized.

Microbial adhesion: The microbe repellence activity of eADF4 (C16) and eADF4(C16)-RGD hydrogels concerning *E. coli* and *P. pastoris* was measured by inoculating the supernatant (100 µL) of the microbe-treated hydrogels (after washing) in fresh media and culturing for additional 12 h at 37 °C. Optical density at 600 nm (OD_{600}; OD600 DiluPhotometer™, IMPLEN) was measured to monitor microbial growth/infection.

BALB/3T3 cultivation: BALB/3T3 mouse fibroblasts (European Collection of Cell Cultures) were cultured in Dulbecco's Modified Eagle Medium (DMEM, Biochrom) supplemented with 10% fetal bovine serum (Biochrom) and 1% (v/v) GlutaMAX (Gibco) in a controlled atmosphere of 5% CO_2, 95% humidity and at 37 °C. Viability and number of cells were analyzed using trypan blue (Sigma-Aldrich) in a Neubauer chamber (Laboroptik, UK).

Post-operative contamination model: eADF4(C16) and eADF4 (C16)-RGD hydrogels with encapsulated BALB/3T3 mouse fibroblasts (i.e. bioinks) were prepared in hanging cell culture inserts using 24-well plates (Merck Millipore) and then exposed to diluted (1:10, corresponding to OD 0.25) bacterial and yeast cells prepared in DMEM for 6 h at 37 °C and 80% relative humidity. Hydrogels were washed three times to remove non-adherent microbes and incubated with fresh DMEM media and cultivated for 10 days under identical conditions. Cell culture medium was changed every 24 h. The cell viability of BALB/3T3 mouse fibroblasts was analyzed using a Live/Dead assay after 3, 6 and 10 days.

Live/Dead assay: Films and hydrogels of eADF4(C16) and eADF4(C16)-RGD were washed with PBS and stained with Calcein acetoxymethylester (Calcein A/M, Invitrogen) and Ethidium Homodimer-1 (EthD-1, Invitrogen) in cell culture medium for the detection of live and dead cells, respectively. Calcein A/M was added to the medium at a final concentration of 0.3 µM, and Ethidium Homodimer-1 was added to the medium at a final concentration of 0.1 µM and incubated for 30 min. After staining, the solution was removed, and fresh PBS was added for imaging. Live and dead cells were visualized and analyzed using a fluorescence microscope (Leica DMi8, Wetzlar) and processed using either Leica Application Suite or Image J.

Scanning electron microscopy (SEM): To analyze the morphological structure using SEM, hydrogels were lyophilized and fixed to SEM stubs using conductive carbon cement solution (Leit-C, PLANO GmbH). Samples were sputter-coated with 2 nm platinum (Sputter Coater 208 HR with 268 MTM 20, Cressington, Watford, U.K.) and then imaged at an accelerating voltage of 2.5 kV using a scanning electron microscope 270 Zeiss Sigma VP 300 (Zeiss, Oberkochen, Germany) and Field Emission Gun (FEG; Apreo VS, ThermoFisher Scientific/FEI, Germany).

CRediT authorship contribution statement

Sushma Kumari: Conceptualization, Methodology, Validation, Formal analysis, Investigation, Data curation, Writing - original draft, Writing - review & editing, Visualization. **Gregor Lang:** Conceptualization, Methodology, Validation, Formal analysis, Investigation, Data curation, Writing - original draft, Writing - review & editing, Visualization. **Elise DeSimone:** Methodology, Formal analysis, Investigation, Data curation, Writing - review & editing. **Christian Spengler:** Methodology, Validation, Formal analysis, Investigation, Data curation. **Vanessa T. Trossmann:** Methodology, Validation, Formal analysis, Investigation, Data curation, Writing - review & editing. **Susanne Lücker:** Methodology, Validation, Formal analysis, Investigation, Data curation. **Martina Hudel:** Methodology, Validation, Formal analysis, Investigation, Data curation. **Karin Jacobs:** Supervision, Funding acquisition, Writing - review & editing. **Norbert Krämer:** Supervision, Writing - review & editing. **Thomas Scheibel:** Conceptualization, Supervision, Funding acquisition, Writing - review & editing.

Declaration of Competing Interest

The authors declare that they have no known competing financial interests or personal relationships that could have appeared to influence the work reported in this paper.

Acknowledgements

The authors thank Dr. Hendrik Bargel for SEM imaging. This project has been funded by the Deutsche Forschungsgemeinschaft (DFG, German Research Foundation)-project number 326998133–TRR225 (funded subprojects and PIs: A07: G.L.; C01: T.S.and JA 905/6: C. S.) as well as SFB840 (A08: T.S.) and SFB 1027 (B2: K.J.).

Author contributions

S.K. and G.L. contributed equally to this work. S.K. performed the in vitro bacterial/ fungal repellent experiments and coculture experiments on films and hydrogels with *E. coli* and *P. pastoris*. G. L. prepared films (smooth and patterned), prepared protein

coated silanized glass slides, performed SEM and analyzed the data. E.D. assisted in designing of coculture experiments. V.T.T. designed, synthesized, and purified the recombinant spider silk variant eADF4(Ω16) and assisted in handing of the protein. S. L., M.H. and N.K. carried out in vitro experiments of *S. mutans* and *C. albicans*. C.S. and K.J. prepared bacterial probes and performed force distance measurements. T.S. designed the experiments and supervised the project. S.K. and G.L wrote the manuscript. E.D., V.T.T., C.S., K.J. and T.S. contributed to writing and editing of the manuscript.

Competing interests

The authors declare the following competing financial interest (s): T.S. is co-founder and shareholder of AMSilk GmbH.

References

[1] L.L. Leape et al., The Nature of adverse events in hospitalized patients, N. Engl. J. Med. 324 (1991) 377–384. http://www.nejm.org/doi/full/10.1056/NEJM199102073240605.

[2] V. Russotto et al., Bacterial contamination of inanimate surfaces and equipment in the intensive care unit, J. Intensive Care 3 (2015) 54, https://doi.org/10.1186/s40560-015-0120-5.

[3] A. Gristina, Biomaterial-centered infection: microbial adhesion versus tissue integration, Science 237 (1987) 1588–1595, https://doi.org/10.1126/science.3629258.

[4] E. Barth et al., In vitro and in vivo comparative colonization of Staphylococcus aureus and Staphylococcus epidermidis on orthopaedic implant materials, Biomaterials 10 (1989) 325–328, https://doi.org/10.1016/0142-9612(89)90073-2.

[5] B. Carpentier, O. Cerf, Biofilms and their consequences, with particular reference to hygiene in the food industry, J. Appl. Bacteriol. 75 (1993) 499–511, https://doi.org/10.1111/j.1365-2672.1993.tb01587.x.

[6] S.B. Levy, B. Marshall, Antibacterial resistance worldwide: causes, challenges and responses, Nat. Med. 10 (2004) S122–S129, https://doi.org/10.1038/nm1145.

[7] D. Davies, Understanding biofilm resistance to antibacterial agents, Nat. Rev. Drug Discov. 2 (2003) 114–122, https://doi.org/10.1038/nrd1008.

[8] G.D. Wright, The antibiotic resistome: the nexus of chemical and genetic diversity, Nat. Rev. Microbiol. 5 (2007) 175–186, https://doi.org/10.1038/nrmicro1614.

[9] J.W. Costerton, P.S. Stewart, E.P. Greenberg, Bacterial biofilms: a common cause of persistent infections, Science 284 (1999) 1318–1322, https://doi.org/10.1172/JCI23825.

[10] P.S. Stewart, J. William Costerton, Antibiotic resistance of bacteria in biofilms, Lancet 358 (2001) 135–138, https://doi.org/10.1016/S0140-6736(01)05321-1.

[11] T.J. Foster, The Staphylococcus aureus "superbug", J. Clin. Invest. 114 (2004) 1693–1696, https://doi.org/10.1172/JCI23825.

[12] E. Binda, F. Marinelli, G.L. Marcone, Old and new glycopeptide antibiotics: action and resistance, Antibiotics 3 (2014) 572–594, https://doi.org/10.3390/antibiotics3040572.

[13] J. Pootoolal, J. Neu, G.D. Wright, Glycopeptide antibiotic resistance, Annu. Rev. Pharmacol. Toxicol. 42 (2002) 381–408, https://doi.org/10.1146/annurev.pharmtox.42.091601.142813.

[14] J. Hasan, R.J. Crawford, E.P. Ivanova, Antibacterial surfaces: the quest for a new generation of biomaterials, Trends Biotechnol. 31 (2013) 295–304, https://doi.org/10.1016/j.tibtech.2013.01.017.

[15] D. Campoccia, L. Montanaro, C.R. Arciola, A review of the clinical implications of anti-infective biomaterials and infection-resistant surfaces, Biomaterials 34 (2013) 8018–8029, https://doi.org/10.1016/j.biomaterials.2013.07.048.

[16] D. Campoccia, L. Montanaro, C.R. Arciola, A review of the biomaterials technologies for infection-resistant surfaces, Biomaterials 34 (2013) 8533–8554, https://doi.org/10.1016/j.biomaterials.2013.07.089.

[17] S. Chen et al., Surface hydration: principles and applications toward low-fouling/nonfouling biomaterials, Polymer 51 (2010) 5283–5293, https://doi.org/10.1016/j.polymer.2010.08.022.

[18] S. Krishnan, C.J. Weinman, C.K. Ober, Advances in polymers for anti-biofouling surfaces, J. Mater. Chem. 18 (2008) 3405–3413, https://doi.org/10.1039/B801491D.

[19] E.-R. Kenawy, S.D. Worley, R. Broughton, The chemistry and applications of antimicrobial polymers: a state-of-the-art review, Biomacromolecules 8 (2007) 1359–1384, https://doi.org/10.1021/bm061150q.

[20] M.R.E. Santos et al., Recent developments in antimicrobial polymers: a review, Materials 9 (2016) 599, https://doi.org/10.3390/ma9070599.

[21] Y. Yang et al., Antimicrobial cationic polymers: from structural design to functional control, Polym. J. 50 (2018) 33–44, https://doi.org/10.1038/pj.2017.72.

[22] M. Zasloff, Antimicrobial peptides of multicellular organisms, Nature 415 (2002) 389–395, https://doi.org/10.1038/415389a.

[23] E.M. Hetrick, M.H. Schoenfisch, Reducing implant-related infections: active release strategies, Chem. Soc. Rev. 35 (2006) 780–789, https://doi.org/10.1039/B515219B.

[24] K.P. Miller et al., Inorganic nanoparticles engineered to attack bacteria, Chem. Soc. Rev. 44 (2015) 7787–7807, https://doi.org/10.1039/C5CS00041F.

[25] Y. Liu et al., Nanotechnology-based antimicrobials and delivery systems for biofilm-infection control, Chem. Soc. Rev. 48 (2019) 428–446, https://doi.org/10.1039/C7CS00807D.

[26] D. Campoccia et al., Antibiotic-loaded biomaterials and the risks for the spread of antibiotic resistance following their prophylactic and therapeutic clinical use, Biomaterials 31 (2010) 6363–6377, https://doi.org/10.1016/j.biomaterials.2010.05.005.

[27] M.M. Harriott, M.C. Noverr, Candida albicans and Staphylococcus aureus form polymicrobial biofilms: effects on antimicrobial resistance, Antimicrob. Agents Chemother. 53 (2009) 3914–3922, https://doi.org/10.1128/AAC.00657-09.

[28] L. Eisoldt, A. Smith, T. Scheibel, Decoding the secrets of spider silk, Mater. Today 14 (2011) 80–86, https://doi.org/10.1016/S1369-7021(11)70057-8.

[29] J.A. Kluge et al., Spider silks and their applications, Trends Biotechnol. 26 (2008) 244–251, https://doi.org/10.1016/j.tibtech.2008.02.006.

[30] S. Wright, S.L. Goodacre, Evidence for antimicrobial activity associated with common house spider silk, BMC Res. Notes 5 (2012) 326, https://doi.org/10.1186/1756-0500-5-326.

[31] A. Sponner et al., Composition and hierarchical organisation of a spider silk, PLOS ONE 2 (2007) e998, https://doi.org/10.1371/journal.pone.0000998.

[32] A.R. Franco et al., Silk-based antimicrobial polymers as a new platform to design drug-free materials to impede microbial infection, Macromol. Biosci. 18 (2018) 1800262, https://doi.org/10.1002/mabi.201800262.

[33] L. Nilebäck et al., Self-assembly of recombinant silk as a strategy for chemical-free formation of bioactive coatings: a real-time study, Biomacromolecules 18 (2017) 846–854, https://doi.org/10.1021/acs.biomac.6b01721.

[34] R.H. Zha et al., Universal nanothin silk coatings via controlled spidroin self-assembly, Biomater. Sci. 7 (2019) 683–695, https://doi.org/10.1039/C8BM01186A.

[35] S. Zhang et al., Nitrogen inaccessibility protects spider silk from bacterial growth, J. Exp. Biol. 222 (2019) jeb214981, https://doi.org/10.1242/jeb.214981.

[36] D. Huemmerich et al., Primary structure elements of spider dragline silks and their contribution to protein solubility, Biochemistry 43 (2004) 13604–13612, https://doi.org/10.1021/bi048983q.

[37] C. Vendrely, T. Scheibel, Biotechnological production of spider-silk proteins enables new applications, Macromol. Biosci. 7 (2007) 401–409, https://doi.org/10.1002/mabi.200600255.

[38] A. Leal-Egaña, T. Scheibel, Silk-based materials for biomedical applications, Biotechnol. Appl. Biochem. 55 (2010) 155–167, https://doi.org/10.1042/BA20090229.

[39] S. Müller-Herrmann, T. Scheibel, Enzymatic degradation of films, particles, and nonwoven meshes made of a recombinant spider silk protein, ACS Biomater. Sci. Eng. 1 (2015) 247–259, https://doi.org/10.1021/ab500147u.

[40] P.H. Zeplin et al., Spider silk coatings as a bioshield to reduce periprosthetic fibrous capsule formation, Adv. Funct. Mater. 24 (2014) 2658–2666, https://doi.org/10.1002/adfm.201302813.

[41] C.B. Borkner et al., Surface modification of polymeric biomaterials using recombinant spider silk proteins, ACS Biomater. Sci. Eng. 3 (5) (2017) 767–775, https://doi.org/10.1021/acsbiomaterials.6b00306.

[42] F. Bauer, S. Wohlrab, T. Scheibel, Controllable cell adhesion, growth and orientation on layered silk protein films, Biomater. Sci. 1 (2013) 1244–1249, https://doi.org/10.1039/C3BM60114E.

[43] A. Leal-Egana et al., Interactions of fibroblasts with different morphologies made of an engineered spider silk protein, Adv. Eng. Mater. 14 (2012) B67–B75, https://doi.org/10.1002/adem.201180072.

[44] S. Wohlrab et al., Cell adhesion and proliferation on RGD-modified recombinant spider silk proteins, Biomaterials 33 (2012) 6650–6659, https://doi.org/10.1016/j.biomaterials.2012.05.069.

[45] K. Schacht et al., Biofabrication of cell-loaded 3D spider silk constructs, Angew. Chem. Int. Ed. 54 (2015) 2816–2820, https://doi.org/10.1002/anie.201409846.
[46] K. Schacht, U. Slotta, M. Suhre, Prevention of biofilm formation with vegan silk polypeptides, Sofw J 143 (2017) 04.
[47] M.V. Graham, N.C. Cady, Nano and microscale topographies for the prevention of bacterial surface fouling, Coatings 4 (2014) 37–59, https://doi.org/10.3390/coatings4010037.
[48] X. Khoo, M.W. Grinstaff, Novel infection-resistant surface coatings: a bioengineering approach, MRS Bulletin 36 (2011) 357–366, https://doi.org/10.1557/mrs.2011.66.
[49] A. Tripathy et al., Natural and bioinspired nanostructured bactericidal surfaces, Adv. Colloid Interface Sci. 248 (2017) 85–104, https://doi.org/10.1016/j.cis.2017.07.030.
[50] S. Erramilli, J. Genzer, Influence of surface topography attributes on settlement and adhesion of natural and synthetic species, Soft Matter 15 (2019) 4045–4067, https://doi.org/10.1039/C9SM00527G.
[51] Y. Cheng, G. Feng, C.I. Moraru, Micro- and nanotopography sensitive bacterial attachment mechanisms: a review, Front. Microbiol. 10 (2019) 191, https://doi.org/10.3389/fmicb.2019.00191.
[52] M. Humenik et al., Ion and seed dependent fibril assembly of a spidroin core domain, J. Struct. Biol. 191 (2015) 130–138, https://doi.org/10.1016/j.jsb.2015.06.021.
[53] U. Slotta et al., Structural analysis of spider silk films, Supramol. Chem. 18 (2006) 465–471, https://doi.org/10.1080/10610270600832042.
[54] E. Metwalli et al., Structural changes of thin films from recombinant spider silk proteins upon post-treatment, Appl. Phys. A 89 (2007) 655–661, https://doi.org/10.1007/s00339-007-4265-5.
[55] K. Spiess, A. Lammel, T. Scheibel, Recombinant spider silk proteins for applications in biomaterials, Macromol. Biosci. 10 (2010) 998–1007, https://doi.org/10.1002/mabi.201000071.
[56] S. Wohlrab, K. Spieß, T. Scheibel, Varying surface hydrophobicities of coatings made of recombinant spider silk proteins, J. Mater. Chem. 22 (2012) 22050–22054, https://doi.org/10.1039/C2JM35075K.
[57] S. Kumari et al., Recombinant spider silk hydrogels for sustained release of biologicals, ACS Biomater. Sci. Eng. 4 (2018) 1750–1759, https://doi.org/10.1021/acsbiomaterials.8b00382.
[58] E. DeSimone et al., Recombinant spider silk-based bioinks, Biofabrication 9 (2017) 044104, https://doi.org/10.1088/1758-5090/aa90db.
[59] C. Thamm, E. DeSimone, T. Scheibel, Characterization of hydrogels made of a novel spider silk protein eMaSp1s and evaluation for 3D printing, Macromol. Biosci. 17 (2017) 1700141, https://doi.org/10.1002/mabi.201700141.
[60] B. Dhandayuthapani et al., Polymeric scaffolds in tissue engineering application: a review, Int. J. Polym. Sci. 2011 (2011) 290602, https://doi.org/10.1155/2011/290602.
[61] J. Jang, H.-G. Yi, D.-W. Cho, 3D printed tissue models: present and future, ACS Biomater. Sci. Eng. 2 (2016) 1722–1731, https://doi.org/10.1021/acsbiomaterials.6b00129.
[62] S. Kumari, et al., Data for microbe resistant engineered recombinant spider silk protein based 2D and 3D materials. Data in Brief, submitted for publication (2020).
[63] N. Thewes et al., A detailed guideline for the fabrication of single bacterial probes used for atomic force spectroscopy, Eur. Phys. J. E 38 (2015) 140, https://doi.org/10.1140/epje/i2015-15140-2.
[64] C. Spengler et al., Strength of bacterial adhesion on nanostructured surfaces quantified by substrate morphometry, Nanoscale 11 (2019) 19713–19722, https://doi.org/10.1039/C9NR04375F.
[65] A. Beaussart et al., Single-cell force spectroscopy of probiotic bacteria, Biophys J. 104 (2013) 1886–1892, https://doi.org/10.1016/j.bpj.2013.03.046.
[66] G. Zeng, T. Müller, R.L. Meyer, Single-cell force spectroscopy of bacteria enabled by naturally derived proteins, Langmuir 30 (2014) 4019–4025, https://doi.org/10.1021/la404673q.
[67] T. Jungst et al., Strategies and molecular design criteria for 3D printable hydrogels, Chem. Rev. 116 (2016) 1496–1539, https://doi.org/10.1021/acs.chemrev.5b00303.
[68] D.N. Rockwood et al., Materials fabrication from Bombyx mori silk fibroin, Nat. Protoc. 6 (2011) 1612–1631, https://doi.org/10.1038/nprot.2011.379.
[69] H. Shirahama et al., Precise tuning of facile one-pot gelatin methacryloyl (GelMA) synthesis, Sci. Rep. 6 (2016) 31036, https://doi.org/10.1038/srep31036.
[70] B.J. Klotz et al., Gelatin-methacryloyl hydrogels: towards biofabrication-based tissue repair, Trend Biotechnol. 34 (2016) 394–407, https://doi.org/10.1016/j.tibtech.2016.01.002.
[71] C.B. Borkner et al., Ultrathin spider silk films: insights into spider silk assembly on surfaces, ACS Appl. Polym. Mater. 1 (2019) 3366–3374, https://doi.org/10.1021/acsapm.9b00792.
[72] A.M. Anton et al., Foundation of the outstanding toughness in biomimetic and natural spider silk, Biomacromolecules 18 (2017) 3954–3962, https://doi.org/10.1021/acs.biomac.7b00990.
[73] C. Guo et al., Structural comparison of various silkworm silks: an insight into the structure-property relationship, Biomacromolecules 19 (2018) 906–917, https://doi.org/10.1021/acs.biomac.7b01687.

7.5. Teilarbeit V

Teilarbeit V wurde 2020 unter dem Titel „*Data for microbe resistant engineered recombinant spider silk protein based 2D and 3D materials*“ im Journal *Data in Brief* veröffentlicht.

Kumari, S.*; Lang, G.*; DeSimone, E.; Spengler, C.; **Trossmann, V. T.**; Lücker, S.; Hudel, M.; Jacobs, K.; Krämer, N. & Scheibel, T. (2020) Data for microbe resistant engineered recombinant spider silk protein based 2D and 3D materials. *Data in Brief* **32**: 106305.

https://doi.org/10.1016/j.dib.2020.106305

* gleichberechtigte Co-Autorenschaft

Teilarbeit V beinhaltet weitere Daten zu Teilarbeit IV (Kumari, S.*; Lang, G.*; DeSimone, E.; Spengler, C.; **Trossmann, V. T.**; Lücker, S.; Hudel, M.; Jacobs, K.; Krämer, N. & Scheibel, T. (2020) Engineered spider silk-based 2D and 3D materials prevent microbial infestation. *Materials Today* **41**: 21.) und ist als zusätzlich publizierte *Supporting Information* zu verstehen.

Data in Brief 32 (2020) 106305

Contents lists available at ScienceDirect

Data in Brief

journal homepage: www.elsevier.com/locate/dib

Data Article

Data for microbe resistant engineered recombinant spider silk protein based 2D and 3D materials

Sushma Kumari[a,†], Gregor Lang[a,b,†], Elise DeSimone[a], Christian Spengler[c], Vanessa T. Trossmann[a], Susanne Lücker[d], Martina Hudel[e], Karin Jacobs[c], Norbert Krämer[d], Thomas Scheibel[a,f,g,h,i,*]

[a] Department of Biomaterials, Faculty of Engineering Science, University of Bayreuth, Prof.-Rüdiger-Bormann-Str. 1, 95447 Bayreuth, Germany
[b] Biopolymer Processing Group, Faculty of Engineering Science, University of Bayreuth, Ludwig-Thoma-Str. 36A, 95447 Bayreuth, Germany
[c] Department of Experimental Physics and Center for Biophysics, Saarland University, 66123 Saarbrücken, Germany
[d] Medical Center for Dentistry, Department of Paediatric Dentistry, Medical Center Gießen and Marburg, Justus-Liebig University Gießen, Schlagenzahl 14, 35392 Gießen, Germany
[e] Institute of Medical Microbiology, Justus-Liebig University Gießen, Schubertstraße 81, 35392 Gießen, Germany
[f] Bayreuth Center for Material Science and Engineering (BayMAT), Germany
[g] Bavarian Polymer Institute (BPI), Germany
[h] Bayreuth Center for Colloids and Interfaces (BZKG), Germany
[i] Bayreuth Center for Molecular Biosciences (BZMB), University of Bayreuth, Universitätsstraße 30, 95447 Bayreuth, Germany

ARTICLE INFO

Article history:
Received 8 July 2020
Revised 7 September 2020
Accepted 8 September 2020
Available online 11 September 2020

ABSTRACT

Data presented in this article describe bacterial and fungal repellent properties of 2D-films and 3D-hydrogels made of different recombinantly produced spider silk proteins based on consensus sequences of Araneus diadematus dragline silk proteins (fibroin 3 and 4). Here, the attachment, growth, and microbial colonization of Streptococcus mutans (S. mutans) as well as Candida albicans (C. albicans) on plane and micro-patterned films were visualized by scanning electron microscopy (SEM). Also, microbial

DOI of original article: 10.1016/j.mattod.2020.06.009
* Corresponding author.
E-mail address: thomas.scheibel@bm.uni-bayreuth.de (T. Scheibel).
† These authors contributed equally to this work.

https://doi.org/10.1016/j.dib.2020.106305

Keywords:
Microbe adhesion
Hydrogels
Patterned films
Biofilm
Bioselective surface
Engineered spider silk proteins

viability data are provided of Escherichia coli (E. coli) and Pichia pastoris (P. pastoris) on hydrogels made of eADF4(C16) and eADF4(C16)-RGD, quantified using the Alamar blue assay. Experimental results, design of a post-operative contamination model of microbes with mammalian cells, and methods in the data article refer to the research paper "Engineered spider silk-based 2D and 3D materials prevent microbial infestation" published recently [1].

Specifications Table

Subject	Biotechnology, Biomaterials
Specific subject area	Microbe repellent recombinant spider silk proteins
Type of data	Table, Microscopy images, Figures
How data were acquired	Adhesion of microbial cells on films was analysed using scanning electron microscopy (SEM). Spider silk and polycaprolactone (PCL) films were incubated in microbial solutions (*S. mutans* and *C. albicans*) for 12 h and at 37 °C. The films were washed with phosphate buffered saline (PBS) and placed in 2.5% v/v glutaraldehyde for 1 h to fix the microbial cells, followed by gradual dehydration using ethanol solutions from 30% (in Milli-Q water) to 100 %. All dried samples were sputter coated with 2 nm platinum and imaged at an accelerating voltage of 2.5 kV using a Zeiss Sigma 660 VP 300, Germany. Adhered microbial cells (*E. coli* and *P. pastoris*) on hydrogels were analysed using the CellTiter-Blue assay. Hydrogels incubated with bacterial and yeast cells were washed with PBS and then incubated with 10% CellTiter Blue in PBS for 3 h at 37 °C. Transformation of the blue fluorescent dye resazurin into red fluorescent resorufin ($\lambda_{ex} = 530$ nm; $\lambda_{em} = 590$ nm) was measured using a plate reader (Mithras LB 940, Berthold, Bad Wildbad) with a counting time of 0.5 s.
Data format	Raw data were analysed and processed using Origin and Adobe illustrator.
Parameters for data collection	Experiments were performed by incubating 2D films (eADF4(C16) and PCL) with *S. mutans* and *C. albicans*, and 3D hydrogels (eADF4(C16) and eADF4(C16)-RGD) with *E. coli and P. pastoris* for 12 h and 24 h, respectively, at 37 °C.
Description of data collection	Films were dried and imaged using SEM. Hydrogels were incubated with 10 % CellTiter-Blue in PBS for 3 h at 37 °C, and transformation of the blue fluorescent dye resazurin into red fluorescent resorufin (λex = 530 nm; λem = 590 nm) was analysed using a plate reader.
Data source location	Institution: University of Bayreuth City/Town/Region: Bayreuth Country: Germany
Data accessibility	The data are supplied with this article.
Related research article	Authors' names: Sushma Kumari, Gregor Lang, Elise DeSimone, Christian Spengler, Vanessa T. Trossmann, Susanne Lücker, Martina Hudel, Karin Jacobs, Norbert Krämer and Thomas Scheibel Title: Engineered spider silk-based 2D and 3D materials prevent microbial infestation Journal: Materials Today DOI: https://doi.org/10.1016/j.mattod.2020.06.009

Value of the Data

- The dataset provides insights into the bacterial and fungal repellence properties of spider silk based 2D-films and 3D-hydrogels as shown in reference (1).
- The data clearly show that both, smooth and patterned eADF films and hydrogels substantially restrict the attachment, growth and microbial colonization of pathogenic bacteria and fungi.

Table 1
Properties of recombinant spider silk proteins.

Recombinant spider silk protein	M_w (kDa)	No. of charged amino acid residues at neutral pH (positive/negative)	pI
eADF4(C16)	47.7	0/16	3.5
eADF4(C32NR4)	104.1	2/34	3.5
eADF4(C16)-RGD	48.5	1/17	3.6
eADF4(Ω16)	47.7	0/0	7.7
$eADF3(AQ)_{12}$	48.0	0/0	5.5

Charged amino acid residues refer to silk sequences only; the T7 tag, present in all constructs, comprises an additional arginine residue. Values for eADF4(C16), eADF4(C32NR4), and eADF3((AQ)12) were taken from Ref. 2, eADF4(C16)-RGD from Ref. 3, and unpublished data of eADF4(Ω16).

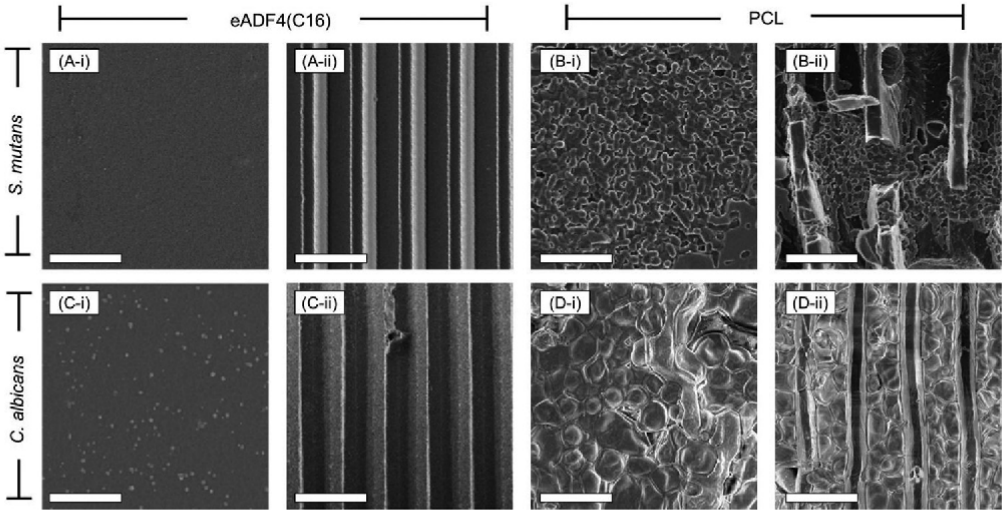

Fig. 1. Bacterial and fungal repellent properties of films made of eADF4(C16). SEM images showing (i) plane and (ii) micro-patterned surfaces of (A & C) eADF4(C16) and (B & D) PCL after 12 h of incubation with (A & B) *S. mutans* and (C & D) *C. albicans* at 37 °C. Scale bars = 5 µm.

- The data are useful to design advanced biopolymers that can selectively repel pathogenic microorganisms without actively killing microbes, and, at the same time, promote mammalian cell growth.
- The data is valuable in understanding and examining the microbe-repellent effects of natural spider silk.
- The data is providing information for researchers in the field of biomedical engineering to develop microbe repellent surfaces for biomedical and technical applications.

1. Data Description

Data presented in this article demonstrate that 2D-films and 3D-hydrogels of recombinantly produced proteins show bacterial and fungal repellent properties without killing microbes upon contact. Table 1 summarizes the properties of two engineered *Araneus diadematus* fibroins eADF3 and eADF4 and variants thereof with respect to their molecular weight, net charge and the presence of a terminal assembly domain. SEM images in Fig. 1 clearly show that both, smooth and patterned eADF4(C16) films significantly restrict the attachment and microbial colonization of *S. mutans* as well as *C. albicans*, as compared to polycaprolactone (PCL) films. The viability of *E. coli* and *P. pastoris* on hydrogels of eADF4(C16) and eADF4(C16)-RGD was quantified over 10 days

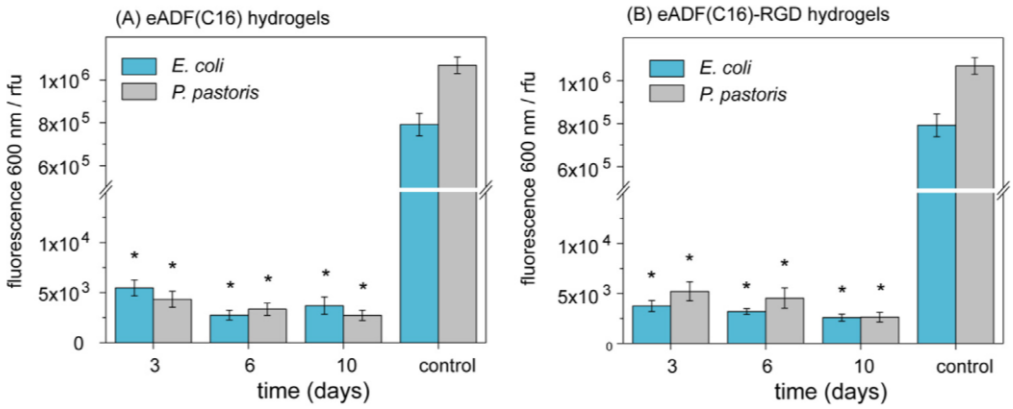

Fig. 2. Bacterial and fungal repellent properties of hydrogels made of two different spider silk variants. Viability of *E. coli* and *P. pastoris cells* on hydrogels of (A) eADF4(C16) and (B) eADF4(C16)-RGD was quantified over 10 days using the CellTiter-Blue assay and analyzing the transformation of the blue fluorescent dye resazurin into red fluorescent resorufin using 530 nm excitation and 600 nm emission filters in a microplate reader. Cell culture treated plates without coating were used as control. Each result is an average of three experiments, and the error bars designate the standard deviations. Student's t-test was performed for statistical analysis, $^{*}p < 0.05$.

Table 2
CellTiter-Blue assay data of eADF4(C16) hydrogels in Fig. 2.

Sample name	Days	Fluorescence measurement, Ex 530 nm/Em 600 nm			Average ± stdev	Student's t. test value
		S1	S2	S3		
eADF4(C16)_*E. coli*	3	4597	6141	5697	5478 ± 795	1.32×10^{-5}
eADF4(C16)_*P. pastoris*	3	5220	3625	4184	4343 ± 809	1.14×10^{-6}
eADF4(C16)_*E. coli*	6	3225	2807	2230	2754 ± 500	1.31×10^{-5}
eADF4(C16)_*P. pastoris*	6	2662	3536	3843	3347 ± 612	1.13×10^{-6}
eADF4(C16)_*E. coli*	10	2829	3721	4559	3703 ± 865	1.31×10^{-5}
eADF4(C16)_*P. pastoris*	10	2502	3316	2368	2729 ± 513	1.13×10^{-6}
Control_*E.coli*	1	741307	846368	788259	791978 ± 52629	
Control_*P. pastoris*	1	1053496	1112205	1039713	1068471 ± 38496	

using the CellTiter-Blue assay and is shown in Fig. 2 and raw data is provided in Table 2 and 3. The experimental design of a post-operative contamination model of bacteria and fungi with mammalian cells in/on hydrogel scaffolds made of eADF4(C16) and RGD-modified eADF4(C16) is shown in Fig. 3. This data specifically demonstrates the aptness of recombinant spider silk in the field of tissue engineering to selectively promote mammalian cell binding and provide microbe repellence at the same time. These data are comprehensively discussed in the reference article [1].

2. Additional Information Concerning the Recombinant Spider Silk Protein Sequences

Engineered *Araneus diadematus*fibroins eADF3 and eADF4 and variants thereof are based on the repetitive consensus sequences (modules C and Ω (ADF4), modules A and Q (ADF3)) of the core domains of the naturally occurring fibroins ADF3 and ADF4 of the dragline silk of the European garden spider *A. diadematus*. The number after the modules depict the amount of repeats (e.g. C16 stands for 16 times the C module).

Amino acid sequence of module C: GSS AAAAAAAA S GPGGY GPENQGPS GPGGY GPGGP
Amino acid sequence of module Ω: GSS AAAAAAAA S GPGGY GPQNQGPS GPGGYGPGGP
Amino acid sequence of module A: GPYGP GASAAAAAA GGYGP GSGQQ
Amino acid sequence of module Q: GPGQQ GPGQQ GPGQQ GPGQQ

Table 3
CellTiter-Blue assay data of eADF4(C16)-RGD hydrogels in Fig. 2.

Sample name	Days	Fluorescence measurement, Ex 530 nm/Em 600 nm			Average ± stdev	Student's t. test value
		S1	S2	S3		
eADF4(C16)-RGD_ *E. coli*	3	3516	4360	3345	3740 ± 543	1.32×10^{-5}
eADF4(C16)-RGD_ *P. pastoris*	3	4272	6189	5143	5201 ± 960	1.14×10^{-6}
eADF4(C16)-RGD_ *E. coli*	6	3074	3528	2986	3196 ± 291	1.31×10^{-5}
eADF4(C16)-RGD_ *P. pastoris*	6	4494	3532	5559	4528 ± 1013	1.13×10^{-6}
eADF4(C16)-RGD_ *E. coli*	10	2185	2847	2559	2707 ± 136	1.32×10^{-5}
eADF4(C16)-RGD_ *P. pastoris*	10	2120	2681	3075	2625 ± 480	1.13×10^{-6}

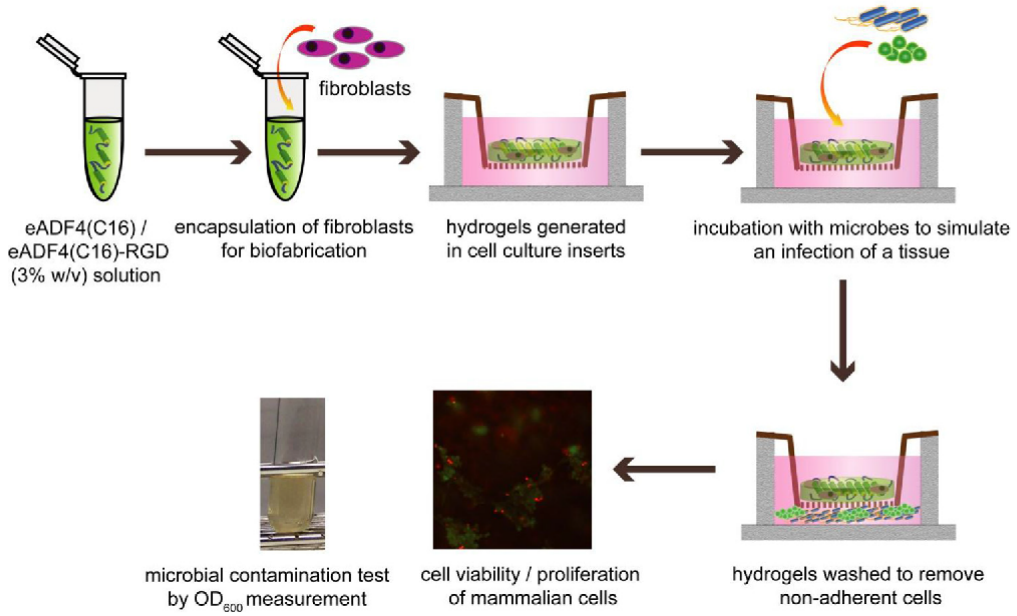

Fig. 3. Schematic illustration demonstrating a post-operative contamination model of microbes (*E. coli* and *P. pastoris*) and mammalian cells (BALB/3T3) in/on hydrogel scaffolds made of eADF4(C16) and eADF4(C16)-RGD. The cell viability of mouse fibroblasts (BALB/3T3) in culture with microbes was evaluated by cell staining with calcein A/M (live cells: green) and ethidium homodimer I (dead cells: red), and microbial growth of *E. coli* and *P. pastoris* in fresh media was measured using the optical density at 600 nm (OD_{600}).

Abbreviations: RGD, Arginylglycylaspartic acid; NR4, non-repetitive region of ADF4.

Design and production of these recombinant proteins have been described in Detail in references [1] and [2].

3. Experimental Design, Materials and Methods

3.1. Bacteria and yeast culture on films

Streptococcus mutans (DSMZ 20523, Braunschweig) and *Candida albicans* (patient isolate), stored at -80 °C, were thawed at room temperature (RT), fractionally spread on Columbia blood

agar (PB 5039A, oxoid, Wesel) and incubated for 48 h at 5 % CO_2 and 37 °C. Afterwards, an overnight culture was prepared in BBL™ Schaedler Broth medium (Becton Dickinson, Sparks MD, USA) and diluted (1:10) with Schaedler Broth medium.

Escherichia coli BL21(DE3)-gold (Novagen, Merck, Darmstadt, Germany), stored at -80 °C, was thawed at RT and inoculated in Luria–Bertani medium (LB) with constant shaking at 150 rpm, 37 °C, until an optical density (OD_{600}) between 0.8 and 1 was reached (corresponding to a viable count of approx. 10^7–10^8 CFU mL^{-1}). The *E. coli* culture was diluted (1:10) with LB medium.

Pichia pastoris X33 (wild type, Invitrogen, Germany) was inoculated in YPD-media and allowed to grow with constant shaking at 150 rpm for 24 h at 30 °C. The *P. pastoris* culture was diluted (1:10) with YPD medium.

Spider silk and PCL films were taken out of 70 % ethanol, subsequently washed with PBS (8.18 g NaCl, 0.2 g KCl, 0.24 g anhydrous KH_2PO_4, 1.78 g Na_2HPO_4 x $2H_2O$, 1 L distilled water, pH 7.4, Sigma Aldrich, St. Louis, Missouri, USA), and incubated in 5 mL of diluted microbial solution (as described above) in petri dishes (Ø 5 cm) for 12 h (5 % CO_2, 37 °C). Then, the films were removed and carefully washed with PBS to remove any non-adherent bacteria and yeast cells, fixed with 2.5 % v/v glutaraldehyde for 1 h, gradually dehydrated with ethanol solutions from 30% (in Milli-Q water) to 100 %, and finally dried at room temperature for subsequent SEM imaging.

***Bacterial and yeast cell viability*:** Adhered *E. coli* and *P. pastoris* on hydrogels were analysed using the CellTiter-Blue assay after culturing for 24 h at 37 °C. Samples incubated with bacterial and yeast cells were washed with phosphate buffered saline (PBS; Sigma-Aldrich) three times and then incubated with 10 % CellTiter-Blue (Promega) in PBS for 3 h at 37 °C. Transformation of the blue fluorescent dye resazurin into red fluorescent resorufin ($\lambda_{ex} = 530$ nm; $\lambda_{em} = 590$ nm) was measured using a plate reader (Mithras LB 940, Berthold, Bad Wildbad) with a counting time of 0.5 s.

***Post-operative contamination model*:** The experimental setup was similar to the previously described ones mimicking post-operative infection in which microbial cells were allowed to adhere on tissue engineering scaffolds for 2–6 h. [4,5,6] eADF4(C16) and eADF4(C16)-RGD hydrogels with encapsulated BALB/3T3 mouse fibroblasts (i.e. bioinks used for biofabricaiton) were prepared in hanging cell culture inserts using 24-well plates (Merck Millipore) and then exposed to diluted (1:10, corresponding to OD 0.25) bacterial and yeast cells prepared in DMEM for 6 h, 80 % relative humidity and at 37 °C. Hydrogels were washed three times to remove non-adherent microbes and incubated with fresh DMEM media and cultivated for 10 days under identical conditions. Cell culture medium was changed every 24 h. The cell viability of BALB/3T3 mouse fibroblasts was analyzed using the Live/Dead assay after 3, 6 and 10 days.

***Scanning electron microscopy (SEM)*:** To analyze the morphological structure using SEM, dried films and lyophilized hydrogels were fixed to SEM stubs using conductive carbon cement solution (Leit-C, PLANO GmbH). Samples were sputter-coated with 2 nm platinum (Sputter Coater 208 HR with 268 MTM 20, Cressington, Watford, UK.) and then imaged at an accelerating voltage of 2.5 kV using a 270 Zeiss Sigma VP 300 (Zeiss, Oberkochen, Germany) and Field Emission Gun (FEG; Apreo VS, ThermoFisher Scientific/FEI, Germany).

Declaration of Competing Interest

The authors declare the following competing financial interest (s): T.S. is co-founder and share-holder of the AMSilk GmbH.

Acknowledgments

This project has been funded by the Deutsche Forschungsgemeinschaft (DFG, German Research Foundation)-project number 326998133–TRR225 (funded subprojects and PIs: A07: G.L. and C01: T.S.) as well as SFB840 (A08: T.S.) and SFB 1027 (B2: KJ).

References

[1] S. Kumari, G. Lang, E. DeSimone, C. Spengler, V.T. Trossmann, S. Lücker, M. Hudel, K. Jacobs, N. Krämer, T. Scheibel, Engineered spider silk-based 2D and 3D materials prevent microbial infestation, Mater. Today (2020) https://doi.org/10.1016/j.mattod.2020.06.009.

[2] D. Huemmerich, C.W. Helsen, S. Quedzuweit, J. Oschmann, R. Rudolph, T. Scheibel, Primary structure elements of spider dragline silks and their contribution to protein solubility, Biochemistry 43 (2004) 13604–13612 https://doi.org/10.1021/bi048983q.

[3] S. Wohlrab, S. Müller, A. Schmidt, S. Neubauer, H. Kessler, A. Leal-Egaña, T. Scheibel, Cell adhesion and proliferation on RGD-modified recombinant spider silk proteins, Biomaterials 33 (2012) 6650–6659 https://doi.org/10.1016/j.biomaterials.2012.05.069.

[4] Y. Zhu, Y. Gu, S. Qiao, L. Zhou, J. Shi, H. Lai, Bacterial and mammalian cells adhesion to tantalum-decorated micro-/nano-structured titanium, J. Biomed. Mater. Res. A. 105 (2017) 871-878, doi:10.1002/jbm.a.35953.

[5] J. Tan, Z. Liu, D. Wang, X. Zhang, S. Qiana, X. Liu, A facile and universal strategy to endow implant materials with antibacterial ability *via* alkalinity disturbing bacterial respiration, Biomater. Sci. 8 (2020) 1815–1829, doi:10.1039/C9BM01793C.

[6] D. Wang, Q. Li, J. Qiu, X. Zhang, N. Ge, X. Liu, Corrosion motivated ROS generation helps endow titanium with broad-spectrum antibacterial abilities, Adv. Mater. Interfaces (6) (2019) 1900514, doi:10.1002/admi.201900514.

7.6. Teilarbeit VI

Teilarbeit VI wurde 2021 unter dem Titel „Recombinant Spider Silk Gels Derived from Aqueous-Organic Solvents as Depots for Drugs“ im Journal *Angewandte Chemie International Edition* veröffentlicht.

Neubauer, V. J.; **Trossmann, V. T.**; Jacobi S.; Döbl, A. & Scheibel, T. (2021) Recombinant Spider Silk Gels Derived from Aqueous-Organic Solvents as Depots for Drugs. *Angewandte Chemie International Edition* **60**: 11847.

https://doi.org/10.1002/anie.202103147

Eine deutsche Version von Teilarbeit VI wurde unter dem Titel „Rekombinante Spinnenseidengele aus wässrig-organischen Mischphasen als Wirkstoffdepots“ in *Angewandte Chemie* veröffentlicht.

Neubauer, V. J.; **Trossmann, V. T.**; Jacobi S.; Döbl, A. & Scheibel, T. (2021) Rekombinante Spinnenseidengele aus wässrig-organischen Mischphasen als Wirkstoffdepots. *Angewandte Chemie* **133**: 11953.

https://doi.org/10.1002/ange.202103147

GDCh Communications Angewandte International Edition Chemie

Hydrogels

How to cite: *Angew. Chem. Int. Ed.* **2021**, *60*, 11847–11851
International Edition: doi.org/10.1002/anie.202103147
German Edition: doi.org/10.1002/ange.202103147

Recombinant Spider Silk Gels Derived from Aqueous–Organic Solvents as Depots for Drugs

*Vanessa J. Neubauer, Vanessa T. Trossmann, Sofia Jacobi, Annika Döbl, and Thomas Scheibel**

Abstract: *Hydrogels are widely used in various biomedical applications, as they cannot only serve as materials for biofabrication but also as depots for the administration of drugs. However, the possibilities of formulation of water-insoluble drugs in hydrogels are rather limited. Herein, we assembled recombinant spider silk gels using a new processing route with aqueous–organic co-solvents, and the properties of these gels could be controlled by the choice of the co-solvent. The presence of the organic co-solvent further enabled the incorporation of hydrophobic drugs as exemplarily shown for 6-mercaptopurine. The developed gels showed shear-thinning behaviour and could be easily injected to serve, for example, as drug depots, and they could even be 3D printed to serve as scaffolds for biofabrication. With this new processing route, the formulation of water-insoluble drugs in spider silk-based depots is possible, circumventing common pharmaceutical solubility issues.*

Hydrogels are used for biomedical applications such as tissue engineering, drug delivery, and recently also biofabrication.[1] Besides polysaccharides, such as alginate[2] or chitosan,[3] proteins such as *Bombyx mori* silkworm silk[4] or gelatine[5] have been processed into hydrogels using various methods. Also, hydrogel formation of the recombinant spider silk protein eADF4(C16), which is engineered based on the repetitive core domain of one of the *Araneus diadematus* dragline silk proteins,[6] has been investigated thoroughly.[7] Spider silk hydrogels exhibit shear-thinning behaviour,[7a] which is a crucial requirement for 3D printing and biofabrication[8] or the administration as drug depots.[9] Modifications during processing allowed incorporating water-soluble biologicals in eADF4(C16) hydrogels and their sustained release.[9] However, several pharmaceutical active agents show only poor water solubility or stability and cannot be delivered using hydrogels. Therefore, the aim of this study was to provide drug depots based on gels with the possibility to formulate both water-soluble and water-insoluble drugs.

Ions such as potassium or phosphate effect folding[10] of spider silk proteins,[11] and this kosmotropic ion-triggered structure formation is part of the natural assembly process of spider silk.[12] However, protein folding effects can be also achieved using non-physiological organic co-solvents when they are fully miscible in water.[13] The presence of organic co-solvents with varying polarity can change the solvation conditions, often leading to protein conformational changes.[13] The assumption that especially hydrophobic interactions and hydrogen bonds are driving forces of protein folding is commonly agreed with.[14] Besides intramolecular folding, also intermolecular structure formation can be obtained in aqueous–organic solvents yielding protein assembly and fibrillisation.[15]

Therefore, we investigated a novel gelation route of recombinant spider silk proteins upon fibril assembly in aqueous–organic micro-heterogeneous phases, including the underlying assembly mechanism, and we provide evidence for the use of gels made therewith as drug depots as well as their 3D printability.

Recombinant spider silk proteins have previously been reported to assemble into fibrils and/or particles upon addition of potassium phosphate, and the gained morphology depends on the concentration of the kosmotropic salt.[6,11,16] Here, we investigated assembly in the presence of co-solvents and -solutes such as DMSO and potassium phosphate and obtained characteristic fibrillisation-based sigmoidal turbidity curves[7a] (Figure 1 A). In order to gain more mechanistic insights into this behaviour, three spider silk protein variants differing in their net charge but with otherwise identical amino acid compositions were analysed (see Experimental Section). Potassium phosphate induced fibrillisation of the negatively charged eADF4(C16),[6] which was used as positive control, and its mechanism of fibrillisation has been reported previously.[11] The positively charged eADF4(κ16)[17] showed accelerated protein aggregation and phase separation in the

[*] V. J. Neubauer, V. T. Trossmann, S. Jacobi, A. Döbl, Prof. T. Scheibel
Lehrstuhl Biomaterialien, Universität Bayreuth
Prof.-Rüdiger-Bormann Strasse 1, 95447 Bayreuth (Germany)
Prof. T. Scheibel
Bayreuther Zentrum für Kolloide und Grenzflächen (BZKG)
Universität Bayreuth
Universitätsstrasse 30, 95440 Bayreuth (Germany),
and
Bayerisches Polymerinstitut (BPI)
Universität Bayreuth
Universitätsstrasse 30, 95440 Bayreuth (Germany),
and
Bayreuther Zentrum für Molekulare Biowissenschaften (BZMB)
Universität Bayreuth
Universitätsstrasse 30, 95440 Bayreuth (Germany),
and
Bayreuther Materialzentrum (BayMAT)
Universität Bayreuth
Universitätsstrasse 30, 95440 Bayreuth (Germany)
E-mail: thomas.scheibel@bm.uni-bayreuth.de
Supporting information and the ORCID identification number(s) for the author(s) of this article can be found under: https://doi.org/10.1002/anie.202103147.

GDCh Communications Angewandte International Edition Chemie

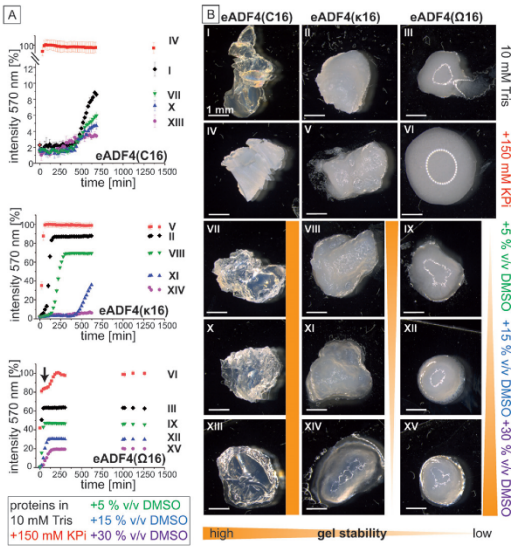

Figure 1. Assembly of three eADF4 variants in presence of different Tris/DMSO volume ratios in comparison to that in presence of 150 mM potassium phosphate (KPi). I–III in 10 mM Tris pH 7.5, IV–VI in presence of 150 mM KPi, VII–IX in presence of 5% (v/v) DMSO, X–XII in presence of 15% (v/v) DMSO, and XIII–XV in presence of 30% (v/v) DMSO. A) Turbidity measurements of eADF4(C16), eADF4(κ16), and eADF4(Ω16) as indicated during fibril formation. Fibril assembly is normalised to KPi samples. The arrow indicates particle formation in case of eADF4(Ω16). B) Stereomicroscopic images of gels at conditions as indicated; scale bars 1 mm. Image VI shows reflections of the light source appearing as a ring. Qualitative gel stabilities are indicated by stability bars.

presence of potassium phosphate, and the uncharged eADF4(Ω16)[18] showed particle formation, indicating a shift towards lower critical potassium phosphate concentrations for particle formation for this variant. The impact of DMSO was analysed in aqueous–organic binary mixtures[19] with different volumes. Like in potassium phosphate, in DMSO the uncharged variant showed the fastest nucleation and fibril growth based on its low electrostatic repulsion, which was least controllable. The positively charged variant showed a fast turbidity increase assuming an aggregation-driven process, yielding gelly morphologies, but no stable gels. The negative variant exhibited the longest lag-phase and yielded well-controllable gels. As this protein is based on the naturally occurring spider silk consensus sequence, the best-controlled assembly behaviour was expected. It has to be mentioned that the addition of DMSO yielded decreased turbidity for all variants and additionally slowed down fibrillisation for eADF4(Ω16) and extended the lag-phase for eADF4(κ16).

Interestingly, gel stability was dependent on both the net charge of the eADF4 variant, as already mentioned above, and the organic additive (Figure 1B), indicating charge-dependent intra- and intermolecular structure formation, as the variants differed in only one amino acid per module in the repetitive sequence. Hydrogen bonds between DMSO and glutamic acid residues within eADF4(C16) were likely the reason for higher gel stability but were independent of the DMSO concentration. In contrast, DMSO seemed to stabilise eADF4(Ω16) gels with increasing concentration, based on hydrogen bonds with glutamine residues. The stability of eADF4(κ16) gelly morphologies decreased with increasing concentration of DMSO, which forms fewer hydrogen bonds with lysine residues.

To investigate the influence of solvent polarity, 3% (w/v) eADF4(C16) solutions, as the best controllable ones, were used in water, and in blends with less polar DMF and with least polar DMSO. Additionally, to gradually increase the concentration of DMSO, 3% (w/v) eADF4(C16) solutions were dialysed against this solvent. The organo-dialysis step allowed a fast solvent exchange and simultaneously lead to highly transparent gels. The effect on protein structure formation was analysed using ATR-FTIR spectroscopy. Secondary structures in gels were derived from the peaks of the amide I and II bands at 1720–1490 cm^{-1} (Figure 2A) and were quantified using Fourier self-deconvolution.

The highest β-sheet content (39 ± 1%) was found in case of Tris-hydrogels as well as gels made in DMSO blends. Tris/DMSO-gels from organo-dialysis showed a lower β-sheet content of 28 ± 5%, which might be caused by faster gelation.

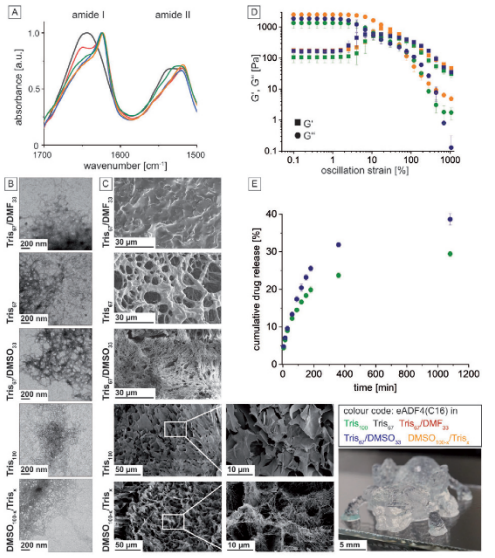

Figure 2. Impact of organic additives on spider silk gels: Comparison of gels from initial 3% (w/v) eADF4(C16) silk solutions in 10 mM Tris pH 7.5 ($Tris_{100}$) diluted with one third volume ratio of the co-solvents water ($Tris_{67}$), DMF ($Tris_{67}/DMF_{33}$), or DMSO ($Tris_{67}/DMSO_{33}$), and gels made upon dialysis against DMSO ($DMSO_{100-x}/Tris_x$). A) Mean ATR-FTIR spectra of the co-solvent gels. B) TEM images of silk fibrils in the co-solvent gels. C) SEM images of the respective co-solvent gels after freeze-drying. D) Mean amplitude sweep rheological measurements of co-solvent gels. E) Normalised cumulative release of 6-mercaptopurine from 2% (w/v) eADF4(C16) $Tris_{100}$ gel (green data points) and from 2% (w/v) eADF4(C16) $Tris_{67}/DMSO_{33}$ gel (blue data points) at 37°C. F) Photo of a 3D printed tarantula from DMSO blend gels ($Tris_{67}/DMSO_{33}$). Scale bar as indicated.

Far fewer β-sheets were found in the presence of water (24 ± 5%) or in case of blends with DMF (22 ± 4%). The formation of fibrillar networks was pronounced in the presence of DMSO, indicated by intertwined fibrils as found in TEM images (Figure 2B). In presence of DMF or water, significantly shorter fibrils were formed. SEM imaging showed a sheet-like structure for lyophilised co-solvent gels with DMF. Fused pore structures were found upon water addition. Strikingly, a highly fibrillary and porous structure was present in case of DMSO-triggered gelation. At higher magnification, pore walls showed fibrillar sub-structures in Tris/DMSO-gels after organo-dialysis (Figure 2C). Sharp pore structures were found in Tris-gels with smooth, sheet-like pores as reported previously.[7a] Fibrils in Tris-hydrogels might have collapsed into these sheet structures upon freeze-drying. Rheological characterisation (Figure 2D) showed slightly higher storage and loss moduli for 2% (w/v) eADF4(C16) Tris/DMSO-gels in comparison to 3% (w/v) eADF4(C16) Tris-hydrogels. Nonetheless, for Tris/DMSO-gels and Tris-hydrogels, moduli were in the same range, and similar yield points were detected, indicating comparable visco-elastic properties. 3% (w/v) eADF4(C16) Tris/DMSO-gels from organo-dialysis showed the highest storage modulus and a slight shift in the yield point towards higher oscillation strain, indicating higher resistance of the material until break.

Nonetheless, the new gels showed typical spider silk hydrogel shear-thinning behaviour and stability (Figure S1A,B). Accordingly, using a RegenHU bioplotter, multilayer scaffolds with high shape stability could be 3D printed using the DMSO blend gels (Figure 2F, Figure S3, and Video S4).

To test the application of such gels as drug depots, fluorescein (FITC) was loaded as a first model substance into Tris/DMSO-gels, and a comparison was made to Tris-hydrogels regarding loading and release at 37°C. Both gel types showed the same release profile (Figure S2), indicating the possibility of generating injectable or transdermal drug-loaded gel depots. Further, the poorly water-soluble 6-mercaptopurine, as clinically relevant cytostatic drug, was loaded into the DMSO-phase of 2% (w/v) eADF4(C16) blend gels. The drug was incorporated by non-covalent interactions, but in case a reversible coupling is intended, a recently published system with a different spider silk variant can be used.[20] Upon non-covalent introduction in Tris-hydrogels, the water-insoluble drug aggregated during the gelation process and accumulated at the bottom of the gel. In the DMSO blend gel, however, loading and release could be accomplished. These results confirmed the suitability of co-solvent-produced spider silk gels with clinically relevant substances as injectable and even 3D printable drug depots.

Finally, we wanted to unravel the driving force of spider silk assembly in presence of co-solvents. The herein reported route towards spider silk gel formation in aqueous–organic binary mixtures is driven in part by structure formation at organic–water interfaces (Scheme 1). eADF4(C16) was found to form water-insoluble β-sheet structures in microcapsules[21] with barrier function[22] upon adsorption at aqueous–organic interfaces. In case of aqueous–organic binary mixtures, micro-

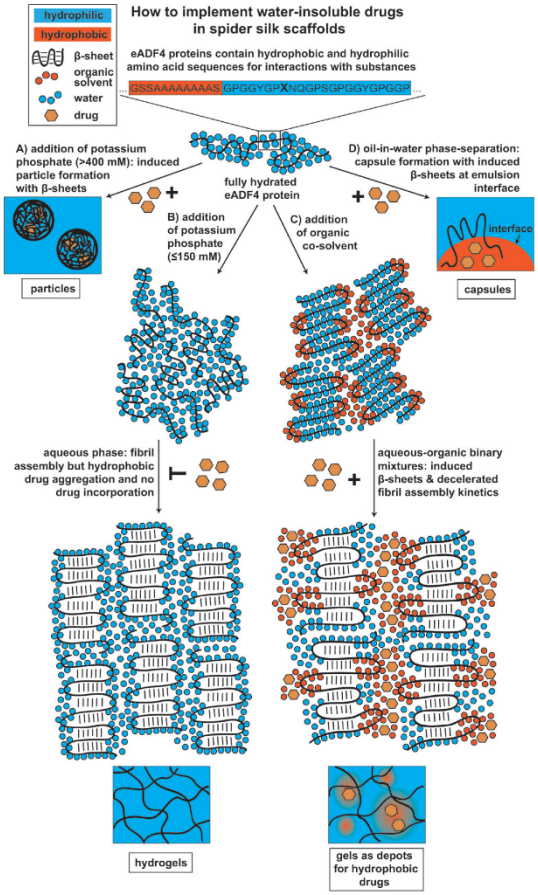

Scheme 1. Illustration of routes towards drug depots made of recombinant spider silk proteins. A) Potassium phosphate-induced co-precipitation of microparticles and any type of drugs. B) Hydrogels cannot incorporate hydrophobic but only hydrophilic drugs during gelation. C) New route of gel formation, allowing the incorporation of hydrophilic as well as hydrophobic drugs. D) Microcapsules can incorporate hydrophilic, hydrophobic, and amphiphilic (at the aqueous–organic interface) drugs. Aqueous–organic binary mixtures as seen in (C) represent intermediate conditions between hydrogel formation in one homogenous (aqueous) phase (B) and phase-separation-induced β-sheet formation at the water–oil interface (D). **X** = selected amino acids of the silk variants, that is, glutamic acid, glutamine, or lysine.

emulsions can form in presence of organic co-solvents such as DMSO[23] or DMF,[13] which are miscible in water.

The formed interphases are micro-heterogeneous[24] and are based on the interaction of hydrogen bond[25] forming molecules. These interphases can be described by a side-by-side arrangement of both solvents in molecular clusters.[25] DMSO and DMF are amphiphilic molecules, which can form hydrogen bonds, for example, with water but also enable hydrophobic interactions among them or with other molecules such as proteins. Similarly, eADF4 exhibits amphiphilic properties due to its amino acid sequence[26] and can therefore

interact with hydrophobic as well as hydrophilic drugs/molecules. Charged amino acid residues can form hydrogen bonds with DMSO to a varying degree, and negatively charged molecules are favoured over uncharged or positively charged ones.[27]

Spider silk gels made out of aqueous–organic co-solvents enlarge the range of applications of spider silk-based materials since material properties can be controlled by the choice of the co-solvent and of the used spider silk variant. DMSO is FDA approved[28] in topical formulations at concentrations at approximately 30% (v/v). Based on our results it can be applied in spider silk gels in pharmaceutical formulations, e.g. for transdermal applications. These gels allow formulation of water-insoluble drugs along with adjustable organic content to yield biocompatible, biodegradable, non-toxic, non-inflammatory, transdermal, injectable, and even 3D printable drug depots. Depending on the application, the drug–silk interaction can be further controlled, for example, by reversible covalent bonds.[20]

Experimental Section

The engineered spider silk protein eADF4(C16) comprises 16 repeats of the consensus sequence GSSAAAAAAAASGPGGYGPENQGPSGPGGYGPGGP (named C-module). The C-module is based on the consensus sequence of the repetitive core domain of the MaSp2 dragline silk fibroin 4 of the European garden spider *Araneus diadematus*.[6] eADF4(C16) was purchased from AMSilk GmbH (Planegg, Germany). In variant eADF4(κ16),[17] all glutamic acid residues are substituted with lysine and in eADF4(Ω16)[18a] with glutamine ones. Both proteins were produced and purified as reported earlier.[6,17,18] Spider silk proteins were dissolved in 6 M guanidinium thiocyanate (Carl Roth, Karlsruhe, Germany) and dialysed against 10 mM Tris buffer, pH 7.5 for several hours, whereas the dialysis of eADF4(Ω16) was done at 4 °C. Concentration adjustment was conducted, if necessary, by follow-up dialysis in 20% (w/v) poly(ethylene glycol) (PEG, 20 kDa, Carl Roth, Karlsruhe, Germany) as reported previously[7a] or using a high vacuum concentrator (Speedvac, Eppendorf). For biphasic gels, co-solvents or co-solute buffers were blended with 3% (w/v) silk solutions and gelled at 37 °C. For organo-dialysis gels, 3% (w/v) silk solutions were dialysed against small volumes (1:100 volume ratio) of DMSO (Carl Roth, Karlsruhe, Germany) at RT for 4 h without further thermal treatment.

For analysis of the gelation kinetics of recombinant spider silk proteins, turbidity changes were monitored at 570 nm using a microplate reader (Mithras LB 940, Berthold Technologies, Germany). Triplicates of 100 µL aliquots were prepared for all solutions (3% (w/v) eADF4(C16), 2% (w/v) eADF4(κ16), and 1% (w/v) eADF4(Ω16)). Spider silk solutions were diluted by addition of different volumes of DMSO to reach final concentrations of 5, 15, and 30% (v/v) DMSO in the blend. As a control, 150 mM potassium phosphate was used as fibrillisation trigger, and data were normalised to this sample's endpoint.

Gel samples were transferred on glass slides for image collection using a Leica M205C stereomicroscope (Wetzlar, Germany) with Leica LAS software and light reflection from dark field mode. The microscope was equipped with a polarisation lens and a 0.63× objective. For scanning electron microscopy (SEM), lyophilised gel samples were investigated after platinum sputtering (2 nm). Images were recorded using a Thermo Scientific (FEI) Apreo VS with a Field Emission Gun at 2 kV and a SE2-detector. Transmission electron microscopy (TEM) images of stained (2% uranyl acetate) spider silk fibrils immobilised on Pioloform-coated 100-mesh copper grids (Plano GmbH, Germany) were recorded using a JEM-2100 TEM (JEOL, Japan), operated at 80 kV, and imaging was carried out using a 4000 × 4000 charge-coupled device camera (UltraScan 4000, Gatan, USA) and Gatan Digital Micrograph software (version 1.83.842).

Rheological behaviour was investigated using a Discovery Hybrid Rheometer 3 (TA, USA) with a plate–plate geometry (diameter 25 mm) at 25 °C. To prevent drying effects on the gels, a wet sponge adapter was used. Amplitude sweeps ($n = 3$) were recorded as triplicates at 31.4 rad s^{-1} and a strain of 0.1–1000%.

Attenuated total reflectance-Fourier transformation infrared spectroscopy (ATR-FTIR) was conducted with lyophilised gel samples. Spectra ($n = 3$) were recorded using a Bruker Tensor 27 (Ettlingen, Germany) with a germanium crystal at a spectral resolution of 2 cm^{-1} with 100 scans. Atmospheric compensation algorithm was applied in OPUS 8.0 software to correct water vapour and carbon dioxide fluctuations during the measurement. Fourier self-deconvolution was carried out as reported previously[29] with band assignment for partial secondary structure determination.[30]

To study the release of 6-mercaptopurine (Sigma, USA) from 2% (w/v) $Tris_{100}$ and 2% (w/v) $Tris_{67}$/$DMSO_{33}$ eADF4(C16) gels, the drug was dissolved in 20 µL DMSO and added to the spider silk solutions or the DMSO-phase. Triplicate release measurements were conducted in 1:1 blends of MilliQ water:DMSO. UV absorbance was monitored using a UV spectrometer (Genesys 10S UV/Vis, Thermo Scientific). Spectra were recorded between 200 and 600 nm, and peak maxima at 328 nm were used to determine cumulative release curves.

3D dispense plotting was carried out using a RegenHU 3D Discovery Gen1 (Switzerland) bioplotter with cartridges size 3cc and according pistons. The printing speed was pre-set to 10 mm s^{-1}. 2% (w/v) $Tris_{67}$/$DMSO_{33}$ eADF4(C16) gels were printed with Luer lock plastic needles with an inner diameter of 0.41 mm and an applied pressure of 0.3 bar.

Acknowledgements

The authors acknowledge the funding from the Deutsche Forschungsgemeinschaft (DFG, German Research Foundation)—project number 326998133-TRR225 (funded subproject: C01 TS) and SCHE603/24-1. The authors thank Anika Winkler for transmission electron microscopy and Hendrik Bargel for scanning electron microscopy. Open access funding enabled and organized by Projekt DEAL.

Conflict of interest

TS is founder and share-holder of AMSilk GmbH.

Keywords: binary mixtures · co-solvent · hydrophobic effect · micro-heterogeneity · self-assembly

[1] J. L. Drury, D. J. Mooney, *Biomaterials* **2003**, *24*, 4337–4351.
[2] a) W.-H. Tan, S. Takeuchi, *Adv. Mater.* **2007**, *19*, 2696–2701; b) A. G. Tabriz, M. A. Hermida, N. R. Leslie, W. Shu, *Biofabrication* **2015**, *7*, 045012.
[3] a) N. Bhattarai, J. Gunn, M. Zhang, *Adv. Drug Delivery Rev.* **2010**, *62*, 83–99; b) Y. Hong, H. Song, Y. Gong, Z. Mao, C. Gao, J. Shen, *Acta Biomater.* **2007**, *3*, 23–31.
[4] N. Wu, H. Yu, M. Sun, Z. Li, F. Zhao, Y. Ao, H. Chen, *ACS Appl. Biol. Mater.* **2020**, *3*, 721–734.
[5] T. Zehnder, B. Sarker, A. R. Boccaccini, R. Detsch, *Biofabrication* **2015**, *7*, 025001.
[6] D. Huemmerich, C. W. Helsen, S. Quedzuweit, J. Oschmann, R. Rudolph, T. Scheibel, *Biochemistry* **2004**, *43*, 13604–13612.

[7] a) K. Schacht, T. Scheibel, *Biomacromolecules* **2011**, *12*, 2488–2495; b) E. DeSimone, K. Schacht, T. Scheibel, *Mater. Lett.* **2016**, *183*, 101–104; c) E. DeSimone, K. Schacht, T. Jüngst, J. Groll, T. Scheibel, *Pure Appl. Chem.* **2015**, *87*, 737–749.
[8] a) K. Schacht, T. Juengst, M. Schweinlin, A. Ewald, J. Groll, T. Scheibel, *Angew. Chem. Int. Ed.* **2015**, *54*, 2816–2820; *Angew. Chem.* **2015**, *127*, 2858–2862; b) E. DeSimone, K. Schacht, A. Pellert, T. Scheibel, *Biofabrication* **2017**, *9*, 044104.
[9] S. Kumari, H. Bargel, M. U. Anby, D. Lafargue, T. Scheibel, *ACS Biomater. Sci. Eng.* **2018**, *4*, 1750–1759.
[10] F. Hofmeister, *Arch. Exp. Pathol. Pharmakol.* **1888**, *24*, 247–260.
[11] U. K. Slotta, S. Rammensee, S. Gorb, T. Scheibel, *Angew. Chem. Int. Ed.* **2008**, *47*, 4592–4594; *Angew. Chem.* **2008**, *120*, 4668–4670.
[12] a) L. Eisoldt, A. Smith, T. Scheibel, *Mater. Today* **2011**, *14*, 80–86; b) E. Doblhofer, A. Heidebrecht, T. Scheibel, *Appl. Microbiol. Biotechnol.* **2015**, *99*, 9361–9380; c) M. Heim, D. Keerl, T. Scheibel, *Angew. Chem. Int. Ed.* **2009**, *48*, 3584–3596; *Angew. Chem.* **2009**, *121*, 3638–3650.
[13] D. R. Canchi, A. E. García, *Annu. Rev. Phys. Chem.* **2013**, *64*, 273–293.
[14] C. N. Pace, S. Treviño, E. Prabhakaran, J. M. Scholtz, *Philos. Trans. R. Soc. London Ser. B* **2004**, *359*, 1225–1235.
[15] N. Javid, K. Vogt, C. Krywka, M. Tolan, R. Winter, *ChemPhysChem* **2007**, *8*, 679–689.
[16] A. Lammel, M. Schwab, U. Slotta, G. Winter, T. Scheibel, *ChemSusChem* **2008**, *1*, 413–416.
[17] E. Doblhofer, T. Scheibel, *J. Pharm. Sci.* **2015**, *104*, 988–994.
[18] a) S. Kumari, G. Lang, E. DeSimone, C. Spengler, V. T. Trossmann, S. Lücker, M. Hudel, K. Jacobs, N. Krämer, T. Scheibel, *Data Brief* **2020**, *32*, 106305; b) S. Kumari, G. Lang, E. DeSimone, C. Spengler, V. T. Trossmann, S. Lücker, M. Hudel, K. Jacobs, N. Krämer, T. Scheibel, *Mater. Today* **2020**, *41*, 21–33.
[19] M. R. Harpham, N. E. Levinger, B. M. Ladanyi, *J. Phys. Chem. B* **2008**, *112*, 283–293.
[20] H. M. Herold, A. Döbl, S. Wohlrab, M. Humenik, T. Scheibel, *Biomacromolecules* **2020**, *21*, 4904–4912.
[21] K. D. Hermanson, D. Huemmerich, T. Scheibel, A. R. Bausch, *Adv. Mater.* **2007**, *19*, 1810–1815.
[22] K. D. Hermanson, M. B. Harasim, T. Scheibel, A. R. Bausch, *Phys. Chem. Chem. Phys.* **2007**, *9*, 6442–6446.
[23] J. Hansen, F. Platten, D. Wagner, S. U. Egelhaaf, *Phys. Chem. Chem. Phys.* **2016**, *18*, 10270–10280.
[24] D. N. Shin, J. W. Wijnen, J. B. F. N. Engberts, A. Wakisaka, *J. Phys. Chem. B* **2002**, *106*, 6014–6020.
[25] a) S. Roy, S. Banerjee, N. Biyani, B. Jana, B. Bagchi, *J. Phys. Chem. B* **2011**, *115*, 685–692; b) A. Wakisaka, H. Abdoul-Carime, Y. Yamamoto, Y. Kiyozumi, *J. Chem. Soc. Faraday Trans.* **1998**, *94*, 369–374; c) A. Wakisaka, T. Ohki, *Faraday Discuss.* **2005**, *129*, 231–245; d) D. B. Wong, K. P. Sokolowsky, M. I. El-Barghouthi, E. E. Fenn, C. H. Giammanco, A. L. Sturlaugson, M. D. Fayer, *J. Phys. Chem. B* **2012**, *116*, 5479–5490.
[26] C. B. Borkner, S. Lentz, M. Müller, A. Fery, T. Scheibel, *ACS Appl. Polym. Mater.* **2019**, *1*, 3366–3374.
[27] K. L. Shaw, G. R. Grimsley, G. I. Yakovlev, A. A. Makarov, C. N. Pace, *Protein Sci.* **2001**, *10*, 1206–1215.
[28] K. Capriotti, J. A. Capriotti, *J. Clin. Aesthet. Dermatol.* **2012**, *5*, 24–26.
[29] J. Petzold, T. B. Aigner, F. Touska, K. Zimmermann, T. Scheibel, F. B. Engel, *Adv. Funct. Mater.* **2017**, *27*, 1701427.
[30] X. Hu, D. Kaplan, P. Cebe, *Macromolecules* **2006**, *39*, 6161–6170.

Manuscript received: March 3, 2021
Accepted manuscript online: March 26, 2021
Version of record online: May 1, 2021

Angewandte Chemie
Eine Zeitschrift der Gesellschaft Deutscher Chemiker

Supporting Information

Recombinant Spider Silk Gels Derived from Aqueous–Organic Solvents as Depots for Drugs

*Vanessa J. Neubauer, Vanessa T. Trossmann, Sofia Jacobi, Annika Döbl, and Thomas Scheibel**

ange_202103147_sm_miscellaneous_information.pdf
ange_202103147_sm_Video.mp4

Experimental section

Rheological characterization of the co-solvent spider silk gels

Rheological behaviour was investigated using a Discovery Hybrid Rheometer 3 (TA, USA) with a plate-plate geometry (diameter 25 mm) at 25 °C. To prevent drying effects, a wet sponge adapter was used. Frequency sweep experiments (n=3) were recorded at angular frequencies between 0.1-100 rad/s and 100-0.1 rad/s for recovery at 50 % strain. Time sweep experiments (n=3) were recorded at angular frequencies of 31.4 rad/s and 0.5 % strain for 120 s.

Release studies of FITC as model substance from co-solvent spider silk gels

To study the release of 5(6)-Carboxy-fluorescein (FITC, Thermo Scientific, Germany) from 2 % w/v Tris- and 2 % w/v $Tris_{67}/DMSO_{33}$ eADF4(C16) gels, FITC was dissolved in 20 µL DMSO and added to the spider silk solutions. Samples without FITC loading served as reference. Triplicate release measurements were done in 1:1 blends of MilliQ water:DMSO. Fluorescence detection was conducted using a fluorescence spectrometer FP-6300 (JASCO, Germany) at an excitation wavelength of 495 nm. Spectra were recorded between 500 and 600 nm, and peak maxima at 517 nm were used to determine release curves. Error bars were calculated according to the law of error propagation.

3D dispense plotting of co-solvent spider silk gels

For 3D dispense plotting, the printing speed of the RegenHu Bioplotter was pre-set to 20 mm/s. 2 % w/v $Tris_{67}/DMSO_{33}$ eADF4(C16) gels were printed with Luer lock plastic and blunt steel needles with an inner diameter of 0.41 mm and an applied pressure of 0.3 - 0.5 bar. 3 % w/v Tris/DMSO-gels after organo-dialysis were printed using Luer lock steel blunt needles with 0.51 mm inner diameter and an applied pressure of 1.06 bar.

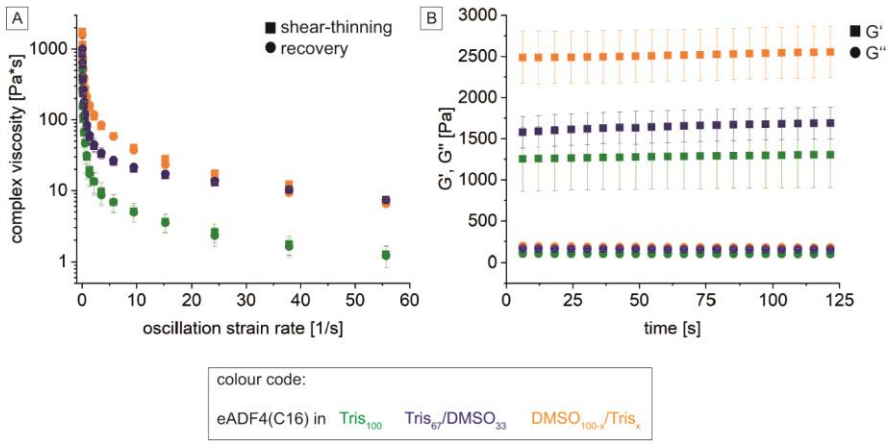

Figure S1: Gels from initial 3 % w/v eADF4(C16) silk solutions in 10 mM Tris pH 7.5 ($Tris_{100}$, green), diluted with 33% v/v of the co-solvent DMSO ($Tris_{67}/DMSO_{33}$, blue), and gels made upon dialysis against DMSO ($DMSO_{100-x}/Tris_x$, orange) were tested concerning the impact of organic additives. A) Mean frequency sweep rheological measurements of co-solvent gels showed shear-thinning behaviour and recovery properties of the gels. B) Mean time sweep rheological measurements of co-solvent gels showed gel stability over time.

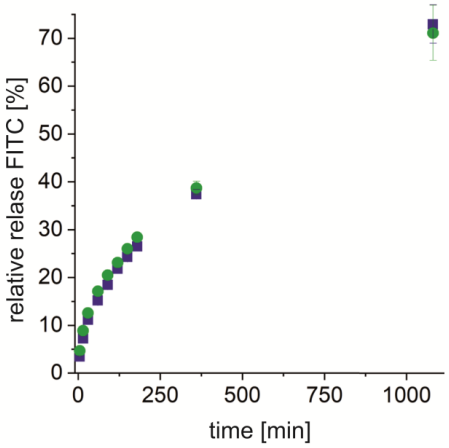

Figure S2: Normalized release of the model drug 5(6)-Carboxy-fluorescein (FITC) from gels at 37 °C: Gels from 2 % w/v eADF4(C16) silk solutions in 10 mM Tris pH 7.5 ($Tris_{100}$, green) and in presence of the co-solvent DMSO ($Tris_{67}/DMSO_{33}$, blue).

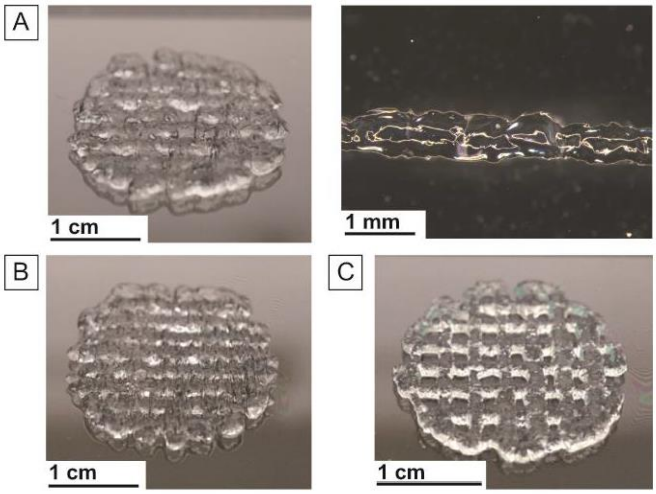

Figure S3: Images of 3D printed scaffolds of A) 2 % w/v $Tris_{67}/DMSO_{33}$ eADF4(C16) gels printed using a conical needle (0.41 mm diameter) on a RegenHU Bioplotter (left) and stereomicroscopic image of one single strand (right); B) 2 % w/v $Tris_{67}/DMSO_{33}$ eADF4(C16) gels printed using a steel needle (0.41 mm diameter); C) 3 % w/v Tris/DMSO-gels from organo-dialysis printed using a steel needle (0.51 mm diameter) and larger line spacing. Scale bars as indicated.

A Video of 3D dispense plotting of a tarantula scaffold is available as Supporting Information Video S4.

7.7. Teilarbeit VII

Teilarbeit VII wurde 2022 unter dem Titel „Selective Topography Directed Cell Adhesion on Spider Silk Surfaces“ im Journal *Advanced Materials Interfaces* veröffentlicht.

Lentz, S.*; **Trossmann, V. T.*** & Scheibel, T. (2022) Selective Topography Directed Cell Adhesion on Spider Silk Surfaces. *Advanced Materials Interfaces* **10**: 2201936.

https://doi.org/10.1002/admi.202201936

* gleichberechtigte Co-Autorenschaft

RESEARCH ARTICLE

ADVANCED MATERIALS INTERFACES
www.advmatinterfaces.de

Selective Topography Directed Cell Adhesion on Spider Silk Surfaces

*Sarah Lentz, Vanessa Tanja Trossmann, and Thomas Scheibel**

For tissue engineering applications, guided cell interaction with a biomaterial surface is one essential feature since, in natural tissue, cells constantly interact with their extracellular matrix, which provides different topographical, mechanical and biochemical stimuli. Therefore, the introduction of topographical surface features is one promising approach to direct material-cell interactions. In this study, maskless lithography and soft lithographic methods are used to produce recombinant spider silk films with size gradient patterns, including grooves, circles, squares, triangles, and stars, to enhance specific cell attachment. The influence of surface features on cell behavior is analyzed using eight different cell lines. It can be shown that surface indentations provide cellular attachment sites and guiding structures for restructuring, aligning, and adopting cell morphology, with a relation of cell to feature size for some of the cell lines investigated. Therefore, specific topographical surface modifications can be used to guide selective cell adhesion, allowing the generation of tissue-specifically modified implant surfaces in the future.

1. Introduction

The interactions of a biomaterial surface with the surrounding biological environment are decisive for the successful performance of a biomaterial.[1] The natural surrounding of cells exposes various external stimuli, including topographical surface features, mechanical properties, or biochemical factors that depend on the composition of the extracellular matrix (ECM).[2] Thus, surface modifications have been investigated to trigger cellular responses, including attachment and alignment of cells for advanced tissue integration.[3] One focus has been on engineering the biomaterial implant surface with topographical features to influence biological responses after cell-material contact.[1c,4] It is well known that substrate topography triggers several important cellular responses after the first cell-surface interaction, such as adhesion, migration, differentiation, morphological changes, and intracellular signaling of cells.[1c,3a,4d–f,5] It must be emphasized that anisotropic topographical surface structures in the nanometer, as well as in the low micrometer range, are perceived by the cells and can cause diverse cellular responses.[4d,5b,c,6] Although surface topography can influence cell adhesion on material surfaces, the appropriate cell response is highly dependent on the respective cell type, and the dimensions and nature of the topographical surface features also play a decisive role.[4e] Thus, for developing biomaterials and implants for tissue engineering applications, it is crucial to know the requirements of tissue-specific cells of the target tissue to adapt the surface topography.[4d–f]

Several studies have been shown that cells can recognize and sense different surface patterns in various dimensions, sizes, and shapes, and can bridge smaller patterns. Interestingly, F-actin assembly correlated with the respective surface pattern, for example, aligned with grooves or on pillar structures.[3a,4d,6b,7] One systematic study analyzed the organization of the cytoskeleton as well as the connection of adhesion forces and surface topography using atomic force microscopy (AFM)-based single-cell force spectroscopy. It was concluded that microstructured surfaces decreased early and enhanced long-term cell adhesion, as adhesion forces increased continuously over time, while nano-topographical surfaces only supported initial cell attachment (<1 h), connected to a different organization of intracellular components and spreading behavior of the cells.[6b] A surface-modified chip (TopoChip) was developed and contained over 2000 different micro-topographies on its surface based on circles, triangles, and rectangles to identify specific topographies influencing differentiation of tonsil-derived stromal cells,[8] tenocytes,[9] or primary human keratinocytes.[10] Structural features and guiding topographies on a biomaterial surface, such as grooves or pores, could mimic the structural,

S. Lentz, V. T. Trossmann, T. Scheibel
Lehrstuhl Biomaterialien
Fakultät für Ingenieurwissenschaften
Universität Bayreuth
Prof-Rüdiger-Bormann-Str. 1, 95447 Bayreuth, Germany
E-mail: thomas.scheibel@bm.uni-bayreuth.de
T. Scheibel
Bayerisches Polymerinstitut (BPI)
Bayreuther Zentrum für Kolloide und Grenzflächen (BZKG)
Bayreuther Zentrum für Molekulare Biowissenschaften (BZMB)
Bayreuther Materialzentrum (BayMAT)
Universität Bayreuth
Universitätsstr. 30, 95447 Bayreuth, Germany

The ORCID identification number(s) for the author(s) of this article can be found under https://doi.org/10.1002/admi.202201936.

DOI: 10.1002/admi.202201936

ADVANCED SCIENCE NEWS
www.advancedsciencenews.com

ADVANCED MATERIALS INTERFACES
www.advmatinterfaces.de

fibrillar composition and landscape of the natural extracellular environment leading to a controlled cellular interaction and guidance.[11] In this context, the term contact guidance was used for the first time by P. Weiss, which means the orientation and direction of cell continuation and migration in response to the shape and topography of the substrate's surface.[12]

On nanopatterned substrates, fibroblasts can respond to the curvature of the underlying substrate and increase their spreading area while reducing their polarization (aspect ratio). However, internal components of the cytoskeleton, such as stress fibers, strongly align along with the underlying topographical pattern.[13] Microtubules have been shown to be the first cellular component involved in cellular orientation along a grooved surface structure located at the bottom of grooves (first 20 min), while aligned actin microfilament bundles were observed afterward (40–60 min) at the wall-ridge edges leading to aligned focal contacts after ≈3 h.[14] Thus, a biomaterial surface could be modified to become cell-attractive, also known as cytophilic, or cell-repellent, also denoted as cytophobic, by adopting the respective surface topography to trigger the biological response of cells.[15]

In the present study, flat recombinant spider silk films, which did per se not support cell adhesion,[16] were modified by applying and introducing differently shaped and sized surface features using a maskless lithographically produced template to enhance cell interaction. Implant materials based on spider silk are highly biocompatible and do not cause any inflammatory response or foreign body reaction.[16b,17] One example are materials made of the recombinant spider silk protein eADF4(C16), which was engineered on the consensus sequence of the *Araneus diadematus* fibroin 4 (ADF4), a spidroin of the European garden spider's dragline silk.[18] Since eADF4(C16) lacks any cell-binding motifs, cell interaction with flat eADF4(C16) films or coatings is very low.[16] Furthermore, catheters coated with an eADF4(C16) spider silk protein layer displayed minimal cell interaction.[16d] The here-introduced features showed areas in the micrometer range, while the height was in the nanometer range. The modification with introduced differently shaped and sized surface patterns supported attachment, morphological restructuring, and alignment of various cell lines on spider silk surfaces.

2. Results and Discussion

2.1. Topography Modification of Recombinant Spider Silk Films

Recombinant eADF4(C16) spider silk scaffolds exhibit promising properties for usage in regenerative and biomedical applications, including versatile processability,[16c] high biocompatibility,[17b] slow biodegradation,[19] and repellence against microbes.[20] However, cell adhesion on unmodified eADF4(C16)-based scaffolds is low since eADF4(C16) lacks any cell interaction sites.[16] Here, spider silk films were modified by applying topographical surface features, namely indentations or protrusions, to enhance cellular interactions, because several cellular responses, including adhesion, spreading, morphological restructuring, migration, and intracellular signaling, are influenced and guided by topographical surface patterns after the first contact of a cell with a material surface.[1c,3a,4d–f,5] Maskless photolithography was used to fabricate a template (Figure S1, Supporting Information), for which a glass slide was covered with a photoresist and a digital mask showing the patterns of interest was designed. One digital mask showing size gradients of different structures (circles, hearts, triangles, squares, hexagons, stars, crosses, and grooves) is exemplary shown in Figure S2, Supporting Information. Such a digital mask can be used for the generation of indentations as well as protrusions on the film surface. The patterns exhibited sizes between ≈ 40 and 100 µm and grooves comprised widths from 6 to 57 µm. After successful template generation, they were covered with polydimethylsiloxane (PDMS) and cured to generate patterned stamps to be used for subsequent film casting. Since PDMS exhibits high wear resistance and shows minimal surface interactions due to its chemical inertness, it was ideally suited as a stamp material.[21] After examining existing literature, it could be concluded that lithography approaches and PDMS molding represent standard, versatile, adjustable, cheap, and high throughput fabrication techniques to generate topographically modified substrate surfaces for cell-contacting surfaces.[3b,c,4f,5b,22]

For patterned film generation, spider silk solutions were cast on ozone-pre-treated polystyrene surfaces, and the appropriate stamps were put on top. After solvent evaporation, the stamps could be removed easily due to the minimized interaction of PDMS with the spider silk surface. The PDMS stamps, the maskless photolithographically produced templates, as well as the received patterned spider silk films were analyzed using light microscopy. The generated structures showed good and uniform shape fidelity for all three surfaces with sharp corners and pronounced edges, which were homogeneously distributed over the whole surface. **Figure 1**A displays light microscopy images of eADF4(C16) spider silk films containing gradients of surface indentations. It is visible that the groove gradient on the film surfaces exhibited different widths for ridges and grooves. For the differently shaped topographies, the size gradient of the different patterns was independent of their geometry. The resulting surface features exhibited dimensions in the predicted range of the digital mask. However, the resolution maximum of the lithography approach was reached because the smaller the individual structures became, the less precisely the edges and corners were pronounced, and the shape increasingly approached a circle. Nevertheless, the resolution of the obtained surface patterns on the films did not deteriorate even after repeated usage of the same PDMS stamp or after producing new PDMS stamps from the lithographically produced template. Thus, it is worth mentioning that both, the coated glass slides and the PDMS stamps, can be reused several times (at least up to 10 times). Furthermore, this method allows the design and production of very diverse surface structures exhibiting different pattern sizes, heights, and shapes.

AFM using tapping mode verified that the patterns had an area size in the micrometer range while the height was in the nanometer range (Figure 1B). The average height of each indentation was determined by analyzing several areas of different patterns, revealing that all indentations exhibited similar heights between 100 and 125 nm with no significant difference between the individual geometries (Figure S3, Supporting Information). Since cells are able to perceive nanometer- and

ADVANCED SCIENCE NEWS
www.advancedsciencenews.com

ADVANCED MATERIALS INTERFACES
www.advmatinterfaces.de

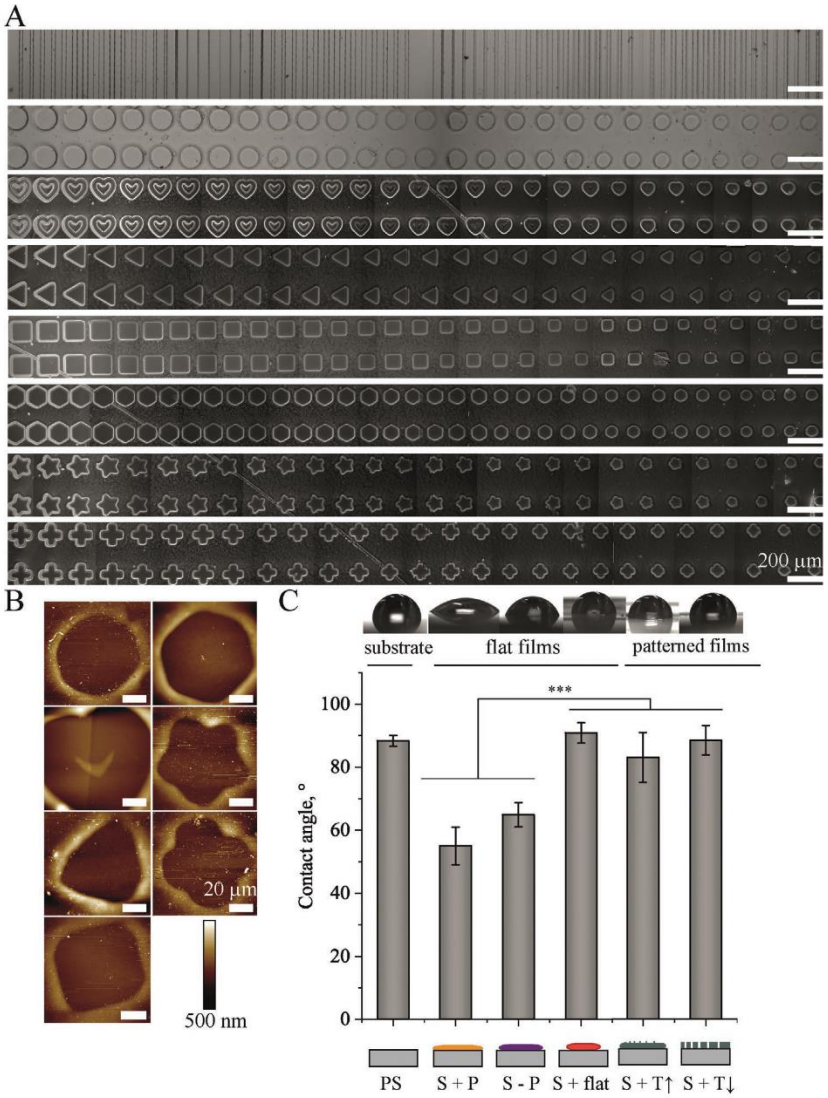

Figure 1. Physicochemical analysis of eADF4(C16) spider silk films with size gradients of various patterns, which are intended to be used for high throughput screening tests for qualitative cell adhesion. A) Displays representative light microscope images of the line and pattern (circles, hearts, triangles, squares, hexagons, stars, and crosses) gradients. Scale bars: 200 µm. B) Represents AFM images for height determination. Scale bars: 20 µm. C) Shows water contact angle measurements on a blank polystyrene substrate (PS), on flat air-dried eADF4(C16) spider silk films with plasma (S + P) and without (S – P) plasma treatment, and on silk films cast with flat PDMS stamps (S + flat) or patterned PDMS stamps (protrusions (S + T↑), indentations (S + T↓)) on top.

micrometer-scaled topographical surface features, these topographical surface features should stimulate diverse cellular reactions.[4d,5b,c,6]

To investigate the influence of the different spider silk film surface topographies on surface hydrophobicity, water contact angles (WCA) were determined using the sessile drop method, and polystyrene (PS) was used as a control (Figure 1C). In general, films cast with a PDMS stamp on top showed a significantly higher WCA (above 80°) than films produced upon evaporation of the solvent without a PDMS stamp (50–60°). A detailed comparison of significance between all spider silk films can be found in Figure S4 and Table S1, Supporting Information. The high hydrophobicity of PDMS stamps[23] led to increased surface hydrophobicity of spider silk films due to the surface exposure of hydrophobic residues of the silk protein. Interestingly, for PDMS cast films, flat surfaces and

ADVANCED SCIENCE NEWS
www.advancedsciencenews.com

ADVANCED MATERIALS INTERFACES
www.advmatinterfaces.de

surfaces exhibiting indentations or protrusions showed similar WCA. In contrast, air-dried films on PS surfaces without pretreatment showed the lowest WCA, while a plasma treatment before film casting already led to increased film hydrophobicity. Therefore, also plasma treatment initiated differences in the spider silk surface.

2.2. Influence of Serum Proteins, Indentations, and Protrusions on Cell Adhesion

Cell adhesion on flat, unmodified eADF4(C16) films has been shown to be low, even in the presence of serum proteins,[16,24] and, therefore, the effect of surface topographies (indentations, protrusions) was analyzed in cell culture using human BJ skin fibroblasts (Figure S5, Supporting Information). Cell binding to spider silk films with grooved, circular, square, and triangular indentations and protrusions was investigated in comparison to that of flat eADF4(C16) films in the presence (w/)/ FCS) and absence (w/o FCS) of fetal calf serum (FCS). It is a known effect that immediately upon contact with body fluids, a protein layer typically adsorbs on the surface of biomaterials, which influences cell adhesion.[1a,c,25] However, in case of the here used eADF4(C16) spider silk films (serum) protein adsorption was very low.[26] Shape fidelity and homogenous pattern distribution on topographically modified eADF4(C16) surfaces were verified using light microscopy before cell culture (Figure S5, Supporting Information). After 4 h adhesion time, unattached BJ fibroblasts were washed off, and adhered cells were fixed and fluorescently stained to visualize cell nuclei (blue) and the F-actin cytoskeleton (red). The fact that 4',6-diamidino-2-phenylindole (DAPI, blue) also interacts with the silk protein to a certain degree was used to stain the film surface and visualize the topographical patterns (Figure S5, Supporting Information).

Comparing similar-sized indentations and protrusions revealed that cells favored the bottom of each topography for primary cell attachment. Thus, in the case of indentations, most cells were found inside the patterns (Figure S5A, Supporting Information). In the case of protrusions, fibroblasts were mainly located around the patterns on the flat spider silk films showing slight morphological adaption (Figure S5B, Supporting Information). On top of these protrusions, cells could be detected only scarcely. One assumption could be the large interspace and distance between the protrusions leading to adhesion and spreading around and not on top of the protrusions. Therefore, subsequent cell culture experiments were carried out only on eADF4(C16) films containing indentations.

In general, it could be seen that the stimulation of cells was clearly enhanced, if the indentations were in the size range of cells. Nevertheless, too large patterns (compared to the cell size) were not identified as topographical stimuli, while patterns smaller than cells could still be recognized. Due to a local spatial 3D structure, topographical surface features reflected attachment points for cells. Their shape influenced cell morphology by guiding the alignment and orientation of the cells (contact guidance). For instance, F-actin staining visualized that cells aligned along present grooves and edges indicated by an elongated cell morphology regardless of having indentations or protrusions. Additionally, as cell attachment and spreading behavior was similar on both surfaces in the presence (w/ FCS) and absence (w/o FCS) of FCS (Figure S5, Supporting Information), it was concluded that, in the present case, primary cell adhesion ($t < 4$ h) on topographically modified eADF4(C16) films was independent of present serum proteins as expected based on our previous study.[26] Thus, the material as well as adsorbed FCS proteins were not responsible for an unspecific cellular attachment on eADF4(C16) film surfaces in accordance with previously published studies.[16,24,26] Therefore, the cell primary attachment was mainly driven by surface topography. However, such behavior might change over time of incubation, since incubating epithelial cells for 12 h on nano- to micrometer-scaled grooved silicon oxide-coated substrates revealed that more cells aligned along the grooves over time showing media-dependent alignment behavior if FCS was present.[7d]

2.3. Influence of Size and Shape of Indentations on Cell Adhesion

Since patterned films made of eADF4(C16) promoted cell adhesion on a per se non-cell-adhesive material, the effect of pattern size and shape on cell behavior was further analyzed. Eight different cell types from different tissues (BJ skin fibroblasts, Balb 3T3 embryonal fibroblasts, MG63 bone fibroblasts, B50 neuronal cells, NG108 neuronal hybrid cells, RN22 Schwann cells, C2C12 muscle myoblasts, HaCaT skin keratinocytes) were seeded on eADF4(C16) films with size gradients and diverse geometries (between 40 and 100 µm) and groove widths (6 to 58 µm). Combining different geometries with a size gradient in one stamp enables the evaluation of various parameters. The approach allows a systematic characterization of how the number of edges and corners, the curvature of pattern edges, the total area of the resulting indentation, and the angles of the individual structures influence the adhesion and spreading of several cell types. A 3D overview of the cell structure and morphology was obtained using confocal laser scanning microscopy (CLSM) upon staining cell nuclei (blue, DAPI) and the F-actin cytoskeleton (red, Phalloidin tetramethyl rhodamine B isothiocyanate (phalloidin-red)) fluorescently (**Figure 2**A). The DAPI background staining of spider silk films was used to visualize the topographical surface indentations. The interaction of DNA intercalating dyes with recombinant spider silk has already been demonstrated with ethidium homodimer, as eADF4(C16)-based hydrogels showed a strong background signal after staining with this dye.[24,27]

Human BJ skin fibroblasts strongly responded to surface indentations and preferentially attached inside these surface features with high contact guidance. Outside the indentations, only sporadically cells could be detected. A preferred surface pattern could not be identified, as the BJ cells attached to all structures indistinguishably. However, a correlation between cell size and pattern size was visible. Since BJ fibroblasts displayed a larger cell size than most other investigated cell types, they also showed spreading and alignment in larger structures. With smaller patterns, one single cell could fill the entire structure. The cells adapted their morphology to the prescribed structure and showed geometric confinement. Moreover, strong

ADVANCED SCIENCE NEWS
www.advancedsciencenews.com

ADVANCED MATERIALS INTERFACES
www.advmatinterfaces.de

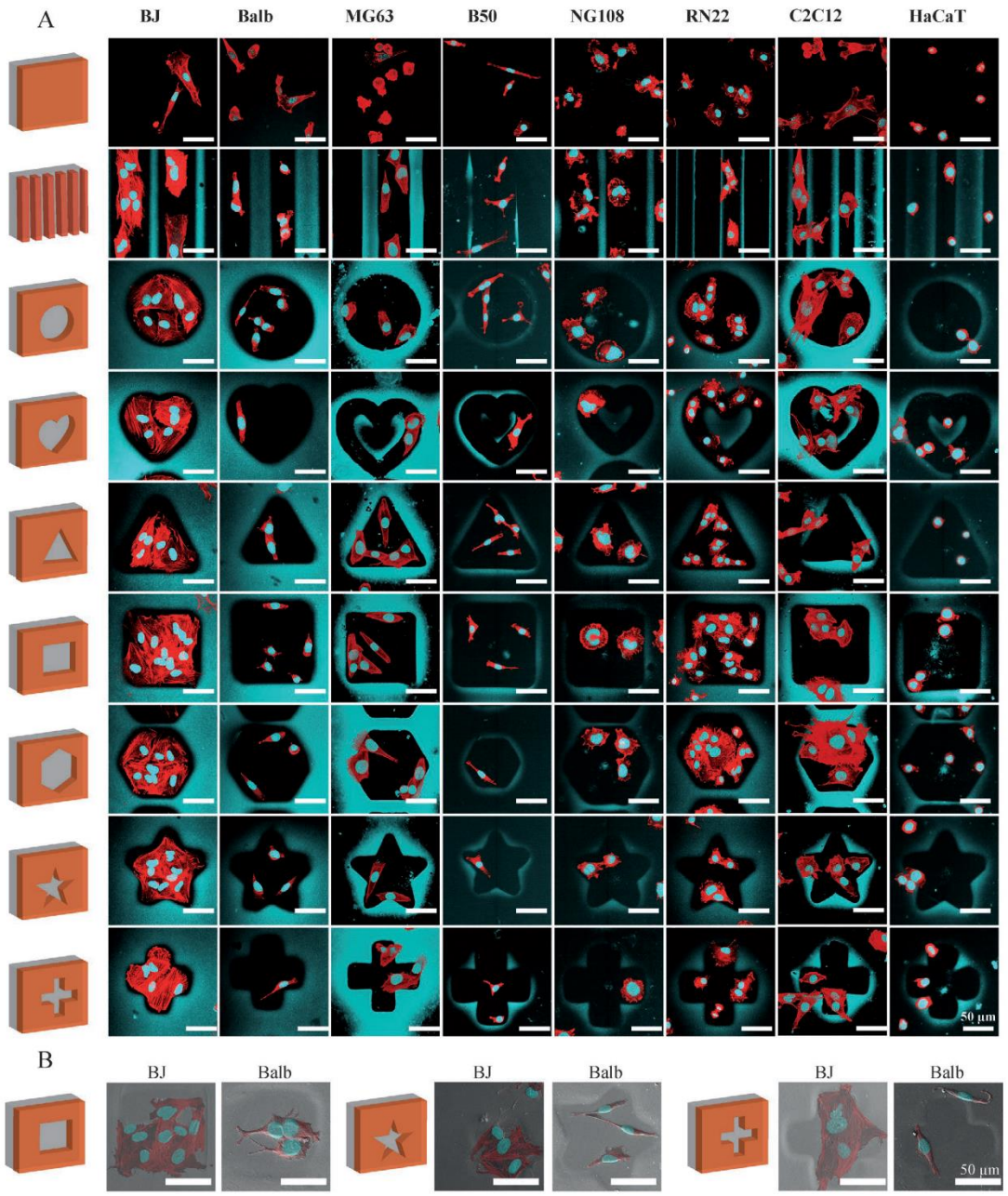

Figure 2. Microscopical analysis of cell adhesion within different topographies (indentations) of patterned eADF4(C16) spider silk films. A) Displays representative confocal laser scanning microscope (CLSM) images of eight different cell types (human BJ skin fibroblasts, mouse Balb 3T3 embryonal fibroblasts, human MG63 bone fibroblasts, rat B50 neuronal cells, mouse-rat NG108 neuronal hybrid cells, rat RN22 Schwann cells, mouse C2C12 myoblasts, and human HaCaT skin keratinocytes) attached to films made of eADF4(C16) showing grooves or topographies (circles, hearts, triangles, squares, hexagons, stars, and crosses as indicated). Flat eADF4(C16) films served as controls. Cell nuclei (blue) and F-actin cytoskeleton (red) were visualized using DAPI and phalloidin-red. DAPI background staining of the spider silk films was used to visualize the different topographies. Scale bars: 50 µm. B) Shows correlative microscopy images of attached BJ and Balb 3T3 fibroblasts inside selected topographies. Correlative images display an overlay of SEM (surface topography) and CLSM (fluorescent cell compartment staining) images to create a structural image. For SEM imaging, CLSM samples were dehydrated and platinum sputter-coated. Scale bars: 50 µm.

ADVANCED SCIENCE NEWS
www.advancedsciencenews.com

ADVANCED MATERIALS INTERFACES
www.advmatinterfaces.de

alignment, orientation, and contact guidance of cells along grooved surfaces were visible. Compared to flat spider silk films, spreading and alignment were enhanced on all structured surfaces.

In contrast, the impact of varying surface topographies on the smaller mouse Balb 3T3 fibroblasts seemed to be neglectable. These fibroblasts attached in an aligned morphology even on flat substrates. Looking at larger patterns, the cells adhered inside the indentations but did not align along with the pattern. Nevertheless, if patterns got smaller, a cell-to-pattern size effect could be identified for this cell line. Smaller patterns, which were in the Balb 3T3 fibroblasts size range, showed an effect on cell alignment and orientation of the F-actin cytoskeleton (especially triangles, circles, squares, hexagons, and crosses).

Since correlative microscopy combines the benefits of different imaging methods, here, scanning electron microscopy (SEM) and CLSM were used to image and characterize precisely the same area of a sample, that is, the identical cell.[28] SEM imaging elaborated surface topographical features of the spherical indentations and the attached cells, while CLSM enabled the detection of fluorescently stained cellular components, including cell nuclei or the F-actin cytoskeleton. Selected correlative overlays of SEM and CLSM images showing BJ and Balb 3T3 fibroblasts inside the square, star- or cross-shaped indentations were generated (Figure 2B). The correlative overlays clearly display focal adhesion and cell anchor sites of attached cells at the edges of the topographical surface patterns.

Interestingly, human MG63 bone fibroblasts strongly reacted to surface patterns. Compared to flat control surfaces (round-shaped cells), MG63 cells displayed cell spreading with focal adhesion formation and adopted their morphology regarding the underlying surface structure on patterned eADF4(C16) films. It seemed that the edges led to contact guidance and cell alignment along with the prescribed surface structure. An adhesion preference of MG63 cells could not be seen, as the cells attached to corners in the cross-shaped as well as along the curved edge in the heart-shaped features. A connection between cell size and pattern size was also visible here. Several cells often interacted with one large surface pattern and aligned therein. If the size of the surface indentation was in the range of the cell size, few cells were able to fill the surface pattern and could adopt their cell morphology to the prescribed structure. Thus, smaller surface patterns showed higher effects.

Rat B50 neuronal cells attached inside the patterns of spider silk films but were not strongly influenced by them. The cells showed a high F-actin expression and focal adhesion formation and spread inside the different surface patterns. Due to their relatively small cell size, more cells could adhere in one large pattern. Nevertheless, for larger structures, the alignment and orientation of the cells along the topographical surface pattern were low compared to that of other cell lines, such as BJ fibroblasts. Interestingly, this cell line used the feature corners as attachments or anchor points.

Mouse-rat NG108 neuronal cells adhered to all introduced patterns. Cells responded little to the topological guidance of the surface patterns. The cells showed similar cell body size on flat and patterned surfaces and adhered independently of the underlying indentation in a round morphology. Their F-actin cytoskeleton was clearly pronounced around the cell nuclei, and many stress fibers could be identified, indicating an unfavorable surface. The formation of neurons could not be detected. Nevertheless, edges and corners seemed to function as anchor points and induced a slight orientation of NG108 cells.

Rat RN22 Schwann cells were preferentially attached to the deepest part of the structured surface inside the pattern. RN22 adopted their cell shape according to the underlying pattern topography (contact guidance). If an edge or a corner was present, the cells also aligned in the prescribed shape. Interestingly, too many corners, as present in cross- or star-shaped patterns, or patterns including the circle or heart with a round shape, seemed to inhibit RN22 alignment. They instead favored hexagons, squares and triangles and adopted their cell orientation toward these topographical structures. Furthermore, a relation between cell and pattern size was identified due to a higher number of cells attached to larger topographical structures, while fewer cells had space in smaller patterns.

Mouse C2C12 myoblasts attached and aligned their cell morphology regarding the underlying surface pattern. Especially, grooves led to enhanced C2C12 cell alignment and contact guidance. The corners and edges seemed to be an attachment or settle point for C2C12 myoblasts. Nevertheless, C2C12 myoblasts were also attached outside the indentation but mainly at the border of a pattern, indicating that they need an anchor point for attachment. C2C12 myoblasts showed a spread morphology on flat surfaces with focal adhesions in different directions. The orientation of these focal adhesions seemed to be influenced by the topographical structure on patterned surfaces.

In contrast to other investigated cell lines, human HaCaT keratinocytes adhered similarly on all investigated surfaces inside and outside the indentations. HaCaT keratinocytes remained a round morphology independent of the underlying substrate, which was not influenced by corners, edges, or grooves.

Interestingly, while cell adhesion to flat eADF4(C16) spider silk films is low,[16] usage of PDMS stamps led to an increase in surface hydrophobicity followed by more cells attaching to the silk surface than in previous studies (Figures 2 and 3, Figure S5, Supporting Information). Our analysis further revealed that linear grooves represent the pattern with the most decisive influence for contact guidance of BJ fibroblasts, Balb 3T3 fibroblasts, MG63 bone fibroblasts, RN22 Schwann cells, and C2C12 myoblasts, which displayed enhanced spreading and strong alignment and orientation of their cell bodies along the straight grooves. In contrast, such modifications did not influence NG108 neuronal cells, B50 cells, and HaCaT keratinocytes. The comparison with existing literature indicated that different types of grooves are the most common topographical surface modifications for guiding cell behavior.[5b,7a,d,11,13,29] However, some studies also investigated other topographies, for instance, circular pits[29d,30] or triangular, circular, rectangular, or star-shaped indentations.[31]

Since our system using size gradients of different surface patterns allows the correlation of biomaterial surface modification and cell-type specific effects, overview images of cell-seeded feature gradients were taken using CLSM to identify future tissue- and cell-specific modification strategies for bioselective adhesion. **Figure 3** displays selected representative indentation gradients (squares, hexagons, stars and grooves)

ADVANCED SCIENCE NEWS
www.advancedsciencenews.com

ADVANCED MATERIALS INTERFACES
www.advmatinterfaces.de

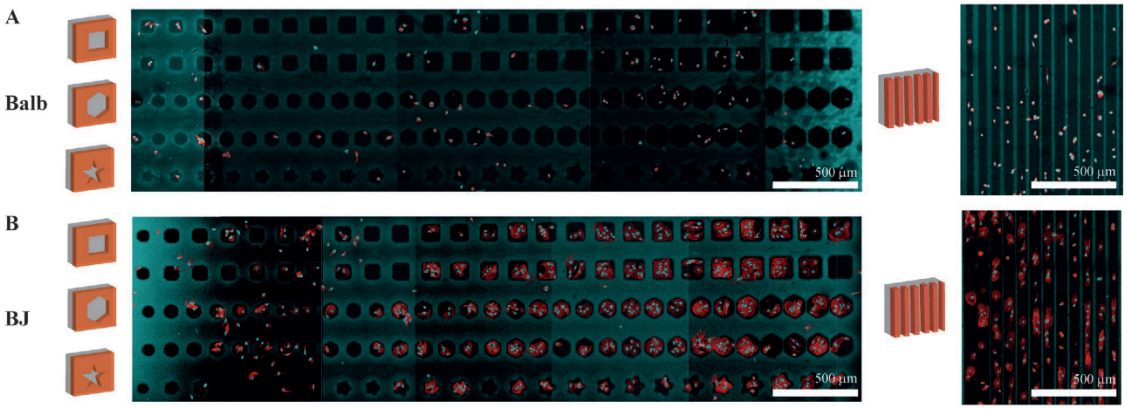

Figure 3. Selected, representative CLSM images of surface topography gradients (squares, hexagons, stars, and grooves as indicated) on eADF4(C16) spider silk films after seeding of A) mouse Balb 3T3 embryonal and B) human BJ skin fibroblasts. Cell nuclei (blue) and F-actin cytoskeleton (red) were visualized using DAPI and phalloidin-red. DAPI background staining of spider silk films was used to visualize the topographies and size gradients. Scale bars: 500 µm.

for Balb 3T3 and BJ fibroblasts for directly comparing different fibroblast cell lines with each other. The relatively small Balb 3T3 fibroblasts mainly attached inside the generated indentations but showed less orientation or alignment. Nevertheless, it was concluded that surface indentations supported Balb 3T3 cell attachment to eADF4(C16) films, even if contact guidance and morphological cell adaption were not detectable. In contrast, human BJ fibroblasts exhibited larger cell sizes and were strongly influenced by surface indentations. Several fibroblasts were attached inside bigger surface patterns and adapted their cell morphology and body regarding the underlying shape of the pattern (geometric confinement).

Our results are in line with another study using BJ fibroblasts and circular indentations (7, 15, or 25 µm diameters). BJ fibroblasts adhered inside the large indentations (25 µm) and adopted their morphology by enhancing their cytoskeleton expression (F-actin and tubulin), while most of the smaller ones (7 µm) were covered by the cells. A size-related cell behavior was described, as fibroblasts entered all indentations, but only cell parts were found inside the structures for smaller ones.[30b] Thus, contact guidance was evident, independent of topographical surface features. Interestingly, outside the indentations, only sparse cells have been found. The results clearly showed that the surface modification with topographical features represents a versatile tool to trigger bioselective cell attachment even of cells with similar features but different origins, for example, fibroblasts from human and mouse.

3. Conclusion and Outlook

Bioselective biomaterial surfaces for various tissue-specific cell types could be generated using topographical surface features on otherwise non-cell-binding spider silk films. Since eADF4(C16) film surfaces are non-cell-adhesive, the impact of surface topography on cell interaction could be studied without significant influences of the material properties. The here shown maskless lithographical modification process for introducing topographical surface features is straightforward, easy, reproducible, and versatile. Furthermore, that system is likely transferable to a variety of other film-forming (bio-)polymers, including other silk proteins or polymers,[20,26,32] since the only prerequisites are polymer solubility in an appropriate solvent (e.g., formic acid), homogenous film formation after evaporation of the used solvent, and biocompatibility of the used polymer. Using a size and structure gradient of various surface topographies in combination with eight cell lines differing in cell size and tissue origin set our approach apart from previous ones. The usual cell non-adhesive (cytophobic) spider silk films are well-suited to screen topographical surface patterns concerning cell-type dependent attachment, adopted spreading behavior, contact guidance, and aligned cell morphology. Cellular responses to topography were strongly cell-type specific and dependent on the shape, size, and structure of the applied topographical feature and the interspace between the surface patterns (**Table 1**), which was only able to evaluate by using the otherwise non-cell-binding spider silk material.

It was detected that the correlation between cell and pattern size is significant, since cells often reacted on geometrical surface features showing dimensions in their cell size range or slightly above. The here-identified cell-specific responses toward geometries allow the generation of tissue-specifically modified biomaterial implants to enable new routes toward enhanced tissue regeneration by triggering cellular responses (**Figure 4**).

4. Experimental Section

Preparation of the Photoresist Templates: Glass slides (Thermo Fisher Scientific, Germany) with 2.5 cm × 2.5 cm were used as substrates for preparing the photoresist templates after cleaning with Piranha solution (3:1 H_2SO_4 : H_2O_2, 10 min, RT). The cleaned glass slides were spin-coated with an adhesion promoter (200 µL/6.25 cm^2, 3000 rpm, 20 s, RT, TI prime, Microchemicals GmbH, Ulm Germany). The adhesion

ADVANCED SCIENCE NEWS
www.advancedsciencenews.com

ADVANCED MATERIALS INTERFACES
www.advmatinterfaces.de

Table 1. Summary of the effects of different eADF4(C16) spider silk film surface topographies on the attachment of eight selected cell lines from various tissues (human BJ skin fibroblasts, mouse Balb 3T3 embryonal fibroblasts, human MG63 bone fibroblasts, rat B50 neuronal cells, mouse-rat NG108 neuronal hybrid cells, rat RN22 Schwann cells, mouse C2C12 myoblasts, and human HaCaT skin keratinocytes), and whether a geometry preference or a cell-pattern-size-effect was detectable.

Cells	Response	Geometry preference	Cell-pattern-size-effect	Effect
BJ	Very strong	No	Yes	Adhesion to all surface topographies, contact guidance, orientation and alignment regarding prescribed structure, enhanced spreading, in smaller patterns fewer cells, in larger patterns more cells attached, geometric confinement
Balb 3T3	Little	No	No	Adhesion is not affected by surface topographies, most cells adhered inside indentations, only smaller patterns affect cell morphology
MG63	Strong	No	Yes	Adhesion to all surface topographies, contact guidance, edges beneficial for orientation, corners served as anchorage points, in smaller patterns fewer cells, in larger patterns more cells attached
B50	Moderate	No	Yes	Adhesion to all surface topographies, alignment regarding present structures, smaller geometries show stronger effects.
NG108	Little	No	No	Adhesion to all surface topographies, alignment or orientation along with corners and edges visible
RN22	Strong	Yes	Yes	Adhesion to all surface topographies, contact guidance, cell morphology depends on topography, too many corners or circular structures hindered RN22 cell spreading, grooves, triangles, squares, and hexagons were preferred, in smaller patterns fewer cells, in larger patterns more cells attached
C2C12	Moderate	Yes	No	Adhesion to all surface topographies, alignment along edges, grooves preferred, cells need anchorage points, morphology adaption if attachment inside the indentation
HaCaT	No	No	No	Adhesion is not affected by surface topographies, no divergent spreading behavior

promoter was cured for 2 min at 120 °C to remove any remaining solvent. The photoresist (500 µL/6.25 cm^2, AZ 4562, Microchemicals GmbH, Ulm, Germany) was spin-coated (4000 rpm, 60 s, RT) onto the adhesion promoter layer and then afterward cured for 8 min at 120 °C.

Photoresist Patterning: The patterns (similar-sized features, structure gradients) were designed in Adobe Illustrator CC 2021 with 1920 × 1080 pixels dimensions due to the format of the SmartPrint device (MICROLIGHT3D, La Tronche, France). Using the shape tool, the desired structure was created. The desired dimensions of the pattern were calculated given by the used objective lens (2.5×) of the SmartPrint. Here one pixel corresponded to 2.84 µm. For gradient patterns, one resulting stamp contained six complete sets of gradients. The digital mask was transferred to the software and was exposed to the photoresist for 90 s. Then the exposed photoresist was developed in developer solution (AZ 400 K, Microchemicals GmbH, Ulm, Germany) for 2 min. Afterward, the photoresist was washed with MQ water.

PDMS Stamp Preparation: The PDMS stamp was prepared using Sylgard 184 Silicone Elastomer (1:10 crosslinker : prepolymer, Dow Corning, Wiesbaden, Germany). The PDMS was mixed, and air was removed upon evacuating the PDMS for 10 min. Afterward, liquid PDMS was poured over the patterned photoresist glass slides. The PDMS was cured for 24 h at room temperature. Then, the PDMS was baked for 2 h at 70 °C, and the stamps were cut out.

Processing of Patterned eADF4(C16) Spider Silk Films: Recombinant eADF4(C16) spider silk protein powder (AmSilk GmbH, Germany) was solved in formic acid (VWR, Germany) at a concentration of 5 mg mL^{-1} for 1–2 h. Before film casting, the surface of 4-well and 8-well µ-slides (ibiTreat, ibidi GmbH, Germany), polystyrene plates (Thermo Fisher Scientific, Germany), or Petri dishes (Sarstaedt, Germany) were treated with oxygen plasma (5 min, 100 W, 0.2 mbar, MiniFlecto, plasma technology, Herrenberg-Gültstein, Germany). 100 µL spider silk solution was pipetted in each well of the 4-well µ-slide. An appropriate patterned PDMS stamp containing the negative imprints of the respective patterns was placed on the spider silk solution. For flat surfaces, 50 µL spider silk solution was drop cast in 8-well µ-slides either without PDMS or with an unpatterned PDMS stamp on top. After evaporation of the solvent (at least overnight) at ambient conditions, the PDMS stamps were removed, and the resulting patterned spider silk films were imaged using a Leica DM IL LED microscope with the associated LAS 4.8 software (both Leica, Germany) ($n = 5$).

Atomic Force Microscopy: To determine the surface morphology, the patterned eADF4(C16) films were analyzed in tapping mode using a Dimension Icon (Bruker Karlsruhe, Germany) with a resolution of 512 by 512 data points at 0.5 Hz. OTESPA-R3 silicon cantilevers (Bruker, Karlsruhe, Germany) were used with a force constant of 26 N m^{-1}. For height determination, nine different spots per image were analyzed ($n = 2$).

Water Contact Angle Measurements: The wettability of the patterned films was analyzed using the sessile drop method with the OEG contact angle system (Surftens Universal, OEG, Frankfurt (Oder), Germany). The shape of the water droplets was analyzed using the SURFTENS software (OEG, Frankfurt (Oder), Germany) and a Laplace Young fit. On each surface, six water droplets were analyzed ($n = 5$).

Cell Culture: Human skin BJ fibroblasts (CRL-2522, ATCC, USA) were cultured in Eagle's Minimum Essential Medium (EMEM, Sigma-Aldrich, Germany) supplemented with 10% v/v fetal calf serum (FCS, BioSell, Germany), 1% v/v GlutaMax (Gibco, Thermo Fisher Scientific, Germany), and 0.1% v/v gentamycin sulfate (Sigma-Aldrich, Germany). Mouse M-MSV Balb/3T3 fibroblasts (ECACC, Sigma-Aldrich, Germany) were cultured in Dulbecco's modified Eagle's medium (DMEM, BioSell, Germany) supplemented with 10% v/v FCS, 1% v/v GlutaMax, and 0.1% v/v gentamycin sulfate. Human bone MG-63 osteosarcoma fibroblasts (CRL-1427, ATCC, USA) were cultured in EMEM supplemented with 10% v/v FCS, 1% v/v GlutaMax, 1% v/v non-essential amino acids (NEAA, Sigma-Aldrich, Germany), and 0.1% v/v gentamycin sulfate. Rat nerve B50 neuronal cells (ECACC, Sigma-Aldrich, Germany) were cultured in DMEM supplemented with 10% v/v FCS, 1% v/v GlutaMax, and 0.1% v/v gentamycin sulfate. Mouse C2C12 myoblasts (CLR-1772, ATCC, USA) were cultured in DMEM supplemented with 10% v/v FCS, 1% v/v GlutaMax, and 0.1% v/v gentamycin sulfate. Mouse-rat NG108-15 somatic cell hybrids from glio- and neuroblastoma (HB-12317, ATCC, USA) were cultured in DMEM supplemented with 10% v/v FCS, 1% v/v GlutaMax, and 0.1% v/v gentamycin sulfate. Human skin HaCaT keratinocytes (DKFZ, CLS, Germany) were cultured in DMEM supplemented with 10% v/v FCS, 1% v/v GlutaMax, and 0.1% v/v gentamycin sulfate. Immature, bipolar rat RN 22 Schwann cells (ECACC, Sigma-Aldrich, Germany) were cultured in DMEM supplemented with 10% v/v FCS, 1% v/v GlutaMax, and 0.1% v/v gentamycin sulfate.

All cell lines were cultivated under humidified conditions and 5% CO_2 in a cell culture incubator (Heracell, Thermo Fisher Scientific, Germany) at 37 °C. Sub-culturing of all cell lines was conducted using trypsin/EDTA (BioSell, Germany) at a low concentration of 0.05% for BJ fibroblasts, Balb/3T3 fibroblasts, C2C12 myoblasts and NG108 hybrids or a higher concentration of 0.25% for HaCaT keratinocytes, MG-63

ADVANCED SCIENCE NEWS
www.advancedsciencenews.com

ADVANCED MATERIALS INTERFACES
www.advmatinterfaces.de

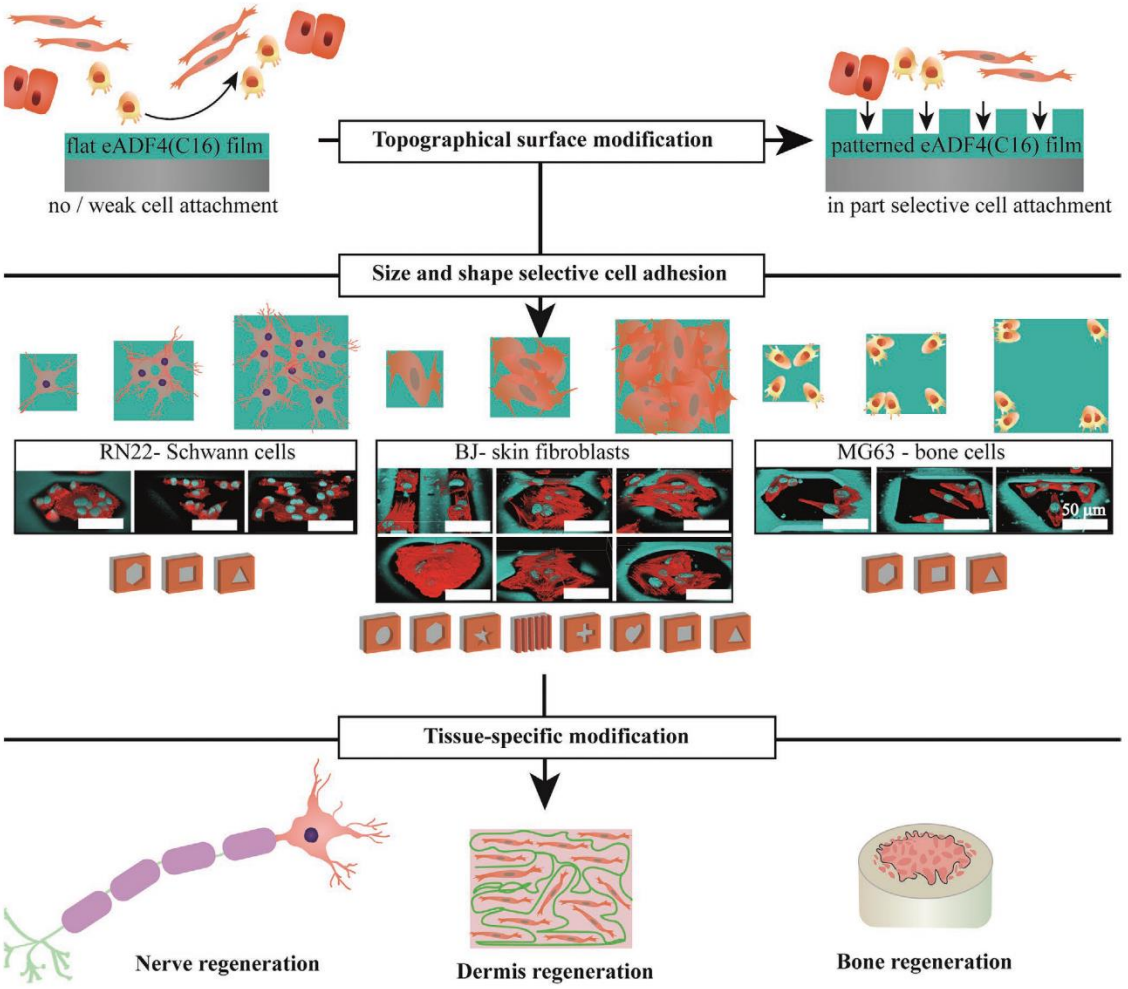

Figure 4. Summary of selected, identified cell-specific responses toward differently shaped and sized topographical surface modifications on eADF4(C16) spider silk films enabling tissue-specific engineering (e.g., nerve, dermis, or bone) of biomaterial implant surfaces by stimulating cellular responses.

osteosarcoma fibroblasts, B50 neuronal cells, and RN 22 Schwann cells. Cells were centrifuged (1200 rpm, 5 min, RT) and resuspended in an appropriate fresh medium. Respective cell numbers were determined using trypan blue (Sigma-Aldrich, Germany) and an automated cell counter (TC20, BioRAD Laboratories, Germany)

Preparation of Spider Silk Films for Cell Culture: The different patterned films made of eADF4(C16) were sterilized for 20–30 min using UV light from the cell culture hood (Herasafe, Thermo Fisher Scientific, Germany). Before use, the surfaces were washed using 1 × phosphate-buffered saline (1×PBS, Sigma-Aldrich, Germany).

Cell Adhesion Assay to Analyze Effects of FCS Components and Impact of Indentations and Protrusions on Cell Attachment: Human BJ fibroblasts were resuspended in EMEM supplemented with 1% v/v GlutaMax and 0.1% v/v gentamycin sulfate without FCS (w/o FCS) or with (w/ FCS) additionally added 10% v/v FCS to analyze the impact of serum proteins in the cell culture media. 10 000 cells per cm^2 were seeded on eADF4(C16) films showing indentations and protrusions (grooves, circles, triangles and squares) and flat films as a control. The samples were incubated for 4 h in a cell culture incubator at 37 °C. Afterward, cell culture media was soaked off, and cells were fixed using 3.7% v/v para-formaldehyde (Roth, Germany) in 1×PBS for 20–30 min at ambient conditions. For each condition, at least four individual wells were analyzed ($n = 5$).

Adhesion assay using eight different cell lines and eADF4(C16) films with indentation gradients to screen for the impact of pattern size and geometry. Human BJ skin fibroblasts, mouse Balb/3T3 embryonal fibroblasts, human MG-63 bone fibroblasts, rat B50 neuronal cells, mouse C2C12 myoblasts, mouse-rat NG108-15 somatic cell hybrids, human HaCaT skin keratinocytes, and rat RN 22 Schwann cells were resuspended in the appropriate complete cell culture media with added 10% v/v FCS to analyze the effect of indentation size and geometry on cell attachment.

On each patterned gradient surface, 10 000 cells per cm^2 were seeded and incubated for 4 h in a cell culture incubator at 37 °C. Afterward, cell culture media was soaked off, and cells were fixed using 3.7% v/v para-formaldehyde (Roth, Germany) in 1×PBS for 20–30 min at ambient conditions. For each pattern geometry, at least four gradients were analyzed ($n = 3$ for BJ and Balb 3T3 fibroblasts, $n = 2$ for other cell lines).

ADVANCED SCIENCE NEWS
www.advancedsciencenews.com

ADVANCED MATERIALS INTERFACES
www.advmatinterfaces.de

Fluorescence Staining of Attached Cells: The fixed cell samples were permeabilized using 0.1% v/v Triton X-100 (Roth, Germany) for 20 min at ambient conditions. Subsequent fluorescence staining of the cell nuclei and the F-actin cytoskeleton was conducted for 60 min in the dark at RT using 300 nM 4',6-Diamidino-2-phenylindole dihydrochloride (DAPI, Sigma-Aldrich, Germany) and 200 nM Phalloidin tetramethyl rhodamine B isothiocyanate (Phalloidin-red, Sigma-Aldrich, Germany) in 1×PBS, respectively.

Fluorescence and Confocal Laser Scanning Microscopy: Fluorescence microscopy of stained cells on patterned spider silk films was conducted using a DMi8 fluorescence microscope and the associated LAS X software (Leica, Germany). Overview images of eADF4(C16) films with indentations were taken using a DMI 8 confocal microscope with the associated LAS X software (both Leica, Germany) equipped with a 10× objective and lasers using excitation wavelengths of 405 (DAPI) and 552 nm (Phalloidin-Red). Z-stacks were recorded using the 63× objective of the DMI 8 confocal microscope and the same lasers to acquire focused images of cells inside indentations.

Scanning Electron Microscopy: CLSM-imaged cell samples were dehydrated using ethanol dehydration set up for subsequent imaging using scanning electron microscopy to generate correlative overlay images. Therefore, 1× PBS was exchanged with 50% (v/v) ethanol and incubated for 30 min. This step was repeated with 60%, 70%, 80%, 90%, and 100% (v/v) ethanol. After the last incubation step, the residual solvent evaporated at ambient conditions. The patterned cell containing spider silk films were fixed on SEM stubs (Plano GmbH, Germany) surrounded by aluminum tape. Afterward, these samples were sputter-coated with a 2 nm platinum layer using a Leica EM ACE 600 sputter coater (Leica, Germany). SEM was performed on a Thermo Scientific (FEI) Apreo VS device equipped with a Field Emission Gun and an SE2-detector operating at 2 kV (Thermo Fisher Scientific, Germany).

Statistical Analysis: The statistical analysis was performed using GraphPad Prism 9.4 (GraphPad Software, San Diego, California, USA) and a nested one-way ANOVA with Tukey's multiple comparisons test. Results are depicted as mean values ± standard deviation. *p*-values ≤0.05 are considered statistically significant.

Supporting Information

Supporting Information is available from the Wiley Online Library or from the author.

Acknowledgements

The authors thank Marcel Höferth for experimental assistance and Hendrik Bargel for help performing the SEM measurements. This work was supported by grant DFG SCHE603/23-1. S.L. and T.S. acknowledge funding from the German Academic Exchange Service (DAAD) through its thematic network Bayreuth-Melbourne Colloid/Polymer Network, sponsored by the Federal Ministry of Education and Research (BMBF) funds. The authors also acknowledge the funding from the Deutsche Forschungsgemeinschaft (DFG, German Research Foundation)-project number 326998133-TRR225 (funded subproject: C01 TS). Support from the Elite Network of Bavaria is also acknowledged (VTT).

Conflict of Interest

T.S. is co-founder and shareholder of the company AMSilk GmbH. All other authors declare that they have no competing financial interests or personal relationships that could have appeared to influence the work reported in the present paper.

Author Contributions

S.L. and V.T.T. contributed equally to this work. S.L., V.T.T., and T.S. designed the study; S.L. and V.T.T. carried out the experimental work and analyzed the data; T.S. supervised the study; V.T.T. and S.L. wrote the original draft; T.S. edited the paper; S.L. performed PDMS stamp generation using photolithography, spider silk film processing, AFM, FTIR and WCA measurements, cell culture, light and fluorescence microscopy and SEM, V.T.T. performed spider silk film processing, cell culture, light and fluorescence microscopy and CLSM.

Data Availability Statement

The data that support the findings of this study are available from the corresponding author upon reasonable request.

Keywords

bioselectivity, contact guidance, correlative microscopy, geometric confinement, gradient materials

Received: September 1, 2022
Revised: November 10, 2022
Published online: December 16, 2022

[1] a) T. R. Kyriakides, in *Host Response to Biomaterials*, (Ed: S. F. Badylak), Academic Press, Oxford **2015**, p. 81; b) Q. Wei, T. Becherer, S. Angioletti-Uberti, J. Dzubiella, C. Wischke, A. T. Neffe, A. Lendlein, M. Ballauff, R. Haag, *Angew. Chem., Int. Ed.* **2014**, *53*, 8004; c) D. M. Kalaskar, F. Alshorner, in *In Situ Tissue Regeneration*, (Eds: S. J. Lee, J. J. Yoo, A. Atala), Academic Press, Boston **2016**, p. 137.

[2] a) T. J. McKee, G. Perlman, M. Morris, S. V. Komarova, *Sci. Rep.* **2019**, *9*, 10542; b) J. K. Kular, S. Basu, R. I. Sharma, *J. Tissue Eng.* **2014**, *5*, 2041731414557112; c) D. Kusindarta, H. Wihadmadyatami, *Tissue Regeneration* (Ed: H. A. E. Kaoud), London **2018**, p. 65, https://doi.org/10.5772/intechopen.75728; d) C. Frantz, K. M. Stewart, V. M. Weaver, *J. Cell Sci.* **2010**, *123*, 4195.

[3] a) J. Rychly, B. J. Nebe, *BioNanomaterials* **2013**, *14*, 153; b) A.-S. Mertgen, V. T. Trossmann, A. G. Guex, K. Maniura-Weber, T. Scheibel, M. Rottmar, *ACS Appl. Mater. Interfaces* **2020**, *12*, 21342; c) S. Cai, C. Wu, W. Yang, W. Liang, H. Yu, L. Liu, *Nanotechnol. Rev.* **2020**, *9*, 971; d) H. Zhang, X. Zheng, W. Ahmed, Y. Yao, J. Bai, Y. Chen, C. Gao, *Biomacromolecules* **2018**, *19*, 1746; e) E. S. Place, N. D. Evans, M. M. Stevens, *Nat. Mater.* **2009**, *8*, 457; f) K. Kyzioł, Ł. Kaczmarek, A. Kyzioł, in *Handbook of Composites from Renewable Materials*, (Eds: V. K. Thakur, M. K. Thakur, M. R. Ressler), Scrivener Publishing LLC, MA **2017**, p. 457; g) R. J. Wade, J. A. Burdick, *Mater. Today* **2012**, *15*, 454; h) H. Arnani, H. Arzaghi, M. Bayandori, A. S. Dezfuli, H. Pazoki-Toroudi, A. Shafiee, L. Moradi, *Adv. Mater. Interfaces* **2019**, *6*, 1900572; i) N. R. Richbourg, N. A. Peppas, V. I. Sikavitsas, *J. Tissue Eng. Regener. Med.* **2019**, *13*, 1275.

[4] a) A. G. Harvey, E. W. Hill, A. Bayat, *Expert Rev. Med. Devices* **2013**, *10*, 257; b) M. Ermis, E. Antmen, V. Hasirci, *Bioact. Mater.* **2018**, *3*, 355; c) E. Luong-Van, I. Rodriguez, H. Y. Low, N. Elmouelhi, B. Lowenhaupt, S. Natarajan, C. T. Lim, R. Prajapati, M. Vyakarnam, K. Cooper, *J. Mater. Res.* **2013**, *28*, 165; d) A. T. Nguyen, S. R. Sathe, E. K. F. Yim, *J. Phys. Condens. Matter* **2016**, *28*, 183001; e) D. W. Hamilton, S. Ghrebi, H. Kim, B. Chehroudi, D. M. Brunette, in *Encyclopedia of Biomaterials and Biomedical Engineering*, Taylor

ADVANCED SCIENCE NEWS
www.advancedsciencenews.com

ADVANCED MATERIALS INTERFACES
www.advmatinterfaces.de

and Francis, New York **2006**, p. 1; f) M. Nikkhah, F. Edalat, S. Manoucheri, A. Khademhosseini, *Biomaterials* **2012**, *33*, 5230.

[5] a) C.-Y. Yang, W.-Y. Huang, L.-H. Chen, N.-W. Liang, H.-C. Wang, J. Lu, X. Wang, T.-W. Wang, *J. Mater. Chem. B* **2021**, *9*, 567; b) R. G. Flemming, C. J. Murphy, G. A. Abrams, S. L. Goodman, P. F. Nealey, *Biomaterials* **1999**, *20*, 573; c) X. Le, G. E. J. Poinern, N. Ali, C. M. Berry, D. Fawcett, *Int. J. Biomater.* **2013**, *2013*, 782549.

[6] a) J. Ballester-Beltran, M. Biggs, M. Dalby, M. Salmerón-Sánchez, A. Leal-Egana, *Front. Mater.* **2015**, *2*, 00039; b) T. Naganuma, *Nanoscale* **2017**, *9*, 13171.

[7] a) X. F. Walboomers, W. Monaghan, A. S. G. Curtis, J. A. Jansen, *J. Biomed. Mater. Res.* **1999**, *46*, 212; b) C. Matschegewski, S. Staehlke, R. Loeffler, R. Lange, F. Chai, D. P. Kern, U. Beck, B. J. Nebe, *Biomaterials* **2010**, *31*, 5729; c) C. Mörke, H. Rebl, B. Finke, M. Dubs, P. Nestler, A. Airoudj, V. Roucoules, M. Schnabelrauch, A. Körtge, K. Anselme, C. A. Helm, J. B. Nebe, *ACS Appl. Mater. Interfaces* **2017**, *9*, 10461; d) A. I. Teixeira, G. A. Abrams, P. J. Bertics, C. J. Murphy, P. F. Nealey, *J. Cell Sci.* **2003**, *116*, 1881; e) C. Matschegewski, S. Staehlke, H. Birkholz, R. Lange, U. Beck, K. Engel, J. B. Nebe, *Materials* **2012**, *5*, 1176; f) X. Liu, R. Liu, B. Cao, K. Ye, S. Li, Y. Gu, Z. Pan, J. Ding, *Biomaterials* **2016**, *111*, 27.

[8] A. S. Vasilevich, F. Mourcin, A. Mentink, F. Hulshof, N. Beijer, Y. Zhao, M. Levers, B. Papenburg, S. Singh, A. E. Carpenter, D. Stamatialis, C. v. Blitterswijk, K. Tarte, J. d. Boer, *Front. Bioeng. Biotechnol.* **2018**, *6*.

[9] S. Vermeulen, A. Vasilevich, D. Tsiapalis, N. Roumans, P. Vroemen, N. R. M. Beijer, A. D. Eren, D. Zeugolis, J. de Boer, *Acta Biomater.* **2019**, *83*, 277.

[10] S. Zijl, A. S. Vasilevich, P. Viswanathan, A. L. Helling, N. R. M. Beijer, G. Walko, C. Chiappini, J. de Boer, F. M. Watt, *Acta Biomater.* **2019**, *84*, 133.

[11] a) G. Abagnale, A. Sechi, M. Steger, Q. Zhou, C.-C. Kuo, G. Aydin, C. Schalla, G. Müller-Newen, M. Zenke, I. G. Costa, P. van Rijn, A. Gillner, W. Wagner, *Stem Cell Rep.* **2017**, *9*, 654; b) P. Clark, P. Connolly, A. S. Curtis, J. A. Dow, C. D. Wilkinson, *J. Cell Sci.* **1991**, *99 (Pt 1)*, 73.

[12] a) G. A. Dunn, J. P. Heath, *Exp. Cell Res.* **1976**, *101*, 1; b) P. Weiss, *J. Exp. Zool.* **1945**, *100*, 353.

[13] A. Mathur, S. W. Moore, M. P. Sheetz, J. Hone, *Acta Biomater.* **2012**, *8*, 2595.

[14] C. Oakley, D. M. Brunette, *J. Cell Sci.* **1993**, *106*, 343.

[15] V. Brunetti, G. Maiorano, L. Rizzello, B. Sorce, S. Sabella, R. Cingolani, P. P. Pompa, *Proc. Natl. Acad. Sci. U. S. A.* **2010**, *107*, 6264.

[16] a) S. Wohlrab, S. Müller, A. Schmidt, S. Neubauer, H. Kessler, A. Leal-Egaña, T. Scheibel, *Biomaterials* **2012**, *33*, 6650; b) P. Zeplin, N. Maksimovikj, M. Jordan, J. Nickel, G. Lang, A. Leimer, L. Römer, T. Scheibel, *Adv. Funct. Mater.* **2014**, *24*, 2568; c) A. Leal-Egaña, G. Lang, C. Mauerer, J. Wickinghoff, M. Weber, S. Geimer, T. Scheibel, *Adv. Eng. Mater.* **2012**, *14*, B67; d) C. B. Borkner, S. Wohlrab, E. Möller, G. Lang, T. Scheibel, *ACS Biomater. Sci. Eng.* **2017**, *3*, 767; e) T. U. Esser, V. T. Trossmann, S. Lentz, F. B. Engel, T. Scheibel, *Mater. Today Bio.* **2021**, *11*, 100114.

[17] a) C. Fredriksson, M. Hedhammar, R. Feinstein, K. Nordling, G. Kratz, J. Johansson, F. Huss, A. Rising, *Materials* **2009**, *2*, 1908; b) M. Lucke, I. Mottas, T. Herbst, C. Hotz, L. Römer, M. Schierling, H. M. Herold, U. Slotta, T. Spinetti, T. Scheibel, G. Winter, C. Bourquin, J. Engert, *Biomaterials* **2018**, *172*, 105; c) S. Salehi, K. Koeck, T. Scheibel, *Molecules* **2020**, *25*, 737; d) T. B. Aigner, E. DeSimone, T. Scheibel, *Adv. Mater.* **2018**, *30*, 1704636.

[18] D. Huemmerich, C. W. Helsen, S. Quedzuweit, J. Oschmann, R. Rudolph, T. Scheibel, *Biochemistry* **2004**, *43*, 13604.

[19] S. Müller-Herrmann, T. Scheibel, *ACS Biomater. Sci. Eng.* **2015**, *1*, 247.

[20] a) S. Kumari, G. Lang, E. DeSimone, C. Spengler, V. T. Trossmann, S. Lücker, M. Hudel, K. Jacobs, N. Krämer, T. Scheibel, *Data Brief* **2020**, *32*, 106305; b) S. Kumari, G. Lang, E. DeSimone, C. Spengler, V. T. Trossmann, S. Lücker, M. Hudel, K. Jacobs, N. Krämer, T. Scheibel, *Mater. Today* **2020**, *41*, 21.

[21] a) X. Wei, J. Shen, Z. Gu, Y. Zhu, F. Chen, M. Zhong, L. Yin, Y. Xie, Z. Liu, W. Jin, M. Nouri, L. Chang, *ACS Appl. Bio Mater.* **2018**, *1*, 2167; b) G. Bartalena, Y. Loosli, T. Zambelli, J. G. Snedeker, *Soft Matter* **2012**, *8*, 673.

[22] H. Kavand, H. van Lintel, S. B. Sichani, S. Bonakdar, H. Kavand, J. Koohsorkhi, P. Renaud, *ACS Appl. Mater. Interfaces* **2019**, *11*, 10559.

[23] A. Mata, A. J. Fleischman, S. Roy, *Biomed. Microdevices* **2005**, *7*, 281.

[24] K. Schacht, T. Jüngst, M. Schweinlin, A. Ewald, J. Groll, T. Scheibel, *Angew. Chem., Int. Ed.* **2015**, *54*, 2816.

[25] a) C. J. Wilson, R. E. Clegg, D. I. Leavesley, M. J. Pearcy, *Tissue Eng.* **2005**, *11*, 1; b) J. M. Anderson, A. Rodriguez, D. T. Chang, *Semin. Immunol.* **2008**, *20*, 86.

[26] S. Lentz, V. T. Trossmann, C. B. Borkner, V. Beyersdorfer, M. Rottmar, T. Scheibel, *ACS Appl. Mater. Interfaces* **2022**, *14*, 31751.

[27] E. DeSimone, K. Schacht, A. Pellert, T. Scheibel, *Biofabrication* **2017**, *9*, 044104.

[28] a) C. L. Fonta, B. M. Humbel, *Arch. Biochem. Biophys.* **2015**, *581*, 98; b) T. Takizawa, J. M. Robinson, *Placenta* **2003**, *24*, 557.

[29] a) A. Leclerc, D. Tremblay, S. Hadjiantoniou, N. V. Bukoreshtliev, J. L. Rogowski, M. Godin, A. E. Pelling, *Biomaterials* **2013**, *34*, 8097; b) W.-T. Su, Y.-F. Liao, I. M. Chu, *Micron* **2007**, *38*, 278; c) A. I. Teixeira, G. A. McKie, J. D. Foley, P. J. Bertics, P. F. Nealey, C. J. Murphy, *Biomaterials* **2006**, *27*, 3945; d) M. J. Dalby, D. McCloy, M. Robertson, C. D. W. Wilkinson, R. O. C. Oreffo, *Biomaterials* **2006**, *27*, 1306.

[30] a) A. Mata, L. Hsu, R. Capito, C. Aparicio, K. Henrikson, S. I. Stupp, *Soft Matter* **2009**, *5*, 1228; b) C. C. Berry, G. Campbell, A. Spadiccino, M. Robertson, A. S. G. Curtis, *Biomaterials* **2004**, *25*, 5781.

[31] J. Sun, N. Jamilpour, F.-Y. Wang, P. K. Wong, *Biomaterials* **2014**, *35*, 3273.

[32] F. Bauer, S. Wohlrab, T. Scheibel, *Biomater. Sci.* **2013**, *1*, 1244.

ADVANCED MATERIALS INTERFACES

Supporting Information

for *Adv. Mater. Interfaces,* DOI: 10.1002/admi.202201936

Selective Topography Directed Cell Adhesion on Spider Silk Surfaces

*Sarah Lentz, Vanessa Tanja Trossmann, and Thomas Scheibel**

WILEY-VCH

Supplementary Information

Topography directed cell adhesion on spider silk surfaces

Sarah Lentz‡, Vanessa Trossmann‡ and Thomas Scheibel

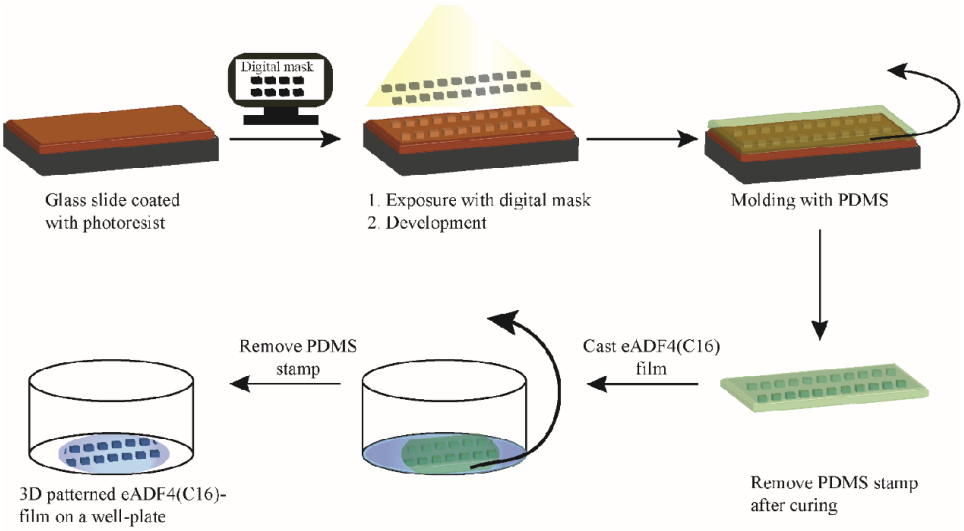

Figure S1: Schematic illustration of the preparation of patterned recombinant eADF4(C16) spider silk films. The first step is the coating of RCA (Radio Corporation of America) cleaned glass slides with a photoresist. Then the digital mask is exposed (UV light) to the glass slide. Afterwards, the exposed photoresist is developed in the developer solution. The exposed parts of the photoresist get removed to obtain a template. This template is covered with PDMS and cured to receive an imprint (stamp). The PDMS stamp gets removed. The recombinant eADF4(C16) spider silk solution is cast into a well-plate. Then, the PDMS stamp is placed in the solution. After the solvent (formic acid) is completely evaporated, the PDMS stamp is removed, and a 3D patterned recombinant spider silk film remains.

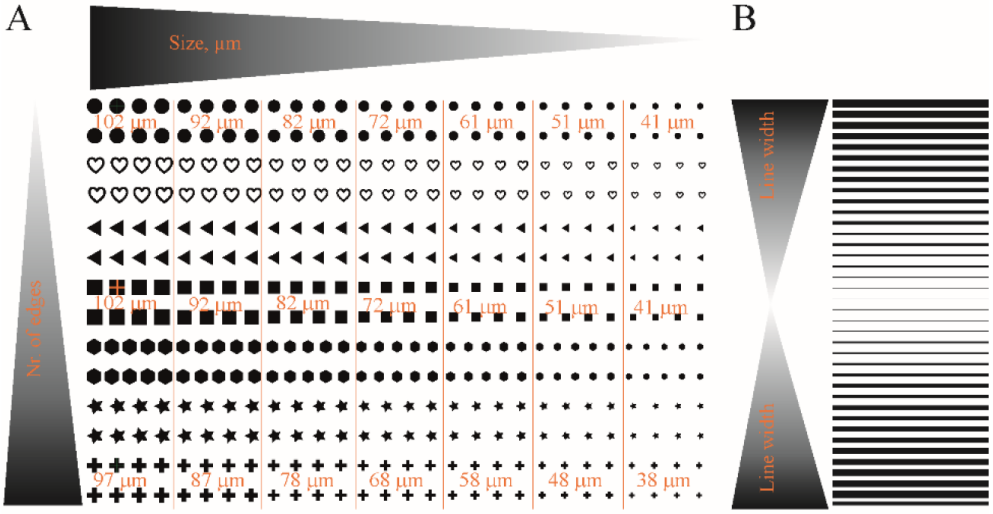

Figure S2: Digital masks showing size gradients of different structures (circles, hearts, triangles, squares, hexagons, stars, and crosses) (A) and grooves exhibiting different groove widths (B). (A) The patterns were arranged regarding their number of edges and their size. The resulting features should show sizes between around 40 µm and 100 µm. (B) the groove gradient is characterized by increasing widths for grooves and ridges.

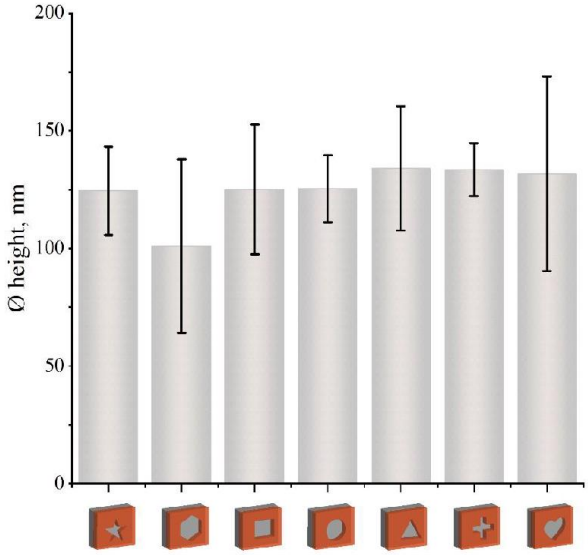

Figure S3: Individual indentation heights of patterns of processed eADF4(C16) spider silk films determined using AFM.

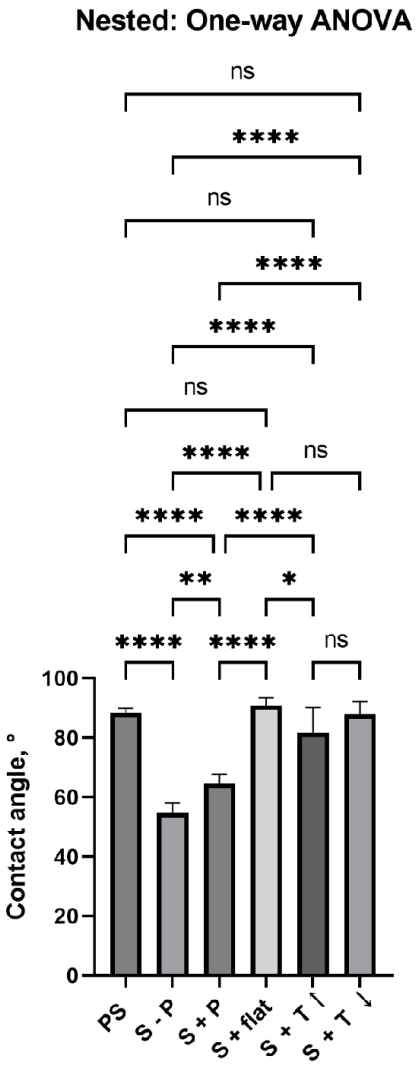

Figure S4: One-way ANOVA plot of water contact angles (°) water contact angle measurements on a blank polystyrene substrate (PS), on flat air-dried eADF4(C16) spider silk films with plasma (S + P) and without (S – P) plasma treatment, and on silk films cast with flat PDMS stamps (S + flat) or patterned PDMS stamps (protrusions (S + T↑), indentations (S + T↓)) on top (n=5). The ANOVA resulted in non-significant (ns) and significant (*, ** or **) differences of the water contact angles.**

Table S1: Results of one-way ANOVA analysis with Turkey´s multiple comparisons test. Every sample was compared. Ns means non-significant. *, **, * and **** indicate significant differences. Mean Diff. stands for the average difference between the two compared patterns. The abbreviations mean the following: blank polystyrene substrate (PS), flat air-dried eADF4(C16) spider silk films with plasma (S + P) and without (S – P) plasma treatment, silk films cast with flat PDMS stamps (S + flat), patterned PDMS stamps with protrusions (S + T↑) and indentations (S + T↓)) on top (n=5).**

Tukey's multiple comparisons test	Mean Diff,	Summary	Adjusted P Value
PS vs. S - P	33,64	****	<0,0001
PS vs. S + P	23,80	****	<0,0001
PS vs. S + flat	-2,506	ns	0,9786
PS vs. S + T↑	6,617	ns	0,4988
PS vs. S + T ↓	0,3857	ns	>0,9999
S - P vs. S + P	-9,839	**	0,0065
S - P vs. S + flat	-36,14	****	<0,0001
S - P vs. S + T↑	-27,02	****	<0,0001
S - P vs. S + T ↓	-33,25	****	<0,0001
S + P vs. S + flat	-26,31	****	<0,0001
S + P vs. S + T↑	-17,18	****	<0,0001
S + P vs. S + T ↓	-23,41	****	<0,0001
S + flat vs. S + T↑	9,122	*	0,0320
S + flat vs. S + T ↓	2,891	ns	0,8293
S + T↑ vs. S + T ↓	-6,231	ns	0,2276

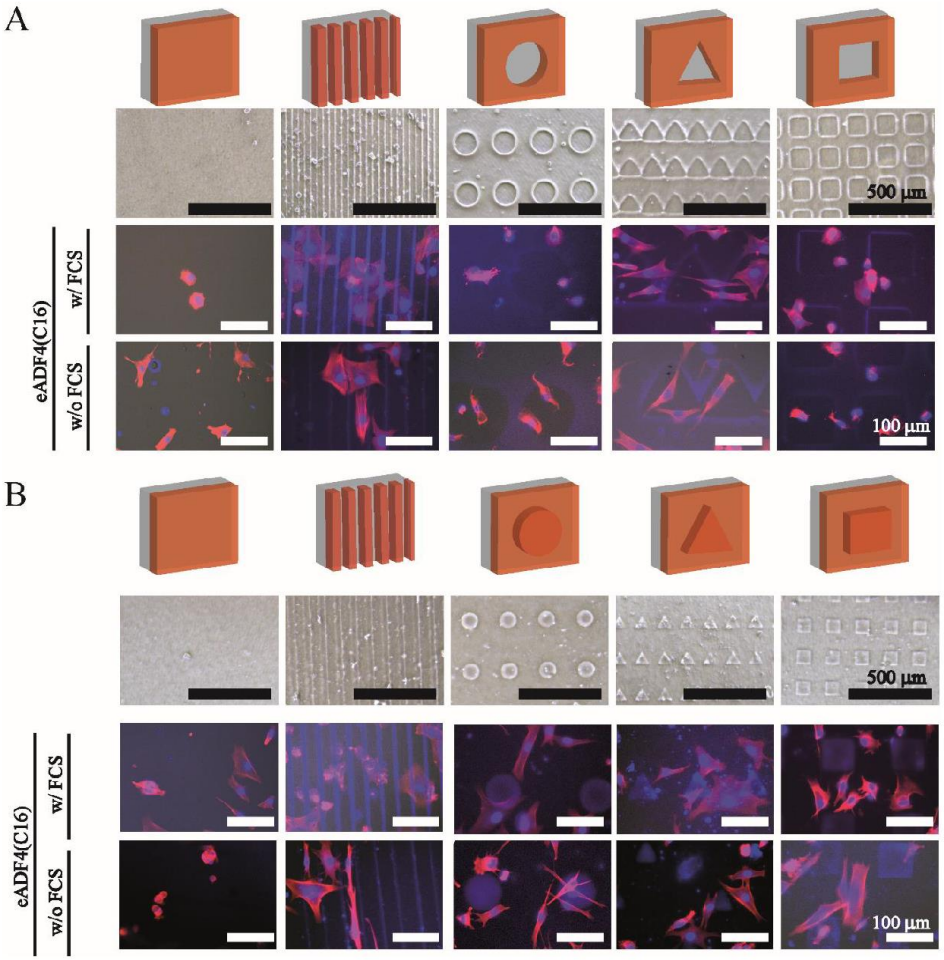

Figure S5: Cell adhesion to eADF4(C16) spider silk films containing indentations (A) or protrusions (B) in the absence (w/o FCS) and presence (w/ FCS) of added fetal calf serum (FCS). Before cell culture experiments, the shape-fidelity of surface topographical patterns was confirmed using light microscopy (upper row). Human BJ skin fibroblasts were incubated for 4 h on flat, grooved and patterned eADF4(C16) spider silk surfaces (circle, triangle and square) in absence and presence of FCS and subsequently stained with DAPI (blue, cell nuclei) and phalloidin-red (red, F-actin cytoskeleton) (n=5). Scale bars as indicated.

7.8. Teilarbeit VIII

Teilarbeit VIII wurde 2021 unter dem Titel „Impact of Cell Loading of Recombinant Spider Silk Based Bioinks on Gelation and Printability" im Journal *Macromolecular Bioscience* veröffentlicht.

Lechner, A.*; **Trossmann, V. T.*** & Scheibel, T. (2021) Impact of Cell Loading of Recombinant Spider Silk Based Bioinks on Gelation and Printability. *Macromolecular Bioscience* **22**: 2100390.

https://doi.org/10.1002/mabi.202100390

* gleichberechtigte Co-Autorenschaft

RESEARCH ARTICLE

Macromolecular Bioscience
www.mbs-journal.de

Impact of Cell Loading of Recombinant Spider Silk Based Bioinks on Gelation and Printability

*Annika Lechner, Vanessa T. Trossmann, and Thomas Scheibel**

Printability of bioinks encompasses considerations concerning rheology and extrudability, characterization of filament formation, shape fidelity, cell viability, and post-printing cellular development. Recombinant spider silk based hydrogels might be a suitable material to be used in bioinks, that is, a formulation of cells and materials to be used for bioprinting. Here, the high shape fidelity of spider silk ink is shown by bioprinting the shape and size of a human aortic valve. Further the influence of the encapsulation of cells has been evaluated on spider silk hydrogel formation, hydrogel mechanics, and shape fidelity upon extrusion based bioprinting. It is shown that the presence of cells impacts the gelation of spider silk proteins differently, depending on the used silk variant. RGD-modified spider silk hydrogels are physically crosslinked by the cells, while there is no active interaction between cells and un-tagged spider silk proteins. Strikingly, even at cell densities up to ten million cells per milliliter, cell viability is high after extrusion-based printing, which is a significant prerequisite for future applications. Shape fidelity of the printed constructs is demonstrated using a filament collapse test in the absence and presence of human cells.

1. Introduction

Extrusion based bioprinting is one of several advanced bottom-up tissue engineering techniques in the evolving field of biofabrication.[1] Typically, continuous strands of a hydrogel (acellular biomaterial ink) or bioink are dispensed through a nozzle in a layer-by-layer fashion.[2] Bioinks contain one or more material components functioning as mimetic scaffolds as well as cells as the living element.[3] Biofabrication enables the simultaneous deposition of cells, materials, and factors into hierarchically structured and personalized constructs.[4] Each application and processing technique requires individually optimized bioinks. On the one hand, the chosen material has to provide appropriate rheological properties, including viscosity, viscoelastic shear moduli, shear stress, and elastic recovery, suitable for the desired processing technique.[5] On the other hand, it has to support cellular survival, proliferation, and maturation before, during, and after the printing process.[6] For bioink formulations, natural polymers are often favored over synthetic materials, as the latter can cause limitations due to toxicity, low biocompatibility and/or the lack of biological binding sites.[7] The choice of cell type dictates maturation from printed constructs to functional tissues or tissue models. However, given the nature of living cells, the interplay with the surrounding material based on, for example, porosity and stiffness or presented biological cues, significantly influences cellular development.[8] Further, mechanics and printability of the bioink are affected by interactions between the materials and the cells and potential structural disruption based thereon.[9] Evaluation of the performance of a bioink includes consideration of rheological parameters, extrudability, and filament characterization including shape fidelity during and after printing.[5] For successful bioprinting, bioinks have to display shear-thinning behavior, with the viscosity decreasing with increasing shear stress during extrusion and rising with the drop of shear stress after printing, and viscoelasticity, which can be described by the storage (G′) and loss (G″) modulus during oscillatory measurements. Ideally, bioinks should show a reversible, fast gel-solid transition, meaning easy flow through the nozzle during extrusion followed by rapid elastic shape retention after dispension.[5,10] Studies looking at the effect of cells on different aspects of bioink printability elucidate the complexity of the underlying factors. For example, collagen based bioinks showed increased storage moduli and viscosities before

A. Lechner, V. T. Trossmann, T. Scheibel
Lehrstuhl Biomaterialien, Universität Bayreuth
Prof.-Rüdiger-Bormann Straße 1, 95447 Bayreuth, Germany
E-mail: thomas.scheibel@bm.uni-bayreuth.de
T. Scheibel
Bayreuther Zentrum für Kolloide und Grenzflächen (BZKG)
Universität Bayreuth
Universitätsstraße 30, 95440 Bayreuth, Germany
T. Scheibel
Bayerisches Polymerinstitut (BPI)
Universität Bayreuth
Universitätsstraße 30, 95440 Bayreuth, Germany
T. Scheibel
Bayreuther Zentrum für Molekulare Biowissenschaften (BZMB)
Universität Bayreuth
Universitätsstraße 30, 95440 Bayreuth, Germany
T. Scheibel
Bayreuther Materialzentrum (BayMAT)
Universität Bayreuth
Universitätsstraße 30, 95440 Bayreuth, Germany

The ORCID identification number(s) for the author(s) of this article can be found under https://doi.org/10.1002/mabi.202100390

DOI: 10.1002/mabi.202100390

ADVANCED SCIENCE NEWS
www.advancedsciencenews.com

Macromolecular Bioscience
www.mbs-journal.de

gelation and decreased storage moduli after gelation with increasing chondrocyte densities. Notably, the printing resolution was increased at higher cell densities.[11] Another study looked into bioinks based on gelatin methacrylate, gelatin gum, and human endothelial cells. While higher cell densities led to increased storage and loss moduli as well as decreased flow points (stress at the G′ G″ crossover point), they had no influence on the reported outcome of the printing.[12]

Amongst other natural polymers, silk based materials are employed as matrix and bioink components within biofabrication applications. They offer non-toxicity, biocompatibility, and biodegradability and can be processed into various morphologies.[7] For example, a silk fibroin solution, prepared after extraction from *Bombyx mori* cocoons, was successfully 3D printed using extrusion bioprinters and by including sacrificial particles and several post-treatment steps, hierarchical structures with tunable pore sizes were generated.[13] A cell-friendly gelation process could be achieved through the addition of the synthetic polymer polyethylene glycol (PEG) which induced β-sheet formation, leading to physical cross-linking without the need for post-treatment.[14] In other studies, gelatin was added to ink formulations, to enhance the rather poor mechanical properties and to tune the degradation profile of silk fibroin hydrogels.[15,16]

Hydrogels made of recombinantly produced spider silk proteins have recently been shown to be suitable as the material component of printable bioinks without the need of additives. Based on the repetitive core sequence of the European garden spider *Araneus diadematus* dragline silk fibroin 4, the protein eADF4(C16) and its integrin-binding-motif-containing variant eADF4(C16)-RGD form physically cross-linked hydrogel networks at aqueous conditions without the need for additional crosslinking.[17–19] Recombinant eADF4(C16)-based spider silk proteins self-assemble from an intrinsically disordered monomeric protein in solution into tightly packed cross-β nanofibrils with a high β-sheet content via intra- and intermolecular physical interactions.[18,20,21] During fibril self-assembly, the poly-alanine stretches $(Ala)_8$ of each C-module form strong, crystalline, antiparallel β-sheets via hydrogen bonding, while the glycine/proline rich sequence repeats (e.g. GPGXY) remain unstructured or fold into helices or turns forming an amorphous, flexible part embedding the β-sheet crystallites.[18,21–23] At higher protein concentrations (above 2% (w/v)) eADF4(C16)-based spider silk proteins self-assemble into stable β-sheet rich hydrogels with a nanofibrillar network stabilized by intra- and intermolecular physical interactions including hydrogen bonds, hydrophobic interactions, and physical entanglement.[18,24–26] Without crosslinking, hydrogels made of recombinant spider silk proteins are stable, while displaying rather soft mechanical properties. The elastic moduli of 3% (w/v) eADF4(C16) hydrogels were determined to be in the lower kilopascal range (≤1 kPa). This means, that hydrogels made of recombinant spider silk proteins, without additional modifications, are well suited for but also limited to the biofabrication of soft tissues. Mechanical properties can, however, be increased to reach the range of muscle, skin, and cartilage tissue,[27] using chemical crosslinking and increasing the protein concentration, which is feasible up to 7% (w/v) in aqueous solution, to strengthen the hydrogel to elastic moduli up to 110 kPa.[18] The presence of salts, by adding cell culture media to the protein solutions, resulted in faster gelation and stiffer hydrogels.[25] Studies on different variants of the recombinant spider silk protein showed a clear influence of the RGD-tag, which has been genetically engineered into the protein, on the stiffness of hydrogels. Measured at the same protein concentration, eADF4(C16)-RGD hydrogels displayed elastic moduli of ≈0.2 kPa, compared to ≈0.02 kPa for hydrogels made eADF4(C16).[28] Consequently, the elastic moduli could be adjusted to be similar by applying different protein concentrations.[26]

The gentle gelation process allows us to simultaneously encapsulate cells within the shear-thinning, viscoelastic hydrogels for 3D bioprinting. The suitability of spider silk based bioinks to print straight-forward and cell-friendly grid structures using micro-valve printing has been previously shown.[24,26] In this study, we further assessed and improved the printability of recombinant spider silk based bioinks. To obtain optimal printing conditions, the influence of temperature on the rheological properties of eADF4(C16) hydrogels was evaluated. It was demonstrated that these hydrogels can be successfully extrusion-printed with high shape-fidelity into the shape of a human aortic heart valve without the need of any additives or chemical crosslinkers. Successful fabrication of biologically active constructs strongly relies on the ability of an ink to encapsulate high amounts of cells, while facilitating printability, cellular survival, and proliferation. Building on previous studies dealing with recombinant spider silk based bioinks, here, cell densities were increased from one million up to ten million cells per milliliter. For the first time, characterization of gelation kinetics as well as rheological evaluation was performed on cell-containing bioinks based on recombinant spider silk proteins. This study shows the ability of recombinant spider silk protein based materials to be used as high cell-content containing bioinks that are printable to yield advanced structures.

2. Results and Discussion

2.1. Printability of Recombinant Spider Silk Inks

To evaluate the previously shown potential of extrusion printing using recombinant spider silk inks[24,26,29] in terms of geometry as well as durability of the gained structures in detail, the shape of a human aortic valve (model source: Cellink) was printed (**Figure 1**A), as well as the filament collapse test was performed (Figure 1B–D)[30] using acellular 3% (w/v) eADF4(C16) hydrogels. Tapered needles, instead of cylindrical ones, improved the printing results for both set-ups. This might be due to reduced pressure and shear stress applied to the material in the tapered geometry,[31] preventing phase separation, which was seen during printing with cylindrical steel needles. Interestingly, the shape-fidelity of the printed human aortic valve could be confirmed using two different extrusion bioprinters, RegenHU's 3D Discovery and Cellink's BioX (Figure 1A). The size and shape of both constructs, as well as the amount of material needed for both prints (3 mL) were almost identical. Most apparent difference were the closed layers on the 3D Discovery's printed structure versus the open pores on the BioX's print. These varieties occurred even though all consumables, like cartridge and nozzle and basic setting, including layer height and infill pattern and density, were identical. This result demonstrated in principle the good

ADVANCED SCIENCE NEWS
www.advancedsciencenews.com

Macromolecular Bioscience
www.mbs-journal.de

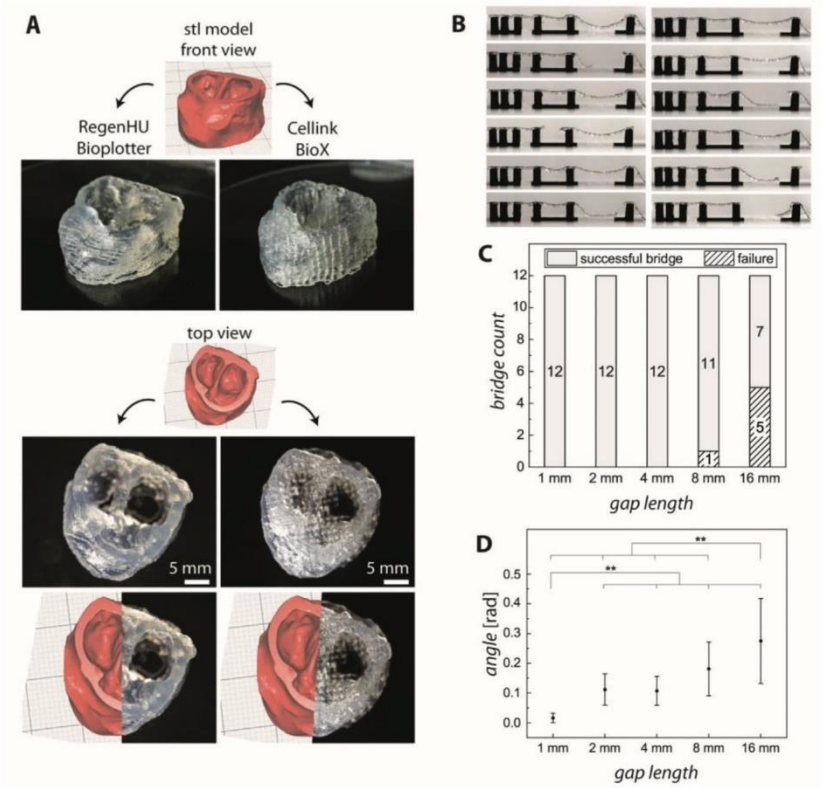

Figure 1. Shape fidelity of extrusion-printed spider silk hydrogels. A) As an example of printed complex scaffold structures, the shape of a human aortic valve (stl-file source: Cellink) was printed with 3% eADF4(C16) hydrogels on two different bioplotters, namely RegenHU's 3D Discovery and Cellinks's BioX. B) Using a 22G tapered tip, one strand of hydrogel filament was printed over a pillar structure, and this process was repeated twelve times. Pictures were taken immediately after printing. C) The failure of the hydrogel to bridge each gap increased with increasing distance. D) Angle of deflection determined graphically from images of filament strands successfully extruded over increasingly spaced pillars (**$p \leq 0.05$).

reproducibility when printing distinct shapes on different printers, but also showed the variation of separately acquired gcodes, meaning the printer's exact instructions, regarding details within the printed shape. Advanced features in these printed structures included overhanging walls and cavities on the inside bridged by upper layers. To quantify the durability of the printed spider silk strands, a filament collapse test was performed. One strand of hydrogel was placed over several pillars with increasing gaps in between (Figure 1B). For a realistic representation, 12 tests, including failed bridges (Figure 1C) are displayed.

The results showed that bridging with the spider silk hydrogels is reliable up to 8 mm without failing. Further, the largest gap with a length of 16 mm was bridged successfully seven out of twelve times. Strand collapses possibly occurred due to small inhomogeneities within the physically cross-linked hydrogel. The angle of deflection was determined as a measure of shape fidelity and the strands ability to hold its own weight against gravity (Figure 1D). With increasing gap size, the angle, and its deviation increased. There was no significant difference between the angles determined for 2, 4, and 8 mm gap lengths. The smallest (1 mm) and largest (16 mm) distance however, resulted in significant smaller or larger angles of deflection compared to all other distances.

eADF4(C16) hydrogels show shear thinning and viscoelastic behavior required for extrusion bioprinting independent of the used silk concentration.[18,24–26] However, during printing of the heart valve and during the filament collapse test, it became apparent that temperature has a severe impact on printability. Therefore, rheology was measured at 25 °C as previously published, but additionally at 4 and at 37 °C. With increasing temperature, higher shear-rate-dependent viscosities (**Figure 2**A), flow points at higher stresses (Figure 2B) and longer linear viscoelastic regions (Figure 2C) were identified. Normally, the viscosity of a sample decreases with increasing temperature. However, if a sample shows temperature dependent hardening, like the recombinant spider silk hydrogels, this effect can be reversed.[10] Generally, higher viscosities and higher yield stresses are linked to better printability, especially regarding filament formation and stiffness after printing, but are also accompanied by an increased pressure and shear stress during printing.[5] This consequence resulting from the rheological changes explained the observation made with recombinant spider silk inks. As already men-

ADVANCED SCIENCE NEWS
www.advancedsciencenews.com

Macromolecular Bioscience
www.mbs-journal.de

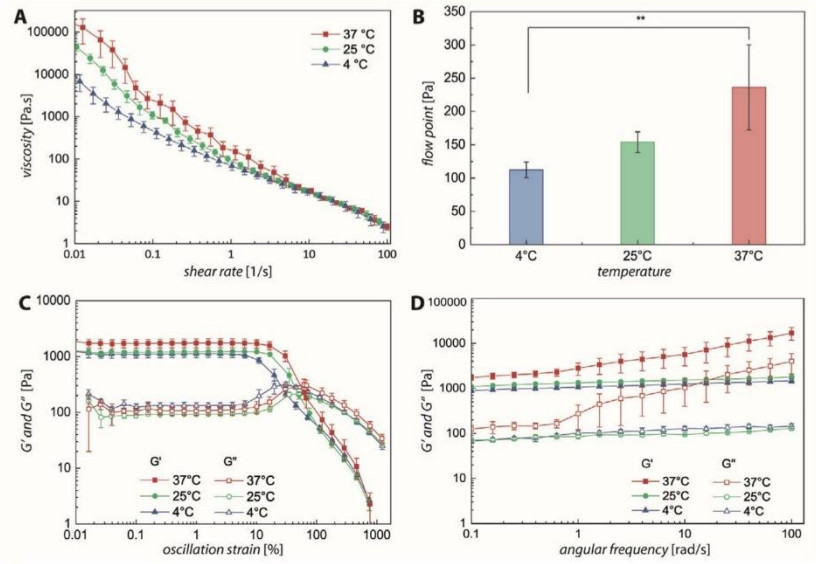

Figure 2. Temperature-dependent rheology of 3% eADF4(C16) hydrogels. Rheological measurements of the spider silk hydrogels were performed at 4, 25, and 37 °C. A) Viscosity was measured while increasing rotational shear rates from 0.01 to 100 s^{-1}. B) Flow points were determined as the crossover of G′ (storage modulus) and G″ (loss modulus) at constant angular frequency (10.0 rad s^{-1}) over increase in strain from 0.01% to 1000.0% using TRIOS software (**$p \leq 0.05$). C) G′ and lG″ at constant angular frequency (10.0 rad s^{-1}) over an increase in strain from 0.01% to 1000.0% and D) at constant strain (1.0%) over an increase in oscillatory frequencies from 0.1 to 100 rad s^{-1}.

tioned above, higher printing pressure led to decreased material homogeneity, occasionally causing inconstant filament extrusion. It turned out that the printing should be done, if compatible with the encapsulated cells, at room temperature. Oscillatory frequency-dependent measurements confirmed that finding (Figure 2D). While at 4 °C and at 25 °C the samples showed stability over the entire range of frequencies applied, at 37 °C a clear instability of storage and loss modulus could be detected over varying angular frequencies.

2.2. Gelation of Spider Silk Based Bioinks

The spider silk hydrogel variants eADF4(C16) and eADF4(C16)-RGD were compared to hydrogels made of eADF4(C16)-RGE in terms of usability in bioinks. eADF4(C16)-RGD and eADF4(C16)-RGE are identical in most physico-chemical properties and differ only in one amino acid: in eADF4(C16)-RGE, the glutamic acid (E) replaces the aspartic acid (D) of the eADF4(C16)-RGD variant. This change has a severe impact on cell binding, since the RGE peptide does not properly fit into the binding pocket of integrins yielding significantly lower binding affinities.[32] However, the total net charge as well as charge distribution remain the same. Not surprisingly, eADF4(C16)-RGE 2D films showed a similar low adhesion and proliferation of Balb 3T3 fibroblasts as eADF4(C16).[19]

In previous studies, we have already shown that eADF4(C16) and eADF4(C16)-RGD hydrogels are suitable matrix materials for cell encapsulation. Further, it has been shown that changing the protein concentration upon gelation allowed us to adjust the mechanical properties of the hydrogels.[18,24,26] Here, gelation of all three spider silk variants was investigated in the presence of RPMI media as well as, for the first time, in presence of the mammalian cell line BxPC-3 (pancreatic adenocarcinoma cell line) to analyze the respective influence on nano-fibril formation and gelation kinetics. Since gelation strongly depends on the silk variant itself, but also on the protein concentration used, it was decided to leave the protein concentrations the same (3%(w/v)) in order to focus on the influence of the silk variant on kinetics in the absence and presence of cells. To reveal the cellular impact on hydrogel formation, cells were added either directly at the beginning of the gelation process or at the end of the lag phase (i.e., nucleus formation for fibril growth followed by hydrogel formation) of spider silk assembly.[33]

Both, eADF4(C16)-RGD and eADF4(C16)-RGE displayed an accelerated fibril formation and gelation in comparison to eADF4(C16) in presence of RPMI media (**Figure 3**A, red curves). Interestingly, eADF4(C16)-RGE showed an increase in turbidity shortly after adding the media with a short lag-phase (≈40 min), while eADF4(C16)-RGD displayed a lag-phase of ≈100 min before exponential fibrillization started. In contrast, eADF4(C16) had the longest lag-phase of 500 min. During the lag-phase (nucleation phase) soluble, intrinsically disordered, mostly unstructured spider silk proteins (monomers) transformed into thermodynamically meta-stable β-sheet rich assemblies (oligomers) by physical interactions. These oligomers acted as nuclei for exponential fibril growth by interaction with further soluble silk monomers (fibril elongation phase) resulting in tightly packed

ADVANCED SCIENCE NEWS
www.advancedsciencenews.com

Macromolecular Bioscience
www.mbs-journal.de

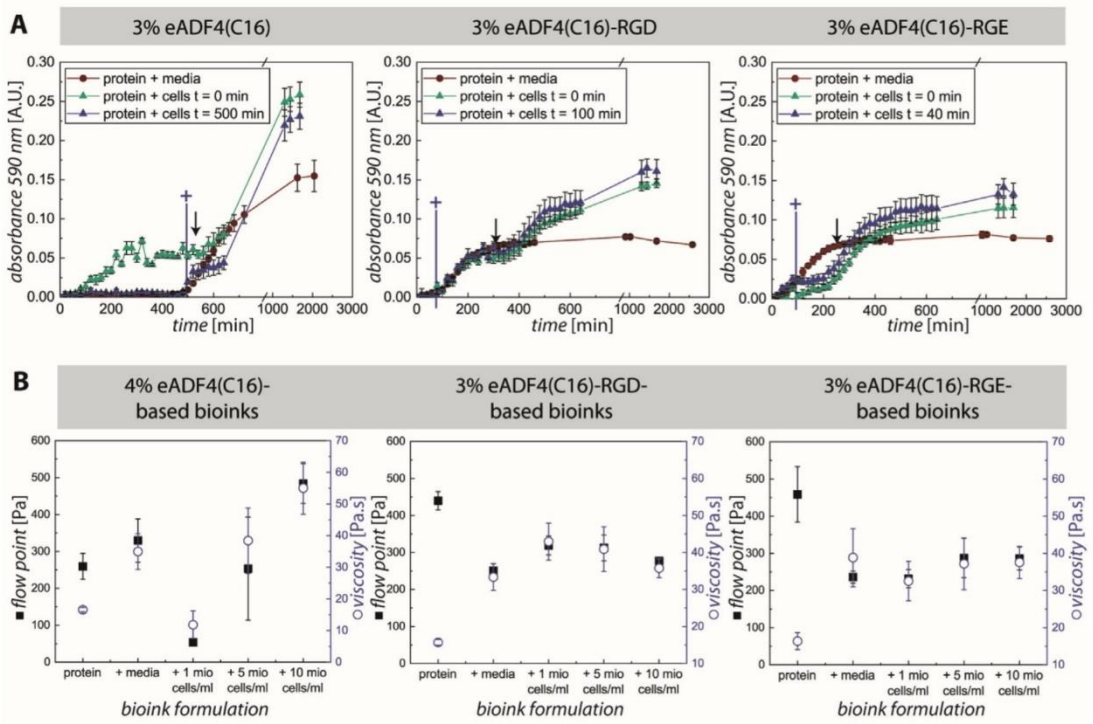

Figure 3. Spider silk gelation in the presence of mammalian cells. A) Protein solutions were mixed with either only media or media plus BxPC-3 cells at finally 1 million cells per milliliter. For each spider silk variant, cells were added either at the beginning of the incubation (t = 0 min) or at the end of the lag phase (nucleation)/beginning of the exponential growth phase of nanofibrils (t = 500 min in case of eADF4(C16), t = 100 min in case of eADF4(C16)-RGD, or t = 40 min in case of eADF4(C16)-RGE; marked with blue crosses). Fibrillization/gelation was quantified measuring the change in turbidity at 570 nm and 37 °C. Appropriate blank values were subtracted and first data points were normalized to zero for better comparability of the curves. Black arrows indicate the intermediate plateau of samples with cells. B) Rheological properties of 4% eADF4(C16), 3% eADF4(C16)-RGD, and 3% eADF4(C16)-RGE hydrogels were analyzed in the absence or presence of BxPC-3 cells (only silk protein, silk protein + 15% (v/v) media, silk protein + 1 mio cells per milliliter, 5 mio cells per milliliter or 10 mio cells per milliliter in 15% (v/v) media). Flow points were determined as crossover of storage (G′) and loss modulus (G″) measured at constant angular frequency (10.0 rad s^{-1}) over increase in strain from 0.01% to 1000.0%. Viscosity was determined at a shear rate of 10 s^{-1}.

thermodynamically stable cross-β nanofibrils with a high β-sheet content.[21] The stationary phase upon completion of fibril formation and gelation was seen after 300 min for both modified variants and after 1500 min for eADF4(C16). These results indicated that both peptide tags accelerated nucleation, fibril formation, and gelation. The acceleration of gelation of eADF4(C16)-RGD and eADF4(C16)-RGE could be resulting from the additional charged amino acid residues ensuring for example ionic bonding with ions from cell culture media.[25]

The addition of BxPC-3 cells before fibrillization (Figure 3A, green curves) affected the nucleation-dependent gelation in different ways: while the initial nucleation of eADF4(C16) was apparently accelerated (shorter lag-phase), in the case of eADF4(C16)-RGE a deceleration was seen (longer lag-phase). Thus, the formation of thermodynamically meta-stable oligomers by intra- and maybe also intermolecular protein interactions was faster in the case of soluble eADF4(C16), but slower in case of eADF4(C16)-RGE. In contrast, initial fibril formation of eADF4(C16)-RGD was not influenced in the presence of cells (identical lag-phase) indicating a similar formation of nuclei independent of cells. Interestingly, for all spider silk variants a similar course of the following exponential fibril growth phase could be detected: after a first increase in turbidity yielding an intermediate plateau (Figure 3A, black arrows), a second turbidity increase was seen until finally the stationary phase was reached. These curves indicated that soluble silk proteins docked on the pre-formed silk nuclei leading to fibril growth (first increase in turbidity). During the intermediate plateau interval, no notable fibrillization took place, and a first hydrogel network was already formed at this intermediate plateau. The second increase in turbidity could be a rearrangement of silk fibrils caused by the present cells leading to the formation of a denser packed, twisted, cell-interconnected network of silk fibrils compared to pure hydrogels without cells. This fibril-cell network would also explain the higher turbidity values of the stationary phase at the end, where gelation was completed. Looking at the single proteins, it could be seen that the exponential fibril growth of eADF4(C16)-RGD was apparently not influenced by present cells, as both

ADVANCED SCIENCE NEWS
www.advancedsciencenews.com

Macromolecular Bioscience
www.mbs-journal.de

curves (with and without cells), overlapped until the intermediate plateau was reached. For eADF4(C16) and eADF4(C16)-RGE the cells caused an acceleration of fibrillization. One reason could be that the present cells minimize the free space in the solution (i.e., a virtually higher protein concentration) forcing the soluble silk proteins to interact with the already present silk nuclei (while not showing protein–cell interactions), leading to an accelerated fibril growth. However, the cells could always interact with the cell-adhesive RGD peptide, regardless of whether the protein is soluble or assembled in nuclei or fibrils. In the case of eADF4(C16)-RGD, such a cell–protein interaction could compensate the acceleration of fibril elongation.

To further analyze the cellular impact on exponential fibril growth behavior of different spider silk variants, BxPC-3 cells were added at the end of the appropriate lag-phases, where first silk nuclei were already formed (Figure 3A, blue curves, plus-sign). In this set-up, the curves overlapped with the curves where only media was contained. Interestingly, the curves after cell addition were similar to the curves where the cells were already included from the beginning. Thus, these results supported the hypothesis of cellular impact on fibril elongation and gelation given above. Nevertheless, compared to the sample without cells, it must be mentioned that in the case of eADF4(C16) and eADF4(C16)-RGE the addition of cells initially slowed down the fibril elongation (gelation), while it remained the same for eADF4(C16)-RGD. One assumption is that the addition of cells at the beginning of the exponential fibril growth phase initially effects a destruction of the already formed network of silk nuclei and fibrils. This event in turn effects a short-term deceleration of fibril elongation due to the reduced interaction of silk nuclei and soluble protein, which could be detected for eADF4(C16) and eADF4(C16)-RGE. In the case of eADF4(C16)-RGD, one assumption is that this destructive effect could be compensated by an interaction of the cells with the RGD peptide independent of whether the protein is soluble or assembled in fibrils, as it is mainly driven by an integrin–RGD interaction.

2.3. Rheological Properties of Spider Silk Based Bioinks

For the following analysis of the silk bioinks regarding rheological behavior, printability, and cell viability, the focus was on the composition of the bioinks, that is, the influence of medium and different cell densities on bioink performance. Therefore, in contrast to the kinetics analysis, here the mechanical properties of the spider silk matrix should be similar. As it was known from previous studies that eADF4(C16)-RGD forms stiffer hydrogels compared to eADF4(C16) at the same protein weight to volume ratio,[24] it was decided to use a concentration of 4% (w/v) for eADF4(C16) and 3% (w/v) for eADF4(C16)-RGD and eADF4(C16)-RGE to focus on the influence of the silk variant in combination with the amounts of cells introduced. Based on these concentrations, flow points and viscosities were determined (Figure 3B). Each hydrogel was analyzed upon addition of cell culture media and further upon increasing cell density (1, 5, and 10 million cells per milliliter). All three silk variant hydrogels showed an increase in viscosity upon the addition of media. While the comparable low flow point of eADF4(C16) hydrogels increased as well, the higher flow points of eADF4(C16)-RGD and eADF4(C16)-RGE ones dropped upon the addition of media. Both, viscosity and flow point of eADF4(C16) inks dropped significantly upon the addition of cells and increased again with increasing cell densities to values higher than initially measured for the acellular hydrogels. The effect of increasing amounts of cells was lower on the flow point and viscosity of inks made of the other two variant hydrogels. While there was an initial increase in both values for eADF4(C16)-RGD inks upon addition of the lowest cell density, the values stayed in the same regime with increasing cell densities (Figure 3B). Recovery experiments focused on stabilities of storage and loss modulus at low shear rate before and after high rotational shear stress (Appendix, Figure S1, Supporting Information). The trend to recover its properties of each ink/bioink was similar to the trend seen for the flow points (with better recovery at lower flow points). For eADF4(C16), the inks without additives, as well as the sample containing one million cells per milliliter showed good recovery. Bioinks with increasing cell densities displayed decreasing ability to recover both, storage and loss moduli. In the case of eADF4(C16)-RGD and eADF4(C16)-RGE, the recovery was significantly improved upon addition of media and cells compared to samples without additives (Appendix, Figure S1, Supporting Information). This direct correlation of higher flow points and lower recovery of inks confirmed the previous observation of unfavorable filament formation related to growing flow points, in the previous case due to temperature increase (see Figure 2B).

2.4. Extrusion Bioprinting of Spider Silk Based Bioinks

Printability of all bioinks was assessed using the filament collapse test (**Figure 4**A). In the case of all eADF4(C16) and eADF4(C16)-RGD based bioinks, rheological differences could be compensated by pressure adjustments. Each of these bioinks were able to bridge all gaps (up to 16 mm) with angles of deflection in the range of 0–0.4 rad, like that determined for 3% eADF4(C16) (Figure 1D). In contrast, for eADF4(C16)-RGE based bioinks, pressure adjustments were not sufficient, since the pressure needed for continuous filament printing resulted in faster extrusion, which could not be counteracted by the maximum speed rate (20 mm s^{-1}) of the used printer (RegenHU's 3D Discovery). Stereo microscopy images of single bridging filament strands showed the optical differences between printed hydrogels and hydrogels containing cell culture media (Figure 4B). While clear and smooth-looking filaments were printed using the hydrogels without additives, strands containing media, especially eADF4(C16) and eADF4(C16)-RGE based ones, appeared opaque, scratchy, and larger in diameter. However, these optical changes did not affect the performance during the filament collapse test (Figure 4A). During printing, the pressure was individually adjusted for optimal outcome and noted afterwards (Figure 4C). Interestingly, the applied pressure differed a lot (400–1400 mbar), but showed the same trend for bioinks made of all three protein variants.

2.5. Cell Viability after Extrusion Bioprinting

For biofabrication, cell survival during encapsulation, after the 3D bioprinting process, and during subsequent cultivation and

ADVANCED SCIENCE NEWS
www.advancedsciencenews.com

Macromolecular Bioscience
www.mbs-journal.de

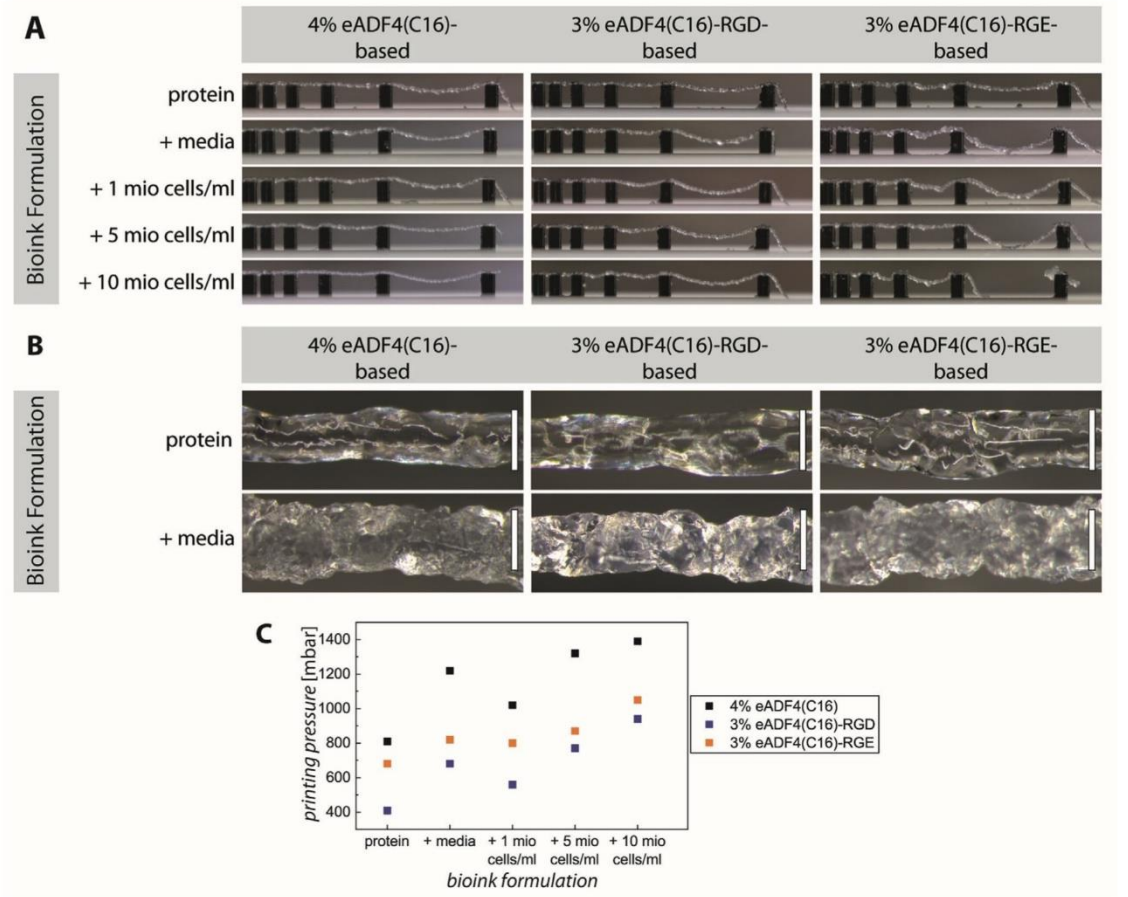

Figure 4. Shape fidelity of extrusion-printed spider silk bioinks. A) Using a 22G tapered tip, one strand of each bioink was printed (RegenHU's 3D Discovery) over a pillar structure; pictures were taken immediately after printing. B) Stereo microscopy images showed hanging strands between two pillars of plain spider silk hydrogels or hydrogels + media (scale bars: 200 µm). C) The printing pressure was manually adjusted for optimal filament extrusion.

maturation is essential. Therefore, live/dead staining directly after printing and after a cultivation time of 7 and 14 days was conducted for all bioinks (**Figure 5** and Figure S2, Supporting Information). Previous studies already showed that eADF4(C16) and eADF4(C16)-RGD hydrogels strongly interact with EthD-I resulting in a red-stained background signal, which is also visible in the here presented images.[24,26] The high cell survival on day 1 directly after 3D bioprinting using tapered needles (viability values for 10 mio cells per milliliter bioinks: 85% ± 1% for eADF4(C16), 83% ± 4% for eADF4(C16)-RGD, and 75% ± 4% for eADF4(C16)-RGE), indicated that the BxPC-3 cells survived on the one hand the encapsulation process using spider silk hydrogels and on the other hand the 3D bioprinting process. Furthermore, the cells were homogeneously distributed in all printed scaffolds without big cell clustering or aggregation. These results are highly important, as previous studies using a micro-valve printhead equipped with a steel needle (inner diameter 0.33 mm) showed cell death rates of up to ≈30%, mainly during the cell encapsulation process, leading to the development of an adopted encapsulation protocol (using more media [15%]) ensuring cell survival.[24,26] Here, the combination of the adjusted and improved encapsulation protocol with cell-friendly pneumatic extrusion using tapered needles was the basis for high cell survival.

Independent of the initial encapsulated cell number, BxPC-3 cells also displayed high cell viability on day 7, however, without increase in cell number. Particularly, the smaller size of viable cells in eADF4(C16)-RGE compared to that in eADF4(C16) and eADF4(C16)-RGD scaffolds should be mentioned. Moreover, BxPC-3 cells already began to die in eADF4(C16) and especially in eADF4(C16)-RGE scaffolds after 7 days as indicated by the enhanced numbers of dead cells. This trend continued to day 14, as a higher number of viable and larger BxPC-3 cells could be

ADVANCED SCIENCE NEWS
www.advancedsciencenews.com

Macromolecular Bioscience
www.mbs-journal.de

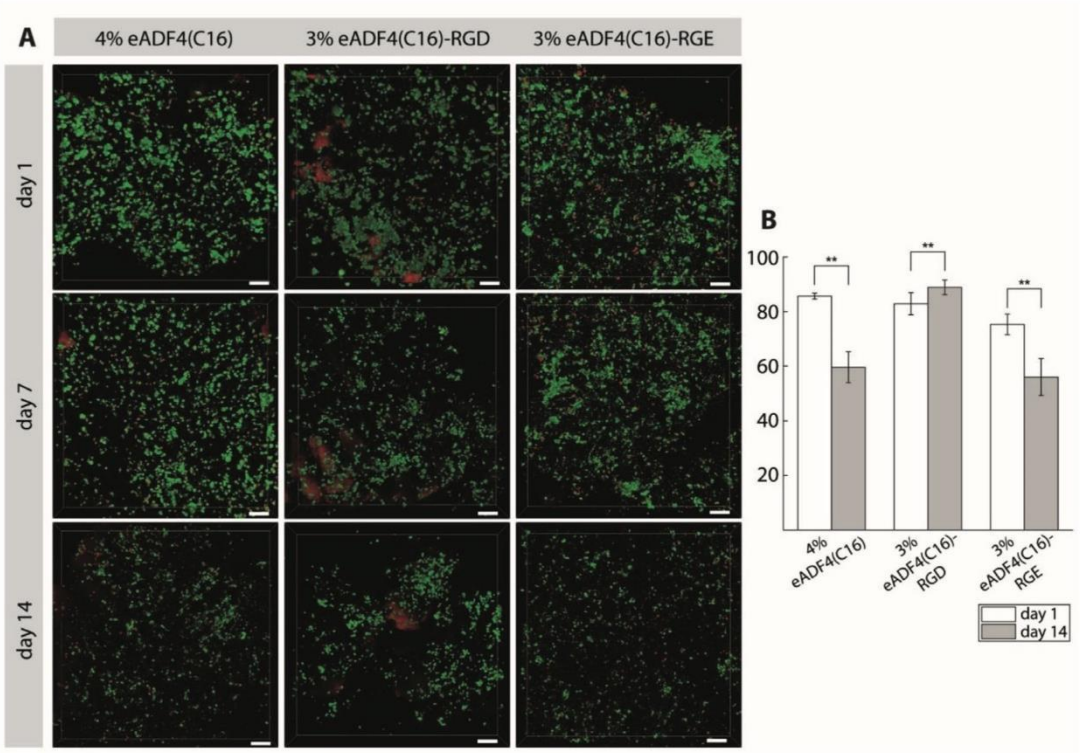

Figure 5. Viability of BxPC-3 cells (10 mio cells per milliliter) in printed constructs comprising 4% eADF4(C16), 3% eADF4(C16)-RGD, or 3% eADF4(C16)-RGE. Spider silk bioinks were printed using a RegenHU Bioplotter with a 22G tapered tip at room temperature and cultivated for up to 14 days at 5% CO2, 95% relative humidity, and 37 °C. A) For CLSM imaging, live cells were stained with Calcein A/M (green) and dead cells with EthD-I (red). Background staining occurs due to interaction of hydrogels with EthD-I (scale bars: 100 µm). B) Quantification of viable cells on day 1 and day 14 (**$p \leq 0.05$).

visualized in eADF4(C16)-RGD (viability: 89% ± 3%) scaffolds compared to eADF4(C16) (viability: 60% ± 6%) and eADF4(C16)-RGE (viability: 56% ± 7%) ones, although cell proliferation could yet not be determined. The lack of cell proliferation inside 3D bioprinted spider silk scaffolds was already shown by DeSimone et al.[26] Factors could be the slow biodegradation of the recombinant spider silk matrix or changed mechanical properties after the printing process coming from structural rearrangement during shear stress.[34–38] Additionally, by using 10 million cells per milliliter, it should be analyzed whether high cell densities have a positive effect on cell survival inside the bioinks. However, the present study showed that the used silk variant had a higher impact on the cell survivability than the initial number of encapsulated cells. As the amino acid sequence of eADF4(C16) lacks any cell binding motifs,[39] the decrease in cell viability over time is not surprising. In contrast, the high cell viability of BxPC-3 cells in eADF4(C16)-RGD scaffolds could be explained by the modification with the integrin binding peptide RGD, which was recognized by cell surface receptors triggering further cellular responses. A recent in vivo silk vascularization study showed that surgically induced angiogenesis, indicated by the formation and sprouting of new blood vessels from an arteriovenous loop, was clearly enhanced in implanted eADF4(C16)-RGD hydrogels compared to eADF4(C16) ones.[40] Thus, the RGD integrin binding tag is highly beneficial and necessary for successful tissue formation and growth. Nevertheless, an inadequate peptide tag, which could not interact with cell surface receptors due to steric hindrance, such as RGE, was counterproductive and led to a decreased cell interaction within the scaffold and finally cell death. It is known that RGD-resembling peptides, such as RGE, showed two to four magnitudes lower affinity to cell receptors.[32]

3. Conclusion

Extrusion based printing of recombinant spider silk bioinks, using tapered tips, reduces the shear stress on cells, resulting in increased cell viabilities. Our results showed that eADF4(C16) and eADF4(C16)-RGD proteins are suitable for the generation of hydrogel based bioinks with high cell densities that can be used in advanced extrusion bioprinting. Even though we saw an influence of different cell densities on rheological properties of the bioinks, we were able to adjust the procedures to accomplish reliable printing results for eADF4(C16) and eADF4(C16)-RGD based inks. For future studies, the application of different types of

ADVANCED SCIENCE NEWS
www.advancedsciencenews.com

Macromolecular Bioscience
www.mbs-journal.de

cells and the examination of biological functions of printed constructs have to be studied. Even though each new bioink composition is expected to require new adjustments, valuable general insights into gelation and the interplay between cell densities, used nozzle, and applied pressure to optimize printing outcome have been gained in this study. In summary, spider silk hydrogels in bioinks show high potential for biofabrication by combining the high biocompatibility of the hydrogels with their ability for gentle cell encapsulation and reliable extrusion printing of advanced structures without the need of additives or crosslinking procedures.

4. Experimental Section

Spider Silk Hydrogel Preparation: The recombinant spider silk protein eADF4(C16) (MW: 47.7 kDa) comprises 16 repeats of a so-called C-module (sequence: GSSAAAAAAAA SGPGGYGPENQGPSGPG-GYGPGGP) originating from the dragline silk of the European garden spider *A. diadematus*.[41] The modified variants eADF4(C16)-RGD (MW: 48.6 kDa) and eADF4(C16) RGE (MW: 48.6 kDa) were generated using genetic engineering.[19] While eADF4(C16)-RGD contains the integrin binding RGD sequence, the eADF4(C16)-RGE spider silk variant served as negative control. The recombinant spider silk proteins were generated as described previously.[19,41] For preparing hydrogels, the lyophilized spider silk proteins were solved in 6 M guanidinium thiocyanate (Roth, Germany) for 1 h at RT, sterile filtered (0.2 µm, Sartorius, Germany) and dialyzed against 10 mM Tris/HCl (Roth, Germany) using dialysis membranes with a molecular weight cutoff of 6–8 kDa (Spectra/Por, Fisher Scientific GmbH, Germany) as described previously.[18,24,26] A subsequent dialysis against 25% w/v poly-ethylene glycol (MW: 20000 g mol^{-1}, Roth, Germany) was conducted to increase protein concentrations using dialysis membranes with a molecular weight cutoff of 6-8 kDa. For subsequent experiments, protein concentrations between 30 and 50 mg mL^{-1} were achieved. In general, hydrogels self-assembled at 37 °C overnight.[18]

Cell Culture: The human BxPC-3 epithelial pancreas cell line (ATCC CRL-1687), derived from an adenocarcinoma, was cultivated in RPMI-1640 medium (Sigma, Germany) supplemented with 10% v/v fetal calf serum (FCS, Biosell, Germany), 1% v/v GlutaMAX (Gibco, USA), and 0.1% v/v gentamycin sulfate (Sigma-Aldrich, Germany) at 37 °C in a humidified incubator (95% relative humidity, 5% CO_2, Heracell, Germany). BxPC-3 cells were split using 0.25% trypsin/EDTA (Gibco, USA). Cell number and viability were determined using trypan blue (Sigma-Aldrich, Germany) and an automated cell counter (BioRad, Germany).

Preparation of Spider Silk Bioinks: To analyze the effect of cell culture medium as well as different cell densities, acellular hydrogel samples, and bioinks were generated at 40 (4% w/v) eADF4(C16) and 30 mg mL^{-1} (3% w/v) eADF4(C16)-RGD or eADF4(C16)-RGE. Therefore, either 47 (4.7% w/v) eADF4(C16) or 35 mg mL^{-1} (3.5% w/v) eADF4(C16)-RGD/eADF4(C16)-RGE solutions were diluted either with 15% v/v water or RPMI medium to obtain acellular hydrogels or with 15% v/v RPMI containing BxPC-3 cells to generate respective bioinks. The solutions were filled in 3cc cartridges with appropriate pistons (both Drifton, Denmark) and sealed using a luer-lock syringe plug (Braun, Germany). For gel formation, the cartridges were fixed on an overhead shaker (Intelli-Mixer RM-2, Germany) and incubated at 37 °C overnight while rotating at 3 rpm to ensure homogenous cell distribution and to prevent sedimentation.

Analysis of Gelation Kinetics: Hydrogel gelation kinetics of the different spider silk proteins were analyzed in the absence and presence of cells upon turbidity changes during nanofibril self-assembly at 570 nm. Therefore, 35 mg mL^{-1} (3.5% w/v) eADF4(C16), eADF4(C16)-RGD, and eADF4(C16)-RGE spider silk solutions were prepared using PEG dialysis as described above. For samples without cells, 15% v/v RPMI medium were added to reach a final protein concentration of 30 mg mL^{-1} (3% w/v). 100 µL triplicates of hydrogel solution were filled in transparent 96 well plates (Nunc, Germany) and incubated at 37 °C under a humidified atmosphere in a cell culture incubator (Heracell, Germany). The increase in turbidity indicating fibril formation was monitored at a wavelength of 570 nm using a microplate reader (Berthold, Germany) in absorbance mode. Furthermore, the impact of BxPC-3 cells, added either directly at the beginning of the gelation process or at the end of the protein-dependent lag phase, was analyzed. Therefore, BxPC 3 cells in 15% v/v RPMI were added with a concentration of one million cells per milliliter at measurement timepoint $t = 0$ min, and $t = 500$ min for eADF4(C16), $t = 100$ min for eADF4(C16)-RGD, or $t = 40$ min for eADF4(C16)-RGE.

Rheology of Spider Silk Bioinks: Rheological measurements were performed on a Discovery HR-2 rheometer (TA instruments, New Castle, DE, USA). Measurements were performed at 4, 25, or 37 °C as triplicates using a 25 mm plate-plate geometry with a gap of 200 µm. Viscosity was measured either at a constant shear rate of 10 s^{-1} or shear rate dependent from 0.01 to 100 s^{-1}. Storage (G′) and loss (G″) moduli were measured at a constant strain of 1.0% at increasing oscillatory frequencies from 0.1 to 100 rad s^{-1} or at a constant angular frequency of 10.0 rad s^{-1}, while increasing the strain from 0.01% to 1000.0%. Flow points were determined as the crossover of G′ and G″ using TRIOS software. Additionally, the samples were treated twice with a constant oscillatory strain of 0.1% for 100 s each. For 400 s in between, a steady increase of rotational shear rate up to 100 s^{-1} was applied. Recovery was recorded as stability of G′ and G″ at low strain before and after the higher shear rate.

4.0.0.1. 3D Printing the Shape of Human Aortic Valves: To demonstrate the printability of recombinant spider silk hydrogels, 3% w/v eADF4(C16) gels were printed in the size and shape of a human aortic valve (CAD-model from Cellink, Sweden). In this context, reproducibility was shown using two different models of extrusion bioprinters, BioX (Cellink, Sweden) and 3D Discovery Bioplotter (RegenHU, Villaz-Saint-Pierre, Switzerland). The stl-file was processed according to the printer's demands. For BioX, the respective G-code was generated on the device, while the 3D Discovery required an iso-file (RegenHU's G-code analogous), which was generated using the software MM Converter. For both printed constructs, the infill was set to 25% and the printing speed to 10 mm s^{-1}. Pneumatic printheads were equipped with a 3cc cartridge, pistons (both Drifton, Denmark), and a 27G (0.2 mm inner diameter) tapered tip (Cellink, Sweden). The printing pressure was set to exactly 400 mbar on the BioX and adjusted manually for optimal printing results on the 3D Discovery (400–420 mbar). In both cases, the constructs were printed on polystyrene surfaces (Sarstaedt, Germany) and imaged using a mirrorless camera and appropriate lenses (Sony Alpha 6000, SELP1650 and SEL30M35).

Filament Collapse Test: The ability of a hydrogel to bridge a certain distance and its degree of collapse can be assessed using the so-called filament collapse test, where a single strand of filament was extruded over a row of pillars with defined gaps in between. The angle of deformation caused by the weight of the filament can be used for quantification.[30] The template was slightly adjusted for more convenient handling. While pillar height, size, and distance remained the same (gaps in millimeter: 1, 2, 4, 8, and 16) as published previously,[30] features were added allowing for precise positioning at the origin of the print bed, like a base plate fitting tightly on the print plate. The pillar structure was printed using an Ultimaker S5 FDM (fused-deposition-modelling) and standard PLA (poly lactic acid) filaments (Ultimaker, Netherlands). During execution of each test, one single strand of spider silk hydrogel or bioink was extruded onto individual pillar constructs (printing speed 10 mm s^{-1}) using the 3D Discovery Bioplotter (RegenHU, Villaz-Saint-Pierre, Switzerland) equipped with a pneumatic printhead and a 22G tapered tip (Drifton, Denmark). Images of extruded strands on pillars were taken directly after printing using a mirrorless camera (Sony Alpha 6000, SELP1650) and a Leica M205C stereomicroscope, equipped with a 0.93× objective and a polarization lens in darkfield mode (Leica, Wetzlar, Germany). The angles of deflection were determined using the taken images and adobe illustrator software.

Live/Dead Staining: To visualize the viability of BxPC-3 cells inside the printed bioinks directly after printing (day 1) and after 7 and 14 days of cultivation, the 3D-printed spider silk scaffolds were stained using calcein acetoxymethyl ester (Calcein A/M) and ethidium homodimer I (EthD-I) (both Invitrogen, Thermo Fisher Scientific, Germany), respectively. Therefore, the printed constructs were incubated in 1× PBS containing final con-

centrations of 2 μM Calcein A/M and 4 μM EthD-I for 45–60 min at 37 °C in a humidified incubator containing 5% CO2 (Heracell, Germany). For subsequent imaging using confocal microscopy, the staining solution was exchanged with fresh 1× PBS. Z-stacks were recorded using a DMI 8 confocal microscope (Leica, Wetzlar, Germany) equipped with lasers using excitation wavelengths of 488 (Calcein A/M) and 552 nm (EthD-I). The viability rates of ten million cells per milliliter bioinks on day 1 and 14 were determined by quantifying live and dead cells from confocal images.

Statistical Analysis: To determine significance between generated data, one-way ANOVA with significance level of $p \leq 0.05$ were performed.

Supporting Information

Supporting Information is available from the Wiley Online Library or from the author.

Acknowledgements

A.L. and V.T.T. contributed equally to this work. The authors acknowledge the funding from the Deutsche Forschungsgemeinschaft (DFG, German Research Foundation)-project number 326998133-TRR225 (funded subproject: C01 TS) and SCHE603/24-1. Support from the Elite Network of Bavaria is also acknowledged.

Open access funding enabled and organized by Projekt DEAL.

Conflict of Interest

The authors declare the following competing financial interest: T.S. is cofounder and shareholder of AMSilk GmbH.

Data Availability Statement

The data that support the findings of this study are available from the corresponding author upon reasonable request.

Keywords

biofabrication, bioprinting, gelation kinetics, physical crosslinking, rheology

Received: September 27, 2021
Revised: November 19, 2021
Published online: December 19, 2021

[1] W. Sun, B. Starly, A. C. Daly, J. A. Burdick, J. Groll, G. Skeldon, W. Shu, Y. Sakai, M. Shinohara, M. Nishikawa, J. Jang, D.-W. Cho, M. Nie, S. Takeuchi, S. Ostrovidov, A. Khademhosseini, R. D. Kamm, V. Mironov, L. Moroni, I. T. Ozbolat, *Biofabrication* **2020**, *12*, 022002.
[2] L. Moroni, T. Boland, J. A. Burdick, C. De Maria, B. Derby, G. Forgacs, J. Groll, Q. Li, J. Malda, V. A. Mironov, C. Mota, M. Nakamura, W. Shu, S. Takeuchi, T. B. F. Woodfield, T. Xu, J. J. Yoo, G. Vozzi, *Trends Biotechnol.* **2018**, *36*, 384.
[3] J. Groll, T. Boland, T. Blunk, J. A. Burdick, D.-W. Cho, P. D. Dalton, B. Derby, G. Forgacs, Q. Li, V. A. Mironov, L. Moroni, M. Nakamura, W. Shu, S. Takeuchi, G. Vozzi, T. B. F. Woodfield, T. Xu, J. J. Yoo, J. Malda, *Biofabrication* **2016**, *8*, 013001.
[4] L. Moroni, J. A. Burdick, C. Highley, S. J. Lee, Y. Morimoto, S. Takeuchi, J. J. Yoo, *Nat. Rev. Mater.* **2018**, *3*, 21.
[5] A. Schwab, R. Levato, M. D'Este, S. Piluso, D. Eglin, J. Malda, *Chem. Rev.* **2020**, *120*, 11028.
[6] R. Levato, T. Jungst, R. G. Scheuring, T. Blunk, J. Groll, J. Malda, *Adv. Mater.* **2020**, *32*, 1906423.
[7] V. J. Neubauer, A. Döbl, T. Scheibel, *Materials* **2021**, *14*, 674.
[8] J. Li, C. Wu, P. K. Chu, M. Gelinsky, *Mater. Sci. Eng., R* **2020**, *140*, 100543.
[9] K. Hölzl, S. Lin, L. Tytgat, S. Van Vlierberghe, L. Gu, A. Ovsianikov, *Biofabrication* **2016**, *8*, 032002.
[10] T. G. Mezger, *The Rheology Handbook*, 4th ed., Vincentz Network, Hannover **2014**.
[11] N. Diamantides, C. Dugopolski, E. Blahut, S. Kennedy, L. J. Bonassar, *Biofabrication* **2019**, *11*, 045016.
[12] G. J. Gillispie, A. Han, M. Uzun-Per, J. Fisher, A. G. Mikos, M. K. K. Niazi, J. J. Yoo, S. J. Lee, A. Atala, *Tissue Eng., Part A* **2020**, *26*, 1349.
[13] M. R. Sommer, M. Schaffner, D. Carnelli, A. R. Studart, *ACS Appl. Mater. Interfaces* **2016**, *8*, 34677.
[14] Z. Zheng, J. Wu, M. Liu, H. Wang, C. Li, M. J. Rodriguez, G. Li, X. Wang, D. L. Kaplan, *Adv. Healthcare Mater.* **2018**, *7*, 1701026.
[15] W. Shi, M. Sun, X. Hu, B. Ren, J. Cheng, C. Li, X. Duan, X. Fu, J. Zhang, H. Chen, Y. Ao, *Adv. Mater.* **2017**, *29*, 1701089.
[16] S. Das, F. Pati, Y.-J. Choi, G. Rijal, J.-H. Shim, S. W. Kim, A. R. Ray, D.-W. Cho, S. Ghosh, *Acta Biomater.* **2015**, *11*, 233.
[17] S. Rammensee, D. Huemmerich, K. D. Hermanson, T. Scheibel, A. R. Bausch, *Appl. Phys. A* **2006**, *82*, 261.
[18] K. Schacht, T. Scheibel, *Biomacromolecules* **2011**, *12*, 2488.
[19] S. Wohlrab, S. Müller, A. Schmidt, S. Neubauer, H. Kessler, A. Leal-Egaña, T. Scheibel, *Biomaterials* **2012**, *33*, 6650.
[20] U. Slotta, S. Hess, K. Spieß, T. Stromer, L. Serpell, T. Scheibel, *Macromol. Biosci.* **2007**, *7*, 183.
[21] M. Humenik, M. Magdeburg, T. Scheibel, *J. Struct. Biol.* **2014**, *186*, 431.
[22] K. Spieß, S. Wohlrab, T. Scheibel, *Soft Matter* **2010**, *6*, 4168.
[23] C. B. Borkner, S. Lentz, M. Müller, A. Fery, T. Scheibel, *ACS Appl. Polym. Mater.* **2019**, *1*, 3366.
[24] K. Schacht, T. Jüngst, M. Schweinlin, A. Ewald, J. Groll, T. Scheibel, *Angew. Chem., Int. Ed.* **2015**, *54*, 2816.
[25] E. DeSimone, K. Schacht, T. Scheibel, *Mater. Lett.* **2016**, *183*, 101.
[26] E. DeSimone, K. Schacht, A. Pellert, T. Scheibel, *Biofabrication* **2017**, *9*, 044104.
[27] N. R. Raia, M. McGill, T. Marcet, S. E. V. Yucha, D. L. Kaplan, *2.6.8 – Soft Tissue Engineering* in *Biomaterials Science (Fourth Edition)* (Eds: W. R. Wagner, S. Sakiyama-Elbert, G. Zhang, M. Yaszemski), Academic Press, Cambridge **2020**, pp. 1399–1414.
[28] K. Schacht, T. Jüngst, M. Schweinlin, A. Ewald, J. Groll, T. Scheibel, *Angew. Chem., Int. Ed.* **2015**, *54*, 2816.
[29] S. Kumari, H. Bargel, M. U. Anby, D. Lafargue, T. Scheibel, *ACS Biomater. Sci. Eng.* **2018**, *4*, 1750.
[30] A. Ribeiro, M. M. Blokzijl, R. Levato, C. W. Visser, M. Castilho, W. E. Hennink, T. Vermonden, J. Malda, *Biofabrication* **2017**, *10*, 014102.
[31] M. Li, X. Tian, D. J. Schreyer, X. Chen, *Biotechnol. Prog.* **2011**, *27*, 1777.
[32] U. Hersel, C. Dahmen, H. Kessler, *Biomaterials* **2003**, *24*, 4385.
[33] M. Humenik, M. Drechsler, T. Scheibel, *Nano Lett.* **2014**, *14*, 3999.
[34] S. Müller-Herrmann, T. Scheibel, *ACS Biomater. Sci. Eng.* **2015**, *1*, 247.
[35] T. B. Aigner, E. DeSimone, T. Scheibel, *Adv. Mater.* **2018**, *30*, 1704636.
[36] S. Salehi, K. Koeck, T. Scheibel, *Molecules* **2020**, *25*, 737.
[37] D. Steiner, G. Lang, L. Fischer, S. Winkler, T. Fey, P. Greil, T. Scheibel, R. E. Horch, A. Arkudas, *Tissue Eng., Part A* **2019**, *25*, 1504.
[38] D. Pasqui, M. De Cagna, R. Barbucci, *Polymers* **2012**, *4*, 1517.
[39] A. Leal-Egaña, G. Lang, C. Mauerer, J. Wickinghoff, M. Weber, S. Geimer, T. Scheibel, *Adv. Eng. Mater.* **2012**, *14*, B67.
[40] D. Steiner, S. Winkler, S. Heltmann-Meyer, V. Trossmann, T. Fey, T. Scheibel, R. E. Horch, A. Arkudas, *Biofabrication* **2021**, *13*, 045003.
[41] D. Huemmerich, C. W. Helsen, S. Quedzuweit, J. Oschmann, R. Rudolph, T. Scheibel, *Biochemistry* **2004**, *43*, 13604.

Macromolecular Bioscience

Supporting Information

for *Macromol. Biosci.*, DOI 10.1002/mabi.202100390

Impact of Cell Loading of Recombinant Spider Silk Based Bioinks on Gelation and Printability

*Annika Lechner, Vanessa T. Trossmann and Thomas Scheibel**

WILEY-VCH

Supporting Information

Impact of Cell Loading of Spider Silk Based Bioinks on Gelation and Printability

*Annika Lechner, Vanessa T. Trossmann, and Thomas Scheibel**

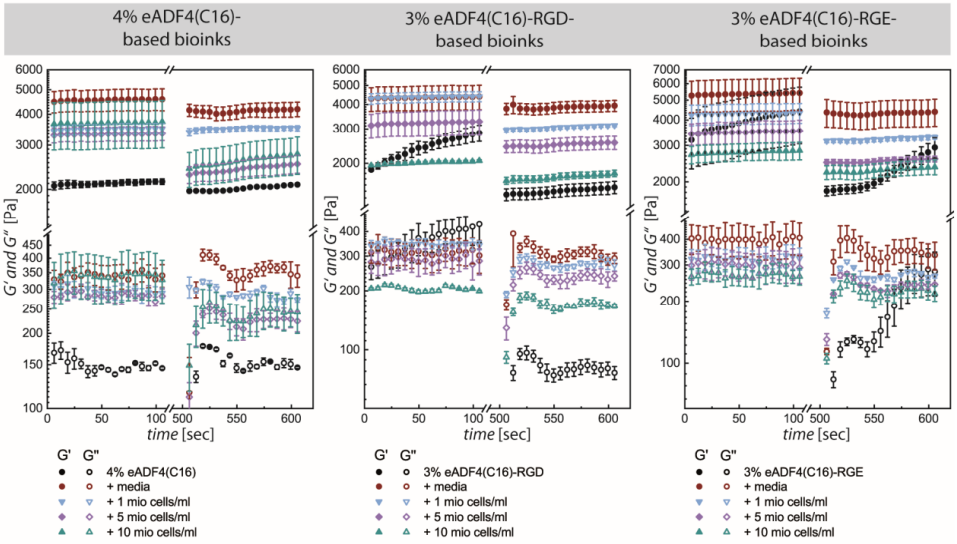

Figure S1. Storage (G') and loss (G'') moduli recovery of recombinant spider silk-based bioinks. Different bioink formulations of 4 % eADF4(C16), 3 % eADF4(C16)-RGD and 3 % eADF4(C16)-RGE + BxPC-3 cells (only protein, protein + 15 % (v/v) media, protein + 1 mio cells/ml, 5 mio cells/ml or 10 mio cells/ml in 15 % (v/v) media) were rheologically analyzed. Samples were treated twice with a constant oscillatory strain of 0.1% for 100 seconds each. For 400 seconds in between, a steady increase of rotational shear rate up to 100 s-1 was applied (data not shown). Recovery was recorded as stability of G' and G'' at low strain before and after high shear rates.

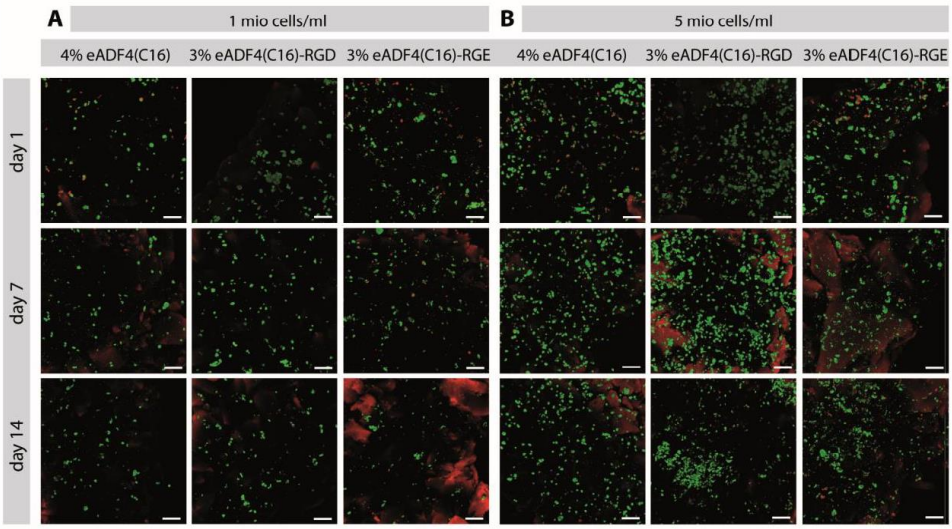

Figure S2. Viability of A) 1 mio cells/ml and B) 5 mio cells/ml BxPC-3 cells in printed constructs made of 4 % eADF4(C16), 3 % eADF4(C16)-RGD or 3 % eADF4(C16)-RGE. Bioinks were printed using a RegenHU Bioplotter with a 22G tapered tip at room temperature and cultivated for up to 14 days at 5 % CO2, 95 % relative humidity and 37 °C. For CLSM imaging, live cells were stained with Calcein A/M (green) and dead cells with EthD-I (red). Background staining occurs due to interaction of hydrogels with EthD-I (scale bars: 100 µm).

7.9. Teilarbeit IX

Teilarbeit IX wurde 2022 unter dem Titel „*Recombinant Spider Silk Bioinks for Continuous Protein Release by Encapsulated Producer Cells*“ im Journal *Biomacromolecules* veröffentlicht.

Trossmann, V. T.*; Heltmann-Meyer, S.*; Amouei, H; Wajant, H.; Horch, R. E.; Steiner, D.[§] & Scheibel, T.[§] (2022) Recombinant Spider Silk Bioinks for Continuous Protein Release by Encapsulated Producer Cells. *Biomacromolecules* **23**: 4427.

https://doi.org/10.1021/acs.biomac.2c00971

* gleichberechtigte Co-Autorenschaft

[§] gleichberechtigte korrespondierende Co-Autorenschaft

pubs.acs.org/Biomac Article

Recombinant Spider Silk Bioinks for Continuous Protein Release by Encapsulated Producer Cells

Vanessa T. Trossmann,[‡] Stefanie Heltmann-Meyer,[‡] Hanna Amouei, Harald Wajant, Raymund E. Horch, Dominik Steiner,* and Thomas Scheibel*

Cite This: *Biomacromolecules* 2022, 23, 4427−4437 Read Online

ACCESS | Metrics & More | Article Recommendations | Supporting Information

ABSTRACT: Targeted therapies using biopharmaceuticals are of growing clinical importance in disease treatment. Currently, there are several limitations of protein-based therapeutics (biologicals), including suboptimal biodistribution, lack of stability, and systemic side effects. A promising approach to overcoming these limitations could be a therapeutic cell-loaded 3D construct consisting of a suitable matrix component that harbors producer cells continuously secreting the biological of interest. Here, the recombinant spider silk proteins eADF4(C16), eADF4(C16)-RGD, and eADF4(C16)-RGE have been processed together with HEK293 producer cells stably secreting the highly traceable reporter biological TNFR2-Fc-GpL, a fusion protein consisting of the extracellular domain of TNFR2, the Fc domain of human IgG1, and the luciferase of *Gaussia princeps* as a reporter domain. eADF4(C16) and eADF4(C16)-RGD hydrogels provide structural and mechanical support, promote HEK293 cell growth, and allow fusion protein production by the latter. Bioink-captured HEK293 producer cells continuously release functional TNFR2-Fc-GpL over 14 days. Thus, the combination of biocompatible, printable spider silk bioinks with drug-producing cells is promising for generating implantable 3D constructs for continuous targeted therapy.

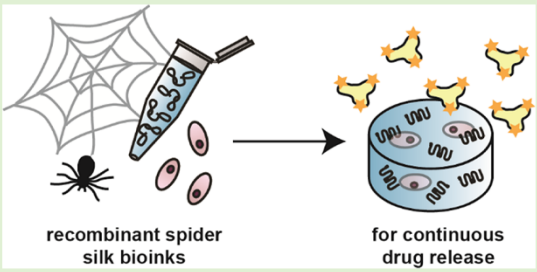

INTRODUCTION

Targeted therapies using different biologicals for the treatment of cancer or autoimmune diseases are of high relevance and are attracting increasing attention in biomedical research.[1] In this context, therapeutically relevant recombinant fusion proteins have been developed, which contain complete or parts of antibodies (e.g., immunotoxins), cytokines, or cell receptor targeting, for instance, interleukins (IL) or the tumor necrosis factor (TNF).[2] TNF is a highly pro-inflammatory cytokine. A fusion protein of the ectodomain of TNF receptor-2 (TNFR2) and the human IgG1 Fc domain (Enbrel/Eternacept) blocking and neutralizing TNF has been approved for the treatment of rheumatoid diseases and psoriasis.[3]

There are various limitations in the broad medical application of a subset of protein-based therapeutics, including low pharmacokinetics, aggregation, lack of stability to enzymatic degradation and hydrolysis, suboptimal biodistribution, and limited permeability across biological barriers. Additionally, due to the short serum half-life of many biologicals, applying these substances requires frequent injections or infusions, which limits efficacy, increases costs, worsens patient compliance, leads to side effects, and risks follow-up infections.[1f,2a,g,4] Chemical and genetic modification of biologicals, their direct or particle-loaded encapsulation in hydrogels, or gene-based therapy (in vivo gene transfer) for therapeutic drug delivery is a current solution to overcome these problems.[1f,2a,g,4d,5]

Further promising approaches to overcome the limitations discussed above could be the matrix-free injection of drug-producing cells (combination of gene and cell therapy)[6] or the implantation of matrix-encapsulated cells directly in the target tissue.[7] In general, it must be distinguished between temporary applications, where only short-living, non-reproducible producer cells are injected locally,[6] and matrix-based cell delivery applications such as cell-containing capsules or other 3D constructs.[7] In the latter case, matrix-encapsulated, proliferating producer cells should be injected or implanted locally for long-term production of a biological directly at the target tissue of interest.[7] In this concept, an appropriate pre-vascularization is helpful for clinical translation to maintain sufficient vascularity of any therapeutic constructs.[8] Furthermore, another crucial factor for therapeutic protein delivery is the

Received: August 4, 2022
Revised: August 18, 2022
Published: September 6, 2022

https://doi.org/10.1021/acs.biomac.2c00971
Biomacromolecules 2022, 23, 4427−4437

used cell type, as stable protein expression, successful scale-up, and long-term production should be guaranteed.[6,9]

Nowadays, many protein-based therapeutic targets (antibodies, fusion proteins, cytokines) are synthesized in mammalian and even human cells, which typically enable high product quality and have the potential to express large and complex biopharmaceuticals.[2e,6,9b,c,10] Especially, for human-derived producer cells, additional advantages ensuring advanced protein folding, secretion, and post-translational modifications are guaranteed as well as minimizing the risk of immunogenic reaction.[2e,6,9b,10a] In this context, human embryonal kidney (HEK) cells, in most cases the HEK293 cell line, are used as a recombinant expression system for the generation of human-like protein therapeutics (for instance, fusion proteins, antibodies, and growth factors (GFs)).[2a,b,d,e,h,6,9b,10a] The HEK293 cell line combines a variety of the before-mentioned advantages, including an efficient transfection system leading to a stable protein expression with high yields as well as the generation of post-translationally modified and glycosylated therapeutic products with reduced immunogenic responses.[2e,6,9b,10a] The identification of a suitable carrier matrix for genetically modified cells producing a biological of interest is one major challenge for such a therapeutic transplant. This matrix should be biocompatible and support the release of the biological into the host organism. To mimic the extracellular matrix for the 3D cell culture, hydrogel-based systems, derived from natural biopolymers including collagens, fibrin, alginate, or silk proteins, or synthetic polymers, such as polyethylene glycol or polylactic acid, have been commonly used, especially due to their possible usage for 3D printing processes.[11]

Recombinant spider silk proteins, based on the dragline silk of the European garden spider *Araneus diadematus*, are desirable and suitable candidates to produce such matrix materials due to the easy processing capabilities for different morphologies including hydrogels for 3D printing together with the low inflammatory response and biodegradability of the materials.[12] The recombinant spider silk variant eADF4(C16) consists of 16 repeats of the so-called C-module, inspired by the repetitive core domain of the natural *Araneus diadematus* fibroin 4,[13] and was genetically modified with the integrin-binding peptide RGD improving the interaction with cells and with the integrin-binding inactive RGE as a control.[14] As eADF4(C16)-based proteins could be processed into physically cross-linked, nano-fibrillar hydrogels without the need of additional cross-linking agents,[15] encapsulation and cultivation of cells inside these gels is possible.[16] Additionally, due to their viscoelastic properties and shear-thinning behavior, 3D bioprinting of acellular hydrogels and bioinks made of spider silk proteins together with cells could be conducted.[16,17] Furthermore, it has been previously shown that different biologicals and drugs could be encapsulated inside and released from recombinant spider silk hydrogels with their activity maintained.[17,18]

In the present study, the beneficial properties of spider silk proteins were exploited to develop a HEK293 producer cell containing spider silk scaffold for the long-term production and release of a highly traceable reporter biological (TNRF2-Fc-GpL) consisting of the ectodomain of TNFR2, the human IgG1 Fc domain, and a *Gaussia princeps* luciferase domain (GpL). HEK293 cell viability, production, release, and activity of the reporter biological were analyzed over a time span of 14 days in 3D bioinks to check the suitability of eADF4(C16)-, eADF4(C16)-RGD-, and eADF4(C16)-RGE-based matrix materials. Finally, as proof of concept for future biofabrication applications, 3D bioprinting was conducted to display high cell survival of encapsulated HEK293 producer cells.

MATERIALS AND METHODS

Production of Recombinant Spider Silk Proteins. The recombinant spider silk protein eADF4(C16) is based on the repetitive consensus sequence of *Araneus diadematus* fibroin 4 (ADF4) of the dragline silk of the European garden spider. For a recombinant production in bacteria, the consensus motive, also called C-module (sequence: GSSAAAAAAAASGPGGYGPENQGPSGPG-GYGP GGP), has been repeated 16 times in one construct.[13] The recombinant spider silk protein eADF4(C16) (MW: 47.7 kDa) was purchased from AMSilk GmbH (Planegg, Germany). The genetically modified spider silk proteins eADF4(C16)-RGD (MW: 48.6 kDa) and eADF4(C16)-RGE (MW: 48.6 kDa) were produced in *E. coli* (BL21 gold (DE3)) upon fed-batch fermentation and purified as described previously using a heating step and ammonium sulfate precipitation.[13,14] eADF4(C16)-RGD contains the cell interaction peptide RGD, while eADF4(C16)-RGE serves as a cell non-binding control. Correct protein synthesis was confirmed using polyacrylamide gel electrophoresis, western blot analysis, and matrix-assisted laser desorption time-of-flight mass spectrometry as described previously.[13,14] All proteins were stored as a lyophilized powder.

Preparation of Spider Silk Hydrogels. For the preparation of spider silk hydrogels, lyophilized spider silk proteins eADF4(C16), eADF4(C16)-RGD, and eADF4(C16)-RGE were dissolved in 6 M guanidinium thiocyanate (Roth, Germany) at a concentration of 20 mg mL^{-1} (1 h, RT) as described previously.[15] The silk solutions were sterile filtered (0.2 μm, Sartorius, Germany) and dialyzed against 10 mM Tris/HCl (Roth, Germany) using dialysis membranes with a molecular weight cutoff of 6−8 kDa (Spectra/Por, Thermo Fisher Scientific GmbH, Germany). Subsequent dialysis against 25% (w/v) polyethylene glycol (PEG, MW: 20000 g mol^{-1}, Roth, Germany) was conducted to increase the protein concentration to 35 mg mL^{-1} by removal of aqueous buffer using the same membranes with a molecular weight cutoff of 6−8 kDa. Protein concentration was determined using a NanoDrop photo spectrometer (PeqLab, VWR, Germany). Over time, spider silk proteins self-assembled into a nano-fibrillar network, forming stable hydrogels by physical interactions.[15]

Transmission Electron Microscopy of Spider Silk Nano-Fibrils. Transmission electron microscopy (TEM) was conducted as described previously to analyze the nano-fibrillar network of the spider silk hydrogels.[16b,19] Therefore, spider silk hydrogels were dissolved in water at a concentration of around 1 mg mL^{-1}. A total of 5 μL of the appropriate spider silk nano-fibrils were pipetted on a pioloform-coated 100-mesh copper TEM grid (Plano GmbH, Germany) and incubated for 5 min at RT. After washing the grid two times with water, the spider silk nano-fibrils were counterstained for 2 min using 2% uranyl acetate solution. The grids were washed once again using water and air-dried in the dark for at least 12 h at RT before imaging. TEM imaging was conducted using a JEM-2100 transmission electron microscope (JEOL, Japan) operating at 80 kV and equipped with a 4000 × 4000 charge-coupled device camera (UltraScan 4000, Gatan, Pleasanton, CA).

Structural Analysis of Spider Silk Hydrogels. Fourier-transform infrared (FTIR) spectroscopy was conducted using a Bruker Tensor 27 FTIR-spectrometer (Bruker, Germany) to analyze the secondary structure content of the spider silk hydrogels. The device was equipped with a mercury cadmium telluride (MCT) detector, a coupled Hyperion 1000 FTIR microscope, and an attenuated total reflection (ATR) lens (20×) (Bruker, Germany). For FTIR measurements, the spider silk hydrogels were frozen in liquid nitrogen and lyophilized. Freeze-dried scaffolds were analyzed on a germanium crystal in ATR mode. The FTIR spectra were recorded in the wavenumber range of 4000 to 800 cm^{-1} in reflectance mode using a spectral resolution of 4 cm^{-1}. In total, 100 scans were recorded for each spectrum. Background spectra with atmospheric compensation

https://doi.org/10.1021/acs.biomac.2c00971
Biomacromolecules 2022, 23, 4427−4437

were recorded using the OPUS 8.0 software and used to correct each spectrum for water- and carbon dioxide-derived signals during the measurement. Furthermore, a Fourier-self-deconvolution (FSD) of the region between 1700 and 1500 cm^{-1} (amide *I* band) was conducted to determine the secondary structure content and β-sheet formation as described previously.[20]

Scanning Electron Microscopy of Spider Silk Hydrogels. Freeze-dried spider silk scaffolds were analyzed by scanning electron microscopy (SEM) to characterize the porous microstructure of the hydrogels as described previously.[15,18] Therefore, lyophilized scaffolds were fixed on SEM stubs (Plano GmbH, Germany) using Leit-C (conductive carbon cement, Plano GmbH, Germany) and aluminum tape. The samples were sputter-coated with a 2 nm platinum layer using a Leica EM ACE 600 sputter coater (Leica, Germany). SEM was conducted on a Thermo Scientific (FEI) Apreo VS device equipped with a field emission gun and an SE2-detector operating at 2 kV (Thermo Scientific, Germany).

Generation of TNFR2-Fc-GpL Producer Cells and Analysis of the GpL Reporter Domain Activity. A scheme of TNFR2-Fc-GpL and its amino acid (aa) sequence are shown in Figure S1. A DNA cassette encoding the extracellular domain of TNFR2 (aa 1-257, accession number NP_001057.1) followed by the human IgG1 Fc domain (aa 251-476, accession number AAA02914.1), a Flag tag (DYKDDDDK), and the *Gaussia princeps* luciferase without its leader sequence (aa 18−185, accession number AAG54095) was obtained by gene synthesis and PCR and inserted in the multi-cloning site of a pCR3 plasmid (Invitrogen, Germany). For generating stable HEK293 transfectants expressing TNFR2-Fc-GpL, HEK293 cells (ATCC CRL-1573) were cultivated in a 15 cm tissue culture dish until confluency. The medium was exchanged to transfection medium. A total of 36 μL of poly-ethylenimine solution (PEI, 1 mg ml^{-1}, Polyscience Inc., USA) was added dropwise with continuous vortexing to 15 mL of serum-free RPMI 1640 medium (Sigma-Aldrich, Germany) supplemented with penicillin−streptomycin (Pen/Strep, Sigma-Aldrich, Germany) and 12 μg of a pCR3-based TNFR2-Fc-GpL encoding expression plasmid to prepare the transfection medium. After incubation for 15 min at room temperature, the DNA/PEI-containing transfection medium was transferred to the HEK293 cells. After overnight incubation, the transfection medium was replaced with RPMI 1640 medium supplemented with 5% (v/v) fetal calf serum (FCS, Gibco, USA). After an additional day, the medium was removed and replaced with RPMI 1640 medium supplemented with 10% (v/v) FCS and 500 μg mL^{-1} geneticin G418 (Gibco, USA) for selecting stably transfected HEK293 cells. After 2 to 3 weeks, single colonies were generated by limiting dilution and assayed for the production of TNFR2-Fc-GpL. TNFR2-Fc-GpL was purified using its internal Flag tag (Figure S1A,B) from cell culture supernatants by affinity chromatography on anti-Flag M2 agarose (Sigma-Aldrich, Germany) according to the manufacturer's recommendations. Therefore, an anti-Flag M2 agarose column (bed volume 1.5 mL) was loaded with a volume of supernatant containing approximately 1.5 mg TNFR2-Fc-GpL by gravity flow and washed with 10−15 mL TBS (tris-buffered saline) buffer. Finally, the bound TNFR2-Fc-GpL was eluted with 10 × 1 mL PBS (phosphate-buffered saline, Sigma-Aldrich, Germany) supplemented with 100 μg/mL Flag peptide. The eluted TNFR2-Fc-GpL was dialyzed against PBS to reduce/remove the Flag peptide. Purity of TNFR2-Fc-GpL was determined using SDS-PAGE, and the visualization of the protein was determined by silver staining (silver staining kit, Thermo Scientific, Rockford, USA). TNFR2-Fc-GpL was co-analyzed with the "Low Molecular Weight Calibration Kit for SDS Electrophoresis" (GE Healthcare UK Limited, Little Chalfont, UK) containing defined amounts of α-lactalbumin, trypsin inhibitor, carbonic anhydrase, ovalbumin, albumin, and phosphorylase-b (Figure S1C).

Cell Culture. HEK293 producer cells were cultured in RPMI 1640 medium (Sigma-Aldrich, Germany) supplemented with 10% (v/v) FCS (BioSell, Germany) and 1% (v/v) Pen/Strep (Gibco, USA) under humidified conditions and 5% CO_2 in a cell culture incubator (Heracell, Thermo Fisher Scientific, Germany) at 37 °C. Sub-culturing of cells was conducted using either accutase (Sigma-Aldrich, Germany) or 0.05% trypsin/EDTA (Gibco, USA). Cells were centrifuged (1200 rpm, 5 min, RT) and resuspended in RPMI 1640 medium. Cell numbers were determined using trypan blue (Sigma-Aldrich, Germany) and an automated cell counter (BioRAD, Germany) or a hemocytometer. The human HeLa epithelial cervix carcinoma cell line was cultivated in RPMI 1640 medium (Sigma-Aldrich, Germany) supplemented with 10% (v/v) FCS (Gibco, USA) and 1% (v/v) Pen/Strep under humidified conditions (5% CO_2, 37 °C) in a cell culture incubator (Heracell, Thermo Fisher Scientific, Germany). Sub-culturing of cells was conducted using 1% trypsin/EDTA (Sigma-Aldrich, Germany). HeLa cells were centrifuged (1200 rpm, 4 min, RT). Cell numbers were determined using trypan blue and a hemocytometer under the microscope before seeding on cell culture plates for further experiments.

Spider Silk Bioink Preparation. Appropriate pre-gelled 3.5% (w/v) spider silk solutions (35 mg ml^{-1}) were mixed with 15% (v/v) RPMI 1640 containing the HEK293 producer cells to reach a final cell density of 5 × 10^6 HEK293 cells per ml to prepare 3% (w/v) spider silk bioinks (30 mg ml^{-1}). This previously developed bioink preparation protocol containing cell culture media was used to ensure high cell viability after the encapsulation process.[16b] Furthermore, 3% (w/v) spider silk hydrogels and bioinks were characterized regarding their gelation behavior in the presence and absence of cells and cell culture media, the diffusion of nutrients and waste products, and their suitability for 3D bioprinting applications.[16,19] Acellular hydrogels containing only RPMI 1640 media served as controls. For 3D cell culture analysis, 100 μL of the respective bioink formulations were filled in 96 well plates (Nunc, Thermo Fisher Scientific, Germany). The samples were incubated at 37 °C to induce hydrogel formation by physical interactions. After 4 h, each hydrogel was overlayed with 100 μL of RPMI 1640 medium. For rheological analysis, acellular hydrogel solutions as well as bioinks were filled into 1 mL syringes (Braun GmbH, Germany) and closed properly. For 3D printing, the respective bioink solutions were filled into 3 cc cartridges (Drifton, Denmark) with associated pistons (Drifton, Denmark), which were sealed using Luer-lock plugs (Braun, Germany). For hydrogel formation, the syringes for rheology and the cartridges for 3D printing were fixed on a rotating shaker (Intelli-Mixer RM-2, Germany) with a rotation speed of 3 rpm, enabling even cell distribution without cell sedimentation in the final bioink, and incubated overnight at 37 °C.

Cell Viability Assay. The metabolic activity of encapsulated cells was measured using the Colorimetric Cell Viability Kit I (WST-8, PromoCell, Germany) according to the manufacturer's protocol after culturing for 1, 3, 7, 10, and 14 days to characterize the viability and proliferation of HEK293 cells in respective 3D silk bioinks. Briefly, 10% (v/v) of the WST-8 solution was added to the cell culture medium and incubated for 2 h at 37 °C. A total of 100 μL of the supernatant was transferred into a black 96-well plate (Greiner Bio-One, Austria), and the absorbance was measured at 450 nm using a microplate reader (Thermo Fisher Scientific, USA).

Protein Release of the TNFR2-Fc-GpL Fusion Protein from Spider Silk Hydrogels and Bioinks. First, TNFR2-Fc-GpL diffusion through and its release from the different, acellular silk hydrogels were analyzed upon adding purified TNFR2-Fc-GpL at a concentration of 1 μg mL^{-1} to the respective silk solution prior to gelation in the absence of cells. A total of 100 μL aliquots of the appropriate formulation was filled in 96 well plates (Nunc, Thermo Fisher Scientific, Germany) and incubated in a humidified atmosphere at 37 °C to induce hydrogel formation. After 4 h, 100 μL of RPMI 1640 cell culture medium was added on top. Furthermore, the TNFR2-Fc-GpL production of encapsulated HEK293 cells in 3D culture and its release from the respective bioinks was characterized. The release of the TNFR2-Fc-GpL from the different acellular spider silk hydrogels as well as the respective bioink formulations was determined by measuring the GpL luciferase activity of TNFR2-Fc-GpL in the supernatant after 1, 3, 7, 10, and 14 days. Therefore, 5 μL of the respective cell culture media supernatants were diluted with 45 μL of fresh medium (RPMI-1640, 0.5% (v/v) FCS and 1% (v/v) Pen/Strep) and transferred to a black 96-well plate (Greiner Bio-One,

https://doi.org/10.1021/acs.biomac.2c00971
Biomacromolecules 2022, 23, 4427−4437

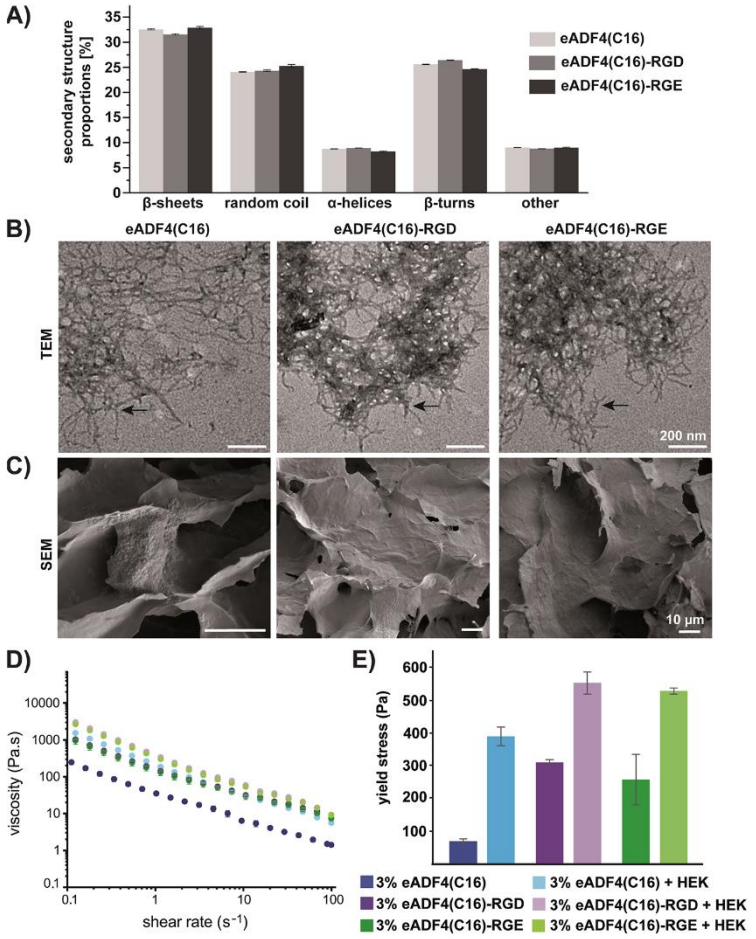

Figure 1. Structural, morphological, and rheological characterization of 3% w/v eADF4(C16), eADF4(C16)-RGD, and eADF4(C16)-RGE spider silk hydrogels: (A) secondary structure proportions of spider silk hydrogels were analyzed using ATR-FTIR-spectroscopy followed by Fourier self-deconvolution (FSD) of the amide I band. (B) TEM images of the self-assembled nano-fibrillary hydrogel networks. Black arrows highlight nano-fibrils. Scale bars: 200 nm. (C) SEM images of freeze-dried spider silk hydrogels. Scale bars: 10 μm. (D) Shear-rate-dependent viscosity of different silk hydrogels in the absence and presence (i.e., bioinks) of HEK293 producer cells during increasing rotational shear rate from 0.01 to 100 s^{-1}. (E) Yield stress of different spider silk hydrogels and bioinks determined from the crossover of storage (G') and loss (G'') moduli. The bioinks contained 5 × 10^6 HEK293 producer cells per mL of silk hydrogel.

Austria). Directly before the measurement, 25 μL of 1.5 μM coelenterazine (Roth, Germany) was added, and the relative light units (RLU) were measured using a luminometer microplate reader (Berthold Technologies, Germany).

Rheology of Spider Silk Hydrogels and Bioinks. Acellular hydrogels and bioinks made of 3% w/v eADF4(C16), eADF4(C16)-RGD, and eADF4(C16)-RGE were analyzed using a Discovery HR-2 rheometer and the TRIOS software (TA instruments, DE, USA) to determine rheological characteristics and the influence of encapsulated cells on bioink mechanics. A total of 200 μL of acellular hydrogel or bioink was measured in triplicates (n = 3) using a 25 mm parallel plate−plate geometry with a gap of 150 μm at 25 °C. Furthermore, a solvent trap with an incorporated wet sponge was used to minimize the evaporation of water from the hydrogels during the measurements. The viscosity of the samples was determined in dependency of the shear rate, which was increased from 0.01 to 100 s^{-1}. Storage (G') and loss (G'') moduli were determined using a frequency sweep with a constant strain of 1% and an increasing angular frequency from 0.1 to 100 rad s^{-1} and an amplitude sweep with constant angular frequency of 10 rad s^{-1} and an increasing strain from 0.01 to 1000%. The appropriate flow points indicated by the yield stress at the crossover of G' and G'' were determined using the TRIOS software. Furthermore, the recovery of the hydrogels and bioinks was determined by measuring the stability of G' and G'' via a time sweep measurement over a time span of 100 s at a low constant strain of 0.1% and angular frequency of 10 rad s^{-1} before and after a flow ramp measurement. This flow ramp measurement was conducted for 500 s with an increased shear rate from 0.001 to 100 s^{-1}.

3D Extrusion Bioprinting of Spider Silk Bioinks and Stereomicroscopy. A single-layered grid structure was printed using a RegenHU 3D Discovery (RegenHU, Switzerland) equipped with a pneumatic printhead to demonstrate that 3% w/v spider silk bioinks could be 3D bioprinted. The underlying G-code was generated using the associated BioCAD software for scaffold design (RegenHU, Switzerland). For 3D printing, the pneumatic printhead was equipped with the bioink-containing 3 cc cartridges and a 22G

https://doi.org/10.1021/acs.biomac.2c00971
Biomacromolecules 2022, 23, 4427−4437

tapered dispensing tip (0.41 mm inner diameter, Drifton, Denmark). The printing speed was set to 10 mm s^{-1}. To obtain optimal results, the printing pressure was adjusted to around 1 bar for each bioink formulation individually. The scaffold was printed on glass slides (Thermo, Germany) for subsequent stereomicroscopic analysis, while for live/dead staining, μ-well chambers (Ibidi GmbH, Germany) were used. Stereomicroscopic images were conducted in the darkfield mode on a Leica M205C stereomicroscope, equipped with a 0.93× objective and a polarization lens (Leica, Germany).

Live/Dead Staining and Confocal Laser Scanning Microscopy. Live/dead staining assessed cell viability and apoptosis of HEK293 cells inside the different bioinks. Therefore, punched cuts of the 100 μL cell-loaded silk bioinks were stained using calcein acetoxymethyl ester (Calcein A/M) for living cells and ethidium homodimer-I (EthD-I) (both Invitrogen, Thermo Fisher Scientific, Germany) for dead cells after culturing for 1, 7, and 14 days. Additionally, 3D bioprinted bioinks were stained directly after printing. All constructs were stained with 2 μM Calcein A/M and 4 μM EthD-I in 1x PBS for 45−60 min in a humidified atmosphere (95% relative humidity, 5% CO_2, 37 °C). Before imaging using confocal laser scanning microscopy, the staining solution was exchanged using fresh 1× PBS. Live and dead stained HEK293 cells inside the bioinks were visualized upon recording z-stacks on a DMi-8 confocal fluorescence microscope (Leica, Germany) equipped with lasers with excitation wavelengths of 488 and 552 nm. The fluorescence emission was detected between 505 and 525 nm for Calcein A/M and between 580 and 605 nm for EthD-I.

TNFR2-Fc-GpL Concentration Determination by Western Blot Analysis. Concentration of TNFR2-Fc-GpL was estimated by anti-human IgG1 western blotting in comparison with TNFR2-Fc (Enbrel/Eternacept, Pfizer, Germany) of known concentration (or alternatively in comparison with a GpL fusion protein of known concentration) and subsequent comparison of band intensities. Subsequently, the purified TNFR2-Fc-GpL was used as a standard to determine concentrations of TNFR2-Fc-GpL in cell culture supernatants and bioinks. For western blot analysis, TNFR2-Fc-GpL containing supernatants were mixed with 4× Laemmli buffer supplemented with phosphatase inhibitor mixture II (Sigma-Aldrich, Germany) and boiled at 95 °C for 5 min. Subsequent sodium dodecyl sulfate-polyacrylamide gel electrophoresis and western blotting were conducted as described previously.[21]

TNF Neutralization Assay. A TNF neutralization assay was conducted to check the functionality of TNFR2-Fc-GpL. Therefore, HeLa cells, which respond to TNF stimulation with Interleukin-8 (IL8) production, were seeded in RPMI 1640 medium with 10% (v/v) FCS in a 96-well plate (20×10^3 cells per well). The next day, cells were stimulated in duplicates with mixtures of 10 ng mL^{-1} TNF and increasing concentrations of TNFR2-Fc-GpL (100 and 900 ng mL^{-1}) obtained from supernatants of bioink-encapsulated HEK293 producer cells. Recombinant, soluble TNF was a kind gift of Prof. Daniela Männel (University of Regensburg) and was originally produced by Knoll AG (Germany). Purified TNFR2-Fc-GpL served as control. After an additional day, the HeLa cell culture supernatants were analyzed for their IL8 content using an enzyme-linked immunosorbent assay (ELISA) according to the instructions of the supplier (BD Biosciences, San Diego, USA).

Statistical Analysis. The statistical analysis was performed with GraphPad Prism 8.00 (GraphPad Software, San Diego, California, USA). Standard distribution was calculated with a Shapiro−Wilk test. Analysis of variance was performed (nonparametrical) in the form of a one-way-ANOVA with a Tukey test (parametrical) or a Kruskal−Wallis test with a post hoc analysis (Dunn's). Results are depicted as mean values ± standard deviation. p-Values ≤0.05 are considered statistically significant.

RESULTS AND DISCUSSION

In order to establish 3D printable spider silk bioinks containing transfected HEK293 cells continuously producing TNFR2-Fc-GpL as a model protein, the bioinks were investigated concerning the influence of variations in the spider silk protein sequence on metabolism and proliferation of the HEK293 cells and production of TNFR2-Fc-GpL. In addition to 3% (w/v) eADF4(C16) hydrogels, two variants were analyzed containing either an integrin-binding peptide RGD for better cell interaction or an RGE peptide as a cell non-binding control. Although eADF4(C16)-RGD and eADF4(C16)-RGE differ only in one amino acid (i.e., in eADF4(C16)-RGE, the aspartic acid residue(D) is changed to a glutamic acid (E)), this change has a significant effect on the interaction with integrins of cells. It is known that integrin surface receptors display a high affinity to different RGD containing peptides, while they show a two to four times lower binding affinity to the RGE peptide.[22] Previous studies have shown that the adhesion and proliferation of Balb 3 T3 fibroblasts were enhanced on eADF4(C16)-RGD films compared to that on eADF4(C16)-RGE and eADF4(C16) ones.[14]

Structural and Morphological Characterization of Acellular Spider Silk Hydrogels. Recombinant spider silk proteins based on eADF4(C16) self-assemble into nano-fibrils accompanied by a transition of the mostly unstructured spider silk proteins to β-sheet rich structures.[15,19] The β-sheet structure formation of the resulting nano-fibrils was analyzed using attenuated total reflection Fourier-transform infrared (ATR-FTIR) spectroscopy on freeze-dried 3% (w/v) hydrogels made of eADF4(C16), eADF4(C16)-RGD, and eADF4(C16)-RGE (Figure 1A). The secondary structure content was quantified using Fourier self-deconvolution (FSD) analysis of the amide I band (1700−1500 cm^{-1}). For all three spider silk hydrogels, a β-sheet content above 30% could be determined. These results verified the transition of an intrinsically unstructured protein into β-sheet-rich nano-fibrils during gelation, which have been described before.[15,19] Furthermore, the self-assembled nano-fibrils of eADF4(C16), eADF4(C16)-RGD, and eADF4(C16)-RGE were visualized using transmission electron microscopy (TEM) (Figure 1B). An ordered interconnected nano-fibrillar network could be detected for all three spider silk variants. Additionally, the nano-fibrils of the three different spider silk variants showed similar dimensions (black arrows, Figure 1B) as mentioned previously.[16b,19] To analyze the macroporous structure of the different hydrogels, they were analyzed using scanning electron microscopy (SEM) (Figure 1C). For all three eADF4(C16)-based hydrogels, smooth and sheet-like structures with sharp pores could be identified.[15,17,18] This smooth and sheet-like surface structure could result from the collapsing nano-fibrillary network during the freeze-drying process.[17] Taken together, these results indicated that the fused peptide tags in case of eADF4(C16)-RGD and eADF4(C16)-RGE did not influence the nucleation-dependent nano-fibril formation of eADF4(C16)-based spider silk proteins.

Rheological Properties of Spider Silk Based Bioinks. Rheological measurements using a plate-to-plate geometry were conducted to analyze mechanical properties of acellular hydrogels made of 3% w/v eADF4(C16), eADF4(C16)-RGD, and eADF4(C16)-RGE and bioinks additionally containing 5×10^6 HEK293 producer cells to characterize the effect of encapsulated cells on mechanical properties. Previously, it has been shown that eADF4(C16)-RGD formed stiffer hydrogels at identical protein concentrations compared to eADF4(C16).[16] Here, the viscosity of acellular spider silk hydrogels and bioinks was shear rate dependently determined to characterize their usability for 3D bioprinting (Figure 1D).

https://doi.org/10.1021/acs.biomac.2c00971
Biomacromolecules 2022, 23, 4427−4437

For all investigated spider silk hydrogels and bioinks, a decrease of viscosity with increasing shear rate could be seen, indicating shear-thinning behavior of the materials. This property is an important feature for 3D bioprinting. Interestingly, eADF4(C16)-RGD and eADF4(C16)-RGE showed similar viscoelastic properties, while eADF4(C16) revealed the already known lower viscosity in direct comparison at the same protein concentrations. Nevertheless, for all three spider silk variants, the viscosity increased upon the addition of HEK293 producer cells, though the bioinks maintained their viscoelastic, shear-thinning behavior. The effect was the highest for eADF4(C16), while the viscosity of acellular hydrogel and bioink converged for eADF4(C16)-RGD and eADF4(C16)-RGE at higher shear rates.

Furthermore, the total yield stress, representing the flow point, of spider silk hydrogels and bioinks was determined using the crossover of storage (G') and loss (G'') moduli after an amplitude sweep measurement (Figure 1E). A similar trend, as seen for the shear-thinning behavior, could be detected, as the yield stress of eADF4(C16)-RGD and eADF4(C16)-RGE hydrogels and bioinks was on a similar level but was enhanced in comparison to that of eADF4(C16) hydrogels and bioinks. For all investigated spider silk variants, the yield stress of bioinks containing HEK293 producer cells was enhanced compared to the hydrogels without cells. Thus, here, encapsulated cells increased the total stiffness and the flow point of the bioinks. A recent study using spider silk bioinks showed similar trends for viscosity and shear-thinning behavior. It also revealed an increase of flow points for eADF4(C16)-RGD and eADF4(C16)-RGE, but a decrease for eADF4(C16), after the addition of human BxPC-3 epithelial pancreas cells.[16c] Nevertheless, the variations could arise from using different cells, which exhibit various cell sizes or different levels of interaction with the spider silk network or varying spider silk bioink concentrations (3% (w/v) versus 4% (w/v)).

Besides shear-thinning behavior, another important prerequisite for potential 3D bioprinting applications is the recovery of the material after extrusion to maintain the form stability of the printed constructs. Rapid recovery is important for successful 3D bioprinting, enabling a homogeneous flow during extrusion without disintegration afterward. Therefore, recovery of different silk hydrogels and bioinks was determined as stability of storage (G') and loss (G'') moduli after deforming the hydrogels and bioinks using a flow ramp measurement with increasing shear rates (Figure S2). All acellular hydrogels and cell-containing bioinks made of spider silk proteins demonstrated rapid recovery, as storage and loss moduli were on similar levels before and after applying high rotational shear stress. Again, the data indicated that the storage and loss moduli of acellular hydrogels and bioinks made of eADF4(C16)-RGD and eADF4(C16)-RGE were enhanced compared to unmodified eADF4(C16) ones. Nevertheless, the presence of HEK293 cells highly increased the storage and loss moduli of unmodified eADF4(C16). Only a slight increase could be detected for eADF4(C16)-RGD bioinks, while for eADF4(C16)-RGE, even a decrease in storage and loss moduli was detected when cells were present. These results indicated that HEK293 producer cells were able to interact with the nano-fibrillar network made of eADF4(C16) and eADF4(C16)-RGD, but not with that of the eADF4(C16)-RGE variant.

HEK293 Producer Cell Proliferation and Viability in Spider Silk Bioinks over 14 Days. For tissue engineering and bioprinting applications, cell survival during the encapsulation process and proliferation afterward in the printed construct are essential. Therefore, bioinks made of 3% w/v eADF4(C16), eADF4(C16)-RGD, and eADF4(C16)-RGE were analyzed concerning their influence on metabolic activity (as a surrogate parameter of proliferation) and cell survival of HEK293 producer cells after encapsulation over 14 days. As shown in Figure 2A, HEK293 producer cells increased their metabolic activity in non-printed bioinks made of the recombinant spider silk variants eADF4(C16) and the modified eADF4(C16)-RGD. In contrast, the metabolic activity decreased for eADF4(C16)-RGE bioinks after day three, indicating that this spider silk variant did not support cellular activities such as proliferation. These findings further revealed that the unmodified eADF4(C16) represented a suitable matrix material for HEK293 producer cells, although the amino acid sequence of eADF4(C16) lacks any cell interaction sites.[23] However, in a previous study, murine MC3T3 osteoblasts were also able to grow on eADF4(C16).[16a] Nevertheless, the RGD variant showed the highest applicability, since a recently published *in vivo* vascularization study of acellular silk hydrogels showed that the presence of the RGD integrin-binding tag clearly supports surgically induced angiogenesis by formation and sprouting of new blood vessels much better than in non-RGD tagged eADF4(C16) hydrogels.[24] Additionally, the higher stability of RGD-modified hydrogels and bioinks compared to eADF4(C16) ones can be a decisive argument for the use of this variant.[16a,24] Furthermore, the enhanced cell proliferation inside the eADF4(C16)-RGD compared to that in the eADF4(C16)-RGE bioink indicated a specific interaction of the cell surface receptors with the RGD peptide tag which RGE tags could not achieve. Thus, an inappropriate peptide tag was counterproductive, as it prevented interactions of cell surface receptors and the surrounding matrix by steric hindrance. Previous studies showed that cell receptors displayed a two to four times lower binding affinity to RGD-resembling peptides, including the RGE peptide.[22]

Additionally, live/dead staining was conducted on days 1, 7, and 14 to visualize the viability of encapsulated HEK293 producer cells (Figure 2B). Only a few dead cells could be detected on day one. Most of the HEK293 producer cells were alive independent of the silk variant confirming a cell-friendly encapsulation process. Moreover, the cells were homogeneously distributed in all spider silk bioinks showing no cell clustering or aggregation. Interestingly, on day seven, the viability was again very high, but the cells seemed to grow in size in comparison to day one. This trend of increased cell size continued until day 14. However, in direct comparison to day seven, fewer cells could be detected in the same area of the hydrogel. One explanation for the larger cell size could be an effect of matrix degradation inside the hydrogel network. When comparing the WST-8 assay results of Figure 2A and the live/dead assay, the WST-8 signal for eADF4(C16) and eADF4(C16)-RGD was only slightly higher on day 14 compared to that on day 7. Here, one assumption is that this enhanced signal could be due to the higher metabolic activity of the larger cells. Interestingly, the outcome for eADF4(C16)-RGE-based matrices seemed different. Although the WST-8 assay indicated a low metabolic activity of the encapsulated HEK293 producer cells over 14 days, the cells were still viable inside the eADF4(C16)-RGE matrix. This finding again confirmed that an inadequate peptide tag, such as RGE, may fail to stimulate

https://doi.org/10.1021/acs.biomac.2c00971
Biomacromolecules 2022, 23, 4427−4437

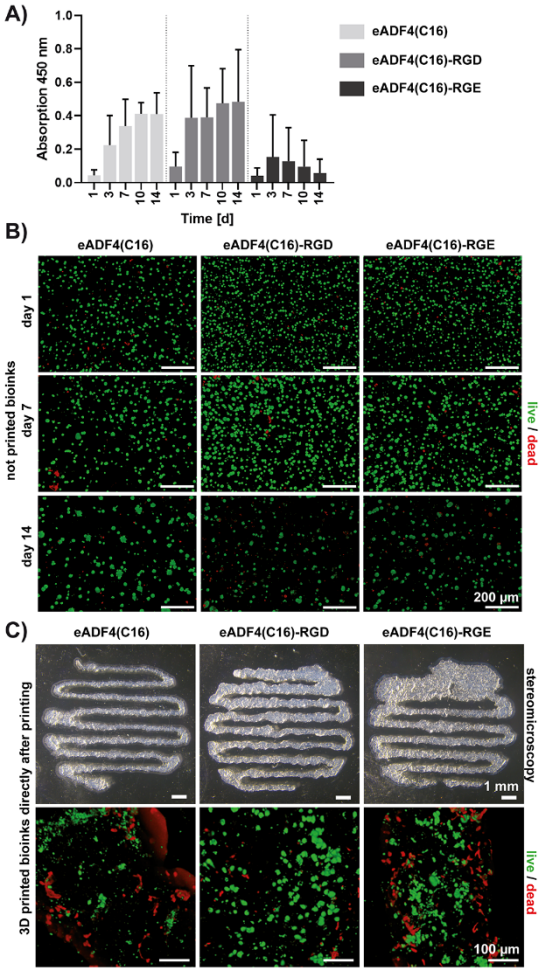

Figure 2. HEK293 proliferation and survival in bioinks comprising 3% w/v spider silk hydrogels made of eADF4(C16), eADF4(C16)-RGD, and eADF4(C16)-RGE: (A) cell proliferation of HEK293 producer cells in non-printed spider silk bioinks over 14 days of cultivation using a WST-8 assay. (B) Confocal microscopy images of bioinks comprising live/dead stained HEK293 cells cultivated in respective spider silk hydrogels after 1, 7, and 14 days of cultivation in a humidified atmosphere containing 5% CO_2 at 37 °C. For (A, B), initially, 500,000 cells were encapsulated in 100 μL of spider silk hydrogels. (C) 3D printing of different spider silk bioinks containing 5×10^6 HEK293 producer cells/mL hydrogel. Stereomicroscopy images of 3D-printed constructs (upper panel) and confocal microscopy images of encapsulated live/dead stained HEK293 producer cells in 3D-printed scaffolds (lower panel) directly after printing. For live/dead staining in (B, C), the cells were stained with Calcein-AM and EthD-1 to visualize live (green) and dead (red) cells, respectively. Scale bars are as indicated.

cell surface receptors preventing a corresponding cell response, for instance, proliferation.

HEK293 Cell Viability in Spider Silk Bioinks after 3D Extrusion Bioprinting. Previous studies have already shown that eADF4(C16) and eADF4(C16)-RGD bioinks can be 3D printed using micro-valve extrusion printing.[16a,b] Here, extrusion printing was used to 3D bioprint the respective bioinks with 5×10^6 encapsulated HEK293 producer cells. As shown in Figure 2C, all three bioinks could be 3D bioprinted, albeit with different resolutions. While eADF4(C16) and eADF4(C16)-RGD allowed a continuous printing with comparable resolution, the eADF4(C16)-RGE bioink appeared to disintegrate. There were some difficulties in generating a scaffold with uniform dimensions made of this variant. Due to the disintegration of the bioink, the pressure had to be increased, leading to an enlarged material extrusion. These findings are in line with the results of a recent study that investigated the printability of these spider silk bioinks with increasing cell numbers.[16c] Besides successful cell encapsulation and printability, another important factor for biofabrication is cell survival after the 3D bioprinting process. Therefore, live/dead staining was conducted directly after printing (Figure 2C). Previous studies have already shown that 3D bioprinted spider silk inks strongly interact with EthD-1 leading to a red-stained background,[16] which could result from the partial decomposition of the hydrogel network during the printing process. Nevertheless, confocal microscopy images displayed that HEK293 producer cells survived the printing process inside the bioinks independent of the silk variant used. Especially inside the eADF4(C16)-RGD bioink, many live cells could be detected, indicating the beneficial synergistic effect of the RGD tag and the higher mechanical stabilities than unmodified eADF4(C16). Furthermore, the enhanced signal inside the eADF4(C16)-RGD compared to the eADF4(C16)-RGE hydrogel confirmed the specific interaction of cell receptors with the RGD peptide. Taken together, the synergistic effect of the RGD peptide as a biochemical stimulus and the good mechanical properties were advantageous for HEK293 producer cell survival within an application using 3D bioprinting.

TNFR2-Fc-GpL Production inside and Its Release from Spider Silk Bioinks. Concerning the potential application as a bioink for continuous drug production, the biological of interest should be released from the bioink and not interact or retain with the surrounding matrix. Therefore, the release of encapsulated TNFR2-Fc-GpL from the nanofibrillar spider silk hydrogel matrix was analyzed first in the absence of cells using luciferase activity measurements of the supernatant over a period of 14 days (Figure 3A). Importantly, it could be seen that a constant, steady-state release could be achieved after 3 days, and no significant change occurred independent of the spider silk bioink used. Nevertheless, a faster release of TNFR2-Fc-GpL from eADF4(C16)-RGE hydrogels could be determined, while less protein was released from eADF4(C16) and eADF4(C16)-RGD hydrogels. These results indicated that TNFR2-Fc-GpL interacts slightly stronger with eADF4(C16) and eADF4(C16)-RGD spider silk compared to eADF4(C16)-RGE. Adsorption studies using quartz crystal microbalance and dissipation (QCM-D) measurements (Figure S3) also revealed that TNFR2-Fc-GpL showed increased interaction with eADF4(C16) and eADF4(C16)-RGD surfaces in comparison to eADF4(C16)-RGE ones.

Next, the production of TNFR2-Fc-GpL by transfected HEK293 cells inside and its release from different spider silk bioinks was analyzed by measuring the luciferase activity in the respective supernatants (Figure 3B). A pre-test using an additional hydrogel layer above the spider silk bioink was conducted to ensure that explicitly bioink-encapsulated

https://doi.org/10.1021/acs.biomac.2c00971
Biomacromolecules 2022, 23, 4427−4437

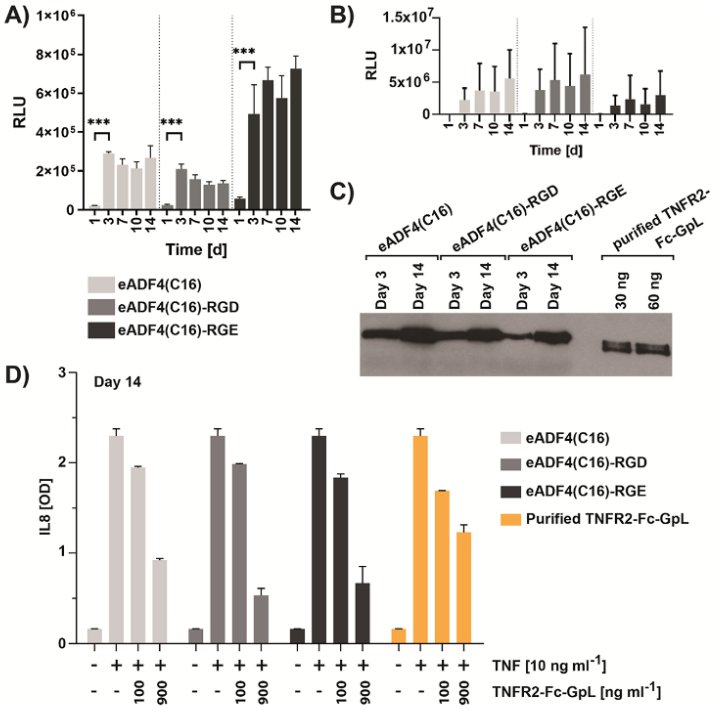

Figure 3. TNFR2-Fc-GpL production and release from 3% w/v spider silk bioinks made of eADF4(C16), eADF4(C16)-RGD, and eADF4(C16)-RGE: (A) luciferase activity of TNFR2-Fc-GpL released from acellular spider silk hydrogels. (B) Luciferase activity of TNFR2-Fc-GpL produced by HEK293 cells encapsulated in the respective bioink and released therefrom over 14 days. (C) Supernatants of TNFR2-Fc-GpL producing HEK293 cells encapsulated in the indicated spider silk inks were harvested after 3 and 14 days and analyzed by western blotting using anti-Flag antibody along with 30 and 60 ng purified TNFR2-Fc-GpL to estimate the fusion protein concentration in the supernatants. (D) The biological activity of TNFR2-Fc-GpL was determined using an enzyme-linked immunosorbent assay (ELISA) of the IL8 content produced by HeLa cells. HeLa cells were treated with 10 ng mL^{-1} TNF and increasing concentrations of TNFR2-Fc-GpL produced by HEK293 producer cells encapsulated in different spider silk bioinks on day 14. Purified TNFR2-Fc-GpL served as control.

HEK293 producer cells and not only surface-exposed ones produced the TNFR2-Fc-GpL (Figure S4). Figure 3B clearly shows that the HEK293 producer cells released functional TNFR2-Fc-GpL from scaffolds made of all three spider silk variants. While the released amount of TNFR2-Fc-GpL was on a similar level for eADF4(C16) and eADF4(C16)-RGD bioinks, less reporter biologicals were released from the eADF4(C16)-RGE scaffolds over time. As already shown in the proliferation assay (Figure 2A), these findings illustrated once again that unmodified eADF4(C16) hydrogels, in addition to the modified, cell-adhesive eADF4(C16)-RGD ones, already represented a suitable matrix for HEK293 producer cells. Furthermore, in addition to cell proliferation, the inadequate RGE peptide tag could not stimulate HEK293 cells to produce TNFR2-Fc-GpL, confirming that a suitable peptide tag is necessary for triggering different cellular responses.

Evaluation of the Biological Activity of TNFR2-Fc-GpL. TNFR2-Fc-GpL production was further analyzed using western blot analysis (Figure 3C) and a TNF neutralization assay (Figure 3D) to check whether the HEK293 cells produce the fusion protein correctly in full-length and functionality. The western blot revealed that more TNFR2-Fc-GpL was produced inside eADF4(C16) and eADF4(C16)-RGD bioinks compared to eADF4(C16)-RGE ones, verifying the results of the luciferase assay (Figure 3B). Additionally, the signal increase (from day 3 to day 14) confirmed the proliferation of HEK293 cells (Figure 2A). The different applied standards enabled calculating how much protein was generated and released to the respective 100 μL supernatant. This was important for the subsequent TNF neutralization assay for checking the biological activity of TNFR2-Fc-GpL by measuring the effect of the TNFR2-Fc-GpL containing supernatants on TNF-induced IL8 production of HeLa cells (Figure 3D). Stimulation of HeLa cells with TNF (10 ng ml^{-1}) resulted in increased production of IL8. The addition of 100 and 900 ng mL^{-1} TNFR2-Fc-GpL from the supernatants of the producer cells in the different spider silk bioinks inhibited the IL8 production, similar to inhibition of control TNFR2-Fc-GpL produced outside a silk matrix (Figure 3D). These results showed that TNFR-Fc-GpL produced by HEK293 cells inside the spider silk bioinks remains fully active, interacts with TNF, and, thus, blocks TNF-triggered cell signaling.

■ CONCLUSIONS

3D cell culture systems provide an artificial extracellular matrix for cells, which is important for drug development and discovery since they mimic the natural tissue environment, which conventional 2D systems cannot achieve. However, in this context, animal- or human-derived scaffolds provide a risk

https://doi.org/10.1021/acs.biomac.2c00971
Biomacromolecules 2022, 23, 4427−4437

of disease transfer, batch-to-batch variability, and lack of reproducibility, scalability, or biofunctionalization.[11a,25] Searching for novel scaffold materials identified recombinant spider silk ones, which combine no cytotoxicity, biodegradability, and no immune response with mechanical tunability.[12] Furthermore, recombinant spider silk proteins can be processed into 3D hydrogels, which are particularly suitable candidates for encapsulation of biologically active substances and cells.[12,15,16,18] Additionally, due to their mechanical properties and shear thinning behavior, these hydrogels can be easily 3D printed.[12,15,16] In the field of pharmaceutical and medical applications, the impact of 3D printing as a precise manufacturing method has risen due to the need for individually developed and adjustable drug delivery systems and dosage therapy forms, personalized tissue engineering and regenerative medicine applications, and disease modeling.[26] This method also enables the processing of various structures with different shapes and sizes for better diffusion.[2a,27] Furthermore, compared to seeding cells in a pre-fabricated, acellular scaffold, encapsulation of cells in a hydrogel matrix shows advantages, including no cell loss during the seeding process, homogeneous cell distribution, and improved cell−material interactions.[28] Thus, 3D printing of cell-loaded, drug-producing delivery systems combines flexibility, individuality, adaptability, and the possibility of personalized therapy.[26a]

Here, the beneficial properties of spider silk hydrogels were combined with HEK293 producer cells to generate a continuously drug-releasing bioink for the long-term production and release of a traceable and active TNRF2-Fc-GpL reporter biological. The highly adjustable system evolved here by combining spider silk bioinks and producer cells is promising for future targeted therapy applications to treat cancer or chronic diseases and reduce side effects. The results correlate with previous studies illustrating that fusion of a GpL domain to TNF, its appropriate receptors (TNFR1 or TNFR2), or other types of antibodies neither affected the activity nor the interaction of the protein and the respective receptor.[2h,i,29] The use of the presented drug-producing bioink for future applications in the field of regenerative medicine could be limited by the lack of vascularization of the matrix. However, the successful vascularization and good biocompatibility of the here-used spider silk matrices has already been previously demonstrated in the AV loop rat model.[24,30]

■ ASSOCIATED CONTENT

Supporting Information

The Supporting Information is available free of charge at https://pubs.acs.org/doi/10.1021/acs.biomac.2c00971.

Recovery of spider silk hydrogels and bioinks (PDF)

■ AUTHOR INFORMATION

Corresponding Authors

Dominik Steiner − *Department of Plastic and Hand Surgery and Laboratory for Tissue Engineering and Regenerative Medicine, University Hospital of Erlangen, Friedrich-Alexander-University Erlangen-Nuremberg (FAU), Erlangen 91054, Germany*; Phone: +49 (0) 9131 85 33 296; Email: steiner_dominik@icloud.com

Thomas Scheibel − *Lehrstuhl Biomaterialien, Fakultät für Ingenieurswissenschaften, Universität Bayreuth, Bayreuth 95447, Germany; Bayreuther Zentrum für Kolloide und Grenzflächen (BZKG), Bayerisches Polymerinstitut (BPI), Bayreuther Zentrum für Molekulare Biowissenschaften (BZMB), Bayreuther Materialzentrum (BayMAT), Universität Bayreuth, Bayreuth 95447, Germany*; orcid.org/0000-0002-0457-2423; Email: thomas.scheibel@bm.uni-bayreuth.de, +49 (0) 921 55 6700

Authors

Vanessa T. Trossmann − *Lehrstuhl Biomaterialien, Fakultät für Ingenieurswissenschaften, Universität Bayreuth, Bayreuth 95447, Germany*

Stefanie Heltmann-Meyer − *Department of Plastic and Hand Surgery and Laboratory for Tissue Engineering and Regenerative Medicine, University Hospital of Erlangen, Friedrich-Alexander-University Erlangen-Nuremberg (FAU), Erlangen 91054, Germany*

Hanna Amouei − *Division of Molecular Internal Medicine, Department of Internal Medicine II, University Hospital of Würzburg, Würzburg 97080, Germany*

Harald Wajant − *Division of Molecular Internal Medicine, Department of Internal Medicine II, University Hospital of Würzburg, Würzburg 97080, Germany*

Raymund E. Horch − *Department of Plastic and Hand Surgery and Laboratory for Tissue Engineering and Regenerative Medicine, University Hospital of Erlangen, Friedrich-Alexander-University Erlangen-Nuremberg (FAU), Erlangen 91054, Germany*

Complete contact information is available at: https://pubs.acs.org/10.1021/acs.biomac.2c00971

Author Contributions

‡V.T.T. and S.H.M. contributed equally to this work. V.T.T., S.H.M., R.E.H., D.S., and T.S. designed the study; V.T.T., S.H.M., and H.A. carried out the experimental work and analyzed the data; R.E.H., D.S., and T.S. supervised the study; V.T.T. wrote the original draft; S.H.M., H.A., H.W., R.E.H., D.S., and T.S. edited the paper; V.T.T. performed the spider silk processing (hydrogels) and the encapsulation of HEK293 cells (bioinks), the structural (FTIR) and rheological characterization and respective data analysis, sample preparation for TEM and SEM, cell staining and confocal microscopy, 3D bioprinting, and stereomicroscopy; S.H.M. conducted WST-8 and luciferase assays and determined the release of the fusion protein from the hydrogels with respective data analysis; H.A. generated the HEK293 producer cells and performed the western blot analysis and the TNF neutralization assay. All authors revised and approved the final version of the manuscript.

Notes

The authors declare the following competing financial interest(s): TS is co-founder and shareholder of the company AMSilk GmbH. All other authors declare that they have no competing financial interests or personal relationships that could have appeared to influence the work reported in the present paper.

■ ACKNOWLEDGMENTS

This work was supported by the Deutsche Forschungsgemeinschaft (DFG, German Research Foundation, grant numbers: Projektnummer 326998133−TRR 225 (subproject C01 to TS and subproject C04 to REH and HW)). The authors would like to thank Anika Winkler for TEM imaging, Claudia

https://doi.org/10.1021/acs.biomac.2c00971
Biomacromolecules 2022, 23, 4427−4437

Stemmann for SEM imaging, and Annika Lechner for scientific discussions. Support from the Elite Network of Bavaria is also acknowledged (VTT).

REFERENCES

(1) (a) Yasunaga, M. Antibody Therapeutics and Immunoregulation in Cancer and Autoimmune Disease. *Semin. Cancer Biol.* **2020**, *64*, 1−12. (b) Petitdemange, A.; Blaess, J.; Sibilia, J.; Felten, R.; Arnaud, L. Shared Development of Targeted Therapies among Autoimmune and Inflammatory Diseases: a Systematic Repurposing Analysis. *Ther. Adv. Musculoskeletal Dis.* **2020**, *12*, 1759720X20969261. (c) Gerber, D. E. Targeted Therapies: a new Generation of Cancer Treatments. *Am. Fam. Physician* **2008**, *77*, 311−319. (d) Caspi, R. R. Immunotherapy of Autoimmunity and Cancer: the Penalty for Success. *Nat. Rev. Immunol.* **2008**, *8*, 970−976. (e) Press, O.; Wijdenes, J.; Glennie, M. J.; Bagshawe, K. D. Targeted Therapy of Cancer and Autoimmune Diseases. In *Pharmacological Sciences: Perspectives for Research and Therapy in the Late 1990s*, Cuello, A. C., Collier, B. Eds.; Birkhäuser Basel, *1995*; pp. 381−389 (f) AlQahtani, A. D.; O'Connor, D.; Domling, A.; Goda, S. K. Strategies for the Production of Long-acting Therapeutics and Efficient Drug Delivery for Cancer Treatment. *Biomed. Pharmacother.* **2019**, *113*, No. 108750.

(2) (a) Ghosh, J. G.; Nguyen, A. A.; Bigelow, C. E.; Poor, S.; Qiu, Y.; Rangaswamy, N.; Ornberg, R.; Jackson, B.; Mak, H.; Ezell, T.; et al. Long-acting Protein Drugs for the Treatment of Ocular Diseases. *Nat. Commun.* **2017**, *8*, 14837. (b) Siegemund, M.; Richter, F.; Seifert, O.; Unverdorben, F.; Kontermann, R. E. Expression and Purification of Recombinant Antibody Formats and Antibody Fusion Proteins. In *Monoclonal Antibodies: Methods and Protocols*; Ossipow, V., Fischer, N. Eds.; Humana Press, 2014; pp. 273−295, DOI: 10.1007/978-1-62703-992-5_18. (c) Kreitman, R. J.; Pastan, I. Antibody Fusion Proteins: Anti-CD22 Recombinant Immunotoxin Moxetumomab Pasudotox. *Clin. Cancer Res.* **2011**, *17*, 6398−6405. (d) Medler, J.; Nelke, J.; Weisenberger, D.; Steinfatt, T.; Rothaug, M.; Berr, S.; Hünig, T.; Beilhack, A.; Wajant, H. TNFRSF Receptor-specific Antibody Fusion Proteins with Targeting Controlled FcγR-independent Agonistic Activity. *Cell Death Dis.* **2019**, *10*, 224. (e) Jäger, V.; Büssow, K.; Wagner, A.; Weber, S.; Hust, M.; Frenzel, A.; Schirrmann, T. High Level Transient Production of Recombinant Antibodies and Antibody Fusion Proteins in HEK293 Cells. *BMC Biotechnol.* **2013**, *13*, 52. (f) Rider, P.; Carmi, Y.; Cohen, I. Biologics for Targeting Inflammatory Cytokines, Clinical Uses, and Limitations. *Int. J. Cell Biol.* **2016**, *2016*, 9259646. (g) Strohl, W. R. Fusion Proteins for Half-Life Extension of Biologics as a Strategy to Make Biobetters. *BioDrugs.* **2015**, *29*, 215−239. (h) Lang, I.; Füllsack, S.; Wajant, H. Lack of Evidence for a Direct Interaction of Progranulin and Tumor Necrosis Factor Receptor-1 and Tumor Necrosis Factor Receptor-2 From Cellular Binding Studies. *Front. Immunol.* **2018**, *9*, 793. (i) Lang, I.; Füllsack, S.; Wyzgol, A.; Fick, A.; Trebing, J.; Arana, J. A. C.; Schäfer, V.; Weisenberger, D.; Wajant, H. Binding Studies of TNF Receptor Superfamily (TNFRSF) Receptors on Intact Cells. *J. Biol. Chem.* **2016**, *291*, 5022−5037. (j) Kiyoshi, M.; Tatematsu, K.-I.; Tada, M.; Sezutsu, H.; Shibata, H.; Ishii-Watabe, A. Structural Insight and Stability of TNFR-Fc Fusion Protein (Etanercept) Produced by Using Transgenic Silkworms. *J. Biochem.* **2021**, *169*, 25−33.

(3) Kivelevitch, D.; Mansouri, B.; Menter, A. Long Term Efficacy and Safety of Etanercept in the Treatment of Psoriasis and Psoriatic Arthritis. *Biologics* **2014**, *8*, 169−182.

(4) (a) Arnold, J. J.; Campain, A.; Barthelmes, D.; Simpson, J. M.; Guymer, R. H.; Hunyor, A. P.; McAllister, I. L.; Essex, R. W.; Morlet, N.; Gillies, M. C.; Hunt, A.; Gillies, M.; Hunt, A.; Hunyor, A. P.; Arnold, J.; Young, S.; Clark, G.; Banerjee, G.; Philips, R.; Perks, M.; Essex, R.; McAllister, I.; Constable, I.; Guymer, R.; Guymer, R.; Lim, L.; Harper, A.; Chow, L. P.; Wickremansinghe, S.; Wickremasinghe, S.; Wickremasinghe, S. Two-Year Outcomes of "Treat and Extend" Intravitreal Therapy for Neovascular Age-Related Macular Degeneration. *Ophthalmology* **2015**, *122*, 1212−1219. (b) Day, S.; Acquah, K.; Mruthyunjaya, P.; Grossman, D. S.; Lee, P. P.; Sloan, F. A. Ocular Complications after Anti-vascular Endothelial Growth Factor Therapy in Medicare Patients with Age-related Macular Degeneration. *Am. J. Ophthalmol.* **2011**, *152*, 266−272. (c) Ibeanu, N.; Egbu, R.; Onyekuru, L.; Javaheri, H.; Tee Khaw, P.; Williams, G. R.; Brocchini, S.; Awwad, S. Injectables and Depots to Prolong Drug Action of Proteins and Peptides. *Pharmaceutics* **2020**, *12*, 999. (d) Jaini, R.; Hannaman, D.; Johnson, J. M.; Bernard, R. M.; Altuntas, C. Z.; de las Alas, M. M.; Kesaraju, P.; Luxembourg, A.; Evans, C. F.; Tuohy, V. K. Gene-Based Intramuscular Interferon-β Therapy for Experimental Autoimmune Encephalomyelitis. *Mol. Ther.* **2006**, *14*, 416−422.

(5) (a) Buwalda, S. J.; Vermonden, T.; Hennink, W. E. Hydrogels for Therapeutic Delivery: Current Developments and Future Directions. *Biomacromolecules* **2017**, *18*, 316−330. (b) Bittner, S. M.; Guo, J. L.; Mikos, A. G. Spatiotemporal Control of Growth Factors in Three-Dimensional Printed Scaffolds. *Bioprinting* **2018**, *12*, No. e00032.

(6) Mobasheri, A.; Choi, H.; Martín-Vasallo, P. Over-Production of Therapeutic Growth Factors for Articular Cartilage Regeneration by Protein Production Platforms and Protein Packaging Cell Lines. *Biology* **2020**, *9*, 330.

(7) (a) Gandhi, J. K.; Opara, E. C.; Brey, E. M. Alginate-based Strategies for Therapeutic Vascularization. *Ther. Deliv.* **2013**, *4*, 327−341. (b) Emerich, D. F.; Orive, G.; Thanos, C.; Tornoe, J.; Wahlberg, L. U. Encapsulated cell therapy for neurodegenerative diseases: From promise to product. *Adv. Drug Delivery Rev.* **2014**, *67-68*, 131−141. (c) Emerich, D. F.; Winn, S. R.; Hantraye, P. M.; Peschanski, M.; Chen, E.-Y.; Chu, Y.; McDermott, P.; Baetge, E. E.; Kordower, J. H. Protective effect of encapsulated cells producing neurotrophic factor CNTF in a monkey model of Huntington's disease. *Nature* **1997**, *386*, 395−399. (d) Mao, A. S.; Özkale, B.; Shah, N. J.; Vining, K. H.; Descombes, T.; Zhang, L.; Tringides, C. M.; Wong, S.-W.; Shin, J.-W.; Scadden, D. T.; Weitz, D. A.; Mooney, D. J. Programmable microencapsulation for enhanced mesenchymal stem cell persistence and immunomodulation. *Proc. Natl. Acad. Sci. U. S. A.* **2019**, *116*, 15392−15397. (e) Hauser, O.; Prieschl-Grassauer, E.; Salmons, B. Encapsulated, genetically modified cells producing in vivo therapeutics. *Curr. Opin. Mol. Ther.* **2004**, *6*, 412−420. (f) Orive, G.; Hernández, R. M.; Gascón, A. R.; Igartua, M.; Pedraz, J. L. Encapsulated cell technology: from research to market. *Trends Biotechnol.* 2002, *20* (9), 382−387. DOI: 10.1016/S0167-7799(02)02037-1. (g) Read, T.-A.; Stensvaag, V.; Vindenes, H.; Ulvestad, E.; Bjerkvig, R.; Thorsen, F. Cells encapsulated in alginate: a potential system for delivery of recombinant proteins to malignant brain tumours. *Int. J. Neurosci.* 1999, *17* (5), 653−663, DOI: 10.1016/S0736-5748(99)00052-0. (h) Read, T.-A.; Sorensen, D. R.; Mahesparan, R.; Enger, P. Ø.; Timpl, R.; Olsen, B. R.; Hjelstuen, M. H. B.; Haraldseth, O.; Bjerkvig, R. Local endostatin treatment of gliomas administered by microencapsulated producer cells. *Nat. Biotechnol.* **2001**, *19*, 29−34. (i) Thorsen, F.; Read, T. A.; Lund-Johansen, M.; Tysnes, B. B.; Bjerkvig, R. Alginate-encapsulated producer cells: a potential new approach for the treatment of malignant brain tumors. *Cell Transplant* **2000**, *9*, 773−783. (j) Zhang, W. Encapsulation of transgenic cells for gene therapy. In *Gene Therapy-Principles and Challenges*, InTech, 2015. (k) Visted, T.; Bjerkvig, R.; Enger, P. Ø. Cell encapsulation technology as a therapeutic strategy for CNS malignancies. *Neuro. Oncol.* **2001**, *3*, 201−210.

(8) (a) Rottensteiner-Brandl, U.; Bertram, U.; Lingens, L. F.; Köhn, K.; Distel, L.; Fey, T.; Körner, C.; Horch, R. E.; Arkudas, A. Free Transplantation of a Tissue Engineered Bone Graft into an Irradiated, Critical-Size Femoral Defect in Rats. *Cell* **2021**, *10*, 2256. (b) Kengelbach-Weigand, A.; Thielen, C.; Bäuerle, T.; Götzl, R.; Gerber, T.; Körner, C.; Beier, J. P.; Horch, R. E.; Boos, A. M. Personalized Medicine for Reconstruction of Critical-size Bone Defects − a Translational Approach with Customizable Vascularized Bone Tissue. *NPJ Regen. Med.* **2021**, *6*, 49.

(9) (a) Dorai, H.; Corisdeo, S.; Ellis, D.; Kinney, C.; Chomo, M.; Hawley-Nelson, P.; Moore, G.; Betenbaugh, M. J.; Ganguly, S. Early

https://doi.org/10.1021/acs.biomac.2c00971
Biomacromolecules 2022, 23, 4427−4437

Prediction of Instability of Chinese Hamster Ovary Cell Lines Expressing Recombinant Antibodies and Antibody-Fusion Proteins. *Biotechnol. Bioeng.* **2012**, *109*, 1016−1030. (b) Chin, C. L.; Goh, J. B.; Srinivasan, H.; Liu, K. I.; Gowher, A.; Shanmugam, R.; Lim, H. L.; Choo, M.; Tang, W. Q.; Tan, A. H.-M.; et al. A Human Expression System Based on HEK293 for the Stable Production of Recombinant Erythropoietin. *Sci. Rep.* **2019**, *9*, 16768. (c) Tripathi, N. K.; Shrivastava, A. Recent Developments in Bioprocessing of Recombinant Proteins: Expression Hosts and Process Development. *Front. Bioeng. Biotechnol.* **2019**, *7*, 420.

(10) (a) Wanscher, A. S. M.; Williamson, M.; Ebersole, T. W.; Streicher, W.; Wikström, M.; Cazzamali, G. Production of Functional Human Insulin-like Growth Factor Binding Proteins (IGFBPs) Using Recombinant Expression in HEK293 Cells. *Protein Expression Purif.* **2015**, *108*, 97−105. (b) Sanchez-Garcia, L.; Martín, L.; Mangues, R.; Ferrer-Miralles, N.; Vázquez, E.; Villaverde, A. Recombinant Pharmaceuticals from Microbial Cells: a 2016 Update. *Microb. Cell Fact.* **2016**, *15*, 33.

(11) (a) Langhans, S. A. Three-Dimensional in Vitro Cell Culture Models in Drug Discovery and Drug Repositioning. *Front. Pharmacol.* **2018**, *9*, 6. (b) Donderwinkel, I.; van Hest, J. C. M.; Cameron, N. R. Bio-inks for 3D Bioprinting: Recent Advances and Future Prospects. *Polym. Chem.* **2017**, *8*, 4451−4471. (c) Hospodiuk, M.; Dey, M.; Sosnoski, D.; Ozbolat, I. T. The Bioink: A Comprehensive Review on Bioprintable Materials. *Biotechnol. Adv.* **2017**, *35*, 217−239. (d) Gungor-Ozkerim, P. S.; Inci, I.; Zhang, Y. S.; Khademhosseini, A.; Dokmeci, M. R. Bioinks for 3D Bioprinting: an Overview. *Biomater. Sci.* **2018**, *6*, 915−946. (e) Malda, J.; Visser, J.; Melchels, F. P.; Jüngst, T.; Hennink, W. E.; Dhert, W. J. A.; Groll, J.; Hutmacher, D. W. 25th Anniversary Article: Engineering Hydrogels for Biofabrication. *Adv. Mater.* **2013**, *25*, 5011−5028.

(12) (a) Salehi, S.; Koeck, K.; Scheibel, T. Spider Silk for Tissue Engineering Applications. *Molecules* **2020**, *25*, 737. (b) Aigner, T. B.; DeSimone, E.; Scheibel, T. Biomedical Applications of Recombinant Silk-Based Materials. *Adv. Mater.* **2018**, *30*, 1704636.

(13) Huemmerich, D.; Helsen, C. W.; Quedzuweit, S.; Oschmann, J.; Rudolph, R.; Scheibel, T. Primary Structure Elements of Spider Dragline Silks and Their Contribution to Protein Solubility. *Biochemistry* **2004**, *43*, 13604−13612.

(14) Wohlrab, S.; Müller, S.; Schmidt, A.; Neubauer, S.; Kessler, H.; Leal-Egaña, A.; Scheibel, T. Cell Adhesion and Proliferation on RGD-modified Recombinant Spider Silk Proteins. *Biomaterials* **2012**, *33*, 6650−6659.

(15) Schacht, K.; Scheibel, T. Controlled Hydrogel Formation of a Recombinant Spider Silk Protein. *Biomacromolecules* **2011**, *12*, 2488−2495.

(16) (a) Schacht, K.; Jüngst, T.; Schweinlin, M.; Ewald, A.; Groll, J.; Scheibel, T. Biofabrication of Cell-Loaded 3D Spider Silk Constructs. *Angew. Chem. Int. Ed. Engl.* **2015**, *54*, 2816−2820. (b) DeSimone, E.; Schacht, K.; Pellert, A.; Scheibel, T. Recombinant Spider Silk-based Bioinks. *Biofabrication* **2017**, *9*, No. 044104. (c) Lechner, A.; Trossmann, V. T.; Scheibel, T. Impact of Cell Loading of Recombinant Spider Silk Based Bioinks on Gelation and Printability. *Macromol. Biosci.* **2022**, *22*, 2100390.

(17) Neubauer, V. J.; Trossmann, V. T.; Jacobi, S.; Döbl, A.; Scheibel, T. Aqueous-Organic Solvent Derived Recombinant Spider Silk Gels as Depots for Drugs. *Angew. Chem., Int. Ed. Engl.* **2021**, *60*, 11847−11851.

(18) Kumari, S.; Bargel, H.; Anby, M. U.; Lafargue, D.; Scheibel, T. Recombinant Spider Silk Hydrogels for Sustained Release of Biologicals. *ACS Biomater. Sci. Eng.* **2018**, *4*, 1750−1759.

(19) DeSimone, E.; Schacht, K.; Scheibel, T. Cations Influence the Cross-linking of Hydrogels made of Recombinant, Polyanionic Spider Silk Proteins. *Mater. Lett.* **2016**, *183*, 101−104.

(20) Hu, X.; Kaplan, D.; Cebe, P. Determining Beta-Sheet Crystallinity in Fibrous Proteins by Thermal Analysis and Infrared Spectroscopy. *Macromolecules* **2006**, *39*, 6161−6170.

(21) Rauert, H.; Wicovsky, A.; Müller, N.; Siegmund, D.; Spindler, V.; Waschke, J.; Kneitz, C.; Wajant, H. Membrane Tumor Necrosis Factor (TNF) Induces p100 Processing via TNF Receptor-2 (TNFR2). *J. Biol. Chem.* **2010**, *285*, 7394−7404.

(22) Hersel, U.; Dahmen, C.; Kessler, H. RGD Modified Polymers: Biomaterials for Stimulated Cell Adhesion and Beyond. *Biomaterials* **2003**, *24*, 4385−4415.

(23) Leal-Egaña, A.; Lang, G.; Mauerer, C.; Wickinghoff, J.; Weber, M.; Geimer, S.; Scheibel, T. Interactions of Fibroblasts with Different Morphologies Made of an Engineered Spider Silk Protein. *Adv. Eng. Mater.* **2012**, *14*, B67−B75.

(24) Steiner, D.; Winkler, S.; Heltmann-Meyer, S.; Trossmann, V. T.; Fey, T.; Scheibel, T.; Horch, R. E.; Arkudas, A. Enhanced Vascularization and de novo Tissue Formation in Hydrogels made of Engineered RGD-tagged Spider Silk Proteins in the Arteriovenous Loop Model. *Biofabrication* **2021**, *13*, No. 045003.

(25) Rimann, M.; Graf-Hausner, U. Synthetic 3D Multicellular Systems for Drug Development. *Curr. Opin. Biotechnol.* **2012**, *23*, 803−809.

(26) (a) Jamróz, W.; Szafraniec, J.; Kurek, M.; Jachowicz, R. 3D Printing in Pharmaceutical and Medical Applications − Recent Achievements and Challenges. *Pharm. Res.* **2018**, *35*, 176. (b) Zhu, X.; Li, H.; Huang, L.; Zhang, M.; Fan, W.; Cui, L. 3D printing Promotes the Development of Drugs. *Biomed. Pharmacother.* **2020**, *131*, No. 110644.

(27) Wang, X.; Zhang, M.; Ma, J.; Xu, M.; Chang, J.; Gelinsky, M.; Wu, C. 3D Printing of Cell-Container-Like Scaffolds for Multicell Tissue Engineering. *Engineering* **2020**, *6*, 1276−1284.

(28) Cidonio, G.; Glinka, M.; Dawson, J. I.; Oreffo, R. O. C. The Cell in the Ink: Improving Biofabrication by Printing Stem Cells for Skeletal Regenerative Medicine. *Biomaterials* **2019**, *209*, 10−24.

(29) (a) Fick, A.; Lang, I.; Schäfer, V.; Seher, A.; Trebing, J.; Weisenberger, D.; Wajant, H. Studies of Binding of Tumor Necrosis Factor (TNF)-like Weak Inducer of Apoptosis (TWEAK) to Fibroblast Growth Factor inducible 14 (Fn14). *J. Biol. Chem.* **2012**, *287*, 484−495. (b) Kums, J.; Nelke, J.; Rüth, B.; Schäfer, V.; Siegmund, D.; Wajant, H. Quantitative Analysis of Cell Surface Antigen-Antibody Interaction using Gaussia princeps Luciferase Antibody Fusion Proteins. *mAbs* **2017**, *9*, 506−520.

(30) Steiner, D.; Lang, G.; Fischer, L.; Winkler, S.; Fey, T.; Greil, P.; Scheibel, T.; Horch, R. E.; Arkudas, A. Intrinsic Vascularization of Recombinant eADF4(C16) Spider Silk Matrices in the Arteriovenous Loop Model. *Tissue Eng. Part A* **2019**, *25*, 1504−1513.

https://doi.org/10.1021/acs.biomac.2c00971
Biomacromolecules 2022, 23, 4427−4437

Supporting Information

Recombinant Spider Silk Bioinks for Continuous Protein Release by Encapsulated Producer Cells

Vanessa T. Trossmann [⊥, ‡], *Stefanie Heltmann-Meyer* [◊, ‡], *Hanna Amouei* [†], *Harald Wajant* [†], *Raymund E. Horch* [◊], *Dominik Steiner* [◊, *], *and Thomas Scheibel* [⊥, §, *]

[⊥] Lehrstuhl Biomaterialien, Fakultät für Ingenieurswissenschaften, Universität Bayreuth, Prof.-Rüdiger-Bormann-Str. 1, 95447 Bayreuth, Germany

[◊] Department of Plastic and Hand Surgery and Laboratory for Tissue Engineering and Regenerative Medicine, University Hospital of Erlangen, Friedrich-Alexander-University Erlangen-Nuremberg (FAU), Krankenhaus-Str. 12, 91054 Erlangen, Germany

[†] Division of Molecular Internal Medicine, Department of Internal Medicine II, University Hospital of Würzburg, Grombühl-Str. 12, 97080 Würzburg, Germany

[§] Bayreuther Zentrum für Kolloide und Grenzflächen (BZKG), Bayerisches Polymerinstitut (BPI), Bayreuther Zentrum für Molekulare Biowissenschaften (BZMB), Bayreuther Materialzentrum (BayMAT), Universität Bayreuth, Universitäts-Str. 30, 95447 Bayreuth, Germany

[‡] Contributed equally to this work

* Co-corresponding authors

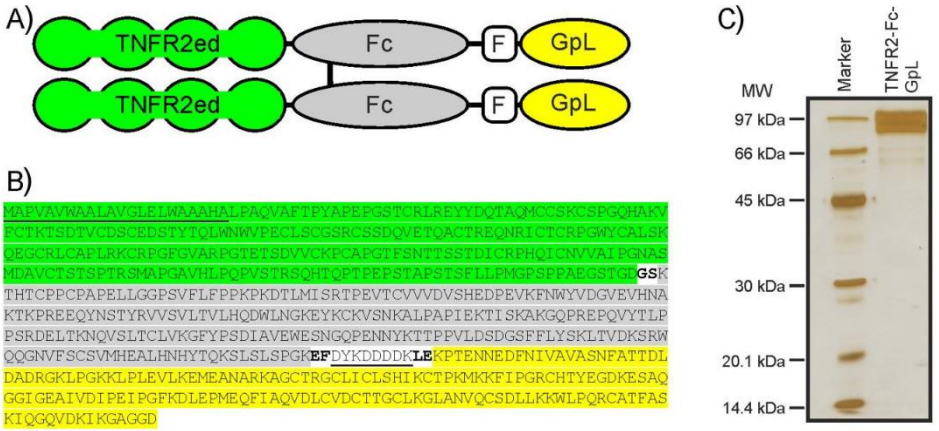

Figure S1. Domain architecture, sequence and purification of TNFR2-Fc-GpL. A) Domain architecture of TNFR2-Fc-GpL: TNFR2ed, extracellular domain of human TNFR2 (green); Fc, Fc domain of human IgG1 (gray); F, Flag tag (white); GpL, *Gaussia princeps* luciferase (yellow). B) Amino acid sequence of TNFR2-Fc-GpL: TNFR2 extracellular domain (green shaded) including signal peptide (green shaded and underlined); Fc domain (grey shaded); GpL domain (yellow shaded); **GS**, **EF** and **LE** represent restriction site encoding amino acids; Flag tag (white shaded and underlined). C) 250 ng TNFR2-Fc-GpL and marker protein mixture (116 ng α-lactalbumin, 80 ng trypsin inhibitor, 83 ng carbonic anhydrase, 147 ng ovalbumin, 83 ng albumin and 67 ng phosphorylase-b) were separated using SDS-PAGE and visualized using silver staining.

2

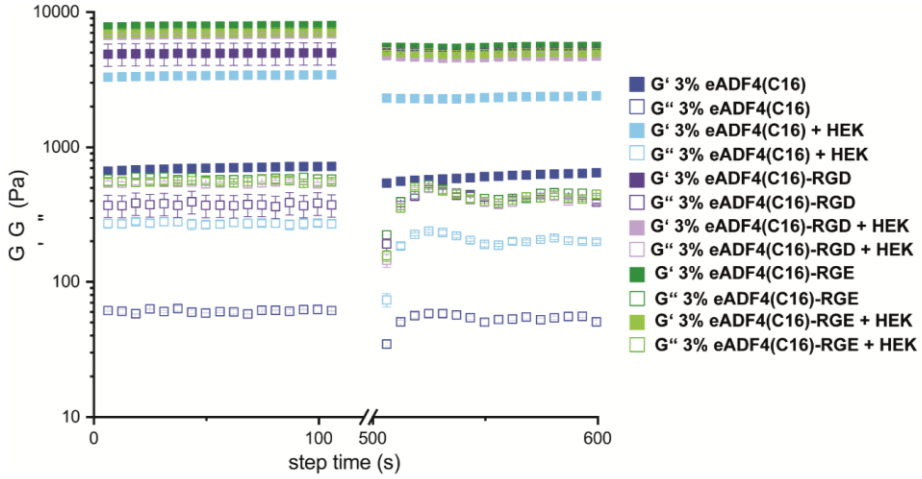

Figure S2. Recovery of 3% w/v hydrogels and bioinks made of eADF4(C16), eADF4(C16)-RGD and eADF4(C16)-RGE: Recovery of different spider silk hydrogels (acellular) and bioinks (hydrogels + cells) as shown by the stability of storage (G') and loss (G'') modulus before and after deformation using a flow ramp measurement with increasing shear rate. The bioinks contained 5 x 10^6 HEK293 producer cells per ml silk hydrogel.

3

Interaction of TNFR2-Fc-GpL with spider silk films

The adsorption of soluble fusion protein on films made of spider silk proteins was analyzed and quantified using a quartz crystal microbalance with dissipation (QCM-D, LOT-QuantumDesign, GmbH, Germany) as described previously [1]. Therefore, eADF4(C16), eADF4(C16)-RGD and eADF4(C16)-RGE were solved in HFIP at a concentration of 5 mg/ml. For uniform coating, UV-ozone cleaned QCM-D gold sensors (5 MHz, AT-cut, Cr/Au, Quartz Pro Sweden AB, Sweden) were spin-coated using 50 µl protein solution (67 rps, 30 s, 3 s acceleration ramp, Schaefer Technologie GmbH, Germany) and post-treated using ethanol vapor in a desiccator overnight to turn the spider silk films water-insoluble. The system equilibration and all adsorption steps of the standard flow-module from Q-Sense E4 (QFM 401, Bioloin Scientific, Sweden) were done in 1x PBS with a volume flow rate of 20 µl/min at 23 °C. First, the sensors were flushed with 1x PBS, followed by TNFR2-Fc-GpL in 1x PBS (concentration 0.1 mg/ml) for 100 min to determine adsorption on the surfaces. Subsequently, the flow modules were washed with 1x PBS again. The frequency and dissipation of the 3rd to 11th overtones were collected for gold, eADF4(C16), eADF4(C16)-RGD and eADF4(C16)-RGD surfaces simultaneously. The areal mass (ng/cm²) was calculated using the 3rd to 11th overtones of frequency and dissipation. Thereby, the areal mass density $\Delta\rho_A$ depends on the change in frequency $\Delta\boldsymbol{f}$ and is proportional to a distinct overtone n. This relation is described by the Sauerbrey equation (1) [2].

$$\Delta\boldsymbol{\rho_A} = -\frac{\boldsymbol{\rho_q h_q}}{\boldsymbol{f_0}}\frac{\boldsymbol{\Delta f}}{\boldsymbol{n}} = -\boldsymbol{C}\frac{\boldsymbol{\Delta f}}{\boldsymbol{n}} \quad (1)$$

The mass sensitivity constant C is the product of the density (ρ_q), the thickness (h_q), and the fundamental frequency (f_0) of the quartz crystal [3]. By converting the thickness into the areal mass, a bulk density of 1350 kg m^{-3} was used as a fitting parameter.

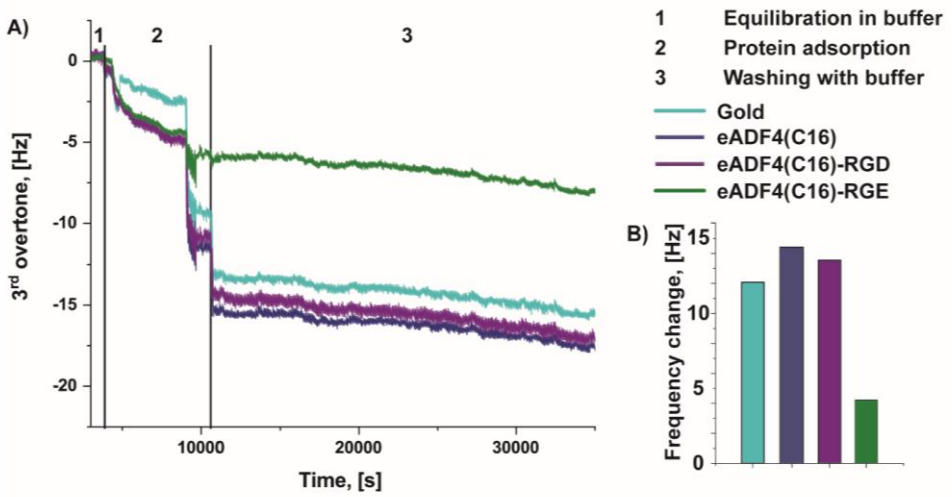

Figure S3. Interaction of TNFR2-Fc-GpL with eADF4(C16), eADF4(C16)-RGD, eADF4(C16)-RGE surfaces and gold as control. QCM-D was used to determine the adsorption of the TNFR2-Fc-GpL fusion protein on spider silk films and gold by frequency change. A) Time-dependent frequency change of the 3rd overtone correlating with adsorption of TNFR2-Fc-GpL on the appropriate surfaces. B) Total amount of adsorbed TNFR2-Fc-GpL indicated by frequency change of the QCM-D measurement.

5

TNFR2-Fc-GpL production by HEK293 producer cells inside spider silk hydrogels

A pre-test using an additional hydrogel layer above the spider silk bioink was conducted, to ensure that bioink-encapsulated HEK293 cells produce functional TNFR2-Fc-GpL, which could diffuse through and released from the spider silk matrix. Therefore, a pre-gelled 3.5 % (w/w) eADF4(C16) solution was mixed with 15 % (v/v) RPMI 1640 containing HEK293 producer cells to reach a final cell density of 5 x 10^6 HEK293 cells per ml final bioink (3 % (w/v)). Moreover, acellular hydrogels containing only media were prepared. In each case, 50 µl of bioink and/or acellular hydrogel solution per well (96 well plate, Nunc) were allowed to gel at 37 °C. For flat control experiments, 5 x 10^3 HEK293 cells per cm^2 were seeded. All samples were covered with 100 µl RPMI 1640 media. The prepared samples were bioink with hydrogel on top (light blue), cells with hydrogel on top (blue), hydrogel with cells on top (dark blue), and cells without any spider silk hydrogel (white). On day 1, 3 and 7 the WST-8 (viability and proliferation) and luciferase (TNFR2-Fc-GpL production) assay were performed (**Figure S4**) as already described in the main manuscript.

6

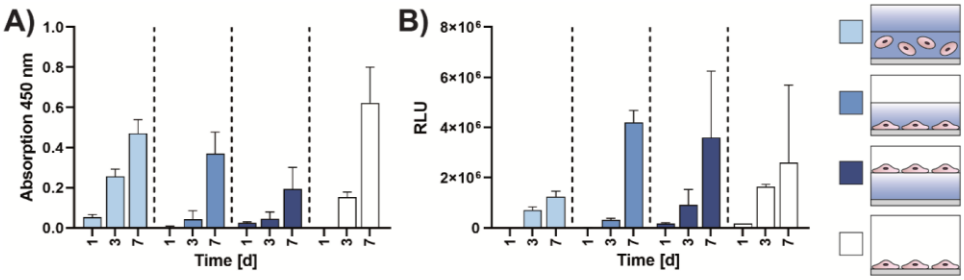

Figure S4. Proliferation (A, WST assay) and TNFR2-Fc-GpL production (B, luciferase activity) of eADF4(C16) bioink-encapsulated HEK293 producer cells covered with an additional eADF4(C16) hydrogel layer (light blue) in comparison to cells cultured on polystyrene surfaces covered with hydrogel (blue), on top of a hydrogel (dark blue) and on polystyrene control surfaces (white). For bioinks, 5 x 10^6 HEK293 producer cells were encapsulated per 1 ml bioink. For flat cultivation, 5000 cells per 1 cm² were seeded.

References

(1) Lentz, S.; Trossmann, V. T.; Borkner, C. B.; Beyersdorfer, V.; Rottmar, M.; Scheibel, T. Structure–Property Relationship Based on the Amino Acid Composition of Recombinant Spider Silk Proteins for Potential Biomedical Applications. *ACS Appl. Mater. Inter.***2022**, *14* (28), 31751-31766. DOI: 10.1021/acsami.2c09590.
(2) Sauerbrey, G. Verwendung von Schwingquarzen zur Wägung dünner Schichten und zur Mikrowägung. *Zeitschrift für Physik* **1959**, *155* (2), 206-222. DOI: 10.1007/BF01337937.
(3) Liu, G.; Zhang, G. *QCM-D Studies on Polymer Behavior at Interfaces*; Springer, 2013. DOI: 10.1007/978-3-642-39790-5.

7.10. Teilarbeit X

Teilarbeit X wurde 2021 unter dem Titel „Enhanced vascularization and de novo tissue formation in hydrogels made of engineered RGD-tagged spider silk proteins in the arteriovenous loop model“ im Journal *Biofabrication* veröffentlicht.

Steiner, D.; Winkler, S.; Heltmann-Meyer, S.; **Trossmann, V. T.**; Fey, T.; Scheibel, T.; Horch, R. E. & Arkudas, A. (2021) Enhanced vascularization and de novo tissue formation in hydrogels made of engineered RGD-tagged spider silk proteins in the arteriovenous loop model. *Biofabrication* **13**: 045003.

https://doi.org/10.1088/1758-5090/ac0d9b

IOP Publishing Biofabrication 13 (2021) 045003 https://doi.org/10.1088/1758-5090/ac0d9b

Biofabrication

OPEN ACCESS

RECEIVED
4 March 2021

REVISED
10 June 2021

ACCEPTED FOR PUBLICATION
22 June 2021

PUBLISHED
13 July 2021

PAPER

Enhanced vascularization and *de novo* tissue formation in hydrogels made of engineered RGD-tagged spider silk proteins in the arteriovenous loop model

Dominik Steiner[1,*], Sophie Winkler[1], Stefanie Heltmann-Meyer[1], Vanessa T Trossmann[2], Tobias Fey[7,8], Thomas Scheibel[2,3,4,5,6], Raymund E Horch[1,*] and Andreas Arkudas[1]

[1] Department of Plastic and Hand Surgery, University Hospital of Erlangen, Friedrich-Alexander-University Erlangen-Nürnberg (FAU), Erlangen, Germany
[2] Faculty of Engineering, Department for Biomaterials, University of Bayreuth, 95447 Bayreuth, Germany
[3] Bayreuth Center for Colloids and Interfaces (BZKG), University of Bayreuth, 95447 Bayreuth, Germany
[4] Bayreuth Center for Molecular Biosciences (BZMB), University of Bayreuth, 95447 Bayreuth, Germany
[5] Center for Material Science and Engineering (BayMAT), University of Bayreuth, 95447 Bayreuth, Germany
[6] Bavarian Polymer Institute (BPI), University of Bayreuth, 95447 Bayreuth, Germany
[7] Department of Materials Science and Engineering, Institute of Glass and Ceramics, Friedrich-Alexander-University Erlangen-Nürnberg (FAU), Erlangen, Germany
[8] Frontier Research Institute for Materials Science, Nagoya Institute of Technology, Gokiso-cho, Showa-ku, Nagoya 466-8555, Japan
* Authors to whom any correspondence should be addressed.

E-mail: dominik.steiner@uk-erlangen.de **and** raymund.horch@uk-erlangen.de

Keywords: engineered recombinant spider silk, biofunctionalization, arteriovenous loop, angiogenesis, tissue formation

Abstract

Due to its low immunogenic potential and the possibility to fine-tune their properties, materials made of recombinant engineered spider silks are promising candidates for tissue engineering applications. However, vascularization of silk-based scaffolds is one critical step for the generation of bioartificial tissues and consequently for clinical application. To circumvent insufficient vascularization, the surgically induced angiogenesis by means of arteriovenous loops (AVL) represents a highly effective methodology. Here, previously established hydrogels consisting of nano-fibrillary recombinant eADF4(C16) were transferred into Teflon isolation chambers and vascularized in the rat AVL model over 4 weeks. To improve vascularization, also RGD-tagged eADF4(C16) hydrogels were implanted in the AVL model over 2 and 4 weeks. Thereafter, the specimen were explanted and analyzed using histology and microcomputed tomography. We were able to confirm biocompatibility and tissue formation over time. Functionalizing eADF4(C16) with RGD-motifs improved hydrogel stability and enhanced vascularization even outperforming other hydrogels, such as fibrin. This study demonstrates that the scaffold ultrastructure as well as biofunctionalization with RGD-motifs are powerful tools to optimize silk-based biomaterials for tissue engineering applications.

1. Introduction

Large volume tissue defects, as a result of trauma or radical tumor resection, often require autologous tissue transfer for defect reconstruction. Although modern reconstructive surgery underwent a continuous development with regard to less invasive surgical methods, autologous tissue transplantation can be associated with a considerable donor site morbidity. The latter one and/or patient specific characteristics (such as previous operations, radiotherapy) can limit tissue availability. First described by O'Shaughnessy and later by Shen *et al* over four decades ago, the principle of flap prefabrication is a promising strategy to generate large vascularized tissues for defect reconstruction mainly in head/neck applications or burn surgery (O'shaughnessy 1936, Guo and Pribaz 2009). Flap prefabrication describes intrinsic vascularization due to the implantation of an axial vascular pedicle. Besides the distal ligation of an artery with its venae comitantes creating an arteriovenous bundle, arteriovenous loops (AVL) are used for flap prefabrication.

Since Erol and Spira first described neovascularization of skin flaps in rats upon implantation of an AVL, a continuous development of the rat AVL model evolved (Erol and Spira 1980). Basically, a venous interponate is microsurgically anastomosed between the femoral vein and artery forming an AVL. Vascularization originating from the AVL starts 10–14 d upon implantation (Polykandriotis *et al* 2008). However, not only tissues can be prefabricated upon implantation of AVL, but also biomaterials for the generation of bioartificial tissues. In this regard, we and others were able to show vascularization of various biomaterials based on alginate or fibrin (Polykandriotis *et al* 2008, Steiner *et al* 2018). Further, as a first attempt, recombinant engineered spider silk fibers have been tested in the AVL model (Steiner *et al* 2019). We have been able to demonstrate that the microvascular network originating from the AVL supports survival of transplanted cells, which is a crucial step for the successful generation of tissue engineering applications (Arkudas *et al* 2007). As mentioned above, hydrogels made of fibrin or alginate dialdehyde (ADA) cross-linked with gelatine (ADA-GEL) were assessed in the rat AVL model and were able to demonstrate scaffold vascularization, biocompatibility and biodegradation. Additionally, we confirmed that cells could be safely transplanted in fibrin and ADA-GEL hydrogels (Arkudas *et al* 2007, Steiner *et al* 2018, Winkler *et al* 2020). On the other hand, both biomaterials also have some disadvantages, such as an almost complete biodegradation after 4 weeks or the potential risk concerning the transmission of infectious agents in case of fibrin (Arkudas *et al* 2009). Moreover, natural polymers such as ADA-GEL have the great disadvantage of batch-to-batch inconsistency making the reproducible use in clinical application problematic (Fu *et al* 2010). Another promising biomaterial for tissue engineering applications is spider silk (Schacht *et al* 2015, Aigner *et al* 2018, Salehi *et al* 2020). Biotechnology allows the production of recombinant silk proteins with distinct material characteristics in high purity and quantity. In this regard, eADF4(C16) is a well-established spider silk protein based on the consensus sequence of *Araneus diadematus* Fibroin 4 (Huemmerich *et al* 2004). In a former AVL study we were able to show biocompatibility, high vascularization, and a slow biodegradation of eADF4(C16) fibrous matrices. Moreover, we were able to demonstrate that the scaffold ultrastructure had a strong influence on vascularization. In this regard we were able to show an inverse correlation between the degree of vascularization and the fiber diameter of eADF4(C16) scaffolds (Steiner *et al* 2019). Given the fact that smaller fiber diameters increase vascularization of eADF4(C16) scaffolds, here hydrogels made of eADF4(C16) were analyzed, which comprise nanofibrils as the basic building blocks (Schacht and Scheibel 2011, Humenik and Scheibel 2014). Since it has been previously shown that cell–silk interactions in hydrogels can be improved in the presence of an integrated RGD sequence (Schacht *et al* 2015, DeSimone *et al* 2017), the influence of the RGD sequence was investigated on vascularization, tissue formation, biocompatibility and biodegradation in the rat AVL model.

2. Materials and methods

2.1. Spider silk matrix preparation

The recombinant spider silk protein eADF4 (C16) consists of 16 repeats of the C-module (sequence: GSSAAAAAAAASGPGGYGPENQGPSG PGGYGPGG), a consensus motif mimicking the repetitive core sequence of the dragline silk fibroin 4 of the European garden spider (*A. diadematus*) (figure 1(A)) (Huemmerich *et al* 2004). As recombinant eADF4(C16) spider silk lacks cell binding motifs and materials made thereof display low cell adhesion behavior (Leal-egana *et al* 2012), an RGD-containing peptide for guided cell adhesion was genetically fused to eADF4(C16) by an established, seamless cloning strategy as described previously (figure 1(B)) (Huemmerich *et al* 2004, Wohlrab *et al* 2012). In brief, the functionalization was done on the genetic level using the eADF4(C16) gene construct, the DNA sequence encoding for the RGD peptide and appropriate cloning sites leading to the C-terminally modified eADF4(C16)-RGD variant. This cloning strategy also allowed the introduction of a T7 tag at the N-terminus of the protein enabling the detection by western blot analysis after protein purification. The recombinant spider silk protein eADF4(C16)-RGD was synthesized as a soluble protein in *Escherichia* coli BL21 gold (DE3) using a time-dependent fed-batch fermentation strategy as described previously (Huemmerich *et al* 2004, Wohlrab *et al* 2012). The subsequent protein purification was conducted according to an established protocol (Huemmerich *et al* 2004, Wohlrab *et al* 2012). In brief, after cell disruption using ultrasonication the soluble, recombinant spider silk protein eADF4(C16)-RGD was purified using a heat step for denaturation of residual *E. coli* proteins. Afterwards, an ammonium sulfate precipitation and washing steps with 8M urea and water were conducted. The precipitated spider silk particles were freeze dried and stored at −20 °C until further usage. The protein quality was verified using UV–Vis spectroscopy, sodium dodecyl sulfate polyacrylamide gel electrophoresis, western blot analysis and fluorescence spectroscopy as described previously (Huemmerich *et al* 2004, Wohlrab *et al* 2012).

To generate sterile spider silk hydrogels, all processing steps were conducted under a sterile hood with laminar flow. Furthermore, all used solutions were prepared with autoclaved double distilled

IOP Publishing Biofabrication 13 (2021) 045003 D Steiner et al

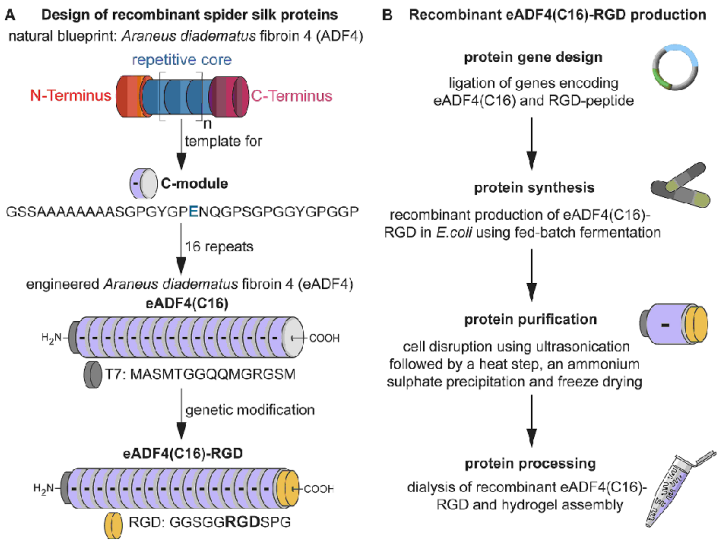

Figure 1. Synthesis of recombinant spider silk proteins. Illustration of the design of the recombinant spider silk eADF4(C16) and the functionalized eADF4(C16)-RGD variant based on the natural occurring *A. diadematus* fibroin 4 (A). Work-flow of the recombinant production or eADF4(C16)-RGD using protein gene design, recombinant synthesis, purification and processing steps (B).

water and sterile filtered stock solutions. The freeze-dried eADF4(C16) and eADF4(C16)-RGD spider silk powder was dissolved in 6M guanidinium thiocyanate (Carl Roth, Karlsruhe, Germany), sterile filtered (pore size 0.2 μm, Sartorius, Germany) and consequently dialyzed against 10 mM Tris/HCl (Carl Roth, Karlsruhe, Germany), pH 7.5 overnight at room temperature using dialysis membranes with a molecular weight cut-off of 6–8 kDa (Thermo Scientific, USA). Subsequent dialysis against 25% (w/v) polyethylene glycol (PEG, 35 000 g mol^{-1},) was conducted to increase the spider silk concentration to 30 mg ml^{-1} (3% w/v) by osmotic pressure driven removal of water. Afterwards, the silk solution was filled in sterile 1 ml syringes (Braun, Germany) and properly closed by parafilm. The gelation occurred by a physically driven assembly of spider silk nanofibrils overnight at 37 °C in a humidified incubator (Heracell, Thermo Scientific, Germany). The spider silk hydrogel containing syringes were sterile-packed in humid environment and stored at 4 °C until implantation.

2.2. Matrix implantation and AV loop operation

The Animal Care Committee of the University of Erlangen and the Government of Mittelfranken approved the animal experiments (AZ 55.2-2532-2-763). The animal experiments were carried out according to the EU Directive 2010/63/EU. Two experimental groups containing eADF4(C16) or eADF4(C16)-RGD hydrogels as scaffold material with an observation period of 4 weeks were designed. Additionally, we performed a eADF4(C16)-RGD subgroup with an observation period of 2 weeks. In the eADF4(C16) group five male Lewis rats with a body weight ranging from 300 to 360 g were used. The eADF4(C16)-RGD group encompassed eight male Lewis rats (Charles River Laboratories, Sulzfeld, Germany) with a body weight ranging from 329 to 373 g. Microsurgery was performed under general anesthesia with isoflurane (op-pharma, Burgdorf, Germany). Briefly, a vein graft from the contralateral leg was interconnected with the left femoral artery and vein forming the AVL. The microsurgical anastomosis for the AVL was performed using Ethilon 11-0 under an operating microscope (Carl Zeiss, Oberkochen, Germany). Afterwards, a Teflon isolation chamber (10 × 10 × 6 mm) was placed in the left groin and half filled with either the eADF4(C16) or eADF4(C16)-RGD hydrogel. Then, the AVL was placed on the matrix, the second half of the spider silk hydrogel was filled into the isolation chamber, and the lid was closed (figure 2). The Teflon isolation chamber was fixed onto the thigh musculature and the skin was closed. Postoperatively, the animals received enoxaparin adapted to the body weight (10 mg kg^{-1}) for 2 days.

2.3. Explantation procedure

Two and four weeks after surgery, intraarterial perfusion with Microfil® (Flow Tech Inc., Carver, USA) was carried out to visualize the vascular network.

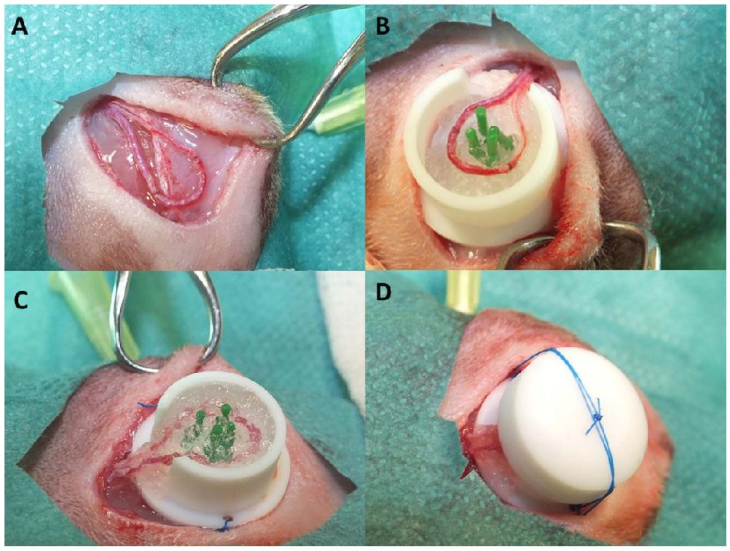

Figure 2. AVL operation. After the microsurgical anastomosis, the AVL was placed on a first layer of spider silk hydrogel (A), (B). Then, the AVL was covered with an additional layer of spider silk hydrogel and the Teflon chamber was closed with a lid (C), (D).

Briefly, a longitudinal laparotomy was performed, the aorta and caval vein identified and dissected. Thereafter, a thin cannula was inserted into the descending aorta, and the inferior caval vein was incised. After flushing the blood volume out with Ringer-heparin (100 IU ml^{-1}) solution, 20 ml yellow-colored Microfil® MV-122 solution with 1.0 ml curing agent was injected into the descending aorta. Polymerization occurred at 4 °C overnight. Afterwards, the constructs were explanted, embedded in Roti®-Histofix 4% (Carl Roth, Karlsruhe, Germany) and microcomputed tomography (μCT) as well as histological analysis were carried out.

2.4. μCT

The evaluation of the microstructure of the vessels in the explanted construct was done using high-resolution μCT scans with a Skyscan 1172 (Skyscan B.V., Leuven, Belgium) equipped with a 11 MP detector and a tungsten tube. The measurement was preformed using a voltage of 80 kV and a current of 100 mA in the oversize scan mode. Additionally, 0.5 mm Al filtering was applied to enhance the contrast of the filled vessels and ensure proper imaging. Each vessel scan was done with a rotation step of 0.23° over 180° and a resolution of 8.95 μm $voxel^{-1}$. The raw data sinograms were reconstructed by Radon back Transformation using the tomographic reconstruction software (NRecon Client and Server 1.6.10.1 with GPU support; Skyscan, Leuven, Belgium) after adjusting the X/Y alignment and joining the partial scans. The reconstructed two-dimensional (2D) cross-sections in 256 gray value levels were exported and the three-dimensional (3D) visual images were generated using an imaging software (Amira 2020.2; Thermo Fisher, Berlin, Germany). These gray value images were used for segmentation of the vessels by a global threshold with automatic 26-side growing algorithm on all layers plus an additional small island removal in the volume. The segmented so called label data was applied to the Autoskeleton module to determine the network structure of the vessels using global thinning algorithms (skeletonization). Using a histogram class width of 10 μm, an accumulated vessel length was calculated for each vessel radius class.

2.5. Histological staining

After μCT analysis, the constructs were embedded in paraffin and cut into 3 μm cross sections, perpendicular to the longitudinal axis of the AVL. According to standard protocols, haematoxylin and eosin (H&E) as well as smooth muscle actin (α-SMA) staining were carried out (Steiner *et al* 2019). As a surrogate parameter for biocompatibility, macrophages were visualized using CD68 staining. Briefly, a blocking solution (Zytomed Systems GmbH, Berlin, Germany) was added to the deparaffinized and rehydrated histological cross sections. Afterwards, an anti-CD68 primary antibody (1:300 dilution, BIO-RAD, Hercules, USA) was added and incubation performed overnight. Color reaction was performed using a second alkaline phosphatase-labeled anti-mouse antibody (AP-Polymer) and Fast Red

TR/Naphthol AS (Sigma) substrate. Haemalaun was used for counterstaining.

In order to differentiate between pro- (M1) and anti-inflammatory (M2) macrophages, we performed CD86 and CD163 immunostaining. After a cooking step for antigen retrieval, a blocking solution (Zytomed Systems GmbH, Berlin, Germany) was added to the deparaffinized and rehydrated histological specimen. Subsequently, either the diluted anti-CD86 (1:250, Abcam, Cambridge, USA) or anti-CD163 (1:500, Leica Biosystems Inc., Buffalo Grove, USA) antibody was added and incubation performed overnight. Staining was carried out using a second alkaline phosphatase-labeled anti-mouse antibody (AP-Polymer), Fast Red TR/Naphthol AS (Sigma) substrate and haemalaun for counterstaining. Endothelial cells were visualized using von Willebrand Factor (vWF) staining. Briefly, the deparaffinized histological cross sections were incubated with a diluted polyclonal vWF antibody (1:100, Biocare Medical, Pacheco, USA) over night. Color reaction was induced with HRP-Green Solution Set as indicated by the manufacturer (life sciences, Bremerhaven, Germany). To visualize matrix degradation as well as the interplay between matrix degradation and angiogenesis, matrix metallopeptidase 3 (MMP3) immunostaining was performed. For heat induced epitope retrieval, the deparaffinized and rehydrated slides were incubated in citrate buffer (pH value: 6) at 121 °C for one minute. Thereafter, the diluted anti-MMP3 antibody (1:50, Sigma-Aldrich, St. Louis, USA) was added to the slides. The slides were washed with Tris-buffered saline and the second antibody conjugated to peroxidase-labeled polymer (Dako REAL EnVision Detection System, Agilent Technologies, Carpinteria, USA) was applied. Afterwards, a further washing step occurred, and immunohistochemical staining was performed using the 3,3′ -Diamin-Benzidin (DAB) substrate. After color reaction the slides were washed with double distilled water and counterstained with hemalaun. Photographs of the histological cross sections were taken using an Olympus IX81 microscope (Olympus, Hamburg, Germany) and the Panoramic Flash scanner 250 and the software CaseViewer 2.4 (3DHISTECH, Budapest, Hungary).

2.6. Semi-automatic histological analysis and statistical methods

We used ImageJ Version 2 (NIH, Bethesda, MD, USA) to quantify vascularization of our constructs. First, the vessels were tagged with a black dot measuring exactly 10 pxl. Then, the microphotographs were transformed into 8 bit RGB color space, and the vessels were counted automatically. Vessel distribution was calculated using the FIJI processing package. Briefly, each marked vessel was assigned to one x- and y-coordinate and the distance between the coordinates of each vessel to the AVL measured. The newly formed tissue in the histological cross sections was marked in GIMP with the 'intelligent scissors' tool. The 'intelligent scissors' tool recognized the newly formed tissue as color difference between adjacent pixels (newly formed tissue vs spider silk) strengthening the objectivity of the evaluation. Subsequently, ImageJ quantified the size of the marked area. GraphPad Prism 7.00 (GraphPad Software, San Diego, USA) was used for statistical analysis. Results are shown as mean arbitrary units ± SD. The results were confirmed for normal distribution first. Thereafter, statistically significant differences were calculated using an unpaired student's t-test. p-values $\leqslant 0.05$ were considered as statistically significant. Due to matrix fragility of the eADF4(C16) constructs, no quantitative histological parameters as well as the construct weight were assessed excluding this experimental group from further statistical analysis.

3. Results

3.1. Postoperative course and macroscopical appearance

The animals tolerated the implantation procedure well. Besides a wound healing disorder in one animal in the eADF4(C16) group no surgical side effects occurred and the postoperative weight course remained unaffected. The Teflon chambers containing the eADF4(C16)-RGD hydrogels did not cause any complications regarding material incompatibility. Four out of five AVL (80%) were patent in the eADF4(C16) group, and all AVL (100%) were patent in the eADF4(C16)-RGD groups. After explantation, the spider silk scaffolds appeared yellow-colored confirming incipient vascularization (figures 3(A) and (B)). Interestingly, compared to eADF4(C16)-RGD explants, eADF4(C16) ones showed less stability, and the eADF4(C16) hydrogel matrix was very brittle.

3.2. Matrix degradation and biocompatibility of eADF4(C16) hydrogels

Comparing the explant weight of the 2 and 4 weeks eADF4(C16)-RGD group, statistically significant differences were detected (0.76 ± 0.03 vs 0.57 ± 0.04 g; $p \leqslant 0.001$; figure 3(C)). The eADF(C16) and the eADF(C16)-RGD group displayed no statistically significant differences after 4 weeks (figure 3(C)). Corresponding to the construct weight, also a statistically smaller construct size was found in the eADF4(C16)-RGD group after 4 weeks (41.1 ± 3.84 vs 57.3 ± 5.49 mm^2, $p \leqslant 0.01$; figure 3(D)). With regard to the initial cross-sectional area (60 cm^2), approximately 96% and 68.5% of the eADF4(C16)-RGD silk matrix were still present after 2 and 4 weeks. Due to matrix fragility the cross-sectional area was not determined in the eADF4(C16) group. Matrix metallopeptidase 3 (MMP-3) was detected in the newly formed tissue, especially in the vascularized construct parts (figure 4).

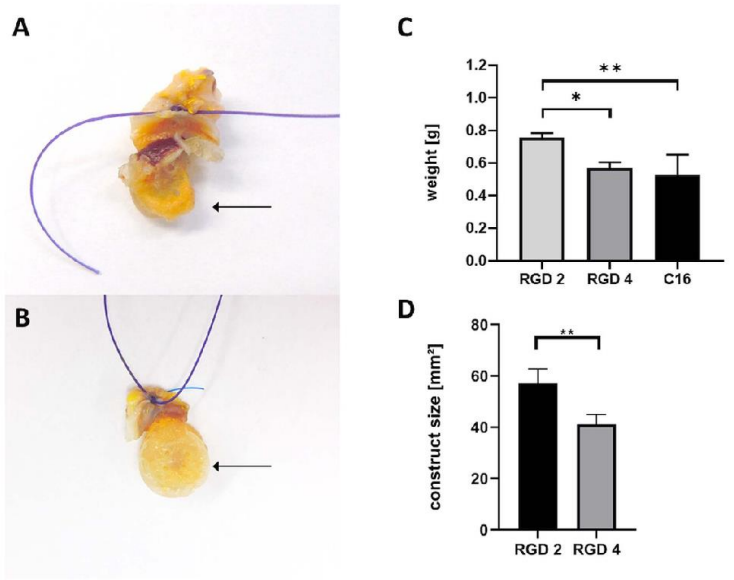

Figure 3. Macroscopic appearance, construct weight and size. The explanted specimen appeared yellow-colored after the perfusion with Microfil® as an indicator of vascularization. Note the arrow depicting the AVL vessels in the construct (A), (B). The eADF4(C16) matrix was very brittle (A) compared to the eADF4(C16)-RGD one (B) after 4 weeks. A significant lower weight was found in the eADF4(C16) and eADF4(C16)-RGD constructs after 4 weeks (RGD4) in comparison to the 2 weeks samples (RGD2) (C). The construct size was significant smaller after 4 weeks in the RGD group (D). Statistically significant differences are indicated for $^{**}p \leqslant 0.01$ and $^{***}p \leqslant 0.001$.

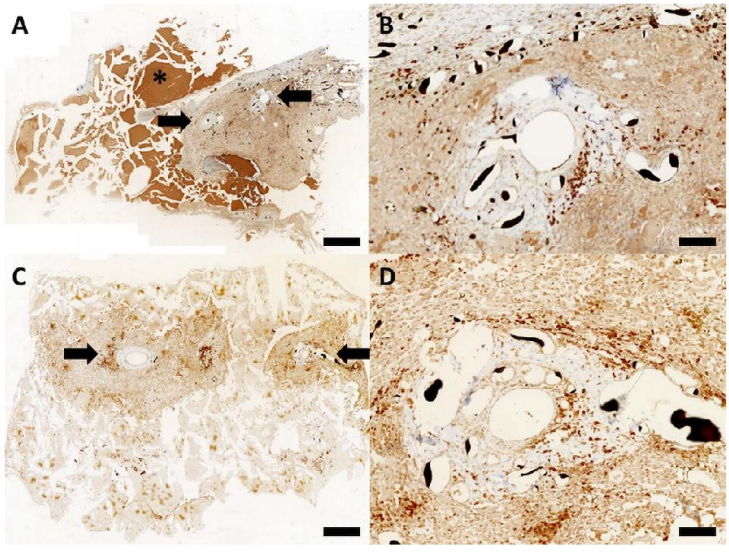

Figure 4. MMP-3 staining. Histological overview (A), (C) and detailed (B), (D) images depicting MMP-3 positive cells in eADF(C16) (A), (B) and eADF4(C16)-RGD hydrogels (C), (D) after 4 weeks. The bold bars indicate the AVL and the asterisk (*) the spider silk hydrogel. MMP-3 appears brown-stained. Note the black Microfil® inside the vessel lumen. Scale bar = 1 mm (A), (C) and 100 μm (B), (D).

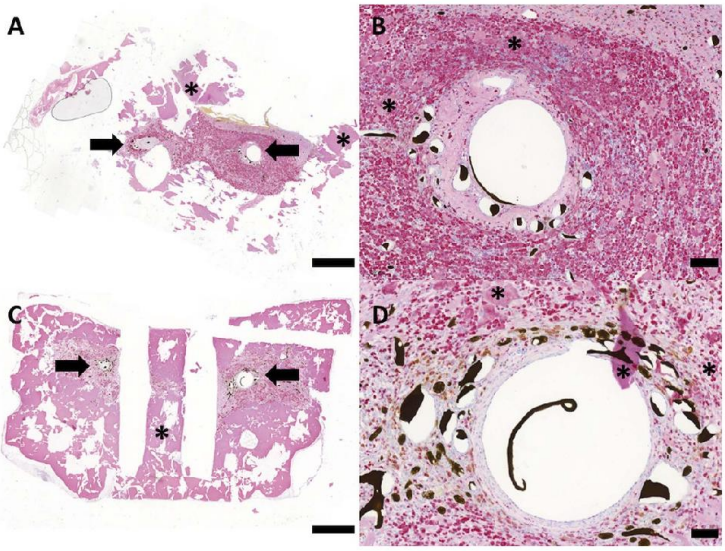

Figure 5. Macrophages as a surrogate parameter for biocompatibility. Macrophages were red-stained using an anti-CD68 antibody. Macrophages were present in the eADF4(C16) (A), (B) control and in the eADF4(C16)-RGD group (C), (D) after 4 weeks. The bold bars indicate the AVL and the asterisks (*) the spider silk hydrogel. Note the black Microfil® inside the vessel lumen. Scale bar = 1 mm (A), (C) and 100 μm (B), (D).

In order to describe the interaction between the newly formed tissue and the spider silk hydrogels in more detail, macrophages were visualized using CD68 staining. In both experimental groups, CD68 positive macrophages could be detected equally distributed in the fibrovascular tissue. No multinuclear giant cells as a surrogate parameter for foreign body reaction were present (figure 5).

To distinguish between pro- (M1) and anti-inflammatory (M2) macrophages, CD86 and CD163 immunostainings were carried out. After 4 weeks, M1 and M2 macrophage subtypes could be detected in the eADF4(C16) as well in the eADF4(C16)-RGD group. Both macrophage subtypes were located perivascular with no predominance of the pro- or anti-inflammatory subtype (figure 6).

3.3. *De novo* vascularized tissue formation inside eADF4(C16) hydrogels

Histological analysis with H&E staining showed newly formed, highly vascularized tissue between the eADF4(C16) and eADF4(C16)-RGD layers (figure 7). Consistent with the macroscopic appearance, the eADF4(C16) hydrogel matrix appeared very brittle in the histological cross sections (figures 7(A) and (B)). Furthermore, it seemed that the RGD sequence enhanced the stability of the constructs containing the eADF4(C16)-RGD silk (figures 7(C) and (E)). As a result of construct fragility, tissue formation and the vessel number were not quantified by histology in the eADF4(C16) group.

Quantifying *de novo* tissue formation in the eADF4(C16)-RGD group revealed a statistically significant higher amount of newly formed tissue after 4 weeks compared to 2 weeks (7.8 ± 1.88 vs 4 ± 0.84 mm^2, $p \leqslant 0.05$). A detailed view on the newly formed vascular network showed that the Microfil® was intraluminal located and not in the interstitium as a surrogate for vessel integrity. Furthermore, von-Willebrand-Factor (vWF) positive cells were found in the intima and α-SMA positive cells were found in the vessel media layer of the newly formed vessel network in the eADF4(C16) (figures 8(A) and (B)) and eADF4(C16)-RGD group (figures 8(C) and (D)). No significant differences regarding the vessel number per cross section were detected after 2 and 4 weeks in the eADF4(C16)-RGD group (235 ± 42 vs 191 ± 79). Furthermore, vessels were equally distributed around the AVL with a mean distance of 2.5 mm (figures 8(E) and (F)).

A holistic approach to visualize and to quantify the newly formed vessel network was performed using μCT scans. Increased vessel sprouting was observed in the eADF4(C16)-RGD specimen after 4 weeks compared to 2 weeks (figures 9(A) and (B)). Furthermore, vessel sprouting in the eADF4(C16) specimen appeared to be lower compared to the eADF4(C16)-RGD ones after 4 weeks (figure 9(C)).

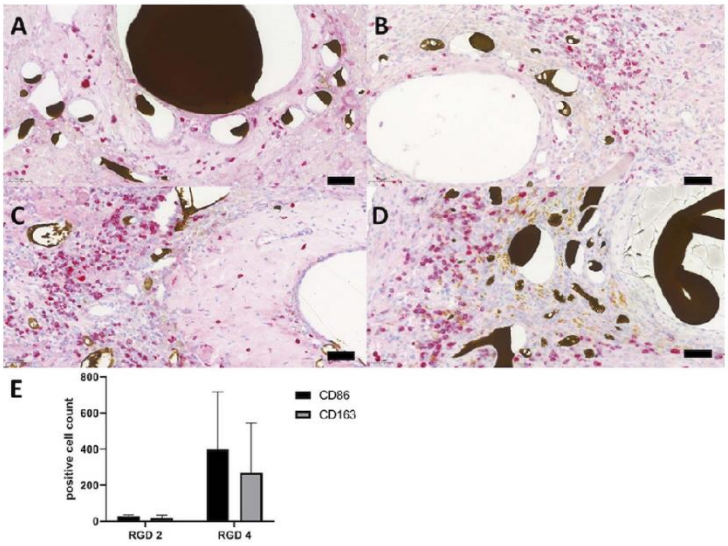

Figure 6. Immunohistochemical staining of anti-(M2) and pro-inflammatory (M1) macrophages. Anti-inflammatory (M2) macrophages were visualized using an anti-CD163 antibody (A), (C). Conversely, pro-inflammatory (M1) macrophages (B), (D) were stained with an anti-CD86 antibody. Histological images of the eADF4(C16) group are shown in (A), (B). Histological images of the eADF4(C16)-RGD group are shown in (C), (D). Equal numbers of M1 and M2 macrophages were found after 4 weeks in the eADF4(C16)-RGD group (E). Macrophages were red-stained. Note the black Microfil® inside the vessel lumen. Scale bar = 50 μm.

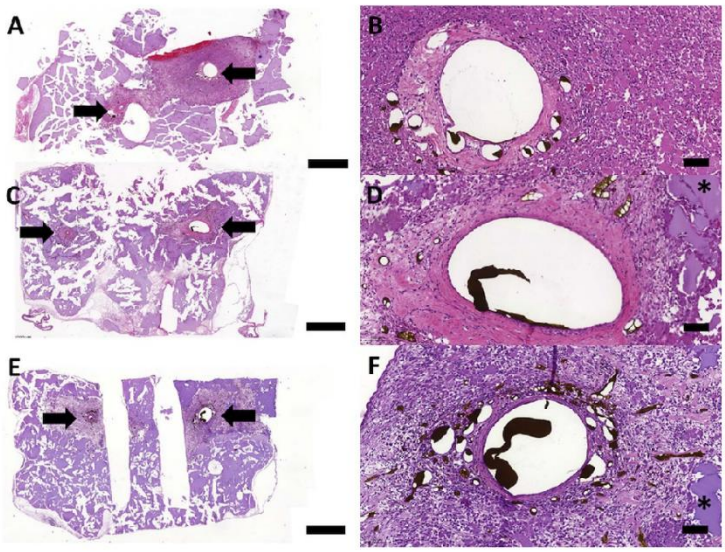

Figure 7. Histological overview and detailed images. The histological specimen were stained with H&E and microphotographs were taken. Newly formed vascularized tissue was found in all groups. In contrast to the eADF4(C16) control group (A), (B), the eADF4(C16)-RGD group displayed a stable matrix after 2 (C), (D) and 4 weeks (E), (F). The bold bars indicate the AVL and the asterisks (*) the spider silk hydrogel. Note the black Microfil® inside the vessel lumen. Scale bar = 1 mm (A), (C), (E) and 100 μm (B), (D), (F).

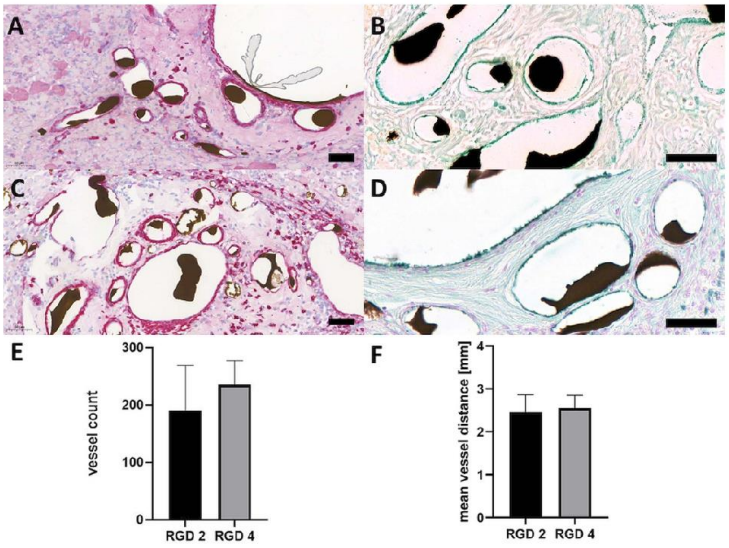

Figure 8. Detailed view on vascularization using α-SMA and vWF staining. The newly formed vessels were red-stained for α-SMA (A), (C). Endothelial cells were green-stained for vWF (B), (D). Histological images of the eADF4(C16) group are shown in (A), (B). Histological images of the eADF4(C16)-RGD group are shown in (C), (D). Note the black Microfil® located inside the vessel lumen. Scale bar = 50 μm. No statistically significant differences were observed concerning the total vessel number per histological cross section (E) and mean vessel distance (F) in the eADF4(C16)-RGD group after 2 (RGD 2) and 4 weeks (RGD4).

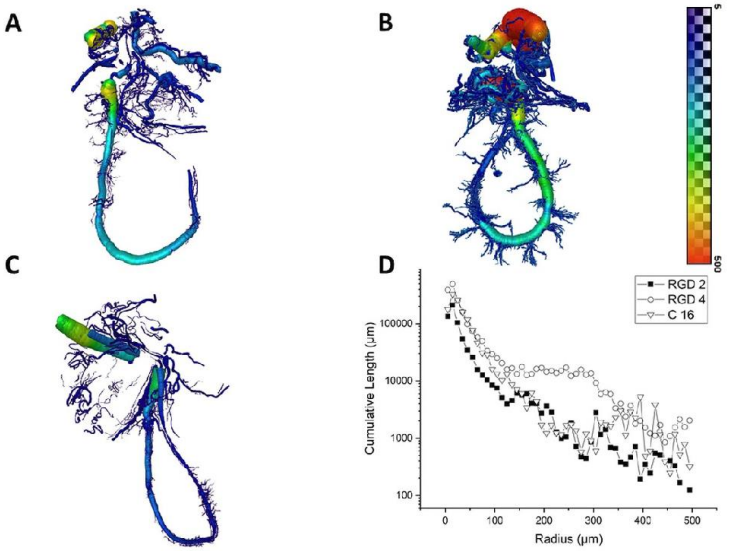

Figure 9. Microcomputer tomography (μCT). After 2 and 4 weeks the eADF4(C16)-RGD (A), (B) and eADF4(C16) group (C) were perfused with Microfil® and underwent μCT analysis. After 4 weeks, a significant increase of vessel formation was detected (B) and quantified by calculating the cumulative vessel length in the eADF4(C16)-RGD group (RGD 4) (D). Note the lower vessel sprouting in the eADF4(C16) group after 4 weeks (C). The scale bar depicts the mean vessel radius in micrometers.

Total length of the newly formed vascular network was assessed by calculating the cumulative vessel length in both experimental groups. In this regard, a statistically significant larger vessel network was found after 4 weeks, if the eADF4(C16) silk matrix contained RGD-motifs (2016.2 ± 83.5 vs 1376.8 ± 54.3 mm; $p \leqslant 0.001$). Moreover, a larger vessel network was detected in the eADF4(C16)-RGD constructs with increasing implantation time (2016.2 ± 83.5 mm after 2 weeks vs 690.3 ± 34.2 mm after 2 weeks; $p \leqslant 0.0001$) (figure 9(D)). Additionally, the diameter of the AVL increased over the implantation time in the eADF4(C16)-RGD specimen. In this regard, the AVL diameter displayed a range between 160 and 230 μm after 2 weeks compared to 230–470 μm after 4 weeks. Furthermore, a larger vessel diameter was observed in the eADF4(C16)-RGD specimen (230–470 μm) compared to the eADF4(C16) ones (290–420 μm) after 4 weeks.

4. Discussion

The successful generation of bioartificial tissues is critically linked to bioactive scaffolds providing an extracellular matrix-like milieu for transplanted cells as well as sufficient vascularization (Schacht *et al* 2015, Horch *et al* 2018, Weigand *et al* 2018, Schmid *et al* 2020, Winkler *et al* 2020). The ideal scaffold biomaterial displays a good biocompatibility and supports vascularization of Tissue Engineering applications. Silk-based scaffolds are promising biomaterials, and biotechnology allows the production of large quantities of high pure custom made silk proteins without batch-to-batch inconsistencies enabling the translational 'from bench to bedside' approach with regard to clinical implementation. In this context, Scheibel *et al* established a silk protein based on the consensus sequence of *A. diadematus* Fibroin 4 (eADF4(C16); MW 48 kDa) (Huemmerich *et al* 2004, Petzold *et al* 2017, Saric and Scheibel 2019, Salehi *et al* 2020). In previous studies, we and others, have demonstrated that silk-based scaffolds are biocompatible without provoking immunological reaction (Zeplin *et al* 2014, Ju *et al* 2016, Zhang *et al* 2017, Steiner *et al* 2019, Hashimoto *et al* 2020, Kramer *et al* 2020). In the present study we were able to show macrophages at the interface between the newly formed tissue and eADF4(C16) hydrogels. Although macrophages positive for CD68 were present after 2 and 4 weeks, no multinuclear giant cells were found indicating the absence of a foreign body reaction. It is worth noting that it has been shown previously that eADF4(C16)-materials are not pro-inflammatory and do not induce unspecific immune responses (Lucke *et al* 2018). Furthermore, the proportion of pro- (CD86) and anti-inflammatory macrophages appeared to be equally underlining the low immunogenicity of silk-based biomaterials (Klopfleisch 2016, Cha *et al* 2017, Liu *et al* 2018). The tripeptide sequence arginine–glycine–aspartic acid (RGD) is well known to support cell adhesion and signal transduction (Wang *et al* 2013). Several extracellular matrix proteins, such as collagens or fibrinogen, display the RGD-motif. These so-called matrikines are involved in extracellular matrix-mediated signal transduction via RGD-motifs and integrins (Hynes 2002a, 2002b, 2009, Ricard-blum and Salza 2014). Several studies demonstrated that biofunctionalizing scaffold materials with the RGD-motif supports recellularization, tissue formation and scaffold integration (Chen *et al* 2011, Kim *et al* 2016, Antonova *et al* 2016a, 2016b). In previous studies, eADF4(C16) has been biofunctionalized with the RGD-motif by genetic engineering leading to enhanced cell attachment, proliferation and viability on materials made thereof (Wohlrab *et al* 2012, Schacht *et al* 2015, DeSimone *et al* 2017, Kramer *et al* 2020). Bearing in mind that vascularization of silk-based scaffolds can be fine-tuned by the fiber diameter and that the RGD-motif supports tissue formation nano-fibrillary eADF4(C16) based hydrogels with and without RGD-sequences were analyzed in the present study (Safari *et al* 2019, Steiner *et al* 2019). Compared to other hydrogels also containing the RGD-motif, such as alginate dialdehyde gelatine (ADA-GEL) or fibrin, we were able to detect significantly more vessels per histological cross section in the eADF4(C16)-RGD group than in fibrin or ADA-GEL after 4 weeks (Arkudas *et al* 2009, Steiner *et al* 2018) (table 1). In a previous study electrospun eADF4(C16) fibrous matrices were filled into a Teflon chamber and vascularized over 4 weeks by means of an AVL (Steiner *et al* 2019). Interestingly, a significant higher construct vascularization was found after 4 weeks in the eADF4(C16)-RGD group compared to the electrospun one as indicated by the vessel number per histological cross section. Our findings are consistent with the cumulative vessel length measured in the μCT indicating the largest vessel network in the eADF4(C16)-RGD group compared to electrospun eADF4(C16) or ADA-GEL after 4 weeks (table 1). Comparing the AVL diameter one might get the impression that the AVL angiogenic potential correlates with the latter one. Considering the histological and μCT findings assessing vascularization after 2 and 4 weeks one has to bear in mind that two different methodologies were used. In this context histology only allows a two-dimensional analysis whereas the μCT enables the exact three-dimensional approach. Interestingly, compared to eADF4(C16)-RGD explants, eADF4(C16) ones showed less stability and the eADF4(C16) hydrogel matrix was very brittle. That was not surprising, because in previous studies 3% (w/v) eADF4(C16) hydrogels displayed lower mechanical properties compared to 3% (w/v) eADF4(C16)-RGD hydrogels. Rheological

Table 1. After 4 weeks, hydrogels consisting of eADF4(C16)-RGD display a higher vascularization and a slower biodegradation compared to ADA-GEL or fibrin. Although vascularization is enhanced in the eADF4(C16)-RGD scaffold, the biodegradation is equal compared to previously published electrospun (ES) eADF4(C16) spider silk scaffolds. Besides the cumulative vessel length (μCT) the other parameters were assessed by histology. Matrix degradation is shown as percentage of the remaining cross-sectional area compared to the initial cross-sectional area (60 mm^2). n.a. = not assessed.

	eADF4(C16)-RGD	eADF4(C16)	ES eADF4(C16)	ADA-GEL	Fibrin
Cumulative vessel length (mm)	2016.2 ± 83.5	1376.8 ± 54.3	477 ± 586	20.8 ± 8	n.a.
Vessel number	235 ± 42	n.a.	99 ± 52	31 ± 24	107 ± 25
Cross-sectional area (mm^2)	41.1 ± 3.8	n.a.	39.7 ± 3.2	14.6 ± 3.7	2.9 ± 1.2
Matrix degradation (%)	31.5	n.a.	33.9	75.7	95.2

analysis revealed that 3% (w/v) eADF4(C16)-RGD hydrogels displayed higher storage and loss moduli compared to eADF4(C16) hydrogels. Furthermore, the elastic modulus of 3% (w/v) eADF4(C16)-RGD hydrogels was ten times higher compared to 3% (w/v) eADF4(C16) ones leading to a higher stiffness of the RGD-tagged silk hydrogel (Schacht *et al* 2015). Using transmission electron microscopy, it could be shown that the nano-fibrillary network of 3% (w/v) eADF4(C16)-RGD hydrogels was slightly denser packed compared to 3% (w/v) eADF4(C16) hydrogels (DeSimone *et al* 2016). Nevertheless, although shear stress and viscosity of 3% (w/v) eADF4(C16)-RGD hydrogels were higher in comparison to 3% (w/v) eADF4(C16) hydrogels, both hydrogels showed viscoelastic and shear-thinning behavior (Schacht *et al* 2015). Beyond providing structural support for transplanted cells, a scaffold should be biodegradable with an inverse correlation between *de novo* tissue formation and degradation rate without producing toxic metabolites (Fan and Wang 2015). The recombinant spider silk scaffolds were slowly degraded providing structural support until the new tissue is formed. Biodegradation was slow with 96% and 68.5% of the eADF4(C16)-RGD matrix remaining after 2 and 4 weeks, respectively. The histologic cross-sectional area was used after 4 weeks as surrogate parameter for biodegradation in order to compare the eADF4(C16)-RGD with other biomaterials from previous AVL studies. A faster biodegradation was found, if the Teflon chambers contained fibrin or ADA-GEL (Arkudas *et al* 2009, Steiner *et al* 2018). No differences regarding biodegradation were found, if electrospun eADF4(C16) fibrous matrices were implanted in the AVL model instead of eADF4(C16)-RGD (Steiner *et al* 2019).

Further, matrix metallopeptidases (MMPs) are critically involved in extracellular matrix degradation during tissue remodeling and angiogenesis (Chang and Werb 2001, Pepper 2001). In a recent study, Jo *et al* demonstrated that matrix metallopeptidase 3 (MMP-3) can degrade silk fibroin (2017). Immunohistochemical staining revealed an accumulation of MMP-3 in the newly formed fibrovascular tissue suggesting a close relationship between angiogenesis and spider silk degradation. Furthermore, we confirmed that recombinant eADF4(C16)-RGD spider silk hydrogels are perfectly suitable for *de novo* tissue formation. In comparison to *de novo* tissue formation after 2 weeks, significant more newly formed tissue was generated in the eADF4(C16)-RGD group after 4 weeks. Compared to electrospun spider silk fibrous matrices without RGD-motif from a previous AVL study, the nano-fibrillary eADF4(C16)-RGD hydrogels displayed more newly formed tissue after 4 weeks (Steiner *et al* 2019).

5. Conclusion

This study successfully demonstrated intrinsic vascularization of eADF4(C16)-RGD spider silk hydrogels in the rat AVL model without causing foreign body reaction. The biocompatible spider silk scaffolds provide structural integrity allowing cell infiltration enabling *de novo* tissue formation accompanied with slow matrix degradation. Our work clearly showed that functionalized recombinant spider silk hydrogels could be used for direct implantations leading to an enhanced tissue formation and vascularization. Furthermore, there is the opportunity to encapsulate tissue specific cells in the silk hydrogels before implantation to generate bioartificial tissues.

Data availability statement

The data that support the findings of this study are available upon reasonable request from the authors.

Acknowledgments

This study was supported by Deutsche Forschungsgemeinschaft (DFG, German Research Foundation)—Project Number 326998133–TRR 225 (subprojects C01 (T S) and C04 (R E H)) and DFG SCHE 603/24-1 (T S).

Conflict of interest

T S is co-founder and shareholder of AMSilk GmbH.

ORCID iDs

Dominik Steiner https://orcid.org/0000-0002-1904-5925
Stefanie Heltmann-Meyer https://orcid.org/0000-0002-3097-854X
Thomas Scheibel https://orcid.org/0000-0002-0457-2423

References

Aigner T B, DeSimone E and Scheibel T 2018 Biomedical applications of recombinant silk-based materials *Adv. Mater.* **30** e1704636
Antonova L V *et al* 2016a Bioabsorbable bypass grafts biofunctionalised with RGD have enhanced biophysical properties and endothelialisation tested *in vivo Front. Pharmacol.* **7** 136
Antonova L V *et al* 2016b Conjugation with RGD peptides and incorporation of vascular endothelial growth factor are equally efficient for biofunctionalization of tissue-engineered vascular grafts *Int. J. Mol. Sci.* **17** 1920
Arkudas A, Beier J P, Heidner K, Tjiawi J, Polykandriotis E, Srour S, Sturzl M, Horch R E and Kneser U 2007 Axial prevascularization of porous matrices using an arteriovenous loop promotes survival and differentiation of transplanted autologous osteoblasts *Tissue Eng.* **13** 1549–60
Arkudas A, Pryymachuk G, Hoereth T, Beier J P, Polykandriotis E, Bleiziffer O, Horch R E and Kneser U 2009 Dose-finding study of fibrin gel-immobilized vascular endothelial growth factor 165 and basic fibroblast growth factor in the arteriovenous loop rat model *Tissue Eng.* A **15** 2501–11
Cha B-H *et al* 2017 Integrin-mediated interactions control macrophage polarization in 3D hydrogels *Adv. Healthcare Mater.* **6** 1700289
Chang C and Werb Z 2001 The many faces of metalloproteases: cell growth, invasion, angiogenesis and metastasis *Trends Cell Biol.* **11** S37–43
Chen J *et al* 2011 *In-vivo* study of adhesion and bone growth around implanted laser groove/RGD-functionalized Ti-6Al-4V pins in rabbit femurs *Mater. Sci. Eng.* C **31** 826–32
DeSimone E, Schacht K, Pellert A and Scheibel T 2017 Recombinant spider silk-based bioinks *Biofabrication* **9** 044104
DeSimone E, Schacht K and Scheibel T 2016 Cations influence the cross-linking of hydrogels made of recombinant, polyanionic spider silk proteins *Mater. Lett.* **183** 101–4
Erol Ö O and Spira M 1980 New capillary bed formation with a surgically constructed arteriovenous fistula *Plast. Reconstr. Surg.* **66** 109–15
Fan C J and Wang D-A 2015 A biodegradable PEG-based micro-cavitary hydrogel as scaffold for cartilage tissue engineering *Eur. Polym. J.* **72** 651–60
Fu S, Thacker A, Sperger D M, Boni R L, Velankar S, Munson E J and Block L H 2010 Rheological evaluation of inter-grade and inter-batch variability of sodium alginate *AAPS PharmSciTech* **11** 1662–74
Guo L and Pribaz J J 2009 Clinical flap prefabrication *Plast. Reconstr. Surg.* **124** e340–50
Hashimoto T, Kojima K and Tamada Y 2020 Higher gene expression related to wound healing by fibroblasts on silk fibroin biomaterial than on collagen *Molecules* **25** 1939
Horch R E, Weigand A, Wajant H, Groll J, Boccaccini A R and Arkudas A 2018 Biofabrication: new approaches for tissue regeneration *Handchir. Mikrochir. Plast. Chir.* **50** 93–100
Huemmerich D, Helsen C W, Quedzuweit S, Oschmann J, Rudolph R and Scheibel T 2004 Primary structure elements of spider dragline silks and their contribution to protein solubility *Biochemistry* **43** 13604–12
Humenik M and Scheibel T 2014 Nanomaterial building blocks based on spider silk-oligonucleotide conjugates *ACS Nano* **8** 1342–9
Hynes R O 2002a Integrins: bidirectional, allosteric signaling machines *Cell* **110** 673–87
Hynes R O 2002b A reevaluation of integrins as regulators of angiogenesis *Nat. Med.* **8** 918–21
Hynes R O 2009 The extracellular matrix: not just pretty fibrils *Science* **326** 1216–9
Jo Y-Y *et al* 2017 Accelerated biodegradation of silk sutures through matrix metalloproteinase activation by incorporating 4-hexylresorcinol *Sci. Rep.* **7** 42441
Ju H W *et al* 2016 Wound healing effect of electrospun silk fibroin nanomatrix in burn-model *Int. J. Biol. Macromol.* **85** 29–39
Kim S, Cui Z-K, Fan J, Fartash A, Aghaloo T L and Lee M 2016 Photocrosslinkable chitosan hydrogels functionalized with the RGD peptide and phosphoserine to enhance osteogenesis *J. Mater. Chem.* B **4** 5289–98
Klopfleisch R 2016 Macrophage reaction against biomaterials in the mouse model—phenotypes, functions and markers *Acta Biomater.* **43** 3–13
Kramer J P M, Aigner T B, Petzold J, Roshanbinfar K, Scheibel T and Engel F B 2020 Recombinant spider silk protein eADF4(C16)-RGD coatings are suitable for cardiac tissue engineering *Sci. Rep.* **10** 8789
Leal-egana A, Lang G, Mauerer C, Wickinghoff J, Weber M, Geimer S and Scheibel T 2012 Interactions of fibroblasts with different morphologies made of an engineered spider silk protein *Adv. Eng. Mater.* **14** B67–B75
Liu B, Zhang M, Zhao J, Zheng M and Yang H 2018 Imbalance of M1/M2 macrophages is linked to severity level of knee osteoarthritis *Exp. Ther. Med.* **16** 5009–14
Lucke M *et al* 2018 Engineered hybrid spider silk particles as delivery system for peptide vaccines *Biomaterials* **172** 105–15
O'shaughnessy L 1936 An experimental method of providing a collateral circulation to the heart *Br. J. Surg.* **23** 665–70
Pepper M S 2001 Role of the matrix metalloproteinase and plasminogen activator-plasmin systems in angiogenesis *Arterioscler. Thromb. Vasc. Biol.* **21** 1104–17
Petzold J, Aigner T B, Touska F, Zimmermann K, Scheibel T and Engel F B 2017 Surface features of recombinant spider silk protein eADF4(kappa 16)-made materials are well-suited for cardiac tissue engineering *Adv. Funct. Mater.* **27** 1701427
Polykandriotis E, Tjiawi J, Euler S, Arkudas A, Hess A, Brune K, Greil P, Lametschwandtner A, Horch R E and Kneser U 2008 The venous graft as an effector of early angiogenesis in a fibrin matrix *Microvasc. Res.* **75** 25–33
Ricard-blum S and Salza R 2014 Matricryptins and matrikines: biologically active fragments of the extracellular matrix *Exp. Dermatol.* **23** 457–63
Safari Z, Soudi S, Jafarzadeh N, Hosseini A Z, Vojoudi E and Sadeghizadeh M 2019 Promotion of angiogenesis by M13 phage and RGD peptide *in vitro* and *in vivo Sci. Rep.* **9** 11182
Salehi S, Koeck K and Scheibel T 2020 Spider silk for tissue engineering applications *Molecules* **25** 737
Saric M and Scheibel T 2019 Engineering of silk proteins for materials applications *Curr. Opin. Biotechnol.* **60** 213–20
Schacht K, Jungst T, Schweinlin M, Ewald A, Groll J and Scheibel T 2015 Biofabrication of cell-loaded 3D spider silk constructs *Angew. Chem., Int. Ed. Engl.* **54** 2816–20
Schacht K and Scheibel T 2011 Controlled hydrogel formation of a recombinant spider silk protein *Biomacromolecules* **12** 2488–95
Schmid R *et al* 2020 Comparison of hydrogels for the development of well-defined 3D cancer models of breast cancer and melanoma *Cancers* **12** 2320
Steiner D *et al* 2018 Encapsulation of mesenchymal stem cells improves vascularization of alginate-based scaffolds *Tissue Eng.* A **24** 1320–31
Steiner D, Lang G, Fischer L, Winkler S, Fey T, Greil P, Scheibel T, Horch R E and Arkudas A 2019 Intrinsic vascularization of

recombinant eADF4(C16) spider silk matrices in the arteriovenous loop model *Tissue Eng.* A **25** 1504–13
Wang F, Li Y, Shen Y, Wang A, Wang S and Xie T 2013 The functions and applications of RGD in tumor therapy and tissue engineering *Int. J. Mol. Sci.* **14** 13447–62
Weigand A, Horch R E, Boos A M, Beier J P and Arkudas A 2018 The arteriovenous loop: engineering of axially vascularized tissue *Eur. Surg. Res.* **59** 286–99
Winkler S *et al* 2020 Human umbilical vein endothelial cell support bone formation of adipose-derived stem cell-loaded and 3D-printed osteogenic matrices in the arteriovenous loop model *Tissue Eng.* A **7** 413–23
Wohlrab S, Muller S, Schmidt A, Neubauer S, Kessler H, Leal-egana A and Scheibel T 2012 Cell adhesion and proliferation on RGD-modified recombinant spider silk proteins *Biomaterials* **33** 6650–9
Zeplin P H, Maksimovikj N C, Jordan M C, Nickel J, Lang G, Leimer A H, Römer L and Scheibel T 2014 Spider silk coatings as a bioshield to reduce periprosthetic fibrous capsule formation *Adv. Funct. Mater.* **24** 2658–66
Zhang W *et al* 2017 Silk fibroin biomaterial shows safe and effective wound healing in animal models and a randomized controlled clinical trial *Adv. Healthcare Mater.* **6** 1700121

7.11. Teilarbeit XI

Teilarbeit XI wurde 2020 unter dem Titel „Multifunctional Biomaterials: Combining Material Modification Strategies for Engineering of Cell-Contacting Surfaces“ im Journal *ACS Applied Materials & Interfaces* veröffentlicht.

Mertgen, A.-S.*; **Trossmann, V. T**.*.; Guex, A. G.[§]; Maniura-Weber, K.; Scheibel, T. & Rottmar, M.[§] (2020) Multifunctional Biomaterials: Combining Material Modification Strategies for Engineering of Cell-Contacting Surfaces. *ACS Applied Materials & Interfaces* **12**: 21342.

https://doi.org/10.1021/acsami.0c01893

* gleichberechtigte Co-Autorenschaft

[§] gleichberechtige korrespondierende Co-Autorenschaft

ACS APPLIED MATERIALS & INTERFACES

www.acsami.org Review

Multifunctional Biomaterials: Combining Material Modification Strategies for Engineering of Cell-Contacting Surfaces

Anne-Sophie Mertgen,[†] Vanessa Tanja Trossmann,[†] Anne Géraldine Guex,* Katharina Maniura-Weber, Thomas Scheibel, and Markus Rottmar*

Cite This: *ACS Appl. Mater. Interfaces* 2020, 12, 21342−21367 Read Online

ACCESS | Metrics & More | Article Recommendations

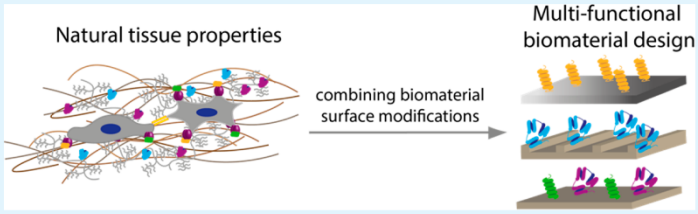

ABSTRACT: In the human body, cells in a tissue are exposed to signals derived from their specific extracellular matrix (ECM), such as architectural structure, mechanical properties, and chemical composition (proteins, growth factors). Research on biomaterials in tissue engineering and regenerative medicine aims to recreate such stimuli using engineered materials to induce a specific response of cells at the interface. Although traditional biomaterials design has been mostly limited to varying individual signals, increasing interest has arisen on combining several features in recent years to improve the mimicry of extracellular matrix properties. Tremendous progress in combinatorial surface modification exploiting, for example, topographical features or variations in mechanics combined with biochemical cues has enabled the identification of their key regulatory characteristics on various cell fate decisions. Gradients especially facilitated such research by enabling the investigation of combined continuous changes of different signals. Despite unravelling important synergies for cellular responses, challenges arise in terms of fabrication and characterization of multifunctional engineered materials. This review summarizes recent work on combinatorial surface modifications that aim to control biological responses. Modification and characterization methods for enhanced control over multifunctional material properties are highlighted and discussed. Thereby, this review deepens the understanding and knowledge of biomimetic combinatorial material modification, their challenges but especially their potential.

KEYWORDS: *biofunctionalization, biomaterials, multifunctionality, biointerface, cell interaction, biochemical functionalization, topographical functionalization, biomimetic*

1. INTRODUCTION

The interaction of implant materials or engineered tissues with their environment and surrounding cells is decisive for their success. Depending on the application, different levels of integration in and interaction of the materials with their surroundings are needed. Although bioinert materials should interact minimally with the surrounding tissue, bioactive or biomimetic materials are designed to actively engage with their biological environment by directing, supporting, and stimulating cellular responses.[1−5] Bioinert materials are important in many applications, e.g., blood contacting devices that have to minimize protein adsorption and prevent blood coagulation on their surfaces.[3,6,7] Surface modification of materials with active or inductive properties creates biointerfaces that have to be specifically designed and functionalized according to the desired target tissue or application in the body.[8−13]

Biomaterials design for tissue engineering and regenerative strategies has been traditionally inspired to mimic single aspects like mechanics, topography, or a chemical cue from the complex natural extracellular matrix (ECM). By combining at least two of those ECM characteristics on multifunctional engineered materials, mimicry of the ECM is enhanced, and elucidation of the interplay between various signals and their effect on cellular behavior can provide a better understanding of material−tissue interactions.

Received: January 31, 2020
Accepted: April 13, 2020
Published: April 14, 2020

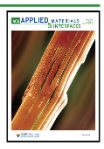

https://dx.doi.org/10.1021/acsami.0c01893
ACS Appl. Mater. Interfaces 2020, 12, 21342−21367

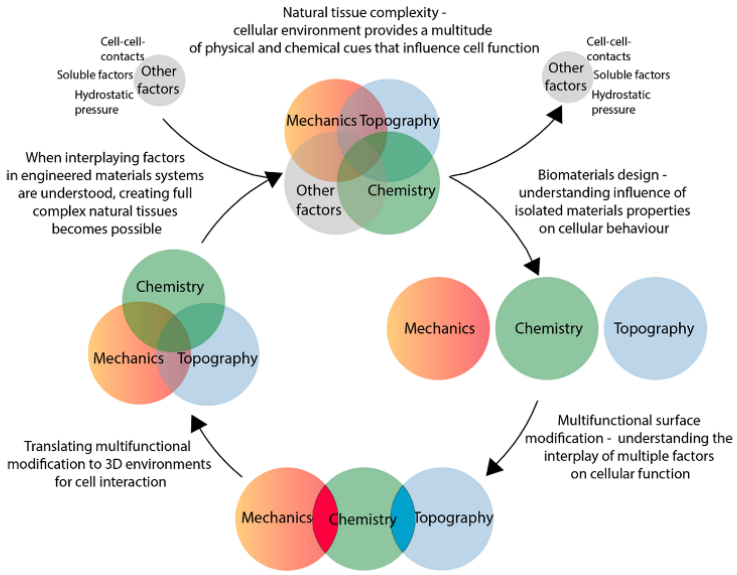

Figure 1. Schematic representing the complexity of the extracellular environment in general and the natural extracellular matrix in particular. Recreating this, combinatorial material functionalization represents a strategy toward biomimetic material design.

Tissues are sophisticated and highly dynamic systems. Their multifunctional microenvironments instruct cellular behavior via a complex interplay of multiple biochemical and physical cues from the ECM, soluble factors such as growth factors, cell–cell contacts, and hydrostatic pressure.[14,15] Depending on the tissue type, distinct compositions of these components induce different mechanics or topography because of altered protein fibril structures and composition of the ECM, influencing cell behavior.[16−24] Cells interact with the ECM in a complex interplay of biochemical and mechanobiological processes. For instance, the adhesion to ECM proteins is mediated via transmembrane proteins (integrins) that recognize specific amino acid sequences (adhesion peptides).[25] However, the generally inactive integrins need to be activated by focal adhesion proteins, which in turn are activated by transmembrane kinases or growth factor receptors.[17,26] The resulting focal adhesion complexes respond to physical and mechanical stimuli by interaction with and alteration of the cytoskeletal organization.[27]

Most tissues, however, are not defined by a definite mechanical value, one topographical feature, or fixed ECM and growth factor composition but consist of gradients or heterogenic distributions. Biophysical and biochemical gradients are known to steer cellular migration and differentiation during embryogenesis, tissue remodeling and regeneration, inflammation, or disease.[28−31] Gradual distributions of such properties are also a prominent structural hallmark in tissues that bridge between two distinct types of tissues, such as in the tendon-to-bone transition zone or in the osteochondral tissue.[32,33]

Because most unmodified synthetic materials do not present suitable surface properties for interaction with living cells and tissues, they require modification or functionalization. To this end, many strategies have been developed to design specific biointerfaces mimicking individual characteristics of natural ECM of the target tissue[5,11,34−40] (Figure 1).

Approaches to controlling cell behavior through the design of biomaterial surfaces have been reviewed recently[11,41,42] and include, for example, surface functionalization with ligands for direct interaction with cellular transmembrane receptors such as ECM proteins, growth factors, or their functional fragments (peptides). Cellular adhesion, cytoskeleton formation, and differentiation can also be influenced by engineering mechanical properties of biomaterials to match the respective cellular environment.[43−45]

Cell behavior is furthermore strongly influenced by the surface roughness (density and dimension of presented topographical surface patterns) of biomaterials,[46] with a highly cell-type specific response to the range and scale of topographical features.[47−51] Especially, differentiation, gene expression, and cell fate decisions of different cell types are affected by various surface topographies.[51−55] Although the size of individual cells is in the micrometer range, they interact with submicrometer-topographical features by actin-fibril-driven filopodia,[55] which contain integrin receptors that identify surface features of just 10 nm in height.[56,57] In this context, studies with ordered and disordered RGD-functionalized gold nanopatterns showed that a distance of around 70 nm between RGD ligands was the crucial ligand density for adhesion of various cell types.[58−62] Furthermore, biochemical, mechanical, or structural gradients can be created to mimic naturally graded tissue or to study cell migration as a function of changing substrate properties.[39,63−69] In the following sections, synergistic effects of combinatorial material modifications on different biological systems and characterization of such systems are presented and discussed, whereas the ones that currently provide the best control over material properties are highlighted.

2. SYNERGISTIC EFFECTS OF MULTIFUNCTIONAL MATERIALS ON CELLULAR INTERACTION

2.1. Combining Chemical Surface Modifications. *Combinations of Various ECM proteins, Growth Factors, and Their*

https://dx.doi.org/10.1021/acsami.0c01893
ACS Appl. Mater. Interfaces 2020, 12, 21342−21367

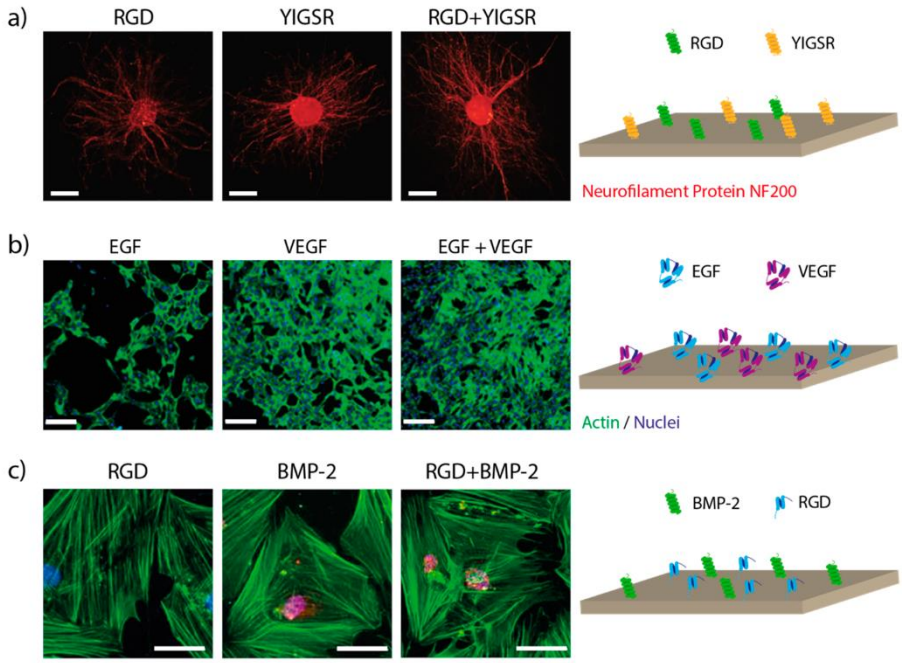

Figure 2. Combination of adhesion motifs, growth factors, or both for synergistic effects on cells: (a) Co-immobilization of RGD and YIGSR peptides enhanced neurite outgrowth from dorsal root ganglions (scale bar = 500 μm). Adapted with permission from ref 78. Copyright 2017 Wiley−VCH. (b) Combination of epidermal growth factor and VEGF enhanced survival of endothelial cells (scale bar = 200 μm). Adapted and reprinted with permission from ref 79. Copyright 2016 Elsevier. (c) Surface functionalization with BMP-2 mimetic peptide and RGD increased osteogenic marker expression (i.e., RunX2) in human bone marrow stem cells (scale bar = 50 μm). Adapted and reprinted from ref 80. Copyright 2016 with permission from Elsevier.

Fragments. Modification of a surface by a combination of several ECM proteins usually promotes cell attachment, spreading, and survival. This was, for instance, shown by increased neurite formation and length of neural cells on combinations of collagen I (Col I) with fibronectin (FN) or laminin (LM) compared to cells seeded on pure collagen I-modified surfaces.[70] In addition, combinations of adhesion peptides enhanced the attachment, spreading, and survival of endothelial cells,[71−75] neuronal cells,[76] fibroblasts,[76,77] or osteoblasts.[77]

Co-immobilizing RGD (from fibronectin) and YIGSR (from laminin) enhanced, for example, endothelial cell adhesion, as measured by cell number and spreading, compared to immobilized single peptides.[72−75] This combination has also been shown to promote neurite outgrowth of dorsal root ganglions[78] (Figure 2a). The presence of other peptide combinations, such as RGD and KRSR or combinations of laminin fragments, also cooperatively enhanced the attachment, spreading, and proliferation of fibroblasts,[76,77] demonstrating a strong dependence of the cell response on the exact ratio of incorporated peptides.[76] Interestingly, however, Castellanos et al. demonstrated that the combination of RGD and REDV, where the latter is known as an endothelial specific peptide derived from fibronectin, did not enhance adhesion of endothelial cells.[71] Hence, the choice of molecule(s) and their concentration and ratio need to be adjusted for each cell type, desired functionality, and target tissue.

In addition to steering attachment and adhesion, the stimulation of cell proliferation, quiescence, or differentiation is essential for the performance of a biomaterial. To this end, different strategies to stimulate angiogenesis,[81] endothelial cell functionality,[79,82] and hepatocyte[83] but also bone or cartilage differentiation[84] have been successfully demonstrated by modifying materials with specific combinations of growth factors (Figure 2b). For instance, the functionalization of collagen scaffolds with a combination of VEGF and angiopoetin-1 induced enhanced angiogenesis compared to their single factor functionalized controls, which was particularly evident when the molecules were covalently immobilized rather than being physisorbed.[81] The coimmobilization of epidermal growth factor and VEGF at a molecular ratio of 4:1 on chondroitin sulfate scaffolds significantly enhanced endothelial attachment and survival. However, other ratios had the opposite effect, resulting in decreased cell attachment compared to VEGF-only controls.[79] This concentration- or ratio-dependent outcome highlights the importance of gaining a better understanding on possible synergistic/antagonistic effects of combined biochemical surface modifications to improve biomaterial designs.

The combined stimulation of adhesion and differentiation by coimmobilization of growth factors and adhesion molecules has been demonstrated in concepts including but not limited to osseointegration,[85−87] endothelialization, and angiogenesis[82,88,89] or liver regeneration[83] (see one example in Figure 2c). Although coimmobilizing RGD with epidermal growth factor enhanced hepatocyte survival and functionality,[83] combining it with VEGF or basic fibroblast growth factor improved endothelial cell functionality.[82,88] The same effect could be observed for combinations of RGD with different growth-factor-derived peptides: The combination of RGD with VEGF mimetic QK peptide synergistically enhanced the angiogenic potential of endothelial cells.[90] Targeting a different tissue, RGD in combination with a BMP-7 mimicking peptide (CGQGFSYPYKAVFSTQ) had a beneficial effect on osteogenic differentiation of mesenchymal stem cells.[91] Brigaud et al. studied the synergistic effect of fibronectin with BMP-2, BMP-6, or BMP-7 adsorbed on titanium-hydroxyapatite samples on the osteogenic commitment and differentiation of C2C12 cells. They observed that BMP-6 was most potent at lower concentrations alone, but BMP-2 was most potent when combined with fibronectin.[85] This highlights the importance of addressing both the concentration as well as the very nature of the molecule.

https://dx.doi.org/10.1021/acsami.0c01893
ACS Appl. Mater. Interfaces 2020, 12, 21342−21367

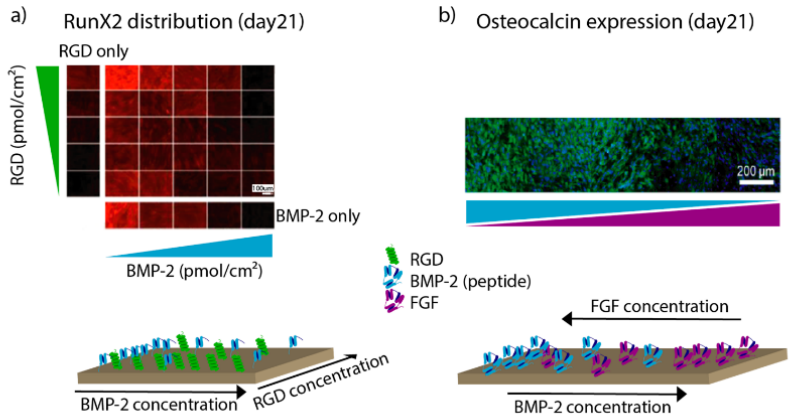

Figure 3. Biochemical ligand gradients: (a) Orthogonal gradient of RGD and BMP-2 peptides allowed to identify optimized combinations and ratios for osteogenic differentiation. Adapted and reprinted with permission from ref 95. Copyright 2016 American Chemical Society. (b) Interfacial tissues, such as tendon to bone, can be replicated with reverse parallel gradients of, for instance, BMP-2 and FGF. Adapted and reprinted with permission from ref 97. Copyright 2016 American Chemical Society.

Combinatorial Gradients of Biochemical Components. As was observed in various of the studies above, the choice of combined chemical signals and their specific concentration and ratio influence the response of cells. To date, the exact concentrations and ratios of such signals in natural tissues are unknown. To strategically analyze mixing ratios and different concentrations of immobilized molecules, we can preferably use arrays and gradients instead of preparing large numbers of samples with different, independent mixing ratios and concentrations. Arrays offer a multitude of different discrete spots to which a cocktail of molecules can be tethered on one single substrate.[92] Gradients on the other hand exhibit gradually increasing concentrations or densities of immobilized molecules on a sample and thereby allow for screening of different ratios, concentrations, or groups within a single experiment, thus providing higher throughput of experiments at higher levels of complexity.[84,86,92,93] Notably, surface gradients can be prepared according to the experimental design along the *x*- or *y*-axis of a sample in parallel, orthogonal, or reverse parallel manner.[84,86,93]

Using an array approach Koepsel et al.[92] and Zhang et al.[94] compared different mixing ratios of different BMP-mimicking peptides with RGD or YIGSR to demonstrate the dependence of osteogenic induction by BMP peptides on the amount of the adhesion peptides. With their arrays, they achieved up to 120 spots on one sample, with up to 16 different groups of peptide mixtures and 9 replicates per condition.[92,94] This work could facilitate the further understanding of peptide combination and concentration-specific effects. However, because array spots contain discrete concentrations over a certain range, optimized concentrations or ratios might be missed.

Dual gradients with continuous concentration changes, on the other hand, were successfully used for identification of molecule ratios showing synergistic effects on osteogenic differentiation (orthogonal or parallel gradients),[86,93,95] for migration studies (parallel gradients)[96] or recreation of tissue transition zones, such as the tendon-to-bone region (reverse gradients).[66,84,97,98] Using a parallel concentration gradient of RGD and BMP-2 mimetic peptide, Moore et al.[86] demonstrated that the combination of both components at the highest concentration (130 pmol/cm^2 combined) synergistically promoted mineralization of human bone marrow stromal cells in vitro.[86] Additionally, Ma et al.[95] created orthogonal gradients of RGD on the *x*-axis and BMP-2 on the *y*-axis of the samples and could reveal that osteogenic differentiation is highest at higher RGD (83 pmol/cm^2) concentrations combined with lower BMP-2 concentrations (0.5 pmol/cm^2) (Figure 3a). The results of these studies are partially contradictory. They highlight the strong dependence of the outcome on the study design (parallel vs orthogonal gradient). Furthermore, the exact concentration of each molecule is not known on the parallel gradient.[95]

By creating parallel gradients of fibronectin and VEGF and single-component gradients of each as control, Liu et al.[96] could show that cell migration from low to high concentrations was significantly increased on the dual gradient, compared to the single gradients. Although this demonstrates that a combination of chemical cues can enhance cell migration on parallel gradients, it is interesting that the slope of the concentrations along the gradient did not have a significant influence.[96] Using reverse dual gradients with BMP-2 and platelet-derived growth factor type BB (PDGF-BB), Ki et al.[84] demonstrated osteogenic differentiation of adipose-derived stem cells (ADSCs) on the BMP-2-rich end and differentiation toward tenocytes on the PDGF-BB-rich end (Figure 3b).[84] Such reverse gradients are a powerful tool to study or recreate tissue interfaces, such as the here-presented bone−tendon interface.

Various studies clearly demonstrated a strong dependency of the cell response on concentration and ratio of the presented peptides or proteins.[58,76,79,85,99] Although current studies focused on the combination of two molecules, the search for enhanced understanding forces researchers to increase the number of "signals" to the point where cues from natural tissues are better reflected. In the next step, it will be interesting to study how the interplay of three molecules influences cell behavior. Although methods for the fabrication of three-component gradients have already been developed,[100,101] immobilization of the biological molecules and subsequent gradient characterization as well as analyzing cell interaction have yet to be achieved. Furthermore, multicomponent chemical surface modification mimics only one aspect of natural tissues. Table 1 summarizes studies combining different chemical surface modifications. For recapitulation of natural tissues, researchers also need to consider surface topography and substrate mechanical properties.

2.2. Combining Biochemical and Topographical Surface Modification. *Effects of Different Spatial Surface Topographies Combined with Biochemical Ligands on Cell Behavior.* The density and the size (macro, micro, nano dimensions) of topographical patterns, which are introduced on the surface of materials, strongly influence cell behavior. Diverging observations have been described regarding the effects of macro-, micro-, or nanoroughness on cell function, with responses being highly cell type specific.[5,105,106] For instance, an increased surface roughness (nano- to micrometer range) promoted proliferation of osteoblasts[50] but decreased fibroblast proliferation.[47,48] Additionally, surfaces with microscale features led to decreased proliferation but enhanced gene expression of osteoblasts.[48,107,108] These studies came to similar conclusions, although topographies differed in their height and width as well as in the fabrication approach. Besides the roughness-dependent differ-

https://dx.doi.org/10.1021/acsami.0c01893
ACS Appl. Mater. Interfaces 2020, 12, 21342−21367

Table 1. Overview of Different Approaches for Chemical Surface Modification and the Respective Characterization Method[a]

substrate	chemistry	molecules	characterization method	cell type	biological effect	ref
Specific Immobilization, Molecule-Specific Characterization						
poly[(4-methylpropiolate-p-xylylene)-co-(p-xylylene)]	alkyne–azide click reaction and thiol-yne reaction; gradients	FGF and BMP-2	IRRAS, WCA, fluorescence	fibroblasts (3T3)	FGF supported cell proliferation on one side of the reverse gradient, BMP-2 induced bone formation on the other side of the gradient.	97
PEA and PMA	adsorption	VEGF, affinity bound to FN	AFM, ELISA, VEGF specific immunogold reaction	endothelial cells (HUVEC)	FN and VEGF induce tube formation of HUVEC. In vivo evaluation in a murine fat pad model induced vascularization.	89
Specific Immobilization, Unspecific Characterization						
UV-ozone activated glass slide	thiol–ene and SPAAC reactions	RGD and BMP-2	XPS	mesenchymal stem cells (hMSC)	Synergistic and concentration-dependent upregulation of osteogenic-specific genes after 14 days.	95
PEG-ylated and gold nanoparticle decorated glass slide	CuAAC click reaction and gold–sulfur affinity	RGD and PHSRN	chymotrypsin assay, QCM	fibroblasts (REF WT)	RGD and PHRSN synergistically enhanced cell attachment, spreading, and focal adhesion assembly.	102
PLLA	EDC/NHS coupling and direct solution spinning	RGD, BCP	XPS, SEM, thermo-gravimetric analysis	mesenchymal stem cells (hMSC)	RGD and BCP synergistically enhanced adhesion, spreading, and ALP activity.	87
Unspecific Immobilization, Molecule-Specific Characterization						
dextran	click chemistry and coiled-coil (KS-ES)	RGD (click) and VEGF (coiled coil)	^{1}H NMR, Ellmann's assay of peptide supernatant, orange II assay,	endothelial cells (HUVEC)	Combining VEGF with RGD enhanced proliferation and attachment of HUVEC.	88
chondroitin sulfate	coiled-coil (Kcoil/Ecoil)	EGF and FGF	ELISA	endothelial cells and smooth muscle cells (HUVEC and AoSMC)	EGF and VEGF synergistically enhanced HUVEC and SMC attachment and viability.	79
poly(L-lysine)/ hyaluronic acid	LbL adsorption and microfluidics; gradients	BMP-2 and BMP-7	fluorescence	skeletal myoblasts (C2C12)	Synergistic effect of BMP-2 and BMP-7 on osteogenic differentiation.	103
collagen	EDC/NHS coupling	VEGF and Angiopoietin-1	indirect ELISA (supernatant)	murine heart endothelial cells (HS V)	VEGF and Ang-1 synergistically enhanced cell proliferation and tube formation.	81
PCL/F127	heparin immobilization; gradient	PDGF-BB and BMP-2	toluidine blue and ELISA	adipose-derived stromal cells (ASC)	A reverse gradient revealed increased tendon-specific protein expression on the PDGF-BB side and increased bone-specific protein expression on the BMP-2 side.	84
PS plates	sulfo-SANPAH chemistry	EGF and IGF	fluorescence and ELISA)	keratinocytes (HaCaT)	EGF and IGF collectively influenced keratinocyte migration and morphology.	104
Unspecific Immobilization, Unspecific Characterization						
gold-coated glass coverslips	SAMs and EDC/NHS coupling	RGD and BMP-2 or heparin mimicking peptides	fluorescence	mesenchymal stem cells (hMSC)	Strongest osteogenic differentiation on RGD combined with BMP-2 peptide.	92
UV-ozone activated glass slide	SAMs and bifunctional PEO linker	RGD and BMP-2-derived peptide (KPSS)	XPS, WCA	mesenchymal stem cells (hMSC)	Synergistic upregulation of osteogenic markers by RGD and BMP-2 peptides.	86
quartz substrates	SAMs and Michaels addition	cyclic RGD and bone forming peptide-1	WCA, XPS	mesenchymal stem cells (MSC)	Synergistic upregulation of osteogenic markers when combining RGD with BMP-7-derived peptide.	91
gold-coated glass coverslips	SAMs and CuAAC click chemistry	RGD, YIGSR, KRSR, KPSS	IR, XPS, ellipsometry, AFM	adipose-derived stromal cells (hADSC) and mouse embryonic fibroblasts (MEF)	Combination of adhesion peptides (RGDS and YIGSR) with BMP-7-derived peptide upregulated bone-specific protein expression.	94
gold-coated glass coverslips	SAMs and EDC/NHS coupling	FN and VEGF	FTIR, XPS, SPR	bovine aortic endothelial cells (BAEC)	BAEC migrated significantly faster on combined gradients of FN and VEGF compared to single-component gradients and compared to nongradient controls.	96
titanium-hydroxyapatite	adsorption	FN and BMP-2 or BMP-6 or BMP-7	BCA assay (amount of molecule), SPR (adsorption kinetics)	skeletal myoblasts (C2C12)	Synergistic effect of FN with either BMP-2, BMP-7, or BMP-6 on the osteogenic differentiation.	85
PU–PEG	EDC/NHS coupling	RGD, YIGSR	WCA, AFM, amino acid analysis, XPS	endothelial cells (HUVEC)	RGD and YIGSR synergistically enhanced EC viability.	73
silk-fibroin	EDC/NHS coupling	RGD and KRSR	absorbance of peptide solutions (UV/vis)	osteoblasts (NHO) and fibroblasts (NHDF)	RGD and KRSR peptide synergistically improved cell attachment, spreading, and viability.	77

https://dx.doi.org/10.1021/acsami.0c01893
ACS Appl. Mater. Interfaces 2020, 12, 21342−21367

Table 1. continued

substrate	chemistry	molecules	characterization method	cell type	biological effect	ref
			Unspecific Immobilization, Unspecific Characterization			
aminated PU–PEG	EDC/NHS coupling	RGD, YIGSR, Heparin	toluidin blue, amino acid analysis	endothelial cells (HUVEC)	Combination of RGD, YIGSR, and heparin led to enhanced cell viability and vascular graft patency.	74
PLCL	polydopamine (Michael type addition)	RGD and bFGF	fluorescamine assay and ELISA, XPS	endothelial cells (HUVEC)	Immobilized RGD and bFGF enhanced HUVEC viability and interconnected monolayer formation.	82
cobalt chrome	CPTES silanization and thiol reaction	RGD, REDV, YIGSR	XPS, surface charge, QCM-d	endothelial cells (HUVEC)	Only the combination of RGD and YIGSR induced strong synergistic increase in cell attachment.	71
PCL–PLGA	urea bond between peptide and NCO-PEG	RGD, YIGSR	fluorescamine assay	endothelial cells (HUVEC and HPMEC)	Synergistic improvement on cell attachment of RGD and YIGSR.	75

[a]Studies are divided into four groups, depending on the immobilization or characterization approach: molecule-specific immobilization and characterization, molecule-specific immobilization and unspecific characterization, unspecific immobilization and molecule-specific characterization, and unspecific immobilization and characterization.

entiation of MSC,[49,109] early inflammatory responses of macrophages were enhanced on 2D films or microfibrous PLLA scaffolds compared to nanofibrous substrates.[110] In these approaches, the cell responses to the materials were generally influenced by the present topography as well as by unspecific protein adsorption from serum-supplemented culture medium to the sample surface.

In this context, Macgregor et al.[111] demonstrated that the dimension of topographical surface nanopattern (16, 38, or 68 nm) could influence the conformation of the protein immobilized on the surface. This fact influenced the cell−surface interaction, in this case, binding of mouse embryonic stem cells (mESC) to FN. They showed that FN could not bind to the surface when 16 nm surface topographies were present, as FN displayed similar size (15 nm length, 9 nm width), which in turn did not occur for larger patterns.[111] Besides surface chemistry, existing surface topographies could lead to protein denaturation and conformational changes after adsorption on the surface, which in turn could lead to a loss of function or bioactivity impairing cell interaction.[5,9,106,112,113] Furthermore, such conformational changes could lead to toxic effects or inflammation,[113,114] which are unwished side effects. However, controlled protein adsorption allowed immobilization of attachment sites on a material surface for guiding cellular interaction.[9,106,112] Thus, surface topography can be further complemented by the functionalization with biochemical ligands to better control the surface characteristics. In general, combining different surface topographies and ECM-derived stimuli enables the investigation of synergistic or antagonistic effects on cell behavior and ultimately the generation of ECM-mimicking cellular microenvironments.[115−118]

It was shown that the size of topographical structures from nano- to micropatterns influenced cell adhesion, spreading, and proliferation, whereas chemical ligands had an impact on self-renewal and differentiation of osteoblasts and stem cells.[111,119] For example, the outward surface modification with spatial hut, dome, or pyramidal nanostructures, functionalized with RGD or FN-coating, led to enhanced proliferation of MSC and drove endothelial cell adhesion. Although the cytoskeleton of endothelial cells was arranged around the pyramids, the focal adhesion formation of MSC was highest on FN-modified, hut-nanostructured (3 nm height, 35 nm width) surfaces, verifying the important influence of nanostructures for these cells.[115,116] However, surface functionalization with RGD-modified pyramids in the microscale (height ∼2 μm) hindered endothelial cell attachment. Le Saux et al.[116] showed that the density of surface-exposed RGD drove spreading, focal adhesion formation, and internal organization of cells, whereas size and scale of surface topography mainly influenced the number of surface-attached cells. This led the authors to propose a two-step model of cell adhesion: initial cell contact to a substrate surface is dominated and guided by topographical surface features, but the attachment is driven by the interaction of cellular surface receptors with surface-exposed chemical cues.[116] Another study showed that osteogenic differentiation of hMSC could be enhanced on surfaces with BMP-2 peptide-modified nanopatterned surfaces in the presence and absence of osteogenic differentiation medium.[120]

Combined gradients of nanopatterns and proteins, for instance, FN and vitronectin, have been investigated to understand synergistic effects on cell behavior, which is especially relevant for tissue transition zones.[121−123] For example, it was shown that spreading and cytoskeleton organization of C2C12 myoblasts increased along topographical gradients of different nanopatterns (bars, rings, and dot pairs) functionalized with vitronectin, and that the pattern length, but not its area, was the critical parameter for cell spreading.[122] On a parallel gradient of BSA/lysozyme and surface roughness in the nanoscale, fibroblasts showed increased cell adhesion in the direction of the gradient.[123] Osteoblasts, however, showed decreased spreading and proliferation along a uniformly RGD-decorated nanoparticle-density gradient.[124]

Biochemical Ligand Functionalized Indentations and Grooves Support Cell Alignment and Differentiation. One aim of combining surface topography with chemical functionalities was to understand and mimic (at least partially) the influence of the ECM on stem cell differentiation,[111,120,125] skeletal muscle tissue engineering,[126,127] peripheral nerve regeneration,[128] and development of functional cells,

https://dx.doi.org/10.1021/acsami.0c01893
ACS Appl. Mater. Interfaces 2020, 12, 21342−21367

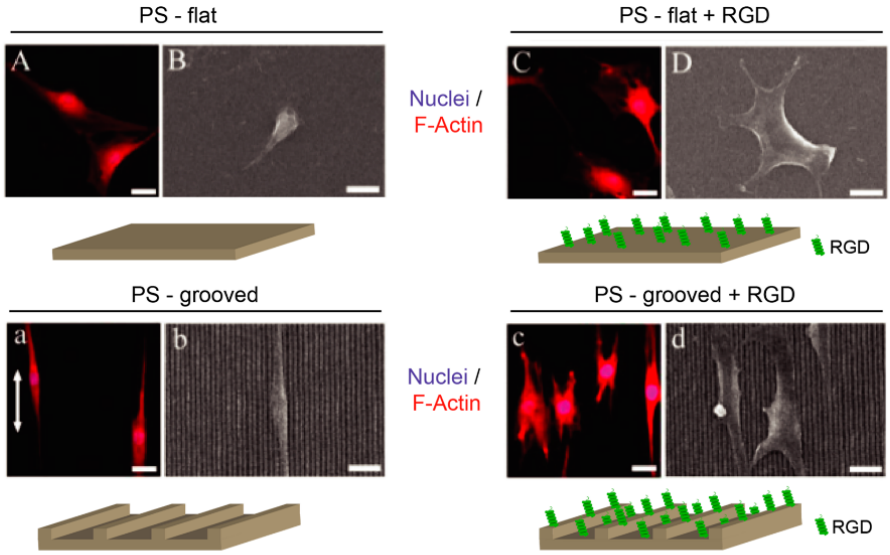

Figure 4. Synergistic influence of spatial surface topography (grooves) and biochemical ligands on cell behavior. Submicrometer grooves on a polystyrene (PS) surface guided alignment and elongation of C2C12 myoblasts along the grooves, whereas RGD functionalization directed their spreading, growth, and differentiation by interaction with cellular surface receptors. The grooves displayed widths from 670 to 920 nm and depths of around 670 nm (cartoon for illustration only, not to scale). Immunofluorescent staining of nuclei (DAPI) and F-actin in C2C12 myoblast was done after 24 h in culture (A, a, C, c). The scale bars in the fluorescence (A, a, C, c) and SEM (B, b, D, d) images are 25 and 10 μm, respectively. The arrow displays the groove direction. Images adapted and reprinted with permission from ref 126. Copyright 2012 Wiley.

such as neurons,[129,130] or on cellular transformation into cancer.[131] Thereby, shape-restriction of biochemical ligands could be used to guide and control cell attachment and differentiation on biomaterial surfaces. For example, MSC displayed more and larger focal adhesions as well as enhanced differentiation toward the osteogenic fate on 100 nm deep indentations, modified with RGD, compared to those with 10 nm depth.[125] Although outgrowth of neuronal cells was rapid on continuous, shallow poly-L-lysine surface features in the micrometer range, it was delayed on interrupted ones. This demonstrated that controlled neuron adhesion and outgrowth were regulated by a chemical compound, whereas topography provided guidance for neurons.[130]

Furthermore, grooves (from the nanometer to the micrometer scale) combined with biochemical ligands were shown to promote alignment and differentiation of cells, including MC3T3-E1 osteoblasts,[132] MG-63 osteoblast-like cells,[133] C2C12 myoblasts,[126,127,134] PC12 cells,[129] hMSC,[120] anterior cruciate ligament fibroblasts (ACLF),[135] and human corneal epithelial cells (HCEC).[136,137] Studies combining such grooves with RGD,[126,127,133,135−137] YIGSR,[127] a LM-derived peptide PPFLMLLKGSTR,[129] BMP-2 peptides,[120] FN,[134] Col I,[129,133] or neuronal GF[128] all demonstrated beneficial and conducive effects on adhesion, growth, differentiation, or alignment of myoblasts (Figure 4),[126,127,134] HCEC,[136,137] hMSC,[120] ACLF,[135] osteoblast-like cells,[133] or PC12 cells.[128,129] The adhesive ligand significantly enhanced attachment, growth, and differentiation of cells, whereas grooves directed the cellular morphology, alignment, and elongation along the topographical pattern (Figure 4).[126−129,133,135]

On surfaces combining microgrooves (4 μm height, 8 μm width) with orthogonally arranged FN microlanes (10 μm width), osteoblasts were predominantly influenced by the topographical feature and aligned preferentially along the grooves.[132] Similarly, fibroblasts showed clearly increased cell elongation and alignment along a parallel, linear, microstructured FN gradient.[121] Another study demonstrated that a microgroove (2 μm height, 20 μm width) induced contact guidance of MG-63 osteoblast-like cells could only be interrupted by an amino functionalization, but not by coupling Col I or RGD on the patterned surface.[133]

In addition, one study, combining grooves in the submicro- to micrometer range (200 nm to 2 μm width) with RGD and different cell culture media, confirmed that cell responses to functionalized surfaces were not only guided by topographical and chemical cues but were also dependent on present soluble factors in the cell culture media, as HCEC alignment differed in serum-containing or GF-defined, serum-free media.[136] This observation could be confirmed on BMP-2 peptide-functionalized nanogrooves, where osteogenic differentiation and cell behavior of hMSC was affected by present soluble factors of an osteoinductive medium. Although the cells aligned to modified grooves in standard growth medium, their spreading and calcium deposition was enhanced in the presence of an osteogenic induction medium.[120]

Fibers Combined with Biochemical Ligands Support Cellular Responses and Function. Fibrous scaffolds as an overall system represent hierarchical surface topography and structures mimicking the physical properties of the ECM. However, single fibers of the substrate show their own inherent surface topography, adding an additional dimension of topographical cues, such as different fiber surface roughness or pore depth, to influence cell response. For instance, this nanoroughness and nanopores led to different osteogenic gene expression of hMSC,[138] enhanced growth of A-172 neuronal cells,[139] different astrocyte-mediated neurite outgrowth[140] or increased adhesion, proliferation, and gene expression of vascular SMCs.[141] Moreover, fibrous topographies from the nano- to the microscale combined with ECM-derived ligands, such as laminin, RGD, and VEGF, have been shown to support engineering of endothelial[142−149] or neuronal tissue.[150−152] Compared to unmodified fibers, endothelial cell adhesion, proliferation, migration and function were clearly enhanced on electrospun nano- or microfibrous poly(ε-caprolactone) (PCL), poly(L-lactic acid-co-ε-caprolactone) (PLLCL) or blended PCL/gelatin and PCL/poly(3-hydroxybutyrate-co-3-hydroxyvalerate) nonwoven meshes modified with RGD[142,144] or with immobilized VEGF.[143,145,146,148,149] The spatial functionalization of fibrous PCL scaffolds in the submicro- and micrometer range with osteopontin-derived and heparin-binding peptides by thiol-maleimide coupling enabled cell-specific adhesion of endothelial cells (HUVEC) and pericytes to promote endothelization and angiogenesis.[147] In another

https://dx.doi.org/10.1021/acsami.0c01893
ACS Appl. Mater. Interfaces 2020, 12, 21342−21367

example, adhesion, proliferation, migration, and axonal growth of Schwann cells was shown to be enhanced on laminin-modified core−shell poly(L-lactide-co-caprolactone) (PLCL) nanofibers[152] and guided on PCL/PEG blend microfibers functionalized with RGD compared to scaffolds without RGD.[151] PC12 cells also demonstrated increased viability on RGD-modified poly-(L-lactic acid) (PLLA) nanofibers and higher neurite outgrowth on blended LM-PLLA nanofibers (diameter ∼100−500 nm).[150] The fibrous structure of such substrates was shown to enable the adhesion, migration, and growth along the fibers, whereas the biochemical ligands represent chemo-attractive, cell-stimulating factors.[142−153] A recent study showed that initial adhesion of bone murine stromal ST-2 cells was topography-driven and even possible on unmodified electrospun PCL microfibers (diameter ∼1.3−1.6 μm), but the proliferation rate was clearly enhanced on FN-functionalized PCL fibers.[154] Table 2 summarizes studies combining chemical and topographical surface modifications and the respective characterization methods as well as the biological response.

2.3. Combining Biochemical Modifications with Different Mechanical Properties. *Substrate Composition and Mechanical Properties Control Initial Cell Material Contacts and Differentiation.* Synergistic effects of physical (mechanical properties) and biochemical signals (growth factors, proteins) on cell behavior are well-known, and several studies have focused on different substrates with varying elastic moduli combined with diverse biochemical ligands, such as full-length ECM proteins, GFs or peptide sequences derived therefrom.[157−168] In general, with increasing substrate rigidity and presence of ECM proteins (e.g., Col I and FN), spreading, actin cytoskeleton organization and proliferation of hMSC,[161,163] smooth muscle cells (SMCs),[169] and keratinocytes[163] as well as adhesion and neurite formation of PC12 cells[160] were enhanced. Furthermore, the modification of substrates with a range of elastic moduli between 0.5 and 423 kPa with peptide sequences, such as RGD,[157,158] KQAGDV,[157] and BMP-2mp,[158] revealed in some cases synergistic, but sometimes also discrete effects on the formation and organization of the F-actin cytoskeleton, proliferation and differentiation of cells.[157,158] It was shown previously that SMC spreading and focal adhesion formation were promoted by the ligand density and identity as well as substrate stiffness. However, there, an increase in elastic modulus led to enhanced proliferation but decreased differentiation independently of the present biochemical cue.[157] Furthermore, the combination of substrates showing mechanical properties matching the target tissue, with hepatocyte GF,[167] PDGF,[168] BMP-2,[165,168] and VEGF,[166] revealed synergistic effects on cell adhesion, migration, and proliferation as well as increased metabolic activity of endothelial cells,[166,167] myoblasts,[165] and ADSC.[168] Taken together, the functionalization of substrates with growth factors can enhance cellular functions or support cellular interactions with an otherwise cell-unfavorable substrate.[165−167,170] Furthermore, the surface-bound presentation of GFs enhanced the efficacy and function of growth factors, such as VEGF,[171] BMP-2,[165] and insulin-like GF,[172] and is closer to physiological conditions in nature, as many GFs are bound to proteins or glycosaminoglycans in the ECM.[19,165,173−175] In this context, researchers hypothesized that the spatial arrangement of the GF on the surface led to a restricted diffusion and increased local availability of the GF as well as an interplay of different cell receptors, such as cell adhesion receptors.[165,176−178] Nevertheless, it was also shown that the concentration of a GF, such as VEGF, is a critical factor for increased, stable vascularization or aberrant angiogenesis.[179,180]

Cell Differentiation Is Influenced by Matrix Composition and Elastic Modulus of the Support Material, but Can Be Dominated by a Biochemical Stimulus. In addition to cell attachment and spreading, cell fate decisions are known to be influenced by the interplay of substrate mechanics and ECM ligands. This has been shown for stem and progenitor cell differentiation and in development and regeneration of functional neuronal,[159,160,162,181,182] muscle,[157−159,161,162] liver,[164] skin,[163] or bone tissue.[158,159,161,162] For example, human MSC were cultured on substrates with different elastic moduli or indentation depths functionalized with ECM proteins, such as collagen I, or other chemical groups. Thereon, the cells showed rigidity-dependent differentiation, with neurogenesis and angiogenesis being enhanced on soft (modulus: 0.1−6.5 kPa), myogenesis on intermediate (modulus: 8−17 kPa) and osteogenesis on slightly stiffer substrates (modulus: 25−80 kPa).[159,161−163] Adult neural stem cells (aNSC) showed differentiation into neurons on softer (modulus: ∼0.1−0.5 kPa) and into glials on harder RGD-modified substrates (modulus: ∼1−10 kPa).[182] Furthermore, when combining growth factors with mechanically different materials, positive effects on osteogenesis,[165,168,170] endothelialization, revascularization, or angiogenesis[166,167,183] as well as the development of skin[184] were demonstrated. For example, the differentiation of myoblasts[170] or endothelial cells[166] as well as osteoblast,[165] endothelial cell,[167] and myoblast[165] function were mainly regulated by the elastic modulus of the substrate.

The influence of combined biochemical and mechanical stimuli on cell differentiation is complex and often crucially dependent on the biochemical stimulus. Between elastic moduli of 4−30 kPa, cholangiocyte differentiation of liver progenitor cells was observed to be mechanics-independent in the presence of Col IV but mechanics-regulated on FN-modified surfaces. Further, hepatocyte differentiation was mainly induced by the biochemical ligand and matrix composition (Figure 5a).[164] Human MSC, on the other hand, favored the myogenic fate on substrates with elastic moduli of 13−17 kPa, whereas osteogenic fate was preferred on substrates with elastic moduli of 45−49 kPa, if the cell-unspecific RGD peptide was used. However, in the presence of the bone-specific BMP-2 peptide, differentiation toward the osteogenic fate was enhanced largely independent of the substrate rigidity, except for very soft substrates (modulus: 0.5−3.5 kPa). On these substrates, differentiation was inhibited because of a reorganization of the F-actin cytoskeleton (Figure 5b).[158]

Furthermore, chemical stimulation in the presence of specific GFs, such as adsorbed HGF[167] or tethered BMP-2[165] or VEGF,[166] could also support cellular responses on mechanically not favored surfaces.[165−167,170] On substrates showing various elastic moduli (2.85−5.05 MPa) the presence of a supporting growth factor, such as PDGF or BMP-2, could inhibit stiffness-dependent regulation of osteogenic and adipogenic differentiation genes of ADSC.[168] In this context, it is also important how a GF is presented to cells, as studies have demonstrated that immobilized GFs, such as BMP-2, had a stronger effect on myoblast behavior, when compared to its soluble form, which was especially apparent on soft substrates (modulus: ∼200 kPa) (Figure 5c).[165] More detailed information on the impact of physical properties, the presentation of GFs, and the interplay of mechanotransduction and GF signaling on cell behavior and their microenvironments is summarized elsewhere.[19,174−178]

Combining Mechanical and Biochemical Gradients to Identify Synergistic Effects. Because of the analysis of materials with different but consistent mechanical properties modified with biochemical ligands, conclusions of their synergistic effects on cells could be drawn. Most tissues do not show a definite mechanical value but rather gradients in mechanical properties[32] and even display concentration gradients of ECM components and GFs.[33] Thus, gradients of elastic modulus play a special role in combination with biologically relevant ligands on a substrate, as both regulate many physiological processes, including cell migration,[31,185−189] spreading, and cytoskeleton organization,[63,185,188,190] as well as differentiation.[187,191] Generally, the combination of gradients of mechanical signals with ECM-derived ligands, such as Col I,[31,185,187,191] FN,[189−191] or RGD,[63,186] showed positive synergistic effects on fibroblasts,[31,63,188,190] MSC,[187] bone-marrow stromal cells,[191] SMC,[185] ADSC,[189] and aortic cells.[186] In addition to enhanced migration or spreading of MSC,[187] SMC,[185] or ADSC,[189] especially fibroblast spreading was dependent on the elastic modulus and increased along the mechanical gradient (Young's modulus from 1 to 240 kPa), when the concentration of immobilized FN was constant (Figure 6a).[190]

The combination of elastic modulus gradients with biochemical ones, for example with an RGD gradient, enabled to better understand complex cell−matrix interactions.[31,63,186,188] Using this approach, increasing substrate rigidity and availability of a biochemical ligand gradient showed positive and synergistic effects on migration and spreading of fibroblasts,[31,63,188] aortic cells,[186] and bone-marrow stromal cells.[191] For instance, on dual gradient scaffolds (elastic

https://dx.doi.org/10.1021/acsami.0c01893
ACS Appl. Mater. Interfaces 2020, 12, 21342−21367

Table 2. Overview of Studies Combining Chemical and Topographical Surface Modifications and the Respective Characterization Methods[a]

substrate	preparation method	topography and range	topographical characterization	immobilized molecules	immobilization method	chemical characterization	cell type	biological effect	ref
Different Spatial Surface Topographies Combined with Biochemical Ligands									
PLA with hydroxyapatite (HAP)	HAP precipitation on Gly, Arg or Asp	rough and irregular surface patterns in the nanometer range	SEM, AFM, WCA	serum proteins	protein adsorption	BCA assay	human osteoblasts (hFOB 1.16)	Increased hFOB proliferation with increased topological roughness.	59
titanium disks with aluminum particles	sandblasting of Al_2O_3 particles	rough and irregular surface patterns in the submicro- and micrometer range	profilometry, SEM, EDX	FN, RGD and/or PHSRN	coupling by tresyl chloride	ELISA	osteoblasts (MC3T3)	FN and peptides enhanced MC3T3 adhesion, proliferation and differentiation.	119
tantalum-coated Ge−Si surfaces	molecular beam epitaxy (MBE) deposition and tantalum coating	variety of nanometer-scaled hut and dome structures	AFM, XPS	FN	protein adsorption	ellipsometry, antibody binding	human dental pulp-derived stem cells (DP-MSC)	DP-MSC proliferation was enhanced on topographical surfaces.	115
PEI	electrostatic adsorption silica particles to PEI	nanoparticle-density gradient	SEM, AFM	RGD	PLL-g-PEG-RGD	cell staining after adhesion	rat calvarial osteoblasts (RCO)	RCO adhesion and spreading increased on unstructured surfaces, decreased with increasing particle gradient.	124
silicon oxide	hole mask colloidal lithography and angled physical vapor deposition	nanopattern gradients with varied bar length, ring diameter, dot pair separation	SEM, QCM	vitronectin	protein adsorption	cell staining after adhesion	skeletal myoblasts (C2C12)	Best at beginning of the gradient, ring: increased spreading with increasing ring diameter, bar: FA elongated with elongation of the pattern.	122
silicon	time-dependent wet chemical etching	nano- and micro-scaled pyramids	AFM	RGD	covalent coupling by urethane bonding	cell staining after adhesion	bovine aortic endothelial cells (BAEC)	RGD density drove spreading and focal adhesion formation of EC, whereas size and scale of pyramids guided adhesion.	116
PAAM	microcontact printing of PDMS stamp	various shapes (round, star-shaped, oval) in the micrometer range	immunofluorescence imaging	FN, Col I, LM	covalent coupling of aldehyde-hydrazine groups	cell staining after adhesion	mesenchymal stem cells (hMSC)	Neurogenesis occurred protein-dependent and protein-independent of anisotropic patterns, adipogenesis observed on FN and if spreading is restricted.	155
Grooved and Longitudinal Surface Topographies Combined with Biochemical Ligands									
HMDS	patterning by reactive ion etching	continuous and interrupted patterns in the micrometer range	SEM, AFM	PLL patterns	acetone liftoff after adsorption of PLL into etched trenches	FITC-PLL	rat hippocampal cells (E18)	Rapid neurite outgrowth on continuous lines, delayed outgrowth on interrupted lines.	130
PET	photolithography	linear patterns in the micrometer range	FITC-labeled peptides, XPS	SVVYGLR peptide	EDC/NHS coupling	FITC-labeled peptides, XPS	endothelial cells (HUVEC)	Narrow linear SVVYGLR-micropatterns enhanced spreading, orientation, migration, and morphogenesis of HUVEC.	156
ODTS	multiphoton excited photochemistry	parallel series of individual linear microstructured gradients	immunofluorescence imaging	FN	multiphoton excited photochemistry coupling	fluorescence	fibroblasts (NIH 3T3)	Increased fibroblasts elongation/alignment along a linear, structured gradient with increasing FN concentration.	121
PLLA	dry phase inversion, casting of polymer particles in longitudinal patterns	longitudinal, topographical surface micropatterns	SEM	β-NGF	coupling by ester-amine reaction, self-assembly, protein−protein interactions	XPS	neuroblasts (PC12)	PC12 aligned along the topographical pattern, β-NGF enhanced growth, with the highest neurite extension at the end with the highest β-NGF amount.	128
PC	hot embossing with a silicon master	holes, grooves, and ridges in the micrometer range	SEM, AFM	FN	coupling to CH_3-by HDT	immunostaining	primary and skeletal (C2C12) myoblasts	Alignment of primary and C2C12 myoblasts to ridges and grooves, no influence on myogenesis.	134
PUA/pGMA	dispensing on a silicon master fabricated by photolithography	grooves and dots in the nanometer range	SEM, AFM	BMP-2 peptide	epoxy-amine coupling via ring-opening reaction	fluorescamine assay of supernatants, XPS	mesenchymal stem cells (hMSC)	Enhanced osteogenic differentiation in presence of BMP-2 peptides and nanopatterns.	120

https://dx.doi.org/10.1021/acsami.0c01893
ACS Appl. Mater. Interfaces 2020, 12, 21342−21367

Table 2. continued

substrate	preparation method	topography and range	topographical characterization	immobilized molecules	immobilization method	chemical characterization	cell type	biological effect	ref
Grooved and Longitudinal Surface Topographies Combined with Biochemical Ligands									
PS	casting on a master silicon wafer	grooves in the nanometer range	AFM	RGD	interaction with dopamine coating	ESCA	anterior cruciate ligament fibroblasts (ACLF)	Elongation and alignment of cells increased with increasing groove depth, RGD enhanced proliferation and spreading, best cell behavior on 700 nm grooves and RGD.	135
PET	time-dependent UV-exposure (254 nm)	micropatterns with depth variation in the nanometer scale	optical 3D profiler system	RGD	EDC/NHS coupling	XPS, high-resolution beta-imager (^{3}[H] lysine)	mesenchymal stem cells (hMSC)	100 nm pattern enhanced adhesion and osteogenic differentiation of hMSC, 10 nm pattern enhanced adhesion.	125
PLGA	solvent-assisted micromolding method of PLGA:PLL-peptide	ridges and grooves in the submicrometer range	AFM, SEM	RGD, YIGSR	EDC/NHS coupling to PLL	ESCA, fluorescence	skeletal myoblasts (C2C12)	Grooves induced C2C12 alignment; RGD had a higher impact than YIGSR on growth and differentiation.	127
PS	electron beam lithography and dry etching a PDMS mold	grooves in the submicrometer range	AFM, SEM,	RGD	EDC/NHS coupling	ESCA, water contact angle	skeletal myoblasts (C2C12)	C2C12 cell attachment increased after RGD modification, alignment along the grooves, highest differentiation when combined.	126
PEGDA	casting on a PDMS mold	grooves in the submicro- and micrometer range	AFM	RGD	Michael-type addition	cell staining after adhesion	human corneal epithelial cells (HCEC)	Parallel alignment of HCEC along the grooves.	137
PEI/PVDMA	layer-by-layer coating on a PDMS stamp	grooves in the submicro- and micrometer range	AFM	RGD	coating with peptide and D-glucamine	cell binding assay with soluble peptides	human corneal epithelial cells (HCEC)	Cell alignment dependent on the scale of the topographical cue, best on 400 and 4000 nm pitches	136
PLGA	solution casting and laser ablation	grooves in the micrometer range	surface profile control technique	Col I, LM-peptide (PPFLMLLKGSTR)	coating	FITC-conjugated LM-peptide	Neuroblasts (PC12)	Enhanced neurite alignment and parallel outgrowth in grooves, LM-peptide and 5 μm grooves showed parallel outgrowth, decreased neurite number and length on micropatterns.	129
polyimide	Hot embossing with a silicon master	grooves in the micrometer range	SEM	FN	μCP by PDMS stamps coated HDT for covalent coupling	SEM, immunostaining	osteoblasts (MC3T3-E1)	Single modification: osteoblasts aligned along the pattern. Combined: alignment along the topographical pattern.	132
silicon wafers with titanium	deep reactive ion etching (DRIE)	grooves in the micrometer range	SEM, AFM	Col I, RGD, amino groups	acetic coating and drying, coupling to APTES/SPDP, plasma process	WCA, zeta potential	human osteoblast-like cells (MG-63)	Cell elongation and alignment along the groove/plateau direction on Col I and RGD, amino modification interrupted topography-induced contact guidance.	133
Fibrous Surface Topographies Combined with Biochemical Ligands									
PLLA	(blended) electrospinning	nanofibrous nonwovens	SEM	LM	EDC/NHS coupling or physical adsorption	FITC-LM, SCM, XPS, MicroBCA protein assay	neuroblasts (PC12)	Enhanced viability on postmodified nanofibers, enhanced neurite outgrowth on blended fibers.	150
PCL	electrospinning	nano- and microfibrous nonwovens	SEM	VEGF	EDC/NHS coupling	XPS, ELISA, immunohistochemistry	endothelial cells (HUVEC)	Immobilized VEGF enhanced endothelial cell adhesion and proliferation.	143
PCL, PLLCL	electrospinning	nonwovens in the submico- and micrometer range	SEM	GRGDSP	covalent grafting of photoreactive peptide after UV irradiation	XPS, WCA	endothelial cells (HUVEC)	Dose-dependent increase in HUVEC adhesion and control over proliferation.	144
PCL	electrospinning	nonwovens in the submicro- and micrometer range	SEM	RGD	grafting with Nap-FFGRGD through self-assembly	fluorescence	rabbit endothelial cells and smooth muscle cells (EC and SMC)	RGD modified grafts enhanced hemocompatibility, EC cell migration, and SMC regeneration.	142

https://dx.doi.org/10.1021/acsami.0c01893
ACS Appl. Mater. Interfaces 2020, 12, 21342−21367

Table 2. continued

substrate	preparation method	topography and range	topographical characterization	immobilized molecules	immobilization method	chemical characterization	cell type	biological effect	ref
Fibrous Surface Topographies Combined with Biochemical Ligands									
PCL	electrospinning	nonwovens in the submicro- and micrometer range	SEM	adhesion peptide: SWVYG LRGCC, heparin binding peptide: CGGGAAALRKKLGKA	covalent coupling to Mal-modified PCL	fluorescence	endothelial cells (HUVEC) and human saphenous vein-derived pericytes (hSVPs)	Enhanced HUVEC-specific adhesion; increased pericyte adhesion and secretion of VEGF.	147
PCL/gelatin	electrospinning	blended microfibrous nonwovens	SEM	VEGF	coupling to heparin after heparin immobilization on gelatin	toluidine blue	endothelial cells (HUVEC)	VEGF enhanced proliferation of HUVEC.	145
PCL	electrospinning	blended microfibrous nonwovens	SEM	VEGF-HGFI	hydrophobic interactions	fluorescence	endothelial cells and smooth muscle cells (HUVEC and SMC)	Lower fibrinogen adsorption, platelet activation and aggregation. Increase in HUVEC functionality, endothelization, enhanced expression of SMCs marker genes.	149
PCL	electrospinning	microfibrous nonwovens	SEM	FN	coating to hydrolyzed PCL or additional ECD + NHS coupling or coaxial electrospinning	ATR-FTIR, ToF-SIMS	bone marine stromal cells (ST-2)	Enhanced ST-2 proliferation, especially on coaxial spun fibers.	154

[a]The biological response in vitro is briefly stated.

modulus gradient from 5 to 15 kPa combined with an orthogonal RGD density gradient from 0 mM to 0.7 mM immobilized peptide) human fibroblasts displayed increased spreading along both gradients, showing the best spreading at the stiffest area with highest RGD density. Especially, by keeping one parameter constant, cells displayed enhanced spreading along the appropriate increasing gradient (Figure 6b).[63] However, biochemical cues can also dominate and direct cell migration and differentiation, as fibroblasts migrated to or stayed at the region with low Young's modulus, but high collagen density (Figure 6c).[31,188] Independent of the elastic modulus of the substrate, bone-marrow stromal cells showed osteogenic or tenoblast differentiation in the presence of FN or Col, respectively,[191] and aortic cell infiltration was enhanced with increasing RGD concentrations.[186] Table 3 summarizes studies combining chemical and mechanical surface modifications and the respective characterization methods as well as the biological response.

Lessons Learned from Combinatorial Surface Approaches. Combining several biochemical moieties or biochemical ligands with either topographical features or different mechanics, generally leads to synergistic enhancement in cell-type-specific responses, such as attachment or differentiation. It is known that adhesion molecules generally lead to enhanced cell attachment and spreading, whereas growth factors stimulate the expression of cell-type-specific functionality. Thereby, specific phenotypes or differentiation combining several adhesion factors could already lead to enhanced functionality.[78] Especially, combining growth factors with adhesion ligands induces enhanced functional cell response.[80,89,91] The type as well as the dimension of surface topography is decisive for cell responses.[115,116,126,156,194] Although chemical adhesive ligands significantly enhanced adhesion, growth, and differentiation of cells, grooved and fibrous topographies directed cell morphology, alignment, and elongation along the pattern.[125−128,135,142−153] Furthermore, restriction of a biochemical ligand pattern guided cell arrangement, orientation, and differentiation.[155,156] An interplay between mechanical properties of the substrate and the presented biochemical stimulus (integrin signaling) for modulating cellular behavior and responses could be seen. Nevertheless, the cell function could be dominated by a chemical stimulus leading to differentiation, even on a mechanically cell-unfavorable substrate.[158,164,165,168]

Furthermore, various studies clearly demonstrated a strong dependency of the cell response on concentration and ratio of the presented biochemical ligands.[58,76,79,85,99] However, the exact concentration of adhesion molecules and GFs needed to induce a desired cell response is often not known. Arrays and gradients provide an excellent method to gain knowledge on cell fate decisions in response to biomolecule functionalization.[66,84,86,92−97,103] Nevertheless, a clear need for further work to better understand the dependence of combinations, concentrations, and ratios of biomolecules, of surface topographies, and of mechanical properties of the support material can be seen, not only to steer cell behavior but also to recreate transition zones of tissues with a natural gradient.

3. CHALLENGES IN FABRICATION AND CHARACTERIZATION OF COMBINATORIAL SURFACE FUNCTIONALIZED BIOMATERIALS

Material Functionalization with Various Biochemical Groups. Control over surface properties becomes challenging when combining various biochemical groups on one substrate. Castellano et al. immobilized combinations of YIGSR, RGDS, and REDV on cobalt−chrome substrates via chloropropyltriethoxysilane silanization and subsequent conjugation of sulfur with chlorine.[71] Notably, this directionally controlled peptide conjugation ensured the availability of the peptide's adhesion sequence for cellular attachment and was used for all different peptides and combinations thereof. Although the functionalized substrates were thoroughly characterized via X-ray photoelectron spectroscopy (XPS), surface charge measurement, and quartz-crystal-microbalance (QCM-d) analysis, none of these

https://dx.doi.org/10.1021/acsami.0c01893
ACS Appl. Mater. Interfaces 2020, 12, 21342−21367

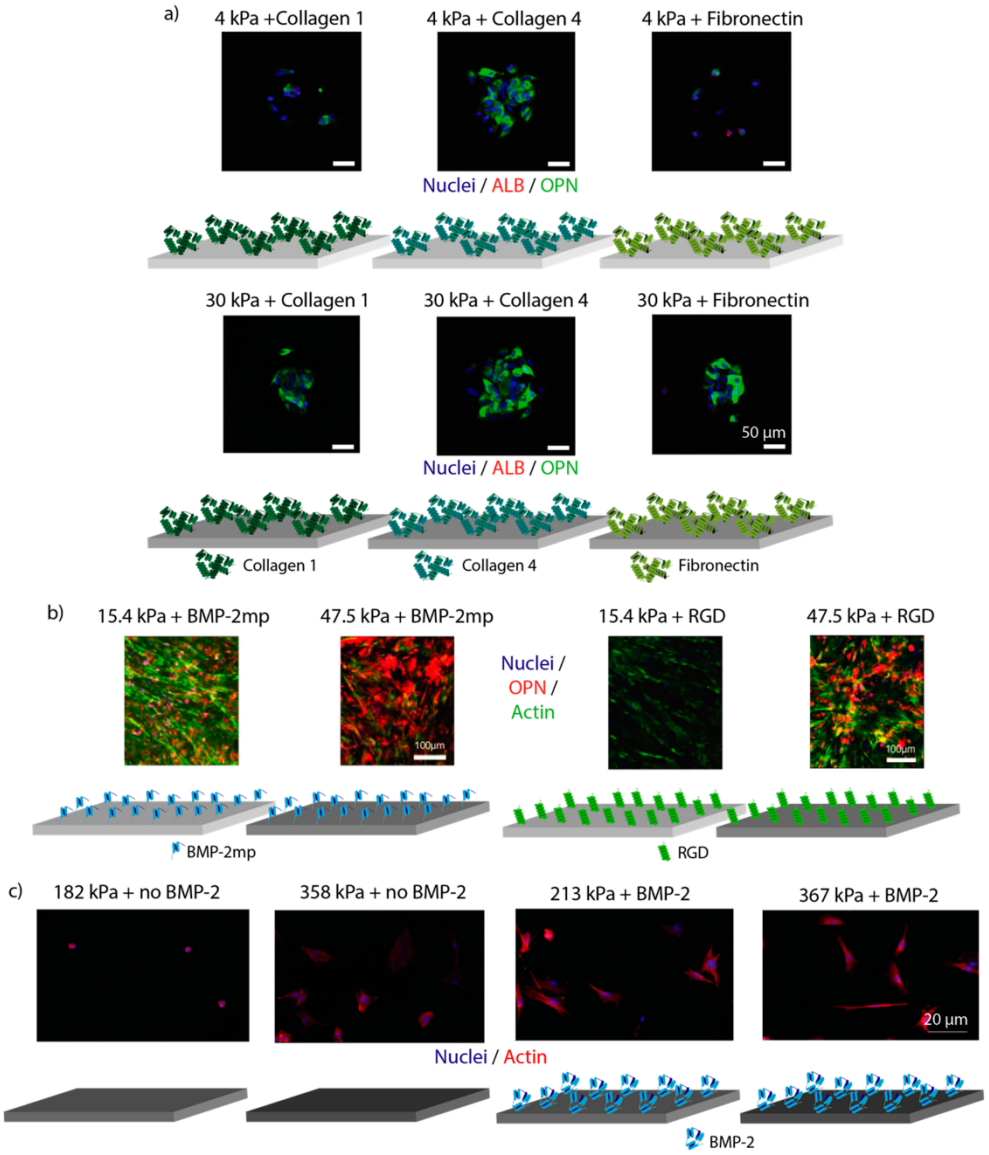

Figure 5. Cell differentiation dependence on mechanical properties of the substrate and the influence of biochemical ligands: Mechanics-dependent cell differentiation on mechanically consistent substrates can be influenced by (a) surface-immobilized ECM proteins, (b) ECM protein- or GF-derived peptides, or (c) GFs. (a) Cholangiocyte differentiation of bipotential mouse embryonic liver cells (BMEL) was independent of the elastic modulus in the presence of Col IV, but regulated by mechanical properties in the presence of FN on different PAAM substrates (4 and 30 kPa). Hepatocyte differentiation of BMEL was mainly independent of elastic modulus and guided by the present biochemical ligand. BMEL stained for cell nuclei (DAPI), albumin (ALB), and osteopontin (OPN). Image (a) reprinted and adapted with permission from ref 164. Copyright 2016 Elsevier. (b) hMSC showed mechanics-independent osteogenic differentiation in the presence of osteogenic ligand BMP-2 mimetic peptide on polyacrylamide-*co*-acrylic acid substrates. In the presence of the adhesion ligand RGD, hMSC displayed differentiation dependent on the elastic modulus: myogenic fate on soft (modulus: 15.4 kPa) and osteogenic fate on slightly stiffer (modulus: 47.5 kPa) substrates. hMSC after 4 weeks stained for actin, osteopontin (OPN), and cell nuclei (DAPI). Image (b) reprinted and adapted from ref 158. Copyright 2013 Elsevier. (c) Adhesion and spreading of C2C12 myoblasts is dependent on the presence of BMP-2 growth factor on soft PLL/HA films (modulus: 200 kPa) but independent of the ligand on substrates showing Young's moduli of around 360 kPa. An immunofluorescent staining of C2C12 was conducted for cell nuclei and actin. Image (c) adapted and reprinted with permission from ref 165. Copyright 2011 Wiley–VCH.

methods was able to distinguish between different peptides. Hence, because of the unspecific immobilization and characterization methods, the ratio of immobilized peptides on the surface is unknown and the reported synergistic effect from

https://dx.doi.org/10.1021/acsami.0c01893
ACS Appl. Mater. Interfaces 2020, 12, 21342−21367

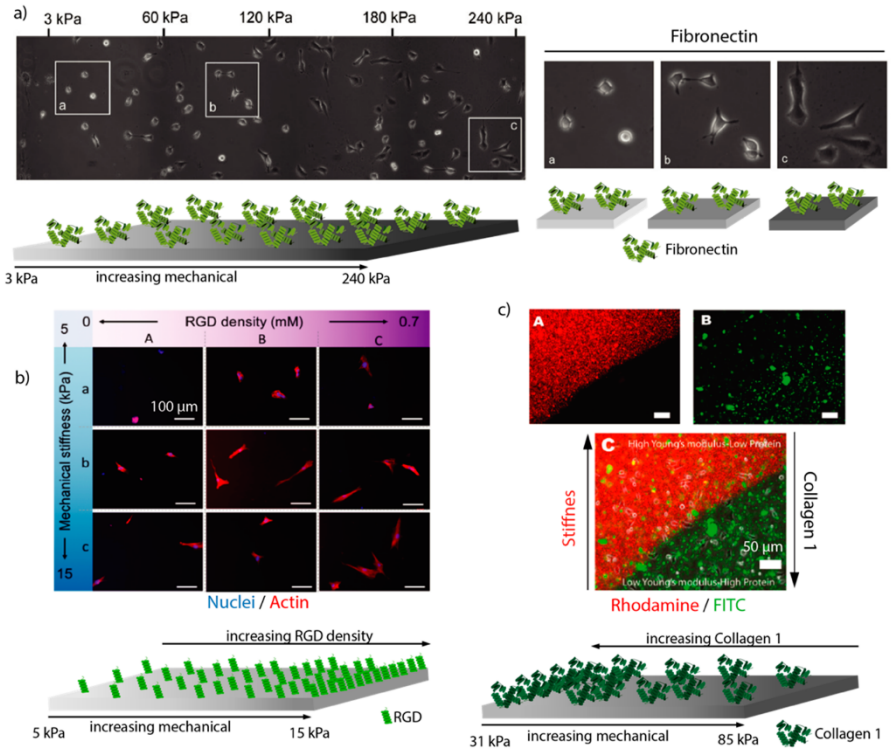

Figure 6. Combined effect of mechanical gradients and biochemical ligands on cell behavior. (a) NIH3T3 fibroblasts adhesion and spreading along a mechanical gradient (modulus: 1 to 240 kPa) of a PAAM substrate was only depending on elastic modulus, regardless of the immobilized present FN functionalization. Image (a) adapted and reprinted from ref. 190 under CC BY license. (b) Human fibroblasts (BJ) showed synergistically enhanced adhesion and spreading along parallel increasing mechanical properties (elastic modulus gradient from 5 to 15 kPa) and RGD adhesion peptide gradients (0–0.7 mM) on PEG substrates. An immunofluorescent staining of fibroblasts was conducted for actin and cell nuclei. Image (b) adopted and reprinted with permission from ref 63. Copyright 2016 American Chemical Society. (c) Adhesion and migration of Balb/c 3T3 fibroblasts is dependent on the present biochemical ligands on orthogonal mechanics (elastic modulus gradient from 31 to 85 kPa) and Col I gradients of PAAM substrates. Over a period of 3 h, fibroblasts migrated to or stayed at regions with high densities of the ligand. Image (c) adapted and reprinted with permission from ref 31. Copyright 2010 American Chemical Society.

peptide combination RGDS/YIGSR on endothelial cell proliferation cannot be correlated to an exact peptide ratio.

This example nicely demonstrates the challenges concerning fabrication and characterization of functionalized biomaterials. Methods for fabrication and characterization of materials functionalized with various biochemical groups are therefore divided here as follows: (a) random immobilization and molecule-unspecific characterization, (b) random immobilization and specific characterization, (c) specific immobilization and unspecific characterization, and (d) molecule-specific immobilization and specific characterization.

Unspecific immobilization methods encompass only one tethering route for all molecules at the same time, with concentration or ratio being only loosely controlled by the composition of the biomolecule solution used for the modification process. These strategies are often based on carbodiimide/n-hydroxysuccinimide chemistry.[74,87,92] They are well established and ensure effective molecule immobilization, but the lack of specificity bears the risk of compromising the bioavailability, as several amino acids of a biological compound might be able to conjugate.[195]

Specific immobilization strategies are mostly based on click chemistry, which is available as thiol–ene reaction, strain-promoted alkyne–azide cycloaddition (SPAAC), oxime ligation, and copper-catalyzed alkyne–azide cycloaddition (CuAAC).[93,97,102,196] In these cases, the different biomolecules can be modified to contain one of the click chemistry partners (e.g., alkyne) and the surface to present the respective other one (e.g., azide) allowing a specific reaction only between the targeted partners. However, although most of these approaches are cytocompatible, copper-catalyzed chemistry should be avoided in biomedical applications because of its toxicity.[197] Another specific immobilization method of tethering FN and VEGF has recently been published by Moulisova et al.[89] They exploited the different surface chemistry and charge of poly(ethyl acrylate) (PEA) and poly(methyl acrylate) (PMA) films to steer the conformation of FN adsorbed to the surface. By doing so, they achieved a globular conformation of FN on PMA and a fibril structure on PEA, with the latter structure exposing both the integrin binding site RGD and the VEGF binding site of FN.[89] This biomimetic presentation of both functionalities ensured their bioavailability.

https://dx.doi.org/10.1021/acsami.0c01893
ACS Appl. Mater. Interfaces 2020, 12, 21342–21367

Table 3. Overview of Studies Combining Chemical and Mechanical Surface Modifications and the Respective Characterization Methods[a]

substrate	preparation method	elastic modulus	mechanical characterization	immobilized molecules	immobilization method	chemical characterization	cell type	biological effect	ref.
Discrete Substrates Varying in Elastic Modulus Combined with Biochemical Ligands									
PAAM	polymerization with varying cross-linker concentration	10 Pa to 10 kPa	rheology	RGD	EDC/NHS and sulfo-SMCC coupling	cell staining after adhesion	adult neural stem cells (aNSC)	Enhanced aNSC spreading and proliferation above 100 Pa, neuronal gene expression at 500 Pa, neuron (100−500 Pa), or glial (1000−10000 Pa) differentiation.	182
PAAM	different polymer-block ratios	7 Pa to 19 kPa	rheology	FN	radiolabeling assay with NHS	radioactive labeling	neuroblasts (PC12)	Stiffness-dependent increase in adhesion and neurite formation of PC12 cells.	160
PAAM	concentration-dependent polymerization	0.1−1 kPa, 8−17 kPa, 25−40 kPa	AFM	Col I	covalent bonding after sulfo-SANPAH activation	fluorescence	mesenchymal stem cells (hMSC)	MSC differentiation in neuronal cells on soft, myogenic cells on intermediate, osteogenic cells on stiff substrates.	159
PAAM Or Collagen	different polymer-block ratios or collagen concentrations	0.5−40 kPa	rheology	Col I, FN, FBS, PDGF	covalent bonding after sulfo-SANPAH activation	cell staining after adhesion	human foreskin fibroblasts (BRS), oncogenic Ras-transformed BRS-Ras, myofibroblasts (BRS-MF)	FBS enhanced fibroblast spreading with increasing ligand density and increasing stiffness; PDGF effect was independent of mechanics or ligand.	192
PAAM	concentration-dependent cross-linking with Irgacure 2959	4−30 kPa		Col I, Col III, Col IV, FN, LM I	covalent bonding after sulfo-SANPAH activation	fluorescence	bipotential mouse embryonic liver progenitor cells (BMEL 9A1)	Hepatocyte differentiation induced by ECM composition; cholangiocyte differentiation in mechanics-independent in the presence of Col IV but mechanically driven on FN.	164
PEGDA, ACPEG	photoinitiated radical poly merization	4−41 kPa	AFM	RGD	EDC/NHS	cell staining after adhesion	fibroblasts (L929)	Enhanced fibroblast spreading above a modulus of 20 kPa.	193
PACAA	free radical polymerization	0.5−70 kPa	dynamic mechanical analysis	RGD and BMP-2 peptide	EDC/NHS coupling	fluorescence, XPS, high-resolution μ-imager (^{3}H-lysine)	mesenchymal stem cells (hMSC)	Mechanical stiffness-dependent and peptide-induced differentiation along the osteogenic or myogenic lineage.	158
PAAM	concentration dependent polymerization	0.7−80 kPa	tensile testing	Col I, Col IV, FN, LM I	covalent bonding after sulfo-SANPAH activation	fluorescence	mesenchymal stem cells (hMSC)	80 kPa and Col I increased osteogenic differentiation; 80 kPa and Col I or LM I, or 25 kPa and FN or Col IV induced myogenic differentiation.	161
PAAM	different polymer-block ratios	5.5−152 kPa	AFM	Col I, amino-, carboxyl-, phosphate-groups	covalent bonding after sulfo-SANPAH activation and plasma polymer deposition	XPS, water contact angle	mesenchymal stem cells (hMSC)	Enhanced adhesion on Col I and spreading on stiffer substrates; osteogenesis on 41 kPa with phosphate; myogenesis on 10−17 kPa with carboxyl; neurogenesis on <10 kPa with carboxyl.	162
PLL, HA	LbL-coating, cross-linking by sulfo-NHS and EDC	182−213 kPa, 358−367 kPa	AFM	BMP-2	postdiffusion and adsorption under acidic conditions	fluorescence	skeletal myoblasts (C2C12)	Immobilized BMP-2 had higher impact on C2C12, especially on soft substrates. Spreading, cytoskeleton formation and migration were enhanced.	165
HA, PLL	LbL-coating, cross-linking by sulfo-NHS and EDC	200−430 kPa	AFM, FT-IR	HGF	diffusion, physical adsorption	QCM-D	endothelial cells (HUVEC)	Increasing stiffness resulted in increased adhesion, migration, proliferation, and spreading. Function enhanced on soft substrates.	167
PDMS, PAAM	varied base to cross-linker ratio; from increasing monomer and cross-linker concentration	PDMS: 0.1 kPa to 2.3 MPa PAA: 0.1−740 kPa	microindentation	Col I, FN	covalent coupling after sulfo-SANPAH activation	immunofluorescence or immuno-histochemistry	mesenchymal stem cells (hMSC) and primary human keratinocytes	Independent of PDMS mechanical properties, keratinocyte and hMSC spreading and differentiation were similar. PAA induced increased spreading and decreasing differentiation of keratinocytes, increasing spreading and osteogenic differentiation of hMSC, but decreased adipogenic differentiation with varying stiffness	163
Col-GAG	different EDC/NHS ratios	2.85−5.05 MPa	tensile testing	BMP-2 PDGF	benzophenone immobilization with UV	fluorescence	adipose-derived stem cells (ADSC)	Substrate rigidity directed osteogenesis of ADSC. On soft substrates, GFs were needed. PDGF increased metabolic activity and proliferation but inhibited differentiation. BMP-2 induced no effect on lineage-specific differentiation.	168

https://dx.doi.org/10.1021/acsami.0c01893
ACS Appl. Mater. Interfaces 2020, 12, 21342−21367

Table 3. continued

substrate	preparation method	elastic modulus	mechanical characterization	immobilized molecules	immobilization method	chemical characterization	cell type	biological effect	ref.
Substrates Combining Mechanical and Biochemical Gradients									
HA/MeHA fibers	27% to 100% MeHA gradient, UV-cross-linking with Irgacure 2959	gradient: ~500 Pa to 10 kPa	AFM, FT-IR, SEM	RGD	gradient flow of two solutions, reaction of thiol-RGD and Me-HA	FT-IR, fluorescence	aortic arch explants	Increased cell infiltration from low to high RGD density/concentration of chick aortic arch explants.	186
PAAM	time-dependent UV cross-linking	gradient: 1–14 kPa	AFM	Col I	covalent bonding after sulfo-SANPAH activation	fluorescence	mesenchymal stem cells (hMSC)	MSC migration to stiffer part, myogenic differentiation.	187
PEG8NB, linear PEG2SH	time-, speed-, and photodependent thiol−ene reaction	gradient: 5–5 kPa	tensile testing	RGD	time- and speed-dependent UV exposure	fluorescence	human fibroblasts (BJ)	Increased fibroblast spreading along both gradients; most pronounced on stiffest end with high RGD concentration.	63
PAAM	different concentrations polymerized via photoinitiation	5–80 kPa, gradient: 1–80 kPa	AFM, uniaxial tensile testing	Col I	covalent bonding after sulfo-SANPAH activation	fluorescence	bovine aortic smooth muscle cells (VSMC)	Uniform gels: cell spreading, polarization, random motility increased with stiffness; gradients: spreading, durotaxis, and cell orientation increased with stiffness, nearly all cells polarized, cell migration to stiffer end.	185
PAAM	different polymer-block concentrations	gradients: 0.1–6.6 kPa, 2.4–38.1 kPa, 3.2–159.2 kPa	AFM, OCT	FN	covalent bonding after sulfo-SANPAH activation	fluorescence (FRET)	adipose-derived stem cells (ADSC) and skeletal myoblasts (C2C12)	ADSC migration to the stiffer end, increasing cell spreading with increasing stiffness, C2C12 spreading increased with stiffness.	189
PAAM	increasing the amount of cross-linker	gradient: 31.2–79.8 kPa	AFM	Col I	addition of FITC-Col I beads	fluorescence	fibroblasts (3T3)	Fibroblasts stayed at high Col I or migrated to the higher Col I concentration.	31
4–12% NuPage	different polymer-block ratios	gradient: 10–100 kPa	indentation, compression and tension	FN, Col I	covalent bonding after sulfo-SANPAH activation	fluorescence	mesenchymal stem cells (hBMSC)	Enhanced hBMSC adhesion and tenoblast differentiation on Col I; enhanced osteogenic differentiation on FN with increasing ligand density and stiffness.	191
PAAM	cross-linking with Irgacure 2959	gradient: 46.7–126.7 kPa	AFM	Col I	chemical conjugation with NHS and SDA and photomask UV-exposure	fluorescence and FN binding assay	fibroblasts (3T3)	Fibroblasts migrated to the soft, Col I-rich part, enhanced organization of the cytoskeleton.	188
PAAM	time-dependent UV cross-linking with Irgacure 2959	gradient: 1–240 kPa	AFM	FN	covalent bonding after sulfo-SANPAH activation	fluorescence	fibroblasts (NIH3T3) and neuroblastoma cells (SY5Y)	Increasing spreading with increasing stiffness.	190

[a]The biological response in vitro is briefly stated.

https://dx.doi.org/10.1021/acsami.0c01893
ACS Appl. Mater. Interfaces 2020, 12, 21342−21367

Special challenges arise, however, when aiming to fabricate parallel, reverse, or orthogonal gradients of two different biomolecules on the surface. There are no standard methods established yet, but a range of different strategies have been described. For instance, Ma et al. used a confined channel diffusion method and combined thiol−ene and SPAAC click chemistry to create a dual orthogonal peptide gradient.[93,95] Guan et al. also used two different click chemistries to achieve a dual reverse gradient by exploiting a temperature gradient for controlled peptide immobilization.[97] Other simpler methods to create gradients are based on time- controlled incubation of the sample in the molecule solution, which can be done by dipping with a linear motion drive[100] or by filling a container with a syringe pump.[101] Here, the same conjugation chemistry can be used for all immobilized molecules. Furthermore, gradient photomasks can be used for UV-mediated molecule immobilization to achieve parallel gradients.[86,104]

Detection and quantification of specific molecules in a mixture of molecules on a surface is challenging, and only a few characterization methods are currently available. Methods including XPS, Fourier-transform infrared spectroscopy (FTIR), atomic force microscopy (AFM), and water contact angle measurement (WCA) are very commonly used for materials chemistry characterization.[71,82,86,95,102] These methods are generally not suitable to detect different biological molecules, because of the chemical similarity of individual functional groups. The same accounts for biochemical methods, such as bicinchoninic acid (BCA) assay[85] or fluorescamine assay.[82,87] Although these methods specifically detect amino acids and thus biomolecules, they cannot differentiate between them. Hence, the actual amount of the different molecules present at the surface is not known and can only be estimated from the composition of the molecule solution. Thereby, control over the surface chemistry is limited, and discriminating effects from different molecules or concentrations on cell behavior become challenging, if not impossible.

On the other hand, enzyme-linked immunosorbent assay (ELISA) is very specific for the identification of single proteins and growth factors. An ELISA has typical detection limits of 0.01 ng per sample and allowed quantification of absolute amounts of molecules as well as analysis of bioavailability of the immobilized molecule and thus information about the conformation and directionality.[79,84,89] However, so far, this method is only available for whole proteins and growth factors but not in a commercial manner for peptides. Furthermore, it is not suitable for gradient characterization.[198] Amino acid analysis after hydrolyzation of molecules from the surface and subsequent analysis by liquid chromatography allowed revealing characteristic amino acids from different peptides.[73,74] This method allows quantitative detection in a pmol/cm^2 range. Direct labeling of biomolecules with fluorescent tags with different emission wavelengths presents a more versatile but less quantitative method.[97,103,104] Although this approach was used for many molecules, such as custom-synthesized peptides, and was suitable for gradient characterization,[198] difficulties can arise from background fluorescence, detection limits, and possible quenching of the fluorophore. Immunostaining of proteins such as FN or VN with nanoparticle-tagged antibodies allowed specific and quantitative detection of the protein with AFM characterization.[199] Time-of-flight secondary ion mass spectrometry (ToF-SIMS) is a promising method for characterization of multicomponent surfaces and gradients.[200] Its high sensitivity and specificity for different chemical groups allows for distinguishing footprints of individual amino acids and gives information about the orientation of the immobilized molecules. However, absolute quantification of chemical groups is not possible.[200−203]

Topographical or Mechanical Modification with Subsequent Chemical Functionalization. When combining topographical modification or modification of mechanical properties with biochemical functionalization, the modification steps are typically performed sequentially. Thus, control over the surface properties is possible, because mechanical and topographical functionalization use inherently different fabrication steps than biochemical ones. Surface topography on the one hand can be produced by a wide variety of methods, including different lithographical approaches,[122,126,156] microcontact printing,[155] multiphoton excited photochemistry,[121] particle adsorption,[111,124] sandblasting,[119] different etching techniques,[116,126,130,133] laser ablation methods,[129] mold casting methods,[120,126,127,135−137] embossing,[132,134] or electrospinning.[142,147,204,205] Modification of mechanical properties, on the other hand, is usually achieved by employing mechanically diverse polymer substrates that can be generated, for example, from polyethylene glycol (PEG),[63,157] PDMS,[163] collagen-GAG,[168] or hyaluronic acid[186] combined with poly-L-lysine[165,167] or poly(acrylamide-*co*-acrylic)acid[158] by varying the appropriate cross-linker amount. A commonly used substrate for varying mechanical properties is polyacrylamide (PAAM),[159,164,166,187−190,192] where distinct mechanical properties can be obtained by varying the amount of acrylamide or biacrylamide (B-AA),[159,166,189,192] by time-dependent UV cross-linking with a photo initiator, such as Irgacure 2959,[187,188] or a combination of both.[164,190]

Although surface topographies are characterized most frequently by atomic force microscopy (AFM)[111,115,116,124,126,127,130,134] and scanning electron microscopy (SEM),[50,119,120,122,128,147,206] mechanical properties of biomaterials (surface and bulk properties) are commonly determined by AFM,[159,185,188,189] mechanical tensile testing,[63,157,161,168,185,191] uniaxial compression measurements by dynamic mechanical analysis,[158] microindentation tests,[163] or rheology.[160,182] Profilometry or confocal 3D optical surface metrology allow quantification of surface roughness, similarly to AFM.[207−209]

Successful single protein or peptide functionalization can be confirmed by XPS,[120,158,162,166] immunostaining,[163,168,187,191] WCA measurement,[111,126,128,133,153] ELISA,[119,143] analysis of fluorescent biomolecules,[127,130,142,147,150,156] the zeta potential of the surface,[133] BCA assay,[50] electron spectroscopy for chemical analysis (ESCA),[135] or QCM-d.[167] However, some methods can be influenced by both chemical and topographical or mechanical properties of the substrates. For example, water contact angles are dependent on surface chemistry (Wenzel model) and on roughness (Cassie−Baxter model), thus limiting the applicability of WCA measurements as sole method for biochemical characterization of topographically modified substrates.[210,211] Furthermore, the same technical limitations described above occur when developing chemical gradients or when using more than one biochemical group for the modification of topographically/mechanically modified materials.

It is also important to consider that mechanical properties are inherently related to materials chemistry and that surface biochemical functionalization could alter surface mechanical properties.[5,212−215] In this context, one study compared

https://dx.doi.org/10.1021/acsami.0c01893
ACS Appl. Mater. Interfaces 2020, 12, 21342−21367

compressive and tensile properties of un- and ECM-coated surfaces and revealed that the standard compression stiffness estimation by indentation-type AFM showed no significant differences in stiffness values because of the dependency of indentation depth perpendicular indentation and the layer thickness of the protein modification. However, a tensile mechanical characterization using a biaxial stretcher showed higher resistance values of FN and Col coatings compared to uncoated regions, causing direction-dependent and ligand-specific mechanical properties, which may affect mechanically driven cellular responses.[215] Another study showed that commonly used AFM-based indentation with colloidal probes measured the micrometer-scale stiffness of a material by deformation, whereas a force−distance measurement with a modified AFM tip could determine nanoscale stiffness of material cross-links on the molecular level, which also mediates cell attachment.[193] A strong interdependence of all properties might be the reason why studies systematically investigating the effect of altered topography and mechanical characteristics are rare.[216−222]

4. CONCLUSION AND FUTURE PERSPECTIVES

Here, we summarized the systematic combination of several surface modifications, such as (I) various biochemical cues immobilized on a surface, (II) the combination of different topographical surface features functionalized with biochemical cues, and (III) the combination of mechanical substrate properties modified with biochemical cues, demonstrating that combinations of these different signals generally elicit positive synergistic effects with regard to a variety of cell responses and fate decisions. Furthermore, we highlight the importance of fabrication and characterization methods that are specific for the individual modification in order to provide control over such complex systems and ensure a correct correlation of effect and outcome.

The lack of comparability between studies on biomaterials and biological responses is one well-known challenge.[223−226] Even though many reviewed studies investigated similar material systems, the comparison of their results is challenging because of differences in chosen material characterization methods (e.g., bulk material tensile testing or surface mechanical nanoindentation), alterations in terminology, or disparities in biomolecule source (e.g., animal-derived vs recombinant proteins).[215,227−230] Furthermore, many different cell types have been used to study the effects of surface properties on cell behavior, and results can fluctuate even in reports using identical cell lines or cells from the same batch, as genetic variability and diversification is common in cell lines.[231]

In order to achieve better comparability between studies in the future, we propose that not only controlled fabrication methods are combined with quantitative characterization techniques but also that the source of biochemical compounds or, for example, design of peptides should be, if possible, based on previous studies in order to provide better comparability.

Surface modification is a very useful step for understanding the interplay of materials with biology and for isolating specific effects. In future studies, we expect to see increased combinations of chemical, topographical and mechanical cues at once as well as increasing combinations of 3+ chemical signals. Especially, larger systematic studies should be conducted in order to be able to derive overall conclusions and lessons for strategic further development.

However, for tissue engineering and regenerative medicine, moving toward 3D is crucial.[232−234] The need for material surface functionalization to enhance cell interaction and mimicry of the natural cell niche is very much needed.[235−240] However, further aspects, such as the substrate/scaffold porosity and architecture, increase the complexity.[213,236,241−246]

For instance, a recent study combining electrospinning and photolithography showed that osteogenic differentiation of hMSC was enhanced on a grooved substrate made of composite electrospun nanofibers.[247] Along this line, some research groups are increasingly focusing on the design and development of smart, functional 3D biomaterials that actively interact with cells and respond to diverse stimuli, including pH, temperature, or ionic strength.[248] Furthermore, high-throughput platforms and multiwell arrays enable rapid screening of different cellular stimuli, such as surface exposed topography or rigidity cues, either simultaneously or in isolatation to assess their influence on cell behavior.[249]

Research on biomaterials for tissue engineering is poised to grow in the future,[250] as personalized regenerative medicine approaches using stem cells are moving toward clinical applications.[251] For scaling up the throughput of groups per experiment, a promising study developed a 3D niche microarray system to better understand cellular responses in a variety of biochemically and physically functionalized 3D microenvironments.[252]

However, we believe the development of this field depends not only on progress within tissue engineering itself but also on parallel progress in basic biology. Basic biology will allow us to increasingly understand the exact properties of ECM: concentrations of chemical signals and their presentation, detailed structures, and mechanical properties.[253−255] Therefore, efforts from both sides should by synergized in more interdisciplinary approaches to strive for optimized mimicry of the extracellular matrix.

Already in 2009, general considerations about biomaterial complexity have been discussed, for example, by Place, Evans, and Stevens,[13] who highlighted that financial aspects limit complexity because multifunctionality decreases the probability of successful clinical translation. They suggested seeking the minimal complexity for achieving the desired functional outcome, such as a particular cell type adhesion, proliferation, or differentiation.[13] We agree that a balance between increasing complexity on the road to clinical applicability and related cost-effectiveness should be aimed for. The here-discussed and motivated technical and scientific advances in material modification and characterization may pave the way for clinical translation of true biomimetic biomaterial concepts in the future.

We strongly believe that multifunctional surface modification approaches will gain increasing relevance, but we cannot emphasize enough that the choice of appropriate methods is of paramount importance for their success and chances for successful clinical translation.

AUTHOR INFORMATION

Corresponding Authors

Markus Rottmar − *Laboratory for Biointerfaces, Empa, Swiss Federal Laboratories for Materials Science and Technology, St. Gallen 9014, Switzerland;* orcid.org/0000-0001-7636-428X; Email: markus.rottmar@empa.ch

Anne Géraldine Guex − *Laboratory for Biointerfaces and Laboratory for Biomimetic Membranes and Textiles, Empa, Swiss*

https://dx.doi.org/10.1021/acsami.0c01893
ACS Appl. Mater. Interfaces 2020, 12, 21342−21367

Federal Laboratories for Materials Science and Technology, St. Gallen 9014, Switzerland; Email: annegeraldine.guex@empa.ch

Authors

Anne-Sophie Mertgen − *Laboratory for Biointerfaces and Laboratory for Biomimetic Membranes and Textiles, Empa, Swiss Federal Laboratories for Materials Science and Technology, St. Gallen 9014, Switzerland*

Vanessa Tanja Trossmann − *Lehrstuhl für Biomaterialien, Universität Bayreuth, Bayreuth 95440, Germany*

Katharina Maniura-Weber − *Laboratory for Biointerfaces, Empa, Swiss Federal Laboratories for Materials Science and Technology, St. Gallen 9014, Switzerland*; orcid.org/0000-0001-7895-3563

Thomas Scheibel − *Lehrstuhl für Biomaterialien, Bayerisches Polymerinstitut (BPI), Bayreuther Zentrum für Kolloide und Grenzflächen (BZKG), Bayreuther Zentrum für Molekulare Biowissenschaften (BZMB), Bayreuther Materialzentrum (BayMAT), Universität Bayreuth, Bayreuth 95440, Germany*

Complete contact information is available at: https://pubs.acs.org/10.1021/acsami.0c01893

Author Contributions

†A.-S.M. and V.T.T. contributed equally to this work.

Notes

The authors declare no competing financial interest.

■ ACKNOWLEDGMENTS

This work is part of the Zurich Heart project under the umbrella of University Medicine Zurich/Hochschulmedizin Zürich. This work was funded by Deutsche Forschungsgemeinschaft (DFG, German Research Foundation) project number 326998133-TRR 225 (subproject C01).

■ ABBREVIATIONS

3D, three-dimensional
AA, acrylic acid
ACLF, anterior cruciate ligament fibroblasts
ACPEG, carboxy poly(ethylene glycol) acrylate
AFM, atomic force microscopy
ALB, albumin
ALP, alkaline phosphatase
aNSC, adult neural stem cells
AoSMCs, aortic smooth muscle cells
APTES, 3-aminopropyltriethoxysilane
ASCs, adipose stem cells
B-AA, biacrylamide
BAEC, bovine aortic endothelial cells
BCA, bicinchoninic acid
BCMN, block copolymer micelle nanolithography
BCP, biphasic calcium phosphate
bFGF, basic-fibroblast growth factor
BMP, bone morphogenic protein
BMEL, bipotential mouse embryonic liver cells
BMSC, bone marrow stem cells
BSA, bovine serum albumin
BSP, bone salioprotein
C2C12, murine myoblast cell line
Col, collagen
CPTES, chloropropyltriethoxysilane
CuAAC, copper-catalyzed alkyne−azide cyloaddition
DMPA, 2,2-dimethoxy-2-phenylacetophenone
DP-MSC, dental pulp-derived mesenchymal stem cells
DRIE, deep reactive ion etching
ECM, extracellular matrix
EDC/NHS, 1-ethyl-3-(3-(dimethylamino)propyl)-carbodiimide hydrochloride/N-succinic anhydride
EDX, energy-dispersive X-ray analysis
EGF, epidermal growth factor
ELISA, enzyme-linked immunosorbent assay
ESCA, electron spectroscopy for chemical analysis
FE-SEM, field-emission scanning electron microscopy
FITC, fluoresceinisothiocyanate
FN, fibronectin
FTIR, Fourier transform infrared spectroscopy
GAG, glycosaminoglycan
GF, growth factor
HA, hyaluronic acid
hADSC, human adipose-derived stem cells
HAP, hydroxyapatite
hBMSC, human bone marrow-derived stem cells
HCEC, human corneal epithelial cells
HDT, hexadecanethiol
HGFI, class I hydrophobin
HMDS, hexamethyldisilazane
hMSC, human mesenchymal stem cells
HPMEC, human pulmonary microvascular endothelial cells
HUVEC, human umbilical cord vein endothelial cells
IGF, insulin-like growth factor
IRRAS, infrared reflection−absorption spectroscopy
KQAGDV, Lys-Gln-Ala-Gly-Asp-Val
KRSR, Lys-Arg-Ser-Lys
LbL, layer-by-layer
LM, laminin
MBA, N,N′-methylenbisacrylamid
MBS, m-maleimidobenzoyl-*N*-hydroxysuccinimide ester
MEF, mouse embryonic fibroblasts
mESC, mouse embryonic stem cell
MSC, mesenchymal stem cell
NGF, neuronal growth factor
ODTS, octadecyltrichlorosilane
OPN, osteopontin
PAA, poly(acrylic acid)
PAAM, poly(acrylamide)
PACAA, poly(acrylamide-*co*-acrylic acid)
PC, poly(carbonate)
PC12 cell, neuronal cell line
PCL, poly(e-caprolactone)
PDGF, platelet-derived growth factor
PDMS, poly(dimethylsiloxane)
PEA, poly(ethyl acrylate)
PEG, poly(ethylene glycol)
PEGDA, PEG-diacrylate
PEI, poly(ethylene imine)
PET, poly(ethylene terephtalate)
pGMA, poly(glycidyl methacrylate)
PLA, polylactic acid
PLCL, poly(L-lactide-*co*-caprolactone)
PLGA, poly(lactic-*co*-glycolic acid)
PLLA, poly(L-lactic acid)
PLLCL, poly(L-lactic acid-*co*-ε-caprolactone)
PMA, poly(methyl acrylate)
PS, poly(styrene)
PU, poly(urethane)

https://dx.doi.org/10.1021/acsami.0c01893
ACS Appl. Mater. Interfaces 2020, 12, 21342−21367

PUA, polyurethane acrylate
PVDMA, 2-vinyl-4,4-dimethylazlactone
QCM-d, quartz crystal microbalance - dissipation
QK, VEGF mimicking peptide (KLTWQELYQLKYKGI)
RCO, rat calvarial osteoblasts
REDV, Arg-Glu-Asp-Val
RGD, Arg-Gly-Asp
SAM, self-assembled monolayer
SEM, scanning electron microscopy
SMC, smooth muscle cell
SPAAC, strain promoted alkyne−azide cycloaddition
SPDP, N-succinimidyl-3-(2-pyridyldithio)propionate
Sulfo-SANPAH, sulfosuccinimidyl 6-(4′-azido-2′-nitrophenylamino)hexanoate
Sulfo-SMCC, sulfosuccinimidyl 4-(N-maleimidomethyl) cyclohexane-1-carboxylate
SVVYGLR, Ser-Val-Val-Tyr-Gly-Leu-Arg
TAMRA, 5-carboxytetramethylrhodamin
ToF-SIMS, time-of-flight secondary ion mass spectrometry
UV/vis, ultraviolet−visible spectroscopy
VEGF, vascular endothelial growth factor
WCA, water contact angle
XPS, X-ray photoelectron spectroscopy
YIGSR, Tyr-Ile-Gly-Ser-Arg
NGF, nerve growth factor

REFERENCES

(1) Chan, B. P.; Leong, K. W. Scaffolding in Tissue Engineering: General Approaches and Tissue-Specific Considerations. *European Spine Journal* **2008**, *17* (4), 467−479.
(2) Bhat, S.; Kumar, A. Biomaterials and Bioengineering Tomorrow's Healthcare. *Biomatter* **2013**, *3* (3), e24717.
(3) Wei, Q.; Becherer, T.; Angioletti-Uberti, S.; Dzubiella, J.; Wischke, C.; Neffe, A. T.; Lendlein, A.; Ballauff, M.; Haag, R. Protein Interactions with Polymer Coatings and Biomaterials. *Angew. Chem., Int. Ed.* **2014**, *53* (31), 8004−8031.
(4) Pacelli, S.; Manoharan, V.; Desalvo, A.; Lomis, N.; Jodha, K. S.; Prakash, S.; Paul, A. Tailoring Biomaterial Surface Properties to Modulate Host-Implant Interactions: Implication in Cardiovascular and Bone Therapy. *J. Mater. Chem. B* **2016**, *4* (9), 1586−1599.
(5) Kyziol, K.; Kaczmarek, L.; Kyziol, A. Surface Functionalization of Biomaterials In *Handbook of Composites from Renewable Materials*; Wiley,2017; Chapter 18 , pp 457−490.
(6) Qi, P.; Maitz, M. F.; Huang, N. Surface Modification of Cardiovascular Materials and Implants. *Surf. Coat. Technol.* **2013**, *233*, 80−90.
(7) Borkner, C. B.; Wohlrab, S.; Möller, E.; Lang, G.; Scheibel, T. Surface Modification of Polymeric Biomaterials Using Recombinant Spider Silk Proteins. *ACS Biomater. Sci. Eng.* **2017**, *3* (5), 767−775.
(8) Aamodt, J. M.; Grainger, D. W. Extracellular Matrix-Based Biomaterial Scaffolds and the Host Response. *Biomaterials* **2016**, *86*, 68−82.
(9) Harvey, A. G.; Hill, E. W.; Bayat, A. Designing Implant Surface Topography for Improved Biocompatibility. *Expert Rev. Med. Devices* **2013**, *10* (2), 257−267.
(10) Li, D.; Zheng, Q.; Wang, Y.; Chen, H. Combining Surface Topography with Polymer Chemistry: Exploring New Interfacial Biological Phenomena. *Polym. Chem.* **2014**, *5* (1), 14−24.
(11) Zhang, H.; Zheng, X.; Ahmed, W.; Yao, Y.; Bai, J.; Chen, Y.; Gao, C. Design and Applications of Cell-Selective Surfaces and Interfaces. *Biomacromolecules* **2018**, *19* (6), 1746−1763.
(12) Hinderer, S.; Layland, S. L.; Schenke-Layland, K. ECM and ECM-Like Materials - Biomaterials for Applications in Regenerative Medicine and Cancer Therapy. *Adv. Drug Delivery Rev.* **2016**, *97*, 260−269.
(13) Place, E. S.; Evans, N. D.; Stevens, M. M. Complexity in Biomaterials for Tissue Engineering. *Nat. Mater.* **2009**, *8*, 457−480.
(14) Duck, F. A. Physical Properties of Tissues. In *Physical Properties of Tissues*; Duck, F. A., Ed.; Academic Press: London, 1990; pp 1−336.
(15) Lin, C.-C.; Anseth, K. S. Cell-Cell Communication Mimicry with Poly(Ethylene Glycol) Hydrogels for Enhancing Beta-Cell Function. *Proc. Natl. Acad. Sci. U. S. A.* **2011**, *108* (16), 6380−6385.
(16) Discher, D. E.; Mooney, D. J.; Zandstra, P. W. Growth Factors, Matrices, and Forces Combine and Control Stem Cells. *Science* **2009**, *324* (5935), 1673−1677.
(17) Janson, I. A.; Putnam, A. J. Extracellular Matrix Elasticity and Topography: Material-Based Cues that Affect Cell Function via Conserved Mechanisms. *J. Biomed. Mater. Res., Part A* **2015**, *103* (3), 1246−1258.
(18) Polo-Corrales, L.; Latorre-Esteves, M.; Ramirez-Vick, J. E. Scaffold Design for Bone Regeneration. *J. Nanosci. Nanotechnol.* **2014**, *14* (1), 15−56.
(19) Martino, M. M.; Briquez, P. S.; Maruyama, K.; Hubbell, J. A. Extracellular Matrix-Inspired Growth Factor Delivery Systems for Bone Regeneration. *Adv. Drug Delivery Rev.* **2015**, *94*, 41−52.
(20) Yurdagul, A., Jr.; Orr, A. W. Blood Brothers: Hemodynamics and Cell-Matrix Interactions in Endothelial Function. *Antioxid. Redox Signaling* **2016**, *25* (7), 415−434.
(21) Yousif, L. F.; Di Russo, J.; Sorokin, L. Laminin Isoforms in Endothelial and Perivascular Basement Membranes. *Cell Adh Migr* **2013**, *7* (1), 101−110.
(22) Augustin, H. G.; Young Koh, G.; Thurston, G.; Alitalo, K. Control of Vascular Morphogenesis and Homeostasis through the Angiopoietin - Tie System. *Nat. Rev. Mol. Cell Biol.* **2009**, *10* (3), 165−177.
(23) García de Vinuesa, A.; Abdelilah-Seyfried, S.; Knaus, P.; Zwijsen, A.; Bailly, S. BMP Signaling in Vascular Biology and Dysfunction. *Cytokine Growth Factor Rev.* **2016**, *27*, 65−79.
(24) Janson, I. A.; Kong, Y. P.; Putnam, A. J. Nanotopographic Substrates of Poly (Methyl Methacrylate) do not Strongly Influence the Osteogenic Phenotype of Mesenchymal Stem Cells In Vitro. *PLoS One* **2014**, *9* (3), No. e90719.
(25) Ruoslahti, E. RGD and Other Recognition Sequences for Integrins. *Annu. Rev. Cell Dev. Biol.* **1996**, *12* (1), 697−715.
(26) Kim, S. H.; Turnbull, J.; Guimond, S. Extracellular Matrix and Cell Signalling: The Dynamic Cooperation of Integrin, Proteoglycan and Growth Factor Receptor. *J. Endocrinol.* **2011**, *209* (2), 139−151.
(27) Geiger, B.; Spatz, J. P.; Bershadsky, A. D. Environmental Sensing through Focal Adhesions. *Nat. Rev. Mol. Cell Biol.* **2009**, *10*, 21−33.
(28) Ashe, H. L.; Briscoe, J. The Interpretation of Morphogen Gradients. *Development* **2006**, *133* (3), 385−394.
(29) Jin, T.; Xu, X.; Hereld, D. Chemotaxis, Chemokine Receptors and Human Disease. *Cytokine* **2008**, *44* (1), 1−8.
(30) Sundararaghavan, H. G.; Monteiro, G. A.; Firestein, B. L.; Shreiber, D. I. Neurite Growth in 3D Collagen Gels with Gradients of Mechanical Properties. *Biotechnol. Bioeng.* **2009**, *102* (2), 632−643.
(31) Hale, N. A.; Yang, Y.; Rajagopalan, P. Cell Migration at the Interface of a Dual Chemical-Mechanical Gradient. *ACS Appl. Mater. Interfaces* **2010**, *2* (8), 2317−2324.
(32) Deymier, A. C.; An, Y.; Boyle, J. J.; Schwartz, A. G.; Birman, V.; Genin, G. M.; Thomopoulos, S.; Barber, A. H. Micro-Mechanical Properties of the Tendon-to-Bone Attachment. *Acta Biomater.* **2017**, *56*, 25−35.
(33) Nguyen, L. H.; Kudva, A. K.; Saxena, N. S.; Roy, K. Engineering Articular Cartilage with Spatially-Varying Matrix Composition and Mechanical Properties from a Single Stem Cell Population Using a Multi-Layered Hydrogel. *Biomaterials* **2011**, *32* (29), 6946−6952.
(34) Kingshott, P.; Andersson, G.; McArthur, S. L.; Griesser, H. J. Surface Modification and Chemical Surface Analysis of Biomaterials. *Curr. Opin. Chem. Biol.* **2011**, *15* (5), 667−676.
(35) Wu, G.; Li, P.; Feng, H.; Zhang, X.; Chu, P. K. Engineering and Functionalization of Biomaterials via Surface Modification. *J. Mater. Chem. B* **2015**, *3* (10), 2024−2042.

https://dx.doi.org/10.1021/acsami.0c01893
ACS Appl. Mater. Interfaces 2020, 12, 21342−21367

(36) Bierbaum, S.; Hintze, V.; Scharnweber, D. Functionalization of Biomaterial Surfaces Using Artificial Extracellular Matrices. *Biomatter* **2012**, *2* (3), 132−141.
(37) Wade, R. J.; Burdick, J. A. Engineering ECM Signals into Biomaterials. *Mater. Today* **2012**, *15* (10), 454−459.
(38) Darnell, M.; Mooney, D. J. Leveraging Advances in Biology to Design Biomaterials. *Nat. Mater.* **2017**, *16*, 1178−1185.
(39) Ross, A. M.; Lahann, J. Surface engineering the cellular microenvironment via patterning and gradients. *J. Polym. Sci., Part B: Polym. Phys.* **2013**, *51* (10), 775−794.
(40) Ermis, M.; Antmen, E.; Hasirci, V. Micro and Nanofabrication Methods to Control Cell-Substrate Interactions and Cell Behavior: A Review from the Tissue Engineering Perspective. *Bioactive Materials* **2018**, *3* (3), 355−369.
(41) Amani, H.; Arzaghi, H.; Bayandori, M.; Dezfuli, A. S.; Pazoki-Toroudi, H.; Shafiee, A.; Moradi, L. Controlling Cell Behavior through the Design of Biomaterial Surfaces: A Focus on Surface Modification Techniques. *Adv. Mater. Interfaces* **2019**, *6* (13), 1900572−1900601.
(42) Richbourg, N. R.; Peppas, N. A.; Sikavitsas, V. I. Tuning the Biomimetic Behavior of Scaffolds for Regenerative Medicine Through Surface Modifications. *J. Tissue Eng. Regener. Med.* **2019**, *13* (8), 1275−1293.
(43) Discher, D. E.; Janmey, P.; Wang, Y.-l. Tissue Cells Feel and Respond to the Stiffness of Their Substrate. *Science* **2005**, *310* (5751), 1139−1143.
(44) Wells, R. G. The Role of Matrix Stiffness in Regulating Cell Behavior. *Hepatology* **2008**, *47* (4), 1394−1400.
(45) Prager-Khoutorsky, M.; Lichtenstein, A.; Krishnan, R.; Rajendran, K.; Mayo, A.; Kam, Z.; Geiger, B.; Bershadsky, A. D. Fibroblast Polarization is a Matrix-Rigidity-Dependent Process Controlled by Focal Adhesion Mechanosensing. *Nat. Cell Biol.* **2011**, *13*, 1457−1465.
(46) Fiedler, J.; Özdemir, B.; Bartholomä, J.; Plettl, A.; Brenner, R. E.; Ziemann, P. The Effect of Substrate Surface Nanotopography on the Behavior of Multipotnent Mesenchymal Stromal Cells and Osteoblasts. *Biomaterials* **2013**, *34* (35), 8851−8859.
(47) Künzler, T. P.; Drobek, T.; Schuler, M.; Spencer, N. D. Systematic Study of Osteoblast and Fibroblast Response to Roughness by means of Surface-Morphology Gradients. *Biomaterials* **2007**, *28* (13), 2175−2182.
(48) Zink, C.; Hall, H.; Brunette, D. M.; Spencer, N. D. Orthogonal Nanometer-Micrometer Roughness Gradients Probe Morphological Influences on Cell Behavior. *Biomaterials* **2012**, *33* (32), 8055−8061.
(49) Faia-Torres, A. B.; Guimond-Lischer, S.; Rottmar, M.; Charnley, M.; Goren, T.; Maniura-Weber, K.; Spencer, N. D.; Reis, R. L.; Textor, M.; Neves, N. M. Differential Regulation of Osteogenic Differentiation of Stem Cells on Surface Roughness Gradients. *Biomaterials* **2014**, *35* (33), 9023−9032.
(50) Yang, G.; Liu, Z.; Guo, Y.; Zhang, J.; Li, H.; Shi, W.; Feng, J.; Wang, K.; Yang, L. Osteoblast Response to the Surface Topography of Hydroxyapatite Two-Dimensional Films. *J. Biomed. Mater. Res., Part A* **2017**, *105* (4), 991−999.
(51) Waddell, S. J.; de Andrés, M. C.; Tsimbouri, P. M.; Alakpa, E. V.; Cusack, M.; Dalby, M. J.; Oreffo, R. O. Biomimetic Oyster Shell-Replicated Topography Alters the Behaviour of Human Skeletal Stem Cells. *J. Tissue Eng.* **2018**, *9*, 2041731418794007.
(52) Vasilevich, A. S.; Mourcin, F.; Mentink, A.; Hulshof, F.; Beijer, N.; Zhao, Y.; Levers, M.; Papenburg, B.; Singh, S.; Carpenter, A. E.; Stamatialis, D.; Blitterswijk, C. v.; Tarte, K.; Boer, J. d. Designed Surface Topographies Control ICAM-1 Expression in Tonsil-Derived Human Stromal Cells. *Front. Bioeng. Biotechnol.* **2018**, *6*, 87.
(53) Vermeulen, S.; Vasilevich, A.; Tsiapalis, D.; Roumans, N.; Vroemen, P.; Beijer, N. R. M.; Dede Eren, A.; Zeugolis, D.; de Boer, J. Identification of Topographical Architectures Supporting the Phenotype of Rat Tenocytes. *Acta Biomater.* **2019**, *83*, 277−290.
(54) Zijl, S.; Vasilevich, A. S.; Viswanathan, P.; Helling, A. L.; Beijer, N. R. M.; Walko, G.; Chiappini, C.; de Boer, J.; Watt, F. M. Micro-Scaled Topographies Direct Differentiation of Human Epidermal Stem Cells. *Acta Biomater.* **2019**, *84*, 133−145.
(55) Allan, C.; Ker, A.; Smith, C.-A.; Tsimbouri, P. M.; Borsoi, J.; O'Neill, S.; Gadegaard, N.; Dalby, M. J.; Dominic Meek, R. Osteoblast Response to Disordered Nanotopography. *J. Tissue Eng.* **2018**, *9*, 2041731418784098.
(56) Dalby, M. J.; Riehle, M. O.; Johnstone, H.; Affrossman, S.; Curtis, A. S. G. Investigating the Limits of Filopodial Sensing: a Brief Report Using SEM to Image the Interaction between 10 nm High Nano-Topography and Fibroblast Filopodia. *Cell Biol. Int.* **2004**, *28* (3), 229−236.
(57) Dalby, M. J.; Gadegaard, N.; Oreffo, R. O. C. Harnessing Nanotopography and Integrin-Matrix Interactions to Influence Stem Cell Fate. *Nat. Mater.* **2014**, *13*, 558−569.
(58) Arnold, M.; Cavalcanti-Adam, E. A.; Glass, R.; Blümmel, J.; Eck, W.; Kantlehner, M.; Kessler, H.; Spatz, J. P. Activation of Integrin Function by Nanopatterned Adhesive Interfaces. *ChemPhysChem* **2004**, *5* (3), 383−388.
(59) Cavalcanti-Adam, E. A.; Volberg, T.; Micoulet, A.; Kessler, H.; Geiger, B.; Spatz, J. P. Cell Spreading and Focal Adhesion Dynamics Are Regulated by Spacing of Integrin Ligands. *Biophys. J.* **2007**, *92* (8), 2964−2974.
(60) Cavalcanti-Adam, E. A.; Aydin, D.; Hirschfeld-Warneken, V. C.; Spatz, J. P. Cell Adhesion and Response to Synthetic Nanopatterned Environments by Steering Receptor Clustering and Spatial Location. *HFSP J.* **2008**, *2* (5), 276−285.
(61) Huang, J.; Gräter, S. V.; Corbellini, F.; Rinck, S.; Bock, E.; Kemkemer, R.; Kessler, H.; Ding, J.; Spatz, J. P. Impact of Order and Disorder in RGD Nanopatterns on Cell Adhesion. *Nano Lett.* **2009**, *9* (3), 1111−1116.
(62) Wang, X.; Yan, C.; Ye, K.; He, Y.; Li, Z.; Ding, J. Effect of RGD Nanospacing on Differentiation of Stem Cells. *Biomaterials* **2013**, *34* (12), 2865−2874.
(63) Tong, X.; Jiang, J.; Zhu, D.; Yang, F. Hydrogels with Dual Gradients of Mechanical and Biochemical Cues for Deciphering Cell-Niche Interactions. *ACS Biomater. Sci. Eng.* **2016**, *2* (5), 845−852.
(64) Genzer, J.; Bhat, R. R. Surface-Bound Soft Matter Gradients. *Langmuir* **2008**, *24* (6), 2294−2317.
(65) Genzer, J. Surface-Bound Gradients for Studies of Soft Materials Behavior. *Annu. Rev. Mater. Res.* **2012**, *42* (1), 435−468.
(66) Seidi, A.; Ramalingam, M.; Elloumi-Hannachi, I.; Ostrovidov, S.; Khademhosseini, A. Gradient Biomaterials for Soft-to-Hard Interface Tissue Engineering. *Acta Biomater.* **2011**, *7* (4), 1441−1451.
(67) Wu, J.; Mao, Z.; Tan, H.; Han, L.; Ren, T.; Gao, C. Gradient Biomaterials and their Influences on Cell Migration. *Interface Focus* **2012**, *2* (3), 337−355.
(68) Zou, B.; Liu, Y.; Luo, X.; Chen, F.; Guo, X.; Li, X. Electrospun Fibrous Scaffolds with Continuous Gradations in Mineral Contents and Biological Cues for Manipulating Cellular Behaviors. *Acta Biomater.* **2012**, *8* (4), 1576−1585.
(69) Smith Callahan, L. A. Gradient Material Strategies for Hydrogel Optimization in Tissue Engineering Applications. *High-Throughput* **2018**, *7* (1), 1−13.
(70) Tate, C. C.; Shear, D. A.; Tate, M. C.; Archer, D. R.; Stein, D. G.; LaPlaca, M. C. Laminin and Fibronectin Scaffolds Enhance Neural Stem Cell Transplantation into the Injured Brain. *J. Tissue Eng. Regener. Med.* **2009**, *3*, 208−217.
(71) Castellanos, M. I.; Mas-Moruno, C.; Grau, A.; Serra-Picamal, X.; Trepat, X.; Albericio, F.; Joner, M.; Gil, F. J.; Ginebra, M. P.; Manero, J. M.; Pegueroles, M. Functionalization of CoCr Surfaces with Cell Adhesive Peptides to Promote HUVECs Adhesion and Proliferation. *Appl. Surf. Sci.* **2017**, *393*, 82−92.
(72) Castellanos, M. I.; Guillem-Marti, J.; Mas-Moruno, C.; Díaz-Ricart, M.; Escolar, G.; Ginebra, M. P.; Gil, F. J.; Pegueroles, M.; Manero, J. M. Cell Adhesive Peptides Functionalized on CoCr Alloy Stimulate Endothelialization and Prevent Thrombogenesis and Restenosis. *J. Biomed. Mater. Res., Part A* **2017**, *105* (4), 973−983.
(73) Choi, W. S.; Bae, J. W.; Joung, Y. K.; Park, K. D.; Lee, M. H.; Park, J.-C.; Kwon, I. K. Fabrication of Endothelial Cell-Specific Polyurethane Surfaces Co-Immobilized with GRGDS and YIGSR Peptides. *Macromol. Res.* **2009**, *17* (7), 458−463.

https://dx.doi.org/10.1021/acsami.0c01893
ACS Appl. Mater. Interfaces 2020, 12, 21342−21367

(74) Choi, W. S.; Joung, Y. K.; Lee, Y.; Bae, J. W.; Park, H. K.; Park, Y. H.; Park, J. C.; Park, K. D. Enhanced Patency and Endothelialization of Small-Caliber Vascular Grafts Fabricated by Coimmobilization of Heparin and Cell-Adhesive Peptides. *ACS Appl. Mater. Interfaces* **2016**, *8* (7), 4336−4346.
(75) Nishiguchi, A.; Singh, S.; Wessling, M.; Kirkpatrick, C. J.; Möller, M. Basement Membrane Mimics of Biofunctionalized Nanofibers for a Bipolar-Cultured Human Primary Alveolar-Capillary Barrier Model. *Biomacromolecules* **2017**, *18* (3), 719−727.
(76) Hozumi, K.; Kumai, J.; Yamada, Y.; Nomizu, M. Active Peptide-Conjugated Chitosan Matrices as an Artificial Basement Membrane. *Polymers* **2015**, *7* (2), 281−297.
(77) Kim, J. W.; Ki, C. S.; Park, Y. H.; Kim, H. J.; Um, I. C. Effect of RGDS and KRSR Peptides Immobilized on Silk Fibroin Nanofibrous Mats for Cell Adhesion and Proliferation. *Macromol. Res.* **2010**, *18* (5), 442−448.
(78) Zhu, L.; Wang, K.; Ma, T.; Huang, L.; Xia, B.; Zhu, S.; Yang, Y.; Liu, Z.; Quan, X.; Luo, K.; Kong, D.; Huang, J.; Luo, Z. Noncovalent Bonding of RGD and YIGSR to an Electrospun Poly(ε-Caprolactone) Conduit through Peptide Self-Assembly to Synergistically Promote Sciatic Nerve Regeneration in Rats. *Adv. Healthcare Mater.* **2017**, *6* (8), 1600860.
(79) Lequoy, P.; Murschel, F.; Liberelle, B.; Lerouge, S.; De Crescenzo, G. Controlled Co-Immobilization of EGF and VEGF to Optimize Vascular Cell Survival. *Acta Biomater.* **2016**, *29*, 239−247.
(80) Bilem, I.; Chevallier, P.; Plawinski, L.; Sone, E. D.; Durrieu, M.-C.; Laroche, G. RGD and BMP-2 Mimetic Peptide Crosstalk Enhances Osteogenic Commitment of Human Bone Marrow Stem Cells. *Acta Biomater.* **2016**, *36*, 132−142.
(81) Chiu, L. L. Y.; Radisic, M. Scaffolds with Covalently Immobilized VEGF and Angiopoietin-1 for Vascularization of Engineered Tissues. *Biomaterials* **2010**, *31*, 226−241.
(82) Lee, Y. B.; Shin, Y. M.; Lee, J. h.; Jun, I.; Kang, J. K.; Park, J. C.; Shin, H. Polydopamine-Mediated Immobilization of Multiple Bioactive Molecules for the Development of Functional Vascular Graft Materials. *Biomaterials* **2012**, *33*, 8343−8352.
(83) Mehta, G.; Williams, C. M.; Alvarez, L.; Lesniewski, M.; Kamm, R. D.; Griffith, L. G. Synergistic Effects of Tethered Growth Factors and Adhesion Ligands on DNA Synthesis and Function of Primary Hepatocytes Cultured on Soft Synthetic Hydrogels. *Biomaterials* **2010**, *31*, 4657−4671.
(84) Min, H. K.; Oh, S. H.; Lee, J. M.; Im, G. I.; Lee, J. H. Porous Membrane with Reverse Gradients of PDGF-BB and BMP-2 for Tendon-to-Bone Repair: In Vitro Evaluation on Adipose-Derived Stem Cell Differentiation. *Acta Biomater.* **2014**, *10*, 1272−1279.
(85) Brigaud, I.; Agniel, R.; Leroy-Dudal, J.; Kellouche, S.; Ponche, A.; Bouceba, T.; Mihailescu, N.; Sopronyi, M.; Viguier, E.; Ristoscu, C.; Sima, F.; Mihailescu, I. N.; Carreira, A. C. O.; Sogayar, M. C.; Gallet, O.; Anselme, K. Synergistic Effects of BMP-2, BMP-6 or BMP-7 with Human Plasma Fibronectin onto Hydroxyapatite Coatings: A Comparative Study. *Acta Biomater.* **2017**, *55*, 481−492.
(86) Moore, N. M.; Lin, N. J.; Gallant, N. D.; Becker, M. L. Synergistic Enhancement of Human Bone Marrow Stromal Cell Proliferation and Osteogenic Differentiation on BMP-2-Derived and RGD Peptide Concentration Gradients. *Acta Biomater.* **2011**, *7* (5), 2091−2100.
(87) Shin, Y. M.; Jo, S. Y.; Park, J. S.; Gwon, H. J.; Jeong, S. I.; Lim, Y. M. Synergistic Effect of Dual-Functionalized Fibrous Scaffold with BCP and RGD Containing Peptide for Improved Osteogenic Differentiation. *Macromol. Biosci.* **2014**, *14* (8), 1190−1198.
(88) Noel, S.; Fortier, C.; Murschel, F.; Belzil, A.; Gaudet, G.; Jolicoeur, M.; De Crescenzo, G. Co-Immobilization of Adhesive Peptides and VEGF within a Dextran-Based Coating for Vascular Applications. *Acta Biomater.* **2016**, *37*, 69−82.
(89) Moulisová, V.; Gonzalez-García, C.; Cantini, M.; Rodrigo-Navarro, A.; Weaver, J.; Costell, M.; Sabater i Serra, R.; Dalby, M. J.; García, A. J.; Salmerón-Sánchez, M. Engineered Microenvironments for Synergistic VEGF - Integrin Signalling during Vascularization. *Biomaterials* **2017**, *126*, 61−74.
(90) Lin, C.-Y.; Wang, Y.-R.; Lin, C.-W.; Wang, S.-W.; Chien, H.-W.; Cheng, N.-C.; Tsai, W.-B.; Yu, J. Peptide-Modified Zwitterionic Porous Hydrogels for Endothelial Cell and Vascular Engineering. *BioRes. Open Access* **2014**, *3* (6), 297−310.
(91) Yin, W.-N.; Cao, F.-Y.; Han, K.; Zeng, X.; Zhuo, R.-X.; Zhang, X.-Z. The Synergistic Effect of a BMP-7 Derived Peptide and Cyclic RGD in Regulating Differentiation Behaviours of Mesenchymal Stem Cells. *J. Mater. Chem. B* **2014**, *2* (47), 8434−8440.
(92) Koepsel, J. T.; Brown, P. T.; Loveland, S. G.; Li, W.-J.; Murphy, W. L. Combinatorial Screening of Chemically Defined Human Mesenchymal Stem Cell Culture Substrates. *J. Mater. Chem.* **2012**, *22* (37), 19474−19481.
(93) Ma, Y.; Zheng, J.; Amond, E. F.; Stafford, C. M.; Becker, M. L. Facile Fabrication of "Dual Click" One- and Two-Dimensional Orthogonal Peptide Concentration Gradients. *Biomacromolecules* **2013**, *14* (3), 665−671.
(94) Zhang, D.; Kilian, K. A. Peptide Microarrays for the Discovery of Bioactive Surfaces that Guide Cellular Processes: a Single Step Azide-Alkyne "Click" Chemistry Approach. *J. Mater. Chem. B* **2014**, *2* (27), 4280−4288.
(95) Ma, Y.; Policastro, G. M.; Li, Q.; Zheng, J.; Jacquet, R.; Landis, W. J.; Becker, M. L. Concentration-Dependent hMSC Differentiation on Orthogonal Concentration Gradients of GRGDS and BMP-2 Peptides. *Biomacromolecules* **2016**, *17* (4), 1486−1495.
(96) Liu, L.; Ratner, B. D.; Sage, E. H.; Jiang, S. Endothelial Cell Migration on Surface-Density Gradients of Fibronectin, VEGF, or Both Proteins. *Langmuir* **2007**, *23* (22), 11168−11173.
(97) Guan, Z. Y.; Wu, C. Y.; Wu, J. T.; Tai, C. H.; Yu, J.; Chen, H. Y. Multifunctional and Continuous Gradients of Biointerfaces Based on Dual Reverse Click Reactions. *ACS Appl. Mater. Interfaces* **2016**, *8* (22), 13812−13818.
(98) Almodóvar, J.; Crouzier, T.; Selimović, Š.; Boudou, T.; Khademhosseini, A.; Picart, C. Gradients of Physical and Biochemical Cues on Polyelectrolyte Multilayer Films Generated via Microfluidics. *Lab Chip* **2013**, *13* (8), 1562−1570.
(99) Aucoin, L.; Griffith, C. M.; Pleizier, G.; Deslandes, Y.; Sheardown, H. Interactions of Corneal Epithelial Cells and Surfaces Modified with Cell Adhesion Peptide Combinations. *J. Biomater. Sci., Polym. Ed.* **2002**, *13* (4), 447−462.
(100) Beurer, E.; Venkataraman, N. V.; Rossi, A.; Bachmann, F.; Engeli, R.; Spencer, N. D. Orthogonal, Three-Component, Alkanethiol-Based Surface-Chemical Gradients on Gold. *Langmuir* **2010**, *26* (11), 8392−8399.
(101) Kim, S.; Nam, J.; Yeo, W.-S. A Method for Generation and Characterization of Orthogonal Three-Component Gradient Surfaces. *Bulletin of the Korean Chemical Society* **2015**, *36* (10), 2501−2505.
(102) Schenk, F. C.; Boehm, H.; Spatz, J. P.; Wegner, S. V. Dual-Functionalized Nanostructured Biointerfaces by Click Chemistry. *Langmuir* **2014**, *30* (23), 6897−6905.
(103) Almodóvar, J.; Guillot, R.; Monge, C.; Vollaire, J.; Selimović, Š.; Coll, J.-L.; Khademhosseini, A.; Picart, C. Spatial Patterning of BMP-2 and BMP-7 on Biopolymeric Films and the Guidance of Muscle Cell Fate. *Biomaterials* **2014**, *35* (13), 3975−3985.
(104) Stefonek-Puccinelli, T. J.; Masters, K. S. Co-Immobilization of Gradient-Patterned Growth Factors for Directed Cell Migration. *Ann. Biomed. Eng.* **2008**, *36* (12), 2121−2133.
(105) Rupp, F.; Liang, L.; Geis-Gerstorfer, J.; Scheideler, L.; Hüttig, F. Surface Characteristics of Dental Implants: A Review. *Dent. Mater.* **2018**, *34* (1), 40−57.
(106) Bacakova, L.; Filova, E.; Parizek, M.; Ruml, T.; Svorcík, V. Modulation of Cell Adhesion, Proliferation and Differentiation on Materials Designed for Body Implants. *Biotechnol. Adv.* **2011**, *29* (6), 739−767.
(107) Kim, H. J.; Kim, S. H.; Kim, M. S.; Lee, E. J.; Oh, H. G.; Oh, W. M.; Park, S. W.; Kim, W. J.; Lee, G. J.; Choi, N. G.; Koh, J. T.; Dinh, D. B.; Hardin, R. R.; Johnson, K.; Sylvia, V. L.; Schmitz, J. P.; Dean, D. D. Varying Ti-6Al-4V Surface Roughness Induces Different Early Morphologic and Molecular Responses in MG63 Osteoblast-Like Cells. *J. Biomed. Mater. Res., Part A* **2005**, *74A* (3), 366−373.

https://dx.doi.org/10.1021/acsami.0c01893
ACS Appl. Mater. Interfaces 2020, 12, 21342−21367

(108) Andrukhov, O.; Huber, R.; Shi, B.; Berner, S.; Rausch-Fan, X.; Moritz, A.; Spencer, N. D.; Schedle, A. Proliferation, Behavior, and Differentiation of Osteoblasts on Surfaces of Different Microroughness. *Dent. Mater.* **2016**, *32* (11), 1374−1384.
(109) Ahn, E. H.; Kim, Y.; Kshitiz; An, S. S.; Afzal, J.; Lee, S.; Kwak, M.; Suh, K.-Y.; Kim, D.-H.; Levchenko, A. Spatial Control of Adult Stem Cell Fate Using Nanotopographic Cues. *Biomaterials* **2014**, *35* (8), 2401−2410.
(110) Saino, E.; Focarete, M. L.; Gualandi, C.; Emanuele, E.; Cornaglia, A. I.; Imbriani, M.; Visai, L. Effect of Electrospun Fiber Diameter and Alignment on Macrophage Activation and Secretion of Proinflammatory Cytokines and Chemokines. *Biomacromolecules* **2011**, *12* (5), 1900−1911.
(111) Macgregor, M.; Williams, R.; Downes, J.; Bachhuka, A.; Vasilev, K. The Role of Controlled Surface Topography and Chemistry on Mouse Embryonic Stem Cell Attachment, Growth and Self-Renewal. *Materials* **2017**, *10* (9), 1081−1093.
(112) Deng, Z. J.; Liang, M.; Toth, I.; Monteiro, M. J.; Minchin, R. F. Molecular Interaction of Poly(acrylic acid) Gold Nanoparticles with Human Fibrinogen. *ACS Nano* **2012**, *6* (10), 8962−8969.
(113) Deng, Z. J.; Liang, M.; Monteiro, M.; Toth, I.; Minchin, R. F. Nanoparticle-Induced Unfolding of Fibrinogen Promotes Mac-1 Receptor Activation and Inflammation. *Nat. Nanotechnol.* **2011**, *6* (1), 39−44.
(114) Valastyan, J. S.; Lindquist, S. Mechanisms of Protein-Folding Diseases at a Glance. *Dis. Model Mech.* **2014**, *7* (1), 9−14.
(115) Dolatshahi-Pirouz, A.; Jensen, T.; Kraft, D. C.; Foss, M.; Kingshott, P.; Hansen, J. L.; Larsen, A. N.; Chevallier, J.; Besenbacher, F. Fibronectin Adsorption, Cell Adhesion, and Proliferation on Nanostructured Tantalum Surfaces. *ACS Nano* **2010**, *4* (5), 2874−2882.
(116) Le Saux, G.; Magenau, A.; Böcking, T.; Gaus, K.; Gooding, J. J. The Relative Importance of Topography and RGD Ligand Density for Endothelial Cell Adhesion. *PLoS One* **2011**, *6* (7), No. e21869.
(117) Lee, J.; Choi, I.; Yeo, W.-S. Preparation of Gradient Surfaces by Using a Simple Chemical Reaction and Investigation of Cell Adhesion on a Two-Component Gradient. *Chem. - Eur. J.* **2013**, *19* (18), 5609−5616.
(118) Lee, Y. J.; Lee, J.-H.; Cho, H.-J.; Kim, H. K.; Yoon, T. R.; Shin, H. Electrospun Fibers Immobilized with Bone Forming Peptide-1 Derived from BMP7 for Guided Bone Regeneration. *Biomaterials* **2013**, *34* (21), 5059−5069.
(119) Pramono, S.; Pugdee, K.; Suwanprateep, J.; Koontongkaew, S. Sandblasting and Fibronectin-Derived Peptide Immobilization on Titanium Surface Increase Adhesion and Differentiation of Osteoblast-like Cells (MC3T3-E1). *Journal of Dental Sciences* **2016**, *11* (4), 427−436.
(120) Kim, M.-J.; Lee, B.; Yang, K.; Park, J.; Jeon, S.; Um, S. H.; Kim, D.-I.; Im, S. G.; Cho, S.-W. BMP-2 Peptide-Functionalized Nanopatterned Substrates for Enhanced Osteogenic Differentiation of Human Mesenchymal Stem Cells. *Biomaterials* **2013**, *34* (30), 7236−7246.
(121) Chen, X.; Su, Y.-D.; Ajeti, V.; Chen, S.-J.; Campagnola, P. J. Cell Adhesion on Micro-Structured Fibronectin Gradients Fabricated by Multiphoton Excited Photochemistry. *Cell. Mol. Bioeng.* **2012**, *5* (3), 307−319.
(122) Bøggild, T.; Runager, K.; Sutherland, D. S. Nanopattern Gradients for Cell Studies Fabricated Using Hole-Mask Colloidal Lithography. *ACS Appl. Mater. Interfaces* **2016**, *8* (24), 14975−14979.
(123) Wang, L.-S.; Duncan, B.; Tang, R.; Lee, Y.-W.; Creran, B.; Elci, S. G.; Zhu, J.; Yesilbag Tonga, G.; Doble, J.; Fessenden, M.; Bayat, M.; Nonnenmann, S.; Vachet, R. W.; Rotello, V. M. Gradient and Patterned Protein Films Stabilized via Nanoimprint Lithography for Engineered Interactions with Cells. *ACS Appl. Mater. Interfaces* **2017**, *9* (1), 42−46.
(124) Künzler, T. P.; Huwiler, C.; Drobek, T.; Vörös, J.; Spencer, N. D. Systematic Study of Osteoblast Response to Nanotopography by means of Nanoparticle-Density Gradients. *Biomaterials* **2007**, *28* (33), 5000−5006.
(125) Zouani, O. F.; Chanseau, C.; Brouillaud, B.; Bareille, R.; Deliane, F.; Foulc, M.-P.; Mehdi, A.; Durrieu, M.-C. Altered Nanofeature Size Dictates Stem Cell Differentiation. *J. Cell Sci.* **2012**, *125* (5), 1217−1224.
(126) Wang, P.-Y.; Thissen, H.; Tsai, W.-B. The Roles of RGD and Grooved Topography in the Adhesion, Morphology, and Differentiation of C2C12 Skeletal Myoblasts. *Biotechnol. Bioeng.* **2012**, *109* (8), 2104−2115.
(127) Wang, P.-Y.; Wu, T.-H.; Tsai, W.-B.; Kuo, W.-H.; Wang, M.-J. Grooved PLGA Films Incorporated with RGD/YIGSR Peptides for Potential Application on Skeletal Muscle Tissue Engineering. *Colloids Surf., B* **2013**, *110*, 88−95.
(128) Uz, M.; Sharma, A. D.; Adhikari, P.; Sakaguchi, D. S.; Mallapragada, S. K. Development of Multifunctional Films for Peripheral Nerve Regeneration. *Acta Biomater.* **2017**, *56*, 141−152.
(129) Yao, L.; Wang, S.; Cui, W.; Sherlock, R.; O'Connell, C.; Damodaran, G.; Gorman, A.; Windebank, A.; Pandit, A. Effect of Functionalized Micropatterned PLGA on Guided Neurite Growth. *Acta Biomater.* **2009**, *5* (2), 580−588.
(130) Greene, A. C.; Washburn, C. M.; Bachand, G. D.; James, C. D. Combined Chemical and Topographical Guidance Cues for Directing Cytoarchitectural Polarization in Primary Neurons. *Biomaterials* **2011**, *32* (34), 8860−8869.
(131) Li, J.; Kwiatkowska, B.; Lu, H.; Voglstätter, M.; Ueda, E.; Grunze, M.; Sleeman, J.; Levkin, P. A.; Nazarenko, I. Collaborative Action of Surface Chemistry and Topography in the Regulation of Mesenchymal and Epithelial Markers and the Shape of Cancer Cells. *ACS Appl. Mater. Interfaces* **2016**, *8* (42), 28554−28565.
(132) Charest, J. L.; Eliason, M. T.; García, A. J.; King, W. P. Combined Microscale Mechanical Topography and Chemical Patterns on Polymer Cell Culture Substrates. *Biomaterials* **2006**, *27* (11), 2487−2494.
(133) Mörke, C.; Rebl, H.; Finke, B.; Dubs, M.; Nestler, P.; Airoudj, A.; Roucoules, V.; Schnabelrauch, M.; Körtge, A.; Anselme, K.; Helm, C. A.; Nebe, J. B. Abrogated Cell Contact Guidance on Amino-Functionalized Microgrooves. *ACS Appl. Mater. Interfaces* **2017**, *9* (12), 10461−10471.
(134) Charest, J. L.; García, A. J.; King, W. P. Myoblast Alignment and Differentiation on Cell Culture Substrates with Microscale Topography and Model Chemistries. *Biomaterials* **2007**, *28* (13), 2202−2210.
(135) Wang, P.-Y.; Wu, T.-H.; Chao, P.-H. G.; Kuo, W.-H.; Wang, M.-J.; Hsu, C.-C.; Tsai, W.-B. Modulation of Cell Attachment and Collagen Production of Anterior Cruciate Ligament Cells via Submicron Grooves/Ridges Structures with Different Cell Affinity. *Biotechnol. Bioeng.* **2013**, *110* (1), 327−337.
(136) Tocce, E. J.; Liliensiek, S. J.; Broderick, A. H.; Jiang, Y.; Murphy, K. C.; Murphy, C. J.; Lynn, D. M.; Nealey, P. F. The Influence of Biomimetic Topographical Features and the Extracellular Matrix Peptide RGD on Human Corneal Epithelial Contact Guidance. *Acta Biomater.* **2013**, *9* (2), 5040−5051.
(137) Yañez-Soto, B.; Liliensiek, S. J.; Murphy, C. J.; Nealey, P. F. Biochemically and Topographically Engineered Poly(Ethylene Glycol) Diacrylate Hydrogels with Biomimetic Characteristics as Substrates for Human Corneal Epithelial Cells. *J. Biomed. Mater. Res., Part A* **2013**, *101A* (4), 1184−1194.
(138) Chen, H.; Huang, X.; Zhang, M.; Damanik, F.; Baker, M. B.; Leferink, A.; Yuan, H.; Truckenmüller, R.; van Blitterswijk, C.; Moroni, L. Tailoring Surface Nanoroughness of Electrospun Scaffolds for Skeletal Tissue Engineering. *Acta Biomater.* **2017**, *59*, 82−93.
(139) Zamani, F.; Amani-Tehran, M.; Latifi, M.; Shokrgozar, M. A. The influence of surface nanoroughness of electrospun PLGA nanofibrous scaffold on nerve cell adhesion and proliferation. *J. Mater. Sci.: Mater. Med.* **2013**, *24* (6), 1551−1560.
(140) Johnson, C. D.; D'Amato, A. R.; Puhl, D. L.; Wich, D. M.; Vesperman, A.; Gilbert, R. J. Electrospun fiber surface nanotopography influences astrocyte-mediated neurite outgrowth. *Biomed Mater.* **2018**, *13* (5), 054101−054101.
(141) Zhou, Q.; Xie, J.; Bao, M.; Yuan, H.; Ye, Z.; Lou, X.; Zhang, Y. Engineering aligned electrospun PLLA microfibers with nano-porous

https://dx.doi.org/10.1021/acsami.0c01893
ACS Appl. Mater. Interfaces 2020, 12, 21342−21367

surface nanotopography for modulating the responses of vascular smooth muscle cells. *J. Mater. Chem. B* **2015**, *3* (21), 4439−4450.
(142) Zheng, W.; Wang, Z.; Song, L.; Zhao, Q.; Zhang, J.; Li, D.; Wang, S.; Han, J.; Zheng, X.-L.; Yang, Z.; Kong, D. Endothelialization and Patency of RGD-Functionalized Vascular Grafts in a Rabbit Carotid Artery Model. *Biomaterials* **2012**, *33* (10), 2880−2891.
(143) Guex, A. G.; Hegemann, D.; Giraud, M. N.; Tevaearai, H. T.; Popa, A. M.; Rossi, R. M.; Fortunato, G. Covalent Immobilisation of VEGF on Plasma-Coated Electrospun Scaffolds for Tissue Engineering Applications. *Colloids Surf., B* **2014**, *123*, 724−733.
(144) Dettin, M.; Zamuner, A.; Roso, M.; Iucci, G.; Samouillan, V.; Danesin, R.; Modesti, M.; Conconi, M. T. Facile and Selective Covalent Grafting of an RGD-Peptide to Electrospun Scaffolds Improves HUVEC Adhesion. *J. Pept. Sci.* **2015**, *21* (10), 786−795.
(145) Wang, K.; Chen, X.; Pan, Y.; Cui, Y.; Zhou, X.; Kong, D.; Zhao, Q. Enhanced Vascularization in Hybrid PCL/Gelatin Fibrous Scaffolds with Sustained Release of VEGF. *BioMed Res. Int.* **2015**, *2015*, 865076.
(146) Antonova, L. V.; Seifalian, A. M.; Kutikhin, A. G.; Sevostyanova, V. V.; Matveeva, V. G.; Velikanova, E. A.; Mironov, A. V.; Shabaev, A. R.; Glushkova, T. V.; Senokosova, E. A.; Vasyukov, G. Y.; Krivkina, E. O.; Burago, A. Y.; Kudryavtseva, Y. A.; Barbarash, O. L.; Barbarash, L. S. Conjugation with RGD Peptides and Incorporation of Vascular Endothelial Growth Factor Are Equally Efficient for Biofunctionalization of Tissue-Engineered Vascular Grafts. *Int. J. Mol. Sci.* **2016**, *17* (11), 1920−1930.
(147) Campagnolo, P.; Gormley, A. J.; Chow, L. W.; Guex, A. G.; Parmar, P. A.; Puetzer, J. L.; Steele, J. A. M.; Breant, A.; Madeddu, P.; Stevens, M. M. Pericyte Seeded Dual Peptide Scaffold with Improved Endothelialization for Vascular Graft Tissue Engineering. *Adv. Healthcare Mater.* **2016**, *5* (23), 3046−3055.
(148) Zhao, L.; Ma, S.; Pan, Y.; Zhang, Q.; Wang, K.; Song, D.; Wang, X.; Feng, G.; Liu, R.; Xu, H.; Zhang, J.; Qiao, M.; Kong, D. Functional Modification of Fibrous PCL Scaffolds with Fusion Protein VEGF-HGFI Enhanced Cellularization and Vascularization. *Adv. Healthcare Mater.* **2016**, *5* (18), 2376−2385.
(149) Wang, K.; Zhang, Q.; Zhao, L.; Pan, Y.; Wang, T.; Zhi, D.; Ma, S.; Zhang, P.; Zhao, T.; Zhang, S.; Li, W.; Zhu, M.; Zhu, Y.; Zhang, J.; Qiao, M.; Kong, D. Functional Modification of Electrospun Poly(ε-caprolactone) Vascular Grafts with the Fusion Protein VEGF-HGFI Enhanced Vascular Regeneration. *ACS Appl. Mater. Interfaces* **2017**, *9* (13), 11415−11427.
(150) Koh, H. S.; Yong, T.; Chan, C. K.; Ramakrishna, S. Enhancement of Neurite Outgrowth Using Nano-Structured Scaffolds Coupled with Laminin. *Biomaterials* **2008**, *29* (26), 3574−3582.
(151) Bockelmann, J.; Klinkhammer, K.; von Holst, A.; Seiler, N.; Faissner, A.; Brook, G. A.; Klee, D.; Mey, J. Functionalization of Electrospun Poly(ε-Caprolactone) Fibers with the Extracellular Matrix-Derived Peptide GRGDS Improves Guidance of Schwann Cell Migration and Axonal Growth. *Tissue Eng., Part A* **2011**, *17* (3−4), 475−486.
(152) Kijeńska, E.; Prabhakaran, M. P.; Swieszkowski, W.; Kurzydlowski, K. J.; Ramakrishna, S. Interaction of Schwann Cells with Laminin Encapsulated PLCL Core-Shell Nanofibers for Nerve Tissue Engineering. *Eur. Polym. J.* **2014**, *50*, 30−38.
(153) Dettin, M.; Zamuner, A.; Roso, M.; Gloria, A.; Iucci, G.; Messina, G. M. L.; D'Amora, U.; Marletta, G.; Modesti, M.; Castagliuolo, I.; Brun, P. Electrospun Scaffolds for Osteoblast Cells: Peptide-Induced Concentration-Dependent Improvements of Polycaprolactone. *PLoS One* **2015**, *10* (9), No. e0137505.
(154) Liverani, L.; Killian, M. S.; Boccaccini, A. R. Fibronectin Functionalized Electrospun Fibers by Using Benign Solvents: Best Way to Achieve Effective Functionalization. *Front. Bioeng. Biotechnol.* **2019**, *7*, 68−68.
(155) Lee, J.; Abdeen, A. A.; Zhang, D.; Kilian, K. A. Directing Stem Cell Fate on Hydrogel Substrates by Controlling Cell Geometry, Matrix Mechanics and Adhesion Ligand Composition. *Biomaterials* **2013**, *34* (33), 8140−8148.
(156) Lei, Y.; Zouani, O. F.; Rémy, M.; Ayela, C.; Durrieu, M.-C. Geometrical Microfeature Cues for Directing Tubulogenesis of Endothelial Cells. *PLoS One* **2012**, *7* (7), No. e41163.
(157) Peyton, S. R.; Raub, C. B.; Keschrumrus, V. P.; Putnam, A. J. The Use of Poly(Ethylene Glycol) Hydrogels to Investigate the Impact of ECM Chemistry and Mechanics on Smooth Muscle Cells. *Biomaterials* **2006**, *27* (28), 4881−4893.
(158) Zouani, O. F.; Kalisky, J.; Ibarboure, E.; Durrieu, M.-C. Effect of BMP-2 from Matrices of Different Stiffnesses for the Modulation of Stem Cell Fate. *Biomaterials* **2013**, *34* (9), 2157−2166.
(159) Engler, A. J.; Sen, S.; Sweeney, H. L.; Discher, D. E. Matrix Elasticity Directs Stem Cell Lineage Specification. *Cell* **2006**, *126* (4), 677−689.
(160) Leach, J. B.; Brown, X. Q.; Jacot, J. G.; DiMilla, P. A.; Wong, J. Y. Neurite Outgrowth and Branching of PC12 Cells on Very Soft Substrates Sharply Decreases Below a Treshold of Substrate Rigidity. *Journal of Neural Engineering* **2007**, *4*, 26−34.
(161) Rowlands, A. S.; George, P. A.; Cooper-White, J. J. Directing Osteogenic and Myogenic Differentiation of MSCs: Interplay of Stiffness and Adhesive Ligand Presentation. *American Journal of Physiology-Cell Physiology* **2008**, *295* (4), C1037−C1044.
(162) Lanniel, M.; Huq, E.; Allen, S.; Buttery, L.; Williams, P. M.; Alexander, M. R. Substrate Induced Differentiation of Human Mesenchymal Stem Cells on Hydrogels with Modified Surface Chemistry and Controlled Modulus. *Soft Matter* **2011**, *7* (14), 6501−6514.
(163) Trappmann, B.; Gautrot, J. E.; Connelly, J. T.; Strange, D. G. T.; Li, Y.; Oyen, M. L.; Cohen Stuart, M. A.; Boehm, H.; Li, B.; Vogel, V.; Spatz, J. P.; Watt, F. M.; Huck, W. T. S. Extracellular-Matrix Tethering Regulates Stem-Cell Fate. *Nat. Mater.* **2012**, *11*, 642−649.
(164) Kourouklis, A. P.; Kaylan, K. B.; Underhill, G. H. Substrate Stiffness and Matrix Composition Coordinately Control the Differentiation of Liver Progenitor Cells. *Biomaterials* **2016**, *99*, 82−94.
(165) Crouzier, T.; Fourel, L.; Boudou, T.; Albigès-Rizo, C.; Picart, C. Presentation of BMP-2 from a Soft Biopolymeric Film Unveils its Activity on Cell Adhesion and Migration. *Adv. Mater.* **2011**, *23* (12), H111−H118.
(166) La, W.-G.; Yang, H. S. Synergistic Effects of Extracellular Matrix Rigidity and Immobilized Vascular Endothelial Growth Factor on Vascular Tube Formation and Cell Morphology of Human Umbilical Vein Endothelial Cells. *Tissue Eng. Regener. Med.* **2015**, *12* (1), 20−27.
(167) Chang, H.; Liu, X.-q.; Hu, M.; Zhang, H.; Li, B.-c.; Ren, K.-f.; Boudou, T.; Albiges-Rizo, C.; Picart, C.; Ji, J. Substrate Stiffness Combined with Hepatocyte Growth Factor Modulates Endothelial Cell Behavior. *Biomacromolecules* **2016**, *17* (9), 2767−2776.
(168) Banks, J. M.; Mozdzen, L. C.; Harley, B. A. C.; Bailey, R. C. The Combined Effects of Matrix Stiffness and Growth Factor Immobilization on the Bioactivity and Differentiation Capabilities of Adipose-Derived Stem Cells. *Biomaterials* **2014**, *35* (32), 8951−8959.
(169) Peyton, S. R.; Kim, P. D.; Ghajar, C. M.; Seliktar, D.; Putnam, A. J. The Effects of Matrix Stiffness and RhoA on the Phenotypic Plasticity of Smooth Muscle Cells in a 3-D Biosynthetic Hydrogel System. *Biomaterials* **2008**, *29* (17), 2597−2607.
(170) Tan, S.; Fang, J. Y.; Yang, Z.; Nimni, M. E.; Han, B. The Synergetic Effect of Hydrogel Stiffness and Growth Factor on Osteogenic Differentiation. *Biomaterials* **2014**, *35* (20), 5294−5306.
(171) Chen, T. T.; Luque, A.; Lee, S.; Anderson, S. M.; Segura, T.; Iruela-Arispe, M. L. Anchorage of VEGF to the extracellular matrix conveys differential signaling responses to endothelial cells. *J. Cell Biol.* **2010**, *188* (4), 595−609.
(172) Davis, M. E.; Hsieh, P. C. H.; Takahashi, T.; Song, Q.; Zhang, S.; Kamm, R. D.; Grodzinsky, A. J.; Anversa, P.; Lee, R. T. Local myocardial insulin-like growth factor 1 (IGF-1) delivery with biotinylated peptide nanofibers improves cell therapy for myocardial infarction. *Proc. Natl. Acad. Sci. U. S. A.* **2006**, *103* (21), 8155−8160.
(173) Hynes, R. O. The extracellular matrix: not just pretty fibrils. *Science* **2009**, *326* (5957), 1216−1219.

https://dx.doi.org/10.1021/acsami.0c01893
ACS Appl. Mater. Interfaces 2020, 12, 21342−21367

(174) Briquez, P. S.; Hubbell, J. A.; Martino, M. M. Extracellular Matrix-Inspired Growth Factor Delivery Systems for Skin Wound Healing. *Adv. Wound Care (New Rochelle)* **2015**, *4* (8), 479−489.
(175) Mitchell, A. C.; Briquez, P. S.; Hubbell, J. A.; Cochran, J. R. Engineering growth factors for regenerative medicine applications. *Acta Biomater.* **2016**, *30*, 1−12.
(176) Salmerón-Sánchez, M.; Dalby, M. J. Synergistic growth factor microenvironments. *Chem. Commun.* **2016**, *52* (91), 13327−13336.
(177) Cipitria, A.; Salmeron-Sanchez, M. Mechanotransduction and Growth Factor Signalling to Engineer Cellular Microenvironments. *Adv. Healthcare Mater.* **2017**, *6* (15), 1700052.
(178) Monteiro, A. I.; Kollmetz, T.; Malmström, J. Engineered systems to study the synergistic signaling between integrin-mediated mechanotransduction and growth factors (Review). *Biointerphases* **2018**, *13* (6), 06D302.
(179) Ozawa, C. R.; Banfi, A.; Glazer, N. L.; Thurston, G.; Springer, M. L.; Kraft, P. E.; McDonald, D. M.; Blau, H. M. Microenvironmental VEGF concentration, not total dose, determines a threshold between normal and aberrant angiogenesis. *J. Clin. Invest.* **2004**, *113* (4), 516−527.
(180) Davies, N.; Dobner, S.; Bezuidenhout, D.; Schmidt, C.; Beck, M.; Zisch, A. H.; Zilla, P. The dosage dependence of VEGF stimulation on scaffold neovascularisation. *Biomaterials* **2008**, *29* (26), 3531−3538.
(181) Farrukh, A.; Ortega, F.; Fan, W.; Marichal, N.; Paez, J. I.; Berninger, B.; Campo, A. d.; Salierno, M. J. Bifunctional Hydrogels Containing the Laminin Motif IKVAV Promote Neurogenesis. *Stem Cell Rep.* **2017**, *9* (5), 1432−1440.
(182) Saha, K.; Keung, A. J.; Irwin, E. F.; Li, Y.; Little, L.; Schaffer, D. V.; Healy, K. E. Substrate Modulus Directs Neural Stem Cell Behavior. *Biophys. J.* **2008**, *95* (9), 4426−4438.
(183) Lavalley, D.; Zanotelli, M.; Bordeleau, F.; Wang, W.; Schwager, S.; Reinhart-King, C. Matrix Stiffness Enhances VEGFR-2 Internalization, Signaling, and Proliferation in Endothelial Cells. *Convergent Science Physical Oncology* **2017**, *3*, 044001.
(184) Kenny, F. N.; Drymoussi, Z.; Delaine-Smith, R.; Kao, A. P.; Laly, A. C.; Knight, M. M.; Philpott, M. P.; Connelly, J. T. Tissue Stiffening Promotes Keratinocyte Proliferation through Activation of Epidermal Growth Factor Signaling. *J. Cell Sci.* **2018**, *131* (10), 215780.
(185) Isenberg, B. C.; DiMilla, P. A.; Walker, M.; Kim, S.; Wong, J. Y. Vascular Smooth Muscle Cell Durotaxis Depends on Substrate Stiffness Gradient Strength. *Biophys. J.* **2009**, *97* (5), 1313−1322.
(186) Sundararaghavan, H. G.; Burdick, J. A. Gradients with Depth in Electrospun Fibrous Scaffolds for Directed Cell Behavior. *Biomacromolecules* **2011**, *12* (6), 2344−2350.
(187) Tse, J. R.; Engler, A. J. Stiffness Gradients Mimicking In Vivo Tissue Variation Regulate Mesenchymal Stem Cell Fate. *PLoS One* **2011**, *6* (1), No. e15978.
(188) Jain, G.; Ford, A. J.; Rajagopalan, P. Opposing Rigidity-Protein Gradients Reverse Fibroblast Durotaxis. *ACS Biomater. Sci. Eng.* **2015**, *1* (8), 621−631.
(189) Hadden, W. J.; Young, J. L.; Holle, A. W.; McFetridge, M. L.; Kim, D. Y.; Wijesinghe, P.; Taylor-Weiner, H.; Wen, J. H.; Lee, A. R.; Bieback, K.; Vo, B.-N.; Sampson, D. D.; Kennedy, B. F.; Spatz, J. P.; Engler, A. J.; Choi, Y. S. Stem Cell Migration and Mechanotransduction on Linear Stiffness Gradient Hydrogels. *Proc. Natl. Acad. Sci. U. S. A.* **2017**, *114* (22), 5647−5652.
(190) Sunyer, R.; Jin, A. J.; Nossal, R.; Sackett, D. L. Fabrication of Hydrogels with Steep Stiffness Gradients for Studying Cell Mechanical Response. *PLoS One* **2012**, *7* (10), No. e46107.
(191) Sharma, R. I.; Snedeker, J. G. Biochemical and Biomechanical Gradients for Directed Bone Marrow Stromal Cell Differentiation toward Tendon and Bone. *Biomaterials* **2010**, *31* (30), 7695−7704.
(192) Grinnell, F.; Ho, C.-H. The Efect of Growth Factor Environment on Fibroblast Morphological Response to Substrate Stiffness. *Biomaterials* **2013**, *34* (4), 965−974.
(193) Çolak, A.; Li, B.; Blass, J.; Koynov, K.; del Campo, A.; Bennewitz, R. The mechanics of single cross-links which mediate cell attachment at a hydrogel surface. *Nanoscale* **2019**, *11* (24), 11596−11604.
(194) Kolind, K.; Leong, K. W.; Besenbacher, F.; Foss, M. Guidance of Stem Cell Fate on 2D Patterned Surfaces. *Biomaterials* **2012**, *33* (28), 6626−6633.
(195) Spicer, C. D.; Pashuck, E. T.; Stevens, M. M. Achieving Controlled Biomolecule-Biomaterial Conjugation. *Chem. Rev.* **2018**, *118*, 7702−7743.
(196) Zheng, J.; Hua, G.; Yu, J.; Lin, F.; Wade, M. B.; Reneker, D. H.; Becker, M. L. Post-Electrospinning "Triclick" Functionalization of Degradable Polymer Nanofibers. *ACS Macro Lett.* **2015**, *4* (2), 207−213.
(197) Liang, L.; Astruc, D. The Copper(I) -Catalyzed Alkyne-Azide Cycloaddition (CuAAC) " Click " Reaction and its Applications. An Overview. *Coord. Chem. Rev.* **2011**, *255*, 2933−2945.
(198) Moore, N. M.; Becker, M. L. Bioactive Self-Assembled Monolayer Gradients. *Soft Matter Gradient Surfaces: Methods and Applications* **2012**, 329−363.
(199) Cantini, M.; Gomide, K.; Moulisova, V.; González-García, C.; Salmerón-Sánchez, M. Vitronectin as a Micromanager of Cell Response in Material-Driven Fibronectin Nanonetworks. *Adv. Biosyst.* **2017**, *1* (9), 1700047.
(200) Li, B.; Ma, Y.; Wang, S.; Moran, P. M. A Technique for Preparing Protein Gradients on Polymeric Surfaces: Effects on PC12 Pheochromocytoma Cells. *Biomaterials* **2005**, *26*, 1487−1495.
(201) Wang, H.; Castner, D. G.; Ratner, B. D.; Jiang, S. Probing the Orientation of Surface-Immobilized Immunoglobulin G by Time-of-Flight Secondary Ion Mass Spectrometry. *Langmuir* **2004**, *20* (5), 1877−1887.
(202) Mathias, J. R.; Dodd, M. E.; Walters, K. B.; Yoo, S. K.; Ranheim, E. A.; Huttenlocher, A. Characterization of Zebrafish Larval Inflammatory Macrophages. *Dev. Comp. Immunol.* **2009**, *33* (11), 1212−1217.
(203) Yokoyama, Y.; Aoyagi, S.; Fujii, M.; Matsuo, J.; Fletcher, J. S.; Lockyer, N. P.; Vickerman, J. C.; Passarelli, M. K.; Havelund, R.; Seah, M. P. Peptide Fragmentation and Surface Structural Analysis by Means of ToF-SIMS Using Large Cluster Ion Sources. *Anal. Chem.* **2016**, *88* (7), 3592−3597.
(204) Wang, X.; Ding, B.; Li, B. Biomimetic electrospun nanofibrous structures for tissue engineering. *Mater. Today* **2013**, *16* (6), 229−241.
(205) Denchai, A.; Tartarini, D.; Mele, E. Cellular Response to Surface Morphology: Electrospinning and Computational Modeling. *Front. Bioeng. Biotechnol.* **2018**, *6*, 155.
(206) Wang, P.-Y.; Bennetsen, D. T.; Foss, M.; Ameringer, T.; Thissen, H.; Kingshott, P. Modulation of Human Mesenchymal Stem Cell Behavior on Ordered Tantalum Nanotopographies Fabricated Using Colloidal Lithography and Glancing Angle Deposition. *ACS Appl. Mater. Interfaces* **2015**, *7* (8), 4979−4989.
(207) Mertgen, A.-S.; Yazgan, G.; Guex, A. G.; Fortunato, G.; Müller, E.; Huber, L.; Schneider, R.; Brunelli, M.; Rossi, R. M.; Maniura-Weber, K.; Rottmar, M. Controlling the Surface Structure of Electrospun Fibers: Effect on Endothelial Cells and Blood Coagulation. *Biointerphases* **2018**, *13* (5), 051001.
(208) Milleret, V.; Hefti, T.; Hall, H.; Vogel, V.; Eberli, D. Influence of the Fiber Diameter and Surface Roughness of Electrospun Vascular Grafts on Blood Activation. *Acta Biomater.* **2012**, *8* (12), 4349−4356.
(209) Guex, A. G.; Kocher, F. M.; Fortunato, G.; Körner, E.; Hegemann, D.; Carrel, T. P.; Tevaearai, H. T.; Giraud, M. N. Fine-Tuning of Substrate Architecture and Surface Chemistry Promotes Muscle Tissue Development. *Acta Biomater.* **2012**, *8* (4), 1481−1489.
(210) Kim, D.; Pugno, N. M.; Ryu, S. Wetting Theory for Small Droplets on Textured Solid Surfaces. *Sci. Rep.* **2016**, *6*, 37813.
(211) Kubiak, K. J.; Wilson, M. C. T.; Mathia, T. G.; Carval, P. Wettability versus Roughness of Engineering Surfaces. *Wear* **2011**, *271*, 523−528.
(212) Kavousanakis, M. E.; Chamakos, N. T.; Papathanasiou, A. G. Connection of Intrinsic Wettability and Surface Topography with the Apparent Wetting Behavior and Adhesion Properties. *J. Phys. Chem. C* **2015**, *119* (27), 15056−15066.

https://dx.doi.org/10.1021/acsami.0c01893
ACS Appl. Mater. Interfaces 2020, 12, 21342−21367

(213) Abbott, R. D.; Kaplan, D. L. Engineering Biomaterials for Enhanced Tissue Regeneration. *Current Stem Cell Reports* **2016**, *2* (2), 140−146.
(214) Lee, J.-H.; Park, H.-K.; Kim, K. S. Intrinsic and Extrinsic Mechanical Properties Related to the Differentiation of Mesenchymal Stem Cells. *Biochem. Biophys. Res. Commun.* **2016**, *473* (3), 752−757.
(215) Horvath, A. N.; Holenstein, C. N.; Silvan, U.; Snedeker, J. G. The Protein Mat(ters)—Revealing the Biologically Relevant Mechanical Contribution of Collagen- and Fibronectin-Coated Micropatterns. *ACS Appl. Mater. Interfaces* **2019**, *11* (44), 41791−41798.
(216) Sinha, R.; Verdonschot, N.; Koopman, B.; Rouwkema, J. Tuning Cell and Tissue Development by Combining Multiple Mechanical Signals. *Tissue Eng., Part B* **2017**, *23* (5), 494−504.
(217) Wu, Y.; Yang, Z.; Law, J. B. K.; He, A. Y.; Abbas, A. A.; Denslin, V.; Kamarul, T.; Hui, J. H. P.; Lee, E. H. The Combined Effect of Substrate Stiffness and Surface Topography on Chondrogenic Differentiation of Mesenchymal Stem Cells. *Tissue Eng., Part A* **2017**, *23* (1−2), 43−54.
(218) Jeon, H.; Tsui, J. H.; Jang, S. I.; Lee, J. H.; Park, S.; Mun, K.; Boo, Y. C.; Kim, D.-H. Combined Effects of Substrate Topography and Stiffness on Endothelial Cytokine and Chemokine Secretion. *ACS Appl. Mater. Interfaces* **2015**, *7* (8), 4525−4532.
(219) Chaterji, S.; Kim, P.; Choe, S. H.; Tsui, J. H.; Lam, C. H.; Ho, D. S.; Baker, A. B.; Kim, D.-H. Synergistic Effects of Matrix Nanotopography and Stiffness on Vascular Smooth Muscle Cell Function. *Tissue Eng., Part A* **2014**, *20* (15−16), 2115−2126.
(220) Niepel, M. S.; Ekambaram, B. K.; Schmelzer, C. E. H.; Groth, T. Polyelectrolyte multilayers of poly (l-lysine) and hyaluronic acid on nanostructured surfaces affect stem cell response. *Nanoscale* **2019**, *11* (6), 2878−2891.
(221) Parandakh, A.; Anbarlou, A.; Tafazzoli-Shadpour, M.; Ardeshirylajimi, A.; Khani, M.-M. Substrate topography interacts with substrate stiffness and culture time to regulate mechanical properties and smooth muscle differentiation of mesenchymal stem cells. *Colloids Surf., B* **2019**, *173*, 194−201.
(222) Charest, J. M.; Califano, J. P.; Carey, S. P.; Reinhart-King, C. A. Fabrication of Substrates with Defined Mechanical Properties and Topographical Features for the Study of Cell Migration. *Macromol. Biosci.* **2012**, *12* (1), 12−20.
(223) Mueller, W. D.; Lucia Nascimento, M.; Lorenzo De Mele, M. F. Critical Discussion of the Results from Different Corrosion Studies of Mg and Mg Alloys for Biomaterial Applications. *Acta Biomater.* **2010**, *6* (5), 1749−1755.
(224) Simon, C. G.; Yaszemski, M. J.; Ratcliffe, A.; Tomlins, P.; Luginbuehl, R.; Tesk, J. A. ASTM International Workshop on Standards and Measurements for Tissue Engineering Scaffolds. *J. Biomed. Mater. Res., Part B* **2015**, *103* (5), 949−959.
(225) Plant, A. L.; Locascio, L. E.; May, W. E.; Gallagher, P. D. Improved Reproducibility by Assuring Confidence in Measurements in Biomedical Research. *Nat. Methods* **2014**, *11* (9), 895−898.
(226) Skoog, S. A.; Kumar, G.; Narayan, R. J.; Goering, P. L. Biological Responses to Immobilized Microscale and Nanoscale Surface Topographies. *Pharmacol. Ther.* **2018**, *182*, 33−55.
(227) Cai, X. Y.; Wake, A.; Gouty, D. Analytical and Bioanalytical Assay Challenges to Support Comparability Studies for Biosimilar Drug Development. *Bioanalysis* **2013**, *5* (5), 517−520.
(228) Perlin, L.; MacNeil, S.; Rimmer, S. Production and Performance of Biomaterials Containing RGD Peptides. *Soft Matter* **2008**, *4* (12), 2331−2349.
(229) Kammerer, P.; Heller, M; Brieger, J; Klein, M.; Al-Nawas, B; Gabriel, M Immobilisation of Linear and Cyclic RGD-Peptides on Titanium Surfaces and their Impact on Endothelial Cell Adhesion and Proliferation. *European Cells and Materials* **2011**, *21*, 364−372.
(230) Dijkgraaf, I.; Liu, S.; Kruijtzer, J. A. W.; Soede, A. C.; Oyen, W. J. G.; Liskamp, R. M. J.; Corstens, F. H. M.; Boerman, O. C. Effects of Linker Variation on the In Vitro and In Vivo Characteristics of an 111In-labeled RGD Peptide. *Nucl. Med. Biol.* **2007**, *34* (1), 29−35.
(231) Ben-David, U.; Siranosian, B.; Ha, G.; Tang, H.; Oren, Y.; Hinohara, K.; Strathdee, C. A.; Dempster, J.; Lyons, N. J.; Burns, R.; Nag, A.; Kugener, G.; Cimini, B.; Tsvetkov, P.; Maruvka, Y. E.; O'Rourke, R.; Garrity, A.; Tubelli, A. A.; Bandopadhayay, P.; Tsherniak, A.; Vazquez, F.; Wong, B.; Birger, C.; Ghandi, M.; Thorner, A. R.; Bittker, J. A.; Meyerson, M.; Getz, G.; Beroukhim, R.; Golub, T. R. Genetic and Transcriptional Evolution Alters Cancer Cell Line Drug Response. *Nature* **2018**, *560* (7718), 325−330.
(232) Duval, K.; Grover, H.; Han, L.-H.; Mou, Y.; Pegoraro, A. F.; Fredberg, J.; Chen, Z. Modeling Physiological Events in 2D vs. 3D Cell Culture. *Physiology* **2017**, *32* (4), 266−277.
(233) Ribeiro, A. S.; Powell, E. M.; Leach, J. B. Neural Stem Cell Differentiation in 2D and 3D Microenvironments. *26th Southern Biomedical Engineering Conference: SBEC 2010* **2010**, *32*, 422−425.
(234) Dumont, C. M.; Karande, P.; Thompson, D. M. Rapid Assessment of Migration and Proliferation: A Novel 3D High-Throughput Platform for Rational and Combinatorial Screening of Tissue-Specific Biomaterials. *Tissue Eng., Part C* **2014**, *20* (8), 620−629.
(235) Carletti, E.; Motta, A.; Migliaresi, C. Scaffolds for Tissue Engineering and 3D Cell Culture. In *3D Cell Culture: Methods and Protocols*; Haycock, J. W., Ed.; Humana Press: Totowa, NJ, 2011; pp 17−39.
(236) Loh, Q. L.; Choong, C. Three-Dimensional Scaffolds for Tissue Engineering Applications: Role of Porosity and Pore Size. *Tissue Eng., Part B* **2013**, *19* (6), 485−502.
(237) Meng, X.; Leslie, P.; Zhang, Y.; Dong, J. Stem Cells in a Three-Dimensional Scaffold Environment. *SpringerPlus* **2014**, *3* (1), 80−87.
(238) Stratton, S.; Shelke, N. B.; Hoshino, K.; Rudraiah, S.; Kumbar, S. G. Bioactive Polymeric Scaffolds for Tissue Engineering. *Bioactive Materials* **2016**, *1* (2), 93−108.
(239) Rödling, L.; Schwedhelm, I.; Kraus, S.; Bieback, K.; Hansmann, J.; Lee-Thedieck, C. 3D Models of the Hematopoietic Stem Cell Niche under Steady-State and Active Conditions. *Sci. Rep.* **2017**, *7* (1), 4625.
(240) Jammalamadaka, U.; Tappa, K. Recent Advances in Biomaterials for 3D Printing and Tissue Engineering. *J. Funct. Biomater.* **2018**, *9* (1), 22−35.
(241) Karageorgiou, V.; Kaplan, D. Porosity of 3D Biomaterial Scaffolds and Osteogenesis. *Biomaterials* **2005**, *26* (27), 5474−5491.
(242) Choi, S.-W.; Zhang, Y.; Xia, Y. Three-Dimensional Scaffolds for Tissue Engineering: The Importance of Uniformity in Pore Size and Structure. *Langmuir* **2010**, *26* (24), 19001−19006.
(243) Mour, M.; Das, D.; Winkler, T.; Hoenig, E.; Mielke, G.; Morlock, M. M.; Schilling, A. F. Advances in Porous Biomaterials for Dental and Orthopaedic Applications. *Materials* **2010**, *3* (5), 2947−2974.
(244) Bružauskaitė, I.; Bironaitė, D.; Bagdonas, E.; Bernotienė, E. Scaffolds and Cells for Tissue Regeneration: Different Scaffold Pore Sizes—Different Cell Effects. *Cytotechnology* **2016**, *68* (3), 355−369.
(245) Di Luca, A.; Ostrowska, B.; Lorenzo-Moldero, I.; Lepedda, A.; Swieszkowski, W.; Van Blitterswijk, C.; Moroni, L. Gradients in Pore Size Enhance the Osteogenic Differentiation of Human Mesenchymal Stromal Cells in Three-Dimensional Scaffolds. *Sci. Rep.* **2016**, *6*, 22898−22910.
(246) Ahumada, M.; Jacques, E.; Calderon, C.; Martínez-Gómez, F. Porosity in Biomaterials: A Key Factor in the Development of Applied Materials in Biomedicine. In *Handbook of Ecomaterials*; Martínez, L. M. T.; Kharissova, O. V.; Kharisov, B. I., Eds.; Springer International Publishing: Cham, Switzerland, 2017; pp 1−20.
(247) Sankar, S.; Sharma, C. S.; Rath, S. N. Enhanced Osteodifferentiation of MSC Spheroids on Patterned Electrospun Fiber Mats - An Advanced 3D Double Strategy for Bone Tissue Regeneration. *Mater. Sci. Eng., C* **2019**, *94*, 703−712.
(248) Khan, F.; Tanaka, M. Designing Smart Biomaterials for Tissue Engineering. *Int. J. Mol. Sci.* **2018**, *19* (1), 17−30.
(249) Huethorst, E.; Cutiongco, M. F. A.; Campbell, F. A.; Saeed, A.; Love, R.; Reynolds, P. M.; Dalby, M. J.; Gadegaard, N. Customizable, Engineered Substrates for Rapid Screening of Cellular Cues. *Biofabrication* **2020**, *12* (2), 025009.
(250) O'Brien, F. J. Biomaterials & Scaffolds for Tissue Engineering. *Mater. Today* **2011**, *14* (3), 88−95.

https://dx.doi.org/10.1021/acsami.0c01893
ACS Appl. Mater. Interfaces 2020, 12, 21342−21367

(251) Neves, L. S.; Rodrigues, M. T.; Reis, R. L.; Gomes, M. E. Current Approaches and Future Perspectives on Strategies for the Development of Personalized Tissue Engineering Therapies. *Expert Review of Precision Medicine and Drug Development* **2016**, *1* (1), 93−108.
(252) Ranga, A.; Gobaa, S.; Okawa, Y.; Mosiewicz, K.; Negro, A.; Lutolf, M. P. 3D Niche Microarrays for Systems-Level Analyses of Cell Fate. *Nat. Commun.* **2014**, *5*, 4324.
(253) Jallerat, Q.; Feinberg, A. W. Extracellular Matrix Structure and Composition in the Early Four-Chambered Embryonic Heart. *Cells* **2020**, *9* (2), 285−298.
(254) Niklason, L. E. Understanding the Extracellular Matrix to Enhance Stem Cell-Based Tissue Regeneration. *Cell stem cell* **2018**, *22* (3), 302−305.
(255) Nielsen, S. H.; Mouton, A. J.; DeLeon-Pennell, K. Y.; Genovese, F.; Karsdal, M.; Lindsey, M. L. Understanding Cardiac Extracellular Matrix Remodeling to Develop Biomarkers of Myocardial Infarction Outcomes. *Matrix Biol.* **2019**, *75*−*76*, 43−57.

https://dx.doi.org/10.1021/acsami.0c01893
ACS Appl. Mater. Interfaces 2020, 12, 21342−21367

7.12. Teilarbeit XII

Teilarbeit XII wurde 2022 unter dem Titel „Bioselectivity of silk protein-based materials and their bio-inspired applications“ im Journal *Beilstein Journal of Nanotechnology* veröffentlicht.

Bargel, H.*; **Trossmann, V. T.***; Sommer, C. & Scheibel, T. (2022) Bioselectivity of silk protein-based materials and their bio-inspired applications. *Beilstein Journal of Nanotechnology* **13**: 902.

* gleichberechtigte Co-Autorenschaft

BEILSTEIN JOURNAL OF NANOTECHNOLOGY

Bioselectivity of silk protein-based materials and their bio-inspired applications

Hendrik Bargel[‡1], Vanessa T. Trossmann[‡1], Christoph Sommer[1] and Thomas Scheibel[*1,2,3,4,5]

Review

Open Access

Address:
[1]Department of Biomaterials, University of Bayreuth, Prof.-Rüdiger-Bormann-Str. 1, 95447 Bayreuth, Germany, [2]Bayreuth Center of Material Science and Engineering (BayMat), University of Bayreuth, Universitätsstr. 30, 95440 Bayreuth, Germany, [3]Bavarian Polymer Institute (BPI), University of Bayreuth, Universitätsstr. 30, 95440 Bayreuth, Germany, [4]Bayreuth Center of Colloids and Interfaces (BZKG), University of Bayreuth, Universitätsstr. 30, 95440 Bayreuth, Germany and [5]Bayreuth Center for Molecular Biosciences (BZMB), University of Bayreuth, Universitätsstr. 30, 95440 Bayreuth, Germany

Email:
Thomas Scheibel[*] - thomas.scheibel@bm.uni-bayreuth.de

* Corresponding author ‡ Equal contributors

Keywords:
antifouling; bacteriostatic; biofouling; bioselective cell adhesion; spider silk protein

Beilstein J. Nanotechnol. **2022,** *13,* 902–921.
https://doi.org/10.3762/bjnano.13.81

Received: 31 March 2022
Accepted: 23 August 2022
Published: 08 September 2022

This article is part of the thematic issue "Biomimetics on the micro- and nanoscale – The 25th anniversary of the lotus effect".

Guest Editor: M. Mail

Abstract

Adhesion to material surfaces is crucial for almost all organisms regarding subsequent biological responses. Mammalian cell attachment to a surrounding biological matrix is essential for maintaining their survival and function concerning tissue formation. Conversely, the adhesion and presence of microbes interferes with important multicellular processes of tissue development. Therefore, tailoring bioselective, biologically active, and multifunctional materials for biomedical applications is a modern focus of biomaterial research. Engineering biomaterials that stimulate and interact with cell receptors to support binding and subsequent physiological responses of multicellular systems attracted much interest in the last years. Further to this, the increasing threat of multidrug resistance of pathogens against antibiotics to human health urgently requires new material concepts for preventing microbial infestation and biofilm formation. Thus, materials exhibiting microbial repellence or antimicrobial behaviour to reduce inflammation, while selectively enhancing regeneration in host tissues are of utmost interest. In this context, protein-based materials are interesting candidates due to their natural origin, biological activity, and structural properties. Silk materials, in particular those made of spider silk proteins and their recombinant counterparts, are characterized by extraordinary properties including excellent biocompatibility, slow biodegradation, low immunogenicity, and non-toxicity, making them ideally suited for tissue engineering and biomedical applications. Furthermore, recombinant production technologies allow for application-specific modification to develop adjustable, bioactive materials. The present review focusses on biological processes and surface interactions involved in the bioselec-

Beilstein J. Nanotechnol. 2022, 13, 902–921.

tive adhesion of mammalian cells and repellence of microbes on protein-based material surfaces. In addition, it highlights the importance of materials made of recombinant spider silk proteins, focussing on the progress regarding bioselectivity.

Review

1 Introduction

1.1 Bioadhesive protein surfaces

Biological adhesion is important for all organisms such as plants, animals, bacteria, and fungi, covering a wide range of biological aspects including reproduction, growth and settlement, dynamic attachment during locomotion, self-healing, protection against as well as attachment of microbes, and prey hunting [1-6]. A variety of different adhesion mechanisms exist to manage the different challenges of interfacial adhesion. In turn, natural biological adhesives are complex materials that have evolved to meet the various functional demands. Bioadhesion can be found in the range of the micro- to the macroscale [7]. Adhesion principles include contact mechanical principles such as capillary interactions, viscous forces, non-covalent interactions (e.g., van der Waals forces), and adhesive chemistry of biopolymers (various types of glues) [5]. On the level of tissues, multiple cell types work together to perform complex tasks, based on their hierarchical arrangement governing the exchange of information between different cell types. To achieve proper organization and communication, cells produce a large number of adhesion molecules that mediate cell contact phenomena based on receptor–ligand interactions [8]. The ability of mammalian cells to adhere to other cells, tissues, or the extracellular matrix (ECM) via specific molecular interactions plays a critical role in many biological processes including embryogenesis, development of neuronal tissue, hemostasis, immune response, and inflammation [9]. The adhesive interactions of cells between each other and with ECM proteins (often of specific molecular nature), have important key functions in embryonic and organ development, the maintenance of vascular and epithelial integrity, and host defense [10].

The so-called cellular adhesion molecules (CAMs) can be generally divided into five discrete groups that include cadherins, selectins, members of the immunoglobulin superfamily (IgSF), integrins, and others such as mucins. Moreover, certain enzymes such as the vascular adhesion protein 1 (VAP-1) are known to be involved in cell adhesion [11,12]. The distinction of CAM subcategories reflects both structural differences as well as binding to different ligands. Cadherins, selectins, and members of the IgSF are known to mediate cell–cell adhesion, while integrins typically bind to extracellular matrix proteins [12]. As a special case, immune cell integrins also bind to ligands both soluble and on other cells. Additional classification of the CAMs relates to their ligands and type of adhesion. Selectins bind to carbohydrates based on calcium-dependent regulation, cadherins form mostly homotypic contacts also in a calcium-regulated manner, while the IgSF subfamily of nectins is able to form both homotypic and heterotypic interactions [10]. Comprehensive overviews of molecular structure and adhesion mechanisms of various CAM can be found in dedicated reviews [9,10,12,13].

Cadherins are associated with cell–cell adhesive interactions in solid tissues and are involved in processes such as embryonic development, formation of the epithelial layers of the skin and intestine, and axonal formation in the nervous system [9]. The structural integrity of cadherin molecules is stabilized by calcium ions, and their essential role in proper adhesion contacts is reflected in the abbreviated protein family name "**cal**cium-**d**ependent ad**her**ent prote**ins**" [14]. The N-terminal domain of cadherin dimers on one cell is responsible for mediating homotypic binding contacts with their homologues on an adjacent cell in an antiparallel manner. This region also defines binding specificity [15]. Some cadherin receptors are also able to bind to different cadherins. Classic cadherin function is involved in key intracellular structures, such as in adherens junctions (zona adherens and adhesion junctions) and protein complexes composed of E-type cadherins tethered to the actin cytoskeleton through the linker protein group of catenins [15]. One example is cardiac muscle, in which β-catenin localizes to adherens junctions, which are critical for electrical and mechanical coupling between adjacent cardiomyocytes [9].

The immunoglobulin superfamily is one of the largest and most diverse protein families. They are characterized by the presence of at least one immunoglobulin or immunoglobulin-like domain. Most members are type-I transmembrane proteins with an extracellular Ig domain, transmembrane domain, and a cytoplasmic tail [16]. IgSF proteins play a critical role in the development of the nervous system, in embryonic development, and in immune and inflammatory responses [9]. Particularly in the immune system, IgSF members play a critical role in cellular adhesion, and well-known examples include major histocompatibility complex (MHC) class I and II molecules, proteins of the T cell receptor (TCR) complex, intercellular adhesion molecules (ICAMs), and vascular cell adhesion molecules (VCAMs) [17]. Mucosal addressing cell adhesion molecule-1 (MAdCAM-1) and activated leukocyte cell adhesion molecules (ALCAMs) also belong to this family of adhesion receptors and are impor-

Beilstein J. Nanotechnol. 2022, 13, 902–921.

tant in leukocyte trafficking events [10]. These proteins serve as ligands for integrins on the endothelial cells. IgSF molecules are divided into several subfamilies, including nectins and selectins. Whereas nectins mediate cell–cell adhesion in various tissues including endothelium, epithelium, and neural tissue [12], selectins are single-chain transmembrane glycoproteins that mediate calcium-dependent binding to sugar moieties [10]. Their most prominent function is associated with the initial stage of the rolling cell adhesion cascade in which selectin binding enables rolling and cell arrest [18].

Integrins are large heterodimeric glycoproteins constituting a diverse family of adhesion molecules. They play a critical role in important biological functions, including embryogenesis, maintenance of tissue integrity, immune response, and inflammation. Integrins consist of two subunits, α- and β- chains, spanning the cell membrane and forming the receptor in the plasma membrane, characterized by noncovalent interactions [10]. Integrins bind to a large variety of ligands, and the majority belong to two categories. The first category are cell surface molecules of the immunoglobulin supergene family, for example, ICAMs and vascular cell adhesion molecule 1 (VCAM-1), and the second category includes larger-sized ECM protein components such as fibronectin, fibrinogen, vitronectin, and complement component iC3b [13]. Divalent cations, such as Mg^{2+} and Ca^{2+}, are involved in ligand binding. Individual integrins can bind more than one ligand, and vice versa. However, the cellular environment may influence ligand specificity within a particular cell interaction [9]. Generally, integrin-mediated interactions involve a complex series of events including activation, ligand binding, reorganization of the cytoskeleton, and adhesion [13]. In this context, integrin activation is regulated in response to signal cascades inside the cell known as an "inside-out" process initiated by other cell surface receptors, such as chemokine receptors and selectins. The subsequent interaction with cytoplasmic factors leads to a conformational switch in the extracellular integrin binding region from a non-adhesive (inactive) to an adhesive state [19]. Moreover, adhesive interactions also include activation outside the cell (outside-in process) mediated by the cytosolic domains of the integrin α- and β-subunits. The recruitment of either leukocytes or platelets from the blood circulation are examples that require both signalling pathways [9].

Cells in their native tissue environment are surrounded by a unique, complex ECM consisting of a variety of molecules and proteins showing a diversity of assembled morphologies, structures and folding states, which are essential for their assigned functions. Besides structural and mechanical support, the present proteins are direct interaction partners for the cellular receptors mentioned above and contain binding sites for further biologically active molecules, including growth factors, which stimulate several subsequent cellular responses, such as growth or differentiation [20-23]. Prominent examples of ECM proteins are collagens, laminins, fibronectin, and elastin, which contain several short peptide recognition and binding motifs in their amino acid sequence for interaction with specific cellular surface integrins or other types of receptors [23]. Within the ECM, fibronectin is the best-known attachment site for cells by interacting with members of the integrin family of cell surface proteins. However, fibronectin is a multifunctional adhesion molecule, also binding to other protein constituents of the ECM such as fibrin, collagen, and heparin [24]. Thus, fibronectin is involved in several physiological events such as embryonic differentiation, cell morphology, cell migration, and thrombosis [19]. The function of fibronectin as a cell-binding molecule involves its recognition by integrins through short peptide motifs, among them the prominent Arg–Gly–Asp (RGD) and Leu–Asp–Val–Pro (LDVP) sequences [19].

1.2 Applications of bio-inspired selective surface modifications

The increasing knowledge on natural receptor–ligand binding mechanisms led to various approaches in the last years to increase both cellular adhesion on surfaces of biomaterials and biosensors, as well as for therapeutic drug carrier systems against infections, inflammatory and auto-immune diseases, and for anti-tumor treatments [10,25]. One main goal in developing bioactive, bioadhesive, and functional biomaterial scaffolds for tissue engineering, is the enhanced support and regeneration of injured or non-functional tissues or parts thereof.

Apart from the development of sophisticated synthetic polymer systems [26,27], protein-based and bioinspired materials have nowadays an enormous impact [28,29]. Biomaterials based on native collagen, keratin, elastin, silk, and their recombinant, engineered counterparts become increasingly popular in biomedicine and tissue engineering, since they exhibit promising chemical and physical properties, such as bioactivity, structural integrity, and cell stimulation [29,30]. Biomimetic materials modulating specific cellular responses and tissue regeneration have been developed by adjusting and modifying materials using bioactive and bioadhesive molecules, such as full-length ECM proteins or functional peptide fragments thereof. These ligands interact with cell receptors for guiding cellular responses, such as cell proliferation or specific matrix degradation [31-34]. Compared to full-length proteins, short, bioactive peptide sequences show several advantages due to their size, including similar function, controllable, inexpensive, and synthetic production in high amounts, facile processing, simple modification, accessibility, and no animal origin [31,33].

Beilstein J. Nanotechnol. 2022, 13, 902–921.

Many reviews have summarized biologically active peptide sequences regarding their natural origin, their functions, their cellular effects, the targeted tissues, or the engineered and designed scaffolds [31-36]. The most prominent and important adhesive peptide sequence used for functionalization and increasing the bioadhesiveness of a material is the tripeptide RGD, naturally occurring in various ECM proteins including fibronectin, vitronectin, laminin, and collagen [34,35,37-41]. This frequently used peptide has been shown to increase the bioadhesiveness of biomaterials by interacting with cellular integrin receptors and, thus, allows for interaction and attachment of many different cell types [23,33,34,36,39,42-44]. Some integrin types interact with their ligands by recognizing specific ligand motifs. For instance, α4 integrins recognize the Leu–Asp–Val–Pro (LDVP) motif in fibronectin, the Leu–Asp–Thr–Ser (LDTS) sequence in MAdCAM-1, and Ile–Asp–Ser (IDS) in VCAM-1 [19]. Another example of selective adhesion of cells expressing one type of integrin has been achieved by click chemistry to immobilize peptidomimetics of α5β1- or αvβ3-selective RGD peptides [45]. Two other commonly used adhesive peptides to promote cellular interactions with biomaterials are the pentapeptides IKVAV (Ile–Lys–Val–Ala–Val) and YIGSR (Tyr–Ile–Gly–Ser–Arg), which are naturally present in laminin and are used for increasing bioadhesiveness and cellular interactions with biomaterials [23,33-35,41,46-48]. Functionalization of material surfaces is consistently one important step in tissue engineering, especially in the case of implants, where the interaction of cells with the surface is desired [32,44]. However, in the case of 3D structures, bioactive factors must be present in the bulk material and surround the incorporated cells [31,33,34]. For the usage as implant, biocompatible biomaterial implant surfaces should demonstrate different properties adopted to the needed requirements to allow for a successful incorporation in the human body depending on the aimed application (Figure 1). Therefore, the interactions of proteins, microbes, and cells should be guided by material-related surface properties to create bioinert, bioactive, or biomimetic biomaterials.

1.3 Antiadhesive and anti-fouling protein surfaces

Nature has evolved a diverse portfolio of anti-adhesive, antimicrobial and antifouling methods. Biofouling can be defined as the undesired attachment and growth of life on artificial surfaces [49]. One general strategy to inhibit

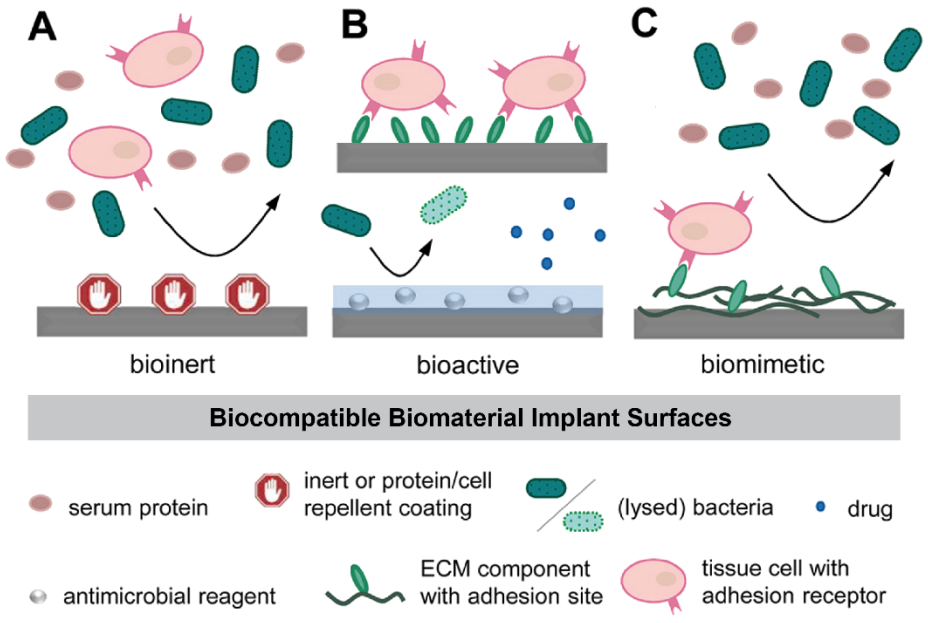

Figure 1: Material-related properties guiding the interactions of proteins, microbes and cells on biomaterial surfaces. (A) Bioinert surfaces hinder the adsorption of proteins, and no interaction and adhesion of cells and microbes is possible. (B) Bioactive surfaces actively stimulate their surrounding by releasing factors or agents to allow for cellular interaction (bioadhesion) or combat against microbes. (C) Biomimetic surfaces are designed to mimic natural ECM composition to guide cellular interactions and tissue regeneration, while repelling proteins and microbes. Figure 1 was adapted from reference [32] (© 2021 S. Spiller et al., published by De Gruyter, distributed under the terms of the Creative Commons Attribution 4.0 International License, https://creativecommons.org/licenses/by/4.0).

Beilstein J. Nanotechnol. 2022, 13, 902–921.

biofilm formation and microbial colonialization is microbial repellence since it targets a direct inhibition of bacterial adherence on a surface. Various approaches can be distinguished according to their basic defense mechanism. These are (A) surface topography, which disturbs and inhibits the initial adhesion based on morphological features, (B) material modification, where intrinsic chemical and physical properties result in microbe-repellence, and (C) additives and coatings that inhibit initial attachment or directly kill microbes (see Figure 2) [50].

Natural surfaces provide many examples of anti-adhesive topography, including nanostructured pikes on Cicada wings [51], micro-structured and patterned riblets of the shark skin scales [52], hierarchically micro- and nanostructured ultrahydrophobic surfaces with self-cleaning ability, such as Lotus leaves and insect wing analogues [53-55], and the superhydrophobic air-retaining surfaces of *Salvinia* floating fern leaves and of the water bug *Notonecta glauca* [53,56]. Based on such blueprints, bioinspired anti-adhesion and antifouling surfaces have been successfully generated by soft photolithography, micromolding or nanopatterning techniques [57]. Moreover, the biomimetic application Sharklet® textured similarly to shark skin has not only been reported to be antiadhesive against green algae spores and bacterial cells but to even display antiviral attachment properties [58]. Superhydrophobic surfaces inspired by the Lotus-effect® (>150° contact angle) have been found to diminish bacterial adhesion due to reduced protein surface adsorption [59-61]. Superhydrophobicity relies on the combination of chemical composition, surface structuring on the micro-/nanoscale, and the introduction of low-surface-energy compounds [62]. Various studies demonstrated that the adhesion of *Staphylococcus aureus, Pseudomonas aeruginosa*, and *Escherichia coli* (*E. coli*) bacteria was significantly reduced on superhydrophobic coatings obtained from fluorinated silica colloids, thin film deposition of silicone elastomers or nanoengineered superhydrophobic surfaces of Teflon®-coated aluminium [63-65]. Superhydrophobic surfaces have also been reported to be unfavorable for mammalian cell attachment and growth. This may be due to the fact that the proteins in the ECM (such as fibronectin, vitronectin, collagen, and laminin) are adsorbed in a denatured state, and their orientation becomes unsuitable for cell binding [66]. Cells (e.g., osteoblasts) are more likely to attach to more hydrophilic surfaces and exhibit

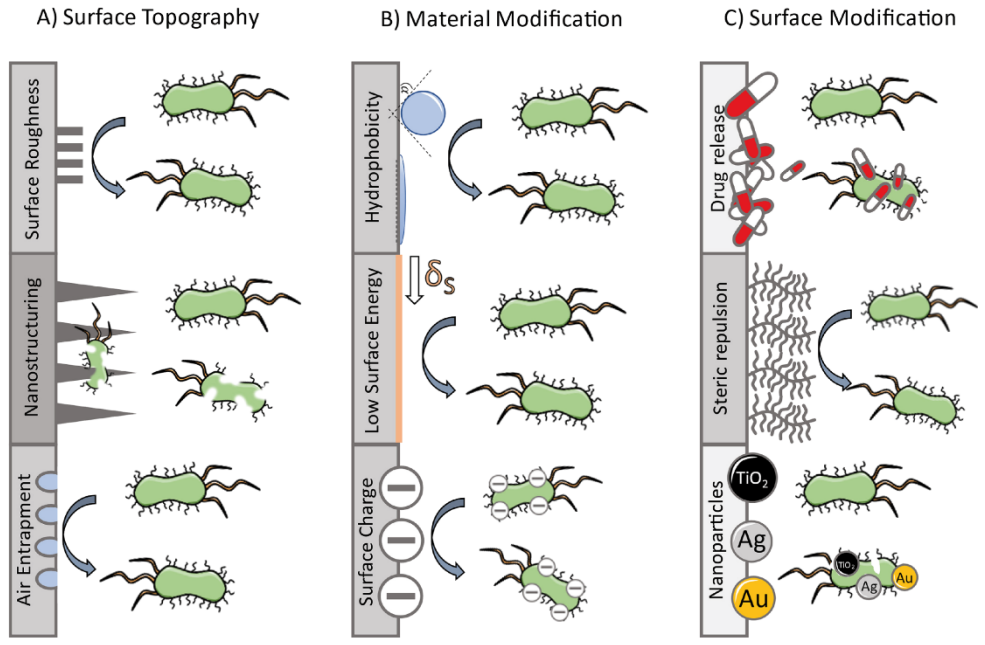

Figure 2: Common antimicrobial approaches regarding the general defense mechanisms (A) surface topography, (B) material modification, and (C) surface modification. Repellent surfaces are displayed in grey, biocide mechanisms in light grey, and contact killing materials in dark grey. Figure 2 was reproduced from reference [50].

the strongest adhesion at contact angles between 60° and 80° [66].

The contrary material property of highly hydrophilic surfaces also effectively reduces protein and, subsequently, microbial adhesion. A theoretical study analysed the contribution to either adhesion or repellency of steric repulsion, van der Waals attraction, and hydrophobic interaction free energies of surface-bound hydrophilic polyethylene oxide (PEO) polymer [67]. Greater surface density and chain length of terminally attached PEO chains were reported to correlate to a lower van der Waals attractive component. In turn, steric repulsion of the polymer chains against protein molecules increases, while a tightly bound water layer creates a physical and energetic barrier and renders interactions with approaching proteins or bacteria thermodynamically unfavorable [50]. The concept of steric repulsion based on a hydration layer through hydrogen bonding and/or ionic solvation has been reported for various materials such as poly(*N*-isopropylacrylamide) (PNIPAAm) [68,69], dextrans [69], poly(ethyleneimine) (PEI) [70,71], and chitosan [72].

Concerning proteins, several studies have reported different molecules to generate effective antiadhesive, antimicrobial, and antibiofouling properties, including the formation of an oriented monolayer of bacterial flagellin proteins on hydrophobic surfaces [73], a reduction of oral bacteria adhesion on dental brackets by more than 95% due to a reduced surface free energy [74], and the fabrication of antifouling coatings through fluorous media-assisted thermal treatment of stable, hydrophilic protein films [75]. One prominent natural route to prevent the colonization and infection with microbes on cells, tissues, and material surfaces is to block adhesion of bacteria and inhibit attachment to host cells. Microbial cells utilize a variety of extracellular structures such as flagella, pili, fimbriae, and curli fibres, as well as outer membrane proteins to attach to almost every surface [50,76]. During the reversible attachment phase of bacterial biofilm formation, surface pre-conditioning occurs due to soluble organic and inorganic macromolecules that absorb on the underlying materials. The various locomotive appendices, the glycocalyx, and hydrophobic molecules mediating non-specific binding interactions help bacterial attachment even in presence of repulsive forces [77,78]. To address the target protein molecules involved in bacterial adhesion, specific drugs are studied that can disrupt the formation of these molecules. One example are pilicides, derivatives of ring-fused 2-pyridones, which block the correct folding of the pili or fimbriae crucial to bacterial pathogenesis by inhibiting the chaperone–usher polymerization pathway in Gram-negative microorganisms involved in pili protein synthesis [79]. For instance, the inhibitor targets pilus chaperone PapD, thereby reducing the adhesion to cell lines by 90% [80]. These pilicides inhibit curli formation in uropathogenic *E. coli* by preventing the polymerization of protein CsgA and FimC, the chaperone protein of the type-I pili [81]. Once in close contact with mammalian cells, bacteria begin to develop quasi-irreversible attachments by forming stronger bonds with the surface mediated by adhesion proteins or polysaccharides also binding to components of the ECM [50]. The most important adhesion proteins produced by numerous bacteria and virus particles involve surface lectins, known as adhesins and hemagglutinins, that bind to complimentary tissue-specific host cell-surface glycoproteins and glycolipids [82]. Blocking these bacterial lectins by their analogues or suitable carbohydrates has been reported as a possible route for preventing and treating microbial infections [78]. For example, a novel group of adhesins widely found in Gram-negative pathogens has been described, termed multivalent adhesion molecule (MAM7) [83]. The adhesin genes are constitutively expressed, and adhesins are themselves involved in the initial attachment phase of pathogens, by interacting with both the host cell receptor phosphatidic acid and the co-receptor fibronectin. Recombinant production of MAM7 and subsequent coupling on polymer beads has been reported to decrease the surface attachment and infection of pathogens, mimicking the bacterial surface display of the adhesins. Pre-treatment of host cells with MAM7-based inhibitors has shown to inhibit bacterial infection with a range of important clinical pathogens, including *Vibrio parahaemolyticus, Vibrio cholerae, Yersinia pseudotuberculosis*, and enteropathogenic *E. coli* [83,84].

Another protein-based antimicrobial strategy in nature is the use of antimicrobial peptides (AMPs) [85]. These molecules are short-length amphipathic peptide molecules (between 10 and 50 amino acids), usually with cationic charges and hydrophobic residues, and are naturally produced by all multicellular organisms as immune response elements. They are involved in multiple interactions in and outside the cells in response to infections and microbial assault [86]. Mammalian AMPs are generally produced in epithelial tissues of the testis, skin, gastrointestinal tract, and respiratory tract, as well as in leukocyte cells such as monocytes, neutrophils, and others, thus forming a central part of mammalian innate immunity [87]. The multitude of immuno-functional roles of the broad-spectrum antimicrobial peptides includes (1) eliminating bacterial growth through direct antimicrobial activity, (2) inhibiting biofilm-specific signalling pathways, and (3) modulating the innate immune responses resulting in the inhibition of potentially harmful inflammation reactions [85,86,88]. In order to highlight the multifaceted nature of AMPs, the term host defense proteins (HDPs) was coined [89]. HDPs are rich in cationic amino acids (e.g., arginine and lysine), and amino acids with hydrophobic side chains (e.g., tryptophan, phenylalanine, tyro-

Beilstein J. Nanotechnol. 2022, 13, 902–921.

sine, leucine, isoleucine, and valine). This composition renders them amphiphilic, which is crucial to their mode of action and promotes their attachment to the bacterial surface/membrane residues [85]. HDPs have properties of cell-penetrating peptides and can translocate across membranes of prokaryotic, but also eukaryotic, cells [90]. The main mode of action of these peptides is promotion of adhesion through the cationic groups to the anionic bacterial membranes and their lipopolysaccharides (a component of the outer membrane of most Gram-negative bacteria), enabling insertion into the membrane driven by clusters of hydrophobic residues [85,91]. As a consequence, the microbial membranes are permeabilized, associated with membrane perturbation and dissipation of the transmembrane potential, which results in bacterial cell lysis and death [92]. In humans, over 120 HDPs have been identified, and typical examples include lysozyme, defensins, histatins, lactoferricin, kinocidins, ribonuclease, dermcidin, and cathelicidins [93]. In the cathelicidin family of HDPs, named by the ability to inhibit the protease cathepsin L, the amphipathic, helical peptide LL-37 is the only cathelicidin-derived HDP found in humans [87,91]. It was reported that this peptide is able to inhibit *Pseudomonas* biofilm formation at 1/16 of its minimum inhibitory concentration (MIC) for planktonic organisms [94], and, subsequently, it was demonstrated that a distinct subset of HDP peptides can be addressed specifically as antibiofilm peptides, with similar overall amino acid compositions but distinct structure–activity relationships compared to those of antimicrobial peptides [95]. As a result of the multiple functionalities of HDPs, several amphiphilic antimicrobial molecules have recently been developed mimicking both structure and functional aspects of the antimicrobial peptides, such as all-D amino acid peptides [96], β-peptides [97], and peptide isomers known as peptoids, (oligo N-substituted glycines) [98]. In addition, the transfer of the general molecular structure of AMPs/HDPs has led to peptide-mimicking polymers and surface-engineered polymeric-brush-tethered AMPs. These approaches are promising for establishing biomaterials and medical devices with antifouling and antibacterial properties, but with reduced susceptibility to enzymatic degradation [85]. General advantages of AMPs/HDPs and mimicking polymer systems over antibiotics as a new generation of antimicrobial agents are their functional diversity, broad spectrum of potential practical applications such as tissue repair, the protection of implanted devices, low potential of bacterial resistance due to their multiple bacterial targets, and host/non-host microbe specificity [85,86,99].

1.4 Importance of (protein-based) bioselective materials

One of the biggest threats to human health worldwide is the rapid emergence of multidrug-resistant pathogens, due to the overuse of broad-spectrum antibiotics [100]. The rising rates of antimicrobial and antiviral resistance of infectious bacteria, viruses, and fungi and their related diseases impact all aspects of modern medicine. Recent outbreaks of severe diseases such as Ebola, influenza, and even more so the severe acute respiratory syndrome (SARS) and the pandemic SARS-CoV-2, have tremendously increased the urgency for new concepts and materials that prevent pathogenic microbial infestation and contact-based spreading due to contaminations of surfaces leading to biofilm formation [101]. In contrast, for biomaterials and their biomedical application (such as implants and wound dressings), cell-friendly and adhesive properties are necessary [66]. Ideally, bioselective materials that promote host cell adhesion while simultaneously preventing microbial infestation and biofouling would exhibit a best-of-both-worlds approach for a number of biomedical applications. For instance, it has been shown that the surface modification of glass substrates with the cell-binding motif RGD of fibronectin and collagen significantly enhanced 3T3 fibroblast cell adhesion. RGD further showed no specific binding affinity towards both clinically relevant bacteria *E. coli* or *S. aureus*, and collagen reduced *E. coli*, but enhanced *Staphylococcus aureus* (*S. aureus*) adhesion [102]. Similar results were obtained for chemically coupled RGD and collagen to an antimicrobial polymeric multilayer composed of dextran sulfate and chitosan [103].

One way to achieve bioselective, biocompatible, and multifunctional materials for biomedical applications is the utilization of natural protein materials shown to accomplish the desired properties and derived bio-inspired materials thereof. Protein-based materials are interesting candidates due to their natural origin, biological activity, and structural properties. Among them are silk materials, in particular one made of spider silk proteins [104]. These are well-studied examples characterized by extraordinary properties including excellent biocompatibility, slow biodegradation, low immunogenicity, and non-toxicity, making them ideally suited for tissue engineering and biomedical applications [105-107]. This review focuses on achievements made with silk-based protein materials and highlights the interaction with mammalian cells and microbes as far as the important aspect of bioselective surfaces is concerned.

2 Natural silk proteins

2.1 Silk protein classification

The term silk generally refers to extracorporeal, proteinaceous structural materials, mostly in the form of threads [108,109]. Silk proteins evolved around 250 million years ago and are present in a variety of recent arthropod families, most prominently in silkworms and spiders, but also in bees, wasps, and ants [110]. Silks fulfill numerous functions, including prey capture, dispersal, reproduction, adhesion, and building cocoons, nests, egg sacs, and stalks [6,110]. Silk proteins are

Beilstein J. Nanotechnol. 2022, 13, 902–921.

biochemically diverse but do share common elements. They usually consist of large proteins that contain long motifs of highly repetitive amino acid sequences rich in alanine, serine, and/or glycine [111]. Moreover, the proteins are stored as highly concentrated silk dope solutions in specialized glands and solidify in a spinning process often associated with shear forces accompanied by their folding into a single dominant secondary structure [112]. Due to both convergent evolution (i.e., silks have been "invented" independently several times), and adaptation to specific functions, the amino acid sequence and protein structure varies considerably, resulting in a versatile class of proteins [112]. Silks are known as semicrystalline materials since they consist of ordered, crystalline structures embedded in an amorphous matrix. The regular secondary structure within one type of silk allows for the condensed packing of protein, as well as the formation of hydrogen bonds, leading to tightly connected intra- and inter-protein chains [111]. While the crystalline regions exhibit a high hydrogen bond density accounting for the strength of a silk fibre, the unordered amorphous regions with less hydrogen bond density induce flexibility [109].

Besides considerable variations in arthropods, the silk of silkworms and related moths, and that of orb-weaving spiders share some features. Their silk proteins are often of high molecular weight, and whilst the termini are hydrophilic, the repetitive cores are composed of alternating large hydrophobic amino acid sequence blocks interspersed with short hydrophilic parts. Interestingly, in both insect (fibroin) and spider (spidroin) silk fibres the core is composed of fibrils that are oriented along the fibre axis and contain nanometre-sized β-sheet crystallites [113,114]. Silkworm silk contains mainly three different proteins, namely a heavy chain fibroin, a light chain fibroin linked via disulfide bonds to the former one, and a P25 glycoprotein associated via noncovalent hydrophobic interactions as a putative stabilizer of the fibre complex integrity [115]. Recently, it has been reported that the accessory Filippi's glands of silkworms appear to regulate posttranslational modifications of fibroin heavy chain molecules, necessary for a tight cocoon architecture [116]. Silk fibroins make up to 75–83 wt % of raw silkworm silk, while sericins, hydrophilic proteins forming a connective coating, constitute 17–25% of the weight of the fibre. Fibroins contain very few cysteine residues, whereas glycine, alanine, serine, and tyrosine make up more than 90 mol %. The fibroins largely contain blocks of $(GAGAGS)_n$, which are responsible for the anisotropic β-sheet-rich nanocrystals [108]. Sericins are based on glue-like serine-rich glycoproteins with rubber-elastic properties [110]. In addition, a further small protein group named seroins was discovered in lepidopteran silk and is known to possess AMP-like antimicrobial activities. It is produced in the silk gland, but also to a lesser extent in the midgut and fat body [117]. As a consequence of its immunogenic and allergic properties, the sericin coating of silkworm silk fibres has to be removed before further processing or use in medical applications in a process known as degumming [108,112].

Spider silks display a much higher degree of diversity, with up to seven different silk types found in the more highly derived group of orb web spiders [108]. This enables spiders to produce mechanically stable web constructions as well as dragline fibres and, at the same time, to wrap their eggs and utilize sticky glue silk for prey capture. The different silks are named after the spidroin-producing spinning glands, such as major and minor ampulla, flagelliform, aggregate and piriform glands, which produce the scaffold thread, an auxiliary spiral, the catching spiral and its glue, and the net anchors. Aciniform and cylindriform silk, in contrast, are used for the egg case [118]. Spider silk consists of 99% spidroins plus some additional lipids, glycoproteins, and ions such as phosphate. The core domain of spidroins consists of short motifs with 10–50 amino acids, which are present in larger modular units, often copied up to several hundred times, giving spidroins a high molecular weight of several hundred kilodaltons [109]. The core domains are flanked by two globular terminal domains, both highly conserved and very similar in many spider species [119]. These globular domains fulfill important control functions concerning protein solubility in the gland reservoir and in the assembly of spidroins into silk threads. The various spidroins of spiders differ in their amino acid sequences to yield the specific properties and functions of the silks. However, some conserved motifs like polyalanine (A_n, poly-A), glycine–alanine (GA), glycine–glycine–X (GGX) and glycine–proline–glycine–$(X)_n$ ($GPG(X)_n$, where X is typically tyrosine, leucine, or glutamine) are abundant in the repetitive core regions in various spidroins [120]. Similar to silkworm silk, poly-A and GA sequences in the spider dragline thread form nanocrystalline hydrophobic β-sheets aligned along the fibre axis, which are embedded in a matrix of more hydrophilic GGX and $GPG(X)_n$ regions responsible for helical and spring-like secondary structures with fewer hydrogen bonds and higher elasticity [114]. The best-studied silk type is the major ampullate silk (MA) used by spiders for web radii and their dragline. It consists of several proteins known as major ampullate spidroins (MaSps). The most prominent spidroins are MaSp1 and MaSp2, differing mainly in their proline content [114], while in some spiders also short MaSp1 variants, and MaSp3 and MaSp4 proteins have been identified [121,122].

2.2 Silk-based materials and their properties

Materials based on arthropod silk proteins attracted increasing attention among material scientists in the last decades. The

Beilstein J. Nanotechnol. 2022, 13, 902–921.

prominent cocoon silk of several silk moths, produced for the wrapping of cocoons during metamorphosis from larvae to adult moths, has been used by humans for millennia [108]. The application of silkworm silk covers a wide range from traditional textiles to technical fabrics and cosmetic articles including skin care, shampoos, and lotions. Traditional utilization of silk fibres as sutures for wounds are known for centuries due to their strength, biocompatibility, and low immunogenicity [104], and silkworm silk surgical threads are commercially available [108]. Moreover, silk-based polymeric materials have also been reported to be suitable as tissue scaffolds due to their biocompatibility and their highly tunable morphologies and mechanical properties. Exemplary, silkworm silk has been studied as a matrix material for tissue-engineered anterior cruciate ligaments [123], and silk fibroin/nanohydroxyapatite composite hydrogels have been studied regarding bone tissue engineering [124].

Spider silk has also been widely used as a multifunctional material for fishing nets, wound coverings, and sutures for surgery for centuries in Australasia and Greece [108]. Since then, it came in focus of researchers worldwide. Natural spider silk has the potential to be used for tissue engineering and biomedical applications. For instance, NIH 3T3 cells showed increased adhesion and proliferation on fabricated, sterilized wovens made of native, unmodified spider dragline silk fibres from *Nephila clavipes* over five days [125]. Furthermore, Wendt et al. showed that naturally occurring spider dragline silk fibres from *Nephila* species could be processed into wovens for culturing first fibroblasts for two weeks before seeding keratinocytes on top to develop a bilayered skin model consisting of an artificial dermis and epidermis [126].

Strikingly, silk materials from silkworms and spiders share a set of highly interesting properties, including mechanical and chemical stability, biocompatibility for mammalian cells and tissues, persistence against microbial degradation and, moreover, potential microbe-repellent and antimicrobial features [50]. Several studies reported antibacterial properties, reduced biofilm formation, and bacterial repellency of both natural silkworm [127-129] and spider silk threads and cocoons [130-136]. However, the status of the intrinsic properties of silk materials in the context of microbial defense is a matter of debate in the scientific community [137,138]. While some of the inconsistencies seem to be related to methodological aspects of the reports in doubt, a misunderstanding of the distinction between the three mechanisms of biofilm inhibition, namely microbial repellency, microbiocidal activity, and contact killing, may foster the discussion on the anti-fouling properties of silk protein materials [50]. Concerning spider silk materials, it has been reported that they seem to prevent bacterial attachment to the surface and biofilm formation instead of being antimicrobial [136].

3 Engineered silk protein-based materials

3.1 Recombinant spider silk technology

The unique properties of spider silk make it a promising candidate for biomedical and tissue engineering applications [105-107]. However, the amounts that could be harvested from spiders are low, and the farming of most spiders is not possible due to their territorial behaviour. Therefore, different recombinant production systems have been developed over time to generate spider silk proteins in appropriate amounts and quality [139,140]. The Johansson research group used the amino acid sequence of the spider *Euprosthenops australis* as inspiration and developed the recombinant spider silk protein 4RepCT comprising four repetitions of a sequence with a polyalanine-rich and a glycine-rich block, as well as a non-repetitive C-terminal domain [141,142]. Another recombinant system is based on the dragline silk of the European garden spider *Araneus diadematus*: Two native spidroins of this silk, namely *Araneus diadematus* fibroin (ADF) 3 and 4, have been used as blueprints for generating the engineered variants eADF3(AQ12) and eADF4(C16). Both proteins contain polyalanine-rich sequences, but eADF4(AQ12) contains two sequence modules (A and Q), while eADF4(C16) comprises only one module (C), repeated either twelve or 16 times, respectively, to generate artificial spider silk proteins [143]. Due to a glutamic acid residue in the C-module, eADF4(C16) is negatively charged [143]. Replacing this amino acid yielded a positively charged eADF4(κ16) and an uncharged eADF4(Ω16) variant, where the glutamic acid residue is exchanged with a lysine or glutamine residue, respectively [144-146]. The dragline silk of *Nephila clavipes* inspired the recombinant spider silk proteins 6mer and 15mer, in which the consensus sequence is repeated six or 15 times, respectively [147]. These recombinant spider silk proteins have been developed using genetic engineering to generate the appropriate gene sequence of interest. In all these cases, recombinant protein production was achieved using bacteria (*E. coli*) [141-143,147]. The usage of genetic engineering further allows for diverse modifications on the genetic level, including site-specific amino acid changes leading to differently charged proteins [144-146] and the addition of short amino acid sequences [114,148-154] or whole domains [155-157] and even proteins [158-160].

3.2 Cell adhesive silk material surfaces

Since the engineered ADF4 sequences lack cell binding sequences, biological interaction and cell attachment is quite limited to recombinant spider silk materials made thereof [161]. Cell culture studies on film surfaces using Balb 3T3 fibroblasts [148], neonatal rat cardiomyocytes [162], human induced

Beilstein J. Nanotechnol. 2022, 13, 902–921.

pluripotent stem cell (hiPSC) derived cardiomyocytes [150], keratinocytes, myoblasts, or neuronal cells [163] revealed that negatively eADF4(C16) and uncharged eADF4(Ω16) surfaces do not allow good and sufficient cell attachment necessary for tissue engineering applications. However, several independent studies showed that the materials made of the positively charged eADF4(κ16) variant enabled partial cell adhesion due to the positive surface charge derived from lysine residues in the primary amino acid sequence [150,162,163]. Since cells expose many negatively charged molecules on their cellular surface, charge modification is often used to guide cellular interaction [164-166]. In the example of the recombinant 4RepCT spider silk, several charged amino acid residues in the primary protein sequence create a material surface that allows for the growth of primary fibroblasts without further modification [167].

As mentioned above, bioselective cell adhesion could be generated by attaching or introducing binding sites, for example, peptide sequences such as RGD, for specific interaction with cellular receptors [41]. In case of recombinant eADF4-based silk, the RGD peptide was genetically (C-terminal) and chemically (N-terminal) coupled to eADF4(C16) to selectively allow for cell attachment on materials made thereof. Fusing the integrin non-binding peptide RGE, showing a residue substitution of aspartate with glutamate thus rendering an identical charge distribution, was applied as a control. Cell culture studies using Balb 3T3 fibroblasts revealed that the RGD peptide enhanced primary cell attachment with increased spread morphology and proliferation on films independently of chemical or genetic modification. The unmodified eADF4(C16) and eADF4(C16)-RGE control surfaces showed less or no cell interaction [148]. In addition, eADF4(C16)-RGD films allowed for adhesion and spreading of neonatal rat cardiomyocytes and hiPSC-derived cardiomyocytes, and further supported their cellular functions, such as beating and contraction [150,168]. The C-terminal genetic modification of the uncharged eADF4(Ω16) and positively charged eADF4(κ16) variant with RGD also enabled the attachment of hiPSC-derived cardiomyocytes and the development of their cell-specific functions on flat films (Figure 3A) [150]. In another study, eADF4(C16) was modified with biomineralization and collagen-binding peptides, yielding an increased osteoblast attachment on these functionalized variants [149].

Genetic modification of 4RepCT led to recombinant spider silk proteins containing linear RGD, RGE, IKVAV, and YIGSR sequences at their N-terminal end. Cell culture analysis using primary cells (fibroblasts, keratinocytes, endothelial, and Schwann cells) revealed that these peptide tags had a clear positive impact on early cell attachment and spreading (Figure 3B). Especially, adhesion and spreading of Schwann cells were influenced in case of the IKVAV modification. Nevertheless, after a longer incubation time (24 h) all modified surfaces supported cell growth [152]. Another study compared the influence of different N-terminally fused RGD-containing peptides on cell behaviour (keratinocytes, endothelial, and human mesenchymal stem cells). It could be shown that all RGD peptides enhanced the adhesiveness of these spider silk surfaces, but the disulfide-bridged, fibronectin-derived integrin-binding RGD peptide showed the highest impact on cell adhesion [151]. RGD-modified FN-4Rep-CT silk could also be used to generate self-assembled membranes, allowing for the adhesion of endothelial cells on the one side and smooth muscle cells on the other side, as well as the diffusion of relevant molecules, making this material promising for vascular tissue engineering [170].

In addition to flat films or coatings, recombinant spider silk proteins based on eADF4 can be processed into 3D scaffolds, such as foams or hydrogels due to their self-assembly properties [169,171-174]. Balb 3T3 fibroblasts adhered to porous foams made of eADF4(C16)-RGD and showed spreading and cell elongation along the foam walls, while cellular aggregates were formed in and on unmodified eADF4(C16) foams, because the cells preferred cell-cell-contacts over cell-material-interactions (Figure 3C) [169]. Additionally, it could be shown that osteoblasts, fibroblasts, keratinocytes, and myoblasts adhere to eADF4(C16)-RGD hydrogels, while they could not attach to unmodified eADF4(C16) hydrogels [174]. A previously published in vivo study of an arteriovenous loop model in rats showed that RGD-functionalized spider silk hydrogels significantly enhanced angiogenesis by forming new blood vessels compared to unmodified eADF4(C16) hydrogels [175].

4RepCT could also be processed in 3D foams for cell culture analysis [154,167,176]. Foams of the genetically modified 4RepCT variants carrying RGD, RGE, IKVAV, and YIGSR sequences were analysed in presence of pancreatic cells for insulin production. While the adhesion and formation of islets was clearly enhanced on RGD-modified foams, a high insulin production was measured for RGD- and YIGSR-modified foams after two days. Although all spider silk scaffolds could be used for culturing pancreatic cells with long-term maintenance of function, the bioactive RGD peptide modification showed the most promising results for in vivo applications (Figure 3D) [154]. One other study analysed the impact of the location of RGD sequences inside the 4RepCT protein on cell behaviour. Therefore, different RGD-containing peptides were genetically introduced at the N-terminus or between repetitive units of the 4RepCT silk protein. The analysis using pancreatic

Beilstein J. Nanotechnol. **2022,** *13,* 902–921.

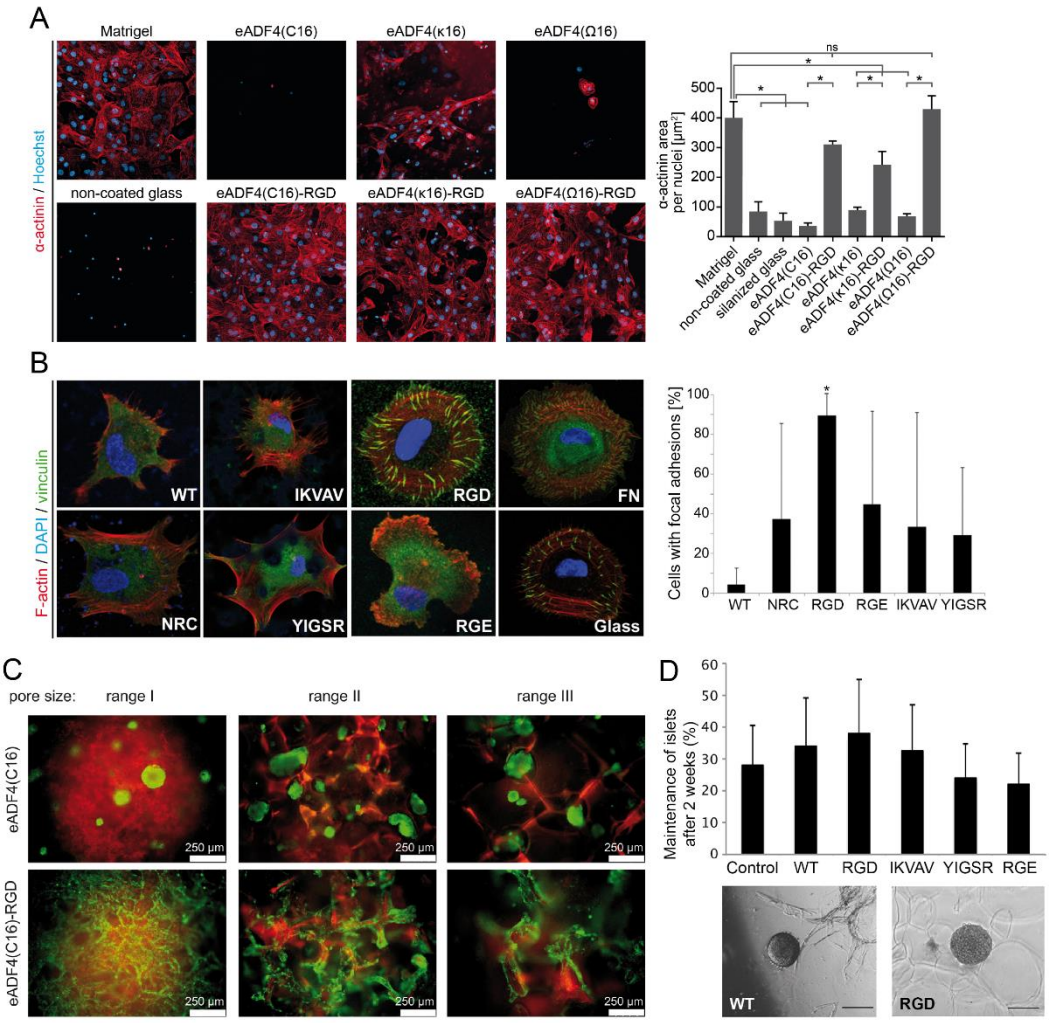

Figure 3: Bioselective, cell adhesive spider silk surfaces. (A) hiPSC-derived cardiomyocytes adhere and spread on spider silk films made of eADF4(C16)-RGD, eADF4(κ16), eADF4(κ16)-RGD, and eADF4(Ω16)-RGD and on control films made of Matrigel. Figure 3A was reprinted from reference [150], Materials Today Bio, vol. 11, by T. U. Esser; V. T. Trossmann; S. Lentz; F. B. Engel; T. Scheibel, "Designing of spider silk proteins for human induced pluripotent stem cell-based cardiac tissue engineering", article no. 100114, Copyright (2021) The Authors, with permission from Elsevier. This content is not subject to CC BY 4.0. (B) Human dermal fibroblasts attachment and spreading behaviour on unmodified (WT) and peptide (NRC, RGD, RGE, IKVAV, and YIGSR)-functionalized 4RepCT spider silk films compared to control surfaces (glass and fibronectin (FN)) after 3 h. Figure 3B was reprinted with slight adaptation from reference [152], Biomaterials, vol. 34, issue 33, by M. Widhe; U. Johansson; C.-O. Hillerdahl; M. Hedhammar, "Recombinant spider silk with cell binding motifs for specific adherence of cells", pages 8223-8234, Copyright (2013), with permission from Elsevier. This content is not subject to CC BY 4.0. (C) Balb 3T3 fibroblasts showed enhanced adhesion, spreading, and elongation on foams made of eADF4(C16)-RGD (lower panel) compared to unmodified eADF4(C16) ones (upper panel) independent of the pore size. Figure 3C was reprinted with permission from [169], Copyright 2016 American Chemical Society. This content is not subject to CC BY 4.0. (D) Human pancreatic islets could adhere, survive, and maintain their function on functionalized foams made of unmodified (WT) and peptide (RGD, RGE, IKVAV, and YIGSR)-functionalized 4RepCT foams. Figure 3D was adapted from reference [154] (© 2015 U. Johansson et al., published by PLOS, distributed under the terms of the Creative Commons Attribution 4.0 International License, https://creativecommons.org/licenses/by/4.0/).

islet cells revealed that peptides inside the protein sequence enhanced cluster formation and total number of these islets, but the viability and functionality of the clusters was enhanced on all RGD-modified substrates [176]. The multitude of studies using functionalized recombinant spider silk in tissue engineering confirmed the high impact and suitability of bioadhe-

Beilstein J. Nanotechnol. 2022, 13, 902–921.

sive spider silk protein-based materials for applications in that field.

3.3 Antimicrobial silk-based surfaces

As already pointed out in section 2.2, no uniform hypothesis has been formulated so far for spider silk surfaces concerning their microbial repellence and persistence against microbial degradation. For example, one study reported increased bacterial growth on spider silk webs of *Linothele fallax* and *Linothele megatheloides* and discussed that spider silk proteins may serve as nutrients for various microbes [177], whereas other studies provided clear evidence that spider silks of the species *Tegenaria domestica, Nephila pilipes, Hippasa holmerae*, and *Cyrtophora moluccensis* are microbe-repellent [131,136]. More species have been studied in other reports, and as one result thereof it is clear that microbial repellence is not a general trait in spider silks [178]. One way to characterize this issue is through the analysis of genetically engineered silk proteins, allowing for a precise control of the design and modifications of the underlying amino acid sequence motifs and the structure–property relationships of tailored silk materials. Thus, intrinsic antimicrobial properties of materials based on recombinant silk proteins can also be analysed in greater detail. Modifications with specific functions, for example, AMPs against biofouling, enzymes, and nanoparticles, open further roads towards antimicrobial or repellent protein-based materials. As an example, Harris et al. studied coatings made of recombinant spider silk proteins based on the dragline silk amino acid sequence of *Nephila clavipes* MaSp1 and MaSp2 on a variety of substrates [179]. The authors reported an intrinsic ability of the recombinant spider silk proteins to prevent biofouling due to bacterial manifestation. In addition, functionalization of the silk proteins with antimicrobial biologicals displayed increased inhibition of surface fouling [179]. Fusion proteins combining recombinant MaSp1 spider silk proteins from *Nephila clavipes* with the AMPs human neutrophil defensin 2 and 4 (HNP-2, HNP-4) and hepcidin, showed antimicrobial activity against Gram-negative *E. coli* and Gram-positive *Staphylococcus aureus* [180]. A more recent study reported on the fusion protein 2Rep-HNP1 consisting of two repeats of the *Euprosthenops australis* MaSp1 repetitive core region and the AMP human neutrophil defensin 1 active peptide (HNP-1) to create antimicrobial silk as a promising new suture material [181]. The tagged 2Rep-HNP1 retained a broad-spectrum antimicrobial activity above 90% against the same bacterial pathogens mentioned above [181]. Another approach aimed to take advantage of the combined usage of natural silk fibroin as a bulk scaffold and a coating with recombinant spider silk proteins functionalized with specific modifications [182]. The recombinant spider silk protein 4RepCT was fused with two AMP motifs with antimicrobial activity, namely magainin I (Mag-4RC) and lactoferricin (Lac-4RC), successfully inhibiting biofilm development of the skin-infecting bacteria *Pseudomonas aeruginosa* (*P. aeruginosa*) and *Staphylococcus epidermidis* (Figure 4A) [183].

Introducing antimicrobial properties on surfaces and coatings using antibacterial agents in silks is an advantageous route to reduce or inhibit microbial infestation. The concentration of the antibacterial agent could be locally increased without exceeding toxicity limits as opposed to conventional antibiotic delivery methods in solution. One approach to make materials antimicrobial is to implement metallic nanoparticles in the bulk material. Silver ions in solution have shown antibacterial properties and are widely used in medicine [185]. The release of silver ions from silver nanoparticles (AgNPs) resulted in enhanced chemical, physical, and biological properties [186,187]. In addition to bactericidal properties, physical damage of bacterial membranes by AgNPs was also observed, causing cell leakage and, eventually, cell death [187,188]. A variety of studies focused on the modification of silkworm silk, including plateless silver coating techniques [189] and various coupling mechanisms of silver or gold nanoparticles [190-192]. In addition, the modification of regenerated sericin using crosslinking or surface-linking to titanium dioxide nanoparticles displayed strong activity against different microbes, resulting in loss of cell integrity and subsequent cell death [193-195]. AgNPs produced with sericin as a reducing agent in situ effectively inhibited the growth of *E. coli*, *S. aureus*, and *P. aeruginosa* in radial diffusion assays [194,195].

The genetic introduction of silver binding sites into recombinant spider silk proteins from *Nephila clavipes* MaSp1 dragline silk has been reported, for example, by Currie and co-workers [196]. The study confirmed the effective chimeric coupling of silver ions from a solution, resulting in potent inhibitory effects on both Gram-positive and Gram-negative bacteria [196]. Apart from silver, carbon in the shape of nanodiamonds incorporated into electrospun silk nanofibres showed antibacterial behaviour [197]. As another example, the antibacterial properties of selenium nanoparticles could further be enhanced by coating them with positively charged recombinant eADF4(κ16) silk proteins (Figure 4B) [184]. In addition, cytotoxicity testing showed that the coated selenium particles are safe to use at certain concentrations in biological applications since they showed acceptable cytotoxicity on Balb 3T3 mouse fibroblasts and HaCaT human skin keratinocytes [184]. Composite films and hydrogels made of recombinant eADF4(C16) spider silk and mesoporous silica nanoparticles (MSN) loaded with the aminoglycoside antibiotics gentamycin, neomycin, and kanamycin as well as the antimycotic amphotericin B, exhibited excellent antimicrobial properties [198]. Surface antimicrobial activities against *E. coli*

Beilstein J. Nanotechnol. **2022,** *13,* 902–921.

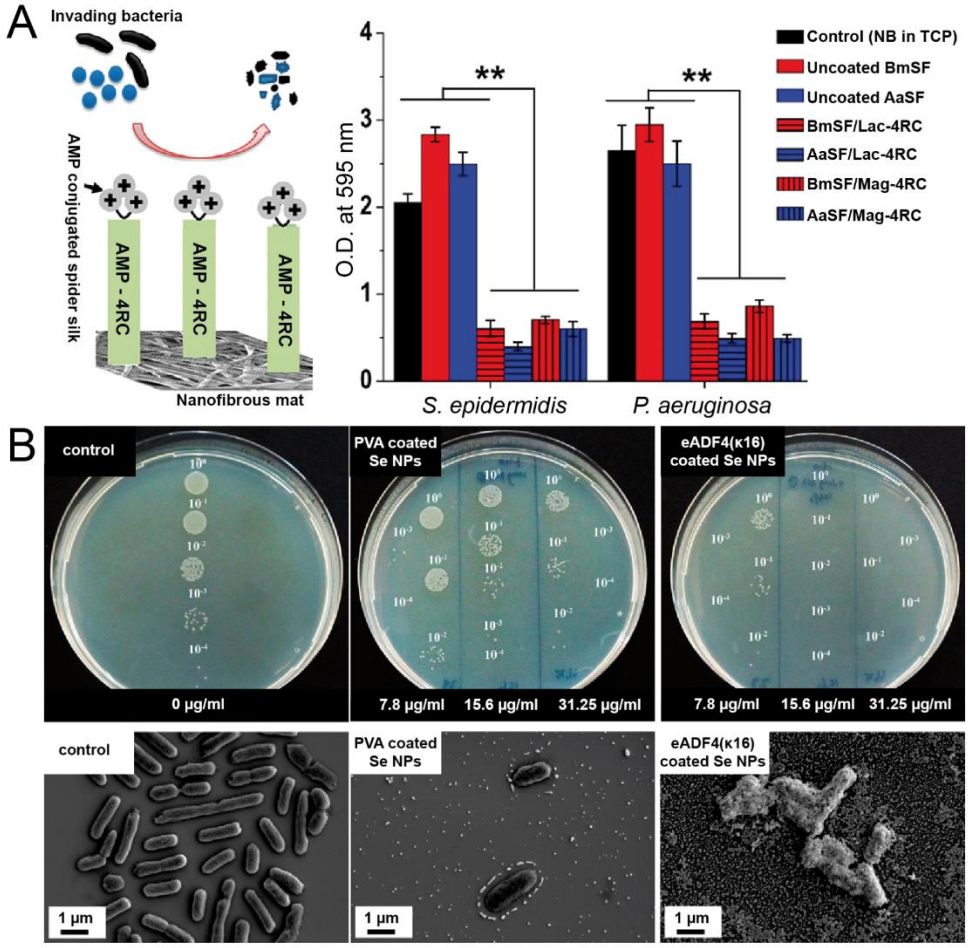

Figure 4: Antimicrobial spider silk materials. (A) Nanofibrous silk fibroin mats (BmSF and AaSF) are coated with recombinant 4RepCT spider silk proteins functionalized with magainin I (Mag-4RC) or lactoferricin (Lac-4RC) cationic antimicrobial peptides. Crystal violet staining (O.D. at 595 nm) of *S. epidermidis* and *P. aeruginosa* bacteria reveals significantly lower biofilm formation on spider silk-coated silk fibroin mats compared to uncoated ones. Figure 4A was adapted with permission from [183], Copyright 2018 American Chemical Society. This content is not subject to CC BY 4.0.
(B) Images of agar plates of a colony-forming unit assay and representative scanning electron images of *E. coli* bacteria without and after a treatment using polyvinyl alcohol (PVA) and eADF4(κ16) spider silk-coated selenium (Se) nanoparticles (NPs) in comparison to a particle-free control. Concentrations as indicated. 10^0 represents the original solution of bacteria without or with appropriate particles, while 10^{-1}, 10^{-2}, 10^{-3}, and 10^{-4} indicate, respectively, 10-, 100-, 1000- and 10000-fold dilutions of the original suspension. Figure 4B was adapted from reference [184] ("Enhanced Antibacterial Activity of Se Nanoparticles Upon Coating with Recombinant Spider Silk Protein eADF4(κ16)", © 2020 Huang et al., published and licensed by Dove Medical Press Ltd., distributed under the terms of the Creative Commons Attribution-NonCommercial 3.0 Unported License, http://creativecommons.org/licenses/by-nc/3.0/). This content is not subject to CC BY 4.0.

and *Pichia pastoris* with sustained release of antibiotics could be monitored over the course of 15 days, even at their MIC [198]. Furthermore, the inclusion of antibiotics/antimycotics did not impair the cytocompatibility of the composite materials and promoted fibroblast cell adhesion and proliferation [198].

By incorporating the non-natural methionine analogue L-azidohomoalanine (L-Aha) into the recombinant 4RepCT spider silk protein, site-specific chemical incorporation of two fluorophores and an antibiotic was conducted using copper-catalysed azide–alkyne cycloaddition (a type of click chemistry) [199]. The assembled silk fibres decorated with the broad-spectrum antibiotic levofloxacin showed significant antibiotic activity over at least five days [199]. In another approach, the same recombinant spider silk was successfully functionalized with bacteriolytic or anti-biofouling enzymes for bioactive surface

Beilstein J. Nanotechnol. 2022, 13, 902–921.

coatings [200]. The group developed recombinant 4RepCT spider silk proteins functionalized with the peptidoglycan degrading endolysin SAL-1 from the staphylococcal bacteriophage SAP-1 and the biofilm-matrix-degrading enzyme dispersin B from *Aggregatibacter actinomycetemcomitans* [200].

3.4 Antiadhesive properties

Besides antimicrobial strategies with a limited number of microbe-killing agents, antiadhesive, anti-fouling, and/or microbe-repellent surfaces are a long-term antimicrobial approach. To this end, it was exemplarily demonstrated that implants and catheters coated with the recombinant spider silk protein eADF4(C16) show significantly reduced adhesion and proliferation of mammalian cells compared to untreated ones [163,201,202]. When transplanted into rats in vivo, eADF4(C16)-coated medical grade silicone implants showed a significant reduction in periprosthetic fibrous capsule formation. Furthermore, the recombinant spider silk protein coatings acted as a bioshield, improved the biocompatibility and significantly decreased the foreign body response to the implant [201,202]. Additionally, it was shown that coatings made of eADF4(C16) silk protein on silicone surfaces could also enhance microbe-repellent properties against four opportunistic infection-related strains, leading to reduced microbial adherence up to 99.7% in comparison to uncoated silicone surfaces [203]. Zhang et al. reported a different repellent effect, due to triboelectric charging of a film made from recombinant spider silk proteins based on a MaSp1 sequence [204]. A potential difference between the positively charged surface and the bacteria was generated by their self-powered triboelectric nanogenerator, which builds up electrical charges of up to 135 V. An extracellular transmission of electrons impairs the bacterial morphology and leads to death of the bacteria by inducing a burst of reactive oxygen species inside the bacterial cytoplasm [204].

Spider silk proteins have also been analysed as far as thrombosis and blood coagulation is concerned. Weiss et al. analysed the effect of surface net charge of several recombinant spider silk variants on the formation of the biomolecular corona in contact with whole blood [205]. The study could show that negatively charged or almost neutral spider silk material surfaces prevented blood clotting, while the positively charged ones interacted predominantly with fibrinogen-based proteins, correlating with increased blood clotting [205]. In another study, silk proteins were functionalized with heparin to prevent thrombosis, reporting an intrinsic ability of the recombinant spider silk proteins to prevent blood clotting [179]. Recently, a heparin-binding and antimicrobial mimicking peptide based on the consensus heparin binding amino acid motif (HBM) was genetically linked to a recombinant MaSp2-based spider silk protein [206]. The fusion protein displayed heparin binding and anticoagulant properties, as well as an intrinsic property to inhibit bacterial growth due to the antimicrobial properties [206].

Finally, a systematic study of different variants of engineered *Araneus diadematus* spidroins ADF3 and ADF4 aimed to demonstrate that the intrinsic microbe-repellence of eADF4(C16) spider silk can be altered by a single amino acid exchange in the repetitive unit. The change of negatively charged glutamate in eADF4(C16) to uncharged glutamine in eADF4(Ω16) resulted in nano-structural changes in films and hydrogels, which in turn resulted in the attachment of some microbes [145,146]. It was concluded that size and distribution of crystalline patches within the silk surface structure are crucial to create anti-fouling, microbe-repellent surfaces, in line with the argumentation that antifouling effects of spider silk surfaces are due to nanostructural features of silk [145,146,207]. Simultaneously, bioselectivity of the silk protein material was achieved by introducing the cell adhesion motif RGD to eADF4(C16), resulting in selective mammalian cell adhesion [145,146]. Figure 5 shows a summary of this recombinant spider silk protein approach for bioselective, microbe-repellent surface effects in comparison to silk fibroin.

Conclusion

Combining microbial repellence with bioselective cell binding is a crucial step towards multifunctional and specific biomaterial applications. A controllable protein-based platform could provide a long-term sustainable and environmentally friendly (in patients and globally) material for this approach. Thus, there is great interest in developing advanced green materials that inhibit microbial adhesion to surfaces while simultaneously promoting selective mammalian cell growth. Arthropod silk materials, and, in particular, spider silk and their recombinant protein mimics, have been demonstrated to be ideally suited candidates to this end. Established recombinant spidroins provide defined protein composition and structure–function relationships, as well as the possibility to incorporate modifications for tailored functionality. Furthermore, such spidroins could be processed into several material forms and are inherently biocompatible and non-toxic. Thus, engineered spider silks provide a huge potential for future biomaterial applications due to the large variety of possible modifications, for instance, the integration of various cell binding motifs or AMPs. These important properties demonstrate the great ability of spider silk-based materials for the usage as bioselective, microbe-resistant coatings for technical as well as biomedical applications and tissue engineering.

Beilstein J. Nanotechnol. **2022,** *13,* 902–921.

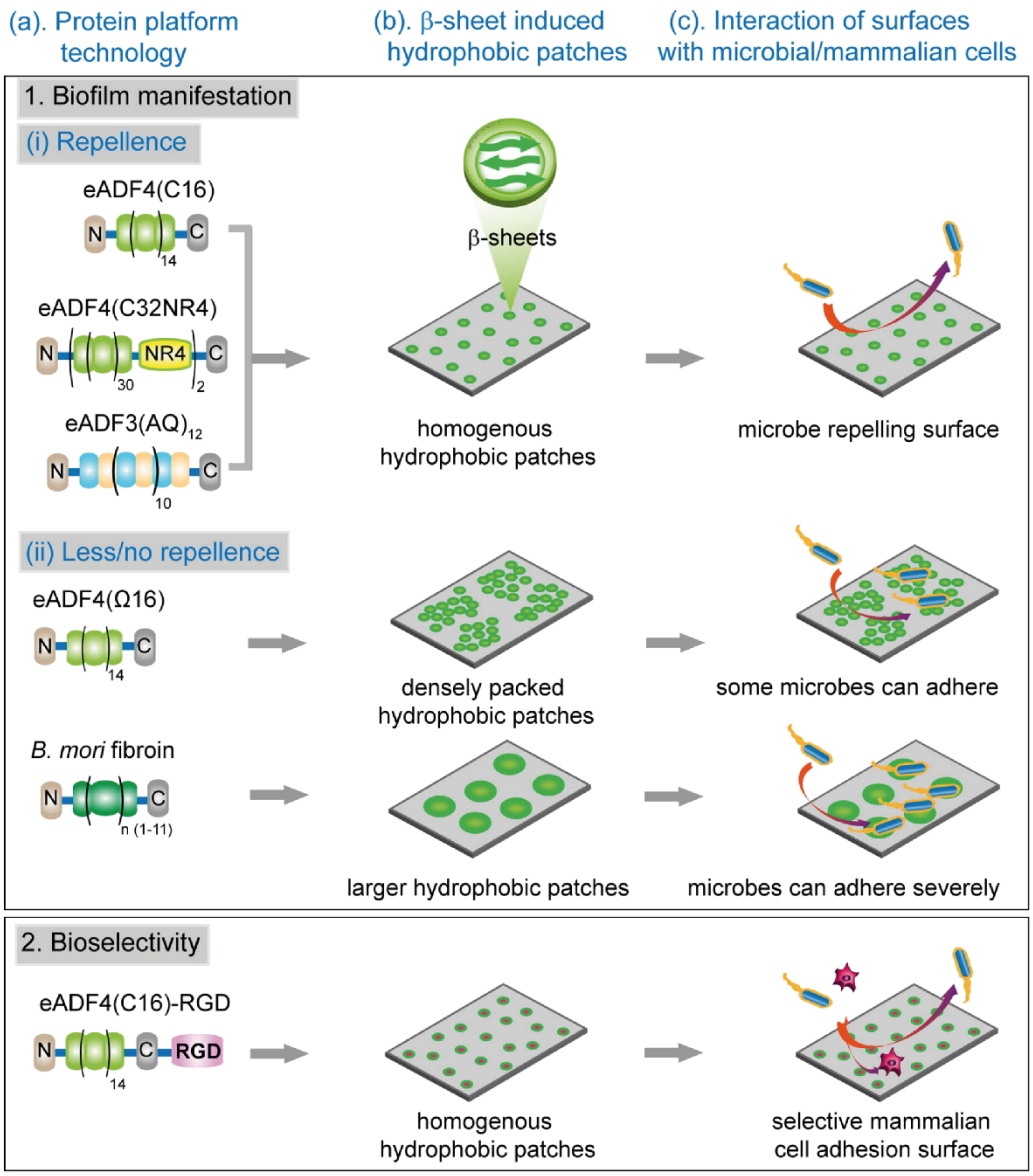

Figure 5: Engineered spider silk proteins for controlled microbial repellence and bioselective cell attachment. Compared to natural silk fibroin from *Bombyx mori*, the recombinant spider silk protein eADF4(C16) shows microbe-repellent behaviour and could be genetically modified (eADF4(C16)-RGD) to selectively allow for the attachment of mammalian cells to generate a multifunctional surface for biomedical applications. Figure 5 was reproduced from reference [146], (© 2020 Kumari et al., published by Elsevier B. V., distributed under the terms of the Creative Commons Attribution-Non-Commercial-NoDerivatives 4.0 International Licence, https://creativecommons.org/licenses/by-nc-nd/4.0/). This content is not subject to CC BY 4.0.

Funding

The authors would like to thank the EU, EFRE-project "Ziel ETZ 2014-2020" grant number 331, and the Federal Ministry of Education and Research (BMBF), project "Silk Repell", grant number 13XP5178A for financial support. Furthermore, the authors thank Nicholas Chan for proofreading the manuscript.

ORCID® iDs

Thomas Scheibel - https://orcid.org/0000-0002-0457-2423

References

1. Fazleabas, A. T.; Kim, J. J. *Science* **2003,** *299,* 355–356. doi:10.1126/science.1081277
2. Keckes, J.; Burgert, I.; Frühmann, K.; Müller, M.; Kölln, K.; Hamilton, M.; Burghammer, M.; Roth, S. V.; Stanzl-Tschegg, S.; Fratzl, P. *Nat. Mater.* **2003,** *2,* 810–813. doi:10.1038/nmat1019
3. Melzer, B.; Steinbrecher, T.; Seidel, R.; Kraft, O.; Schwaiger, R.; Speck, T. *J. R. Soc., Interface* **2010,** *7,* 1383–1389. doi:10.1098/rsif.2010.0140
4. Hofman, A. H.; van Hees, I. A.; Yang, J.; Kamperman, M. *Adv. Mater. (Weinheim, Ger.)* **2018,** *30,* 1704640. doi:10.1002/adma.201704640
5. Gorb, S. N. *Philos. Trans. R. Soc., A* **2008,** *366,* 1557–1574. doi:10.1098/rsta.2007.2172
6. Grunwald, I.; Rischka, K.; Kast, S. M.; Scheibel, T.; Bargel, H. *Philos. Trans. R. Soc., A* **2009,** *367,* 1727–1747. doi:10.1098/rsta.2009.0012
7. Smith, A. M. *Biological Adhesion,* 2nd ed.; Springer: Cham, Switzerland, 2016; p 378.
8. Rozario, T.; DeSimone, D. W. *Dev. Biol. (Amsterdam, Neth.)* **2010,** *341,* 126–140. doi:10.1016/j.ydbio.2009.10.026
9. Petruzzelli, L.; Takami, M.; Humes, H. D. *Am. J. Med.* **1999,** *106,* 467–476. doi:10.1016/s0002-9343(99)00058-3
10. Harjunpää, H.; Llort Asens, M.; Guenther, C.; Fagerholm, S. C. *Front. Immunol.* **2019,** *10,* 1078. doi:10.3389/fimmu.2019.01078
11. Sperandio, M. *FEBS J.* **2006,** *273,* 4377–4389. doi:10.1111/j.1742-4658.2006.05437.x
12. Samanta, D.; Almo, S. C. *Cell. Mol. Life Sci.* **2015,** *72,* 645–658. doi:10.1007/s00018-014-1763-4
13. Aplin, A.; Howe, A.; Alahari, S.; Juliano, R. *Pharmacol. Rev.* **1998,** *50,* 197–263.
14. Patel, S. D.; Chen, C. P.; Bahna, F.; Honig, B.; Shapiro, L. *Curr. Opin. Struct. Biol.* **2003,** *13,* 690–698. doi:10.1016/j.sbi.2003.10.007
15. Yap, A. S.; Brieher, W. M.; Gumbiner, B. M. *Annu. Rev. Cell Dev. Biol.* **1997,** *13,* 119–146. doi:10.1146/annurev.cellbio.13.1.119
16. Wai Wong, C.; Dye, D. E.; Coombe, D. R. *Int. J. Cell Biol.* **2012,** 340296. doi:10.1155/2012/340296
17. Cayrol, R.; Wosik, K.; Berard, J. L.; Dodelet-Devillers, A.; Ifergan, I.; Kebir, H.; Haqqani, A. S.; Kreymborg, K.; Krug, S.; Moumdjian, R.; Bouthillier, A.; Becher, B.; Arbour, N.; David, S.; Stanimirovic, D.; Prat, A. *Nat. Immunol.* **2008,** *9,* 137–145. doi:10.1038/ni1551
18. Kappelmayer, J.; Nagy, B. *BioMed Res. Int.* **2017,** 6138145. doi:10.1155/2017/6138145
19. Zhao, J.; Santino, F.; Giacomini, D.; Gentilucci, L. *Biomedicines* **2020,** *8,* 307. doi:10.3390/biomedicines8090307
20. Hynes, R. O. *Science* **2009,** *326,* 1216–1219. doi:10.1126/science.1176009
21. Berrier, A. L.; Yamada, K. M. *J. Cell. Physiol.* **2007,** *213,* 565–573. doi:10.1002/jcp.21237
22. Legate, K. R.; Wickström, S. A.; Fässler, R. *Genes Dev.* **2009,** *23,* 397–418. doi:10.1101/gad.1758709
23. Han, W. M.; Jang, Y. C.; García, A. J. The Extracellular Matrix and Cell–Biomaterial Interactions. In *Biomaterials Science,* 4th ed.; Wagner, W. R.; Sakiyama-Elbert, S. E.; Zhang, G.; Yaszemski, M. J., Eds.; Academic Press, 2020; pp 701–715. doi:10.1016/b978-0-12-816137-1.00045-3
24. Pankov, R.; Yamada, K. M. *J. Cell Sci.* **2002,** *115,* 3861–3863. doi:10.1242/jcs.00059
25. De Marco, R.; Greco, A.; Calonghi, N.; Dattoli, S. D.; Baiula, M.; Spampinato, S.; Picchetti, P.; De Cola, L.; Anselmi, M.; Cipriani, F.; Gentilucci, L. *Pept. Sci.* **2018,** *110,* e23081. doi:10.1002/bip.23081
26. Zhang, J.; Jiang, X.; Wen, X.; Xu, Q.; Zeng, H.; Zhao, Y.; Liu, M.; Wang, Z.; Hu, X.; Wang, Y. *JPhys Mater.* **2019,** *2,* 032004. doi:10.1088/2515-7639/ab1af5
27. Mano, J. F. *Adv. Eng. Mater.* **2008,** *10,* 515–527. doi:10.1002/adem.200700355
28. Gagner, J. E.; Kim, W.; Chaikof, E. L. *Acta Biomater.* **2014,** *10,* 1542–1557. doi:10.1016/j.actbio.2013.10.001
29. Choi, S. M.; Chaudhry, P.; Zo, S. M.; Han, S. S. Advances in Protein-Based Materials: From Origin to Novel Biomaterials. In *Cutting-Edge Enabling Technologies for Regenerative Medicine;* Chun, H. J.; Park, C. H.; Kwon, I. K.; Khang, G., Eds.; Springer: Singapore, 2018; pp 161–210. doi:10.1007/978-981-13-0950-2_10
30. Annabi, N.; Mithieux, S. M.; Camci-Unal, G.; Dokmeci, M. R.; Weiss, A. S.; Khademhosseini, A. *Biochem. Eng. J.* **2013,** *77,* 110–118. doi:10.1016/j.bej.2013.05.006
31. Shin, H.; Jo, S.; Mikos, A. G. *Biomaterials* **2003,** *24,* 4353–4364. doi:10.1016/s0142-9612(03)00339-9
32. Spiller, S.; Clauder, F.; Bellmann-Sickert, K.; Beck-Sickinger, A. G. *Biol. Chem.* **2021,** *402,* 1271–1288. doi:10.1515/hsz-2021-0144
33. Hosoyama, K.; Lazurko, C.; Muñoz, M.; McTiernan, C. D.; Alarcon, E. I. *Front. Bioeng. Biotechnol.* **2019,** *7,* 205. doi:10.3389/fbioe.2019.00205
34. Huettner, N.; Dargaville, T. R.; Forget, A. *Trends Biotechnol.* **2018,** *36,* 372–383. doi:10.1016/j.tibtech.2018.01.008
35. Yamada, K. M. *J. Biol. Chem.* **1991,** *266,* 12809–12812. doi:10.1016/s0021-9258(18)98761-2
36. Pountos, I.; Panteli, M.; Lampropoulos, A.; Jones, E.; Calori, G. M.; Giannoudis, P. V. *BMC Med.* **2016,** *14,* 103. doi:10.1186/s12916-016-0646-y
37. Ruoslahti, E.; Pierschbacher, M. D. *Cell* **1986,** *44,* 517–518. doi:10.1016/0092-8674(86)90259-x
38. Pierschbacher, M. D.; Hayman, E. G.; Ruoslahti, E. *J. Cell. Biochem.* **1985,** *28,* 115–126. doi:10.1002/jcb.240280205
39. Hersel, U.; Dahmen, C.; Kessler, H. *Biomaterials* **2003,** *24,* 4385–4415. doi:10.1016/s0142-9612(03)00343-0
40. Pierschbacher, M. D.; Ruoslahti, E. *Nature* **1984,** *309,* 30–33. doi:10.1038/309030a0
41. Ruoslahti, E. *Annu. Rev. Cell Dev. Biol.* **1996,** *12,* 697–715. doi:10.1146/annurev.cellbio.12.1.697
42. Bellis, S. L. *Biomaterials* **2011,** *32,* 4205–4210. doi:10.1016/j.biomaterials.2011.02.029
43. Pfaff, M. Recognition Sites of RGD-Dependent Integrins. *Integrin-Ligand Interaction;* Springer: Boston, MA, USA, 1997; pp 101–121. doi:10.1007/978-1-4757-4064-6_4
44. Mertgen, A.-S.; Trossmann, V. T.; Guex, A. G.; Maniura-Weber, K.; Scheibel, T.; Rottmar, M. *ACS Appl. Mater. Interfaces* **2020,** *12,* 21342–21367. doi:10.1021/acsami.0c01893

45. Rechenmacher, F.; Neubauer, S.; Mas-Moruno, C.; Dorfner, P. M.; Polleux, J.; Guasch, J.; Conings, B.; Boyen, H.-G.; Bochen, A.; Sobahi, T. R.; Burgkart, R.; Spatz, J. P.; Fässler, R.; Kessler, H. *Chem. – Eur. J.* **2013,** *19,* 9218–9223. doi:10.1002/chem.201301478
46. Grant, D. S.; Tashiro, K.-I.; Segui-Real, B.; Yamada, Y.; Martin, G. R.; Kleinman, H. K. *Cell* **1989,** *58,* 933–943. doi:10.1016/0092-8674(89)90945-8
47. Graf, J.; Iwamoto, Y.; Sasaki, M.; Martin, G. R.; Kleinman, H. K.; Robey, F. A.; Yamada, Y. *Cell* **1987,** *48,* 989–996. doi:10.1016/0092-8674(87)90707-0
48. Graf, J.; Ogle, R. C.; Robey, F. A.; Sasaki, M.; Martin, G. R.; Yamada, Y.; Kleinman, H. K. *Biochemistry* **1987,** *26,* 6896–6900. doi:10.1021/bi00396a004
49. Sullivan, T.; O'Callaghan, I. *Biomimetics* **2020,** *5,* 58. doi:10.3390/biomimetics5040058
50. Sonnleitner, D.; Sommer, C.; Scheibel, T.; Lang, G. *Mater. Sci. Eng., C* **2021,** *131,* 112458. doi:10.1016/j.msec.2021.112458
51. Ivanova, E. P.; Hasan, J.; Webb, H. K.; Truong, V. K.; Watson, G. S.; Watson, J. A.; Baulin, V. A.; Pogodin, S.; Wang, J. Y.; Tobin, M. J.; Löbbe, C.; Crawford, R. J. *Small* **2012,** *8,* 2489–2494. doi:10.1002/smll.201200528
52. May, R. M.; Magin, C. M.; Mann, E. E.; Drinker, M. C.; Fraser, J. C.; Siedlecki, C. A.; Brennan, A. B.; Reddy, S. T. *Clin. Transl. Med.* **2015,** *4,* 9. doi:10.1186/s40169-015-0050-9
53. Barthlott, W.; Mail, M.; Bhushan, B.; Koch, K. *Nano-Micro Lett.* **2017,** *9,* 23. doi:10.1007/s40820-016-0125-1
54. Watson, G. S.; Green, D. W.; Cribb, B. W.; Brown, C. L.; Meritt, C. R.; Tobin, M. J.; Vongsvivut, J.; Sun, M.; Liang, A.-P.; Watson, J. A. *ACS Appl. Mater. Interfaces* **2017,** *9,* 24381–24392. doi:10.1021/acsami.7b08368
55. Barthlott, W.; Neinhuis, C. *Planta* **1997,** *202,* 1–8. doi:10.1007/s004250050096
56. Barthlott, W.; Schimmel, T.; Wiersch, S.; Koch, K.; Brede, M.; Barczewski, M.; Walheim, S.; Weis, A.; Kaltenmaier, A.; Leder, A.; Bohn, H. F. *Adv. Mater. (Weinheim, Ger.)* **2010,** *22,* 2325–2328. doi:10.1002/adma.200904411
57. Tripathy, A.; Sen, P.; Su, B.; Briscoe, W. H. *Adv. Colloid Interface Sci.* **2017,** *248,* 85–104. doi:10.1016/j.cis.2017.07.030
58. Liu, Q.; Brookbank, L.; Ho, A.; Coffey, J.; Brennan, A. B.; Jones, C. J. *PLoS One* **2020,** *15,* e0244518. doi:10.1371/journal.pone.0244518
59. Koc, Y.; de Mello, A. J.; McHale, G.; Newton, M. I.; Roach, P.; Shirtcliffe, N. J. *Lab Chip* **2008,** *8,* 582–586. doi:10.1039/b716509a
60. Pernites, R. B.; Santos, C. M.; Maldonado, M.; Ponnapati, R. R.; Rodrigues, D. F.; Advincula, R. C. *Chem. Mater.* **2012,** *24,* 870–880. doi:10.1021/cm2007044
61. Stallard, C. P.; McDonnell, K. A.; Onayemi, O. D.; O'Gara, J. P.; Dowling, D. P. *Biointerphases* **2012,** *7,* 31. doi:10.1007/s13758-012-0031-0
62. Zhu, H.; Guo, Z.; Liu, W. *Chem. Commun.* **2014,** *50,* 3900–3913. doi:10.1039/c3cc47818a
63. Privett, B. J.; Youn, J.; Hong, S. A.; Lee, J.; Han, J.; Shin, J. H.; Schoenfisch, M. H. *Langmuir* **2011,** *27,* 9597–9601. doi:10.1021/la201801e
64. Crick, C. R.; Ismail, S.; Pratten, J.; Parkin, I. P. *Thin Solid Films* **2011,** *519,* 3722–3727. doi:10.1016/j.tsf.2011.01.282
65. Hizal, F.; Rungraeng, N.; Lee, J.; Jun, S.; Busscher, H. J.; van der Mei, H. C.; Choi, C.-H. *ACS Appl. Mater. Interfaces* **2017,** *9,* 12118–12129. doi:10.1021/acsami.7b01322
66. Cai, S.; Wu, C.; Yang, W.; Liang, W.; Yu, H.; Liu, L. *Nanotechnol. Rev.* **2020,** *9,* 971–989. doi:10.1515/ntrev-2020-0076
67. Jeon, S. I.; Lee, J. H.; Andrade, J. D.; De Gennes, P. G. *J. Colloid Interface Sci.* **1991,** *142,* 149–158. doi:10.1016/0021-9797(91)90043-8
68. Ista, L. K.; Mendez, S.; Lopez, G. P. *Biofouling* **2010,** *26,* 111–118. doi:10.1080/08927010903383455
69. Bosker, W. T. E.; Patzsch, K.; Stuart, M. A. C.; Norde, W. *Soft Matter* **2007,** *3,* 754–762. doi:10.1039/b618259c
70. Haldar, J.; An, D.; Álvarez de Cienfuegos, L.; Chen, J.; Klibanov, A. M. *Proc. Natl. Acad. Sci. U. S. A.* **2006,** *103,* 17667–17671. doi:10.1073/pnas.0608803103
71. Wong, S. Y.; Li, Q.; Veselinovic, J.; Kim, B.-S.; Klibanov, A. M.; Hammond, P. T. *Biomaterials* **2010,** *31,* 4079–4087. doi:10.1016/j.biomaterials.2010.01.119
72. Buzzacchera, I.; Vorobii, M.; Kostina, N. Y.; de los Santos Pereira, A.; Riedel, T.; Bruns, M.; Ogieglo, W.; Möller, M.; Wilson, C. J.; Rodriguez-Emmenegger, C. *Biomacromolecules* **2017,** *18,* 1983–1992. doi:10.1021/acs.biomac.7b00516
73. Kovacs, B.; Patko, D.; Klein, A.; Kakasi, B.; Saftics, A.; Kurunczi, S.; Vonderviszt, F.; Horvath, R. *Sens. Actuators, B* **2018,** *257,* 839–845. doi:10.1016/j.snb.2017.11.027
74. Liu, X.; Peng, L.; Meng, J.; Zhu, Z.; Han, B.; Wang, S. *Nanoscale* **2018,** *10,* 2711–2714. doi:10.1039/c7nr08844b
75. Wang, L.-S.; Gopalakrishnan, S.; Lee, Y.-W.; Zhu, J.; Nonnenmann, S. S.; Rotello, V. M. *Mater. Horiz.* **2018,** *5,* 268–274. doi:10.1039/c7mh00933j
76. Bullitt, E.; Makowski, L. *Nature* **1995,** *373,* 164–167. doi:10.1038/373164a0
77. Garrett, T. R.; Bhakoo, M.; Zhang, Z. *Prog. Nat. Sci.* **2008,** *18,* 1049–1056. doi:10.1016/j.pnsc.2008.04.001
78. Asadi, A.; Razavi, S.; Talebi, M.; Gholami, M. *Infection (Munich, Ger.)* **2019,** *47,* 13–23. doi:10.1007/s15010-018-1222-5
79. Piatek, R.; Zalewska-Piatek, B.; Dzierzbicka, K.; Makowiec, S.; Pilipczuk, J.; Szemiako, K.; Cyranka-Czaja, A.; Wojciechowski, M. *BMC Microbiol.* **2013,** *13,* 131. doi:10.1186/1471-2180-13-131
80. Pinkner, J. S.; Remaut, H.; Buelens, F.; Miller, E.; Åberg, V.; Pemberton, N.; Hedenström, M.; Larsson, A.; Seed, P.; Waksman, G.; Hultgren, S. J.; Almqvist, F. *Proc. Natl. Acad. Sci. U. S. A.* **2006,** *103,* 17897–17902. doi:10.1073/pnas.0606795103
81. Eidam, O.; Dworkowski, F. S. N.; Glockshuber, R.; Grütter, M. G.; Capitani, G. *FEBS Lett.* **2008,** *582,* 651–655. doi:10.1016/j.febslet.2008.01.030
82. Soto, G. E.; Hultgren, S. J. *J. Bacteriol.* **1999,** *181,* 1059–1071. doi:10.1128/jb.181.4.1059-1071.1999
83. Krachler, A. M.; Ham, H.; Orth, K. *Proc. Natl. Acad. Sci. U. S. A.* **2011,** *108,* 11614–11619. doi:10.1073/pnas.1102360108
84. Krachler, A. M.; Mende, K.; Murray, C.; Orth, K. *Virulence* **2012,** *3,* 389–399. doi:10.4161/viru.20816
85. Etayash, H.; Hancock, R. E. W. *Pharmaceutics* **2021,** *13,* 1820. doi:10.3390/pharmaceutics13111820
86. Zasloff, M. *Nature* **2002,** *415,* 389–395. doi:10.1038/415389a
87. Dürr, U. H. N.; Sudheendra, U. S.; Ramamoorthy, A. *Biochim. Biophys. Acta, Biomembr.* **2006,** *1758,* 1408–1425. doi:10.1016/j.bbamem.2006.03.030
88. Lai, Y.; Gallo, R. L. *Trends Immunol.* **2009,** *30,* 131–141. doi:10.1016/j.it.2008.12.003
89. Hancock, R. E. W.; Sahl, H.-G. *Nat. Biotechnol.* **2006,** *24,* 1551–1557. doi:10.1038/nbt1267

90. Lau, Y. E.; Rozek, A.; Scott, M. G.; Goosney, D. L.; Davidson, D. J.; Hancock, R. E. W. *Infect. Immun.* **2005,** *73,* 583–591. doi:10.1128/iai.73.1.583-591.2005
91. Duplantier, A. J.; van Hoek, M. L. *Front. Immunol.* **2013,** *4,* 143. doi:10.3389/fimmu.2013.00143
92. Wimley, W. C.; Hristova, K. *J. Membr. Biol.* **2011,** *239,* 27–34. doi:10.1007/s00232-011-9343-0
93. Wang, G.; Li, X.; Wang, Z. *Nucleic Acids Res.* **2016,** *44,* D1087–D1093. doi:10.1093/nar/gkv1278
94. Overhage, J.; Campisano, A.; Bains, M.; Torfs, E. C. W.; Rehm, B. H. A.; Hancock, R. E. W. *Infect. Immun.* **2008,** *76,* 4176–4182. doi:10.1128/iai.00318-08
95. de la Fuente-Núñez, C.; Korolik, V.; Bains, M.; Nguyen, U.; Breidenstein, E. B. M.; Horsman, S.; Lewenza, S.; Burrows, L.; Hancock, R. E. W. *Antimicrob. Agents Chemother.* **2012,** *56,* 2696–2704. doi:10.1128/aac.00064-12
96. Lee, J.-K.; Park, Y. *Int. J. Mol. Sci.* **2020,** *21,* 5632. doi:10.3390/ijms21165632
97. Godballe, T.; Nilsson, L. L.; Petersen, P. D.; Jenssen, H. *Chem. Biol. Drug Des.* **2011,** *77,* 107–116. doi:10.1111/j.1747-0285.2010.01067.x
98. Bicker, K. L.; Cobb, S. L. *Chem. Commun.* **2020,** *56,* 11158–11168. doi:10.1039/d0cc04704j
99. Beckloff, N.; Laube, D.; Castro, T.; Furgang, D.; Park, S.; Perlin, D.; Clements, D.; Tang, H.; Scott, R. W.; Tew, G. N.; Diamond, G. *Antimicrob. Agents Chemother.* **2007,** *51,* 4125–4132. doi:10.1128/aac.00208-07
100. Tagliabue, A.; Rappuoli, R. *Front. Immunol.* **2018,** *9,* 1068. doi:10.3389/fimmu.2018.01068
101. Bloom, D. E.; Cadarette, D. *Front. Immunol.* **2019,** *10,* 549. doi:10.3389/fimmu.2019.00549
102. He, T.; Shi, Z. L.; Fang, N.; Neoh, K. G.; Kang, E. T.; Chan, V. *Biomaterials* **2009,** *30,* 317–326. doi:10.1016/j.biomaterials.2008.09.049
103. He, T.; Zhang, Y.; Lai, A. C. K.; Chan, V. *Biomed. Mater.* **2015,** *10,* 015015. doi:10.1088/1748-6041/10/1/015015
104. Altman, G. H.; Diaz, F.; Jakuba, C.; Calabro, T.; Horan, R. L.; Chen, J.; Lu, H.; Richmond, J.; Kaplan, D. L. *Biomaterials* **2003,** *24,* 401–416. doi:10.1016/s0142-9612(02)00353-8
105. Salehi, S.; Koeck, K.; Scheibel, T. *Molecules* **2020,** *25,* 737. doi:10.3390/molecules25030737
106. Aigner, T. B.; DeSimone, E.; Scheibel, T. *Adv. Mater. (Weinheim, Ger.)* **2018,** *30,* 1704636. doi:10.1002/adma.201704636
107. Kiseleva, A. P.; Krivoshapkin, P. V.; Krivoshapkina, E. F. *Front. Chem. (Lausanne, Switz.)* **2020,** *8,* 554. doi:10.3389/fchem.2020.00554
108. Scheibel, T.; Zahn, H.; Krasowski, A. Silk. *Ullmann's Encyclopedia of Industrial Chemistry;* John Wiley & Sons, 2016; pp 1–15. doi:10.1002/14356007.a24_095.pub2
109. Herold, H. M.; Scheibel, T. *Z. Naturforsch., C: J. Biosci.* **2017,** *72,* 365–385. doi:10.1515/znc-2017-0050
110. Sehnal, F.; Sutherland, T. *Prion* **2008,** *2,* 145–153. doi:10.4161/pri.2.4.7489
111. Garb, J. E.; Ayoub, N. A.; Hayashi, C. Y. *BMC Evol. Biol.* **2010,** *10,* 243. doi:10.1186/1471-2148-10-243
112. Sutherland, T. D.; Young, J. H.; Weisman, S.; Hayashi, C. Y.; Merritt, D. J. *Annu. Rev. Entomol.* **2010,** *55,* 171–188. doi:10.1146/annurev-ento-112408-085401
113. Andersson, M.; Johansson, J.; Rising, A. *Int. J. Mol. Sci.* **2016,** *17,* 1290. doi:10.3390/ijms17081290
114. Saric, M.; Scheibel, T. *Curr. Opin. Biotechnol.* **2019,** *60,* 213–220. doi:10.1016/j.copbio.2019.05.005
115. Inoue, S.; Tanaka, K.; Arisaka, F.; Kimura, S.; Ohtomo, K.; Mizuno, S. *J. Biol. Chem.* **2000,** *275,* 40517–40528. doi:10.1074/jbc.m006897200
116. Sehadova, H.; Zavodska, R.; Rouhova, L.; Zurovec, M.; Sauman, I. *Int. J. Mol. Sci.* **2021,** *22,* 13523. doi:10.3390/ijms222413523
117. Kucerova, L.; Zurovec, M.; Kludkiewicz, B.; Hradilova, M.; Strnad, H.; Sehnal, F. *Sci. Rep.* **2019,** *9,* 3797. doi:10.1038/s41598-019-40401-3
118. Eisoldt, L.; Smith, A.; Scheibel, T. *Mater. Today* **2011,** *14,* 80–86. doi:10.1016/s1369-7021(11)70057-8
119. Eisoldt, L.; Thamm, C.; Scheibel, T. *Biopolymers* **2012,** *97,* 355–361. doi:10.1002/bip.22006
120. Bittencourt, D.; Oliveira, P. F.; Prosdocimi, F.; Rech, E. L. *Genet. Mol. Res.* **2012,** *11,* 2360–2380. doi:10.4238/2012.august.13.10
121. Thamm, C.; Scheibel, T. *Biomacromolecules* **2017,** *18,* 1365–1372. doi:10.1021/acs.biomac.7b00090
122. Collin, M. A.; Clarke, T. H., III; Ayoub, N. A.; Hayashi, C. Y. *Int. J. Biol. Macromol.* **2018,** *113,* 829–840. doi:10.1016/j.ijbiomac.2018.02.032
123. Altman, G. H.; Horan, R. L.; Lu, H. H.; Moreau, J.; Martin, I.; Richmond, J. C.; Kaplan, D. L. *Biomaterials* **2002,** *23,* 4131–4141. doi:10.1016/s0142-9612(02)00156-4
124. Ribeiro, M.; de Moraes, M. A.; Beppu, M. M.; Garcia, M. P.; Fernandes, M. H.; Monteiro, F. J.; Ferraz, M. P. *Eur. Polym. J.* **2015,** *67,* 66–77. doi:10.1016/j.eurpolymj.2015.03.056
125. Kuhbier, J. W.; Allmeling, C.; Reimers, K.; Hillmer, A.; Kasper, C.; Menger, B.; Brandes, G.; Guggenheim, M.; Vogt, P. M. *PLoS One* **2010,** *5,* e12032. doi:10.1371/journal.pone.0012032
126. Wendt, H.; Hillmer, A.; Reimers, K.; Kuhbier, J. W.; Schäfer-Nolte, F.; Allmeling, C.; Kasper, C.; Vogt, P. M. *PLoS One* **2011,** *6,* e21833. doi:10.1371/journal.pone.0021833
127. Yang, M.; Shuai, Y.; Zhou, G.; Mandal, N.; Zhu, L.; Mao, C. *ACS Appl. Mater. Interfaces* **2014,** *6,* 13782–13789. doi:10.1021/am503214g
128. Pedregal-Cortés, R.; Toriz, G.; Delgado, E.; Pollack, G. H. *Biofouling* **2019,** *35,* 732–741. doi:10.1080/08927014.2019.1653863
129. Chigama, H.; Yokoi, T.; Furuya, M.; Yokota, K.; Kanetaka, H.; Kawashita, M. *J. Mater. Sci.: Mater. Med.* **2020,** *31,* 49. doi:10.1007/s10856-020-06388-4
130. Amaley, A.; Gawali, A. A.; Akarte, S. R. *Indian J. Arachnol.* **2014,** *3,* 8–11.
131. Wright, S.; Goodacre, S. L. *BMC Res. Notes* **2012,** *5,* 326. doi:10.1186/1756-0500-5-326
132. Tahir, H. M.; Zaheer, A.; Rasheed, A.; Mukhtar, M. K.; Yaqoob, R.; Liaqat, I.; Ahsan, M. M. *Acta Zool. Bulg.* **2018,** *70,* 593–598.
133. Tahir, M.; Sattar, A.; Qamar, S.; Mukhtar, M.; Liaqat, I.; Ali, M.; Zaheer, A.; Arshad, N.; Yaqoob, R.; Naseem, S. *J. Anim. Plant Sci.* **2019,** *29,* 625–628.
134. Carl, N. K.; Alexander, E. D.; Taylor, A. S.; Jessica, A. R.; Jonathan, N. P. *J. Arachnol.* **2015,** *43,* 394–399.
135. Makover, V.; Ronen, Z.; Lubin, Y.; Khalaila, I. *J. R. Soc., Interface* **2019,** *16,* 20180581. doi:10.1098/rsif.2018.0581
136. Zhang, S.; Piorkowski, D.; Lin, W.-R.; Lee, Y.-R.; Liao, C.-P.; Wang, P.-H.; Tso, I.-M. *J. Exp. Biol.* **2019,** *222,* jeb214981. doi:10.1242/jeb.214981
137. Kaur, J.; Rajkhowa, R.; Afrin, T.; Tsuzuki, T.; Wang, X. *Biopolymers* **2014,** *101,* 237–245. doi:10.1002/bip.22323

138. Fruergaard, S.; Lund, M. B.; Schramm, A.; Vosegaard, T.; Bilde, T. *iScience* **2021,** *24,* 103125. doi:10.1016/j.isci.2021.103125
139. Whittall, D. R.; Baker, K. V.; Breitling, R.; Takano, E. *Trends Biotechnol.* **2021,** *39,* 560–573. doi:10.1016/j.tibtech.2020.09.007
140. Heidebrecht, A.; Scheibel, T. *Adv. Appl. Microbiol.* **2013,** *82,* 115–153. doi:10.1016/b978-0-12-407679-2.00004-1
141. Hedhammar, M.; Rising, A.; Grip, S.; Martinez, A. S.; Nordling, K.; Casals, C.; Stark, M.; Johansson, J. *Biochemistry* **2008,** *47,* 3407–3417. doi:10.1021/bi702432y
142. Stark, M.; Grip, S.; Rising, A.; Hedhammar, M.; Engström, W.; Hjälm, G.; Johansson, J. *Biomacromolecules* **2007,** *8,* 1695–1701. doi:10.1021/bm070049y
143. Huemmerich, D.; Helsen, C. W.; Quedzuweit, S.; Oschmann, J.; Rudolph, R.; Scheibel, T. *Biochemistry* **2004,** *43,* 13604–13612. doi:10.1021/bi048983q
144. Doblhofer, E.; Scheibel, T. *J. Pharm. Sci.* **2015,** *104,* 988–994. doi:10.1002/jps.24300
145. Kumari, S.; Lang, G.; DeSimone, E.; Spengler, C.; Trossmann, V. T.; Lücker, S.; Hudel, M.; Jacobs, K.; Krämer, N.; Scheibel, T. *Data Brief* **2020,** *32,* 106305. doi:10.1016/j.dib.2020.106305
146. Kumari, S.; Lang, G.; DeSimone, E.; Spengler, C.; Trossmann, V. T.; Lücker, S.; Hudel, M.; Jacobs, K.; Krämer, N.; Scheibel, T. *Mater. Today* **2020,** *41,* 21–33. doi:10.1016/j.mattod.2020.06.009
147. Rabotyagova, O. S.; Cebe, P.; Kaplan, D. L. *Biomacromolecules* **2009,** *10,* 229–236. doi:10.1021/bm800930x
148. Wohlrab, S.; Müller, S.; Schmidt, A.; Neubauer, S.; Kessler, H.; Leal-Egaña, A.; Scheibel, T. *Biomaterials* **2012,** *33,* 6650–6659. doi:10.1016/j.biomaterials.2012.05.069
149. Neubauer, V. J.; Scheibel, T. *ACS Biomater. Sci. Eng.* **2020,** *6,* 5599–5608. doi:10.1021/acsbiomaterials.0c00818
150. Esser, T. U.; Trossmann, V. T.; Lentz, S.; Engel, F. B.; Scheibel, T. *Mater. Today Bio* **2021,** *11,* 100114. doi:10.1016/j.mtbio.2021.100114
151. Widhe, M.; Shalaly, N. D.; Hedhammar, M. *Biomaterials* **2016,** *74,* 256–266. doi:10.1016/j.biomaterials.2015.10.013
152. Widhe, M.; Johansson, U.; Hillerdahl, C.-O.; Hedhammar, M. *Biomaterials* **2013,** *34,* 8223–8234. doi:10.1016/j.biomaterials.2013.07.058
153. Nilebäck, L.; Hedin, J.; Widhe, M.; Floderus, L. S.; Krona, A.; Bysell, H.; Hedhammar, M. *Biomacromolecules* **2017,** *18,* 846–854. doi:10.1021/acs.biomac.6b01721
154. Johansson, U.; Ria, M.; Åvall, K.; Dekki Shalaly, N.; Zaitsev, S. V.; Berggren, P.-O.; Hedhammar, M. *PLoS One* **2015,** *10,* e0130169. doi:10.1371/journal.pone.0130169
155. Saric, M.; Eisoldt, L.; Döring, V.; Scheibel, T. *Adv. Mater. (Weinheim, Ger.)* **2021,** *33,* 2006499. doi:10.1002/adma.202006499
156. Jansson, R.; Lau, C. H.; Ishida, T.; Ramström, M.; Sandgren, M.; Hedhammar, M. *Biotechnol. J.* **2016,** *11,* 687–699. doi:10.1002/biot.201500412
157. Jansson, R.; Thatikonda, N.; Lindberg, D.; Rising, A.; Johansson, J.; Nygren, P.-Å.; Hedhammar, M. *Biomacromolecules* **2014,** *15,* 1696–1706. doi:10.1021/bm500114e
158. Humenik, M.; Mohrand, M.; Scheibel, T. *Bioconjugate Chem.* **2018,** *29,* 898–904. doi:10.1021/acs.bioconjchem.7b00759
159. Thatikonda, N.; Nilebäck, L.; Kempe, A.; Widhe, M.; Hedhammar, M. *ACS Biomater. Sci. Eng.* **2018,** *4,* 3384–3396. doi:10.1021/acsbiomaterials.8b00844
160. Thatikonda, N.; Delfani, P.; Jansson, R.; Petersson, L.; Lindberg, D.; Wingren, C.; Hedhammar, M. *Biotechnol. J.* **2016,** *11,* 437–448. doi:10.1002/biot.201500297
161. Leal-Egaña, A.; Lang, G.; Mauerer, C.; Wickinghoff, J.; Weber, M.; Geimer, S.; Scheibel, T. *Adv. Eng. Mater.* **2012,** *14,* B67–B75. doi:10.1002/adem.201180072
162. Petzold, J.; Aigner, T. B.; Touska, F.; Zimmermann, K.; Scheibel, T.; Engel, F. B. *Adv. Funct. Mater.* **2017,** *27,* 1701427. doi:10.1002/adfm.201701427
163. Borkner, C. B.; Wohlrab, S.; Möller, E.; Lang, G.; Scheibel, T. *ACS Biomater. Sci. Eng.* **2017,** *3,* 767–775. doi:10.1021/acsbiomaterials.6b00306
164. Leal-Egaña, A.; Díaz-Cuenca, A.; Boccaccini, A. R. *Adv. Mater. (Weinheim, Ger.)* **2013,** *25,* 4049–4057. doi:10.1002/adma.201301227
165. Blau, A. *Curr. Opin. Colloid Interface Sci.* **2013,** *18,* 481–492. doi:10.1016/j.cocis.2013.07.005
166. De Rosa, M.; Carteni', M.; Petillo, O.; Calarco, A.; Margarucci, S.; Rosso, F.; De Rosa, A.; Farina, E.; Grippo, P.; Peluso, G. *J. Cell. Physiol.* **2004,** *198,* 133–143. doi:10.1002/jcp.10397
167. Widhe, M.; Bysell, H.; Nystedt, S.; Schenning, I.; Malmsten, M.; Johansson, J.; Rising, A.; Hedhammar, M. *Biomaterials* **2010,** *31,* 9575–9585. doi:10.1016/j.biomaterials.2010.08.061
168. Kramer, J. P. M.; Aigner, T. B.; Petzold, J.; Roshanbinfar, K.; Scheibel, T.; Engel, F. B. *Sci. Rep.* **2020,** *10,* 8789. doi:10.1038/s41598-020-65786-4
169. Schacht, K.; Vogt, J.; Scheibel, T. *ACS Biomater. Sci. Eng.* **2016,** *2,* 517–525. doi:10.1021/acsbiomaterials.5b00483
170. Tasiopoulos, C. P.; Gustafsson, L.; van der Wijngaart, W.; Hedhammar, M. *ACS Biomater. Sci. Eng.* **2021,** *7,* 3332–3339. doi:10.1021/acsbiomaterials.1c00612
171. Schacht, K.; Scheibel, T. *Biomacromolecules* **2011,** *12,* 2488–2495. doi:10.1021/bm200154k
172. DeSimone, E.; Schacht, K.; Pellert, A.; Scheibel, T. *Biofabrication* **2017,** *9,* 044104. doi:10.1088/1758-5090/aa90db
173. Neubauer, V. J.; Trossmann, V. T.; Jacobi, S.; Döbl, A.; Scheibel, T. *Angew. Chem., Int. Ed.* **2021,** *60,* 11847–11851. doi:10.1002/anie.202103147
174. Schacht, K.; Jüngst, T.; Schweinlin, M.; Ewald, A.; Groll, J.; Scheibel, T. *Angew. Chem., Int. Ed.* **2015,** *54,* 2816–2820. doi:10.1002/anie.201409846
175. Steiner, D.; Winkler, S.; Heltmann-Meyer, S.; Trossmann, V. T.; Fey, T.; Scheibel, T.; Horch, R. E.; Arkudas, A. *Biofabrication* **2021,** *13,* 045003. doi:10.1088/1758-5090/ac0d9b
176. Shalaly, N. D.; Ria, M.; Johansson, U.; Åvall, K.; Berggren, P.-O.; Hedhammar, M. *Biomaterials* **2016,** *90,* 50–61. doi:10.1016/j.biomaterials.2016.03.006
177. Szymkowiak, P.; Tsiareshyna, M.; Koczura, R. *Biologia (Cham, Switz.)* **2020,** *75,* 1679–1683. doi:10.2478/s11756-020-00426-w
178. Alicea-Serrano, A. M.; Bender, K.; Jurestovsky, D. *J. Arachnol.* **2020,** *48,* 84–89. doi:10.1636/0161-8202-48.1.84
179. Harris, T. I.; Gaztambide, D. A.; Day, B. A.; Brock, C. L.; Ruben, A. L.; Jones, J. A.; Lewis, R. V. *Biomacromolecules* **2016,** *17,* 3761–3772. doi:10.1021/acs.biomac.6b01267
180. Gomes, S. C.; Leonor, I. B.; Mano, J. F.; Reis, R. L.; Kaplan, D. L. *Biomaterials* **2011,** *32,* 4255–4266. doi:10.1016/j.biomaterials.2011.02.040
181. Liu, F. Y. C. *bioRxiv* **2021**. doi:10.1101/2021.03.26.437269

182.Nilebäck, L.; Chouhan, D.; Jansson, R.; Widhe, M.; Mandal, B. B.; Hedhammar, M. *ACS Appl. Mater. Interfaces* **2017,** *9,* 31634–31644. doi:10.1021/acsami.7b10874
183.Chouhan, D.; Thatikonda, N.; Nilebäck, L.; Widhe, M.; Hedhammar, M.; Mandal, B. B. *ACS Appl. Mater. Interfaces* **2018,** *10,* 23560–23572. doi:10.1021/acsami.8b05853
184.Huang, T.; Kumari, S.; Herold, H.; Bargel, H.; Aigner, T. B.; Heath, D. E.; O'Brien-Simpson, N. M.; O'Connor, A. J.; Scheibel, T. *Int. J. Nanomed.* **2020,** *15,* 4275–4288. doi:10.2147/ijn.s255833
185.Brennan, S. A.; Ní Fhoghlú, C.; Devitt, B. M.; O'Mahony, F. J.; Brabazon, D.; Walsh, A. *Bone Jt. J.* **2015,** *97-B,* 582–589. doi:10.1302/0301-620x.97b5.33336
186.Li, Y.; Lin, Z.; Zhao, M.; Xu, T.; Wang, C.; Hua, L.; Wang, H.; Xia, H.; Zhu, B. *ACS Appl. Mater. Interfaces* **2016,** *8,* 24385–24393. doi:10.1021/acsami.6b06613
187.Seong, M.; Lee, D. G. *Curr. Microbiol.* **2017,** *74,* 661–670. doi:10.1007/s00284-017-1235-9
188.Khalandi, B.; Asadi, N.; Milani, M.; Davaran, S.; Abadi, A. J. N.; Abasi, E.; Akbarzadeh, A. *Drug Res. (Stuttgart, Ger.)* **2017,** *67,* 70–76. doi:10.1055/s-0042-113383
189.Yu, D.; Kang, G.; Tian, W.; Lin, L.; Wang, W. *Appl. Surf. Sci.* **2015,** *357,* 1157–1162. doi:10.1016/j.apsusc.2015.09.074
190.Tang, B.; Li, J.; Hou, X.; Afrin, T.; Sun, L.; Wang, X. *Ind. Eng. Chem. Res.* **2013,** *52,* 4556–4563. doi:10.1021/ie3033872
191.Tang, B.; Sun, L.; Kaur, J.; Yu, Y.; Wang, X. *Dyes Pigm.* **2014,** *103,* 183–190. doi:10.1016/j.dyepig.2013.12.008
192.Nadiger, V. G.; Shukla, S. R. *J. Text. Inst.* **2016,** *107,* 1543–1553. doi:10.1080/00405000.2015.1129756
193.Doakhan, S.; Montazer, M.; Rashidi, A.; Moniri, R.; Moghadam, M. B. *Carbohydr. Polym.* **2013,** *94,* 737–748. doi:10.1016/j.carbpol.2013.01.023
194.He, H.; Cai, R.; Wang, Y.; Tao, G.; Guo, P.; Zuo, H.; Chen, L.; Liu, X.; Zhao, P.; Xia, Q. *Int. J. Biol. Macromol.* **2017,** *104,* 457–464. doi:10.1016/j.ijbiomac.2017.06.009
195.Tao, G.; Cai, R.; Wang, Y.; Liu, L.; Zuo, H.; Zhao, P.; Umar, A.; Mao, C.; Xia, Q.; He, H. *Mater. Des.* **2019,** *180,* 107940. doi:10.1016/j.matdes.2019.107940
196.Currie, H. A.; Deschaume, O.; Naik, R. R.; Perry, C. C.; Kaplan, D. L. *Adv. Funct. Mater.* **2011,** *21,* 2889–2895. doi:10.1002/adfm.201100249
197.Khalid, A.; Bai, D.; Abraham, A. N.; Jadhav, A.; Linklater, D.; Matusica, A.; Nguyen, D.; Murdoch, B. J.; Zakhartchouk, N.; Dekiwadia, C.; Reineck, P.; Simpson, D.; Vidanapathirana, A. K.; Houshyar, S.; Bursill, C. A.; Ivanova, E. P.; Gibson, B. C. *ACS Appl. Mater. Interfaces* **2020,** *12,* 48408–48419. doi:10.1021/acsami.0c15612
198.Kumari, S.; Bargel, H.; Scheibel, T. *Macromol. Rapid Commun.* **2020,** *41,* 1900426. doi:10.1002/marc.201900426
199.Harvey, D.; Bardelang, P.; Goodacre, S. L.; Cockayne, A.; Thomas, N. R. *Adv. Mater. (Weinheim, Ger.)* **2017,** *29,* 1604245. doi:10.1002/adma.201604245
200.Seijsing, F.; Nilebäck, L.; Öhman, O.; Pasupuleti, R.; Ståhl, C.; Seijsing, J.; Hedhammar, M. *MicrobiologyOpen* **2020,** *9,* e993. doi:10.1002/mbo3.993
201.Zeplin, P. H.; Berninger, A.-K.; Maksimovikj, N. C.; van Gelder, P.; Scheibel, T.; Walles, H. *Handchir., Mikrochir., Plast. Chir.* **2014,** *46,* 336–341. doi:10.1055/s-0034-1395558
202.Zeplin, P. H.; Maksimovikj, N. C.; Jordan, M. C.; Nickel, J.; Lang, G.; Leimer, A. H.; Römer, L.; Scheibel, T. *Adv. Funct. Mater.* **2014,** *24,* 2658–2666. doi:10.1002/adfm.201302813
203.Sommer, C.; Bargel, H.; Raßmann, N.; Scheibel, T. *MRS Commun.* **2021,** *11,* 356–362. doi:10.1557/s43579-021-00034-y
204.Zhang, Y.; Zhou, Z.; Sun, L.; Liu, Z.; Xia, X.; Tao, T. H. *Adv. Mater. (Weinheim, Ger.)* **2018,** *30,* 1805722. doi:10.1002/adma.201805722
205.Weiss, A. C. G.; Herold, H. M.; Lentz, S.; Faria, M.; Besford, Q. A.; Ang, C.-S.; Caruso, F.; Scheibel, T. *ACS Appl. Mater. Interfaces* **2020,** *12,* 24635–24643. doi:10.1021/acsami.0c06344
206.Mulinti, P.; Diekjürgen, D.; Kurtzeborn, K.; Balasubramanian, N.; Stafslien, S. J.; Grainger, D. W.; Brooks, A. E. *Bioengineering* **2022,** *9,* 46. doi:10.3390/bioengineering9020046
207.Zha, R. H.; Delparastan, P.; Fink, T. D.; Bauer, J.; Scheibel, T.; Messersmith, P. B. *Biomater. Sci.* **2019,** *7,* 683–695. doi:10.1039/c8bm01186a

License and Terms

Danksagung

Da die Fertigstellung einer Doktorarbeit ein langer und oftmals beschwerlicher Weg ist, möchte ich mich an dieser Stelle bei allen bedanken, die mich während meiner Promotion begleitet und stets unterstützt haben.

Mein erster und besonderer Dank gilt meinem Doktorvater Prof. Dr. Thomas Scheibel. Unter seiner Betreuung konnte ich ein spannendes und vielseitiges Thema bearbeiten. Ich hatte stets die Freiheiten meine eigenen Ideen einbringen und verfolgen zu dürfen. Dabei konnte ich mich immer auf seine Unterstützung und hilfreichen Ratschläge verlassen. Das entgegengebrachte Vertrauen ermöglichte es mir zudem, eine einzigartige wissenschaftliche und persönliche Entwicklung durchleben zu dürfen. Bei dieser Gelegenheit möchte ich mich vor allem für die Möglichkeiten zur Teilnahme am Elitestudienprogramm „Macromolecular Science“, die Mitarbeit im TRR225 und für den Auslandsaufenthalt in Australien bedanken.

In diesem Zusammenhang möchte ich mich bei meinen Kooperationspartnern um Prof. Dr. Felix Engel und Tilman Esser (Erlangen), Prof. Dr. Raymund Horch, Dr. Dominik Steiner und Stefanie Heltmann-Meyer (Erlangen), Prof. Dr. Harald Wajant und Hanna Amouei (Würzburg) sowie Markus Rottmar und Anne-Sophie Mertgen (St. Gallen) bedanken. Durch gemeinsame Projekte sind einige Teilarbeiten dieser Dissertation entstanden.

Bei dieser Gelegenheit möchte ich allen weiteren Ko-Autoren und Ko-Autorinnen der hier gezeigten Teilarbeiten danken. Mein besonderer Dank geht dabei an Dr. Sarah Lentz, Dr. Annika Lechner, Dr. Vanessa Neubauer, Dr. Sushma Kumari, Dr. Gregor Lang, Dr. Hendrik Bargel, PD Dr. Martin Humenik durch deren Hilfe viele Projekte und Publikationen zu einem erfolgreichen Abschluss gekommen sind.

Ich möchte mich auch bei Dr. Tamara Aigner und Anika Winkler für die Transmissionselektronenmikroskopie-Aufnahmen, bei Dr. Hendrik Bargel, Dr. Sarah Lentz, Dr. Annika Lechner, Claudia Stemmann und Tim Schiller für die Rasterelektronen-mikroskopie-Aufnahmen sowie Dr. Sarah Lentz für die Rasterkraftmikroskopie-Aufnahmen bedanken. Weiterhin möchte ich mich auch bei allen Studierenden bedanken, die eine Forschungsarbeit bei mir absolviert und mich bei meinen Projekten unterstützt haben.

Ich bin außerdem für die immense Unterstützung unserer TAs, Johannes Diehl, Andreas Schmidt, Alexandra Pellert, Claudia Stemmann, Nicole Pittel und Eva Möller, sowie Heike Haase dankbar. Der Laboralltag wäre ohne euch nicht so einfach und produktiv gewesen.

Weiterhin möchte ich den Sekretärinnen Sabrina Schwägerl, Andrea Bodner und Christa Vogel meinen Dank aussprechen. Ich konnte mit jedem noch so kleinen organisatorischen Problem zu euch kommen.

Ein besonderer Dank gilt auch unseren akademischen Räten Dr. Melanie Scheibel, PD Dr. Martin Humenik und Dr. Hendrik Bargel. Ihre offenen Ohren für meine Probleme sowie die kritischen Diskussionen und hilfreichen Ratschläge haben mir während der Promotion sehr weiter geholfen.

Die Promotion am Lehrstuhl Biomaterialien ermöglichte mir außerdem viele interessante Menschen kennenlernen zu dürfen. Ich bedanke mich daher beim gesamten „Fiberlab“ für eine unvergessliche Zeit, eine tolle Atmosphäre und anregende Gespräche. Ich habe mich in diesem vielfältigen Team jederzeit willkommen und gut aufgehoben gefühlt.

Elena Doblhofer, Adrian Golser und Martin Neuenfeldt haben mich damals in ihrem Büro aufgenommen und mir den Beginn der Promotion sehr angenehm gemacht.

Mein besonderer Dank gilt jedoch dem „Jungle Office & Friends“. Annika Lechner, Sarah Lentz, Vanessa Neubauer, Anika Winkler und Merisa Saric sind nicht nur Arbeitskollegen, sondern zu wahren Freunden geworden. Unsere Freundschaft reicht über unsere gemeinsame Zeit am Lehrstuhl Biomaterialien hinaus. Der riesige Zusammenhalt, das gegenseitige Verständnis und eure Unterstützung werden mir immer in Erinnerung bleiben, Ich bin mir sicher, dass unsere gemeinsamen Erlebnisse uns oft mit Freude an die Zeit in der „BioMat“ zurückdenken lassen.

Dennoch möchte ich mich auch bei Tim Schiller, Christina Heinritz, Xuen Ng, Kathrin Döhla, Kai Mayer und Kathrin Neuber bedanken, die mir den Abschied vom „Jungle Office & Friends“ erleichtert haben und jederzeit ein offenes Ohr für meine Probleme hatten.

Zuletzt möchte ich mich aus vollem Herzen und mit großer Liebe bei meiner Familie bedanken, die mich in jeder Lebenslage liebevoll unterstützt hat. Ich bin unendlich dankbar, dass ich euch in meinem Leben habe. Ohne eure Unterstützung hätte ich das alles nicht so geschafft. Ihr seid wie Felsen in der Brandung und gebt mir zu jeder Zeit die nötige Kraft. Meine Eltern Gudrun und Norbert haben mich seit jeher unterstützt und mir ermöglicht, meinen Weg zu gehen. Auch mein Bruder Philipp und seine Freundin Christina waren jederzeit eine große Stütze und wichtige Ansprechpartner. Unsere Familienhündin Schaggi hatte immer eine beruhigende und stärkende Wirkung auf mich. Meinem Freund Tim gilt ein besonderer Dank. Er war in dieser anstrengenden Phase für mich da und hat mich stets aufgefangen sowie den Rücken gestärkt. Ich danke dir für deine ruhige, verständnisvolle Art und liebevolle Unterstützung.

Eidesstattliche Versicherungen und Erklärungen

(§ 9 Satz 2 Nr. 3 PromO BayNAT)

Hiermit versichere ich eidesstattlich, dass ich die Arbeit selbstständig verfasst und keine anderen als die von mir angegebenen Quellen und Hilfsmittel benutzt habe (vgl. Art. 64 Abs. 1 Satz 6 BayHSchG).

(§ 9 Satz 2 Nr. 3 PromO BayNAT)

Hiermit erkläre ich, dass ich die Dissertation nicht bereits zur Erlangung eines akademischen Grades eingereicht habe und dass ich nicht bereits diese oder eine gleichartige Doktorprüfung endgültig nicht bestanden habe.

(§ 9 Satz 2 Nr. 4 PromO BayNAT)

Hiermit erkläre ich, dass ich Hilfe von gewerblichen Promotionsberatern bzw. -vermittlern oder ähnlichen Dienstleistern weder bisher in Anspruch genommen habe noch künftig in Anspruch nehmen werde.

(§ 9 Satz 2 Nr. 7 PromO BayNAT)

Hiermit erkläre ich mein Einverständnis, dass die elektronische Fassung meiner Dissertation unter Wahrung meiner Urheberrechte und des Datenschutzes einer gesonderten Überprüfung unterzogen werden kann.

(§ 9 Satz 2 Nr. 8 PromO BayNAT)

Hiermit erkläre ich mein Einverständnis, dass bei Verdacht wissenschaftlichen Fehlverhaltens Ermittlungen durch universitätsinterne Organe der wissenschaftlichen Selbstkontrolle stattfinden können.

Bayreuth, den …… ……

Vanessa Tanja Trossmann